

VOLUME 16 NO. 2 1996

ISSN: 0955-2219

JOURNAL OF THE EUROPEAN CERAMIC SOCIETY

Special Issue

Mullite '94

E CERS

19990115 045

ELSEVIER

JOURNAL OF THE EUROPEAN CERAMIC SOCIETY

The *Journal of the European Ceramic Society* publishes the results of original research relating to the structure, properties and processing of ceramic materials. Papers of either an experimental or theoretical character will be welcomed on a fully international basis. Papers may cover any of the branches of ceramic science and technology and may relate to any of the so called categories, structural, functional and traditional ceramics. The central objective will be to sustain a high standard of research quality by means of appropriate reviewing procedures.

Editorial Board

R. J. Brook

Editor
University of Oxford,
Department of Materials,
Parks Road, Oxford OX1 3PH, UK

G. N. Babini

President ECerS
CNR-IRTEC,
Via Granarolo 64, 48018 Faenza, Italy

J. L. Baptista

Universidade de Aveiro,
Departamento de Engenharia
Ceramica e do Vidro,
P-3800 Aveiro, Portugal

P. Boch

ESPCI, 10 Rue Vauquelin,
F-75231 Paris Cedex, France

A. J. Burggraaf

University of Twente,
Laboratory of Inorganic Chemistry,
Materials Science and Catalysis,
PO Box 217, NL-7500 AE Enschede,
The Netherlands

F. Cambier

CRIBC, 4 Avenue Gouverneur Cornez,
B-7000 Mons, Belgium

M. A. Delgado Mendez

Immediate Past President ECerS
CSIC,
Sociedad Espanola de Ceramica y Vidrio,
Carretera Valencia, km. 24, 300,
E-28500 Arganda del Rey (Madrid), Spain

J. L. Holm

NTH,
University of Trondheim,
Institute of Inorganic Chemistry,
N-7034 NTH Trondheim, Norway

J. R. Jurado-Egea

Instituto de Ceramica y Vidrio,
CSIC, Ctra. Valencia, km. 24,300,
28500 Arganda del Rey, Madrid, Spain

R. N. Katz

North American Co-ordinator
Department of Mechanical Engineering,
Worcester Polytechnic Institute,
100 Institute Road, Worcester,
Massachusetts 01609-2280, USA

D. Kolar

Institute Jozef Stefan,
Jamova 39, YU-61111 Ljubljana,
Slovenia

R. Pampuch

Department of Advanced Ceramics,
AGH, Cracow,
al. Mickiewicza 30, Poland

G. C. Pellacani

c/o Universita' di Modena,
Via Campi 183, 41100 Modena, Italy

R. Pompe

Swedish Ceramic Institute,
S-402 29 Göteborg, Sweden

P. Popper

22 Pembroke Drive,
Newcastle under Lyme,
Staffordshire ST5 2JN, UK

S. Sōmiya

Japanese Co-ordinator
Nishi Tokyo University,
3-7-19, Seijo,
Setagaya, Tokyo 157, Japan

D. Taylor

Fairey Tecramics Ltd,
Mount Industrial Estate, Filleybrooks,
Stone, Staffs ST15 0PU, UK

G. de With

Philips Research Laboratories,
WA-1-2-42, Prof Holstlaan 4,
5656 AA Eindhoven, The Netherlands

G. Ziegler

Universität Bayreuth,
Institut für Materialwissenschaft (IMA),
Lehrstuhl Keramik und Verbundwerkstoffe,
Postfach 3008, D-8580 Bayreuth,
Germany

SUBSCRIPTIONS

1996—One volume, 12 issues per volume (Volume 16). Annual Institutional Subscription Rates 1996: £625.00/US\$994.00. **Members of the European Ceramic Society can subscribe to the journal at the special rate of £110.00/US\$175.00.** Subscription prices exclude VAT. Non-VAT registered customers in the European Community will be charged the appropriate VAT in addition to the price listed. Prices include postage and insurance and are subject to change without notice. All journals are distributed worldwide by air-speeded delivery at no extra cost to the subscriber. US Mailing Agent: USA Postmaster: Second Class postage paid at Newark, New Jersey and additional entry points. The *Journal of the European Ceramic Society* (ISSN 0955-2219) is published monthly, January to December in one volume, by Elsevier Science Ltd, The Boulevard, Langford Lane, Kidlington, Oxford OX5 1GB, UK. The annual subscription in the USA is \$994. The *Journal of the European Ceramic Society* is distributed by Virgin Mailing and Distribution, 10 Camptown Road, Irvington, New Jersey 07111-1105. POSTMASTER: Please send address corrections to *Journal of the European Ceramic Society*, c/o Elsevier Science Inc., 660 White Plains Road, Tarrytown, NY 10591-5153. Subscription orders should be addressed to:

THE OXFORD FULFILMENT CENTRE
PO Box 800, Kidlington, Oxford, OX5 1DX, England

In the United States and Canada: For further information contact:

Elsevier Science Inc., 660 White Plains Road,
Tarrytown, NY 10591-5153, USA

DISTRIBUTION STATEMENT 1

Approved for public release
Distribution Unlimited

1. AGENCY USE ONLY (Leave blank)	2. REPORT DATE	3. REPORT TYPE AND DATES COVERED	
	1994	Conference Proceedings	
4. TITLE AND SUBTITLE		5. FUNDING NUMBERS	
Mullite and Mullite Ceramics		F6170894W0696	
6. AUTHOR(S)			
Conference Committee			
7. PERFORMING ORGANIZATION NAME(S) AND ADDRESS(ES)		8. PERFORMING ORGANIZATION REPORT NUMBER	
Institut fur Werkstoff-Forschung des DLR Porz-Wahnheide, Linder Hohe Koln 51147 Germany		N/A	
9. SPONSORING/MONITORING AGENCY NAME(S) AND ADDRESS(ES)		10. SPONSORING/MONITORING AGENCY REPORT NUMBER	
EOARD PSC 802 BOX 14 FPO 09499-0200		CSP 94-1021	
11. SUPPLEMENTARY NOTES			
2 Volumes - Journal of the European Ceramic Society and International Workshop Abstracts			
12a. DISTRIBUTION/AVAILABILITY STATEMENT		12b. DISTRIBUTION CODE	
Approved for public release; distribution is unlimited.		A	
13. ABSTRACT (Maximum 200 words)			
The Final Proceedings for Mullite and Mullite Ceramics, 7 September 1994 - 9 September 1994			
14. SUBJECT TERMS		15. NUMBER OF PAGES	
EOARD		420 (Estimated)	
		16. PRICE CODE	
		N/A	
17. SECURITY CLASSIFICATION OF REPORT	18. SECURITY CLASSIFICATION OF THIS PAGE	19. SECURITY CLASSIFICATION OF ABSTRACT	20. LIMITATION OF ABSTRACT
UNCLASSIFIED	UNCLASSIFIED	UNCLASSIFIED	UL

NSN 7540-01-280-5500

Standard Form 298 (Rev. 2-89)
Prescribed by ANSI Std. Z39-18
298-102

JOURNAL OF THE EUROPEAN CERAMIC SOCIETY

VOL. 16 1996

Special Issue
Mullite '94
Irsee, Germany
7-9 September 1994

ELSEVIER

DO NOT QUALITY CONTROLLED

Preceding Pages Blank

AQF99-04-0645

Copyright © 1996 Elsevier Science Ltd

It is a condition of publication that manuscripts submitted to this Journal have not been published and will not be simultaneously submitted or published elsewhere. By submitting a manuscript, the authors agree that the copyright for their article is transferred to the Publisher if and when the article is accepted for publication. However, assignment of copyright is not required from authors who work for organizations which do not permit such assignment. The copyright covers the exclusive rights to reproduce and distribute the article, including reprints, photographic reproductions, microform or any other reproductions of similar nature, and translations. No part of this publication may be reproduced, stored in a retrieval system or transmitted in any form or by any means, electronic, electrostatic, magnetic tape, mechanical, photocopying, recording or otherwise, without permission in writing from the copyright holder.

Photocopying information for users in the USA. The Item-fee Code for this publication indicates that authorization to photocopy items for internal or personal use is granted by the copyright holder for libraries and other users registered with the Copyright Clearance Center (CCC) Transactional Reporting Service provided the stated fee for copying, beyond that permitted by Section 107 or 108 of the United States Copyright Law, is paid. The appropriate remittance of \$15.00 per copy per article is paid directly to the Copyright Clearance Center Inc., 222 Rosewood Drive, Danvers, MA 01923, USA.

Permission for other use. The copyright owner's consent does not extend to copying for general distribution, for promotion, for creating new works, or for resale. Specific written permission must be obtained from the Publisher for such copying.

Disclaimer. Whilst every effort is made by the Publisher and Editorial Board to see that no inaccurate or misleading data, opinion or statement appear in this Journal, they wish to make it clear that the data and opinions appearing in the articles and advertisements herein are the sole responsibility of the contributor or advertiser concerned. Accordingly, the Publisher, the Editorial Board and Editors and their respective employees, officers and agents accept no responsibility or liability whatsoever for the consequences of any such inaccurate or misleading data, opinion or statement.

Back Issues: Back issues of all previously published volumes are available direct from Elsevier Science Offices (Oxford and New York). Complete volumes and single issues can be purchased for 1991-1995. Earlier issues are available in high quality photo-duplicated copies as complete volumes only. Back volumes on microfilm are available from UMI, 300 North Zeeb Road, Ann Arbor, MI 48106, USA.

The Item-fee Code for this publication is: 0955-2219/96 \$15.00+0.00

Printed in Great Britain by Galliard (Printers) Ltd, Great Yarmouth

Contents

Volume 16 Number 2

Special Issue: Mullite '94

99 Foreword

101 Importance of Starting Materials on Reactions and Phase Equilibria in the Al_2O_3 – SiO_2 System
J. A. PASK (USA)

109 Formation of Aluminium Rich 9:1 Mullite and its Transformation to Low Alumina Mullite upon Heating
R. X. FISCHER, H. SCHNEIDER & D. VOLL (Germany)

115 The Formation of Mullite from Kaolinite under Various Reaction Atmospheres
K. J. D. MACKENZIE, R. H. MEINHOLD, I. W. M. BROWN & G. V. WHITE (New Zealand)

121 Mullitization and Densification of $(3\text{Al}_2\text{O}_3 + 2\text{SiO}_2)$ Powder Compacts by Microwave Sintering
P. PILUSO, L. GAILLARD, N. LEQUEUX & P. BOCH (France)

127 Characterization of Low Temperature Mullitization
T. BAN, S. HAYASHI, A. YASUMORI & K. OKADA (Japan)

133 Anisotropic Grain Growth in Seeded and B_2O_3 -doped Diphasic Mullite Gels
S.-H. HONG, W. CERMIGNANI & G. L. MESSING (USA)

143 Single-phase and Diphasic Aerogels and Xerogels of Mullite: Preparation and Characterization
S. KOMARNENI & C. RUTISER (USA)

149 Effect of Aging Temperature on the Structure of Mullite Precursor Prepared from Tetraethoxysilane and Aluminum Nitrate in Ethanol Solution
K. OKADA, C. AOKI, T. BAN, S. HAYASHI & A. YASUMORI (Japan)

155 New Aqueous Mullite Precursor Synthesis. Structural Study by ^{27}Al and ^{29}Si NMR Spectroscopy
I. JAYMES & A. DOUY (France)

161 Germanium Mullite: Structure and Vibrational Spectra of Gels, Glasses and Ceramics
D. MICHEL, Ph. COLOMBAN, S. ABOLHASSANI, F. VOYRON & A. KAHN-HARARI (France)

169 Infra-red Spectroscopic Investigation in the Mullite Field of Composition: $\text{Al}_2(\text{Al}_{2+2x}\text{Si}_{2-2x})\text{O}_{10-x}$ with $0.55 > x > 0.25$
C. H. RÜSCHER, G. SCHRADER & M. GÖTTE (Germany)

177 Interpretation of Mullite Real Structure via Inter-Vacancy Correlation Vectors
S. H. RAHMAN, S. STROTHENK, C. PAULMANN & U. FEUSTEL (Germany)

187 Local Structural Information of Mullite Obtained from Diffuse X-ray Scattering
T. R. WELBERRY & B. D. BUTLER (Australia)

195 Time-Resolved Fluorescence Spectroscopy of Cr^{3+} in Mullite
B. PIRIOU (France), H. RAGER & H. SCHNEIDER (Germany)

203 EXAFS Studies of Cr-doped Mullite
K. R. BAUCHSPIEß (Australia), H. SCHNEIDER (Germany) & A. KULIKOV (Russia)

211 Electron Paramagnetic Resonance and Optical Absorption Studies on Cr-doped Mullite Precursors
H. SCHNEIDER (Germany), K. IKEDA (Japan), B. SARUHAN & H. RAGER (Germany)

217 Mechanical Properties of Mullite Materials
M. I. OSENDI & C. BAUDÍN (Spain)

225 Mechanical Properties of High Purity Mullite at Elevated Temperatures
H. OHIRA, M. G. M. U. ISMAIL, Y. YAMAMOTO, T. AKIBA & S. SŌMIYA (Japan)

231 Microstructure and Mechanical Properties of Mullite/Zirconia Composites Prepared from Alumina and Zircon under Various Firing Conditions
T. KOYAMA, S. HAYASHI, A. YASUMORI, K. OKADA (Japan), M. SCHMUCKER & H. SCHNEIDER (Germany)

239 Phase Transformation and Grain Coarsening of Zirconia/Mullite Composites
W.-C. J. WEI, H. C. KAO & M. H. LO (Republic of China)

249 Mullite-Aluminosilicate Glassy Matrix Substrates Obtained by Reactive Coating
J. REQUENA, J. F. BARTOLOMÉ, J. S. MOYA, S. DE AZA, F. GUITIAN (Spain) & G. THOMAS (USA)

255 Fabrication of Low-to-Zero Shrinkage Reaction-Bonded Mullite Composites
D. HOLZ, S. PAGEL (Germany), C. BOWEN (UK), S. WU (USA) & N. CLAUSSEN (Germany)

261 Processing of Mullite-based Long-fibre Composites via Slurry Routes and by Oxidation of an Al–Si Alloy Powder
J. BRANDT & R. LUNDBERG (Sweden)

269 Preliminary Results on a Novel Fabrication Route for α -Al₂O₃ Single Crystal Monofilament-reinforced Reaction-bonded Mullite (RBM)
B. SARUHAN, W. LUXEM & H. SCHNEIDER (Germany)

275 Effects of Composition and Atmosphere on Reactive Metal Penetration of Aluminium in Mullite
E. SAIZ, A. P. TOMSIA, R. E. LOEHMAN & K. EWSUK (USA)

281 High Temperature Behaviour of Polycrystalline Aluminosilicate Fibres with Mullite Bulk Composition. I. Microstructure and Strength Properties
M. SCHMÜCKER, F. FLUCHT & H. SCHNEIDER (Germany)

287 High Temperature Behaviour of Polycrystalline Aluminosilicate Fibres with Mullite Bulk Composition. II. Kinetics of Mullite Formation
B. O. HILDMANN, H. SCHNEIDER & M. SCHMÜCKER (Germany)

293 Processing, Structure, and Properties of Mullite Fiber/Mullite Matrix Composites
K. K. CHAWLA, Z. R. XU & J.-S. HA (USA)

301 Sol-gel Mullite Matrix-SiC and -Mullite 2D Woven Fabric Composites with or without Zirconia Containing Interphase: Elaboration and Properties
Ph. COLOMBAN, E. BRUNETON, J. L. LAGRANGE & E. MOUCHON (France)

315 Processing and Mechanical Properties of Laminated Composites of Mullite/Woven Fabrics of Si–Ti–C–O Fibers
Y. HIRATA, M. MATSUDA, K. TAKESHIMA, R. YAMASHITA, M. SHIBUYA (Japan), M. SCHMÜCKER & H. SCHNEIDER (Germany)

Foreword

The name of mullite comes from the Island of Mull in Western Scotland, where it was first found in nature. It was in 1924 that Bowen and Greig published their basic work on the occurrence of mullite. Bowen and Greig stated: 'Since this paper was written we have discovered crystals of the 3:2 compound in natural rocks from the Island of Mull. We propose the name mullite to designate the compound in a forthcoming paper of the *Journal of the Washington Academy of Science* where this natural occurrence of the mineral is described.'

Because of its high temperature-low pressure formation conditions, mullite occurs only very rarely in nature. It sometimes is found in high temperature metamorphosed rocks of the sanidine facies and at the contact of alumina-rich sedimentary rocks with basaltic melts (so-called buchites or sillimanite buchites). Mullite formation was also described in hornfelses (porcellanite) which develop on the contact of bauxite with olivine dolerite intrusions.

In spite of its rareness in natural rocks, mullite is perhaps the most important phase in the field of traditional ceramics. This can be explained by its occurrence as a main constituent in pottery, porcelains, sanitary ceramics, and structural clay products such as building bricks, pipes, tiles, and in refractories. Based on the importance of mullite for technical refractory and ceramic products, in 1956 Robert B. Sosman made a rather poetic statement about mullite in comparing a journey to

the Isle of Mull with a pilgrimage. Though our less sentimental generation may have problems seeing things in a similar way, many of us agree with Sosman that mullite is one of the most important ceramic phases.

Beside its value for conventional ceramics, mullite has become a strong candidate material for advanced structural and functional ceramics in recent years. The use of mullite has, e.g. been discussed for high temperature engineering materials, electronic packaging materials, optical materials, porous materials and as a matrix for ceramic composites. The reasons for this development are the outstanding thermo-mechanical properties of mullite:

- Low thermal expansion
- Low thermal conductivity
- Excellent creep resistance
- Good chemical stability
- Oxidation resistance

Congresses and workshops especially dedicated to crystal chemistry, processing, characterization and properties of mullite took place in Tokyo, Japan, in 1987, and in Seattle, USA, in 1990. The international conference in Irsee 1994 was the third to be held on mullite. This workshop brought together basic science researchers with material scientists, and with engineers occupied with the production of technical compounds from all over the world (Fig. 1).

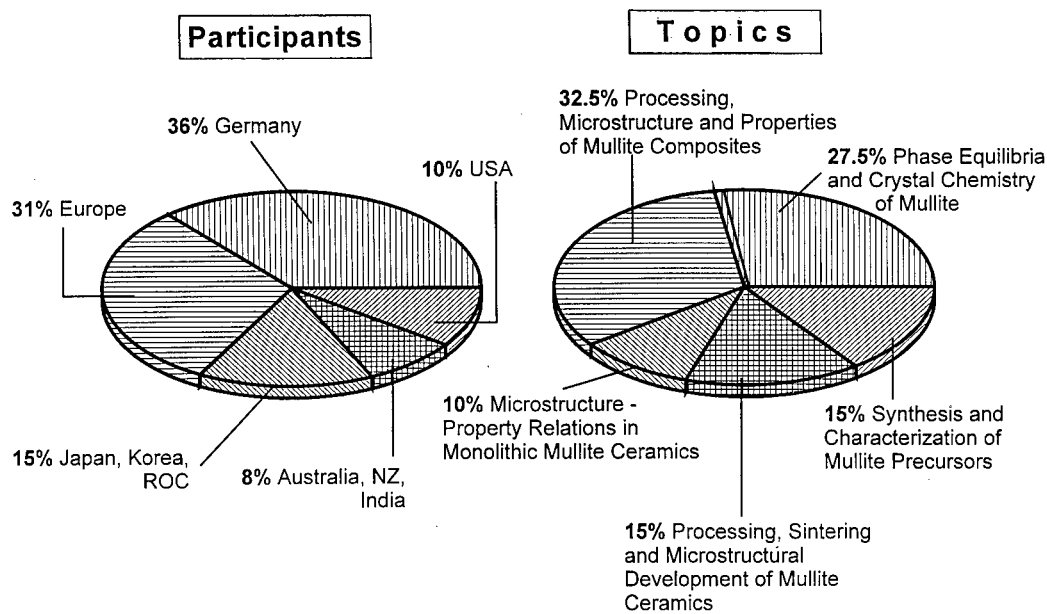


Fig. 1. International Mullite Workshop in Irsee 1994 (Mullite '94). Participants (total number: 52) and topics of scientific sessions.

Topics of the conference were:

- Phase equilibria and crystal chemistry of mullite
- Synthesis and characterization of mullite precursors
- Processing, sintering and microstructural development of mullite ceramics
- Microstructure–property relations in monolithic mullite ceramics
- Processing, microstructure and properties of mullite composites.

The Mullite '94 Workshop provided new, and some most interesting results, which often were discussed late into the night. I believe that most participants will agree that this was a very success-

ful meeting, which was also due to the beautiful environment and the relaxed atmosphere in the old Swabian 'Kloster Irsee'.

On behalf of the participants I gratefully acknowledge the indispensable financial support of the United States Air Force European Office of Aerospace Research and Development (EOARD) and the German Aerospace Research Establishment (DLR). I also thank the staff of the Institute for Materials Research of the DLR, especially Dr B. Saruhan, Mr J. Hermanns and W. Luxem for their help in organizing the meeting.

H. Schneider, German Aerospace Research Establishment (DLR), Institute for Materials Research, 51147 Köln, Germany

Importance of Starting Materials on Reactions and Phase Equilibria in the Al_2O_3 - SiO_2 System

Joseph A. Pask

Department of Materials Science & Mineral Engineering, University of California, Berkeley, CA 94720, USA

(Accepted 22 July 1995)

Abstract

Disagreements in the high Al_2O_3 side of the phase equilibrium diagram for the Al_2O_3 - SiO_2 system have been reported consistently. Some of the disagreements are significantly different and have been reported many times. It is thus necessary to eliminate experimental errors as being primarily responsible. An examination and analysis of the starting materials and the development of a fundamental understanding of the chemical reactions that take place provide an explanation for the reported differences. The objective of this report is to briefly review the disagreements and correlate them with the starting materials and the associated solid-state reactions that occur in reaching stable or metastable equilibrium.

1 Literature Review

A review of a chronological assemblage of selected papers brings out the disagreements. In 1909 Shepherd *et al.*¹ published the first phase equilibrium diagram which indicated that sillimanite ($\text{Al}_2\text{O}_3\text{-SiO}_2$, 62.92 wt% Al_2O_3) was the only binary compound in the Al_2O_3 - SiO_2 system; this compound was subsequently shown to be metastable at standard conditions of temperature and pressure and stable only at high pressures. In 1924, Bowen and Greig^{2,3} published the first phase equilibrium at standard conditions which showed that mullite ($3\text{Al}_2\text{O}_3\text{-}2\text{SiO}_2$, 71.80 wt% Al_2O_3) was the only compound and that it melted incongruently at 1828°C with no solid solution range determined (Fig. 1). In 1950 and 1951, Bauer *et al.*^{4,5} grew a single crystal of mullite containing about 83 wt% Al_2O_3 ($3\text{Al}_2\text{O}_3\text{-SiO}_2$) by the flame fusion process. These experiments raised doubts as to the reported incongruent melting of mullite.

In 1951, Toropov and Galakhov⁶ heated mixtures of alumina gel and quartz; the mullite that formed melted congruently at about 1900°C. In

1954, Shears and Archibald⁷ reported mullite with a solid solution range from $3\text{Al}_2\text{O}_3\text{-}2\text{SiO}_2$ to $2\text{Al}_2\text{O}_3\text{-SiO}_2$ (77.24 wt% Al_2O_3) which melted congruently at approximately 1810°C. In 1960, Welch⁸ supported the proposed solid solution range and incongruent melting. In 1958, Trömel *et al.*⁹ showed some data mostly in support of congruent melting behaviour. However, they also showed data generally indicating that in short time runs no corundum was obtained when it should have been found with incongruent melting, but that increasing the time caused the corundum to appear.

In 1962, Aramaki and Roy¹⁰ showed mullite with a solid solution range of 71.8–74.3 wt% Al_2O_3 and a congruent melting point that was supported by the position of the α - Al_2O_3 liquidus (Fig. 1). They also determined that the solid solution range was extended to 77.3 wt% Al_2O_3 under metastable conditions which is not shown in the figure. They employed samples prepared from dry mixtures of reagent grade α - Al_2O_3 and powdered fused SiO_2 glass. The samples were held at temperature and quenched in mercury or water.

In 1972, Davis and Pask,¹¹ using semi-infinite diffusion couples of sapphire (α - Al_2O_3) and fused SiO_2 at temperatures up to 1750°C, determined the solid solution range of mullite as 71.0–74.0 wt% Al_2O_3 . In 1975, Aksay and Pask¹² extended these experiments to higher temperatures and reported an α - Al_2O_3 liquidus profile (Fig. 2) that was similar to that of Bowen and Greig^{2,3} with a peritectic at ~55 wt% Al_2O_3 which supported mullite as having an incongruent melting point. Single crystals of mullite were grown by the Czochralski technique in 1974 by Guse¹³ and Guse and Mateika¹⁴ of the 2:1 type instead of the 3:1 type obtained by the flame fusion process. In 1980, Shindo¹⁵ also grew single crystals of the 2:1 type by the 'slow cooling float zone method' but showed incongruent melting.

In 1983, Prochazka and Klug¹⁶ showed a solid solution range that shifted to higher Al_2O_3 contents with increase in temperature from 1600°C up

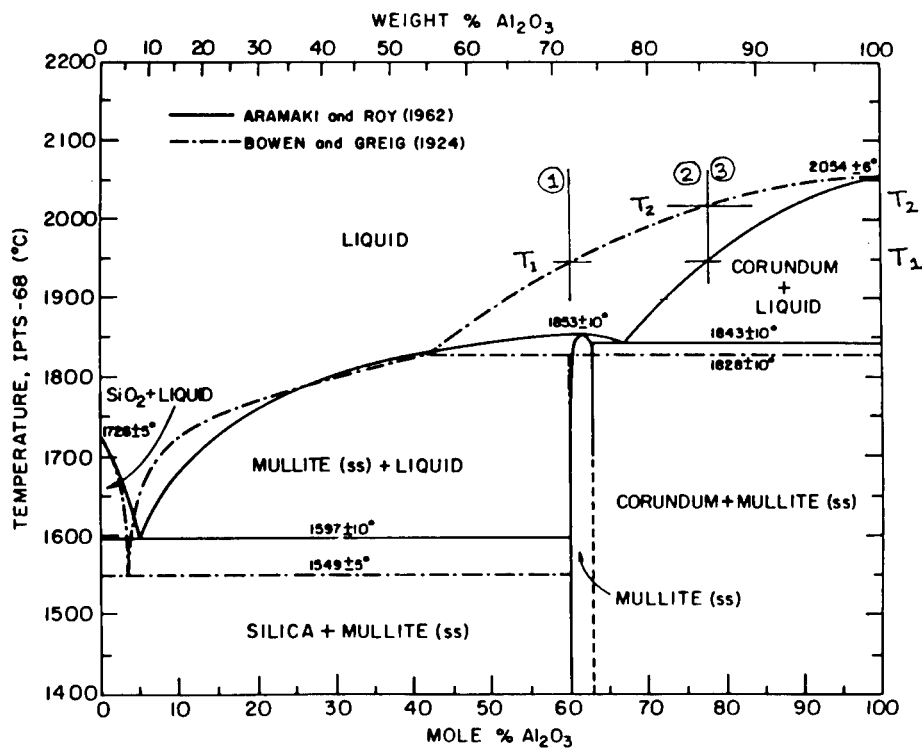


Fig. 1. Superimposed SiO_2 – Al_2O_3 phase equilibrium diagrams as determined by Bowen and Greig^{2,3} and Aramaki and Roy.¹⁰

to about 1890°C, where the mullite reached the 2:1 composition (77.2 wt% Al_2O_3) and melted congruently since the peritectic composition had a slightly higher Al_2O_3 content. In 1987, Klug *et al.*¹⁷ modified the diagram wherein the α - Al_2O_3 liquidus peritectic composition shifted to a slightly lower Al_2O_3 content than 77.2 wt% Al_2O_3 which technically indicated that the mullite melted incongruently. The latter diagram is included in Fig. 2. In both papers, homogeneous aluminosilicate powders produced by sol–gel processing from AlO(OH) and tetraethyl orthosilicate (TEOS) were used.

Many other studies on this system have been published. Sufficient experimental support is available for either opinion. It is thus not necessary to review them in detail. More extensive discussions of the phase equilibria are presented in several other review papers.^{18–21} The diagrams shown in Figs 1 and 2 will suffice for further discussions.

2 Starting Materials

Various starting materials have been used to provide the Al_2O_3 and SiO_2 molecules for a desired composition. In the earlier studies Al_2O_3 was introduced primarily as α - Al_2O_3 powders of controlled particle size. It was mixed with fine ground fused SiO_2 , quartz or cristobalite. A given mixture was normally heated above the liquidus temperature until it formed a homogeneous liquid phase, lowered to and held at the test temperature, and quenched. The homogenization step is critical since α - Al_2O_3 does not react rapidly because of the sluggishness of the liquid due to some covalency and high bond strength of α - Al_2O_3 . On the other hand, if α - Al_2O_3 is melted completely, then nucleation and precipitation also may not occur easily on cooling especially when the aluminosilicate liquid does not become saturated with Al_2O_3 molecules. Kinetic problems then arise.

More recent studies utilized starting materials prepared chemically from alkoxides and sol–gels so that single-phase and diphasic gels were attained, i.e. no Al_2O_3 is introduced as α - Al_2O_3 . Any segre-

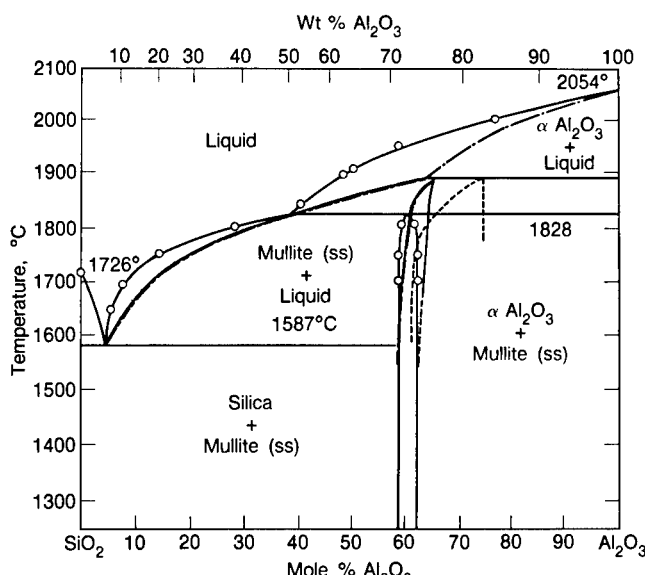


Fig. 2. Phase equilibrium diagrams by Klug *et al.*¹⁷ (dot-dash line) and Aksay and Pask¹² (light solid line) superimposed. Nature of reported solid solution regions for mullite illustrated.

gation or clustering of like atoms in single-phase gels could be critical since they can lead to nucleation and formation of colloidal particles, i.e. diphasic gel mixtures. Single-phase gels have also been called polymeric gels.^{22,23} The basic objective of this approach is to attain or approach homogeneous mixing on an atomic or molecular basis. Sacks *et al.*²⁴ have reviewed the literature on the preparation of starting materials.

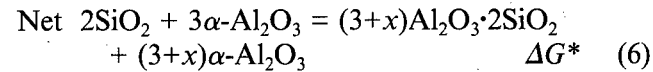
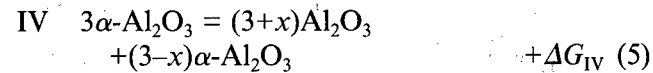
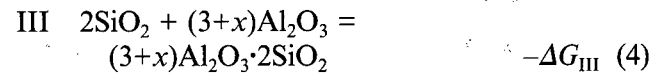
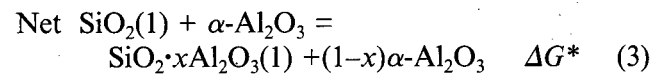
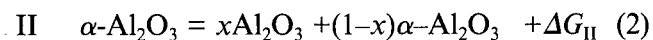
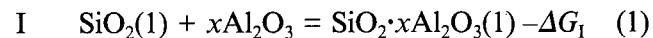
3 Mechanisms of Reactions

The critical factor in determining the nature of the solid-state reactions that occur in reaching equilibrium compositions at elevated temperatures in this system is the presence or absence of α - Al_2O_3 in the starting materials as a source of Al_2O_3 molecules. The α - Al_2O_3 particles react with SiO_2 at their interfaces to form mullite at temperatures below about 1828°C by interdiffusion of the cations through the forming mullite, which is a slow process. This kinetic effect could be counteracted in powder mixtures by reducing the particle size of α - Al_2O_3 and thereby increasing the overall rate by increasing the interfacial area. At temperatures above 1828°C mullite does not form, and α - Al_2O_3 is dissolved in the SiO_2 liquid to form aluminosilicate liquids. The most reactive precursors are those chemically prepared, wherein homogeneous atomic mixtures are formed in the absence of α - Al_2O_3 as a constituent. In this case the reaction rates are considerably faster.

Davis and Pask¹¹ developed the technique of using diffusion couples of sapphire single crystals and fused SiO_2 up to 1750°C to obtain kinetic data on mullite formation as well as equilibrium compositions. Aksay and Pask¹² extended the technique to higher temperatures. Analysis of polished cross-sections at a number of temperatures for Al and Si with an electron microprobe provided data for calculating concentration profiles for Al_2O_3 and SiO_2 and determining equilibrium compositions at the interfaces. It was determined that the reaction rates at the interfaces are faster than the diffusion rates away from them. The composition at a given temperature thus remained constant at a given interface and maintained equilibrium. Below about 1828°C and down to about 1634°C mullite grew at the α - Al_2O_3/SiO_2 interface and the resulting compositions at the liquid/mullite and mullite/ α - Al_2O_3 interfaces were also at equilibrium. The fact that the Al_2O_3 content of about 55 wt% at the peritectic at 1828°C remains constant and is less than that of mullite theoretically indicates incongruent decomposition of mullite in the presence of α - Al_2O_3 .

It is now necessary to determine the nature of the driving forces for the solid-state reactions occurring at the interfaces of the α - Al_2O_3/SiO_2 diffusion couples since they determine the composition of the α - Al_2O_3 liquidus. Experimental temperatures above 1828°C will be considered first. SiO_2 dissolves Al_2O_3 . The driving force is the reduction of the internal free energy of the fused SiO_2 as Al_2O_3 molecules are incorporated into the liquid's atomic structure according to step I (Eqn (1)). The Al_2O_3 molecules are obtained by surface dissociation of crystalline Al_2O_3 by breaking bonds for which energy is required according to step II (Eqn (2)). The required energy is provided by the release of internal free energy by the siliceous liquid as it incorporates Al_2O_3 molecules into its structure. Summation of these step reactions above 1828°C results in the observed net reaction (Eqn (3)).

At experimental temperatures below 1828°C mullite forms at the interface. Energetically it appears more favourable to form mullite than to continue dissolving α - Al_2O_3 , i.e. $\Delta G_{III} > \Delta G_I$ (Eqn (4) > Eqn (1)). ΔG_{III} is greater than ΔG_{IV} (Eqn (5)) which results in the net reaction (Eqn (6)) being negative and the determining occurrence of the reaction. If $\Delta G_{IV} > \Delta G_{III}$, then the net ΔG^* is positive and the reaction will not take place.



With the formation of mullite two interfaces have to be considered: liquid/mullite and mullite/ α - Al_2O_3 . In this case the α - Al_2O_3 atomic structure does not change with temperature but the SiO_2 content of the mullite decreases slightly at temperatures approaching dissociation. The bulk structures and compositions along the interfaces at a given temperature are at equilibrium as represented in Eqns (4), (5) and (6), and provide data for the phase equilibrium diagram.

The relative values for the free energies for the step reactions (1) plus (2) and (4) plus (5) determine the amount of solution and compositions. As the solution proceeds, ΔG_I and ΔG_{III} become

less negative until ΔG^* becomes zero in both cases with the establishment of equilibrium for the test temperature. With continuation of the reaction, when large quantities of the reactants are present, the equilibrium compositions are maintained at the interfaces because the reaction rates are faster than the diffusion rates. In an experimental study, the constancy of the compositions at the interface were verified.^{11,12} It is evident that these reactions do not continue when one of the reactants is consumed.

It should be further evident that at these points the chemical potentials for Al_2O_3 and SiO_2 are equal in the silicate liquid and the mullite but neither phase is necessarily saturated with Al_2O_3 molecules. The limiting factor in these cases is established by the bond strength of the $\alpha\text{-Al}_2\text{O}_3$ atomic structure, which determines the amount of energy necessary to dissociate an Al_2O_3 molecule (Eqns (2) and (5)). Thus, if another source of Al_2O_3 is used whose atomic bond strength is weaker, i.e. ΔG_{II} and ΔG_{IV} are smaller, then the aluminosilicate liquid could dissolve more Al_2O_3 molecules before equilibrium is reached or until the liquid structure itself becomes saturated with Al_2O_3 molecules. In such cases, the liquid is supersaturated relative to $\alpha\text{-Al}_2\text{O}_3$, but it tends to retain the dissolved Al_2O_3 molecules in the absence of saturation and $\alpha\text{-Al}_2\text{O}_3$ nuclei or particles.

In the reported studies, the maximum availability of Al_2O_3 molecules is provided by single-phase sol-gel mixtures wherein essentially atomic homogeneity is present in the absence of any clusters or colloidal assemblages. Compounds can form by rearrangement of atoms and molecules or by short-range diffusion. In the absence of strong $\alpha\text{-Al}_2\text{O}_3$ bonds, more Al_2O_3 molecules can become available for the mullite composition which can vary within the solid solution range with temperature.

The alumina-silica system is subject to significant indications of metastability based on equally verified equilibria experiments. At present, because of lack of adequate thermodynamic data, it is difficult to unequivocally claim that one of the experimentally determined phase equilibria diagrams is stable and others are metastable. It is thus more logical to differentiate them on the basis of the nature of the critical starting materials. In this system that material is alumina. It has been shown that the nature of the most controversial equilibria are dependent on the presence or absence of $\alpha\text{-Al}_2\text{O}_3$ as the starting material for a source of Al_2O_3 molecules. Thus, the diagrams can be differentiated on this basis. The earliest reported diagrams were derived with the use of fine-ground $\alpha\text{-Al}_2\text{O}_3$ or forms of alumina, e.g. $\gamma\text{-Al}_2\text{O}_3$, that

readily converted to $\alpha\text{-Al}_2\text{O}_3$ before they were completely reacted. Silica was added as fine-ground, fused or crystalline SiO_2 . Later diagrams were determined with sol-gel or alkoxide type of starting materials. In these cases the objective was to introduce the Al_2O_3 molecules on the basis of a homogeneous atomic mixture.

In summary, the significance of the types of starting materials used is that the bond strengths of the different types are dependent on their atomic and electronic structures. $\alpha\text{-Al}_2\text{O}_3$ has strong bonds requiring a relatively large amount of energy for release of Al_2O_3 molecules in comparison with the energy requirement for dissociation from a sol-gel type of starting material. Silica has a high degree of covalency which makes restructuring more difficult. Both states lead to difficulties affecting the kinetics of nucleation and precipitation of $\alpha\text{-Al}_2\text{O}_3$. Another factor that leads to slow kinetics is the nature of the structure and bonding of aluminosilicate liquids, which at present are not completely understood.

An illustration of the above discussions can be made by use of Fig. 1. When the $\alpha\text{-Al}_2\text{O}_3/\text{SiO}_2$ diffusion couple is held at 1950°C, the equilibrium liquid composition (about 72 wt% Al_2O_3) at the interface is indicated by pt. 1 which provides a point on the $\alpha\text{-Al}_2\text{O}_3$ liquidus of Bowen and Greig's^{2,3} diagram. Aramaki and Roy,¹⁰ on the other hand, used dried mixtures of reagent-grade activated $\alpha\text{-Al}_2\text{O}_3$ and powdered SiO_2 glass, homogenized them at temperatures above the 'high temperature liquidus' so that all of the $\alpha\text{-Al}_2\text{O}_3$ particles were dissolved to form an aluminosilicate liquid, and lowered the temperature to the test temperature. They found that a composition equivalent to pt. 2 (about 86 wt% Al_2O_3) was in equilibrium with $\alpha\text{-Al}_2\text{O}_3$ at 1950°C.

At this point it is important to consider, on the basis of basic principles, the general behaviour of aluminosilicate liquids with changes in composition and temperature at standard pressures. Mixtures of various condensed phases equivalent to aluminosilicate liquid compositions undergo complete melting on raising the temperature above the liquidus temperatures. The atomic and molecular homogeneity of the liquid, if not present, would be expected to increase with increase in temperature and/or time. With decrease in temperature some clustering would be expected. On dropping below the liquidus with saturation, nuclei formation would be started. Their type and rate of actual formation would be controlled by kinetic factors and their composition. On cooling liquids with more than 55 wt% Al_2O_3 too rapidly, $\alpha\text{-Al}_2\text{O}_3$ nuclei may not form easily because the liquid is not saturated with Al_2O_3 molecules.

Dropping below the melting temperature of mullite, the liquid structure and composition are such that it becomes saturated with mullite which precipitates.

This behaviour can be illustrated by experiments with a series of starting mixtures with an increasing amount of Al_2O_3 from about 55 wt%.²⁵ The mixtures are first homogenized above the liquidus temperature and then cooled rapidly or quenched. Mixtures with increasing amounts of Al_2O_3 up to about 84 wt% do not easily nucleate $\alpha-Al_2O_3$ and mullite is precipitated whose Al_2O_3 content is higher than that of the starting mixture, with which it converges at about 83 wt%. With still higher amounts of Al_2O_3 in the starting mixture, liquid becomes saturated with Al_2O_3 and the first precipitates are spherulites of $\alpha-Al_2O_3$ followed by mullite with a lower Al_2O_3 content. The coprecipitates of mullite have about 77 wt% Al_2O_3 , which corresponds to $2Al_2O_3 \cdot SiO_2$ mullite. These results indicate that at 1950°C the aluminosilicate liquids become saturated with Al_2O_3 at a total content of about 83 wt% Al_2O_3 .

X-ray diffraction analyses of mullites by Kriven and Pask²⁶ showed that mullite with increasing amounts of Al_2O_3 up to about 77 wt% Al_2O_3 saturated the Si sites with Al atoms. Further increase of Al_2O_3 up to about 83 wt% resulted in the formation of a crystallographic superstructure superimposed on the mullite structure. These Al_2O_3 values for mullite supported the Al_2O_3 content of about 83 wt% for the single crystal grown by the flame fusion process,^{4,5} and about 77 wt% for the crystal grown at a constant temperature by the Czochralski technique.^{13,14}

The experimental variations in the Al_2O_3 content of mullite indicate that structures and bond strengths of the mullite are critically dependent on the reaction environment. Competition for Al_2O_3 molecules between the aluminosilicate structures and Al_2O_3 when present as part of the reacting mixture, as pointed out above, determines the composition variabilities that have been reported in the literature. Use of chemically-prepared starting mixtures to give more homogeneous atomic structures also introduces some variability because the atomic structure of the amorphous mixtures are expected to change with increasing temperature and changing conditions. The development of better homogeneity could result in increasing availability of Al_2O_3 molecules from the liquid structure. This behaviour would account for the increasing Al_2O_3 content of the mullite with temperature as seen in the diagram of Klug *et al.*¹⁷ shown in Fig. 2. It is thus supported experimentally that the maximum content of Al_2O_3 in the mullite structure is about 77 wt%. In the presence

of $\alpha-Al_2O_3$ at the time of mullite growth, however, the maximum amount is about 74 wt% because of the lesser availability of Al_2O_3 molecules. The mullites with Al_2O_3 contents above 77 wt% up to about 84 wt% appear only on quenching melts from above the liquidus temperature. The Al_2O_3 molecules in excess of the total available Si/Al atomic sites are accommodated by a crystallographic superstructure as pointed out by Kriven and Pask.²⁶ At about 84 wt% Al_2O_3 the aluminosilicate structure becomes saturated with Al_2O_3 molecules. Further additions cause the primary precipitation of Al_2O_3 spherulites on cooling.

3.1 Effect of rate of cooling

There have been several definitive experiments indicating the importance of kinetics in determining the nature of the phase equilibria with different cooling rates.¹² Three diffusion couples of sapphire/fused SiO_2 were heated together at 1900°C for 15 min. They were cooled together by turning off the furnace and directing the flow of a stream of He gas onto the assembly of sealed crucibles so that small differences existed in their rate of cooling.

Figure 3 shows polished cross-sections perpendicular to the interfaces of the three specimens, with the sapphire on the bottom of the photographs. The specimen in photo A, which was cooled the fastest, shows precipitates of mullite; the specimen in photo C, which was cooled the slowest, shows precipitates of Al_2O_3 ; and the photo B specimen, which was cooled at an intermediate rate, shows large mullite precipitates with small precipitates of Al_2O_3 in the glass phase between. Average diffusion profiles into the fused SiO_2 established at 1900°C were identical for all three specimens with an overall composition of 63 wt% Al_2O_3 in the aluminosilicate at the interfaces. This composition liquid was in equilibrium with Al_2O_3 but its structure was not saturated with Al_2O_3 molecules as previously described. In photo C, the cooling rate was slow enough so that $\alpha-Al_2O_3$ nuclei formed at the interface, leading to the formation of elongated $\alpha-Al_2O_3$ crystals. In photo A, with a faster cooling rate, sufficient time for rearrangement and assembly to form $\alpha-Al_2O_3$ nuclei and crystals was not available before the temperature was reached at which the liquid was saturated with mullite, leading to the nucleation and growth of the elongated mullite crystals. This behaviour supports the concept that $\alpha-Al_2O_3$ does not nucleate easily unless the aluminosilicate atomic structure becomes saturated with Al_2O_3 molecules.

3.2 Mullite peritectic reaction

Another significant experiment is one that showed



Fig. 3. Microstructures of diffusion zones in couples of sapphire (bottom) and fused silica annealed at 1900°C for 15 min and (A) quenched, (B) cooled at a relatively moderate rate and (C) cooled relatively slowly. Precipitates in diffusion zone in (A) are mullite (light grey), in (B) alumina (light grey needles) and mullite (fine precipitates between alumina needles) and in (C) alumina (light grey needles); precipitates along interface in (B) and (C) are also alumina.

the formation of mullite by a peritectic reaction.¹² A mixture containing 71.8 wt% Al_2O_3 was homogenized in a sealed Mo crucible at 1950°C for 460 min, cooled to 1750°C in 30 min, annealed at 1750°C for 29.4 days, and quenched. A polished cross-section is shown in Fig. 4. The light grey crystals are $\alpha\text{-Al}_2\text{O}_3$ surrounded by medium grey growths of mullite, with a dark grey aluminosilicate glass between the mullite growths. The concentration profiles across the mullite growths correspond to those obtained in $\alpha\text{-Al}_2\text{O}_3/\text{SiO}_2$ diffusion couples at 1750°C. The reactions at the interface are fast and maintain equilibrium compositions for 1750°C at the interfaces. The overall reaction is slow because the rate-determining step is interdiffusion through the forming mullite, which is slow.

The formation of $\alpha\text{-Al}_2\text{O}_3$ crystals which participate in the formation of mullite in a melt of this composition clearly indicates that mullite melts incongruently. If mullite had formed directly from the melt and thus melted congruently, then it would have been impossible to form as a stable phase under the above conditions. It could also be pointed out that if Bowen and Greig,^{2,3} using $\alpha\text{-Al}_2\text{O}_3$ particles as part of their starting materials, did not completely dissolve it into their starting mixture and performed experiments at about 70 wt% Al_2O_3 and temperatures of about 1900°C, $\alpha\text{-Al}_2\text{O}_3$ could not have persisted under these conditions if mullite melted congruently. Concentration profile discontinuities across the phase

boundaries provide very accurate information about the stable composition range of the phase fields.

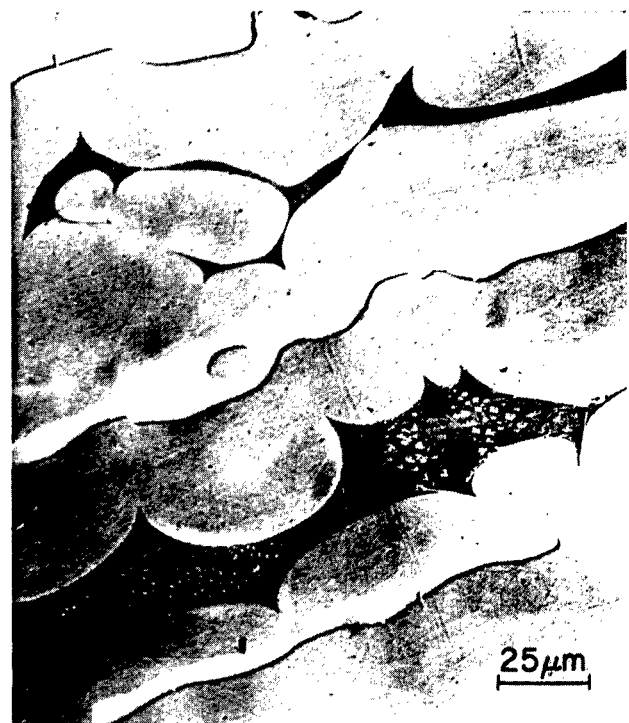


Fig. 4. Microstructure of specimen containing 71.8 wt% Al_2O_3 held at 1950°C for 7.7 h, cooled to 1750°C in 30 min, annealed at 1750°C for 29.4 days, and quenched to room temperature. Light grey precipitates are alumina completely surrounded by layer of mullite. Dark grey portions between mullite layers are glass containing precipitates of mullite formed on quenching. The microstructure formed during the heating schedule indicates a peritectic reaction.

4 Summary and Conclusions

A critical study of the mechanisms and kinetics of the solid-state chemical reactions that take place with different starting materials provides an explanation for the differences that have been reported in the high alumina region of the phase equilibria diagrams for the Al_2O_3 – SiO_2 system. Since the equilibria are formed by reactions, the bond strengths, atomic structures and free energies of the participating phases are critical. The nature of the reactions and their driving forces are the principal factors. Both the source of Al_2O_3 molecules and the nature of the aluminosilicate liquid structures are important in this system.

The Al_2O_3 sources have been either as α - Al_2O_3 particles or chemically-prepared sol–gel aluminosilicates or alkoxides. The α - Al_2O_3 has a high negative free energy of formation. Thus, the energy necessary to break its bonds to provide Al_2O_3 molecules is relatively high. This energy is provided by the aluminosilicate liquid since its free energy is lowered by incorporating Al_2O_3 molecules into its atomic structure. A thermodynamic balance is reached when the free energy change for the overall reaction becomes zero and the chemical potentials for each of the components are equal in both participants at the reacting interface. The source of the phase equilibria differences is the fact that, at this point, equilibria are reached because of insufficient energy to make more Al_2O_3 molecules available. The aluminosilicate liquid at this point, thus, does not become saturated with Al_2O_3 molecules.

In the case of the sol–gel source of Al_2O_3 , the bond strengths are weaker and Al_2O_3 molecules are more readily available. Thus, the aluminosilicate liquid becomes saturated, or near-saturated, with Al_2O_3 molecules. The additional significance of this fact is that in intermediate Al_2O_3 compositions the liquid can be saturated with Al_2O_3 but supersaturated with respect to α - Al_2O_3 . Because of this situation and the high covalency of its bonding, nucleation and growth of α - Al_2O_3 are sluggish in the aluminosilicate liquids.

Consequently, there are two phase equilibria diagrams for the Al_2O_3 – SiO_2 system. The controlling factor is whether α - Al_2O_3 is present or absent throughout the reactions leading to the steady or equilibrium state. In the presence of α - Al_2O_3 , the peritectic composition is 55 wt% Al_2O_3 , mullite corresponds to the 3:2 type and melts incongruently at 1828°C. Its solid solution range remains essentially constant with temperature. In the absence of α - Al_2O_3 , mullite corresponds to the 2:1 type and melts congruently at 1890°C; its solid solution range increases in Al_2O_3 up to 77 wt%

Al_2O_3 but would be expected to vary with the nature of the chemically-prepared source of Al_2O_3 . The 3:1 type of mullite is only formed on quenching homogenized aluminosilicate liquids from above the high temperature α - Al_2O_3 liquidus. This behaviour is the basis of a third phase equilibrium diagram for the Al_2O_3 – SiO_2 system which has not been extensively studied.

Aramaki and Roy²⁷ also performed experiments with ternary mixtures composed of additions of MgO or CaO to Al_2O_3 and SiO_2 . These were used to support the arguments that mullite melted congruently on the basis of the position of the boundary between the primary fields of mullite and α - Al_2O_3 in the corresponding ternary phase equilibrium diagrams. However, since the starting materials were first completely homogenized above the liquidus temperatures, the equilibrium phase compositions were obtained in the absence of α - Al_2O_3 as a starting material.

In summary, the controlling factor in determining the nature of the phase equilibrium diagram for the Al_2O_3 – SiO_2 system is the presence or absence of α - Al_2O_3 during the reactions leading to stable or metastable equilibrium. In the presence of α - Al_2O_3 , the higher temperature α - Al_2O_3 liquidus represents an atomic structure thermodynamically in equilibrium with α - Al_2O_3 but not saturated with Al_2O_3 molecules. In the absence of α - Al_2O_3 as a source of Al_2O_3 molecules, the lower temperature α - Al_2O_3 liquidus represents an atomic structure that is saturated with Al_2O_3 molecules. On cooling, α - Al_2O_3 nucleates and precipitates from liquids when they become saturated with Al_2O_3 molecules. The region between the two liquidus represents liquid structures that are supersaturated with respect to α - Al_2O_3 . In order to further differentiate the two conditions, the phase equilibrium diagram derived in the presence of α - Al_2O_3 as one of the starting materials could be identified as the α - Al_2O_3 – SiO_2 system; and in the absence of α - Al_2O_3 , the phase equilibrium diagram could be identified as the Al_2O_3 – SiO_2 system.

References

1. Shepherd, E. S., Rankin G. A. & Wright, W., *Am J. Sci.*, **28** (1909) 301.
2. Bowen, N. L. & Greig, J. W., *J. Am. Ceram. Soc.*, **7** (1924) 238.
3. Bowen, N. L. & Greig, J. W., *J. Am. Ceram. Soc.*, **7** (1924) 410.
4. Bauer, W. H. & Gordon, I., *J. Am. Ceram. Soc.*, **33** (1950) 140.
5. Bauer, W. H. & Gordon, I., *J. Am. Ceram. Soc.*, **34** (1951) 250.
6. Toropov, N. A. & Galakhov, F. Y., *Dokl. Akad. Nauk. SSSR*, **78** (1951) 299.
7. Shears, E. C. & Archibald, W. A., *Iron Steel (London)*, **27** (1954) 26.

8. Welch, J. H., *Nature (London)*, **186** (4724) (1960) 545.
9. Trömel, S., Obst, K. H., Konopicky, K., Bauer, H. & Patzk, L., *Ber. Deut. Keram. Ges.*, **34** (1958) 108.
10. Aramaki, S. & Roy, R., *J. Am. Ceram. Soc.*, **45** (1962) 229.
11. Davis, R. F. & Pask, J. A., *J. Am. Ceram. Soc.*, **55** (1972) 525.
12. Aksay, I. A. & Pask, J. A., *J. Am. Ceram. Soc.*, **58** (1975) 507.
13. Guse, W., *J. Crystal Growth*, **26** (1974) 151.
14. Guse, W. & Mateika, D., *J. Crystal Growth*, **26** (1974) 237.
15. Shindo, I., D.Sc. Thesis, Tohoku University, Japan, 1980.
16. Prochazka, S. & Klug, F. J., *J. Am. Ceram. Soc.*, **66** (1983) 874.
17. Klug, F. J., Prochazka S. & Doremus, R. H., *J. Am. Ceram. Soc.*, **70** (1987) 750.
18. Davis, R. F. & Pask, J. A., *High Temperature Oxides, Part IV*, ed. A. M. Alper, 1971, p. 37.
19. Pask, J. A., *Mullite and Mullite Matrix Composites*, eds S. Somiya, R. F. Davis & J. A. Pask, Am. Ceram. Soc. Trans., Vol. 6, 1990, p. 1.
20. Pask, J. A., *Ceramics Int.*, **9** (1983) 107.
21. Pask, J. A., *Ceramics Developments—Materials Science Forum, Part I*, eds C. C. Sorrel & B. Ben-Nisan, 1988, p. 1.
22. Yoldas, B. E., *Mullite and Mullite Matrix Composites*, eds S. Somiya, R. F. Davis & J. A. Pask, Am. Ceram. Soc. Trans., Vol. 6, 1990, p. 255.
23. Zhang, X. W., Tomsia, A. P., Yoldas, B. E. & Pask, J. A., *J. Am. Ceram. Soc.*, **70** (1987) 704.
24. Sacks, M. D., Lee, H.-W. & Pask J. A., *Mullite and Mullite Matrix Composites*, eds S. Somiya, R. F. Davis & J. A. Pask, Am. Ceram. Soc. Trans., Vol. 6, 1990, p. 167.
25. Risbud, S. H., Draper, V. F. & Pask, J. A., *J. Am. Ceram. Soc.*, **61** (1978) 471.
26. Kriven, W. M. & Pask, J. A., *J. Am. Ceram. Soc.*, **66** (1983) 649.
27. Aramaki, S. & Roy, R., *J. Am. Ceram. Soc.*, **42** (1959) 644.

Formation of Aluminum Rich 9:1 Mullite and its Transformation to Low Alumina Mullite upon Heating

Reinhard X. Fischer,^{a*} Hartmut Schneider^b & Dietmar Voll^b

^aInstitut für Geowissenschaften der Universität, D-55099 Mainz, Germany

^bGerman Aerospace Research Establishment (DLR), Institute for Materials Research, D-51140 Köln, Germany

(Accepted 22 July 1995)

Abstract

The formation of aluminum rich mullites $Al_{4+2x}Si_{2-2x}O_{10-x}$ with $x > 2/3$ has been studied at annealing temperatures between 700 and 1650°C. Calcination of the amorphous precursor at 700°C yields a mullite with 88 mol% Al_2O_3 corresponding to an x -value of 0.809. Simultaneously, a γ -alumina phase is formed. Further increase of the annealing temperature yields an increase in the aluminum incorporation up to 92.1 mol% Al_2O_3 at 1000°C derived from the refined lattice constants. This is the highest amount of Al observed so far in a mullite except the supposed end member γ - Al_2O_3 which, however, has not yet been established unambiguously. Above 1000°C, the aluminum content in mullite is reduced. This is accompanied by a transformation of the spinel-type phase to a superstructure of a θ -alumina like phase. The final product at 1650°C consists of 34 mol% of a 'normal' mullite with $x = 0.32$ and 66 mol% corundum.

1 Introduction

An aluminum rich mullite with 89% Al_2O_3 and lattice constants $a > b$ has been described recently^{1,2} and it was shown that the linear relationship between lattice constant a and the molar content of Al_2O_3 can be extrapolated beyond the crossover point of a and b lattice parameters. In the work described here we show that a sample prepared by sol-gel synthesis exhibits an even higher aluminum content at annealing temperatures below 1000°C. This sample is used to elucidate the crystallization process of mullites at the high alumina end of the solid solution series.

2 Experimental

The sample was prepared as described in Refs 1 and 2. After heating at a rate of 300°C/h, the samples were kept at the respective temperatures for 15 h and subsequently quenched in air. A portion of the sample was retained for the X-ray investigations and the bulk of the sample was further heated to the next temperature step. X-ray powder diffraction data were collected with a Seifert automatic powder diffractometer with $CuK\alpha$ radiation and a graphite monochromator in the diffracted beam. Samples were filled into a flat sample holder with a bottom silicon crystal to diminish background scattering. Background was subtracted by hand with a linear interpolation between consecutive breakpoints in the pattern. Phase analyses were performed by simulation of the mullite powder diagrams using the PC Rietveld plus program.³ Calculated intensities were corrected for automatic divergence slit effects in the Rietveld procedure.⁴ Data were collected in step scan mode between 10 and 100° 2θ with steps of 0.03° and a counting time of 30 s per step, except for the final data set of the 1650°C sample which was measured between 5 and 140° 2θ with 10 s per step.

3 Results and Discussion

Crystallization of mullite starts at about 700°C, together with the formation of a γ -alumina phase (Figs 1(a-d)). High background intensities indicate the presence of a relatively large amount of a coexisting amorphous phase. Mullite formed at 700°C exhibits broad X-ray lines of low intensity. X-ray line intensities gradually increase upon heating accompanied by a sharpening of the line widths, especially at temperatures above 900°C. This indicates an increasing degree of structural order in $a > b$ mullites heat-treated above ≈ 900 °C.

*Present address: Fachbereich Geowissenschaften der Universität, D-28334 Bremen, Germany.

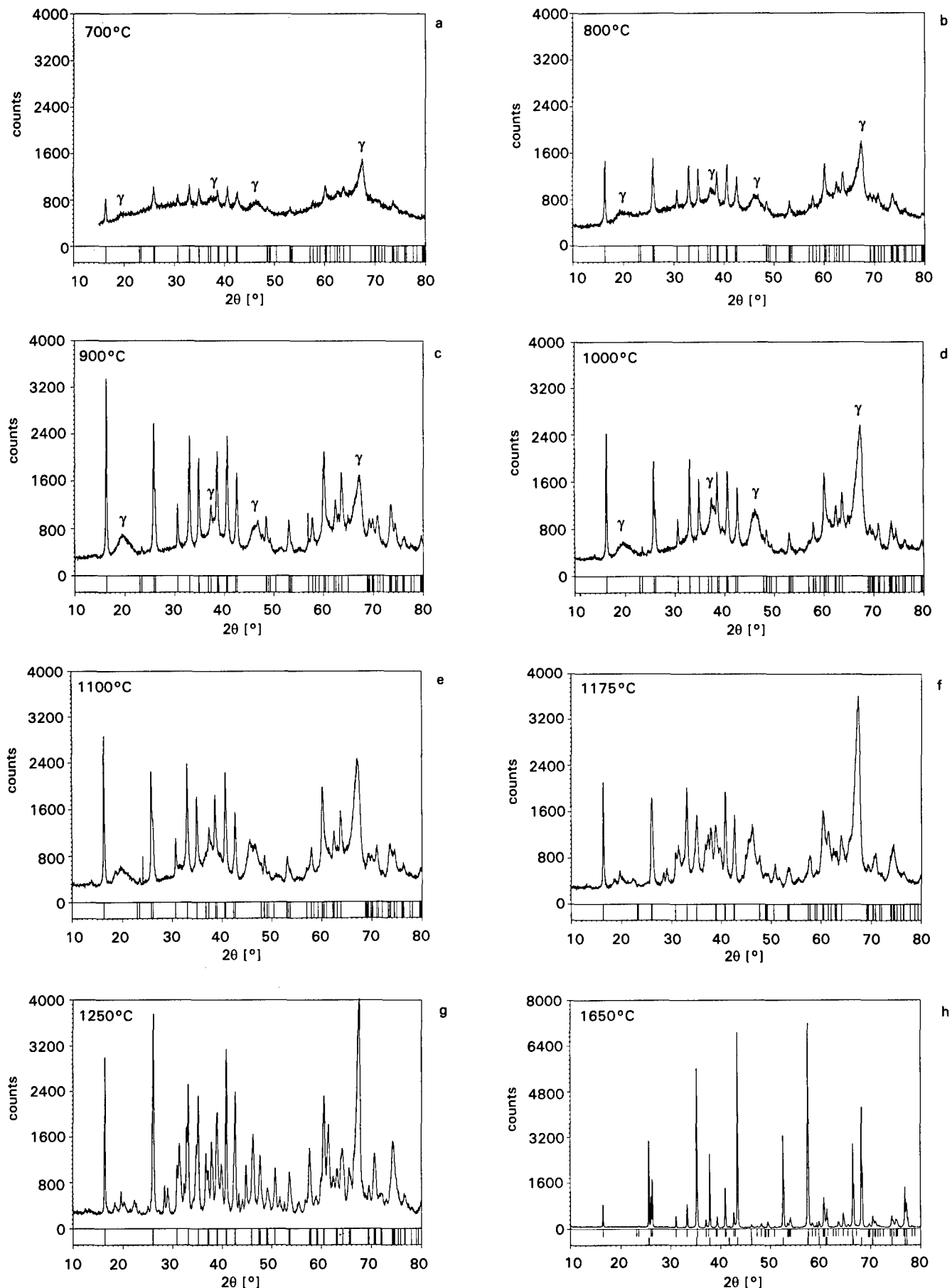


Fig. 1. Observed powder patterns of mullite samples at various annealing temperatures given in the upper left corner of the diagram frames. Mullite reflections are indicated by tickmarks underneath the powder diagrams. The broad peaks belonging to the γ -alumina phase are labeled with the Greek letter γ in Figs 1(a-d). Reflections without tickmarks in Figs 1(e-g) belong to a transformed alumina phase. Fig. 1(h) shows the powder diagrams of mullite (upper row of tickmarks) and corundum, α -alumina (bottom set of tickmarks). The sharp features at $57^\circ 2\theta$ in Fig. 1(c) and at $24^\circ 2\theta$ in Fig. 1(e) are spurious intensities from instrumental effects; they are eliminated in the analyses.

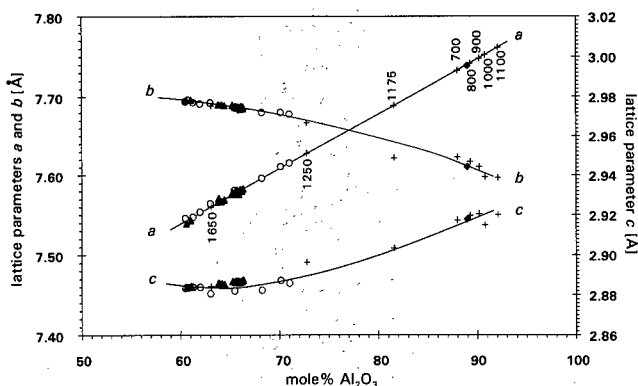


Fig. 2. Lattice parameters a , b , and c of mullites from recent determinations (♦ Ref. 2, ▲ Ref. 5, ○ Ref. 6) with the additional data points (+) from this work. The straight line for a results from linear regression, the curves for b and c are fitted by hand. Data points of this work are labeled with the respective annealing temperatures (°C).

This observation is in agreement with HRTEM studies on $a > b$ mullites prepared at 1000°C which yielded evidence for an ordered sequence of domains with high and low O_c oxygen vacancy concentrations.⁵ The γ -alumina phase has the characteristic broad peaks in the powder diagram at 20, 46, and 67° 2θ . Above $\approx 1100^\circ\text{C}$ (Figs 1(e–g)), the reflections of the alumina phase become sharper. Splitting of the peaks indicates a phase transition or an ordering of the highly disordered defect spinel. At 1650°C (Fig. 1(h)), the alumina spinel phase transforms to α -alumina (corundum) and mullite exhibits very sharp diffraction peaks.

The chemical composition of the low-temperature mullites were derived from the linear relationship between its lattice constant a and the molar content of Al_2O_3 . Using the more recent data of mullite determinations^{6,7} in the low alumina region extended by the data from the high alumina mullite,² we get the relationships shown in Fig. 2. A linear regression based on these data (represented by the open circles, solid triangles, and the diamond symbol) yields the line drawn for lattice constant a . The curves for lattice constants b and

c are fitted by hand. Slope A and intercept B are derived from the linear regression yielding the relation to calculate the molar content m of Al_2O_3 in mullite

$$a = A \cdot m + B = 0.00692 \cdot m + 7.124$$

and

$$m = 144.5 \cdot a - 1029.5$$

The uncertainties are 0.00008 for A and 0.005 for B yielding an error of about 1.5 mol% for the determination of m with this equation.

Lattice constants were determined by the Rietveld refining method. The accuracy of the refinements depends strongly on the accuracy of the crystal structure parameters which are used for the powder pattern simulation. Therefore, the refinement has been performed iteratively with an average structure of mullite as an initial model. This initial refinement yielded improved lattice constants which were used to redetermine the chemical composition from the curves shown in Fig. 2. The occupation factors of the Al and Si atoms were set to values derived from the x -values according to the formula given below (see also footnote in Table 1). This process was repeated two or three times until the best fit was achieved with the most accurate lattice constants. Regions of the spinel phase in the powder diagrams were excluded from the refinements. The resulting lattice constants, related to the molar content of Al_2O_3 , can be used to derive the x -value in the formula of the mullite chemical composition and, consequently, the occupation factors of the respective atom sites. The x -value is given by

$$x = 10 - 6 \cdot \frac{m + 200}{m + 100}$$

The results are listed in Table 1. The lattice constants are added to Fig. 2 (+ symbols). While the a parameters inevitably lie on the straight line (since they were derived from the linear regression), the parameters b and c give a good measure for the shape of these lattice parameter curves.

Table 1. Lattice constants a , b , c (Å) from Rietveld refinements, molar content, m of Al_2O_3 (%) from linear regression, and atom site occupancies

T (°C)	a	b	c	m	x	Number per unit cell			
						Si in T	T^*, Oc^*	T^{**}	Oc
700	7.7328(24)	7.6229(23)	2.9175(6)	88.0	0.809	0.383	1.191	0.426	0
800	7.7419(12)	7.6172(11)	2.9197(3)	89.3	0.830	0.340	1.170	0.489	0
900	7.7480(6)	7.6106(6)	2.9205(2)	90.2	0.845	0.311	1.155	0.534	0
1000	7.7616(9)	7.5969(8)	2.9201(2)	92.1	0.877	0.245	1.123	0.632	0
1100	7.7525(10)	7.5978(9)	2.9150(3)	90.8	0.855	0.289	1.144	0.567	0
1175	7.6889(26)	7.6222(26)	2.9034(6)	81.6	0.697	0.606	1.303	0.091	0
1250	7.6278(20)	7.6671(20)	2.8964(5)	72.8	0.528	0.944	1.056	0	0.416
1650	7.5603(3)	7.6886(3)	2.8843(1)	63.1	0.320	1.360	0.640	0	1.040

$\text{Si in } T = 2 - 2x$, $T^*, \text{Oc}^* = 2 - x$ for samples with $x > 2/3$ (700–1175°C) and $2x$ for samples with $x < 2/3$, $T^{**} = 3x - 2$ for samples with $x > 2/3$ else 0, $\text{Oc} = 2 - 3x$ for samples with $x < 2/3$ else 0 (see Ref. 2 for explanation).

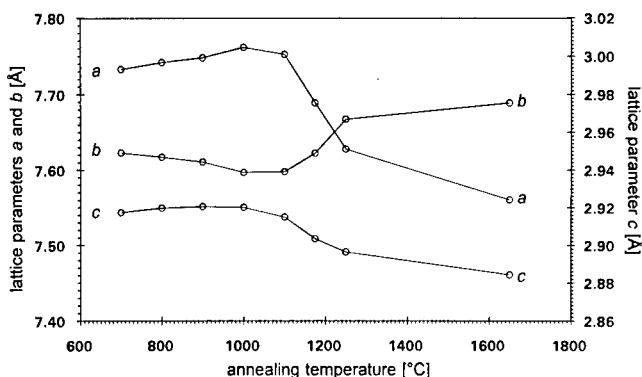


Fig. 3. Plot of lattice constants versus annealing temperature.

The deviations of the parameters of the 1175 and 1250°C samples might be caused by the severe overlap of the mullite reflections with the spinel phase reflections. An improvement in the accuracy of the lattice constant determinations could be achieved by a simultaneous simulation of mullite and γ -alumina. The multiphase refinement could not be performed because of difficulties in the crystal structure determination of the spinel phase. Further work is in progress. However, the results are sufficiently accurate for a discussion of the phase formation. Figure 3 shows a plot of the lattice constants versus the annealing temperature and Fig. 4 shows the corresponding molar relationship derived from data in Fig. 2. It is notable that the lattice constant a , and consequently the molar content of Al_2O_3 , increase upon heating between 700 and 1000°C. In this region, the mullite phase corresponds to the new type of mullite described in Ref. 2 (see also data in Table 1). Above 1000°C, the aluminum content is reduced, rapidly falling to values which represent a 'normal' mullite at 1250°C with lattice constants $a < b$ and with x -values $< 2/3$ corresponding to mullites with less than 80 mol% Al_2O_3 . At the final temperature, at 1650°C, the sample consists of α -alumina (corundum) and a well crystallized mullite with 63% Al_2O_3 . Simultaneously with the reduction in the aluminum content at 1100°C, a transformation of the spinel phase is observed indicated by the narrowing and splitting of the broad reflections at $20^\circ 2\theta$ and $46^\circ 2\theta$ (Fig. 1(e)). At 1250°C, further transformation to a θ -alumina like phase is observed with very sharp reflections indicating a well crystallized product. However, several reflections which do not fit into the monoclinic cell of θ -alumina⁸ indicate a supercell with bigger lattice parameters which has not been observed before for the transition aluminas. We suspect that the reduction of the aluminum content in mullite above 1000°C is directly related to the formation of the new deformed spinel phase. Considering that the spinel phase could incorporate silicon as

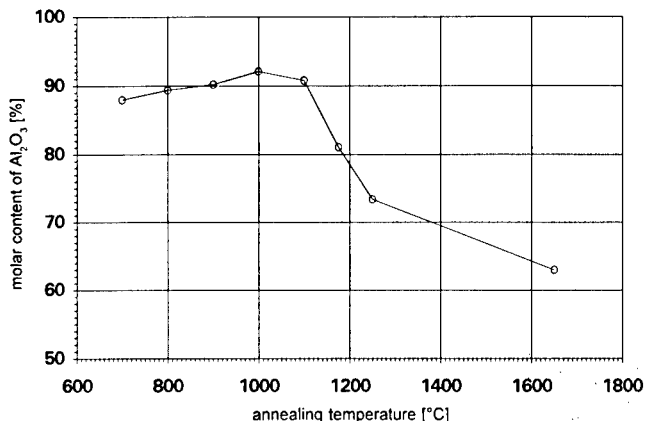


Fig. 4. Plot of molar content of Al_2O_3 versus annealing temperature.

well⁹ a discussion of the exact phase relations in this system is very difficult as long as the structure of the defect spinel has not been determined.

The final product at 1650°C contains 34 mol% mullite ($\text{Al}_{4.64}\text{Si}_{1.36}\text{O}_{9.68}$) and 66 mol% corundum (Al_2O_3) derived from the standardless quantitative Rietveld analysis with an absolute error of about 3%. Here, we assume that the amorphous phase completely disappeared. This corresponds roughly to a Al/Si ratio of 6:1 in the bulk composition of this sample which indicates a loss of silicon in the vigorous hydrolytic reaction of the starting materials with an initial Al/Si ratio of about 4:1.^{1,2}

Acknowledgements

We thank the Deutsche Forschungsgemeinschaft (DFG) for financial support under grant Fi442/2. The award of a Heisenberg fellowship to RXF is gratefully acknowledged. We thank R. D. Shannon for reading the manuscript. Computing facilities were financially supported by the Materialwissenschaftliches Forschungszentrum of the University of Mainz.

References

1. Schneider, H., Fischer, R. X. & Voll, D., Mullite with lattice constants $a > b$. *J. Am. Ceram. Soc.*, **76** (1993) 1879–81.
2. Fischer, R. X., Schneider, H. & Schmücker, M., Crystal structure of Al-rich mullite. *Am. Mineral.*, **79** (1994) 983–90.
3. Fischer, R. X., Lengauer, C., Tillmanns, E., Ensink, R. J., Reiss, C. A. & Fantner, E. J., PC-Rietveld plus, a comprehensive Rietveld analysis package for PC. *Materials Science Forum* **133–136** (1993) 287–92.
4. Fischer, R. X., Divergence slit corrections for Bragg-Brentano diffractometers with rectangular sample surface. *Powder Diffraction*, in press.
5. Schneider, H., Okada, Y., Pask, J. A., *Mullite and mullite ceramics*. Wiley & Sons, Chichester, 1994, pp. 33–4.
6. Klug, F. J., Prochazka, S. & Doremus, R. H., Alumina-silica phase diagram in the mullite region. *Ceramic Transactions*, **6** (1990) 15–43.

7. Ban, T. & Okada, K., Structure refinement of mullite by the Rietveld method and a new method for estimation of chemical composition. *J. Am Ceram. Soc.*, **75** (1992) 227-30.
8. Zhou, R. -S. & Snyder, R. L., Structures and transformation mechanisms of the η , γ and θ transition aluminas. *Acta. Cryst.*, **B47** (1991) 617-30.
9. Schneider, H., Voll, D., Saruhan, B., Schmücker, M., Schaller, T. & Sebald, A., Constitution of the γ -alumina phase in chemically produced mullite precursors. *J. Europ. Ceram. Soc.*, **13** (1994) 441-8.

The Formation of Mullite from Kaolinite Under Various Reaction Atmospheres

K. J. D. MacKenzie, R. H. Meinhold, I. W. M. Brown & G. V. White

New Zealand Institute for Industrial Research and Development, PO Box 31-310, Lower Hutt, New Zealand

(Accepted 22 July 1995)

Abstract

In addition to its importance as a high-technology ceramic, mullite is also an intermediate phase in the formation of non-oxide ceramics (sialons) by carbothermal reduction of clay minerals. This reaction involved the formation of mullite under non-oxidizing atmospheres and in the presence of carbon. The effect of eight different reaction atmospheres on mullite formation from kaolinite in the presence and absence of carbon was studied by X-ray diffraction, ^{27}Al and ^{29}Si magic angle spinning nuclear magnetic resonance (MAS NMR) spectroscopy. Generally, a greater amount of mullite is formed at 1200°C under vacuum and reducing atmospheres, which also produce mullites that are slightly more silica-rich (as deduced from X-ray lattice parameter measurements) but contain higher proportions of tetrahedral ^{27}Al NMR resonance at ≈ 46 ppm, probably associated with Al^ sites. Reaction systems containing either nitrogen or ammonia in the presence of carbon show NMR evidence of previously unreported early stage formation of $\text{Si}-\text{O}-\text{N}$ bonds. Thermodynamic calculations are presented which suggest that the formation of SiO is an important factor in the complex interactions between the various solid and gaseous reactants.*

1 Introduction

Mullite is an important high-technology ceramic in its own right, especially when prepared in high purity, by contrast with the product generally formed by heating clay minerals. However, the mullite resulting from the thermal reaction of clays plays an important role in the formation of sialons (silicon aluminium oxynitrides), another class of high-technology materials. The synthesis of sialon from natural aluminosilicates involves heating a clay such as kaolinite with carbon in a nitrogen atmosphere, but if other inert atmospheres such as argon are used, equally useful

carbide phases can be formed.¹ The practical importance of such synthesis reactions has led us to study the effect of a number of different reaction atmospheres on the formation of mullite from kaolinite, both in the presence and absence of carbon.

The aim of these studies was to measure the effect of eight different reaction atmospheres on:

- (1) the amount of mullite formed under standard conditions (2 h heating at 1200°C),
- (2) the composition of the mullite formed, and
- (3) the structure of the mullite formed.

The amount and composition of the product was measured by X-ray diffraction (XRD), from peak intensities and unit cell dimensions respectively, while aspects of the bonding and structure were studied by ^{29}Si and ^{27}Al solid-state magic angle spinning nuclear magnetic resonance (MAS NMR) spectroscopy. A thermodynamic analysis was also made, to clarify some of the details of the complex interactions occurring in these reacting systems.

2 Experimental

Kaolinite of high purity and good crystallinity ('Light' grade, supplied by British Drug Houses) was ball milled with an excess (25 wt%) Degussa lampblack under hexane for 16 h, extruded into 2 mm diameter rods, dried and heated in an alumina boat in an electric tube furnace under various flowing gases (flow rate 150 ml min⁻¹). The maximum temperature, at which the samples were held for 10 min, was 1200°C. A parallel set of experiments was also made omitting the carbon. After rapid cooling, maintaining the gas atmosphere, the samples were ground and examined by powder XRD (Philips PW1700 automatic diffractometer with $\text{CoK}\alpha$ radiation) and solid-state nuclear magnetic resonance spectroscopy (Varian Unity 500 spectrometer). All the NMR

spectra were acquired at 11.7 T using a 5 mm Doty magic angle probe spinning up to 12 kHz. The recycle delay time used for the ^{29}Si spectra was 300 s, to allow for the possible presence of species with very long relaxation times.

The thermodynamic calculations were made using a computer program² which uses tabulated thermodynamic data to determine the concentration of the various gas and solid species in complex systems as a function of gas concentration and reaction temperature.

3 Results and Discussion

Figure 1 shows the amount of mullite formation from kaolinite at 1200°C under the various reaction atmospheres, estimated semi-quantitatively from the height of the major mullite XRD peak at 3.4 Å. In the absence of carbon, oxidizing atmospheres produce the least mullite, while reducing atmospheres, which include ammonia and CO_2 , produce the greatest amount. Inert atmospheres are intermediate in their effect. In the presence of carbon the reaction atmosphere clearly changes, with inert gases producing the most mullite, but oxidizing gases still producing the least mullite, due to the fact that the carbon burns off very readily under these conditions.

Figure 2 shows the alumina content of the mullites, estimated from the unit cell dimensions using the relationship of Cameron.³ The unit cells were determined from careful measurements of at least 11 mullite XRD peaks, with angular corrections

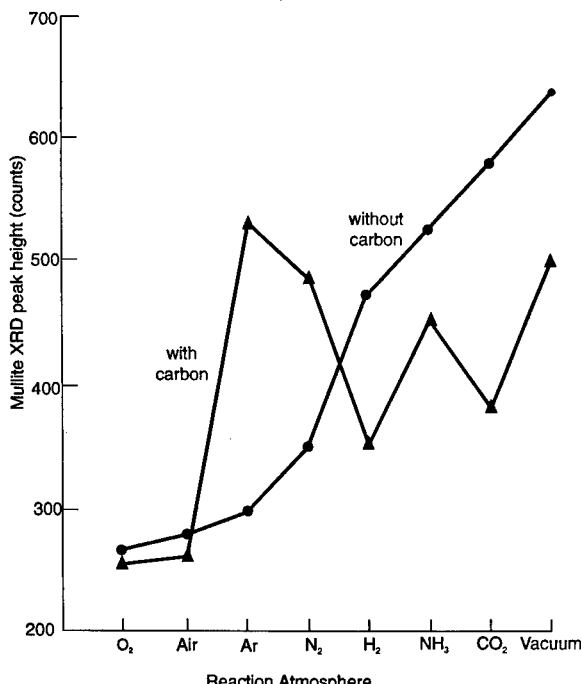


Fig. 1. Mullite formation in kaolinite (1200°C, 10 min) under various atmospheres, with and without carbon.

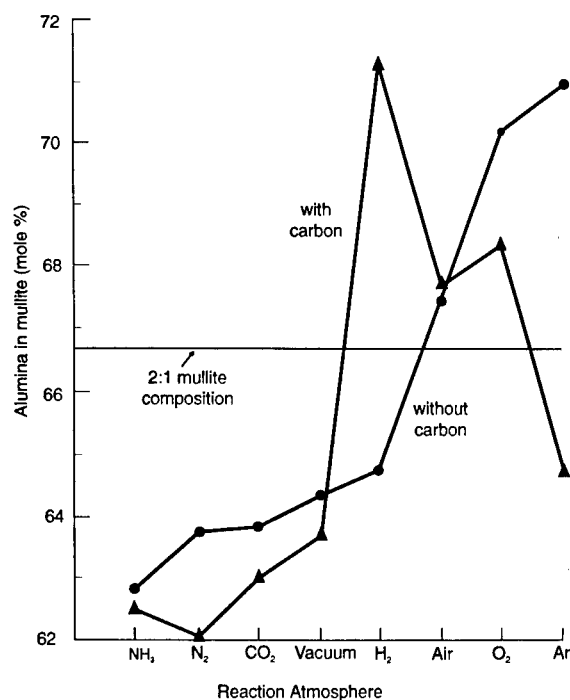


Fig. 2. Composition of mullites formed from kaolinite (1200°C, 10 min) under various atmospheres, with and without carbon.

made using an external silicon standard. In the absence of carbon, the alumina content of the mullite is highest under oxidizing conditions and argon, whereas under reducing conditions and vacuum, the composition is intermediate between 3:2 and 2:1 mullite. A similar situation occurs in the presence of carbon, except that hydrogen atmospheres now produce mullite with the highest alumina content.

Examples of the more interesting ^{29}Si and ^{27}Al spectra are shown in Fig. 3. The ^{29}Si MAS NMR spectra of all the mullites of this study are broad, but show the typical mullite peak at -87 ppm⁴ and a higher-field peak at about -106 ppm due to the free silica which separates from the kaolinite during the reactions preceding mullite formation. However, differences were found in the ^{29}Si spectra of samples heated with carbon in nitrogen (Fig. 3(A)) and heated without carbon in ammonia. In both these spectra there is evidence of broad spectral intensity downfield of the mullite peak. This is in the region of Si-N bonds, and in the spectral simulation of the sample heated in nitrogen (Fig. 3(B)) a peak centred at about -58 ppm could be fitted, the broadness of which suggests the presence of a continuum of nitride and oxynitride species. A similar situation was found in the ^{29}Si spectrum of the sample heated in ammonia, in which two peaks were fitted in this region, their positions (-40 ppm and -68 ppm) consistent with silicon nitride and silicon oxynitride, respectively. Both these samples have experienced the combination of a reducing atmosphere

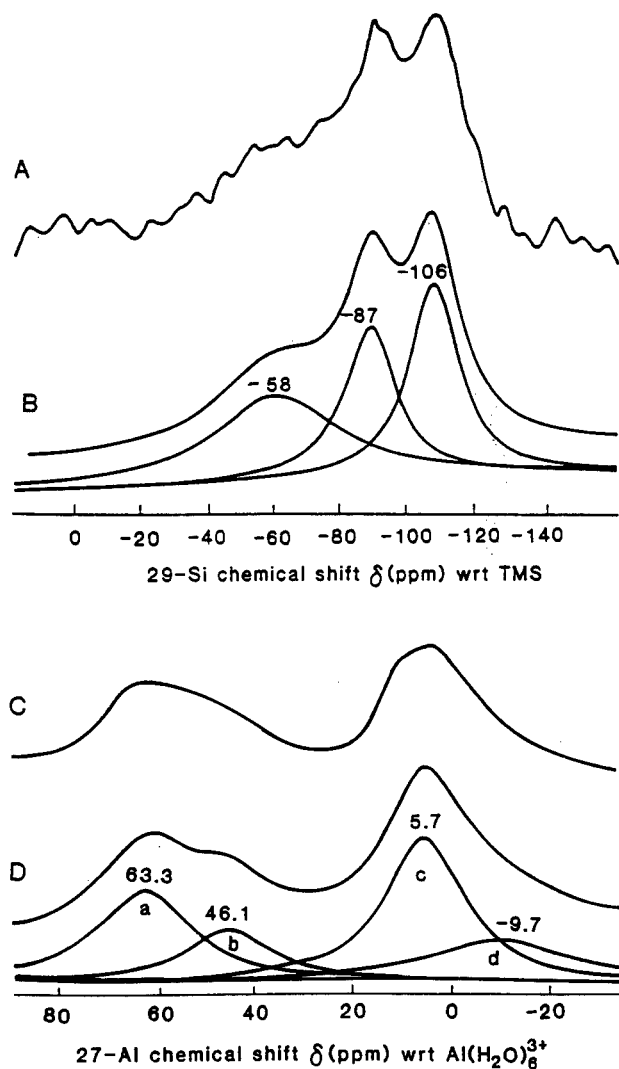


Fig. 3. Observed and simulated solid-state MAS NMR spectra of kaolinite reacted at 1200°C for 10 min: (A) ^{29}Si spectrum of sample containing carbon, in N_2 ; (B) simulation of A; (C) ^{27}Al spectrum of sample containing carbon, in H_2 ; (D) simulation of C.

and nitrogen, which seems to encourage the formation of Si-N bonding even at this low temperature.

The ^{27}Al MAS NMR spectra (Fig. 3(C)) are typical for mullite, containing an octahedral resonance at 1–6 ppm and a tetrahedral resonance at about 59 ppm. The octahedral resonance shows a marked tail on the upfield side which in the simulation of (Fig. 3(D)) has been fitted to a small broad peak (d); this tailing is commonly found in association with octahedral resonances and does not indicate a second site, but arises from electric field gradient (EFG) effects. The tetrahedral resonance at about 59 ppm can also be resolved into two overlapping peaks in a number of the samples (Fig. 3(D)). Following the reasoning of Merwin *et al.*,⁴ the tetrahedral peak at about 46 ppm may be due to the site associated with an oxygen defect. There is no readily discernible relationship between the area of this resonance and factors such as the amount of mullite formed or its total alumina content.

3.1 Thermodynamic calculations for these systems

There is clearly some complex chemistry occurring between the aluminosilicate lattice and the gas atmosphere, which can be modified by the presence of the carbon. Thermodynamic calculations were made in an attempt to interpret the behaviour of the various systems. Although these thermodynamic calculations refer to equilibrium conditions, and the present experiments were conducted under dynamic conditions, it was thought that the calculations could provide an insight into the various processes occurring, provided the results are treated with caution.

For the purpose of the calculations, the system was assumed to be anhydrous, with the composition of kaolinite from which the structural water had been removed (metakaolinite). The thermodynamic calculations predicted that this decomposes to silica and γ -alumina in most cases, with the formation of mullite, which is also taken into account in the calculations. Vacuum conditions were approximated by extremely high concentrations of an inert gas such as Ar, in which the dilution effect mimics the removal of gas by pumping. In all other cases, an ample excess of reactant gas (100 moles) and carbon (10 moles) was assumed. A range of temperatures was calculated, but the greatest attention was paid to the calculations at 1200°C.

3.2 Reactions in the absence of carbon

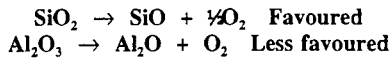
Under these conditions at 1200°C, vacuum, CO_2 and reducing atmospheres were found by experiment to be of most assistance to mullite formation. The conclusions of the thermodynamic calculations for these more beneficial atmospheres are summarized in Fig. 4.

The calculations predict that at 1200°C, vacuum conditions should facilitate the decomposition of the silica to SiO but the alumina component should remain intact. The calculations for the system containing CO_2 indicate that the CO_2/CO equilibrium lies heavily to the left, although under the dynamic gas flow conditions of the experiment it may be shifted more to the right. The resulting CO would also favour the formation of SiO . At 1200°C, ammonia is completely dissociated into H_2 and N_2 ; the resulting hydrogen again facilitates SiO formation but does not form appreciable Al_2O at 1200°C (Fig. 4). Reaction between the silica component and the N_2 in the presence of the dissociated H_2 to form silicon nitride or silicon oxynitride is not predicted, but the formation of AlN from the alumina component is slightly favoured (although not observed experimentally here). Thus, the thermodynamic calculations for all the atmospheres which were found to assist mullite formation suggest that the silica phase is

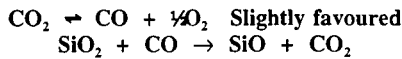
KAOLINITE WITHOUT CARBON

Experimental order for mullite formation:
Vacuum > CO₂ > NH₃ > H₂

A. Vacuum



B. Carbon Dioxide



C. Ammonia

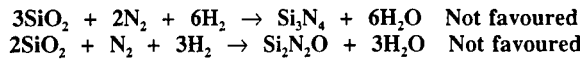
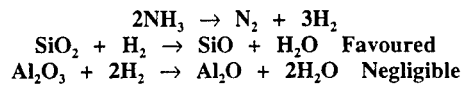


Fig. 4. Conclusions drawn from thermodynamic calculations for aluminosilicate systems reacted at 1200°C in the absence of carbon.

reacting with the gas in all cases, but the alumina component is much more stable.

3.3 Reactions in the presence of carbon

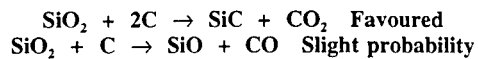
In the presence of carbon, the experimental results indicate that reducing conditions again exert a beneficial influence on the formation of mullite, but, by contrast with the results in the absence of carbon, the inert atmospheres Ar and N₂ now also strongly promote mullite formation. The primary action of the inert gases will be to maintain the carbon in its elemental form. The predictions of thermodynamic calculations at 1200°C for the inert and reducing gases in the presence of carbon are summarized in Fig. 5.

In both argon and vacuum, reaction between the silica component and carbon to form SiC is predicted, although this product was not experimentally observed. Because of its ability to be removed in the gas stream, the formation of SiO is probably more significant than it would be under the equilibrium conditions of the thermodynamic calculations. In nitrogen, the formation of silicon oxynitride from the silica component is strongly favoured in the presence of carbon (Fig. 5), consistent with the ²⁹Si NMR spectrum of this sample (Fig. 3(A)), but the alumina component is predicted to remain unreacted. In ammonia, reaction between the dissociated H₂ and the carbon to form CH₄ is predicted at lower temperatures, but by 1200°C, the equilibrium has shifted back again to the left. Thus, ammonia in the presence of carbon is predicted to form silicon oxynitride, this reaction being confirmed by ²⁹Si NMR. In hydrogen

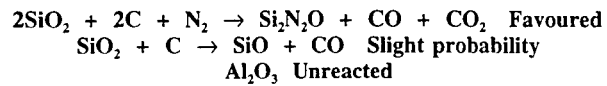
KAOLINITE WITH CARBON

Experimental order for mullite formation:
Ar > Vacuum > N₂ > NH₃ > H₂ > CO₂

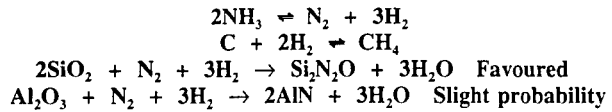
A. Argon and Vacuum



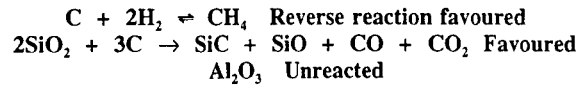
B. Nitrogen



C. Ammonia



D. Hydrogen



E. Carbon Dioxide

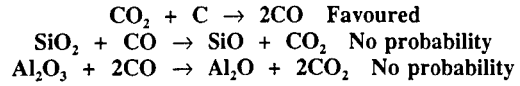


Fig. 5. Conclusions drawn from thermodynamic calculations for aluminosilicate systems reacted at 1200°C in the presence of carbon.

alone, the formation of SiC and SiO is predicted at 1200°C, but the alumina component of the reactant remains unreacted. As with Ar and vacuum atmospheres, the SiC is not experimentally observed. At 1200°C, CO₂ is predicted to react with carbon to form CO, but the thermodynamic probability of further reaction between CO and silica or alumina is low.

Thus, the thermodynamic calculations suggest that both in the presence and absence of carbon, the silica component is most affected by the various atmospheres, especially reducing atmospheres and those with the potential to become reducing. When the free silica in the reacting system has been consumed by the formation of SiO or Si₂N₂O, the silica component of the mullite present will be progressively decomposed by similar reactions (i.e. the formation of SiO, SiC or silicon oxynitrides). Removal of SiO in the gas stream will decrease the silicon concentration of the system unless it is retained by reacting with the alumina-rich components to form further mullite. A relationship between mullite formation and the tendency of the system to form SiO is illustrated in Fig. 6, in which the observed degree of mullite formation is plotted against the calculated SiO concentration for each system.

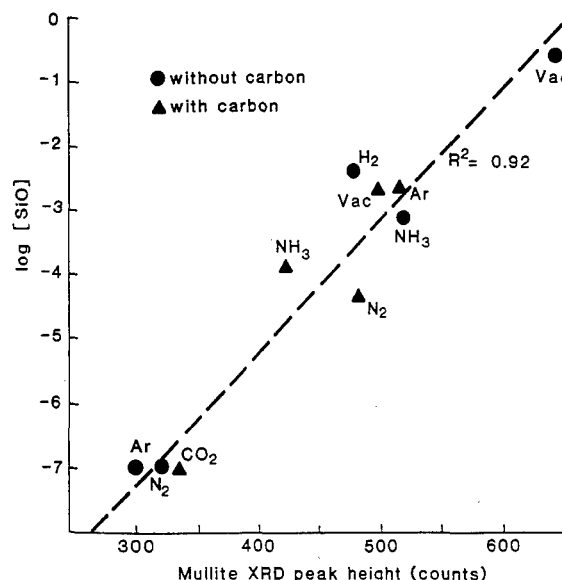


Fig. 6. Calculated SiO concentrations in systems of kaolinite composition, reacted in different atmospheres at 1200°C in the presence and absence of carbon, as a function of the experimentally determined mullite concentration.

The relationship shown in Fig. 6 is better than expected in view of the equilibrium assumptions of the thermodynamic calculations, which are very different from the present experimental conditions. Since the formation of mullite in these systems appears to be closely associated with their tendency to form SiO, the temperature dependence of SiO formation is also of interest (Fig. 7).

Although the calculated thermodynamic predictions of Fig. 7 must again be treated with caution, they indicate very different temperature dependences in the various atmospheres with and without carbon. In all but the two hydrogen-containing systems (H_2 and NH_3), the presence of carbon lowers the onset temperature for SiO formation, and in the case of Ar and N_2 , increases the eventual SiO concentration. These results suggest that the relative behaviour in the various reaction systems (and also the effect on mullite formation) may change markedly with reaction temperature.

The mechanism of mullite formation under reactive atmospheres which decompose the siliceous component to form SiO probably depends on the enhanced reactivity of the gas-phase SiO species for the more alumina-rich components. Alternatively, if discrete SiO is not directly formed, the increased lability of the Si-O bonds in the solid silica or aluminosilicate phases may be sufficient to promote further reaction and an increase in the silica content of the mullite.

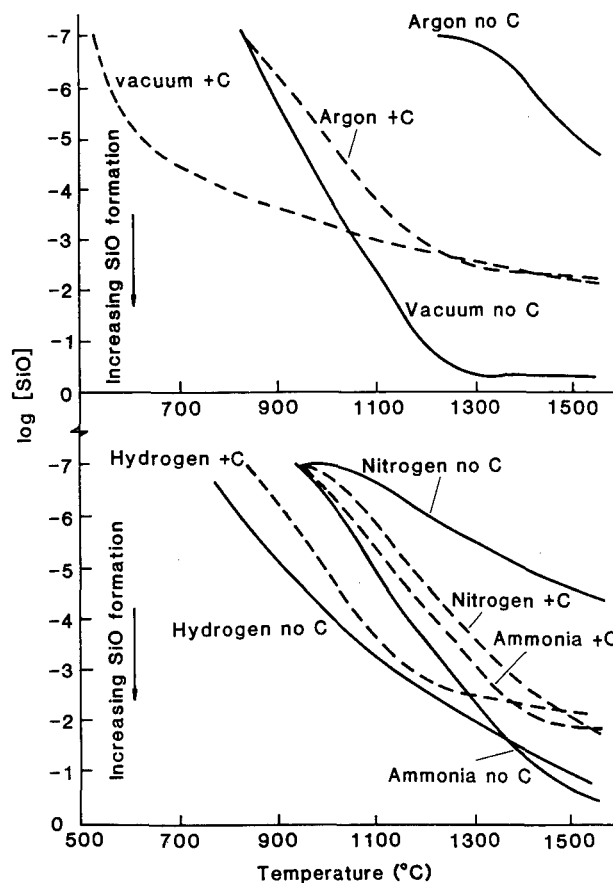


Fig. 7. Temperature dependence of calculated SiO formation in systems of kaolinite composition, under different atmospheres in the presence and absence of carbon.

Although the thermodynamic predictions must be applied with caution to the results of dynamic experiments, they shed interesting light on the relative importance of the various competing reactions occurring in complex gas-solid systems such as mullite-forming systems under various atmospheres.

References

1. MacKenzie, K. J. D., Meinhold, R. H., White, G. V., Sheppard, C. M. & Sherriff, B. L., Carbothermal formation of β -sialon from kaolinite and halloysite studied by ^{29}Si and ^{27}Al solid state MAS NMR. *J. Mater. Sci.*, **29** (1994) 2611-19.
2. Turnbull, A. G. & Wadsley, M. W., CSIRO Thermochemistry System, Version 5.1, 1988.
3. Cameron, W. E., Composition and cell dimensions of mullite. *Am. Ceram. Soc. Bull.*, **56** (1977) 1003-11.
4. Merwin, L. H., Sebald, A., Rager, H. & Schneider, H., ^{29}Si and ^{27}Al MAS NMR spectroscopy of mullite. *Phys. Chem. Minerals*, **18** (1991) 47-52.

Mullitization and Densification of $(3\text{Al}_2\text{O}_3 + 2\text{SiO}_2)$ Powder Compacts by Microwave Sintering

P. Piluso, L. Gaillard, N. Lequeux & P. Boch

Laboratoire Céramiques et Matériaux Minéraux, Ecole Supérieure de Physique et de Chimie Industrielles, 10 rue Vauquelin, 75231 Paris Cedex 05, France

(Accepted 22 July 1995)

Abstract

Reaction sintering of $(3\text{Al}_2\text{O}_3 + 2\text{SiO}_2)$ powder compacts was studied using either a conventional electric furnace or a 2.45 GHz microwave furnace. Special attention was paid to temperature measurement within the microwave furnace. The reality of a microwave effect that accelerates the kinetics and therefore, decreases the temperatures of mullitization and densification, remains uncertain. In any case, such an effect does not exceed $\approx 50^\circ\text{C}$, which is in the order of the temperature gradient between the core and the surface of microwave heated specimens.

1 Introduction

Many studies have been devoted to microwave sintering of ceramics.¹⁻⁵ Microwave treatments have been reported to lead to a decrease in the temperature of sintering. In alumina, this decrease was said to be as large as 400°C ,⁶⁻⁸ which suggests the existence of a 'microwave effect' that accelerates the diffusion kinetics. However, there are large discrepancies in experimental data, and no definitive explanation has been proposed for the microwave effect.

The microwave effect has been most studied for densification without chemical change, but if it is not an artefact it should affect chemical reactions as well. Reaction sintering is a good way of combining reaction mechanisms and densification mechanisms. The present work was devoted to the preparation by reaction sintering⁹⁻¹⁴ of mullite ceramics. The influence of conventional heat treatments was compared to that of microwave treatments in order to investigate the existence of a microwave effect on densification and reaction (mullitization). The evidence of a microwave effect being related to a decrease in the temperature of densification (or of reaction), the accuracy of the

temperature measurements is of major importance. Therefore, special attention was paid to temperature measurement in the microwave furnace.

2 Experimental

2.1 The microwave furnace

The microwave-energy per unit volume (U) that is absorbed within a given material is expressed as:

$$U \approx 2\pi f E_{\text{int}}^2 \epsilon_0 \epsilon'' \quad (1)$$

E_{int} being the microwave electric field within the material, f the frequency, and ϵ'' and ϵ_0 the permittivity of free space and the effective relative loss factor, respectively.

Ceramic oxides such as Al_2O_3 or SiO_2 exhibit low dielectric losses, and are, therefore, difficult to heat in a commercial microwave furnace. We have built a microwave furnace specially designed to heat such low-loss materials.¹⁰⁻¹⁴ The furnace is shown in Fig. 1. It consists of a 2.45 GHz microwave generator with an adjustable 1.2 kW power output. The microwaves are directed into the applicator (which is a resonant, TE_{10n} single mode cavity) through a waveguide. A coupling iris minimizes the reflected power. The resonance of the cavity is controlled using an adjustable short-circuit. The incident and reflected powers are measured using two microwave-power meters and are recorded via a computer. The specimen is a cylinder of 13 mm in diameter and 3.5 mm thick. Its temperature is measured by a thermocouple (10% Rh-90% Pt/Pt) located in a hole drilled to the center of the specimen. The heating cycle is monitored by a programmable controller that regulates the incident power to follow a programmed temperature-to-time law.

In the absence of a theoretical model for the microwave effect, there is no evident choice for the frequency that would optimize the effect.

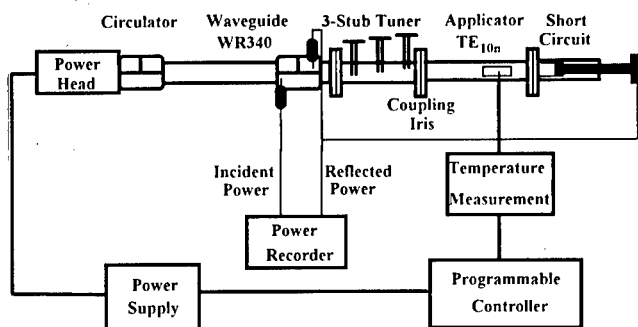
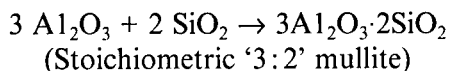


Fig. 1. The microwave furnace.

However, the frequency of 2.45 GHz is practically imposed by international regulations, which severely limit the industrial use of other, (e.g. 28 GHz) frequencies. Any industrial development of microwave sintering should satisfy the regulations and this is the reason why we have chosen a frequency of 2.45 GHz.

2.2 Green body preparation

Mullite ceramics were prepared by reaction sintering of alumina + silica powder compacts:



Alumina was α - Al_2O_3 (CR30 Baikowski®, 99.99% pure, $d_{50} = 0.5 \mu\text{m}$). Silica was cristobalite (M5000 Sifrac®, 99% pure, $d_{50} = 1.8 \mu\text{m}$). Powder mixtures were ball-milled for 5 h in a jar with dissociated ZrSiO_4 ($\text{ZrO}_2 + \text{SiO}_2$) balls in alcoholic medium (ethanol) with deflocculant (0.3 wt% of phosphate ester). A binder (3 wt% of polyvinylbutyral) was then added to improve the mechanical strength of the green material. Powders were granulated through a 200 μm sieve, then uniaxially pressed (150 MPa) to form pellets of 13 mm diameter and 3.5 mm thick.

2.3 Heat treatment

The first stage of heat treatment was pyrolysis of organic-binder and pre-sintering (2 h at 1000°C, in a conventional furnace). The resultant relative density (d/d_{th}) was 0.50. The second stage of heat treatment was reaction sintering, in either the

conventional electric or the microwave furnace. The temperature cycles were similar in both cases: heating at 20°C mn^{-1} from room temperature to the firing temperature (T_f), soaking for 1 h at T_f , then cooling at 20°C mn^{-1} to room temperature. T_f ranged from 1300 to 1600°C. Figure 2 shows a temperature-to-time curve for a $(3\text{Al}_2\text{O}_3 + 2\text{SiO}_2)$ powder compact, microwave heated to 1500°C.

2.4 Characterization of materials

Density of sintered materials was estimated by Archimedes' method. Portions of specimens were diamond sawn, polished with diamond paste, and thermally etched to observe the microstructure by optical and scanning electron microscopy. Microwave reaction-sintered specimens were sawn to cut a slice along the diameter parallel to the thermocouple hole, then the slice was cut into three portions labelled as left, central, and right. X-ray diffraction experiments ($\text{Cu}-\text{K}\alpha$ radiation) were performed on those portions and the results were compared to XRD data of reference mixtures of known composition, to analyze the extent of reaction quantitatively. Two ratios of XRD peak areas were considered:

$$\frac{I_{(220)\text{mullite}}}{I_{(220)\text{mullite}} + I_{(204)\text{alumina}}} \text{ and}$$

$$\frac{I_{(121)\text{mullite}}}{I_{(121)\text{mullite}} + I_{(204)\text{alumina}}}.$$

3 Results and Discussion

3.1 Temperature calibration

A study of the microwave effect requires that the accuracy of temperature measurement be as accurate as possible. However, temperature measurement is difficult in a microwave furnace. Firstly, microwave heating is a volumetric process that generates temperature gradients that are the opposite of what conventional heating produces, the core being warmer than the surface ('inverse gradients'). Secondly, the dielectric-loss factor of the heated material usually rises very rapidly when temperature exceeds a critical value. This leads to a sudden increase in the temperature of the specimen ('thermal runaway'). Thirdly, the large electromagnetic field inside the applicator can disturb temperature measurement.

Both radiation pyrometers and thermocouples can be used. Pyrometers are best suited to measure the surface temperature of a specimen whereas thermocouples are best suited to measure the core temperature. Pyrometers do not interfere with microwaves whereas metallic thermocouples can disturb the electric field in the cavity or be affected by it. We tried using both radiation pyrometers and thermocouples. Pyrometers require

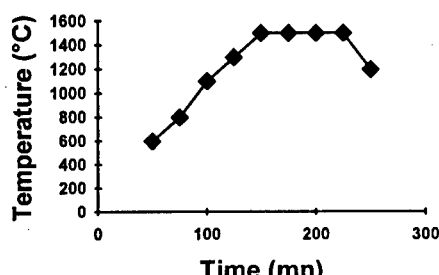


Fig. 2. Temperature versus time for a $(3\text{Al}_2\text{O}_3 + 2\text{SiO}_2)$ powder compact microwave heated to 1500°C.

knowledge of emissivity of the ceramics that were tested, which do not behave as a black body. Thermocouples gave reproducible results if placed perpendicularly to the electric field and protected by a metallic shield. We used thermocouples with small diameters (1 and 0.5 mm) to limit the heat losses by conduction.

The thermocouples were calibrated as follows:

3.1.1 Using 1 mm diameter thermocouples

These were tested using eutectic composition (49.4 wt% CaO + 50.6 wt% Al_2O_3), which melts at $1360^{\circ}C$,¹⁵ as confirmed by the experiments in the conventional furnace. The assumption was that eutectic melting is not sensitive to any microwave effect. However, the eutectic temperature that was measured in the microwave furnace was $1320^{\circ}C$. This meant that the temperature in the microwave furnace was under-estimated by about $40^{\circ}C$ (furnace was at $T \approx 1360^{\circ}C$) and the discrepancy must be due to heat conduction through the thermocouple. Because conduction decreases when the thermocouple diameter decreases, 0.5 mm thermocouples should behave better than 1 mm ones, as will be confirmed later on.

3.1.2 Using 0.5 mm diameter thermocouples

These were tested by comparison with an IR pyrometer focused on a hole bored into an alumina specimen and shaped to behave as a black body, due to multiple reflections of light. In the conventional furnace, the calibration showed that the emissivity of alumina at $1000^{\circ}C$ was of about 0.6 whereas that of the 'black-body hole' was of about 0.9 (instead of 1 for a perfect black body). In the microwave furnace, the tip of the 0.5 mm thermocouple was located at the center of the black-body hole in the alumina specimen and the specimen was thermally insulated by alumina fibers. The difference between the temperature given by the thermocouple and that given by the pyrometer was small over all the temperature range. It was of $10^{\circ}C$ at $T = 1000^{\circ}C$, to be compared with $40^{\circ}C$ for the under-estimation induced by the 1 mm thermocouple. This confirms that 0.5 mm thermocouples behave better than 1 mm ones and, therefore, 0.5 mm thermocouples were used for the rest of the study.

3.2 Temperature gradients

Microwave heating is a volumetric process. In the simplest case where the absorbed power is homogeneous across the specimen, the temperature is heterogeneous, the core being warmer than the surface. This is the opposite of what is observed in conventional heating: microwave heating induces 'inverse gradients', instead of the 'normal gradi-

ents' of conventional heating. The absorbed power is not homogeneous across the specimen due to changes in E_{int} and ϵ'' (see Eqn (1)). Usually, the effect of such changes is to increase the (inverse) gradients. To minimize the gradients, the heating rate must be kept at a low value ($\leq 20^{\circ}C\ mn^{-1}$) to avoid hot spots due to local thermal runaway. This requires a careful control of the microwave power, which must be kept at a low level (≤ 200 W). Moreover, the heated specimen must be situated at the place in the single-mode resonant cavity where the electric field is maximum, and the size of specimen (13 mm in diameter and 3.5 mm thick) must be small in comparison with the wavelength of microwaves ($\lambda \approx 20$ mm at 2.45 GHz). Finally, the heated specimen must be thermally insulated using low-conduction alumina fibers. In the absence of such insulation, the temperature difference between the core and the surface of specimen can exceed $500^{\circ}C$.

3.3 Mullitization

The extent of mullitization was quantified by XRD data obtained for reaction sintered specimens. The conventionally heated specimens were found to be homogeneously mullitized throughout their cross section, which indicated that their temperature had been homogeneous during reaction sintering. Conversely, the microwave heated specimens were found to be heterogeneously mullitized throughout their cross section, which indicated that they had been subjected to inverse temperature gradients during reaction sintering. For those specimens, the 'mullitization index' was determined from XRD data corresponding to the central section of the slice cut parallel to the thermocouple hole.

For a given mullitization index, the difference between the registered temperatures of conventional and microwave treatments was $\leq 65^{\circ}C$ (Fig. 3). Due to the underestimation of $\approx 10^{\circ}C$ in the microwave furnace, one sees that the present data are in favor of the existence of a microwave effect on mullitization whose magnitude is $\approx 50^{\circ}C$.

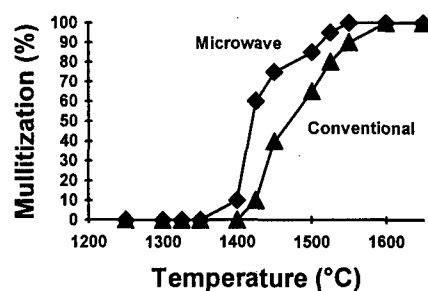


Fig. 3. Mullitization versus temperature (heating rate = $20^{\circ}C\ mn^{-1}$, soaking time = 1 h), for conventional and microwave heating.

Table 1. Mullitization and estimated temperature in a pellet microwave heated to 1400°C

Portion	Left	Central	Right
Mullitization (wt%)	60	75	60
Measured Temperature (°C)	1360	1400	1360
Estimated			

Mullitization gradients in microwave heated materials were analyzed by XRD, using various portions cut from reaction sintered pellets. For example, a specimen treated at 1400°C was found to be mullitized to 75 wt% in the central zone but to only 60 wt% in the superficial zone.

The mullitization gradients can be used to evaluate the temperature gradients, using reaction-to-temperature plots. Table 1 shows that the difference of temperature between center and surface for a pellet microwave heated to 1400°C is $\approx 40^\circ\text{C}$. This temperature difference is similar to the temperature difference that would correspond to the microwave effect.

3.4 Densification

Theoretical density was estimated from a rule of mixture having found the specimen composition that was given by quantitative XRD phase analysis. Apparent density was determined by averaging data from a whole specimen, which means we were not able to take into account any densification gradient.

Microwave heating seems to accelerate densification in comparison to conventional heating. However, specimens with the same mullitization index show the same densification, whatever the nature of heating. The temperature difference between conventional and microwave heating is a maximum for fully mullitized specimens, where densification is $\approx 75\%$. At its maximum, the microwave effect on densification is $\approx 50\text{--}60^\circ\text{C}$, which corresponds to the microwave effect on mullitization. This temperature difference is much

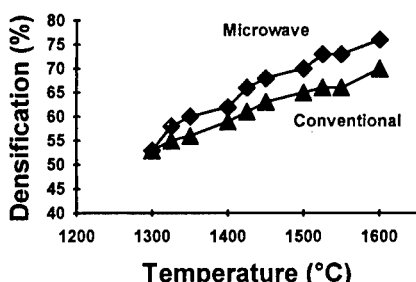


Fig. 4. Densification versus temperature (heating rate = 20°C mn^{-1} , soaking time = 1 h), for conventional and microwave heating.



Fig. 5. SEM micrographs of a microwave heated specimen (1580°C , 35 mn): (a) core; (b) surface.

smaller than the difference of $300\text{--}400^\circ\text{C}$ reported by Kimrey *et al.* in 28 GHz microwave sintered alumina.⁶

Microstructural observations confirmed that the microwave heated specimens were heterogeneous. The core exhibits higher densification and larger grain size than the surface (Fig. 5). For a given densification, conventional heated and microwave heated specimens exhibited similar microstructures, with no noticeable difference in grain shape, (i.e. equiaxial versus elongated).

4 Conclusions

The study of reaction sintering of $3\text{Al}_2\text{O}_3 + 2\text{SiO}_2$ powder compacts treated by conventional or microwave heating does not disprove the possibility of a microwave effect, which would slightly accelerate both reaction and densification. However, the decrease in temperature associated with such an effect would be $\approx 50^\circ\text{C}$, at most, which is much lower than what was sometimes claimed. This

temperature difference is in the order of the temperature gradients across the specimens.

It may be that the experimental conditions we used, in particular the choice of a frequency of 2.45 GHz instead of a higher frequency, were not the best to detect the microwave effect. Moreover, results on alumina-plus-silica mixtures cannot be extrapolated to results on ceramic materials having very different electric properties, in particular ionic conductors or semiconductors. However, it is a fact that, from older to newer data,^{1-3,16} the trend is continuously changing toward a decrease in extent of the microwave effect. The present work shows that, for mullitic materials, the microwave effect cannot be expected to accelerate the densification (or reaction) kinetics at a rate sufficient to reimburse the extra cost of sophisticated microwave equipment. This comment refers to the preparation of homogeneous objects. On the other hand, the existence of noticeable 'inverse' gradients and the possibility of changing the heating rate by changing the dielectric properties make microwave heating an excellent technique for producing non-homogeneous objects. Objects with gradients in properties such as in the new family of functional gradient materials (FGM),¹⁷ ceramic-to-ceramic joining, and ceramic-ceramic composites are examples.

Acknowledgements

The authors acknowledge Electricité de France and Ministère de la Recherche for their support to this study.

References

1. Microwave Processing of Materials, eds W. H. Sutton, M. H. Brooks & I. J. Chabinsky, *Mat. Res. Proc.*, **124** Pittsburgh, USA, 1998.
2. Microwave Processing of Materials II, eds W. B. Snyder, W. H. Sutton, M. F. Iskander & D. L. Johnson, *Mat. Res. Proc.*, **189** Pittsburgh, USA, 1991.
3. Microwave: Theory and Applications in Materials Processing, eds D. E. Clark, F. D. Gac & W. H. Sutton, *Ceram. Trans.*, **21**, Am. Ceram. Soc., 1991.
4. Microwave Processing of Materials III, eds R. L. Beatty, W. H. Sutton & M. F. Iskander, *Mat. Res. Proc.*, **269**, Pittsburgh, USA, 1992.
5. Sutton, W. H., Microwave Processing of Materials, *Ceramic Bulletin*, **68**(2) (1989) 376.
6. Janney, M. A. & Kimrey, H. D., Microwave sintering of alumina at 28 GHz. In *Ceramic Powder Science*, eds G. L. Messing, E. R. Fuller & H. Haussner, *Am. Ceram Soc.*, Westerville, USA, **II**, 1988, 919.
7. Janney, M. A., Kimrey, H. D., Schmidt, M. A. & Kiggans, J. O., Alumina grain growth in a microwave field, *J. Am. Ceram. Soc.*, **74**(7) (1991) 1675.
8. Janney, M. A. & Kimrey, H. D., Diffusion-controlled processes in microwave-fired ceramics, in Ref. 2, p. 215.
9. Patil, D., Mutsuddy, B. & Garard, R., Microwave reaction sintering of oxide ceramics, *J. Microwave Power and Electromagnetic Energy*, **27** (1992) 49.
10. Boch, P., Lequeux, N. & Piluso, P., Reaction sintering of ceramic materials by microwave heating, in Ref. 3, p. 211.
11. Piluso, P., Lequeux, N. & Boch, P., Microwave sintering of ceramics. In *Euro-Ceramics*, eds G. Ziegler & H. Haussner, Deutsche Keramische Ges. Publ., Köln, Germany, 1993, p. 557.
12. Piluso, P., Lequeux, N. & Boch, P., Microwave reaction-sintering of aluminium titanate and mullite ceramics. In *Third Euro-Ceramics*, eds P. Duran & J. F. Fernandez, Faenza Editrice Publ., San Vicente, Spain, Vol I, 1993 p. 1017.
13. Piluso, P., Lequeux, N. & Boch, P., Reaction and densification of mullite and aluminium titanate ceramics heat-treated in a 2.45 GHz microwave furnace. In *Nanostructure and Properties of Materials*, eds N. Igata & Dimitrov, Annales de Chimie - Science des Matériaux Publ., Paris, France, 1993 p. 101.
14. Piluso, P., Thèse, Etude du frittage réactif de la mullite et du titanate d'aluminium par chauffage micro-onde, Université Pierre et Marie Curie, Paris, France, September 1993, (in French).
15. Nurse, R. W., Welch, J. H. & Majundar A. J., System $CaO-Al_2O_3$ in a moisture-free atmosphere. In *Phase Diagrams for Ceramists, III*, The Am. Ceram. Soc., Westerville, USA, 1975, p. 103.
16. Microwave Processing of Materials IV, eds M. F. Iskander, R. J. Lauf & W. H. Sutton, *Mat. Res. Proc.*, **347** Pittsburgh, USA, 1994.
17. See *M. R. S. Bulletin*, **XX**, 1 (1995), for a review on Functionally Gradient Materials.

Characterization of Low Temperature Mullitization

Takayuki Ban, Shigeo Hayashi, Atsuo Yasumori & Kiyoshi Okada

Department of Inorganic Materials, Tokyo Institute of Technology, O-Okayama, Meguro, Tokyo 152, Japan

(Accepted 22 July 1995)

Abstract

Anomalously low temperature mullitization was observed in the precursor prepared by the Nishio and Fujiki's method using aluminum nitrate nonahydrate (ANN), aluminum iso-propoxide (AIP), and silicon ethoxide (TEOS) and its mechanism was examined by various methods. The low temperature mullitization was found to occur only when the precursor was once heat-treated at 250°C before heating up to crystallization. The heat-treated precursor showed two-step mullitization with small amounts of mullitization at 450°C and large amount of mullitization at 900°C. On the other hand, the as-prepared precursor showed one-step mullitization at around 900°C. The presence of two small regions with slightly different chemical composition was found in the particles of the heat-treated precursor samples by ^{29}Si nuclear magnetic resonance (NMR) spectra, small angle X-ray scattering (SAXS) and X-ray Rietveld analysis. The low temperature mullitization was considered to occur at the interfaces of the two small regions because they acted as the heterogeneous nucleation sites.

Introduction

Since mullite, $\text{Al}_{4+2x}\text{Si}_{2-2x}\text{O}_{10-x}$, is one of the important ceramic materials, mullitization from various starting materials has been intensively investigated by many workers.^{1,2} Mullite precursors prepared by various methods are known to be grouped into two types of mullitization pathways. One type shows direct mullitization from the amorphous phase at around 1000°C whereas another one shows formation of the spinel phase at similar temperatures and mullitization occurring at higher temperatures, i.e. around 1200°C. The former precursor is considered to be in the homogeneous mixing state for SiO_2 and Al_2O_3 components, whilst the latter precursor is considered to be in an unhomogeneous state.³ On the other hand, some workers recently reported the mullitization which could not be grouped into

these two categories. Mullitization by these precursors occurred at much lower temperatures than those of the mullitization at around 1000°C. Hulding and Messing⁴ first reported such low temperature mullitization phenomena. They prepared precursors by drying a sol prepared from ANN and TEOS, followed by aging the gel in a steamed atmosphere at 80°C. The precursor crystallized directly to orthorhombic mullite at 700°C. Fischer *et al.*⁵ reported similarly low temperature mullitization for the precursors prepared from aluminum sec-butylate and silicon chloride. Mullite formed by low temperature mullitization was extremely richer in the Al_2O_3 composition (88 mol%) than the ordinary composition (60 mol%) and its lattice showed $a > b$ relation; the opposite to those of the ordinary mullites. Nishio and Fujiki⁶ prepared mullite long fibers using the sol-gel method. They found that mullite started to crystallize at 600°C from the amorphous state when it was heated, as fibers formed though mullitization occurred at around 1000°C when the powdered sample was heated. We have categorized this as low temperature mullitization in this paper because the mullitization occurred below 900°C.

A different feature was suggested in low temperature mullitization compared with those of the ordinary mullitizations which occur at around 1000°C and/or above 1000°C. However, the mechanisms of low temperature mullitization has not been extensively investigated. The purpose of this study is, therefore, to prepare a precursor which shows low temperature mullitization and to characterize the low temperature mullitization process.

Experimental Procedure

The preparation of precursors used in this study was based on the method reported by Nishio and Fujiki.⁶ In this preparation, ANN was first dissolved in deionized water and AIP and TEOS were added to this solution in that order. The aqueous solution was stirred for 2 days at room temperature, and then gelled and dried at 110°C

for 36 h. This xerogel was designated as the as-prepared sample. A part of the as-prepared xerogel was heat-treated at 250°C for 16 h and was referred as the heat-treated sample. In order to compare the mullitization behavior of these samples, two other samples were prepared the following way. The starting solution was prepared by dissolving ANN in ethanol and then by adding TEOS. It was stirred at room temperature for 3 h. Then, a homogeneous type precursor was prepared by slowly hydrolyzing TEOS and gelling the solution by water included in ANN at 60°C for 4 weeks. An unhomogeneous type precursor was prepared by adding ammonia into the solution which formed a precipitation. The homogeneous and unhomogeneous type precursors were designated as the slowly hydrolyzed (SH) method sample and the rapidly hydrolyzed (RH) method sample, respectively. Chemical composition of all these samples was arranged to $\text{Al}_2\text{O}_3 = 60$ mol%, i.e. $3\text{Al}_2\text{O}_3 \cdot 2\text{SiO}_2$ composition.

High resolution solid state magic angle spinning nuclear magnetic resonance (MAS-NMR) spectra were obtained at 70.26 MHz for ^{27}Al and 53.4 MHz for ^{29}Si using a JEOL GX-270 system. The samples were contained in the zirconia rotor. The ^{29}Si spectra were obtained using a pulse width of 2 μs and a recycle delay of 60 s. The ^{27}Al spectra were obtained using a pulse width of 1 μs and a recycle delay of 10 s. The spinning frequency for the both spectra was 3.8 kHz. The chemical shift (δ) of ^{29}Si spectra was referenced by tetramethylsilane at $\delta = 0.0$ ppm, in which the chemical shift was referenced by polydimethylsilane at $\delta = -33.8$ ppm. The chemical shift of ^{27}Al spectra was referenced by $\text{Al}_2(\text{SO}_4)_3 \cdot 18\text{H}_2\text{O}$ at $\delta = 0$ ppm.

Infrared absorption (IR) spectra were obtained by the KBr disk method using a JEOL JIR-6000 system. A pellet was prepared by mixing 0.01 g of sample with 0.25 g of KBr powder and formed by a uniaxial press. The spectra were measured for a wave number range between 400 and 4000 cm^{-1} . Differential thermal analysis (DTA) curves were measured from room temperature to 1100°C at a heating rate of 10°C/min using about 20 mg of sample. Small angle X-ray scattering (SAXS) measurements were carried out using a glass cell 10 mm in width. The range measured was between 0.1 and 3.0 nm^{-1} in a scattering vector using Mo $\text{K}\alpha$ radiation.

Each sample was fired at 400–1000°C for 1 h and the crystalline phase in their samples were examined by powder X-ray diffraction (XRD) using Cu $\text{K}\alpha$ radiation monochromated by a graphite. The XRD measurements were performed by two scanning methods. Measurements for identification of the crystalline phase were made by

the usual continuous scanning method with a scanning speed of 1°/min for a scanning range from 10–50° in 2θ . Structural parameters for some mullites were refined by the Rietveld method⁷ using the RIETAN program.⁸ The XRD profiles for the Rietveld analysis were measured using the step scanning method with a step scanning width of 0.02° and a fixed time of 20 s for a scanning range from 30 to 100° in 2θ . The details of the structure refinement procedure was reported elsewhere.⁹ The amount of mullite formed was evaluated from the scale factor obtained by the Rietveld analysis.

Results and Discussion

Figure 1 shows the XRD patterns of the as-prepared samples and the heat-treated samples heated at various temperatures. The as-prepared sample heated at 400–800°C showed an amorphous pattern. Mullite and a small amount of spinel phase were observed in the as-prepared sample heated at 1000°C. In contrast, mullite began to crystallize at 450°C in the heat-treated sample.

Mullite formation curves in the as-prepared sample, the heat-treated sample, the SH method

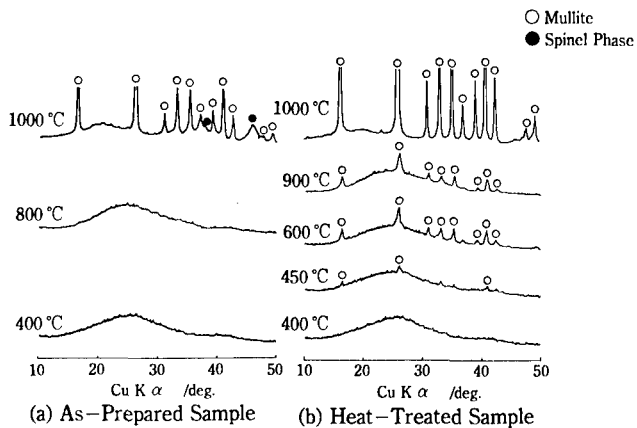


Fig. 1. XRD patterns of the as-prepared sample (a) and the heat-treated sample (b) fired at various temperatures for 1 h.

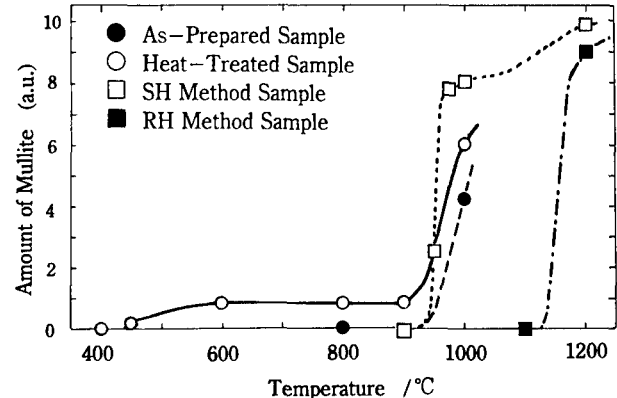


Fig. 2. Formation curves of mullite in the as-prepared sample (●), the heat-treated sample (○), the SH method sample (□) and the RH method sample (■).

sample and the RH method sample are shown in Fig. 2. In the as-prepared sample and the SH method sample, mullite started to crystallize from around 900°C and the amount increased very rapidly by 950°C, especially in the SH method sample. Mullitization in the as-prepared sample was similar to that in the SH method sample. The lower mullite formation content of the as-prepared sample can be interpreted by the co-presence of spinel phase in this sample. In the RH method sample, mullite started to crystallize from around 1100°C and the amount increased very rapidly to around 1200°C. The higher mullitization temperature of this sample was attributed to the formation of the spinel phase at around 1000°C before mullitization. On the other hand, mullite started to crystallize from around 450°C in the heat-treated sample. The amount of formed mullite was, however, very small and did not increase up to 900°C. The amount of mullite rapidly increased from 900°C, and no spinel phase formation was observed at 1000°C as shown in Fig. 1. The mullite formation curve of the heat-treated sample was largely different with respect to the starting temperature of mullitization but was similar with respect to the temperature in which most of the sample crystallized to mullite, i.e. the temperature was at around 1000°C and was similar to those of the as-prepared sample and the SH method sample.

In order to examine the influence of the heating time for the low temperature mullitization, the heat-treated sample was heated at 800°C for 24 h but there was no significant increase in the amount of mullite formed.

Chemical composition of the mullites formed at 600, 800 and 900°C was analyzed by the X-ray Rietveld method. We also evaluated the chemical composition of the mullites from the length of a -axis. The chemical compositions of the mullites obtained from both methods were around 66 mol% Al_2O_3 . The XRD of these mullites showed the similar pattern with those of the tetragonal-like mullite¹⁰ but did not show the XRD pattern of orthorhombic mullite as reported by Huling and Messing⁴ and also the relation of $a > b$ as reported by Fischer *et al.*⁵

Figure 3 shows ^{29}Si and ^{27}Al NMR spectra of the heat-treated sample, the SH method sample, and the RH method sample. All the samples were calcined at 600°C for 1 h. The ^{27}Al NMR spectra showed a complex profile and two or three peaks overlapped. Peaks were observed at around 5, 40 and 60 ppm and were assigned to six-, five- and four-coordinated Al atoms, respectively.¹¹ The intensity of the five-coordinated Al peak showed a trend to decrease as the mullitization temperature of the samples increased and no five-coordinated

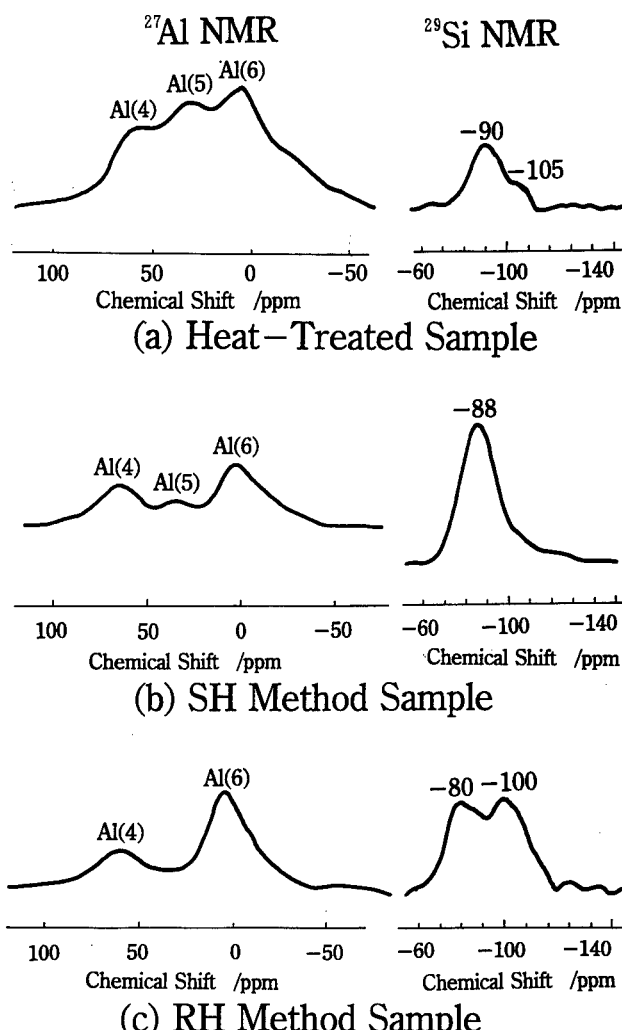


Fig. 3. ^{29}Si and ^{27}Al NMR spectra of the heat-treated sample (a), the SH method sample (b) and the RH method sample (c). All samples were calcined at 600°C for 1 h.

Al peak was observed in the RH method sample. The ^{29}Si NMR spectra showed one or two peaks depending upon the samples. The spectrum of the SH method sample showed only a single peak at around -88 ppm. This peak may be assigned to $\text{Q}^4(2\text{Al})$ or $\text{Q}^4(3\text{Al})$,¹¹ i.e. corresponding to the Q^2 or Q^1 state for the SiO_4 tetrahedral structure. On the other hand, two peaks at around -80 and -100 ppm were observed in the spectrum of the RH method sample. They may be assigned to the Q^0 and Q^3 or Q^4 structures, respectively. The spectrum of the heat-treated sample also showed two peaks and they were observed at around -90 and -105 ppm. Therefore, they may be assigned to the Q^1 or Q^2 and Q^3 or Q^4 structures, respectively.

The following models are proposed for the structure of precursors from the results of ^{27}Al and ^{29}Si NMR spectra. The precursor of the SH method sample has a homogeneous structural state and SiO_2 and Al_2O_3 components are considered to be uniformly mixed at the molecular level. On the other hand, the precursor of the RH method sample consisted of two different structural regions

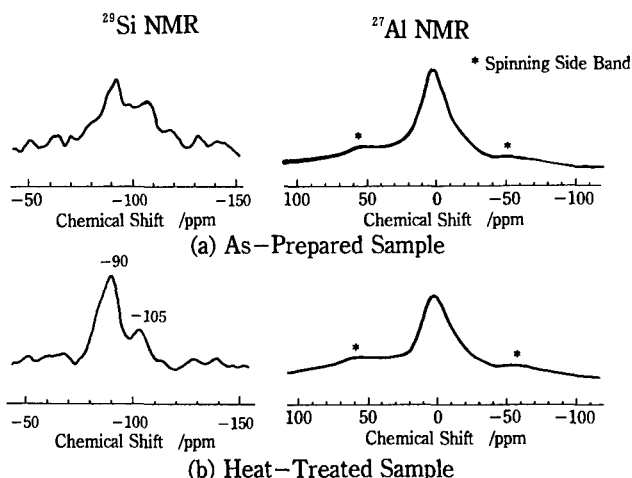


Fig. 4. ²⁹Si and ²⁷Al NMR spectra of the as-prepared sample (a) and the heat-treated sample (b).

which may correspond to an Al-rich and Si-rich chemical composition. Such a separation of chemical composition in the precursor is the reason for the phase change into the spinel phase and amorphous silica at around 1000°C before mullitization.¹ The precursor of the heat-treated sample may also consist of two different composition regions with a slightly Al-rich and Al-poor composition from the starting bulk composition.

In order to elucidate further details of the heat-treated sample, ²⁹Si and ²⁷Al NMR spectra of the heat-treated and the as-prepared samples are compared and are shown in Fig. 4. In the ²⁷Al NMR spectra of both samples, little difference was observed except for some broadening of the six-coordinated Al peak in the heat-treated sample. However, there was a certain difference between their ²⁹Si NMR spectra. The spectrum of the as-prepared sample showed broad complex peaks ranging from -80 to -120 ppm, therefore, they were considered to consist of a number of overlapped peaks. This indicates that there were various polymerization states in SiO₄ tetrahedra of this sample. On the other hand, the spectrum of the heat-treated sample showed two clear peaks at -90 and -105 ppm. These peaks can be assigned to Q¹ or Q² and Q³ or Q⁴ structures, respectively. It may indicate that there were two different states in the polymerization structure of SiO₄ tetrahedra of the heat-treated sample. Since this sample shows low temperature mullitization, whereas the as-prepared sample shows no low temperature mullitization, the difference of these polymerization states of SiO₄ tetrahedra is suggested to correspond to the difference of mullitization in the both samples.

Figure 5 shows SAXS curves of the as-prepared sample and the heat-treated sample. In the as-prepared sample, SAXS was observed only in the small scattering vector (q) range of $q < 0.2 \text{ nm}^{-1}$.

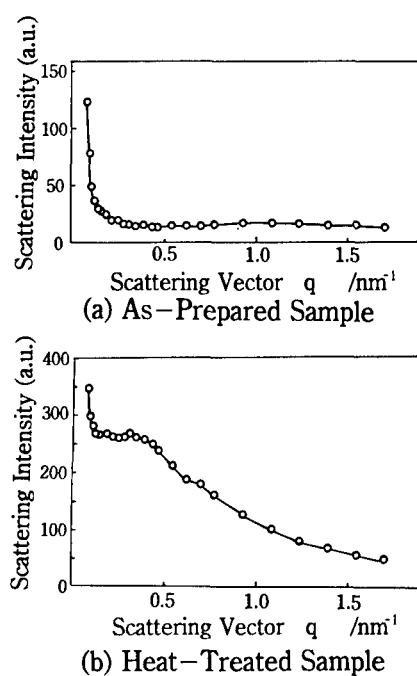


Fig. 5. SAXS curves of the as-prepared sample (a) and the heat-treated sample (b).

It is attributed to scattering from considerably larger scattering species corresponding to the sub-micron size region, in which size corresponds to the particle size of the precursor samples. On the other hand, the SAXS curve of the heat-treated sample showed not only the scattering in the range of $q < 0.2 \text{ nm}^{-1}$ but also the broad scattering in the range of $q > 0.2 \text{ nm}^{-1}$. This broad scattering is attributed to the scattering from relatively smaller scattering species corresponding from angstrom to nanometer order size region. From these SAXS data, we can conclude that the heat-treatment of the sample at 250°C caused very small unhomogeneous structure regions in nanometer size within the precursor particles.

The DTA curves of the as-prepared sample and the heat-treated sample are shown in Fig. 6. Some difference was observed between the two DTA curves. In the DTA curve of the as-prepared sample, endothermic reaction was observed in a wide temperature range from 100 to 400°C. They consisted of some numbers of overlapped endothermic peaks, which were caused due to the various reactions such as dehydration, dehydroxylation and the decomposition of nitrate and alkoxy groups. On the other hand, the DTA curve of the heat-treated sample differed largely from that of the as-prepared sample and showed a clear single endothermic peak at 360°C. During the heat-treatment at 250°C, a partial thermal decomposition of the hydroxyl groups and the rearrangement of the precursor structure are suggested to occur in the sample. In the DTA curve of the heat-treated sample, a weak and broad exothermic peak was

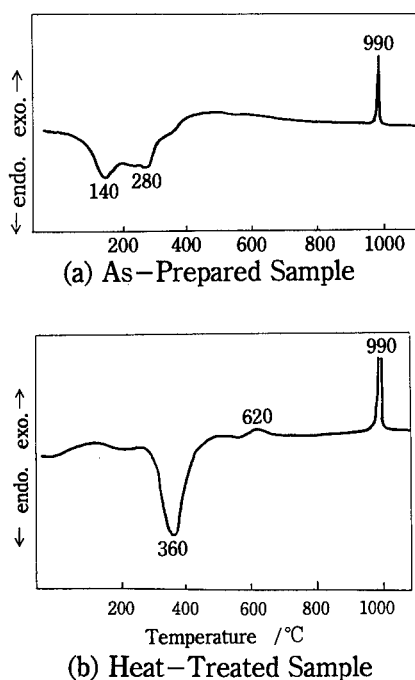


Fig. 6. DTA curves of the as-prepared sample (a) and the heat-treated sample (b).

detected at around 620°C but was not observed in that of the as-prepared sample. This exothermic peak may be corresponding to the low temperature mullitization. On the other hand, the exothermic peak at 990°C was attributed to the crystallization of mullite. Although the intensity of the exothermic peaks in these samples showed little difference, it can be interpreted by the difference of weight loss of the samples with and without heat-treatment at 250°C.

As mentioned in Fig. 1, mullite started to crystallize at 450°C in the heat-treated sample. Therefore, the endothermic peak at 360°C is considered to be important for low temperature mullitization. To examine the structural change by

this endothermic reaction, the heat-treated sample was further heated at 400°C for 1 h. The IR and NMR spectra of the heat-treated sample and the sample further heated at 400°C are shown in Fig. 7. The ^{27}Al NMR spectrum of the heat-treated sample showed only a single peak at 0 ppm, which is assigned to six-coordinated Al structure. On the other hand, the ^{27}Al NMR spectrum of the sample heated at 400°C showed three peaks at 0, 30, and 60 ppm, which are assigned to six-, five-, and four-coordinated Al structures, respectively. Evolution of the four- and five-coordinated Al structures were found in the sample heated at 400°C and this structural change was considered to be derived from the dehydration of Al-OH. On the other hand, changes in the ^{29}Si NMR spectra was not observed except for a little broadening of the peaks and the two peaks still remained at -90 and -105 ppm in both samples. The broadening of the peaks may be related to the condensation reaction of Si-OH and Al-OH by dehydration. In the IR spectrum of the heat-treated sample, a weak absorption band was observed at 950 cm⁻¹, in which the absorption band resembles that of the OH group in diaspore (α -AlOOH).¹² In the IR spectrum of the sample heated at 400°C the absorption band was not observed, whereas a weak and broad absorption band at 850 cm⁻¹ was observed. Since the absorption band at 850 cm⁻¹ may be assigned to that of the condensed AlO₄ tetrahedra,¹² it is also a comparable result to explain the condensation reaction of Al polyhedra by heating at 400°C.

We found that heat-treatment at 250°C was very important in causing low temperature mullitization. Structural change during this treatment was characterized by various methods and the following change was observed: dehydration and

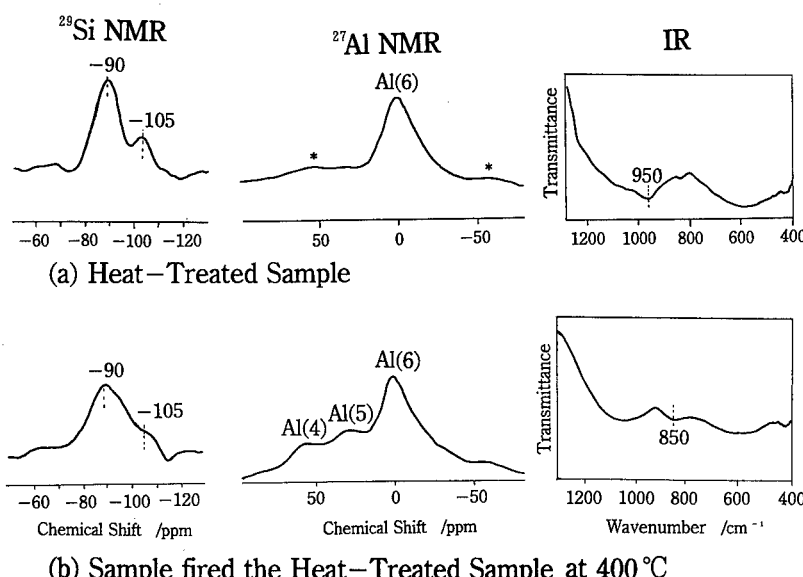


Fig. 7. IR and ^{29}Si and ^{27}Al NMR spectra of the heat-treated sample (a) and the sample further heated the heat-treated sample at 400°C (b).

decomposition of part of the nitrate and alkoxy groups occurred due to the treatment. This change introduced very small unhomogeneous structural regions with a slightly different chemical composition in the precursor particles. These two regions remained even after heating at 400°C, by which temperature condensation and re-arrangement of the precursor were considered. When such small regions with different chemical compositions are present within the particles, the interfaces between them are considered to be energetically active and can act as the heterogeneous nucleation sites. Therefore, low temperature mullitization can occur in the interfaces only by heating at relatively low temperatures. The amount of mullite formed by low temperature mullitization was, however, small because the mullitization occurred only in the interfaces of two regions in the precursor particles. The experimental result was that no apparent increase in the formation amount of mullite occurred, even though the duration at the low mullitization temperature is compatible with the consideration mentioned above.

Conclusions

Mullite precursor was prepared from the combination of ANN, AIP and TEOS based on the Nishio and Fujiki's method⁶ and the mullitization process was examined using various methods. The following conclusions were obtained:

- (1) Heat-treatment at 250°C was essentially necessary for the low temperature mullitization and the heat-treated precursor started to show mullitization at 450°C.
- (2) The formation curve of mullite in low temperature mullitization showed a two-step curve with small amount of mullitization at 450°C and large amount of mullitization at 900°C.

- (3) The precursor to show the low temperature mullitization had two small regions with slightly different chemical composition within the precursor particles.
- (4) The interfaces between these two regions in the precursor particles played an important role as the heterogeneous nucleation sites for low temperature mullitization.

References

1. Okada, K., Otsuka, N. & Soma, S., Review of Mullite synthesis routes in Japan. *Am. Ceram. Soc. Bull.*, **70** (1991) 1633-40.
2. Aksay, I. A., Dabbs, D. M. & Sarikaya, M., Mullite for structural, electronic, and optical applications. *J. Am. Ceram. Soc.*, **74** (1991) 2343-58.
3. Okada, K. & Otsuka, N., Characterization of the spinel phase from $\text{SiO}_2\text{-Al}_2\text{O}_3$ xerogels and the formation process of mullite. *J. Am. Ceram. Soc.*, **69** (1986) 652-6.
4. Huling, J. C. & Messing, G. L., Chemistry-crystallization relations in molecular mullite gels. *J. Non-Crystall. Solids*, **147/148** (1992) 213-21.
5. Fischer, R. X., Schneider, H. & Voll, D., The crystallization process of high alumina mullites. *J. Eur. Ceram. Soc.*, **16** (1996) 109-13.
6. Nishio, T. & Fujiki, Y., Preparation of mullite fiber by sol-gel method. *J. Ceram. Soc. Jpn.*, **99** (1991) 654-9.
7. Rietveld, H. M., A profile refinement method for nuclear and magnetic structure. *J. Appl. Crystallogr.*, **2** (1969) 65-71.
8. Izumi, F., A software package for the Rietveld analysis of X-ray and neutron diffraction patterns. *Nippon Kessho Gakkaishi*, **27** (1985) 23-31.
9. Ban, T. & Okada, K., Structure refinement of mullite by the Rietveld method and a new method for estimation of chemical composition. *J. Am. Ceram. Soc.*, **75** (1992) 227-30.
10. Schneider, H. & Lipinski, T. R., Occurrence of pseudo-tetragonal mullite. *J. Am. Ceram. Soc.*, **71** (1988) C162-4.
11. Kirkpatrick, R. J., Smith, K. A., Schramm, S. E., Turner, G. & Yang, W. H., Solid-state nuclear magnetic resonance spectroscopy of minerals. *Ann. Rev. Earth Planet. Sci.*, **13** (1985) 29-47.
12. Ryskin, Ya. I., The vibrations of protons in minerals: hydroxyl, water and ammonium. In *The Infrared Spectra of Minerals*, ed. V. C. Farmer. Mineralogical Society, London, 1974, pp. 137-81.

Anisotropic Grain Growth in Seeded and B_2O_3 -doped Diphasic Mullite Gels

S.-H. Hong, W. Cermignani & G. L. Messing

Department of Materials Science and Engineering, The Pennsylvania State University, University Park, PA 16802, USA

(Accepted 22 July 1995)

Abstract

Anisotropic grain growth in mullite was investigated in B_2O_3 -doped diphasic gels seeded with either mullite particles or whiskers. Anisotropic grain growth was observed in all systems. The largest anisotropic grains were obtained with a system seeded with 2 wt% mullite whiskers and doped with 2 wt% B_2O_3 . The mullite whiskers act as sites for multiple nucleation and subsequently as templates for mullite overgrowth. Boria lowered the mullite formation temperature by 150°C and it significantly enhanced anisotropic grain growth independent of the presence of seed particles. This enhancement was attributed to increased dissolution of alumina.

1 Introduction

Anisotropic grain growth is one class of *in situ* reaction that is relatively unexplored but appears to offer significant opportunity for the development of new materials with self-reinforcing microstructures. Silicon nitride (Si_3N_4) is exemplary of how the mechanical properties of a polycrystalline ceramic can be improved by optimizing grain growth of anisotropic β -silicon nitride grains during the α to β - Si_3N_4 phase transformation. Today, silicon nitrides with fracture toughnesses of 10–20 MPa $m^{1/2}$ can be routinely produced. Such highly fracture-resistant materials are a result of extensive experimentation. There is surprisingly little fundamental understanding about the processes leading to growth of anisotropic grains. Although silicon nitride has excellent mechanical characteristics, its low oxidation resistance limits its use in high temperature applications. Clearly, there is a need for oxide ceramics having similar self-reinforcing microstructures.

Mullite ($3Al_2O_3 \cdot 2SiO_2$) has been recognised as an important structural and optical material due to its excellent high temperature strength, creep resistance, good chemical and thermal stability,

low thermal expansion coefficient and infrared transparency.^{1–3} The stable crystal structure of mullite is orthorhombic with lattice parameters $a = 7.5456 \text{ \AA}$, $b = 7.6898 \text{ \AA}$ and $c = 2.8842 \text{ \AA}$ (JCPDS Card # 15-776), and is composed of octahedral AlO_6 chains aligned in the c -direction and crosslinked by corner-shared AlO_4 and SiO_4 tetrahedra.⁴ Thus, unrestricted growth parallel to the c -axis favours the development of anisotropic grains.

A number of authors have demonstrated that sol–gel processes can be designed to control the degree of alumina–silica mixing and, consequently, control mullite crystallization kinetics, densification and microstructure evolution.⁵ Several authors^{6–10} have studied microstructural development of aluminosilicates with compositions near the single-phase mullite region. Equiaxed grains in alumina-rich mullites have been attributed to the kinetic limitation of material transport by solid-state diffusion whereas the presence of a liquid phase has been suggested to facilitate the growth of anisotropic grains in silica-rich mullites (i.e. <74 wt% Al_2O_3). While a sol–gel polymeric mixture resulted in the equiaxed microstructure, variations in local chemical heterogeneity in a sol–gel colloidal mixture lead to anisotropic mullite grains at the same composition (72 wt% Al_2O_3).⁵

In ceramic systems which transform by nucleation and growth, another way to control microstructure evolution is to seed the precursor material. A homogeneous, fine-grained matrix ceramic can be obtained by using seed concentrations $> 10^{13}$ seed particles/cm³ of matrix material. Huling and Messing¹¹ demonstrated that a fully dense, nominally 0.2 μm grain size mullite was obtained by seeding a diphasic gel with 30 wt% polymeric gels. They also reported that a hybrid gel consisting of polymeric and diphasic gels could be designed to control the nucleation frequency, reduce the grain size, and increase the microstructural homogeneity in a manner analogous to particle seeding. Mroz and Laughner¹² utilized

seeding to enhance anisotropic grain growth of mullite and reported that a dense, equiaxed grain structure was developed at a relatively high seed concentration, whereas highly anisotropic, large grains dispersed in a matrix of small, equiaxed grains were obtained at a low seed concentration.

Important factors affecting grain growth processes are: (1) the grain size of the microstructure when the sintered products become fully dense, and able to support grain growth (i.e. free of boundary inhibiting pores); and (2) the transport rate and solubility in systems with liquid phases. A dense, fine-grain microstructure has a large surface free energy associated with the grain boundaries and, thus, a large driving force for grain growth. The importance of a fine initial microstructure for anisotropic grain growth was recently demonstrated in TiO_2 -doped alumina obtained by seeding an alumina gel.¹³

In the mullite system, it is known that densification is aided by viscous flow of the amorphous silica phase and that this glass phase also enhances the development of anisotropic grains. The viscosity of the glass phase in mullite can be decreased by several orders of magnitude by adding glass-forming oxides such as boron oxide (B_2O_3) and phosphorous oxide (P_2O_5). Na_2O , which is known to lower the viscosity of silica glasses, did not enhance either the mullite crystallization kinetics or the densification rate.¹⁴ However, the grain size increased and grain morphology changed from equiaxed to anisotropic with increasing Na_2O concentration. When B_2O_3 was added to a mullite precursor, it was reported to react first with alumina to form aluminum borate, $9Al_2O_3 \cdot 2B_2O_3$, a stable crystalline compound,¹⁵ and then to form the mullite phase. Thus, B_2O_3 significantly decreased the temperature of mullite formation.

The crystal structure of aluminum borate ($9Al_2O_3 \cdot 2B_2O_3$) is orthorhombic, it has lattice parameters $a = 7.6874(8)$ Å, $b = 15.0127(5)$ Å and $c = 5.6643(6)$ Å (JCPDS Card # 32-3) and it consists of AlO_6 octahedra, AlO_4 tetrahedra, AlO_5 coordination polyhedra and B_2O_3 triangles.¹⁶ Based on similarities in the crystal structure and lattice parameters, it is reasonable to propose that aluminum borate can act as an epitaxial substrate for mullite nucleation and growth. Based on transmission electron microscope analysis, Richards *et al.* reported that the glass-forming oxides such as B_2O_3 or P_2O_5 do not exist as free glassy phases at the grain boundaries in sol-gel derived mullite fibres.¹⁷

While anisotropic grains are often observed in mullite ceramics, there have been few attempts to develop a self-reinforcing mullite microstructure. Also, it is not well understood how boria affects the mullite transformation kinetics and micro-

structural development. In this paper, we report a series of experiments designed to learn how the initial microstructure and the grain boundary chemistry can be adjusted to obtain a self-reinforced mullite microstructure. The objective of these initial studies is to learn about the fundamental factors controlling anisotropic grain growth in mullite.

2 Experimental Procedure

Microstructural development was evaluated for two series of samples. The first series of samples was seeded with either mullite seed particles or mullite whiskers. Any differences between these samples can be attributed primarily to the effect of the seeds on the mullite formation and subsequent microstructure evolution. Boria was added to a second series of samples to investigate the role of phase equilibria and transport on the mullite formation and anisotropic grain growth.

The diphasic sols were prepared from boehmite [$\gamma-AlO(OH)$] powder (Catapal D, Vista Chemical Co., Houston, TX) and a silica sol (Ludox AS-40, Du Pont Co., Wilmington, DE). Additional details are described elsewhere.¹¹ All samples contained identical Al_2O_3/SiO_2 ratios prior to calcination and were within the single-phase mullite region (~73 wt% Al_2O_3).

A mullite seed dispersion was prepared by dispersing a commercial mullite powder (Chichibu Cement Co., Ltd, Saitama, Japan) in distilled water adjusted to pH 3 with nitric acid. The dispersion was stirred for 3 days, sonicated and centrifuged at 2000 rev min⁻¹ for 30 min and the particles in suspension were used for seeding. The particle size distribution of the mullite seed particles was measured by a laser scattering technique (Horiba LA-900, Horiba Instrument Inc., Irvine, CA). The mullite whiskers (MW-10, Chichibu Cement Co. Ltd, Saitama, Japan) were dispersed in a manner similar to the mullite powder. The boria was introduced to the sol system as boric acid (H_3BO_3).

After heterocoagulating the boehmite and silica sol, they were gelled at 80°C. The gels were dried for 12 h at 80°C, ground with an alumina mortar and pestle, and sieved to < 74 μm (~200 mesh). The powder was dry pressed at low pressure and then pellets, 12.7 mm diameter and 3 mm thickness, were cold isostatically pressed at 200 MPa. The pressed pellets were heated in air from 1600 to 1650°C for 1 to 10 h. For microstructure observation, the sintered samples were cut in half, polished with 0.1 μm diamond paste and thermally etched at 100°C below the sintering temperature.

The micrographs were taken near the centre of the sample. An apparent aspect ratio was measured on the polished surface, but so far we have not attempted to calculate or measure the true aspect ratio.

The mullite formation temperature was determined by differential thermal analysis (DTA) at $10^\circ\text{C min}^{-1}$ in air (Thermal Analyst 2100, TA Instrument, New Castle, DE). X-ray diffraction (XRD) was used to determine the phases present after calcination, and the apparent density of the sintered samples was measured by the Archimedes method.

3 Results and Discussion

3.1 Mullite particle seeding

As determined by inductively coupled plasma emission spectroscopy (Leeman Labs PS3000UV), the composition of the mullite powder is 71.5 wt% Al_2O_3 and 28.5 wt% SiO_2 . This composition is very close to that of 3:2 mullite (~ 71.8 wt% Al_2O_3). From the XRD measurement of the mullite powder, there was no angular separation of the reflection pair $(1\ 2\ 0)/(2\ 1\ 0)$ around $26^\circ 2\theta$, indicating that the seed particles are pseudotetragonal mullite.¹⁸ The median particle size of the as-received powder was $\sim 1.6\ \mu\text{m}$ and the median size of the mullite seed particles was $\sim 0.14\ \mu\text{m}$, with the size range from 0.05 to $0.4\ \mu\text{m}$. The mullite seed particles are spherical and agglomerate-free as confirmed by scanning electron microscopy (SEM).

The mullite formation temperature in the diphasic gels was determined from the DTA exothermic peak maximum. As shown in Fig. 1, the mullite formation temperature decreases from 1345 to 1330°C at 2 wt% seeding. At 10 wt% seeding, the

temperature decreases to 1318°C . The $\sim 30^\circ\text{C}$ decrease in mullite formation temperature relative to the unseeded diphasic gel is comparable to earlier results by Huling and Messing.¹¹ With increasing particle seed concentration, the exothermic mullite formation peak broadens and is obscured by the background. Broadening of the exothermic peak with increasing seed concentration indicates that mullite formation occurs over a wide temperature range. The plateau in mullite formation temperature was shown earlier to be a result of a change in the mullite formation mechanism from nucleation control to interface reaction control.¹⁹

The unseeded and seeded samples were $\sim 97\%$ dense after sintering for 5 h at 1650°C . The microstructures of the unseeded and seeded diphasic gels sintered at 1650°C for 5 h are compared in Fig. 2. In the unseeded samples (Fig. 2(A)), most of the grains are equiaxed with a small number of anisotropic grains whose largest aspect ratio does not exceed 3. The as-received mullite powder, which was sintered at the same sintering condition, yields the same microstructure and approximately the same sintered density as the unseeded colloidal sample. The microstructure of the 0.05 wt% seeded sample (Fig. 2(B)) is similar to the unseeded sample and shows both inter- and intragranular pores. The 0.05 wt% seed concentration corresponds to $\sim 4 \times 10^{11}$ seed particles/ cm^3 of mullite powder and is the same order of magnitude as the intrinsic nucleation density in a similar diphasic mullite system.²⁰ In the 2 wt% seeded sample (Fig. 2(C)), anisotropic grains with an aspect ratio of $\sim 5\text{--}6$ are distributed in a matrix of micrometre-sized grains. Most of the intragranular pores were eliminated as a result of the grain size refinement.¹¹ The aspect ratio in the 10 wt% seeded sample (Fig. 2(D)) does not change much relative to the 2 wt% seeding concentration, but a larger fraction of anisotropic grains was observed. The matrix grains were free of intragranular pores and were $\sim 2\ \mu\text{m}$ in size with rectangular or square shapes. The grains with the polyhedral shapes are most likely end-on views of anisotropic mullite grains.

To determine how the anisotropic grains develop, the 2 wt% seeded samples were sintered at 1600 and 1650°C for 1 to 10 h. After 5 h at 1600°C , the samples are dense with only a few intragranular pores and quite small intergranular pores. The microstructure consists of some anisotropic grains with aspect ratios between 2 and 3 in a matrix of equiaxed, micrometre-sized grains (Fig. 3(A)). A similar microstructure is observed after sintering for 1 h at 1650°C (Fig. 3(B)). Larger anisotropic grains are formed and the aspect ratio increases with increasing sintering

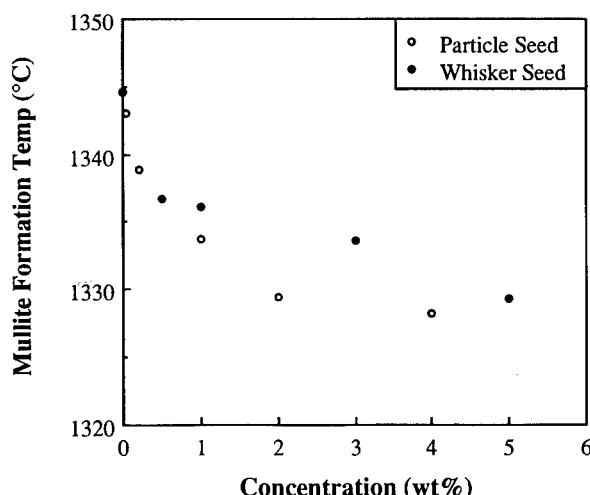


Fig. 1. Temperature of DTA exothermic peak maximum for mullite formation as a function of mullite particle and whisker concentration (heating rate: $10^\circ\text{C min}^{-1}$).

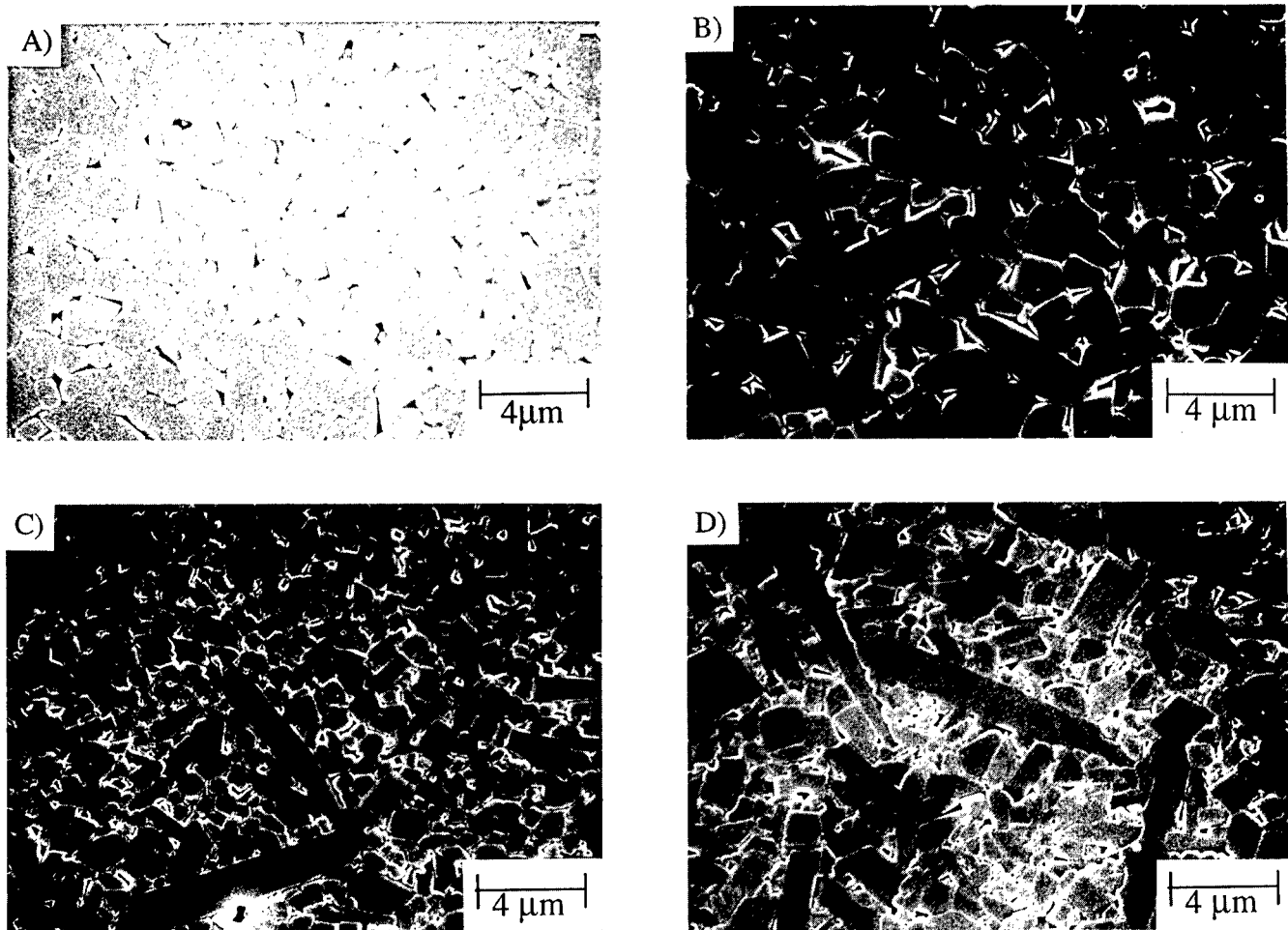


Fig. 2. SEM micrographs of polished diphasic mullite gels heated at 1650°C, 5 h. (A) unseeded; (B) 0.05 wt% mullite seeds; (C) 2 wt% mullite seeds; and (D) 10 wt% mullite seeds.

time and temperature, even though the surrounding equiaxed grains change little. This suggests that the anisotropic grains are nucleated early in the process. With increasing time and temperature, the anisotropic grains impinge and thicken to yield a microstructure of highly anisotropic grains with no intragranular pore.

The evolution of the above microstructure can be explained in terms of the driving force for grain growth and diffusion distance for pore elimination. For low or no seeding, there is a small number of mullite nuclei and grains grow from these nuclei by consuming the amorphous matrix. Thus, as pointed out earlier,²¹ mullite grain boundaries sweep through a larger volume and hence, more pores during the conversion to mullite, thus leaving some of the pores isolated within the grains (Figs 2(A) and 2(B)). In the samples which were seeded above the intrinsic nucleation density, mullite seeds are the active nucleation sites, and thus reduce the grain size after complete mullite conversion. The smaller grains have a large driving force for grain growth. Some grains begin to grow at the expense of the surrounding smaller grains, and these grains become anisotropic (Fig. 2(C)). After a longer sintering time, the anisotropic

grains continue to grow until they impinge. The impinged anisotropic grains cannot grow further, thus these grains begin to thicken. In highly seeded samples (Fig. 2(D)), such as 10 wt% seeding, the grains are initially much finer and the driving force for sintering and grain growth is larger than for lower seeding concentrations. Therefore, samples with a high seed concentration, sintered for a shorter time, develop a microstructure similar to samples with a lower seed concentration, but sintered for a longer time, as shown in Fig. 2(D) and in Fig. 3(D), respectively.

3.2 Mullite whisker seeding

The single crystal mullite whiskers shown in Fig. 4 have an average length of $\sim 5 \mu\text{m}$ and a diameter of $\sim 1 \mu\text{m}$. The chemical composition of the mullite whisker is 73 wt% Al_2O_3 ; the same as that of the diphasic matrix.

The apparent density decreases slightly with increasing whisker seed concentration, and the relative density of 5 wt% whisker seeded samples sintered at 1650°C for 5 h decreased to 95%.

The mullite formation temperature decreases with increasing whisker concentration (Fig. 1). At 5 wt% whisker seed concentration, the mullite

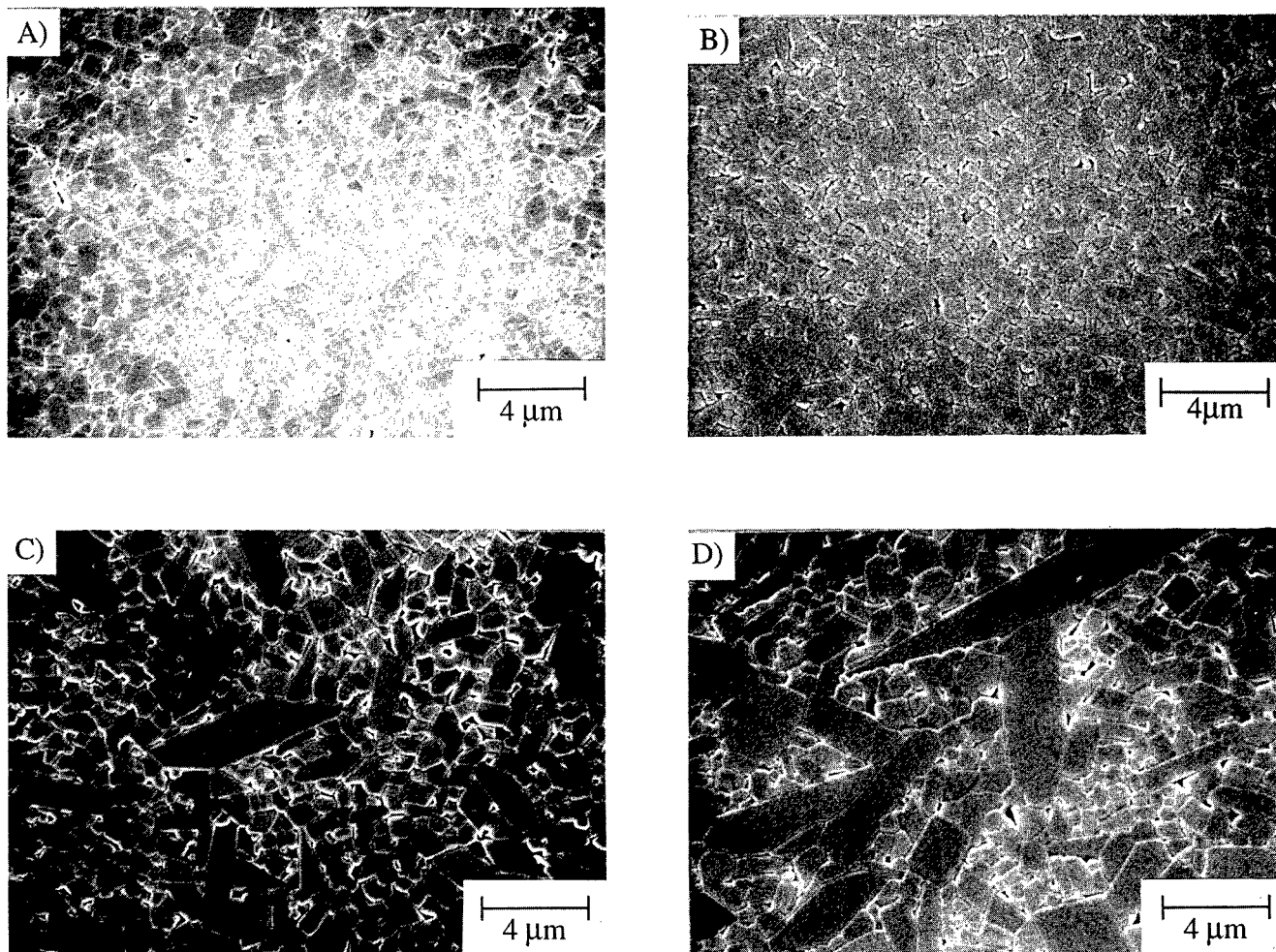


Fig. 3. Effect of time and temperature on the microstructural development of 2 wt% particle seeded mullite gels: (A) 1600°C, 5 h; (B) 1650°C, 1 h; (C) 1650°C, 5 h; and (D) 1650°C, 10 h.

formation temperature decreases by 15°C relative to that of the unseeded sample. In the whisker seeding case, the number of particles per unit weight of seeds is significantly less than in the particle seeding case but interestingly the mullite formation temperature is approximately the same. This suggests that each whisker acts as a site for multiple nucleation.

The micrographs of 1 wt% and 5 wt% whisker seeded samples sintered at 1650°C for 5 h are

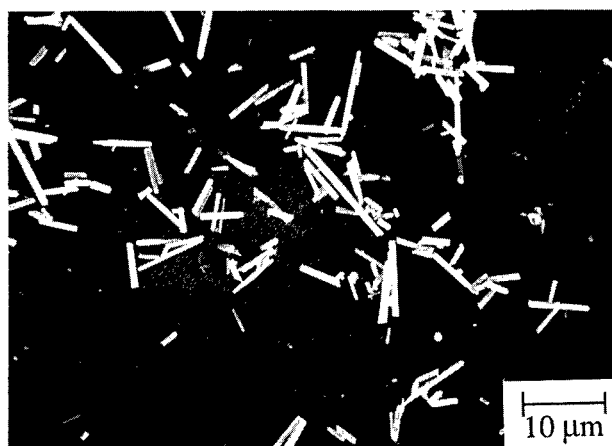


Fig. 4. SEM micrograph of single crystal mullite whiskers.

shown in Fig. 5. As a result of the preparation method, the whisker seeds are randomly distributed. At 1 wt% whiskers, the mullite grains appear to grow more in the axial direction rather than in the radial direction, which leads to an aspect ratio of ~8. At 5 wt% whisker concentration, many randomly distributed, anisotropic grains form and impinge to form a three-dimensionally interlocked microstructure. Again, the whiskers do not continue to grow in the axial direction, but grow in the radial direction, thus thickening the anisotropic grains and reducing the aspect ratio.

The microstructure of the 2 wt% whisker seeded colloidal mullite sample sintered at 1500°C and chemically etched with hydrofluoric acid (HF) for 15 min is shown in Fig. 6. It is evident that the whisker-shaped grain in the centre of the micrograph acted as a site for multiple nucleation. In this sample and many others observed, the anisotropic grains appear to have a mullite whisker core surrounded by an overgrowth layer as demonstrated by the presence of intragranular pores. The intragranular pores in this sample are reduced with increasing temperature and are completely eliminated at 1650°C.

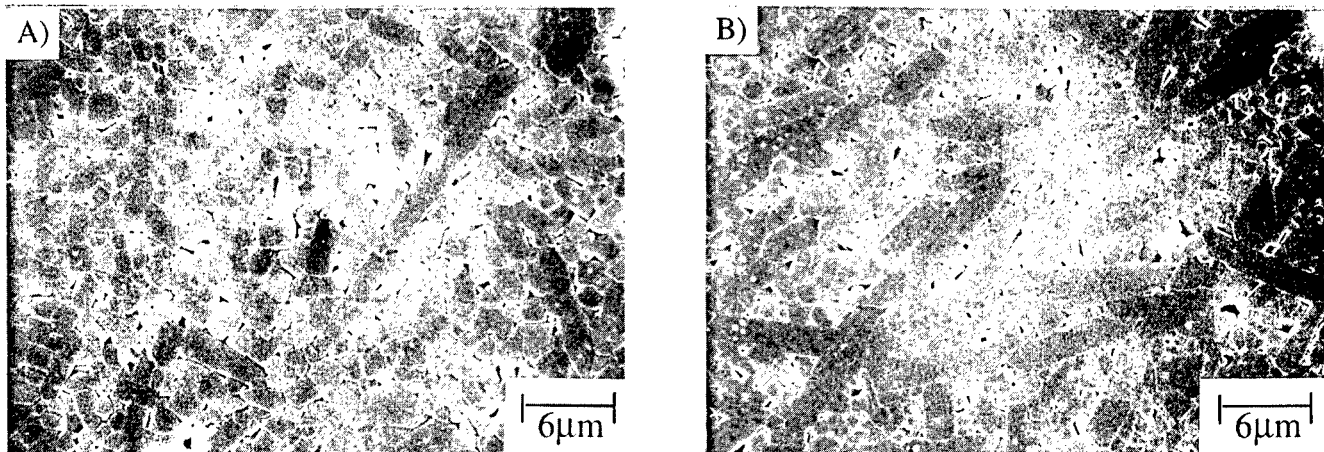


Fig. 5. SEM micrographs of mullite whisker seeded diphasic mullite gels heated at 1650°C for 5 h: (A) 1 wt% mullite whiskers; and (B) 5 wt% mullite whiskers.

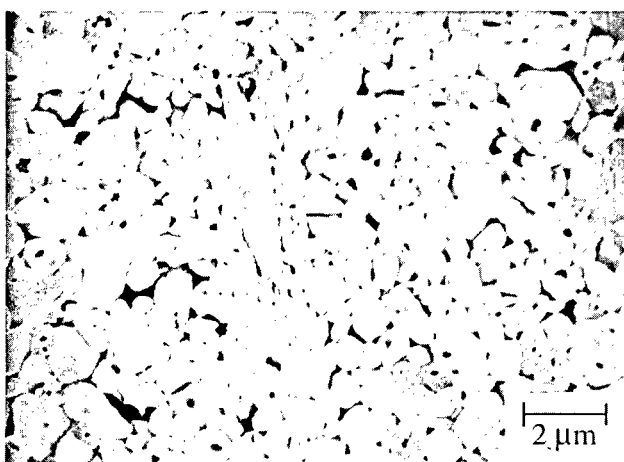


Fig. 6. SEM micrograph of chemically etched, whisker seeded diphasic mullite gel sintered at 1500°C for 5 h.

In both particle seeding and whisker seeding, the same microstructure was developed. However, seeding with whiskers allows for the possibility of aligning the elongated grains: e.g. if another forming method, such as tape casting or extrusion, is used, it is possible to develop a two-dimensionally textured microstructure.^{22,23}

3.3 Boria-doped gels

As expected, the apparent density decreases with increasing boria concentration. For example, the apparent density of the 5 wt% B₂O₃-doped sample is 2.994 g cm⁻³. The lower density may be due to the large pores surrounding the anisotropic grains as well as the lower theoretical density of B₂O₃.

Sowman¹⁵ reported that in the Al₂O₃-B₂O₃-SiO₂ system, aluminum borate (9Al₂O₃·2B₂O₃) forms first in a polymeric gel and then aluminum borosilicate crystalline phase forms by a solid solution reaction with SiO₂. He attributed the sharp exothermic peak at 885°C to the formation of an aluminum borate compound. Richards *et al.*¹⁷ noted that this composition is not in the

stable mullite phase field and contains a high B₂O₃ concentration (12.5 wt%). In 2 wt% boria-doped sol-gel derived mullite fibre, a sharp exothermic peak at 911°C was confirmed by XRD to be associated with the formation of the spinel phase, and no aluminum borate phase was detected.

In our experiments, up to 5 wt% boria was added to a diphasic gel. However, no sharp exothermic peak was observed around 885°C but a strong exothermic peak was observed between 1200 and 1350°C, which is associated with the mullite formation. No diffraction peaks for aluminum borate or aluminum borosilicate phase were detected before mullite formation, and only mullite was observed after mullite formation. A broad peak at low diffraction angles in the XRD increased with increasing boria concentration, suggesting an increase in glass content with increasing B₂O₃. The diffraction pattern of the sample sintered at 1650°C for 5 h shows an increase in (111), (121) and (331) peak intensities relative to the undoped mullite sample. This may be due to the incorporation of boron into the mullite, although this is still under investigation.

Based on chemical analysis, 60 wt% of the boria remained in the 5 wt% boria-doped sample after sintering at 1650°C for 5 h. Richards *et al.*¹⁷ reported that after 60 h at 1400°C, 65 wt% of the B₂O₃ in their fibres volatilized. Even though our samples were sintered at higher temperature, a higher percentage of boria remained in the samples. This may be due to differences in sample dimensions and geometry. For example, the diffusion distance from the mullite fibres of Richards *et al.*¹⁷ is significantly less than the bulk pellet samples used in this study.

The mullite formation temperature is plotted in Fig. 7 as a function of boria concentration for both unseeded and 2 wt% mullite particle seeded samples. The mullite formation temperature

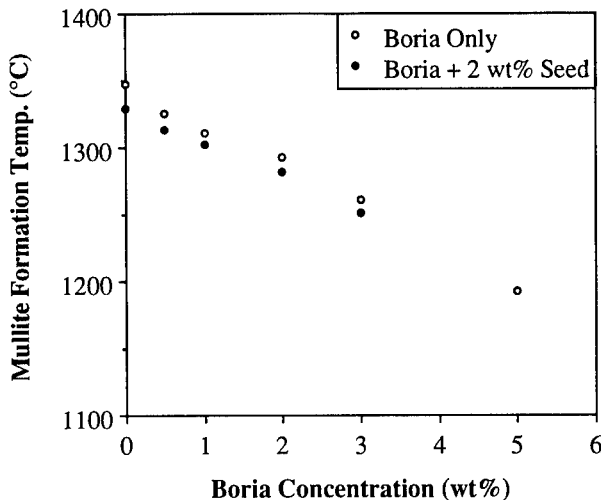


Fig. 7. Temperature of DTA exothermic peak maximum for unseeded and 2 wt% mullite particle seeded diphasic mullite gels as a function of boria addition.

decreases with increasing boria concentration for both samples. At 5 wt% boria, the mullite formation temperature decreases by 150°C relative to the undoped diphasic gel. This indicates that boria has a more dominant effect on the transformation kinetics than seeding. One possibility is that the boroaluminosilicate glass promotes mullite forma-

tion by increasing the solubility of alumina and diffusion rate in the glass phase.

Note that the microstructures of the 2 wt% particle seeded and unseeded samples are similar when B_2O_3 is present. As in the powder seeding and whisker seeding cases, the transformation peak broadened with higher boria concentrations, such that a distinct exotherm could not be observed for the 5 wt% B_2O_3 , 2 wt% particle seeded sample.

Micrographs of the unseeded and 2 wt% particle seeded samples containing B_2O_3 sintered at 1650°C for 5 h are shown in Fig. 8. There is no major difference between the two samples at the same B_2O_3 concentration. In both systems, increasing the boria concentration causes the growth of highly anisotropic grains. At 5 wt% boria, most of the grains are anisotropic and their cross-sections are square or rectangular shaped. There are only a few equiaxed grains. Also, there are several intergranular pores around the anisotropic grain surfaces while there are very few intragranular pores.

3.4 Whisker seeded diphasic mullite with boria

To combine the whisker seeding and boria doping

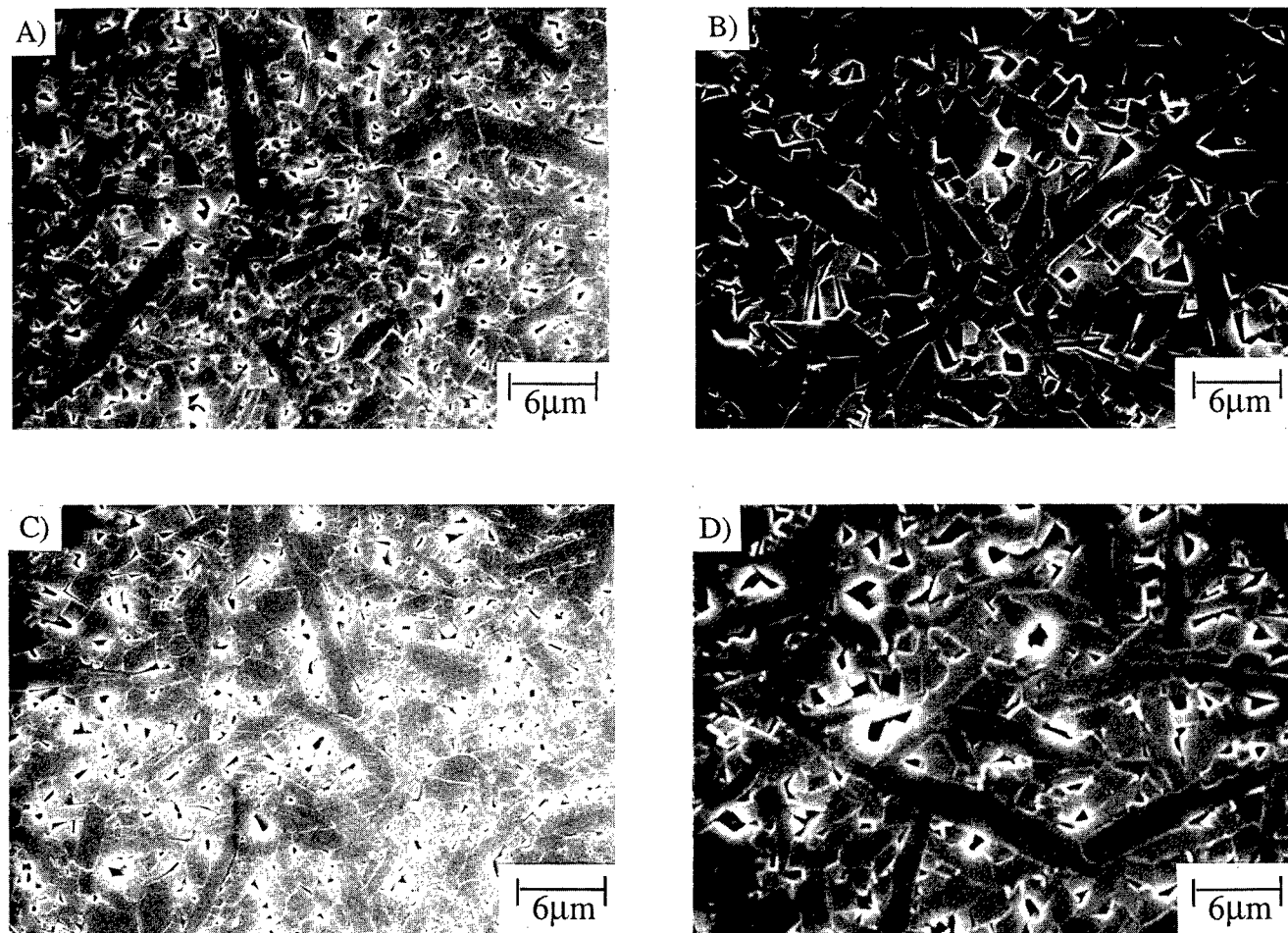


Fig. 8. SEM micrographs of samples heated at 1650°C, 5 h. Diphasic mullite gels doped with: (A) 2 wt% boria; (B) 5 wt% boria; and 2 wt% mullite particle seeded diphasic mullite doped with: (C) 2 wt% boria, (D) 5 wt% boria.

effects, 2 wt% boria was added to 2 wt% whisker seeded diphasic mullite sample. The mullite formation temperature is similar to the 2 wt% boria-doped diphasic mullite. Clearly, a microstructure of three-dimensionally interlocked, anisotropic grains is developed when this system was heated at 1650°C for 5 h (Fig. 9). Some highly anisotropic grains have an aspect ratio of >10 and a length of $>30 \mu\text{m}$.

A model for the microstructure development in whisker seeded and boria-doped diphasic mullite is shown in Fig. 10. Initially, the mullite whiskers are randomly distributed in the amorphous matrix which contains boria (stage A in Fig. 10). The single crystal whiskers provide multiple nucleation sites for overgrowth of mullite. At the same time, intrinsic nucleation occurs in the amorphous matrix (stage B). It is proposed that the boria-containing amorphous matrix facilitates the transport of diffusing ions to their preferred site along the *c*-axis of the whisker. Thus, the exaggerated, anisotropic grains develop by oriented overgrowth on the whiskers. At the same time, the surrounding grains are only slightly anisotropic at this stage. With further heating, a highly anisotropic microstructure is developed when the matrix grains also undergo anisotropic growth (stage C).

4 Summary

Seeding a diphasic mullite gel with mullite particles results in a decrease in the mullite formation temperature and the development of a fine-grained microstructure. Fine grains have a large driving force for grain growth and promote the preferential growth of mullite along its *c*-axis by coalescence of the surrounding fine grains to yield an anisotropic grain microstructure. At high seed concentration or at longer sintering time, the aspect ratio is limited by the impingement of the elongated grains and thickening occurs instead.

The mullite whiskers act as multiple nucleation sites for the diphasic precursor to form an 'overgrowth' layer. This overgrowth layer continues to grow with increasing temperature, resulting in highly anisotropic grains. Increasing the whisker concentration results in a gradual decrease in aspect ratio due to earlier impingement of the grains.

The boria-containing matrix enhances the mullite transformation kinetics and decreases the transformation temperature by 150°C compared with unseeded, undoped colloidal samples. The lower temperature appears to result from increased alumina solubility. By seeding with whiskers and doping with boria, highly anisotropic microstructures

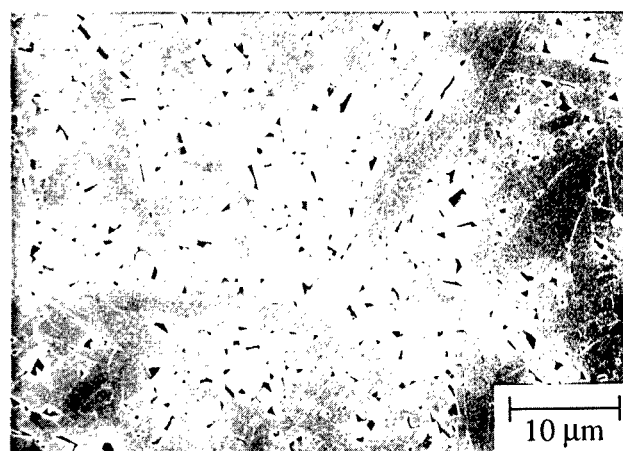
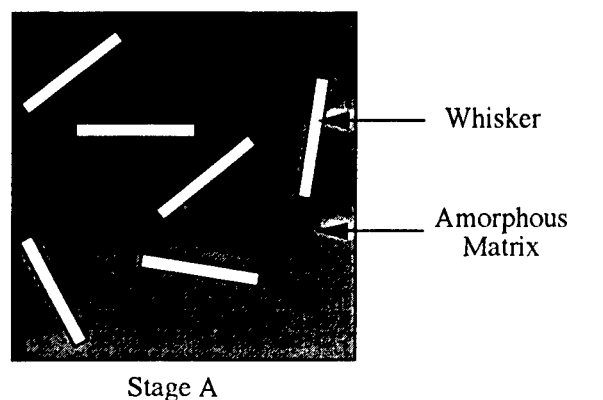
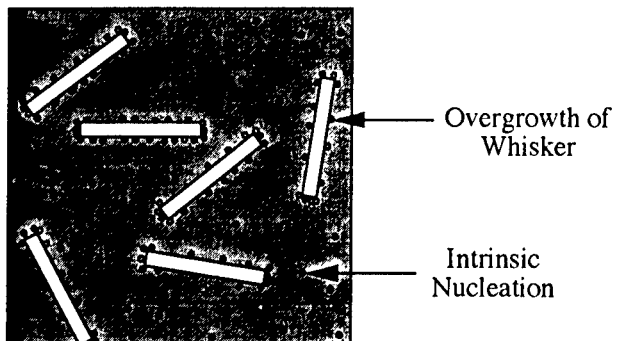


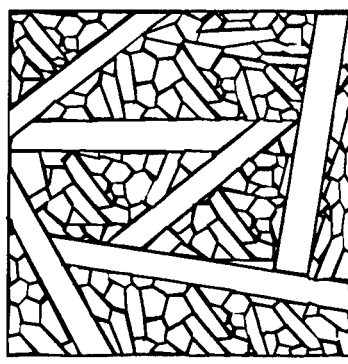
Fig. 9. SEM micrograph of 2 wt% whisker seeded and 2 wt% boria-doped diphasic mullite gel sintered at 1650°C for 5 h.



Stage A



Stage B



Stage C

Fig. 10. Schematic model of microstructural development in whisker seeded and boria-doped diphasic mullite gel.

consisting of anisotropic grains with lengths as long as 30 μm and aspect ratios as high as 10 were developed.

Acknowledgements

The authors gratefully acknowledge the support of the Office of Naval Research under grant number N00014-94-1-0007. One of us (W.C.) thanks the Cooperative Research Program of the Center for Advanced Materials at Penn State for support.

References

1. Aksay, I. A., Dabbs, D. M. & Sarikaya, M., Mullite for structural, electronic, and optical applications. *J. Am. Ceram. Soc.*, **74**(10) (1991) 2343-58.
2. Lessing, P. A., Gordon, R. S. & Mazdiyasni, K. S., Creep of polycrystalline mullite. *J. Am. Ceram. Soc.*, **58**(3-4) (1975) 149.
3. Prochazka, S. & Klug, F. J., Infrared-transparent mullite ceramic. *J. Am. Ceram. Soc.*, **66**(12) (1983) 874-80.
4. Yla-Jaaski, J. & Nissen, H.-U., Investigation of superstructures in mullite by high resolution electron microscopy and electron diffraction. *Phys. Chem. Minerals*, **10** (1983) 47-54.
5. Pask, J. A., Zhang, X. W., Tomsia, A. P. & Yoldas, B. E., Effect of sol-gel mixing on mullite microstructure and phase equilibria in the $\alpha\text{-Al}_2\text{O}_3\text{-SiO}_2$ system. *J. Am. Ceram. Soc.*, **70**(10) (1987) 704-7.
6. Von Lohre, W. & Urban, H., Contribution to the morphology of mullite. *Ber. Dtsch Keram. Ges.*, **37** (1960) 249-51.
7. Ismail, M. G. U., Arai, H., Nakai, Z. & Akiba, T., Mullite whiskers from precursor gel powders. *J. Am. Ceram. Soc.*, **73**(9) (1990) 2736-9.
8. Sacks, M. D. & Pask, J. A., Sintering of mullite-containing materials: I, effect of composition. *J. Am. Ceram. Soc.*, **65**(2) (1982) 65-70.
9. Perry, G. S., Microwave dielectric properties of mullite. *Trans. Brit. Ceram. Soc.*, **72** (1973) 279-83.
10. Ohashi, M., Tabata, H., Abe, O., Kanzaki, S., Mitachi, S. & Kumazawa, T., Preparation of translucent mullite ceramics. *J. Mater. Sci. Lett.*, **6** (1987) 528-30.
11. Huling, J. C. & Messing, G. L., Hybrid gels for homoepitactic nucleation of mullite. *J. Am. Ceram. Soc.*, **72**(9) (1989) 1725-9.
12. Mroz, T. J. & Laughner, J. W., Microstructures of mullite sintered from seeded sol-gels. *J. Am. Ceram. Soc.*, **72**(3) (1989) 508-9.
13. Horn, D. S. & Messing, G. L., Anisotropic grain growth in titania-doped alumina. *Mat. Sci. Eng. A.*, **A195** (1995) 169-78.
14. Fahrenholtz, W. G. & Smith, D. M., Densification and microstructure of sodium-doped colloidal mullite. *J. Am. Ceram. Soc.*, **77**(5) (1994) 1377-80.
15. Sowman, H. G., Alumina-boria-silica ceramic fibers from the sol-gel process. In *Sol-Gel Technoloy for Thin Films, Fibers, Performs, Electronics, and Specialty Shapes*, ed. L. C. Klein, Noyes, Park Ridge, NJ, 1988, pp. 162-82.
16. Ihara, M., Imai, K., Fukunaga, J. & Yoshida, N., Crystal structure of boro-aluminate, $9\text{Al}_2\text{O}_3\cdot2\text{SiO}_2$. *Yogyo Kyokaishi*, **33**(2) (1980) 2605-9.
17. Richards, E. A., Goodbrake C. J. & Sowman, H. G., Reactions and microstructure development in mullite fibers. *J. Am. Ceram Soc.*, **74**(10) (1991) 2404-9.
18. Schneider, H. & Lipinski, T. R., Occurrence of pseudo-tetragonal mullite. *J. Am. Ceram. Soc.*, **71**(3) (1988) C-162-4.
19. Huling, J. C. & Messing, G. L., Epitactic nucleation of spinel in aluminosilicate gels and its effect on mullite crystallization. *J. Am. Ceram. Soc.*, **74**(10) (1991) 2374-81.
20. Wei, W.-C. & Halloran, J. W., Transformation kinetics of diphasic aluminosilicate gels. *J. Am. Ceram. Soc.*, **71**(1) (1988) 581-7.
21. Huling, J. C. & Messing, G. L., Hybrid gels designed for nucleation and crystallization control of mullite. In *Better Ceramics Through Chemistry IV (Materials Research Society Symposium Proceedings Vol. 180)*, eds B. J. J. Zelinski, C. J. Brinker, D. E. Clark & D. R. Ulrich, Materials Research Society, Pittsburgh, PA, 1990, pp. 515-26.
22. Sabol, S. M., Messing, G. L. & Tressler, R. E., Textured alumina fibers with elongated grains. *HiTemp Review 1992*, Vol. 1, NASA CP-10104, 21-1-14, 1992.
23. Wu, M. & Messing, G. L., Fabrication of oriented SiC whisker-reinforced mullite matrix composites by tape casting. *J. Am. Ceram. Soc.*, **77**(10) (1994) 2586-92.

Single-phase and Diphasic Aerogels and Xerogels of Mullite: Preparation and Characterization

Sridhar Komarneni* & Claire Rutiser

Intercollege Materials Research Laboratory, The Pennsylvania State University, University Park, PA 16802, USA

(Accepted 22 July 1995)

Abstract

Single-phase mullite composition gels have been synthesized using tetraethoxysilane [$Si(OC_2H_5)_4$] and aluminum nitrate nonahydrate as precursors. Diphasic mullite gels have been prepared using colloidal silica and boehmite as precursors. Xerogels and aerogels of both the above gels have been obtained by ordinary drying in air at 60°C and critical point drying in methanol, respectively. Single-phase xerogels show an intense exothermic peak at about 980°C while their counterparts, aerogels, do not show any detectable exotherm by differential thermal analysis (DTA). These results suggest that the structure of single phase gels changed during critical point drying and the structural changes were investigated by solid-state ^{27}Al magic angle spinning nuclear magnetic resonance (MAS NMR) spectroscopy. No differences between diphasic xerogels and aerogels could be detected by DTA because there was little or no effect of drying on the discrete silica and alumina phases. The tetrahedral coordination of Al in single-phase mullite gel changed to octahedral coordination as detected by MAS NMR during critical point drying, which suggests that the alumina component segregated. Both single-phase and diphasic aerogels of mullite composition showed very high surface areas in the temperature range 1000–1400°C and these may be useful for high temperature catalytic applications.

Introduction

The concept of diphasic nanocomposites for the synthesis of mullite, $Al_6Si_2O_{13}$ and other compositions was first introduced by us.^{1–3} The diphasic mullite gels led to enhanced densification at very low temperatures.^{4–5} The mechanism of nucleation and densification in single and diphasic gels has been studied by numerous investigators.^{6–12} Solid-

state nuclear magnetic resonance studies of ^{27}Al and ^{29}Si have revealed that single-phase gels made from aluminum nitrate and tetraethoxysilane are mixed on an atomic to molecular level while the diphasic gels are mixed on a nanometre scale.^{13–14}

The single-phase gels crystallize to mullite at lower temperatures than the diphasic gels. The rapid crystallization of mullite in the former gels is not conducive for densification while the diphasic gels led to enhanced densification apparently due to densification and crystallization in a very narrow temperature range.¹⁵ The enormous worldwide interest in mullite for high temperature structural applications is due to its high creep and thermal shock resistance as well as its high strength at very high temperatures. For extremely good mechanical properties, the achievement of full densification with fine microstructure and without any glassy phase is imperative. This is the reason why there are numerous studies on mullite densification. The study of porous mullite ceramics for high temperature catalysis, separations, etc., has, however, been neglected. Thus the objectives of this study are (1) to prepare and characterize single-phase and diphasic aerogels and xerogels of mullite and (2) to characterize the porosity characteristics of these mullite gels after sintering to high temperatures.

Experimental

Preparation of mullite single-phase gels

Mullite single-phase gels and diphasic gels were made by the procedure used previously.^{1,4,5} Aluminum nitrate nonahydrate (56.16 g) was mixed with 95% ethyl alcohol (75 ml) and stirred for 1 h. Tetraethylorthosilicate (TEOS) (11.1 ml) was added and the sol was poured into tubes and kept at 60°C until gelation. After gelation, gels were exchanged in methanol for 4–12 days more. Aerogels were made by critical point drying and xerogels were made by drying at 60°C.

*Also with the Department of Agronomy.

Preparation of mullite diphasic gels

Mullite diphasic gels, with excess Al_2O_3 (nominal composition: 86.5% Al_2O_3 –13.5% SiO_2) were made by mixing boehmite (39.34 g) with 160 ml of distilled water for 30 min. Concentrated nitric acid was added to bring the pH to 3. Commercial colloidal silica (Ludox AS40) was added (12.12 g) and the sol was stirred. The sol was poured into glass tubes and gelled. After gelation the diphasic gels were exchanged with methanol. Diphasic mullite aerogels and xerogels were made in the same fashion as those of single-phase mullite gels.

Aerogel preparation by supercritical drying

Both the single-phase and diphasic mullite gels were aged in methanol at room temperature for 4–12 days to exchange residual water out of the pores of the gels. Aerogels were produced by methanol or ethanol critical point drying at 260 or 270°C and 8.27 MPa in a 50 ml Hastalloy C autoclave (Autoclave Engineers). Both single-phase and diphasic mullite gels were run simultaneously so they would have identical drying conditions. The two types of gel in Pyrex tubes were critical point dried in each 4 h run of the autoclave. Two tubes were placed in the autoclave, and 15 ml of alcohol was added to maintain alcohol vapour pressure during the heating period to prevent the premature loss of pore fluid from the gel. An anti-seize compound (Permatex Industrial anti-seize lubricant) was added to the threads, and the vessel was sealed. The autoclave was pre-pressurized with nitrogen to 8.27 MPa, and a three-stage program was activated on the Omega CN 2041 programmable temperature controller. The first stage heated the autoclave from room temperature to 260 or 270°C over 3 h. The pressure was released manually every 15–30 min to maintain the autoclave pressure in the range 8.27 to 8.96 MPa. For the second stage, the pressure was maintained at 8.27 MPa and the temperature was kept at 260 or 270°C. After 15 min into this second stage, the argon valve was opened and the autoclave exhaust valve was opened slightly to purge the supercritical methanol from the chamber. After 15 min of purging, the pressure on the autoclave vessel was released and the temperature was allowed to decrease slowly.

Sintering of aerogels

Sintering was carried out on unground samples. Each individual aerogel sample was sub-sampled for nitrogen BET analysis. Then samples of about 0.1 g each were removed for sintering. The aerogel and xerogel samples were sintered at 900, 1000, 1200 and 1400°C for 2 h. A Lindberg programmable furnace was used with a heating rate of 2°C

min^{-1} ; cooling rates were no greater than 2°C min^{-1} . Samples were weighed before and after sintering to determine weight loss. Sintering was carried out in platinum trays with platinum foil covering the samples.

Characterization of aerogels

The aerogels were characterized to determine thermal stability, analyse the phases present, and measure textural properties. BET nitrogen adsorption analysis was the primary characterization technique for textural properties.

Powder X-ray diffraction of variously treated aerogels and xerogels

Powder X-ray diffraction (XRD) was carried out using a Scintag X-ray diffractometer with Ni-filtered CuK_α radiation. Powders were dispersed on glass slides using ethanol. The diffraction data were analysed using standard commercial software and the standard diffraction data provided by the Joint Committee on Powder Diffraction Standards (JCPDS).

Differential thermal analysis

The xerogels and aerogels were characterized by differential thermal analysis (DTA) with a Perkin-Elmer DTA 1700 instrument using a heating rate of 10°C min^{-1} in air.

^{27}Al magic angle spinning nuclear magnetic resonance (MAS NMR) spectroscopy

The mullite aerogel and xerogel samples were characterized by ^{27}Al MAS NMR spectroscopy using a SDS 360 instrument operating at a Larmor frequency of 94.669 MHz. The samples were spun at 8.5 to 10.5 kHz and the chemical shifts are reported as ppm with respect to $[\text{Al}(\text{H}_2\text{O})_6]^{3+}$ as an external standard.

Scanning electron microscopy (SEM)

An ISI DS-130 scanning electron microscope was used for determining the particle size and morphology of the as-prepared and sintered single-phase and diphasic aerogels.

BET nitrogen adsorption analysis

Surface area analysis and pore size distribution were determined by multi-point BET analysis and by adsorption and desorption isotherms of nitrogen using an Autosorb-1 (Quantachrome, Syosset, New York). As-prepared aerogels and sintered aerogels were ground gently in an agate mortar with a pestle. Powders (0.04 to 0.08 g) were weighed and transferred to glass BET tubes of known weight. The samples were degassed at 60°C for 30 min or longer. The samples were weighed in

BET tubes and true sample weights were calculated, following standard procedures.

Twenty-point adsorption isotherms and 20-point desorption isotherms were obtained for each sample. The multipoint BET surface area was determined using up to eight adsorption points. Pore size distribution was determined using desorption $D(v)dr$ plots. For comparison purposes, a numerical pore size figure was determined by measuring the centre of the peak at half of the maximum peak amplitude.

Results and Discussion

Differential thermal analysis curves of aerogels and xerogels are shown in Fig. 1. The single-phase xerogel shows an intense exotherm at about 980°C (Fig. 1(A)), as expected based on previous studies, due to atomic or molecular scale mixing of alumina and silica components.^{13,14} The single-phase aerogel, however, shows no exotherm (Fig. 1(B)) in the high temperature range 500–1200°C in a similar way to that of a diphasic mullite gel (Fig. 1(C)). The absence of an exotherm at 980°C in single-phase mullite aerogel was unexpected, but it was expected in the case of diphasic mullite aerogel, the latter being based on previous studies

of diphasic xerogels.¹ Thus, the single-phase mullite aerogel is showing a thermal behaviour similar to that of a diphasic aerogel or xerogel. The above implies that the single-phase mullite gel may have altered during methanol critical point drying to a type of diphasic gel, probably due to the segregation and crystallization of alumina phase.

This hypothesis was tested by powder XRD and ^{27}Al MAS NMR spectroscopy. The as-prepared single-phase xerogel and aerogel show somewhat similar XRD patterns (not shown) with little or no crystallinity and, thus, no difference between the two can be detected. Boehmite could not be detected in the as-prepared aerogel by XRD. The as-prepared diphasic aerogel shows boehmite which is one of the starting phases. The amorphous silica sol cannot be detected by XRD, as expected. The segregation and crystallization of alumina phase to boehmite-like phase during critical point drying of single-phase mullite gel at 270°C is uncertain based on these XRD studies. For this reason, ^{27}Al MAS NMR spectra of the three different gels (Fig. 2) were obtained to detect any differences. The single-phase xerogel (Fig. 2(A)) shows two ^{27}Al resonances, one at 54.56 ppm and another at 0.449 ppm which can be attributed to the tetrahedral and octahedral

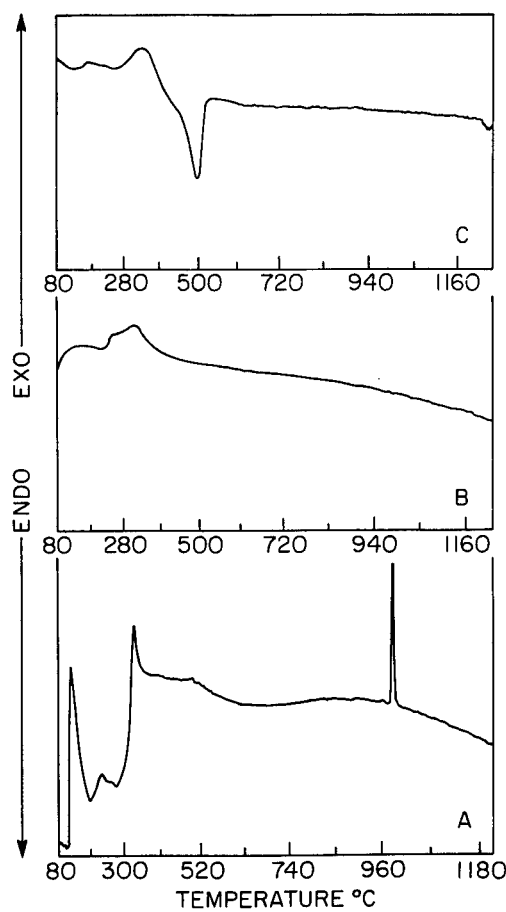


Fig. 1. Differential thermal analysis curves of (A) single-phase mullite xerogel, (B) single-phase mullite aerogel and (C) diphasic mullite aerogel.

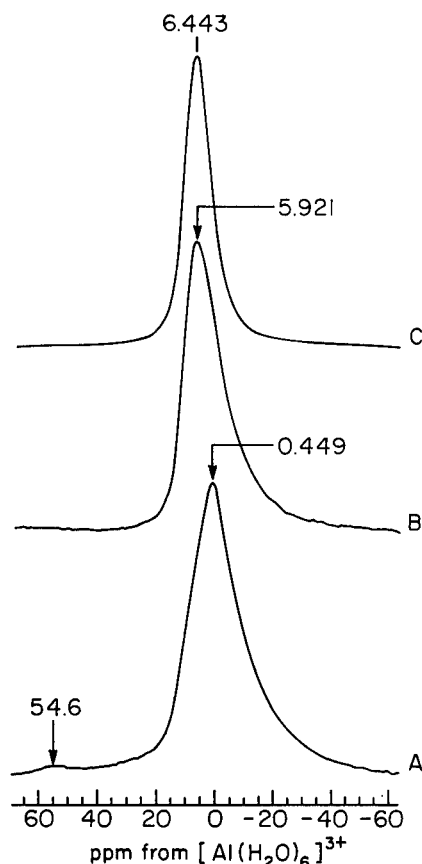


Fig. 2. ^{27}Al MAS NMR spectra of (A) single-phase mullite xerogel, (B) single-phase mullite aerogel and (C) diphasic mullite aerogel. Since these chemical shifts are not corrected for quadrupolar effects, the decimals have no significance.

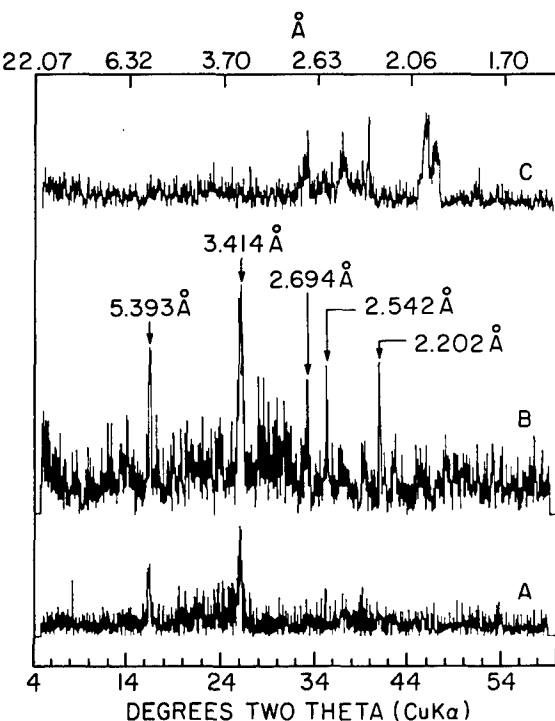


Fig. 3. Powder X-ray diffraction patterns of different mullite gels after DTA run to 1250°C: (A) single-phase xerogel shows mullite peaks, (B) single-phase aerogel shows mullite peaks and (C) diphasic aerogel shows delta alumina peaks.

coordinations, respectively. The tetrahedral coordination of Al implies that part of the Al is in the nearest neighbour environment of silicon due to atomic-scale mixing. When the single-phase gel was dried under supercritical conditions to prepare the aerogel, the ^{27}Al resonance at 54.56 ppm disappeared and only the octahedral ^{27}Al resonance at 5.92 ppm was present (Fig. 2(B)). The diphasic aerogel shows only one resonance at 6.44 ppm (Fig. 3(C)) representing all Al in octahedral coordination because boehmite is one of the starting phases which has Al in octahedral coordination only. Thus the ^{27}Al MAS NMR data show that the alumina component segregated during critical point drying of the single-phase gel to form a boehmite-like phase. These results are supported by the work of Mizushima and Hori,¹⁶ who showed that small boehmite crystals recrystallized to larger crystals during long (72 h) critical point drying of boehmite aerogels.

Powder XRD results of single-phase xerogel and aerogel and diphasic aerogel after heat treatment to 1250°C in the differential thermal equipment shows the formation of mullite in both the single-

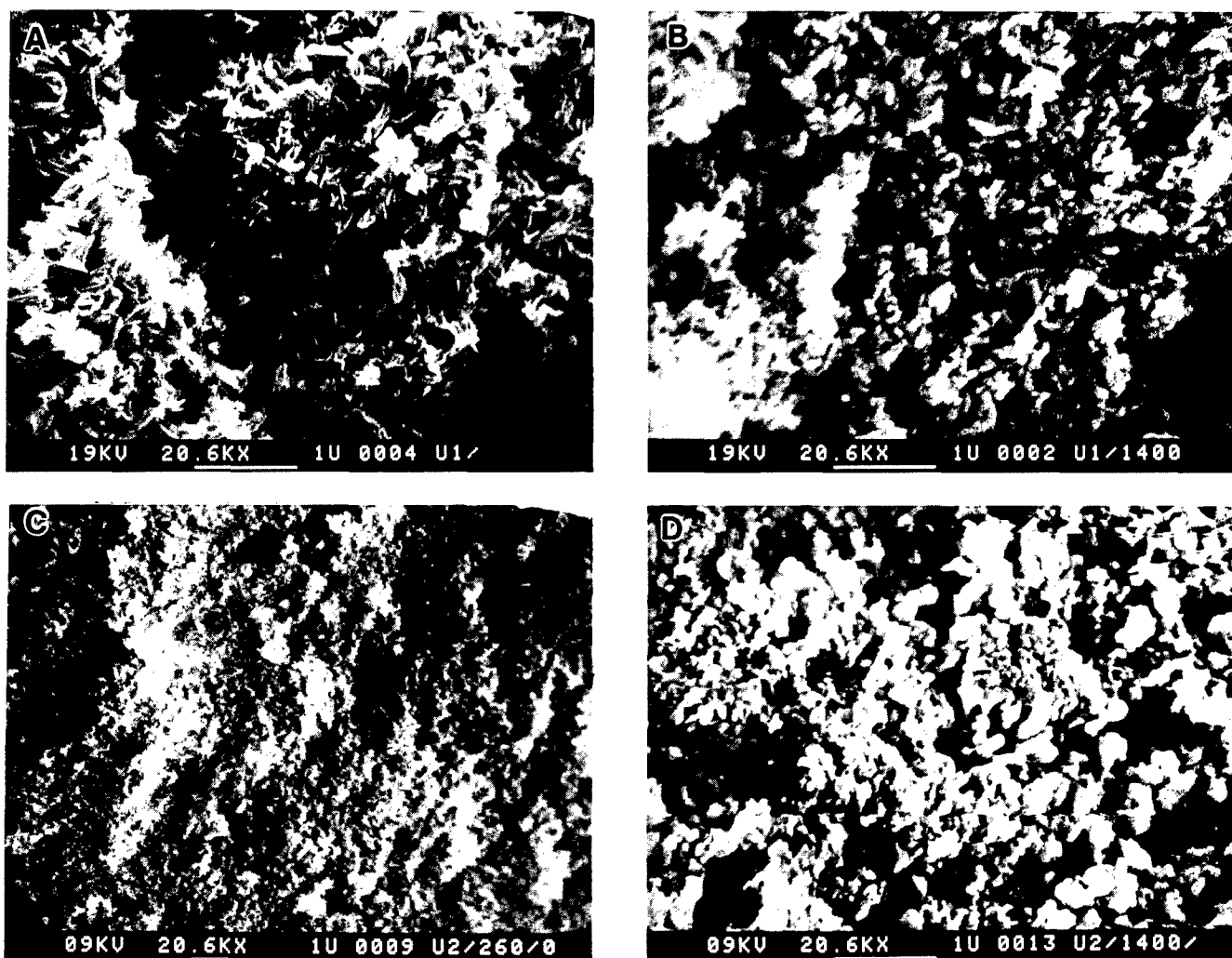


Fig. 4. Scanning electron micrographs of mullite gels: (A) as-prepared single-phase gel, (B) single-phase gel sintered at 1400°C/2 h, (C) as-prepared diphasic gel and (D) diphasic gel sintered at 1400°C 2 h.

Table 1. Surface area and pore sizes of as-prepared and sintered single-phase and diphasic aerogels of mullite composition

	As prepared, 260°C		As prepared, 270°C		Sintered ^a at 1000°C, 2 h		Sintered ^a at 1200°C, 2 h		Sintered ^a at 1400°C, 2 h	
	Surface area (m ² g ⁻¹)	Pore radius (nm)								
Single phase	334	1.8; 17 ^b	434	2.1; 13 ^b	309	1.8; 15 ^b	66	nd ^c	27	1.3; 4 ^b
Diphasic	152	13	180	22	148	1.4	93	20	15.7	1.3; 3.2; 26 ^b

^aSintered samples were critical point dried at 260°C.

^bTwo or more numbers indicate different pore radii in the same gel in order of their abundance as determined by the areas of peaks from pore-size distribution plots.

^cNot determined.

phase xerogel and aerogel. The diphasic aerogel, however, shows only delta alumina under the dynamic heating condition (10°C min⁻¹) of the DTA. These results show that the alteration of single-phase gel to diphasic gel during critical point drying can be detected by both DTA and ²⁷Al MAS NMR but not by XRD. Thus DTA and ²⁷Al MAS NMR techniques are more sensitive than XRD in identifying phase segregation in mullite gels.

The scanning electron micrograph of the as-prepared single-phase mullite aerogel shows porosity and an interesting acicular morphology (Fig. 4(A)). This aerogel sample sintered to 1400°C also shows needle-shaped mullite crystals (Fig. 4(B)). The as-prepared diphasic gel shows porosity and a very fine grained structure (Fig. 4(C)) as expected, because of the two mixed sols. The sintered diphasic porous mullite shows equiaxed, submicrometre grains (Fig. 4(D)). All the mullite composition gels showed mullite by XRD after sintering at 1400°C.

The textural properties of the as-prepared and sintered single-phase and diphasic mullite gels are shown in Table 1. The different aerogels of mullite retain high surface areas in the temperature range 1000–1400°C, which suggests that these can be tailored for high-temperature catalytic applications.

Conclusions

Both single and diphasic aerogels of mullite composition exhibit high surface areas after sintering in the temperature range 1000–1400°C. Segregation of the alumina component occurred during critical point drying of single-phase mullite composition gels. Sintered aerogels of mullite composition may be useful for high temperature catalytic applications.

Acknowledgement

This research was supported by the US Department of Energy under Grant No. DE-FGO2-85ER45204.

References

- Hoffman, D. W., Roy, R. & Komarneni, S., Diphasic xerogels, a new class of materials: phases in the Al₂O₃–SiO₂ system. *J. Am. Ceram. Soc.*, **67** (7) (1984) 468–71.
- Hoffman, D. W., Roy, R. & Komarneni, S., Diphasic ceramic composites via a sol–gel method. *Mater. Lett.*, **2** (1984) 245–7.
- Vilmin, G., Komarneni, S. & Roy, R., Crystallization of ThSiO₄ from structurally and/or compositionally diphasic gels. *J. Mater. Res.*, **2** (1987) 489–93.
- Komarneni, S., Suwa, Y. & Roy, R., Application of compositionally diphasic xerogels for enhanced densification: the system Al₂O₃–SiO₂. *J. Am. Ceram. Soc.*, **69**(7) (1986) C-155–6.
- Komarneni, S. & Roy, R., Mullite derived from diphasic gels. In *Mullite and Mullite Matrix Composites, Ceramic Transactions*, eds S. Somiya, R. F. Davis & J. A. Pask, The American Ceramic Society, Westerville, OH, Vol. 6, 1990, pp. 209–20.
- Yoldas, B. E. & Partlow, D. P., Formation of mullite and other alumina-based ceramics via hydrolytic polycondensation of alkoxides and resultant ultra- and micro-structural effects. *J. Mater. Sci.*, **23**(5) (1988) 1895–900.
- Columban, Ph., Gel technology in ceramics, glass-ceramics and ceramic–ceramic composites. *Ceramics Int.*, **15**(2) (1989) 23–50.
- Wei, W. C. & Halloran, J. W., Phase transformation of diphasic aluminosilicate gels. *J. Am. Ceram. Soc.*, **71**(3) (1988) 166–72.
- Huling, J. C. & Messing, G. L., Hybrid gels for homoepitactic nucleation of mullite. *J. Am. Ceram. Soc.*, **72**(9) (1989) 1725–9.
- Okada, K., Otsuka, N. & Somiya, S., Recent mullitization studies in Japan. *Am. Ceram. Soc. Bull.*, **70**(10) (1991) 2414–18.
- Wei, W. C. & Halloran, J. W., Transformation kinetics of diphasic aluminosilicate gels. *J. Am. Ceram. Soc.*, **71**(3) (1988) 166–72.
- Wang, Y., Li, D. X. & Thomson, W. J., *Mater. Res.*, **8**(1) (1993) 195–205.
- Komarneni, S., Roy, R., Fyfe, C. A., Kennedy, G. J. & Strobl, H., Solid state ²⁷Al and ²⁹Si Magic-angle spinning NMR of aluminosilicate gels. *J. Am. Ceram. Soc.*, **69** (1986) C42–4.
- Selvaraj, U., Komarneni, S. & Roy, R., Structural differences in mullite xerogels from different precursors characterized by ²⁷Al and ²⁹Si MAS NMR. *J. Solid State Chem.*, **106** (1993) 73–82.
- Pach, L., Iratni, A., Hrabe, Z., Svetik, S. & Komarneni, S., Sintering and characterization of mullite in diphasic gels. *J. Mater. Sci.* (submitted).
- Mizushima, Y. & Hori, M., Properties of alumina aerogels prepared under different conditions. *J. Non-Cryst. Solids*, **167** (1994) 1–8.

Effect of Aging Temperature on the Structure of Mullite Precursor Prepared from Tetraethoxysilane and Aluminum Nitrate in Ethanol Solution

Kiyoshi Okada,* Chikako Aoki,[†] Takayuki Ban, Shigeo Hayashi & Atsuo Yasumori

Department of Inorganic Materials, Tokyo Institute of Technology, O-Okayama, Meguro, Tokyo 152, Japan

Abstract

The effect of aging temperature on the structure of mullite precursor prepared by dissolving tetraethoxysilane (TEOS) and aluminum nitrate nonahydrate (ANN) in ethanol was investigated by liquid state ²⁹Si and ²⁷Al nuclear magnetic resonance (NMR) spectroscopy, small angle X-ray scattering (SAXS), powder X-ray diffraction (XRD) and solubility of ANN in ethanol. The aging temperatures examined were from 25 to 60°C. With increasing aging temperature, polymerization of TEOS progressed, size of sol particles increased, and solubility of ANN largely increased but little change occurred in the coordination state of the Al ion. Mullite was obtained as the main crystalline phase only when the precursor solution aged at 60°C was fired at 1000°C, whereas the spinel phase was obtained as the main crystalline phase instead of mullite from the solutions aged at the other temperatures. It was therefore concluded that silica and alumina components in the precursor solution were in an intimately mixed state when the precursor solution was aged at 60°C, but those aged under 60°C were not as intimately mixed as the former. Intimate mixing of both components was achieved in the precursor solution aged at 60°C by trapping of ANN solution in silica gel network.

1 Introduction

Mullite has been actively investigated by many workers during the last decade¹ and its good mechanical properties, especially at high temperature, are recognized. It is, therefore, expected to be a candidate material for high temperature applica-

tions under an oxidizing atmosphere. Various kinds of starting materials and preparation methods were studied as the raw materials for mullite ceramics.¹ Generally, their starting materials are in an amorphous state and mullitization occurs at high temperature before the densification. Although a variety of results on this subject were reported, mullitization pathways can be divided into two types on the whole as reviewed by Okada *et al.*² One type shows direct mullitization from an amorphous state and the other type shows a spinel phase³ formation before mullitization. The former type occurs in the starting materials with a good mixture of silica and alumina components, whereas the latter occurs in starting materials with a poor mixture of silica and alumina components. These two types have been widely accepted by many workers. In Ref. 4, however, we found that the crystalline phase of the thin film fired at 1000°C and prepared by dip-coating the solution by dissolving TEOS and ANN in ethanol varied from mullite to spinel phase by changing the aging time of the same solution at room temperature. In order to elucidate this phenomenon the structural state of the mullite precursor in the solution and the effects of the aging time at room temperature were investigated by liquid state ²⁹Si and ²⁷Al NMR, SAXS and XRD techniques.⁵ The following results were obtained: polymerization of TEOS progressed very quickly and most of the Si atoms formed Q³ and Q⁴ structures within a very short reaction time. Here, the superscript figures in Q represent the number of Si-O-Si bonds per one Si atom. On the other hand, Al atoms showed a monomer state and formed an octahedral structure and it did not change throughout the experimented aging time. It was, therefore, found that the precursor did not form an aluminosilicate complex and silica and alumina components were not so homogeneously mixed in the solution.

In this paper, we investigate the effect of aging

*To whom correspondence should be addressed.

[†]Now with Japanese Patent Office, 3-4-3 Kasumigaseki, Chiyoda, Tokyo 100, Japan.

temperature on the structure of mullite precursor prepared by dissolving TEOS and ANN in ethanol to further elucidate this subject.

2 Experimental Procedure

Precursor solution with $3\text{Al}_2\text{O}_3\text{SiO}_2$ composition was prepared by dissolving 0.24 mol/l of TEOS and 0.72 mol/l of ANN in ethanol. Since ANN contains $9\text{H}_2\text{O}$ per one Al atom, the $\text{H}_2\text{O}/\text{TEOS}$ is 27 and this amount of water is highly excessive for polymerization of TEOS. The precursor solution was aged at various temperatures in a sealed plastic bottle up to 100 days. The aging temperatures experimented were 25, 40, 50 and 60°C.

Liquid state NMR measurements were performed by JEOL JNM-GSX500 equipment. The spectra of ^{29}Si NMR were recorded at 99.361 MHz using a pulse width of 14.9 μs and a delay time of 1 s. The spectrum was obtained by accumulating 6000 times because the spectrum signal was very weak. A teflon tube instead of a glass tube was used for the measurements to avoid the signal from a glass tube. Chromium acetylacetone and tetraethoxysilane were added to the solution just before the measurements were made and mixed. The former reagent was used to reduce the spin-lattice relaxation time and the latter one was used as an internal chemical shift standard. The spectra of ^{27}Al NMR were recorded at 130.315 MHz using a pulse width of 1.5 μs and a delay time of 1 s. The spectra were obtained only by accumulating 240 times because the spectrum signal was strong enough in this case. A silica glass tube was used for the measurements. ANN solution was used as an external chemical shift standard.

SAXS measurements were performed by Rigaku RINT-1500 equipment using Ni-filtered Cu $\text{K}\alpha$ radiation (50 kV and 300 mA) through an evacuated beam path. The sample solution was mounted in a glass capillary 3 mm in diameter and 8 μm in thickness. Intensity measurements were made in the scattering angle 2θ from 0.13 to 3.49° with a step interval of 0.02° and a fixed time of 10 s. Since the obtained intensity (I_0) didn't show a linear relation for $\log (I_0)$ versus S^2 (S : scattering vector), the radius of gyration was calculated using the Fankuchen methods.⁶ This value was further recalculated to particle size by assuming sphere shape.⁶ The detection limit of particle size by the present experimental conditions was estimated to be up to around 100 nm.

XRD measurements were performed by Rigaku Geigerflex diffractometer using graphite monochromated Cu $\text{K}\alpha$ radiation (40 kV and 20 mA). The samples for the XRD were prepared by

inserting the precursor solution (2 ml) in an alumina crucible to a furnace kept at 500°C for 15 min to instantly dry and burn out any nitrate and alcohol, and then fired at 1000°C for 6 h.

Solubility of ANN in ethanol at each temperature was measured by a conventional method.

3 Results

3.1 Liquid state ^{29}Si and ^{27}Al NMR

Figure 1 shows ^{29}Si NMR spectra of the precursor solutions aged for 5 days at various temperatures. The spectrum of the solution aged at 25°C showed three peaks at around -91, -100 and -107 ppm. They are assigned to Q^2 , Q^3 and Q^4 structures,⁷ respectively. With increasing aging temperature, the peaks became weak and broad. The spectrum of the sample aged at 60°C showed no apparent peak and only a halo was observed due to the background signal by the teflon tube. Such a change in the spectra can be related to the hydrolysis and polymerization of TEOS to form a three-dimensional silica framework structure. The lack of peaks in the NMR spectrum can be explained by the formation of sol particles, in which structural information can not be detected by the liquid state NMR technique.

All the ^{27}Al NMR spectra of the precursor solutions aged for 5 days showed very sharp peaks at around 0 ppm. No significant differences were found among these spectra. These peaks are same as that of ANN used as an external standard. Therefore, Al atoms are considered to be in a monomer state with a regular octahedral structure. The spectra showed no change even with the

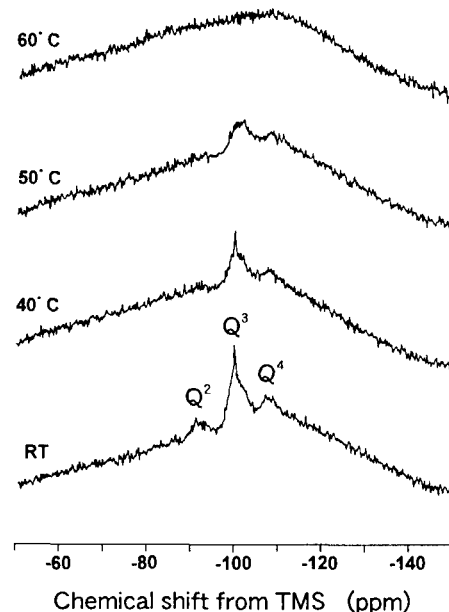


Fig. 1. Liquid state ^{29}Si NMR spectra of the samples aged for 5 days at various temperatures. The superscript figures in Q represent number of Si-O-Si bond per one Si atom.

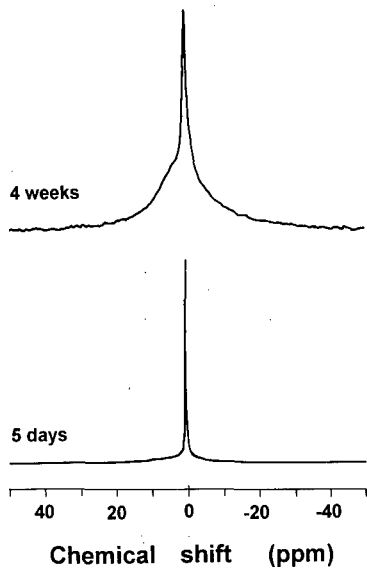


Fig. 2. Liquid state ^{27}Al NMR spectra of the samples aged at 60°C for 5 days and 4 weeks.

longer aging time when they were aged at 40 and 50°C just as in the case of room temperature aging reported before.⁵ On the other hand, a certain change was observed in the spectra when they were aged at 60°C for a long time. The spectra aged at 60°C for 5 days and 28 days are shown in Fig. 2. The full width at half maximum (FWHM) of the peak at around 0 ppm apparently increased and a shoulder also appeared at around several ppm. The increase of FWHM can be attributed to the distortion of octahedra and the shoulder can be assigned to the polymerization of Al-octahedra such as dimer and/or oligomer from a monomer.

3.2 Sol particle size by SAXS

The size of sol particles was measured for the three samples, i.e. aged for 5 days at 25 , 50 and 60°C . No clear indication of small angle X-ray scattering was observed for the sample aged at 25°C except for that from the instrument. It was, therefore, unclear whether sol particles were already formed in this solution or not. Even if the sol particles were present in the sample, they were smaller than several nm in size because this was a detection limit of the present experimental conditions. The other two samples showed small angle X-ray scattering corresponding to sol particles. The size of the sol particles was not uniform and had a distribution. By the Fankuchen method,⁶ they were approximated by two particle size distributions for the both samples. Their particle sizes in the sample aged at 50°C were 7 and 14 nm whereas those at 60°C were 9 and 26 nm. Increase of the larger particle size was clear between these two samples and it may correspond to coalescence of small sol particles.

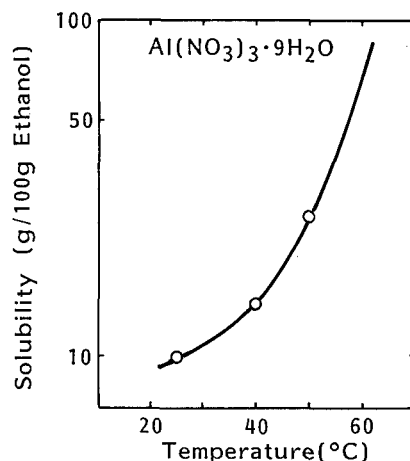


Fig. 3. Solubility curve of aluminum nitrate nonahydrate in ethanol as a function of temperature.

3.3 Solubility of ANN in ethanol

Figure 3 shows the solubility curve of ANN in ethanol. The solubility of ANN at 25°C is around 10 g in 100 g ethanol and is not very high. The solubility increased to 26 g at 50°C . We, however, could not accurately determine the solubility limit of ANN at 60°C because the solution became viscous and evolution of NO_x gas was observed due to the decomposition of nitrate ion.

3.4 Crystalline phase at 1000°C

Intensities for the strongest reflection of mullite, which has fully overlapped peaks of 120 and 210 reflections and 400 reflection of spinel phase were qualitatively measured for the samples fired at 1000°C for 6 h. Their results are shown in Fig. 4. The sample aged at 25°C showed very weak reflections of mullite and spinel phase. Amount of crystalline phases was found to be low compared with the other samples. The samples aged at 40 and 50°C showed relatively intense spinel phase reflections but very weak mullite reflections. On the other hand, only the sample aged at 60°C showed

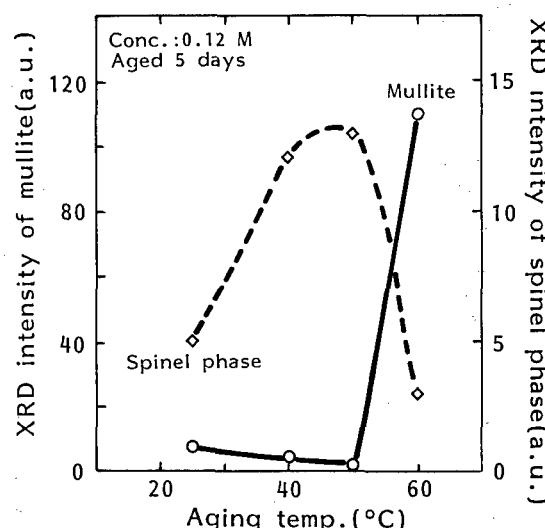


Fig. 4. XRD intensity of crystalline phases in the samples fired at 1000°C for 6 h aged at various temperatures.

strong mullite reflections with only a trace of spinel phase reflections. Thus, the crystalline phases formed by firing the precursor solutions at 1000°C were found to largely differ by the aging temperatures of the samples. Mullite formation was found to be only dominant in the sample aged at 60°C.

The crystalline phase in the samples aged for various times at various temperatures was also examined to clarify the effect of aging time. No dominant mullitization was found in all the samples aged for various times under 60°C. In the samples aged at 60°C, intensity of the mullite reflection of the 1 day aged sample was small. However, the mullite intensity increased with longer aging time and remained constant by aging over 5 days.

4 Discussion

Liquid state NMR data showed that polymerization of TEOS largely progressed but no change occurred in the monomer octahedral coordination of Al atoms with increasing aging temperature. No aluminosilicate complex was detected in the sol solution of the present preparation system. The presence of silica sol particles was also confirmed from the SAXS data. It was, therefore, concluded that the precursor was not in the molecularly mixed state in the solution, though direct mullitization occurred in the samples aged at 60°C. The precursors which show direct mullitization at around 1000°C have been considered to be in a very good mixing state and the silica and alumina components are molecularly mixed.⁸ This may be generally true but it has been found from our results that it is not always necessarily true.

We observed a clear difference in the mullitization pathways between the precursors aged at 60°C and those aged under 60°C. What is the most important point to cause such a difference? Since the precursor did not form an aluminosilicate complex, both components need to be mixed to yield mullite directly. Two things are considered to be important for this. First, it is necessary for polymerized silica to be in small particles and it should form a gel network structure with them. Since the present solution is a very strong acid and contains a high concentration of salt in the present precursor system, the present experimental conditions are considered to be applicable to develop a gel structure rather than particles which is obtained using basic conditions.⁹ The present SAXS data are compatible with this model. Second, the particles of the alumina component, which are considered to be nitrate, are also required to be

small and present around silica gel. As mentioned before, the solubility of ANN in ethanol largely increased with increasing aging temperature. This means that ANN can be dissolved in ethanol up to a very high concentration when they are prepared at higher aging temperature. It is suitable to form a gel structure with a trapped solution of dissolved ANN in the silica gel network structure. The mixed state in silica and alumina is thought to be formed in this way in the sample aged at 60°C and these samples show direct mullitization as a result as has been shown by others previously.^{10,11}

The present and previously reported results,⁴ show that the crystalline phases are found to change not only by the aging conditions of the precursor but also by the firing conditions. The main crystalline phase by firing at 1000°C is mullite in the dip-coated thin films⁴ from the solution aged at room temperature for short time, but it is the spinel phase in the present experiments. In this case the amount of precursor solution for firing is considered to be important and a cause of this difference. A very small amount of precursor was fired in the dip-coating⁴ and was considered to be preferable for mullitization because of the rapid evaporation of the solvent. Recently, Nishio *et al.*¹² reported that the crystallization behaviour of mullite precursor prepared by the solution method changes due to the firing conditions such as the heating rate. We (Ref. 13) also found this and reported similar behavior recently. It is considered that heat treatment under several hundreds °C plays an important role on various reactions such as dehydration and decomposition of nitrates and alkoxy groups which causes rearrangement of the precursor structure.

5 Conclusions

- (1) With increasing aging temperature, polymerization of TEOS to form silica sol progressed.
- (2) No apparent change was observed for a monomer octahedral structure of Al atoms irrespective of the aging temperature in a short aging time.
- (3) Solubility of ANN in ethanol increased with increasing aging temperature.
- (4) The main crystalline phase obtained by firing at 1000°C is mullite when the precursor solution was aged at 60°C, whereas it is the spinel phase when they were aged under 60°C.
- (5) The mullite precursor in the present system was found not to form aluminosilicate com-

plex and silica and alumina components were not in a molecularly mixed state in the solution. Aging at 60°C was, however, suitable to prepare a well mixed state in silica and alumina components and yielded direct mullitization at 1000°C.

Acknowledgements

We thank Professor I. Ando and Dr. H. Kurosu of Tokyo Institute of Technology for use of the NMR instrument and various fruitful suggestions for the NMR measurements. A part of this study is financially supported by the 1991 Corning Research Grant.

References

1. Schneider, H., Okada, K. & Pask, J. A., *Mullite and Mullite Ceramics*, John Wiley & Sons, London, 1994.
2. Okada, K., Otsuka, N. & Somiya, S., Review of mullite synthesis routes in Japan. *Am. Ceram. Soc. Bull.*, **70** (1991) 1633-9.
3. Brindley, G. W. & Nakahira, M., The kaolinite-mullite reaction series: III. The high-temperature phases. *J. Am. Ceram. Soc.*, **42** (1959) 319-24.
4. Okada, K. & Otsuka, N., Preparation of transparent mullite films by dip-coating method. In *Ceramic Transactions, Vol.6, Mullite and Mullite Matrix Composites*, eds S. Somiya, R. F. Davis & J. A. Pask. Am. Ceram. Soc., Westerville, OH, 1990, pp. 425-34.
5. Aoki, C., Ban, T., Hayashi, S. & Okada, K., Characterization of polymeric structure of aluminosilicate complex in sol-gel solution. In *Third Euro-Ceramics*, eds P. Duran & J. F. Fernandez. Faenza Editrice Iberica S.L., Madrid, 1993, Vol. 1, pp. 387-92.
6. Nitta, I., *X-ray Crystallography (II)*. Maruzen, Tokyo, 1961, pp. 555-6.
7. Pouixviel, J. C., Boilot, J. S., Beloeil, J. C. & Zallemand, J. J., NMR study of the sol/gel polymerization. *J. Non-Cryst. Solids*, **89** (1987) 345-60.
8. Aksay, I. A., Dabbs, D. M. & Sarikaya, M., Mullite for structural, electronic, and optical applications. *J. Am. Ceram. Soc.*, **74** (1991) 2343-58.
9. Iler, R. K., *The Chemistry of Silica*, John Wiley & Sons, London, 1979, p. 174-6.
10. Hoffman, D., Roy, R. & Komarneni, S., Diphasic xerogels, a new class of materials: phases in the Al_2O_3 - SiO_2 system. *J. Am. Ceram. Soc.*, **67** (1984) 468-71.
11. Komarneni, S., Roy, R., Fyfe, C. A., Kennedy, G. T. & Strokl, H., Solid-state ^{27}Al and ^{29}Si magic-angle spinning NMR of aluminosilicate gels. *J. Am. Ceram. Soc.*, **69** (1986) C42-4.
12. Nishio, T., Kijima, K., Kajiwara, K. & Fujiki, Y., The influence of preparation procedure in the mullite preparation by solution method to the mixing of Al and Si and the crystallization behavior. *J. Ceram. Soc. Jpn.*, **102** (1994) 462-70.
13. Ban, T., Hayashi, S., Yasumori, A. & Okada, K., Low temperature mullitization. *J. Eur. Ceram. Soc.*, submitted.

New Aqueous Mullite Precursor Synthesis. Structural Study by ^{27}Al and ^{29}Si NMR Spectroscopy

Isabelle Jaymes & André Douy

CNRS, Centre de Recherches sur la Physique des Hautes Températures 1D, Avenue de la Recherche Scientifique, F-45071 Orléans Cedex 02, France

(Accepted 22 July 1995)

Abstract

A mullite precursor gel is prepared by the slow and homogeneous generation of ammonia inside an aqueous solution of aluminium nitrate and silicic acid, urea being used as the base generator. At 80–100°C a silica gel is rapidly formed, by a catalytic reaction, and then this gel is slowly digested by the partially hydrolysed aluminium atoms which link to silica by Si–O–Al bonds. The structural evolution has been studied by ^{27}Al and ^{29}Si NMR spectroscopy. The first aluminium atoms are incorporated in tetrahedral symmetry and the following ones remain hexacoordinated. The system evolves to soluble aluminosilicate colloids with a local structure close to that of imogolite or allophane: each silicon atom being linked to three AlO_6 hexahedra and a hydroxyl group. By the completion of the hydrolysis the colloids are cross linked to a gel precursor of mullite. With thermal treatment the imogolite-like orthosilicate units arrangement is rapidly lost, but the xerogel remains chemically homogeneous with a random distribution of Al and Si atoms in the lattice, the Al atoms being four-, five- and six-fold coordinated. The xerogel crystallises at 980°C into an alumina-rich mullite and amorphous silica, and the $3\text{Al}_2\text{O}_3\cdot 2\text{SiO}_2$ stoichiometry is reached at 1300°C by reincorporating the silica in the lattice.

1 Introduction

Due to their excellent high-temperature properties, mullite, $3\text{Al}_2\text{O}_3\cdot 2\text{SiO}_2$, and mullite-matrix composites have received much attention during the last decade.^{1,2} The chemical synthesis of mullite has been exemplary.³ It is well known that single phase precursors crystallize into mullite at ~980°C while for diphasic precursors this crystallization is delayed to higher temperatures (~1250°C) through transient alumina phases. The synthesis of single

phase aluminosilicate gels has been generally performed by organic processes, using all alkoxides or silicon alkoxide (TEOS) and aluminium nitrate. Aqueous processes, starting with colloids or salts, lead usually to diphasic gels. However chemically homogeneous mullite precursors may also be obtained by aqueous routes. The precursor solution may be conveniently prepared by hydrolysing tetraethoxysilane (TEOS) in a solution of aluminium nitrate. This precursor solution, of aluminium nitrate and silicic acid, may be transformed into chemically homogeneous amorphous materials by an organic gel-assisted process,⁴ by spray-drying⁵ or by rapid precipitation into an alcoholic solution of a base.⁶ While by the addition of a base to hydrolyse the aluminium salt a diphasic precursor is generally obtained, here we present the synthesis of a chemically very homogeneous gel precursor of mullite, by the slow *in situ* generation of ammonia, using urea as the base generator. ^{27}Al and ^{29}Si NMR spectroscopy has been used to study the different steps of the synthesis, from the solution to the ceramic.

2 Experimental

2.1 Synthesis

Tetraethoxysilane (TEOS), $\text{Si}(\text{OC}_2\text{H}_5)_4$ (Merck), was added in the stoichiometric ratio to a stirred 0.6 M aqueous solution of aluminium nitrate nonahydrate (Aldrich). By hydrolysis of TEOS a clear solution was obtained. Urea $\text{CO}(\text{NH}_2)_2$ (Merck) was added (1.8 urea mole per aluminium nitrate mole) and the solution was stored at 80°C. A gel was obtained after a few hours, a clear sol after 3 days, and a second gel after a week. This gel was filtered, washed with water, dried at 100°C, and further calcined to different temperatures. Preparations were also made by adding various quantities of urea to the precursor solution, and storing at 80°C for 20 days or 100°C for 7–10 days. These

preparations corresponded to different degrees of partial hydrolysis of the aluminium cations. For some preparations gadolinium was added from nitrate as a paramagnetic relaxation agent for the ^{29}Si NMR spectroscopy study (0.04 wt% Gd_2O_3 in the final oxide).

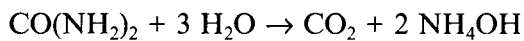
2.2 Characterisation

NMR experiments were recorded on a Bruker MSL 300 spectrometer operating at a magnetic field of 7.04 Tesla. For ^{27}Al a pulse length of 0.6 μs and a recycle time of 1 s were used, and for ^{29}Si a pulse length of 2 μs and a recycle time of 10 s. High resolution solid state MAS-NMR spectra were obtained in zirconia rotors spinning the samples at the magic angle ($54^\circ 44'$) at 15 kHz and 4 kHz respectively for Al and Si. The chemical shifts are given with respect to tetramethylsilane and $[\text{Al}(\text{H}_2\text{O})_6]^{3+}$ in aqueous aluminium nitrate. The isotropic chemical shift positions (δ_{iso}) and the estimated minimum quadrupolar frequencies (ν_Q) are measured using central and satellite transitions as proposed by Jäger⁷ and Massiot *et al.*⁸

3 Results and Discussion

When TEOS is added to an acidic solution of aluminium nitrate ($\text{pH} \sim 2$) it is hydrolysed into silicic acid. At this pH the rate of hydrolysis is maximum while that of polycondensation of silicic acid is minimum.⁹ If no base is added to this solution the silicic acid will slowly polymerise into silica gel, after several weeks at room temperature or a few days at 100°C. This silica gel may be filtered and carefully washed and dried. By analysis of the gel and the filtrate it is shown that no reaction occurs between the silicated and aluminate species.

Urea has been used as a base generator in the preparation of oxide ceramics.^{10,11} At temperatures higher than 60°C, urea is hydrolysed in aqueous solutions:¹²



For the solution of aluminium nitrate and silicic acid the slow *in situ* generation of ammonia will hydrolyse and polycondense the aluminium species while increasing the pH will result in polycondensation of the silicic acid, although the raising of the pH is significant only at the end of the hydrolysis of the aluminium nitrate. A copolycondensation, or at least a good level of mixing of aluminate and

silicate species may be expected by this reaction. In fact the reaction proceeds by a very different way. When 1.8 mole of urea per mole of aluminium nitrate are added to the solution, that is in slight excess for the complete hydrolysis of aluminium (which would require 1.5 mole of urea), at 80°C a gel is formed within a few hours. Then this gel is slowly desegregated and a clear colloidal sol is obtained after 3 days and a second gel after a week. For the study of the reactions occurring during the synthesis, a series of preparations were made with precise quantities of urea corresponding to partial hydrolyses of aluminium. By storing at 80°C for 20 days or at 100°C for 7–10 days it was considered that practically all the urea had reacted. Even by ageing at 100°C for much longer times the obtained gels or sols did not apparently evolve. In these conditions gels were obtained for degrees of hydrolysis $h = \text{OH/Al} < 0.7$, clear sols for $0.8 < h < 2.7$ and gels for $h > 2.8$.

3.1 First gels ($h < 0.7$)

The chemical compositions in silicon and aluminium for the first gels and the sols are given in Table 1, determined by EDX analysis on the gels filtered and carefully washed and dried, and on the freeze-dried materials obtained from the concentrated and dialysed sols. The first gel which is formed is probably a pure silica gel; as aluminium is hydrolysed it reacts with this silica gel and is responsible for its digestion to small particles of aluminosilicate species.

The ^{29}Si MAS NMR spectra confirm the nature of the first gels (Fig. 1). For $h = 0.1$ the spectrum is characteristic of polymerised silica with main resonances at -110 ppm (Q^4) and -102 ppm (Q^3). In this Q^n notation,¹³ Q represents a silicon atom in a SiO_4 tetrahedron and n indicates the number of other Q units attached to it. Q^4 denotes three-dimensionally cross-linked tetrahedra, that is fully polymerised silica, and Q^3 chain-branching sites. As the hydrolysis progresses we note a shift of the resonance bands to lower fields. The intensity of the band at -110 ppm decreases and other bands appear at -90 and -78 ppm. Two different phenomena may contribute to this shifting of the resonance lines: the depolymerisation of the silica network and the replacement of silicon by aluminium in the second sphere of coordination of the silicon atoms. Each depolymerisation step (breaking of $\text{Si}-\text{O}-\text{Si}$ to $\text{Si}-\text{O}-\text{OH}$) results in a shift of ca 10 ppm, while for each replacement of $\text{Si}-\text{O}-\text{Si}$ bonds by $\text{Si}-\text{O}-\text{Al}$ bonds a chemical shift

Table 1. Evolution of the Al/Si ratio in the gels and the colloids with the degree of hydrolysis h of aluminium nitrate

$h = \text{OH/Al}$	0.2	0.4	0.6	0.8	1.0	1.2	1.5	1.8	2.0	2.4	2.6
Al/Si	0.11	0.21	0.38	0.67	0.82	1.1	1.3	1.7	1.95	2.2	2.55

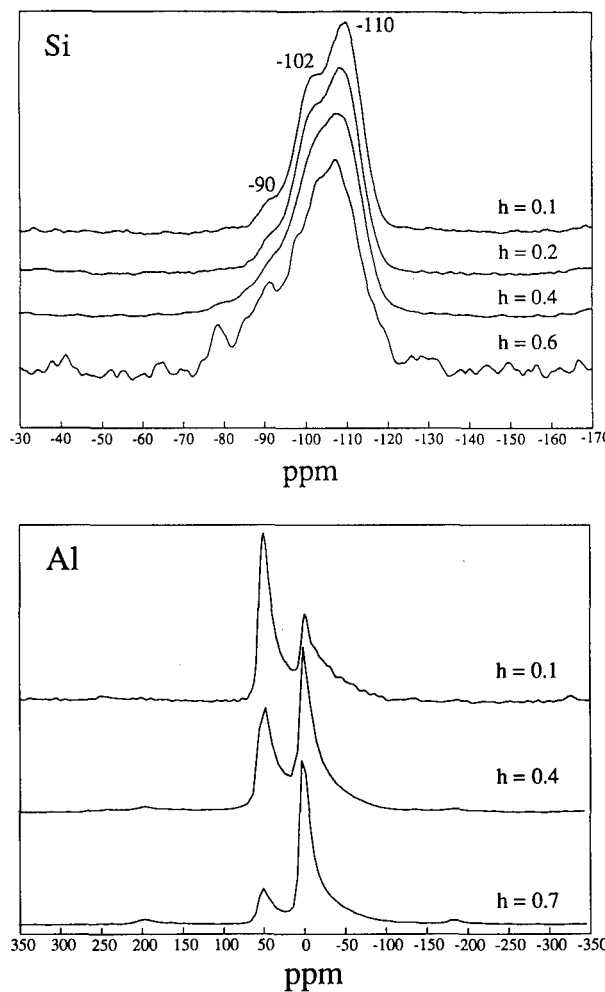


Fig. 1. ^{29}Si and ^{27}Al MAS NMR spectra of the first gels for different degrees of hydrolysis for aluminium.

of ca 5 ppm is expected for the silicon atoms.¹³ The two reactions occur during the hydrolysis and further studies are necessary for precise attribution of the new lines appearing on the NMR spectra.

The first aluminium atoms incorporated in the silica gel are mainly tetracoordinated, with the apparent chemical shift at 50 ppm (Fig. 1) for this quadrupolar nucleus, characteristic of AlO_4 tetrahedra. Some Al also occurs in hexacoordinated symmetry, at 0 ppm, characteristic of AlO_6 octahedra. As the hydrolysis progresses the ratio $\text{Al(VI)}/\text{Al(IV)}$ increases and the majority of the aluminium atoms incorporated in the gel are hexacoordinated.

Whatever the quantity of urea added to the precursor solution, a silica gel is always formed in the first step of the reaction. Urea acts as a catalyst in the polycondensation of silicic acid in the presence of aluminium nitrate. The incorporation of the first aluminium atoms in tetrahedral symmetry is in agreement with other reports on silica-rich single phase aluminosilicate gels.¹⁴ When the content in alumina increased the ratio $\text{Al(VI)}/\text{Al(IV)}$ also increased.¹⁵

3.2 Colloidal sols ($0.8 < h < 2.7$)

The ^{29}Si and ^{27}Al NMR spectra of the colloidal sols (Fig. 2) show an evolution of the environments for the silicon atoms. For the ^{29}Si NMR spectroscopy the colloidal sols have been greatly concentrated but remained optically clear. The remaining resonance bands at -110 and -102 ppm, predominant in the first gel progressively disappear and are replaced by lines at -90 and -85 ppm. These lines then disappear in their turn and the evolution is towards a single resonance at -78 ppm for a degree of hydrolysis h slightly higher than 2.4.

The static ^{27}Al NMR spectra show only a band at 0 ppm corresponding to hexacoordinated aluminium atoms, including the non hydrolysed aluminium cations $[\text{Al}(\text{H}_2\text{O})_6]^{3+}$. But due to molecular-weight broadening effects associated with the quadrupolar aluminium nucleus in highly distorted symmetry, many Al species may be not observable by NMR spectroscopy under static conditions.

The size of the colloidal particles has been determined by dynamic light scattering.¹⁶ For a series of colloidal samples aged at 100°C for 10

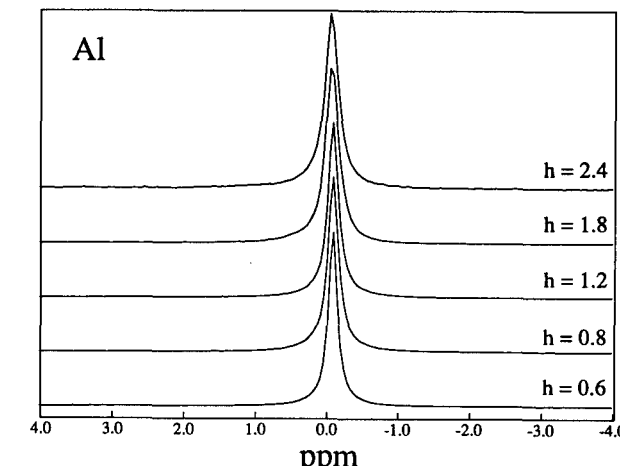
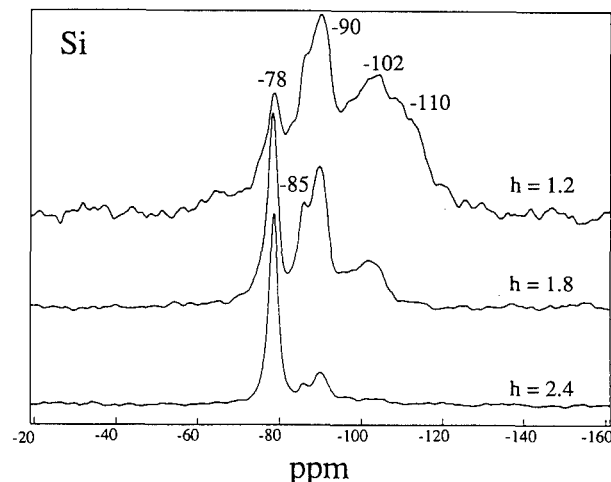


Fig. 2. ^{29}Si and ^{27}Al NMR spectra of concentrated colloidal sols (Si) and colloidal sols (Al) corresponding to different degrees of hydrolysis h for aluminium.

days, the Stokes radius decreases rapidly to values close to 2 nm. A minimum of 1.64 nm is observed around $h = 2.6$, with a narrow size distribution (± 0.03 nm). For higher h values the size of the particles increases sharply just before the second gelation.

3.3 The second gel ($h > 2.8$)

For degrees of hydrolysis higher than 2.8 another gel is obtained, resulting from the cross linking of the colloidal particles by the condensation of the last aluminium atoms being hydrolysed. By further ageing syneresis occurs with cracking of the gel. The gel is filtered and washed to eliminate the ammonium nitrate formed during the hydrolysis and dried. Since no aluminium or silicon were found in the filtrate, this gel is an aluminosilicate gel precursor of stoichiometric 3:2 mullite.

The ^{29}Si and ^{27}Al MAS NMR spectra (Fig. 3) show for silicon atoms a sharp resonance at ~ 78 ppm as in the colloidal sols for high degrees of hydrolysis, and for aluminium atoms practically a single hexacoordinated symmetry at ~ 0 ppm. There remains however some tetrahedrally coordinated atoms (at ~ 50 ppm) not visible in static conditions in the colloidal samples, even though probably present. These local environments for silicon and aluminium atoms are very similar to

those in natural imogolite.¹⁷⁻¹⁹ In this tubular mineral each silicon atom is linked to three hexacoordinated aluminium atoms via oxo bridges and to one hydroxyl group, and the NMR spectrum exhibits a unique resonance band at ~ 78 ppm; and all the aluminium atoms are hexacoordinated. The high degree of similarity in the local structure and the sharpness of resonance bands indicate a very high degree of chemical homogeneity in the colloidal samples before the gelation and in the gel. However the particle size of the colloidal species before gelation, substantially too low for a tubular morphology, and the chemical composition ($\text{Al/Si} = 2.5-3$) are more related to allophane than imogolite. While in imogolite the Al/Si atomic ratio is about 2, for allophanes, very poorly crystalline hydrous aluminosilicates with a hollow spheroidal structure, a much wider range of composition is available.²⁰⁻²² Allophanes usually also possess imogolite-like orthosilicate units giving rise to a sharp resonance at ~ 78 ppm.²²

3.4 Structural evolution with heat-treatment

Heated at $10^\circ\text{C}/\text{min}$ the second gel ($h = 3$) exhibits only a single and strong exotherm at 980°C , on differential scanning calorimetry. By X-ray diffraction this thermal event is checked to be the crystallization into mullite. For the NMR spectroscopy study samples were calcined for 1 h at different temperatures (Fig. 3). There is a strong modification in the local environments of the cations at low temperature treatment, between 100 and 300°C . At 300°C the site distribution for the silicon atoms is much broader than at 100°C , with a shift to higher fields which may result from the condensation of hydroxyl groups. This broad line indicates a random distribution of Si and Al atoms in the lattice. For the aluminium atoms tetrahedral ($\delta_{\text{iso}} = 70-72$ ppm) and 'pentahedral' ($\delta_{\text{iso}} = 41$ ppm) coordinations appear. So the imogolite-like local structure is rapidly lost by heat-treatment. This behaviour is also more characteristic of allophane than imogolite. In imogolite the sharp resonance is still the major band at 400°C (15 min) while in allophane it disappears at about 200°C .^{19,22}

With increasing temperature above 300°C , the structural evolution of this precursor becomes more similar to those of other single phase aluminosilicate gel precursors of mullite.²³⁻²⁶ There is a regular shift of the maximum of the broad resonance for the silicon atoms until 900°C . For the aluminium atoms, the Al(IV) and Al(V) signals increase and are at their apparent maximum intensities at 900°C , before the crystallization temperature.

At 1000°C the sample is crystallised and the environments of the atoms are modified. The 'pen-

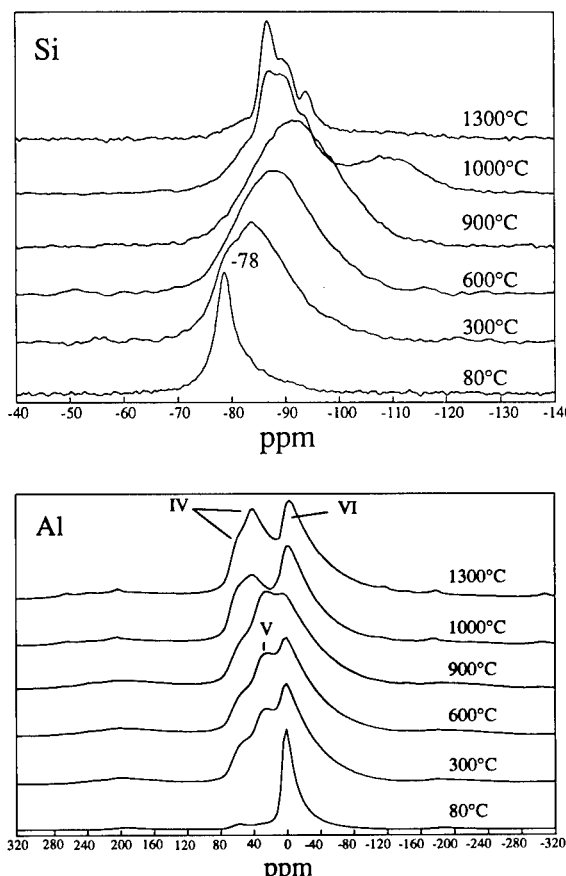


Fig. 3. ^{29}Si and ^{27}Al MAS NMR spectra of the mullite precursor gel to the ceramic after heat treatment for 1 h at different temperatures.

tacoordinated' aluminium atoms have disappeared and there are now three Al sites in mullite: one octahedral ($\delta_{\text{iso}} = 10$ ppm) and two tetrahedral, assigned by Merwin and Schneider^{27,28} to T and T* sites of the mullite structure,²⁹ at 70 and 41 ppm respectively for the isotropic positions. T* refers to trilcluster distorted Al tetrahedra, explaining the low chemical shift for Al(IV), at a similar isotropic position to the 'pentacoordinated' atoms in the amorphous state. For silicon atoms the broad signal at -90 ppm is replaced by the characteristic resonances of mullite at -86, -90, -94 and -80 ppm, and a broad signal at -110 ppm, characteristic of silica. This reflects the segregation occurring during the crystallization. The crystallised mullite is richer in alumina and a part of silica is expelled from the lattice.

On further heating, to 1300°C, the free amorphous silica has re-entered the mullite structure and the signal at -110 ppm has disappeared. The material is orthorhombic 3:2 mullite.²⁸⁻³⁰ The main resonance at -86 ppm corresponds to Si atoms in a sillimanite-type (Al_2SiO_5) arrangement, while the lines at -90 and -94 ppm reflect a mullite-type Al/Si ordering. The change in the mullite composition from 1000 to 1300°C is accompanied by an apparent increase of the Al(IV)/Al (VI) ratio.

4 Conclusion

This synthesis of mullite precursor proceeds through unexpected reactions. It is shown that a silica gel may be digested by partially hydrolysed aluminium species homogeneously generated inside its network. This leads to aluminosilicate colloids and gels with aluminium and silicon atoms environments close to those in imogolite or allophane. This local arrangement is thermodynamically lost by thermal treatment but a very high degree of mixing of aluminium and silicon atoms is preserved in the amorphous state, and the xerogel crystallises into mullite at low temperature. This synthesis, with the use of urea as a base generator, is well suited to all compositions single phase aluminosilicate gels and especially to mullite precursors.

Acknowledgements

The Région Centre is acknowledged for financial support. The authors are grateful to Dr D. Massiot for NMR discussions, and to Prof. J. P. Busnel for the dynamic light scattering experiments.

References

1. Ceramic Transactions. Vol 6. In *Mullite and Mullite Matrix Composites*, eds S. Somiya, R. F. Davies & J. A. Pask, American Ceramic Society, Westerville, OH, 1990.
2. Proceedings of the Symposium Mullite Processing, Structure and Properties, 43rd Pacific Coast Regional Meeting, The American Ceramic Society, *J. Am. Ceram. Soc.*, **74**(10) (1990).
3. Sacks, M. D., Lee, H. W. & Pask J. A., A review of powder preparation methods and densification procedures for fabricating high density mullite. In ref. 1, pp. 167-207.
4. Douy, A., Organic gels in the preparation of silicate powders. 1. Mullite. *J. Eur. Ceram. Soc.*, **7** (1991) 117-23.
5. Jaymes, I. & Douy, A., Homogeneous mullite-forming powders by spray drying aqueous solutions. *J. Am. Ceram. Soc.*, **75** (1992) 3154-6.
6. Jaymes, I. & Douy, A., Homogeneous precipitation of mullite precursors. *J. Sol-Gel Sci. & Technol.*, **4** (1995) 7-13.
7. Jäger, C., How to get more from ^{27}Al MAS NMR by high speed satellite transition spectroscopy. *J. Magn. Reson.*, **99** (1992) 353-62.
8. Massiot, D., Coté, B., Taulelle, F. & Coutures, J. P., ^{27}Al MAS NMR of crystalline and amorphous materials. In *Applications of NMR to Cement Sciences*, eds P. Colombe & A. R. Grimmer, Gordon and Breach, New York, 1994, pp. 153-69.
9. Iler, P. K., *The Chemistry of Silica*, Wiley, New York, 1979.
10. Kato, A., Inoue, K. & Katata, Y., Sintering behavior of yttria-stabilized zirconia (YSZ) powder prepared by homogeneous precipitation. *Mat. Res. Bull.*, **22** (1987) 1275-81.
11. Wood, T. E., Siedle, A. R., Hill, J. R., Skarjune, R. P. & Goodbrake, C. J., Hydrolysis of aluminum. Are all gels created equal? *Mat. Res. Symp. Proc.*, **180** (1990) 97-116.
12. Shaw, W. H. R. & Bordeaux, J. J., The decomposition of urea in aqueous media. *J. Am. Chem. Soc.*, **77** (1955) 4729-33.
13. Engelhardt, G. & Mitchell, D., *High Resolution Solid State NMR of Silicates and Zeolites*, Wiley, New York, 1987.
14. Irwin, A. D., Holmgren, J. S. & Jonas, J., ^{27}Al and ^{29}Si NMR study of sol-gel derived aluminosilicates and sodium aluminosilicates. *J. Mat. Sci.*, **23** (1988) 2908-12.
15. Komarneni, S., Roy, R., Fyfe, C. A., Kennedy G. J. & Strobl, H., Solid state ^{27}Al and ^{29}Si magic angle spinning NMR of aluminosilicate gels. *J. Am. Ceram. Soc.*, **69**, (1986) C-42-4.
16. Jaymes, I., Douy, A., Massiot, D. & Busnel, J. P., to be published.
17. Barron, P. F., Wilson, M. A., Campbell, A. S. & Frost, R. L., Detection of imogolite in soils using ^{29}Si NMR. *Nature*, **299** (1982) 616-18.
18. Goodman, B. A., Russel, J. D., Montez, B., Oldfield E. & Kirkpatrick, R. J., Structural studies of imogolite and allophanes by aluminum-27 and silicon-29 nuclear magnetic resonance spectroscopy. *Phys. Chem. Mineral.*, **12** (1985) 342-6.
19. MacKenzie, K. J. D., Bowden, M. E., Brown, I. V. M. & Meinhold, R. H., Structure and thermal transformations of imogolite studied by ^{29}Si and ^{27}Al high-resolution solid-state nuclear magnetic resonance. *Clays & Clay Minerals*, **37** (1989) 317-24.
20. Farmer, V. C., Adams, M. J., Fraser, A. R. & Palmieri, F., Synthetic imogolite: properties, synthesis and possible applications. *Clay Miner.*, **18** (1983) 459-72.
21. Wada, S. I., Eto, A. & Wada, K., Synthetic allophane and imogolite. *J. Soil Sci.*, **30** (1979) 347-55.
22. MacKenzie, K. J. D., Bowden, M. E. & Meinhold, R. H., The structure and thermal transformations of allophanes studied by ^{29}Si and ^{27}Al high-resolution solid-state nuclear magnetic resonance. *Clays & Clay Minerals*, **39** (1991) 337-46.
23. Sanz, J., Sobrados, I., Cavalieri, A. L., Pena, P., de Aza, S. & Moya, J. S., Structural changes induced on mullite

precursors by thermal treatment: a ^{27}Al MAS NMR investigation. *J. Am. Ceram. Soc.*, **74** (1991) 2398–403.

- 24. Yoldas, B. E., Effect of ultrastructure on crystallization of mullite. *J. Mat. Sci.*, **27** (1992) 6667–72.
- 25. Selvaraj, U., Komarneni, S. & Roy, R., Structural differences in mullite xerogels from different precursors characterized by ^{27}Al and ^{29}Si MAS NMR. *J. Solid State Chem.*, **106** (1993) 73–82.
- 26. Jaymes, I., Douy, A., Florian, P., Massiot, D. & Coutures, J. P., New synthesis of mullite. Structural evolution study by ^{17}O , ^{27}Al and ^{29}Si MAS NMR spectroscopy. *J. Sol-Gel Sci. & Technol.*, **4** (1995) 7–13.
- 27. Merwin, L. H., Sebald, A., Rager, H. & Schneider, H., ^{29}Si and ^{27}Al MAS NMR spectroscopy of mullite. *Phys. Chem. Miner.*, **18** (1991) 47–52.
- 28. Schneider, H., Merwin, L. & Sebald, A., Mullite formation from non-crystalline precursors. *J. Mat. Sci.*, **27** (1992) 805–12.
- 29. Angel, R. J. & Previt, C. T., Crystal structure of mullite: a reexamination of the average structure. *Am. Mineral.*, **71** (1986) 1476–82.
- 30. Ban, T. & Okada, K., Analysis of local cation arrangement in mullite using ^{29}Si MAS NMR spectra. *J. Am. Ceram. Soc.*, **76** (1993) 291–6.

Germanium Mullite: Structure and Vibrational Spectra of Gels, Glasses and Ceramics

D. Michel,^a Ph. Colombar,^{b*} S. Abolhassani,^{c†} F. Voyron^c & A. Kahn-Harari^c

^aCECM, CNRS UPR 2801, 15 rue G. Urbain, 94407 Vitry, France

^bLASIR, CNRS UPR 2631, 2 rue H. Dunant, 94320 Thiais, France

^cENSCP, URA CNRS 1466, 11 rue P. et M. Curie, 75005 Paris, France

(Accepted 22 July 1995)

Abstract

The Raman spectra of mullite phases in $\text{GeO}_2\text{-Al}_2\text{O}_3$ and $\text{GeO}_2\text{-Ga}_2\text{O}_3$ systems are compared with those of silicon mullite and sillimanite. Replacement of silicon by germanium and aluminium by gallium modifies the wavenumbers of certain lines, especially at high frequency. However, all germanium mullites present similar features which reflect their disordered character. Even for compositions Al_2GeO_5 and Ga_2GeO_5 which are homologous to that of sillimanite, Raman spectra consist of broad bands, as previously observed in silicon mullites. The evolution of spectra is discussed for a series of $\text{Al}_{4+2x}\text{Ge}_{2-2x}\text{O}_{10-x}$ mullite phases with $0 < x < 0.47$. The spectra of amorphous gels and glasses prepared by slow hydrolysis-polycondensation of aluminium and germanium (silicon) alkoxide mixtures show rather narrow bands. This indicates that the polymeric arrangement of molecular entities is less distorted in non-crystalline precursors than in crystalline mullite. Finally, a phase relation diagram is proposed for the sol-gel route.

Introduction

Phases isostuctural with silicon mullites exist in the $\text{GeO}_2\text{-Al}_2\text{O}_3$ phase diagram.¹⁻⁵ However, whereas at atmospheric pressure mullite is the only aluminosilicate formed, two other stable compounds exist with germanium: Al_2GeO_5 , isostructural with the high-pressure silicate kyanite,⁴ and $\text{Al}_2\text{Ge}_2\text{O}_7$ in which Al atoms are in five-fold oxygen coordination.⁶ In addition, the metastable phase Al_4GeO_8 , isostructural to $\beta\text{-Ga}_4\text{GeO}_8$, can be obtained.⁷

*To whom correspondence should be addressed.

†Present address: Electron Microscopy Center, University of Lausanne, Bugnon 27, 1005 Lausanne, Switzerland.

As well as $\text{Al}_{4+2x}\text{Si}_{2-2x}\text{O}_{10-x}$ mullites,⁸ Ge mullites have an extended stability range, but the domain of stability differs for germanates and silicates.^{4,8,9} In particular, the Ge mullite range of composition includes Al_2GeO_5 ($x = 0$), which corresponds to that of high-pressure Al_2SiO_5 sillimanite.

An 'ideal' mullite structure ($x = 0$) can be described as a disordered variety of sillimanite in which aluminium and silicon atoms are randomly distributed on the tetrahedral sites.¹⁰⁻¹² On the contrary, in sillimanite, Al and Si atoms regularly alternate along the tetrahedral chains. This leads to a doubling of the c lattice constant and to a change in the space group from Pbam to Pbnm (Pnma in a standard setting after permutation of axes). In addition to the disorder on tetrahedral sites, $\text{Al}_{4+2x}\text{Si}(\text{or Ge})_{2-2x}\text{O}_{10-x}$ mullites are non-stoichiometric phases with oxygen vacancies when $x \neq 0$. Structure refinements on Si or Ge mullites indicate that the vacancies affect a special set of oxygen positions usually labelled O_c and that the neighbouring cations occupy new sites (Tet*) in order to maintain a tetrahedral environment, as shown in Fig. 1.⁹⁻¹⁴ Consequently, the local structure of mullite is very complex. In particular, various states of order have been observed on germanium mullites depending on composition and thermal treatments.¹⁵⁻¹⁸

The present work reports a Raman scattering study on Ge mullites in a large range of composition, $0 < x < 0.47$ (from 50 to 70 mol% Al_2O_3). In addition, the spectrum of mullite Ga_2GeO_5 clarifies the effect of substitution of aluminium by gallium. Results on crystallized mullite ceramics obtained by high temperature processes are compared with those of monoliths prepared from a sol-gel route in order to understand structural changes in glass ceramics and poorly crystallized samples from modifications of their Raman spectra.

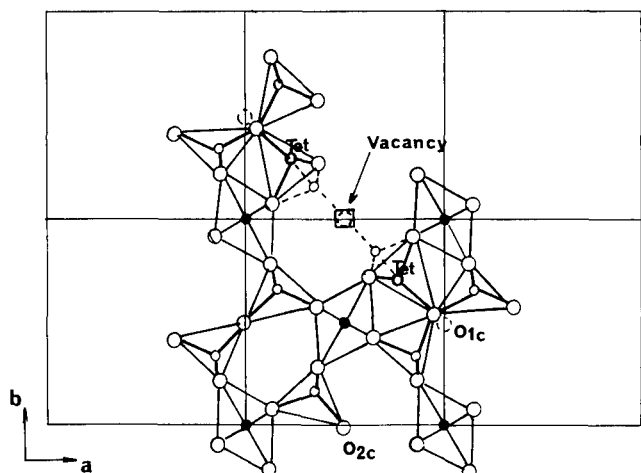


Fig. 1. Projection of the structure of mullite on (0 0 1) showing the environment of an oxygen vacancy on O_c positions and occupancy of new tetrahedral sites Tet*.

Experimental Procedure

Samples were prepared by two methods. The first method was used to obtain well-crystallized Al and Ga germanates giving the reference Raman spectra of the various phases. In this case, the synthesis route was coprecipitation with ammonia of mixed germanium oxide (quartz form soluble in hot water) and Al(or Ga)(NO₃)₃·9H₂O aqueous solutions. Atomic absorption analysis on the residual solutions verified that cation losses during the process are negligible. After dehydration, powders were pressed into pellets and heat-treated for 15 h at 1500°C in sealed platinum tubes to prevent GeO₂ volatilization. Then, samples were annealed for 30 h at 1330°C. The characterization of resulting phases and determination of their lattice constants were performed by X-ray diffraction and the results are reported elsewhere.¹⁸ Raman spectra of these samples were recorded with a Jobin-Yvon Ramanor HG2S apparatus with a double monochromator using the blue ($\lambda = 488.0$ nm) or green ($\lambda = 514.5$ nm) lines of an Ar laser. The slit width was kept to about 1–2 cm⁻¹.

The second series of samples was obtained within the framework of studies on mullite formation and sintering using the sol-gel route.^{19–23} In particular, the substitution of germanium to silicon strongly decreases the refractivity and helps to densify mullite composites.²⁴ Monolithic, optically clear gels were prepared by slow hydrolysis (several months) of mixed aluminium secondary butoxide and germanium ethoxide or silicon methoxide diluted in hexane (ratio alkoxide/hexane = 1/5 by volume). Due to the highly hygroscopic nature of the alkoxides, mixture preparation was performed under argon in a glove box free of water traces (H₂O < 20 ppm). Hydrolysis and evacuation of hexane and alcohols resulting from

hydrolysis–polycondensation then proceeds in air through the polyethylene stopper of a glass flask as previously described.²¹ The mixture becomes viscous, gels and, because of its volume contraction, separates from the flask. Heat treatments were then applied in air at various temperatures. Materials remain optically clear up to 1110–1200°C depending on composition. The crystallization process and phase transitions were followed by differential thermal analysis (DTA), dilatometry and X-ray diffraction. The composition and homogeneity were checked by EDX analysis. Hot-pressed pellets were also prepared using graphite dyes and resistors.

The Raman spectra of samples prepared from organic precursors were recorded with a XY Dilor multichannel spectrometer equipped with a Wright 1200-300 CCD detector cooled with nitrogen. Light was collected with an Olympus microscope at a magnification of 1000 \times . Laser excitation was made by the 514.5 nm argon line. Due to the very weak intensity of some spectra, artefacts coming from the collection optics appeared on some spectra around 550 and 1080 cm⁻¹ (broad bands) and 842 and 916 cm⁻¹ (narrow lines). These artefacts are labelled on Fig. 3

Results and Discussion

Relation between spectra of mullite and sillimanite

The Raman spectra of silicon mullites and alumina–silica glass obtained by fast quenching were studied by McMillan and Piriou.²⁵ A complete interpretation of the Raman spectra of sillimanite was made from the study of polarized spectra by Salje and Werneke²⁶ and the effect of pressure was discussed by Mernagh and Liu.²⁷ These results give a useful classification for the Raman modes and have been of considerable help for our interpretation of spectra of germanates with parent structures.

The irreducible representations corresponding to sillimanite are

$$\Gamma = 13 A_g + 13 B_{1g} + 8 B_{2g} + 8 B_{3g} + 11 B_u + 11 B_{1u} + 16 B_{2u} + 16 B_{3u}$$

including the acoustical modes

$$\Gamma_{\text{acoust.}} = B_{1u} + B_{2u} + B_{3u}$$

Therefore, there are 42 Raman active (13 A_g + 13 B_{1g} + 8 B_{2g} + 8 B_{3g}) and 40 infra-red active (10 B_{1u} + 15 B_{2u} + 15 B_{3u}) modes for sillimanite.

For an ‘ideal’ mullite with no oxygen vacancies ($x = 0$), the irreducible representations decompose as follows :

$$\Gamma = 6 A_g + 6 B_{1g} + 3 B_{2g} + 3 B_{3g} + 5 A_u + 5 B_{1u} + 10 B_{2u} + 10 B_{3u}$$

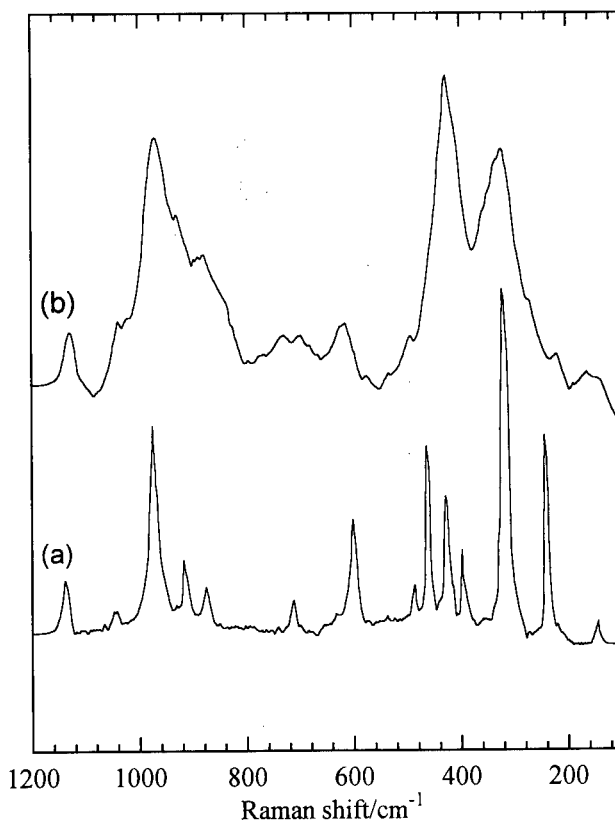


Fig. 2. Raman spectra of: (a) sillimanite from Pinet *et al.*,³⁰ (b) a 55 mol% Al_2O_3 mullite ($x = 0.13$) from McMillan and Piriou.²⁵

including

$$\Gamma_{\text{acoust.}} = \mathbf{B}_{1u} + \mathbf{B}_{2u} + \mathbf{B}_{3u}$$

There are 18 Raman ($6 \text{ A}_g + 6 \text{ B}_{1g} + 3 \text{ B}_{2g} + 3 \text{ B}_{3g}$) and 22 infra-red ($4 \text{ B}_{1u} + 9 \text{ B}_{2u} + 9 \text{ B}_{3u}$) active modes.

It should be pointed out that in mullite and sillimanite the Al atoms in octahedral sites are on an inversion centre and do not participate in the Raman activity. Scattering coming from cations concerns only tetrahedral Al and Si(or Ge) atoms. For the same reason, the O_c atoms in mullite located at the common corner of two tetrahedra (2a Wyckoff positions) are not involved in the Raman spectra. By symmetry, all the Raman modes of a mullite with $x = 0$ directly derive from degeneracy of sillimanite Raman modes. In particular, mullite modes corresponding to metal and oxygen atoms in 4h Wyckoff positions are split into two for sillimanite. Atoms of type O_c are no longer on an inversion centre in sillimanite and six Raman active modes ($2\text{A}_g + 2\text{B}_{1g} + \text{B}_{2g} + \text{B}_{3g}$) are due to vibration of these atoms.

In mullite, the random occupancy of tetrahedral sites by Al and Si, as well as the presence of oxygen vacancies and of new tetrahedral sites when $x \neq 0$, induce breakdown of the translational symmetry of the crystal. In the case of mixed crystals

and solid solutions containing a high content of such massive point defects, the selection rules do not apply and Raman spectra consists of broad bands which tend to reproduce the phonon density of states. A good example can be found in stabilized zirconias, the spectrum of which consists of a broad continuum.^{28,29} Similar features have actually been observed on silicon mullites, as shown in the spectrum of a 55 mol% Al_2O_3 mullite obtained by McMillan and Piriou²⁵ given in Fig. 2(b). Figure 2(a) represents the spectrum of sillimanite obtained by Pinet *et al.*³⁰ Contrary to sillimanite which displays narrow and precisely defined lines, the mullite spectrum consists of broad lines, but each Raman band of mullite can be directly related to corresponding lines in sillimanite. This illustrates well the structural relation between mullite and sillimanite, which possess the same framework of octahedral and tetrahedral chains.

The spectra of Si mullites with compositions $x = 0.25$ and 0.5 prepared from the sol-gel route are given in Fig. 3 and results on mullite and sillimanite spectra are gathered in Table 1. Silicon

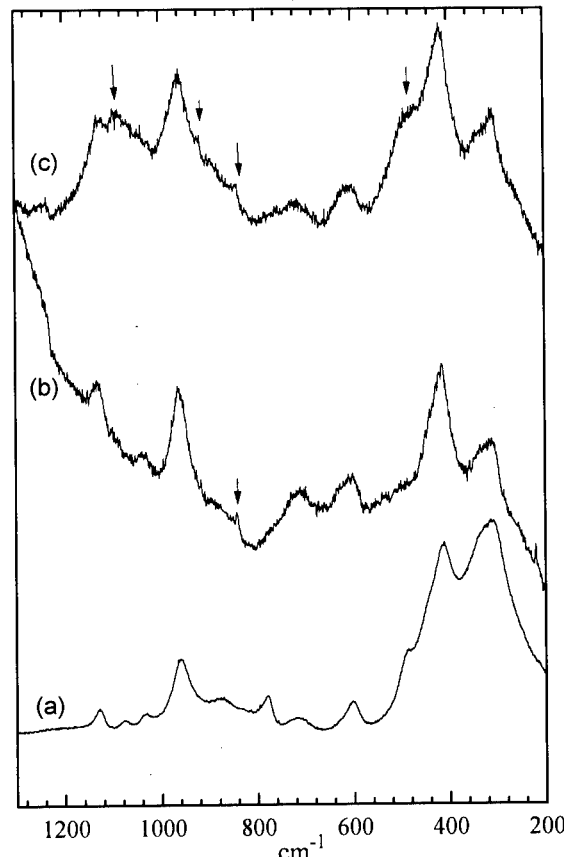


Fig. 3. Raman spectra of silicon mullites with various compositions prepared by a sol-gel route: (a) optically clear nanocrystalline glass-ceramic monolith after 4 days at 1100°C (composition $\text{Al}_2\text{O}_3-2\text{SiO}_2$); (b) pellet ($x = 0.25$, 60 mol% Al_2O_3) hot-pressed at 1600°C for 2 h (the broad band above 1200 cm^{-1} is due to graphitic precipitates); (c) pellet ($x = 0.5$, 71 mol% Al_2O_3) sintered at 1650°C for 3 h in air (arrows indicate the bands arising from the optics).

Table 1. Raman frequencies of sillimanite and Si-mullites

$Al_2O_3-2SiO_2$ Sillimanite (Ref. 30)	Mullite $x = 0.25$, sol-gel route, 1100°C	Mullite $x = 0.5$, sol-gel route, 1600°C	Mullite $x = 0.5$, sol-gel route, 1650°C
144 w			
236 s			
311 vs	310 vs	314 m	308 m
393 w			310 s
413 w	413 m	415 s	416 s
423 m			410 s
459 s			
485 w			
597 m	603 w	607 m	607 m
706 w	715 vw	711 m	718 w
849 vw	780 w	873 w	875 sh
874 w	873 w	873 w	880 sh
910 w			
966 s	960 m	962 s	960 s
1036 w	1033 vw	1033 w	1040 m
1060 w	1077 vw	1080 w	1090 w
1132 w	1129 w	1130 m	1125 w
			1160 m

s: Strong; m: medium; w: weak; vw: very weak; sh: shoulder.

mullites, as well as silicon-containing glasses and gels, are generally poor Raman scatterers^{19,20} and this explains the high noise level in the spectra of Figs 2(a), 3(b) and 3(c). However, the spectrum of the nanocrystalline glass-ceramic monolith (Fig. 3(a)) is better resolved. Local arrangements in the first steps of crystallization from gels seem to be less distorted and better defined than after high-temperature treatments.

Spectra of germanium mullites

The Raman spectra of germanium mullites with various compositions, prepared by coprecipitation and by the sol-gel route, are given in Figs 4 and 5, respectively. For the same composition, the Raman spectra of samples prepared by the two methods are very similar. This indicates that the evolution of Raman spectra with composition represents the intrinsic structural change. Corresponding wavenumbers are gathered in Table 2.

All these spectra are very similar to those of silicon mullites except for the wavenumbers, which are shifted towards low values for most lines. For all compositions, the spectra consist of broad lines as for Si mullite. The line width at half maximum amounts to about 40 cm^{-1} , which is more than twice than in sillimanite. In addition, broader bands with asymmetric profiles around 300 and 600 cm^{-1} are probably the envelope of two or more lines. For the Al_2GeO_5 compound where no oxygen vacancies are present ($x = 0$), these features can be only attributed to a disordered distribution of Al and Ge on tetrahedral sites. This confirms previous results obtained by infra-red spectroscopy^{4,31} and by electron and X-ray diffrac-

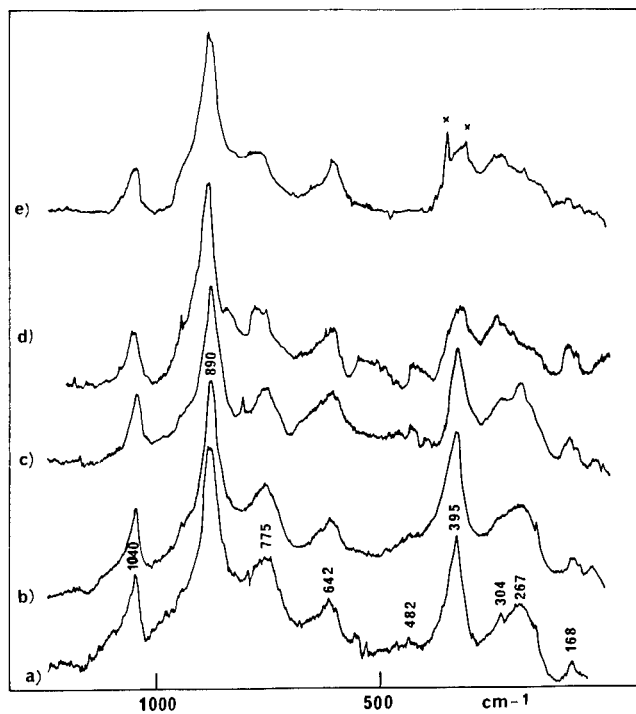


Fig. 4. Raman spectra of $\text{Al}_{4+2x}\text{Si}_{2-2x}\text{O}_{10-x}$ germanium mullites annealed at 1330°C: (a) $x = 0$ (50 mol% Al_2O_3); (b) $x = 0.13$ (55 mol% Al_2O_3); (c) $x = 0.25$ (60 mol% Al_2O_3); (d) $x = 0.40$ (67 mol% Al_2O_3); (e) $x = 0.47$ (70 mol% Al_2O_3). Traces of a Al_2O_3 are revealed by the lines at 380 and 417 cm^{-1} indicated by x.

tion patterns, as there is no diffraction spot or diffuse scattering indicating a double periodicity along the *c*-axis.¹⁷

The general aspect of the spectra remains essentially unchanged with composition for the series of

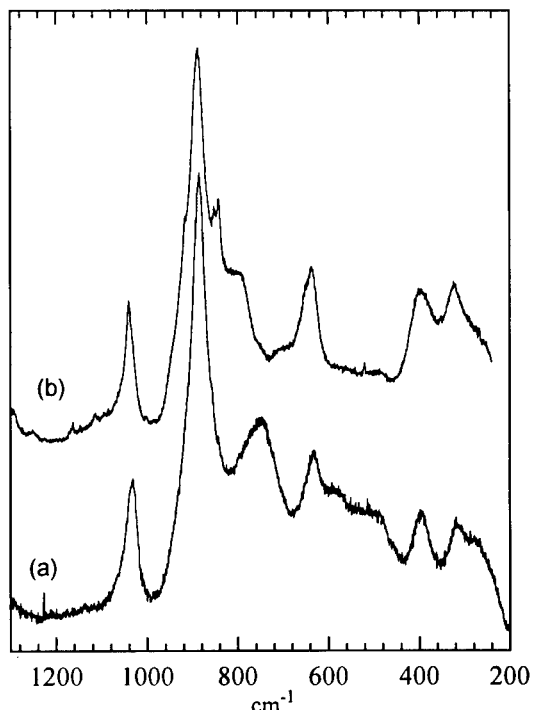


Fig. 5. Raman spectra of $\text{Al}_{4+2x}\text{Ge}_{2-2x}\text{O}_{10-x}$ germanium mullites prepared by sol-gel route: (a) optically clear monolith $x = 0.15$ (56 mol% Al_2O_3) obtained after 3 h at 1000°C; (b) translucent monolith $x = 0.25$ (60 mol% Al_2O_3) obtained at 1250°C.

Table 2. Raman frequencies of $\text{Al}_{4+2x}\text{Ge}_{2-2x}\text{O}_{10-x}$ germanium mullites as a function of composition (mol%). Samples prepared by sol-gel route are indicated by *

50% Al_2O_3 $x = 0$, 1330°C	55% Al_2O_3 $x = 0.13$, 1330°C	56% Al_2O_3 $x = 0.15$, 1000°C*	60% Al_2O_3 $x = 0.25$, 1330°C	60% Al_2O_3 $x = 0.25$, 1250°C*	67% Al_2O_3 $x = 0.40$, 1330°C	70% Al_2O_3 $x = 0.47$, 1330°C
170 w	165 w	^a	170 w	^a	170 w	170 w
265 m	270 m	270 w	250 m		260 m	260 m
305 m	305 sh	315 w	300 m	320 m	300 m	310 s
395 s	395 s	395 s	395 s	395 m	395 s	395 m
480 vw	480 vw	490 vw		480 vw	480 vw	
570 vw		580 vw	570 vw		570 vw	
640 m	640 m	635 m	640 m	635 m	640 m	640 m
775 m	780 m	790 m	785 m	790 m	785 m	795 m
890 vs	890 vs	890 vs	890 vs	890 vs	890 vs	890 w
945 sh	945 sh		945 sh		945 sh	950 sh
1040 m	1040 m	1040 m	1045 m	1040 m	1050 m	1055 sh

s: Strong; m: medium; w: weak; vw: very weak; sh: shoulder.

^a Not studied below 200 cm^{-1} .

Fig. 4. However, modification occurs in the shape, intensity or position of certain bands. Wavenumbers are slightly shifted towards lower frequencies as the alumina content increases for two high frequency lines (from 1040 to 1055 cm^{-1} and from 775 to 795 cm^{-1}). On the other hand, the location of the 640 and 395 cm^{-1} lines does not vary, though the 395 cm^{-1} line decreases and broadens as the alumina content increases. Noticeable intensity changes are also observed for the 260 and 310 cm^{-1} lines depending on composition.

The Raman spectrum of a Ga_2GeO_5 mullite ($x = 0$) given in Fig. 6 has a close resemblance with that of Al_2GeO_5 despite a significant shift towards low frequency (about 50 cm^{-1}) for the bands in the region 700–1100 cm^{-1} . Another difference is the better resolution of the broad band between 200 and 350 cm^{-1} for the gallium compound. This result is in agreement with the observation by Schneider³¹ of some band splitting in infra-red spectroscopy which was interpreted in terms of slight ordering.

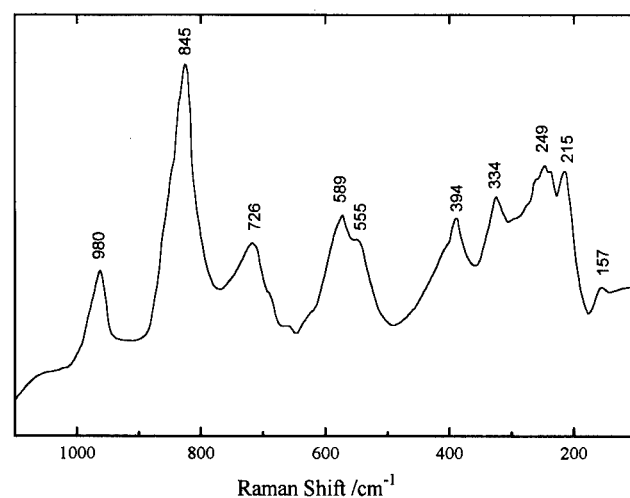


Fig. 6. Raman spectrum of Ga_2GeO_5 mullite.

The high frequency modes of $\text{Al}(\text{or Ga})_2\text{GeO}_5$ mullites (1045, 950, 885 and 785 cm^{-1} with Al and 980, 845 and 726 cm^{-1} with Ga) correspond to the v_1 and v_3 internal modes of GeO_4 groups. These modes are found at much higher wavenumbers than for isolated GeO_4 groups. They appear, for instance, in the range 800–700 cm^{-1} in scheelite orthogermanates.³² Salje and Werneke suggested that the coupling with neighbouring Al–O bonds explains the increased frequencies of SiO_4 stretching vibrations in andalusite and sillimanite.²⁶ The frequency difference in Ga and Al compounds that we observed probably results from the weaker Ga–O stretching force constants and the larger unit-cell parameters in Ga_2GeO_5 . In silicon mullites, the corresponding modes are found at higher frequencies, respectively at 1140, 1040, 960 and 880 cm^{-1} ,²⁵ in good agreement with the difference usually observed between Ge–O and Si–O stretching.³³

The asymmetric band at 640 cm^{-1} in Al–Ge mullite may be assigned to Al–O vibrations and those at 555 and 589 cm^{-1} in Ga_2GeO_5 to Ga–O vibrations. Actually, they are located in the same mid-wavenumber region where McMillan and Piriou have suggested to attribute Al–O displacement in mullite.²⁵ Moreover, Mernagh and Liu found lower Gruneisen parameters for the 708 and 594 cm^{-1} sillimanite modes which is indicative of more ionic bonding and may correspond to Al–O vibrations.²⁷

A relatively well-defined line appears at 395 cm^{-1} in Al_2GeO_5 ($x = 0$) in the region corresponding to O–Ge–O bending in orthogermanates.³² This line is severely affected when the alumina content increases and this is attributed to the decrease of the number of GeO_4 tetrahedra at the expense of AlO_4 units. Moreover, a similar line is found in Ga_2GeO_5 practically at the same frequency whereas in silicon mullite this band is at 410 cm^{-1} .

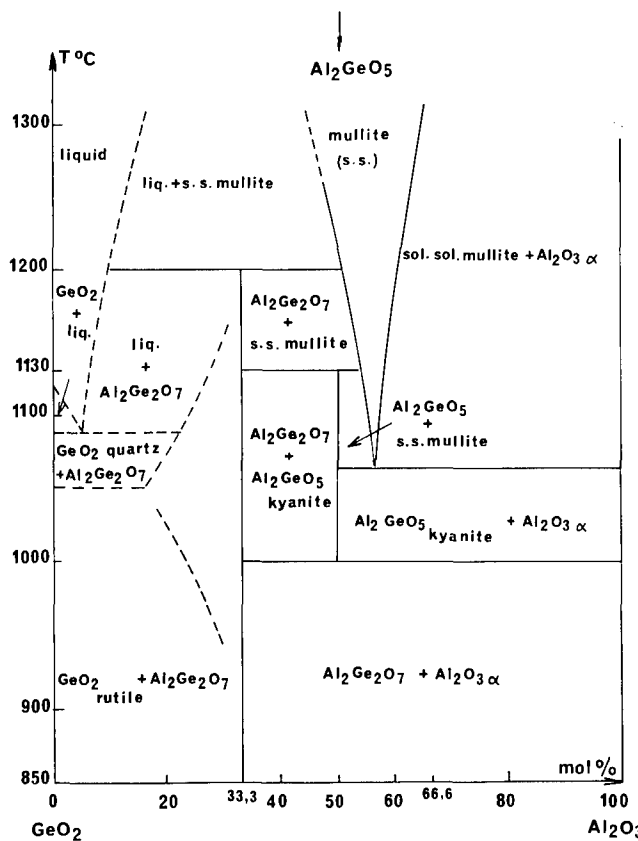


Fig. 7. $\text{GeO}_2\text{--Al}_2\text{O}_3$ phase diagram, after Perez y Jorba.⁴

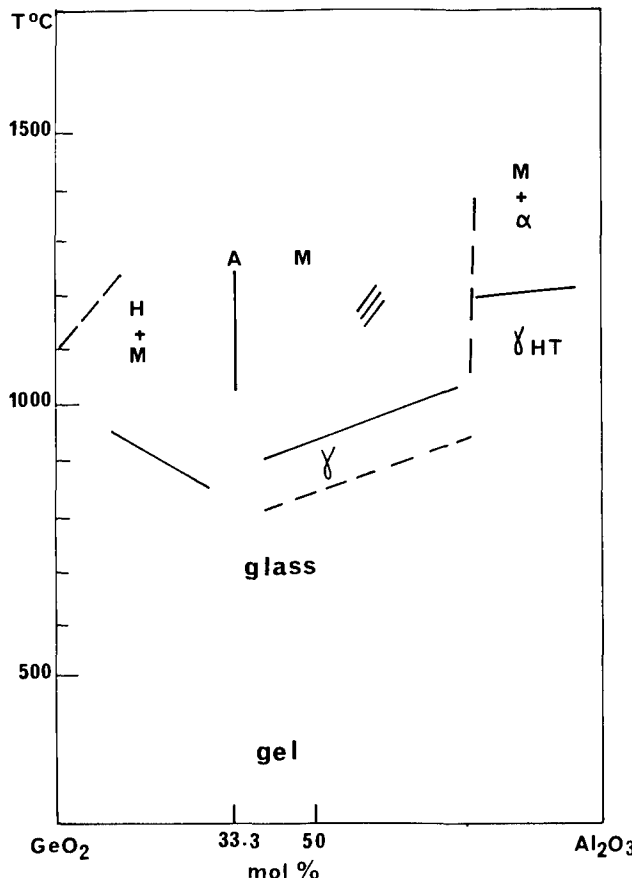


Fig. 8. Phase boundaries observed for gels prepared by slow alkoxide hydrolysis as a function of the composition and thermal treatment (H = hexagonal GeO_2 (quartz-form), M = mullite, $\alpha = \text{Al}_2\text{O}_3$ (corundum), γ = disordered phase exhibiting a spinel-like X-ray diffraction pattern, γ_{HT} = spinel phase, A = monoclinic $\text{Al}_2\text{Ge}_2\text{O}_7$, // = metastable Al_4GeO_8).

The new local arrangements formed as the alumina content increases, in particular the groups of three tetrahedra linked by the same corner (Fig. 1), are expected to modify the Raman activity concerning collective vibrations. The observed change in the shape and intensity of bands with the Al/Ge ratio in the region below 380 cm^{-1} , which corresponds to external rotational and translational modes, is probably associated with these modifications.

Mullite formation and $\text{GeO}_2\text{--Al}_2\text{O}_3$ phase diagram

$\text{GeO}_2\text{--Al}_2\text{O}_3$ phase diagrams established by the study of materials prepared solely by solid-state reaction lead to a rather simple diagram, including mullite as the only binary compound similarly to that of $\text{SiO}_2\text{--Al}_2\text{O}_3$.^{2,5} On the contrary, when the composition-temperature range is precisely explored using reactive powders, a more complex phase diagram is achieved (Fig. 7). Similarly, the crystal-

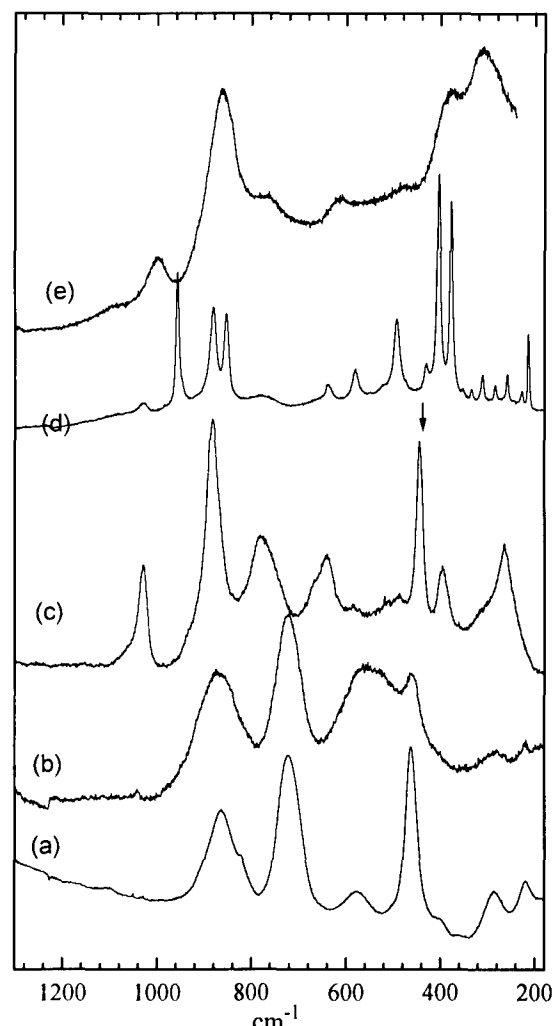


Fig. 9. Evolution of Raman spectra for the composition 2 $\text{GeO}_2\text{--Al}_2\text{O}_3$ (33.3 mol% Al_2O_3) depending on temperature: (a) water-containing gel (room temperature); (b) mesoporous glass obtained after heating at 800°C ; (c) crystallized mullite + hexagonal GeO_2 (indicated by arrow) obtained after heating at 1020°C ; (d) monoclinic $\text{Al}_2\text{Ge}_2\text{O}_7$ obtained after heating for 30 min at 1250°C ; (e) high temperature mullite obtained after heating for 3 min at 1450°C .

lization of homogeneous gels leads to a variety of stable or metastable phases. Figure 8 summarizes the results obtained by annealing optically clear Al_2O_3 – GeO_2 gels and gives the domains where the various phases are formed depending on temperature and the Al/Ge ratio. An example of successive structural changes is shown by Fig. 9, which reports the Raman spectra obtained after heating Al_2O_3 – $2\text{GeO}_{2-x}\text{H}_2\text{O}$ gels at various temperatures. Corresponding wavenumbers are given in Table 3. In the gel state, the Raman spectrum consists of well-defined bands (Fig. 9(a)) that can be assigned to the vibrations of GeO_4 (460 and 565 cm^{-1}) and GeO_6 (720 and 870 cm^{-1}) entities because this spectrum looks like the superimposition of quartz (443 and 880 cm^{-1}) and rutile (695 and 870 cm^{-1}) germania. Dehydration of this gel leads to a mesoporous glass which possesses the same Raman lines, but which are noticeably broadened. In addition, a very broad band which is characteristic of GeO_2 glass³⁴ is observed around 570 cm^{-1} (Fig. 9(b)). At higher temperature, crystallized phases are obtained, the first of which is mullite with some GeO_2 (quartz form). The Raman lines of this mullite phase (Fig. 9(c)) are relatively well defined. Mullite and GeO_2 quartz then transform into the monoclinic $\text{Al}_2\text{Ge}_2\text{O}_7$ compound. Its Raman spectrum (Fig. 9(d)) contains only very sharp lines in agreement with X-ray results on single crystals which indicated that the structure of $\text{Al}_2\text{Ge}_2\text{O}_7$ is

completely ordered.⁶ The polyhedra present in this compound are Ge_2O_7 groups consisting of two tetrahedra linked by one corner and AlO_5 bipyramids.⁶ According to the phase diagram given in Fig. 7, $\text{Al}_2\text{Ge}_2\text{O}_7$ is the phase stable below 1200°C ; however, crystallization of gels leads first to mullite rather than directly into $\text{Al}_2\text{Ge}_2\text{O}_7$. It is likely that the preparation from hydrolysis–polycondensation favours a connected tetrahedra network and induces crystallization into mullite that contains similar arrangements. At higher temperature, the stable phase mullite appears again, but the significant line width of Raman bands reveals a large amount of disorder (Fig. 9(e)).

Conclusions

Raman scattering studies demonstrated that both silicon and germanium mullites are strongly disordered at the molecular scale. In the case of the GeO_2 – Al_2O_3 system, in addition to mullites with various degrees of order, (which can be estimated from Raman line width), several phases can be prepared with methods which favour mixing at molecular scale: $\text{Al}_2\text{Ge}_2\text{O}_7$, Al_2GeO_5 (kyanite form), Al_4GeO_8 and spinel-like phases. Furthermore, the lower melting point of GeO_2 enhances the achievement of the stable state at lower temperature than in silicon-containing homologues.

Acknowledgements

The authors are indebted to Drs B. Piriou (CNRS, Ecole Centrale, Chatenay-Malabry) and B. Lasnier (University of Nantes) for helpful discussion and for kindly communicating their results on Raman spectra of silicon mullite and sillimanite.

References

1. Perez y Jorba, M., Tarte, P. & Collongues, R., Structure and properties of alumina–germanium dioxide compounds. *C.R. Acad. Sci.*, **257** (1963) 3417–20.
2. Miller, J. L. Jr., McCormick, G. R. & Ampian, S. G., Phase equilibria in the system GeO_2 – Al_2O_3 . *J. Am. Ceram. Soc.*, **50** (1967) 268–9.
3. Perez y Jorba, M., GeO_2 – Al_2O_3 and GeO_2 – Fe_2O_3 systems. Comparison with the silica corresponding systems. *Silicates Industriels*, **1** (1968) 11–7.
4. Perez y Jorba, M., Study of phases between germanium dioxide and some oxides of trivalent elements. *Rev. Int. Hautes Temp. et Refract.*, **6** (1969) 283–98.
5. Prochazka, S., Sintering and properties of dense aluminum germanates, In *Ceramics Powders*, ed. P. Vincenzini, Elsevier, Amsterdam, 1983, pp. 861–70.
6. Agafonov, V., Kahn, A., Michel, D. & Perez y Jorba, M., Crystal structure of a new digermanate $\text{Al}_2\text{Ge}_2\text{O}_7$. *J. Solid State Chem.*, **62** (1986) 402–4.

Table 3. Raman frequencies of the spectra of Fig. 9. Samples prepared by sol–gel route at the composition 2 GeO_2 – Al_2O_3 (33.3 mol% Al_2O_3)

Gel, 20°C	Glass, 800°C	Mullite + GeO_2 , 1020°C	$\text{Al}_2\text{Ge}_2\text{O}_7$, 1250°C	Mullite, 1450°C
220 m	220 vw		214 m	
		265 m	228 vw 256 w	
285 m	283 w	312 m	284 w	
			311 w 334 vw 352 vw	300 m,b
400 vw	400 v w		378 s	
		443 s	403 s 430 w	390 s,b
462 s	461 m	487 w	492 m	
			591 w	600 m,b
575 m	570 s,b	641 m	638 w	
			670 sh	
722 s	723 s	780 m	776 w,b	780 m,b
			854 s	
780 m,b	869 m,b	883 s	881 m	890 s,b
			957 m	
823 sh		1030 m	1030 w	1030 m,b

s: Strong; m: medium; w: weak; vw: very weak; sh: shoulder; b: broad.

7. Kahn, A., Agafonov, V., Michel, D. & Perez y Jorba, M., New gallium germanates with tunnel structures: α -Ga₄GeO₈ and Ga₄Ge₃O₁₂. *J. Solid State Chem.*, **65** (1986) 377–82.
8. Cameron, W. E., Mullite: a substituted alumina. *Am. Mineral.*, **62** (1977) 747–55.
9. Michel, D., Abolhassani, S., Kahn, A., Agafonov, V. & Perez y Jorba, M., Aluminum, gallium and iron (III) germanates with aluminum silicate structures. In *Mullite and Mullite Matrix Composites*, Ceramic Transactions, Vol. 6, eds S. Somiya, R. F. Davies & J. A. Pask, The American Ceramic Society, Westerville, OH, 1990, pp. 159–66.
10. Burnham, C. W., Crystal structure of mullite. *Carnegie Inst. Washington Yearbk.*, **63** (1964) 223–7.
11. Burnham, C. W., Composition limits of mullite and the sillimanite–mullite solid solution problem. *Carnegie Inst. Washington Yearbk.*, **63** (1964) 227–8.
12. Durovic, S., Isomorphism between sillimanite and mullite. *J. Am. Ceram. Soc.*, **45** (1962) 157–61.
13. Durovic, S. & Fedji, P., Synthesis and crystal structure of germanium mullite and crystallographic parameters of D-mullites. *Silikaty*, **20** (1976) 97–112.
14. Angel, R. J. & Prewitt, C. T., Crystal structure of mullite: a re-examination of the average structure. *Am. Mineral.*, **71** (1986) 1476–82.
15. Saalfeld, H. & Guse, W., Mullite single crystal growth and characterization. In *Mullite and Mullite Matrix Composites*, Ceramic Transactions, Vol. 6, eds S. Somiya, R. F. Davies & J. A. Pask, The American Ceramic Society, Westerville, OH, 1990, pp. 73–101.
16. Perez-Ramirez, J. G., Michel, D. & Portier, J. R., Enhancing of small isolated domains and superstructures in high resolution of oxides. *Mater. Res. Soc. Proc.*, **139** (1989) 321–6.
17. Kahn-Harari, A., Abolhassani, S., Perez-Ramirez, J. G., Michel, D., Mazerolles, L., Portier, R. & Perez-Ramirez, J. G., Observation of ordering in silicon and germanium mullites. *J. Solid State Chem.*, **90** (1991) 234–48.
18. Abolhassani, S., Contribution to the study of mullite-type aluminum germanates. Thesis, University of Paris-Sud, 1991.
19. Colomban, Ph., Structure of oxide gels and glasses by IR and Raman scattering. II, mullites. *J. Mater. Sci.*, **24** (1989) 3011–20.
20. Colomban, Ph., Gel–glass–mullite transition and microstructure as a function of powder preparation, Stoichiometry and Zr(Ti) addition. In *Ceramic Powder Processing Science*, eds H. Hausner, E. R. Fuller & G. D. Messing. The American Ceramic Society, Westerville, OH, 1989, pp. 85–92.
21. Colomban, Ph. & Mazerolles, L., Nanocomposites in mullite–ZrO₂ and mullite–TiO₂ systems synthesized through hydrolysis gel routes. Microstructure and fractography. *J. Mater. Sci.*, **26** (1991) 3503–10.
22. Colomban, Ph., Jones, D. J., Grandjean, D. & Flank, A. M., EXAFS and XANES study of (Si, Ge) mullites gels and glasses prepared by slow hydrolysis of alkoxides. *J. Non-Cryst. Solids*, **147–148**, (1992) 135–40.
23. Colomban, Ph. & Vendange, V., Sintering of alumina and mullites prepared by slow hydrolysis of alkoxides: the role of the protonic species and pore topology. *J. Non-Cryst. Solids*, **147–148**, (1992) 245–50.
24. Colomban, Ph., Lagrange, J. L., Bruneton, E. & Mouchon, E., Sol–gel mullite matrix–SiC 2D woven fabrics composites with and without zirconia interphase. *J. Eur. Ceram. Soc.*, in press.
25. McMillan, P. & Piriou, B., The structures and vibrational spectra of crystals and glasses in the silica–alumina system. *J. Non-Cryst. Solids*, **53** (1982) 279–98.
26. Salje, E. & Werneke, C., The phase equilibrium between sillimanite and andalusite as determined from lattice vibrations. *Contrib. Miner. Petrol.*, **79** (1982) 56–67.
27. Mernagh, T. & Liu, L. G., Raman spectra from the Al₂SiO₅ polymorphs at high pressure and room temperature. *Phys. Chem. Minerals*, **18** (1991) 126–30.
28. Keramidas, V. G. & White, W. B., Raman scattering from Ca_xZr_{1-x}O_{2-x}, a system with massive point defects. *J. Chem. Phys.*, **34** (1973) 1873–8.
29. Michel, D., Perez y Jorba, M. & Collongues, R., Study by Raman spectroscopy of order–disorder phenomena occurring in some binary oxides with fluorite-related structures. *J. Raman Spectrosc.*, **5** (1976) 163.
30. Pinet, M., Smith, D. C. & Lasnier, B., Raman microprobe in gemmology. *Revue de Géomologie*, (June 1992) 11–60.
31. Schneider, H., Infrared spectroscopic investigation of andalusite and mullite-type structures in the Al₂GeO₅–Fe₂GeO₅ and Al₂GeO₅–Ga₂GeO₅ systems. *N. Jb. Miner. Abh.*, **142** (1981) 11–123.
32. Vandenborre, M. T., Michel, D. & Ennaciri, A., Vibrational spectra and force fields of scheelite-type germanates. *Spectrochim. Acta*, **45A** (1989) 721–7.
33. Lazarev, A. I., Mirgorodskii, A. P. & Ignatiev, *Vibrational Spectra of Complex Oxides: Silicates and Analogs*, Nauka, Leningrad, 1975.
34. Henderson, G. S., Bancroft, G. M., Fleet, M. E. & Rogers D. J., Raman spectra of gallium and germanium substituted silicate glasses: variation in intermediate order. *Am. Mineral.*, **70** (1985) 946–60.

Infra-red Spectroscopic Investigation in the Mullite Field of Composition: $\text{Al}_2(\text{Al}_{2+2x}\text{Si}_{2-2x})\text{O}_{10-x}$ with $0.55 > x > 0.25$

C. H. Rüscher, G. Schrader & M. Götte

Institut für Mineralogie der Universität Hannover und SFB 173, Welfengarten 1, 30167 Hannover, Germany

(Accepted 22 July 1995)

Abstract

The infra-red absorption of 2:1 and 3:2 mullites, and a series of heat-treated mullite starting materials of nominal composition $3\text{Al}_2\text{O}_3 \cdot 2\text{SiO}_2$ prepared by the sol-gel process, are investigated in the spectral range $400\text{--}1400\text{ cm}^{-1}$ using the KBr powder method. It is shown that the intensity variation of the absorption band in the spectral range $1100\text{--}1200\text{ cm}^{-1}$ provides a useful empirical scale for the determination of mullite compositions. This absorption feature exhibits the superposition of three peaks, which are related to vibrations of the mullite specific tetrahedral units $[\text{SiO}_4]$, $[\text{AlO}_4]$ and $[\text{Al}^*\text{O}_4]$ with frequency maxima at about 1165 , 1130 and 1108 cm^{-1} , respectively.

1 Introduction

Mullite, $\text{Al}_2(\text{Al}_{2+2x}\text{Si}_{2-2x})\text{O}_{10-x}\text{V}_x$, is one of the most important ceramic products. The stability field of mullite depends on the ability to accommodate oxygen vacancies (V), which is commonly described by the exchange reaction $2\text{Si}^{4+} + \text{O}^{2-} \rightarrow 2\text{Al}^{3+} + \text{V}$. Cameron^{1,2} put forward the view of a solid solution in the stability field of mullite. The silica-rich limit has been observed for $x \approx 0.17$, possessing a hypothetical miscibility gap to the structurally closely related mineral sillimanite of $x = 0$ composition. This relationship can be seen by assuming an Al-Si disorder on the tetrahedral sites of the sillimanite structure. The field of solid solution, on the other hand, is implied by the incorporation of oxygen vacancies and the development of the lattice constants on x . The **a**-lattice parameter of the orthorhombic unit cell (*Pbam*) of mullite increases linearly from about $a = 0.754\text{ nm}$ for so-called 3:2 'ideal'¹ sinter mullite ($x = 0.25$) to $a = 0.757\text{ nm}$ for 2:1 melt mullite ($x = 0.4$). Along this route of compositions the **c** and **b** lattice parameters

also vary systematically; however, more smoothly compared with the **a** values ($b \approx 0.768\text{--}0.769\text{ nm}$; $c \approx 0.2886\text{--}0.289\text{ nm}$). The linear increase of the **a** lattice parameter still holds towards higher x values, while the **b** parameter drops down slightly and shows $a = b \approx 0.766\text{ nm}$ for $x \approx 0.67$ ^{1,2} (see also Ref. 3 and references therein). Thus, the empirical rule of the development of the lattice parameters (commonly the **a** lattice constant) can be used for an estimation of the composition of mullite ceramics and powders using X-ray diffraction techniques, as has often been reported (compare Ref. 3).

Another potential technique to estimate the composition of mullite has also been suggested by Cameron.¹ By using KBr diluted pressed pellets of various mullites, Cameron¹ observed a systematic change in the line profile of the infra-red absorption in the spectral range 1100 to 1200 cm^{-1} as a function of Al_2O_3 content. On the other hand, the infra-red technique has been used by various authors to investigate mullite crystallization (compare, e.g., Ref. 4) without, however, exploring the possibility of characterization of the mullite composition in any detail, an oversight which will be addressed in this study.

It is proposed here to follow the crystallization of mullite from base non-crystalline mullites of composition $x = 0.25$ (3:2 mullite), prepared by the sol-gel process with different methods of hydrolysis. The synthesis and structural characterization of these materials (precursor material) have been given in detail previously,^{5,6} and it has been shown that so-called types I, II and III precursors show crystallization of mullite at 900 , 1200 and 1200°C , respectively. It is known that type I precursors show a gradual change from initial mullite with high Al_2O_3 content to mullite of bulk composition $x = 0.25$ (above $\sim 1400^\circ\text{C}$), similar to observations reported by Okada and Otsuka⁷ (see also Refs 3, 5, 6, 8). Type II and III precursors, on the other hand, form $\gamma\text{-Al}_2\text{O}_3$ prior

to the crystallization of mullite.^{3,5,8,9} Thus, by investigating these crystallization processes, information on the applicability of the KBr infra-red spectroscopic technique to the determination of mullite compositions can be expected.

It may be noted that MacKenzie¹⁰ was the first to obtain an assignment of infra-red frequencies of a mullite of composition $x = 0.25$ (3:2 mullite), using simplified structural models in comparison with a KBr powder spectrum. MacKenzie¹⁰ could resolve about eight oscillator frequencies. However, it has been shown recently,¹¹ on the basis of single crystal infra-red investigations of mullite of composition $x = 0.4$ (2:1 mullite), that the spectra show strong anisotropy and that 14, 14 and nine oscillator frequencies can be resolved for the polarizations $E||a$, $E||b$ and $E||c$, respectively. The absorption bands are all close together, distributed mainly in the spectral range 300 to 1000 cm^{-1} and 1100 to 1200 cm^{-1} . This indeed creates serious problems in achieving any accurate determination of oscillator frequencies from KBr powder spectra, a point which will also be discussed here.

2 Experimental

The non-crystalline mullite base materials used in this study were kindly provided by Schneider and co-workers (DLR, Germany). These materials were synthesized starting from tetraethyl orthosilicate (TEOS) and aluminium-sec-butylate (Al-O-Bu). The educts were formulated with the stoichiometric composition $3 \text{ Al}_2\text{O}_3 : 2 \text{ SiO}_2$. After different routes of hydrolysis (type I: low water content, slow hydrolysis; types II and III: high water content and fast hydrolysis with pH values of >10 and <10 , respectively), the materials were calcined at 350°C for preservation. Details of the preparation techniques and further characterization of the precursors are given by Schneider and co-workers.^{5,6} A series of samples was prepared from each batch, these samples being subjected to further heat treatments at temperatures between 800 and 1650°C. Each sample (100 mg) was placed in a Pt crucible, heated up to its defined burning temperature at 300°C min^{-1} and quenched by removing the sample from the furnace. The holding time at the burning temperature was 15 h in each case.

The products were investigated by standard X-ray powder methods (Guinier camera) and by infra-red (IR) spectroscopic means (Bruker FTIR IFS88). For the IR measurements the samples were ground to an average particle size of $\sim 1 \mu\text{m}$ and diluted with KBr (sample:KBr = 1:250 wt%; total weight $\approx 1 \text{ g}$). From these mixtures 250 mg were taken and pressed to obtain clear discs for

the measurements. All spectra are plotted in absorption units according to $-\ln(I/I_0)$. I , I_0 = transmitted intensity of the sample plus KBr and pure KBr discs, respectively. For comparison, mullite samples of known 3:2 composition (extracted from sintered mullites) and 2:1 mullites (extracted from melt mullites) were investigated using the same route.

3 Results

KBr powder spectra of pure mullites of known composition $x = 0.25$ ($3\text{Al}_2\text{O}_3\cdot2\text{SiO}_2$) and $x = 0.4$ ($2\text{Al}_2\text{O}_3\cdot\text{SiO}_2$) are shown in Fig 1. Although the line shapes of the spectra look similar, there are characteristic distinctions. The main features observed in the spectrum of the 2:1 mullite are marked by dotted lines. Their vertical extensions are shown for better comparison with the spectrum of the 3:2 mullite. Below about 500 cm^{-1} the spectral line profiles indicate slight differences that are, however, hard to resolve systematically because of experimental difficulties. The peak maximum at $\sim 545 \text{ cm}^{-1}$ in the 2:1 spectrum appears to be shifted to $\sim 575 \text{ cm}^{-1}$ in the 3:2 spectrum. There is a sharper peak structure at $\sim 740 \text{ cm}^{-1}$ in the 3:2 spectrum compared with the 2:1 one. This feature could be related to the difference in intensity of the peak structures at $\sim 810 \text{ cm}^{-1}$ and 895 cm^{-1} . The most prominent spectral difference is observed in the absorption line profile in the spectral range 1100 to 1200 cm^{-1} . The spectrum of the 3:2 mullite is in sufficient agreement with the KBr powder spectrum of a 3:2 mullite reported by MacKenzie.¹⁰ MacKenzie¹⁰ related the peak structure in the spectral range 1100 to 1200 cm^{-1}

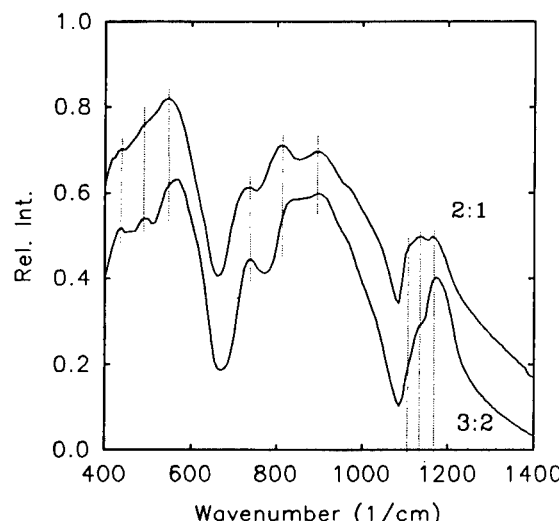


Fig. 1. IR absorption spectra of two mullites of known composition: $2\text{Al}_2\text{O}_3\cdot\text{SiO}_2$ (2:1 mullite, $x = 0.4$) and $3\text{Al}_2\text{O}_3\cdot2\text{SiO}_2$ (3:2 mullite, $x = 0.25$). Dotted vertical lines are given as a guide for the eye, to enable comparison (see text). The spectra are shifted vertically for better comparison.

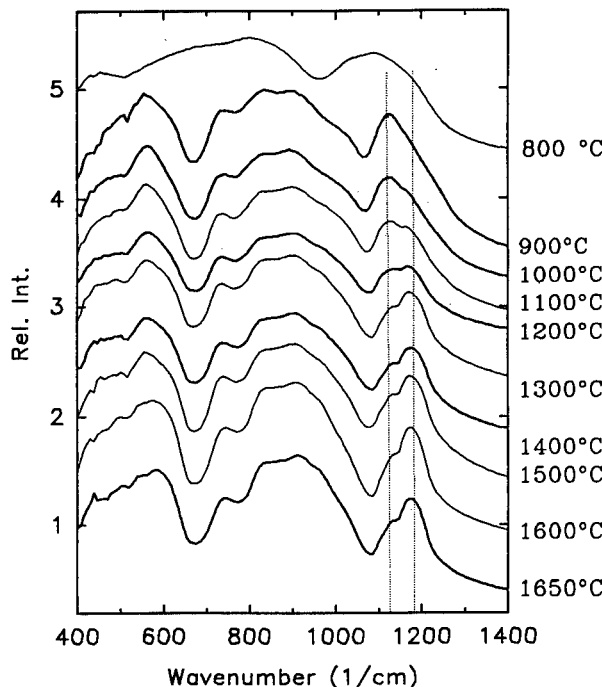


Fig. 2. IR absorption spectra of route of crystallization of type I precursor starting material with the burning temperatures as shown. The spectra are shifted vertically for better comparison. Dotted lines are a guide for the eye.

to a superposition of two peaks of high and low intensity, which were assigned to $[\text{AlO}_4]$ (1165 cm^{-1}) and $[\text{SiO}_4]$ (1125 cm^{-1}) species, respectively. In the spectra shown here, there are three positions marked that will be discussed further below.

The spectra observed for the route of crystallization of type I, II and III precursor starting materials are shown in Figs 2, 3 and 4, respectively. It has been shown earlier⁵ that precursor starting material of type I shows a higher degree of homogeneity than types II and III, i.e. there are larger Al-rich clusters in the type II and III materials.

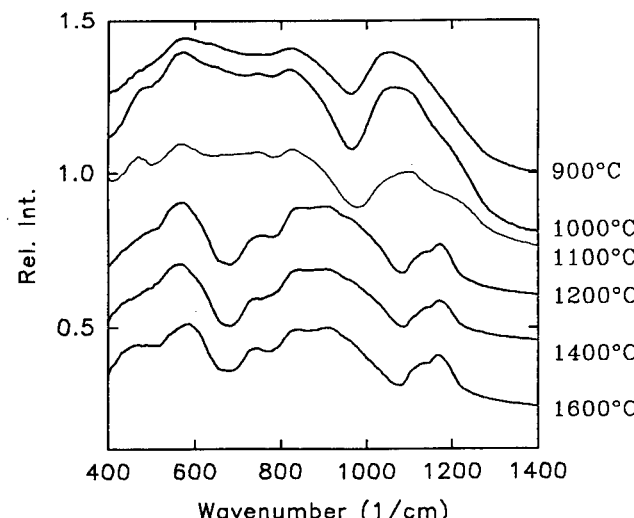


Fig. 3. IR absorption spectra of route of crystallization of type II precursor starting material with the burning temperatures as shown. The spectra are shifted vertically for better comparison.

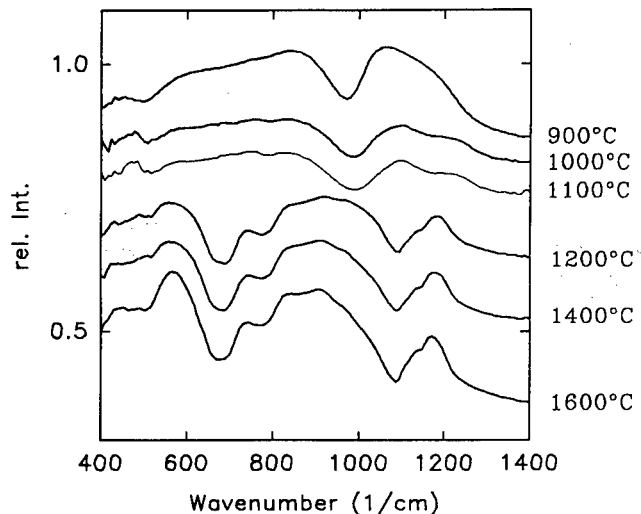


Fig. 4. IR absorption spectra of route of crystallization of type III precursor starting material with the burning temperatures as shown. The spectra are shifted vertically for better comparison.

Therefore, it can be understood that $\gamma\text{-Al}_2\text{O}_3$ crystallizes first⁵ (compare also Ref. 8) in these cases. Inspection of the spectra in Figs 3, 4 and 1 shows that mullite crystallization is proved for the material burned at 1200°C without significant changes in the mullite spectra towards higher burning temperatures. These findings are in agreement with the X-ray results. The changes in the spectra for 900 to 1100°C may be related to prior crystallization ($\gamma\text{-Al}_2\text{O}_3$). In contrast to this, the infra-red absorption spectra show that the formation of mullite for type I precursor material has already occurred at 900°C, with, however, significant changes observed in the 1100 to 1200 cm^{-1} absorption profiles at higher firing temperatures. These changes are in close agreement with observations reported by Cameron¹ for mullites of different Al_2O_3 to SiO_2 ratios ($0.6 < x < 0.25$). It may be noted that the mullite spectra in Fig. 2 also show a systematic decrease of the intensity of the peak structures at 810 cm^{-1} relative to the one at 895 cm^{-1} , but these changes are too small to be followed in detail.

For a first rough determination of the evolution of the absorption profile in the spectral range 1100 to 1200 cm^{-1} , the intensities in the spectra of the series of samples of type I (Fig. 2) were measured at 1130 cm^{-1} and 1170 cm^{-1} relative to the baseline for zero intensity obtained at 2000 cm^{-1} (not shown; note that the spectra are shifted vertically for better comparison). The ratios of the intensities $I(1130 \text{ cm}^{-1})/I(1170 \text{ cm}^{-1})$ are shown in Fig. 5 as a function of the firing temperatures. Also indicated in this figure are the ratios obtained for the 2:1 and 3:1 mullites from Fig. 1. The systematic variation of the data implies that the composition of the mullite changes gradually from Al-rich mullite

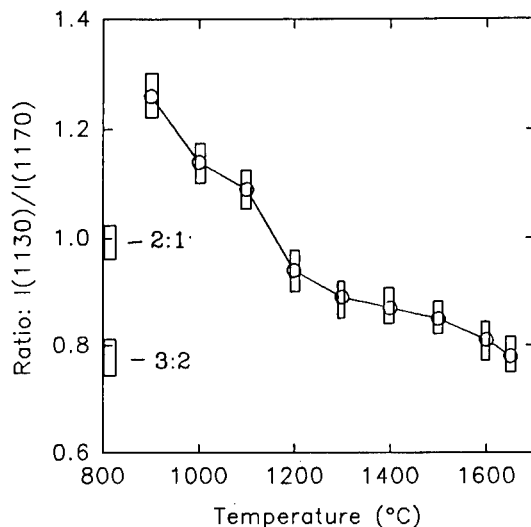


Fig. 5. Ratio of absorption measured at 1130 and 1170 cm^{-1} of the spectra given in Fig. 2 as a function of temperature. Values obtained for ideal 3:2 and 2:1 mullites (Fig. 1) are marked. Boxes indicate the experimental uncertainty. Solid line is a guide for the eye.

to bulk 3:2 mullite as a function of increasing temperature of the firing process. This suggestion is supported by the behaviour of the lattice parameters, which are shown in Fig. 6. Okada and Otsuka⁷ also obtained a similar functional dependence of the lattice constants of so-called 'xerogel' starting materials. These authors were also able to prove the change in Al content of the various mullite products by analytical transmission electron microscopy investigations. A similar phenomenon was also reported by Brown *et al.*¹² in the kaolinite–mullite reaction path, using ^{29}Si and ^{27}Al solid-state nuclear magnetic resonance spectroscopy.

The composition of the mullite products obtained here can be determined by inspecting Fig. 7, in which the intensity ratios are plotted as a function of the \mathbf{a} lattice parameter. Also shown is the x

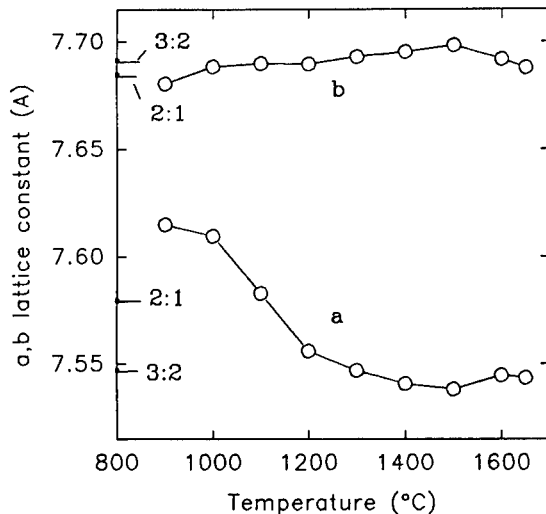


Fig. 6. Refined \mathbf{a} and \mathbf{b} lattice constants for the mullite sample according to the firing processes of type I precursors. ($c = 2.888 \pm 0.001 \text{ \AA}$, not shown). \mathbf{a} and \mathbf{b} values for the mullites of composition 3:2 and 2:1 are marked by horizontal lines.

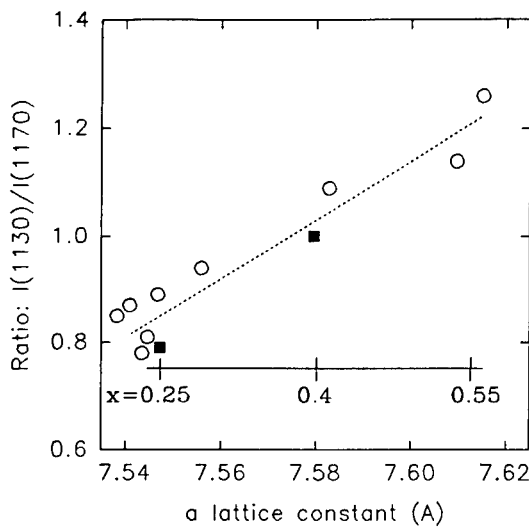


Fig. 7. Intensity ratio $I(1130 \text{ cm}^{-1})/I(1170 \text{ cm}^{-1})$ as a function of \mathbf{a} lattice constants for mullites of composition 3:2 and 2:1 (black squares) and mullites obtained from the firing of type I precursors (open circles), with dotted line as a guide for the eye. Also shown is the linear scale of mullite compositions according to $\text{Al}_2(\text{Al}_{2+2x}\text{Si}_{2-2x})\text{O}_{10-x}$ related on the \mathbf{a} lattice constants.

scale for the chemical composition $[\text{Al}_2(\text{Al}_{2+2x}\text{Si}_{2-2x})\text{O}_{10-x}]$ according to the linear relationship to the \mathbf{a} lattice constant. It is of interest to note that this linear dependence holds irrespective of different ordering patterns of the oxygen vacancies,¹³ providing a conclusive measure of the concentration of oxygen vacancies x . Thus, the IR data of the intensity ratio $I(1130)/I(1170)$ also imply a quasi linear relationship with the chemical composition of mullite. It may be noted that the absorption ratios $I(1130)/I(1170)$ for the mullite products of type II and III precursors (Figs 3 and 4) would indicate $x \approx 0.25$, i.e. there is no change in composition as a function of firing temperature between 1200 and 1600°C.

IR spectra of mullites in the field of nominal composition $x = 0$ to $x = 0.7$ were also shown by Colombari.⁴ Comparison of the 1100 to 1200 cm^{-1} absorption features to results presented here would tentatively indicate Si-rich mullite ($x < 0.4$) in the presentation in Ref. 4. However, discrimination between mullites of various compositions from the 1100–1200 cm^{-1} absorption characteristics was not considered in that study and therefore will not be discussed further here.

4 Discussion

It has been shown above that the intensity ratio of the absorption $I(1130 \text{ cm}^{-1})/I(1170 \text{ cm}^{-1})$ follows an approximately linear relationship with the composition of mullite $\text{Al}_2(\text{Al}_{2+2x}\text{Si}_{2-2x})\text{O}_{10-x}$. Therefore this ratio might be used as an empirical scale for the determination of mullite compositions. Okada

and Otsuka⁷ and Voll⁹ (compare also Schneider *et al.*³) reported a discontinuous development of the compositional dependence of mullite as a function of the firing process for type I (homogeneous) precursors. These authors observed plateau-like behaviour of the **a** lattice constant (and some anomalies in the **b** and **c** parameters) for temperatures in the range 1000 to 1100°C. However, these features cannot be resolved from the present data and can be disregarded for the further discussion here.

Problems with the use of the empirical scale of the IR absorption in the range 1100 to 1200 cm⁻¹ could be related to the coexistence of an amorphous (glassy) phase with the mullite crystals. This phase has to be considered in the crystallization route of the type I precursor, because SiO₂ or $(n\text{SiO}_2) \cdot (m\text{Al}_2\text{O}_3)$ glass phase is known to show an absorption peak in the spectral range 1000 to 1100 cm⁻¹. Thus, with the gradual formation of mullites with $x \approx 0.55$ at 900°C to $x \approx 0.25$ above 1300°C, the volume fraction of the residual amorphous phase should gradually decrease, which could be indicated by decrease of the absorption intensity observed at ~ 1130 cm⁻¹ (Fig. 2). On the other hand, there are indications – at least for the formation of mullite from type I precursors above 1000°C – that the volume fractions of the amorphous state show less influence* than the mullite absorption cross-sections. This may be verified by inspecting the absorption profiles of pure phases of 3:2 and 2:1 mullite shown in Fig. 1 and comparing them with the various spectra in Fig. 2. Additionally, this conclusion is supported by the 1100 to 1200 cm⁻¹ absorption spectra for pure mullite phases of different compositions reported by Cameron,¹ where the line profiles show a similar dependence as obtained in Fig. 2.

A deeper understanding of the changes in the absorption line profiles requires a detailed line profile analysis. This is not a simple task for powder-related spectra and anisotropic materials with a high number of atoms per unit cell, like mullite. With simple structural models ([AlO₆], [AlO₄] and [SiO₄] units), MacKenzie¹⁰ calculated the phonon frequencies of nine fundamental vibrations and related them to peak positions of the KBr powder spectra of a 3:2 mullite in the spectral range 400 to 1200 cm⁻¹. On the other hand, the number of IR active modes expected for the average structure of mullite (4B_{1u}, 9B_{2u}, 9B_{3u};¹¹ compare also Ref. 14 from this issue) already indicates that the true number of IR active modes could largely be

enhanced, compared with those resolved by the KBr experiment. The *average structure of mullite* (see, e.g., Refs 15 and 16) can most easily be understood by assuming an idealized half of the sillimanite unit cell ($c/2 \approx 2.888$ Å) according to a statistical distribution of Al and Si on tetrahedral sites. Edge-sharing [AlO₆] octahedra form chains, which run parallel to the *z*-axis. The centres of these octahedra are at (0, 0, 0) and (1/2, 1/2, 0). The oxygens of the (000) centred octahedra [on O_d sites (*x*, *y*, 0) and (*x*, *y*, 1)] and one oxygen of the second octahedron [O_{ab} at (*x*, *y*, 1/2)] form together with a fourth oxygen (O_c) at (0, 1/2, 1/2) or at (1/2, 0, 1/2) a tetrahedral unit, which is occupied by Si or Al (T₁ site). Thus, two T₁ tetrahedra always have a common O_c oxygen. The *real structure of mullite*, on the other hand, accommodates oxygen vacancies on the O_c sites, which are,

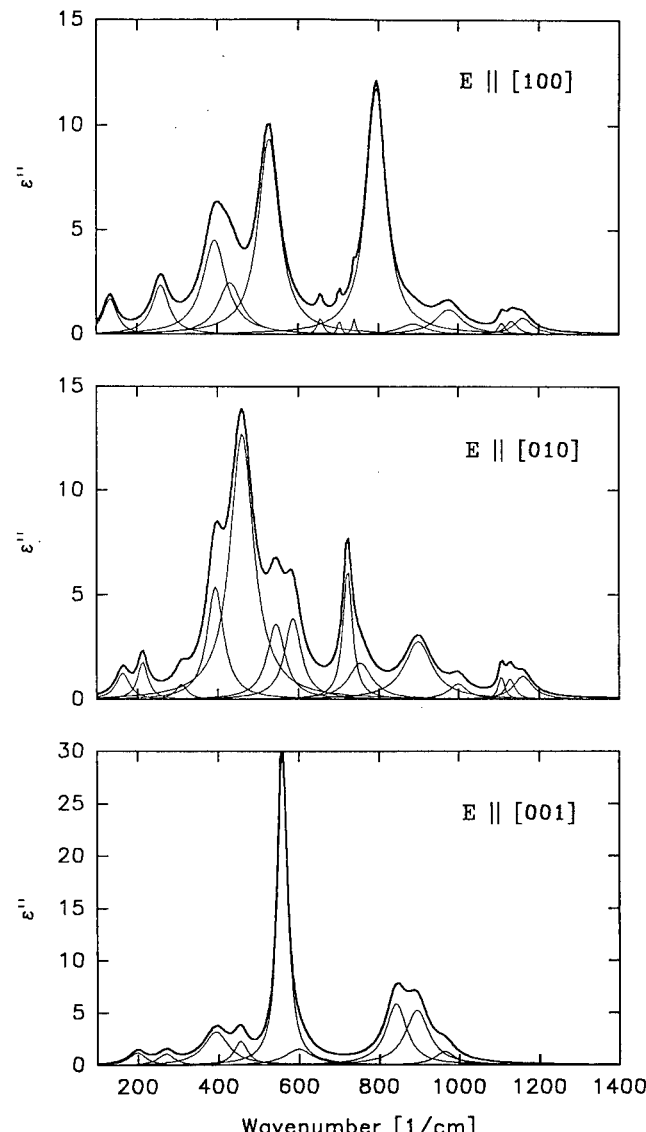


Fig. 8. Imaginary part of the dielectric function obtained by Kramers-Kronig transformation of the single crystal reflectivity of a 2:1 mullite (replotted from Ref. 11). Shown are the results of deconvolution into oscillator terms (thin lines) and their sum thick lines for the different polarizations.

*The contribution of the amorphous (glassy) phase to the IR absorption cross-section has still to be checked more accurately, e.g. by probing the cross-section of the pure phases.

therefore, fractionally occupied. Additionally, charge neutrality requires the substitution of $2\text{Si}^{4+} + \text{O}^{2-} = 2\text{Al}^{3+} + \text{V}$ ($\text{V} = \text{O}_c$ vacancy). These aluminiums can be related to new Al^* tetrahedral sites, creating O_c^* oxygen sites, which are shifted from the O_c positions. Thus, Al^* , O_c , O_c^* and T_1 positions ought all to be fractionally occupied. By taking all atomic positions into account and assuming the rather hypothetical case of full occupation, the number of IR active modes are 13B_{3u} , 13B_{2u} and 6B_{1u} according to polarizations parallel to the a , b and c lattice directions, respectively. For the sake of better comparison, the IR absorption spectra obtained from single crystal investigations of mullite of composition $x = 0.4$ (2:1 mullite) are shown in Fig. 8 (for details see Ref. 11). The deconvolution of these spectra results in 14, 14 and 9 absorption bands with polarizations parallel to the $[1\ 0\ 0]$, $[0\ 1\ 0]$ and $[0\ 0\ 1]$ lattice directions, respectively. According to this it can be concluded that the structural details of mullite result in a large number of modes, that are difficult to resolve in any detail from the KBr powder spectra (see Fig. 1), which sum over all directions of polarizations. However, the triplicate peak structure in the range 1100 to 1200 cm^{-1} can be separated and related back to the peaks in the B_{3u} and B_{2u} related spectra. For comparison, the KBr powder spectrum of 2:1 mullite and the summed single crystal absorption spectrum are shown in Fig. 9 (see also Fig. 1, where the three peak positions are marked). It may be noted that both spectra are in generally good agreement and that small discrepancies have to be related to the different measurement techniques.

Finally, it is interesting to get an assignment for the peak structure used to show the variation in the field of mullite of variable composition. MacKenzie¹⁰ and Cameron¹ suggested only a duplicate peak structure in the spectral range 1100 to

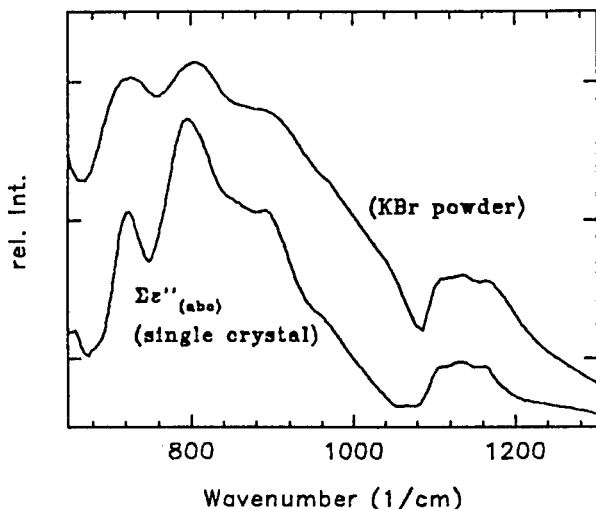


Fig. 9. Comparison of a KBr powder spectra to the summed ϵ'' spectra from Fig. 8.

1200 cm^{-1} in relation to $[\text{AlO}_4]$ and $[\text{SiO}_4]$ structural units. However, it is clear from the present study and from Ref. 11 that a third peak in this spectral range has to be taken into account for mullite, which might be assigned to an $[\text{Al}^*\text{O}_4]$ related tetrahedral vibration. According to this, the chemical variation of mullites $\text{Al}_2^{\text{VI}}(\text{Al}_2^{\text{IV}}\text{Al}_{2x}^*\text{Si}_{2-2x}^{\text{IV}})\text{O}_{10-x}$ should lead to a dependence of the intensity ratio $I(1108\text{ cm}^{-1})/I(1165\text{ cm}^{-1})$ as $2x/(2-2x)$, assuming no frequency shifts and no changes of absorption cross-section of each species as a function of x . Similarly, for the ratio $I(1130\text{ cm}^{-1})/I(1165\text{ cm}^{-1})$ a dependence according to $2/(2-2x)$ is expected, which increases more smoothly as a function of x than does the former. This increase seems to be justified by the observed dependence for the crystallization of type I precursors (see Fig. 7). However, for better information about this, the observed line profiles in the spectral range 1100 to 1200 cm^{-1} have to be deconvoluted quantitatively, which will be the task of further studies.

Acknowledgements

The authors would like to express their thanks to Dr H. Schneider and co-workers (German Aerospace Establishment, Köln) for preparing the precursor starting materials for the present study. Professor E. Eberhard is gratefully acknowledged for his encouragement of this study and for many helpful discussions. Finally, we express our thanks to Professor K. J. D. MacKenzie for many helpful comments on the manuscript.

References

1. Cameron, W. E., Composition and cell dimensions of mullite. *Am. Ceram. Soc. Bull.*, **56** (1977) 1003–11.
2. Cameron, W. E., Mullite: a substituted alumina. *Am. Mineral.*, **62** (1977) 747–55.
3. Schneider, H., Okada, K. & Pask, J. A., *Mullite and Mullite Ceramics*, John Wiley and Sons, 1994, p. 31.
4. Colomban, Ph., Structure of oxide gels and glasses by infra-red and Raman scattering. *J. Mater. Sci.*, **24** (1989) 3011–20.
5. Schneider, H., Saruhan, B., Voll, D., Merwin, L. & Sebald, A., Mullite precursor phases. *J. Eur. Ceram. Soc.*, **11** (1993) 87–97.
6. Schneider, H., Voll, D., Saruhan, B., Sanz, J., Schrader, G., Rüscher, C. H. & Mosset, A., Synthesis and structural characterization of non-crystalline mullite precursors. *J. Non-Crystalline Solids*, **178** C19.
7. Okada, K. & Otsuka, N., Change in chemical composition of mullite formed from $2\text{SiO}_2^*3\text{Al}_2\text{O}_3$ xerogel during the formation process. *J. Am. Ceram. Soc.*, **70** (1987) C245–47.
8. Li, D. X. & Thomson, W. J., Tetragonal to orthorhombic transformation during mullite formation. *J. Mater. Res.*, **6** (1991) 819–24.
9. Voll, D., Mullitprecursoren: Synthese, temperaturabhängige

Entwicklung der strukturellen Ordnung und Kristallisationsverhalten. Dr Thesis, University Hannover, 1994.

- 10. MacKenzie, K. J. D., Infrared frequency calculations for ideal mullite ($3\text{Al}_2\text{O}_3 \cdot 2\text{SiO}_2$). *J. Am. Ceram. Soc.*, **55** (1972) 68–70.
- 11. Rüscher, C. H., Lattice vibrations of 2:1 mullite in infrared and Raman spectra. Submitted.
- 12. Brown, I. W. M., MacKenzie, K. J. D., Bowden, M. E. & Meinholt, R. H., Outstanding problems in the kaolinite–mullite reaction sequence investigated by ^{29}Si and ^{27}Al solid state nuclear magnetic resonance: II, high-temperature transformations of metakaolinite. *J. Am. Ceram. Soc.*, **68** (1985) 298–301.
- 13. Eberhard, E., Private communication, 1994.
- 14. Michel, D., Colombe, Ph., Abolhassani, S., Voyron, F. & Kahn-Harari, A., Germanium mullite: structure, phase relations and vibrational spectra of gels, glasses and ceramics. *J. Eur. Ceram. Soc.*, **16** (1996) 161–8.
- 15. Sadagana, R., Tokonami, M. & Takeuchi, Y., The structure of mullite, $2\text{Al}_2\text{O}_3 \cdot \text{SiO}_2$, and relationship with the structure of sillimanite and andalusite. *Acta Crystallogr.*, **15** (1962) 65–8.
- 16. Angel, R. J. & Prewitt, C. T., Crystal structure of mullite: a reexamination of the average structure. *Am. Mineral.*, **71** (1986) 1476–82.

Interpretation of Mullite Real Structure via Inter-vacancy Correlation Vectors

S. H. Rahman,^a S. Strothenk,^a C. Paulmann^b & U. Feustel^a

^aInstitut für Mineralogie, Universität Hannover, Welfengarten 1, 30167 Hannover, Germany

^bMineralogisch-Petrographisches Institut, Universität Hamburg, Grindelallee 48, 20146 Hamburg, Germany

(Accepted 22 July 1995)

Abstract

High resolution electron microscopy (HREM) results yield that the oxygen vacancies in mullite form domains with higher oxygen vacancy concentrations and specific preferred directions. The domains are more or less statistically distributed in a disordered matrix. In the (010) plane the oxygen vacancies are arranged along [102] and [10-2] over two to four unit cells. In addition, ordered domains with higher amounts of vacancies exhibit a doubling of the c-axis which can already be seen in $h01$ diffraction patterns. Vacancy arrangements in the (100) plane are characterized by preferred orientations along [012] and [01-2] and [001], resulting in an average direction parallel to [013] and [01-3]. Columns with higher vacancy concentrations usually reveal distances of 1.5b and 5 to 6c.

Considering the above-mentioned HREM results, the real structure configuration of 2:1 mullite has been established using the videographic two-dimensional and three-dimensional simulation method. The ordering scheme of the oxygen vacancies can be described via inter-vacancy correlation vectors (short-range order vectors $1mn$; $1=a/2$, $m=b/2$, $n=c$). It has been confirmed that the inter-vacancy correlation vectors $\langle 111 \rangle$, $\langle 201 \rangle$ and $\langle 310 \rangle$ are preferred but a complete structure description can only be obtained by considering the correlation vectors $\langle 022 \rangle$, $\langle 330 \rangle$, $\langle 130 \rangle$, $\langle 401 \rangle$, $\langle 113 \rangle$, $\langle 040 \rangle$, $\langle 222 \rangle$, $\langle 223 \rangle$, $\langle 600 \rangle$ and $\langle 312 \rangle$ additionally. These inter-vacancy vectors, especially $\langle 022 \rangle$ and $\langle 330 \rangle$, play an important role for the formation of the diffuse scattering in the $h01$ and $0k1$ plane.

Introduction

Deviations from the ideal periodic arrangement (point defects, modulations, short-range order, domain boundaries, etc.) strongly influence the physical properties of crystalline solids. Hence,

determination of the real structure becomes a major task in examining the influence of structural disorder on the physical behaviour of materials.

Characteristic features in diffraction patterns of disordered crystals are diffuse scattering and/or satellite reflections apart from the Bragg reflections, the latter being attributed to the average structure. Diffuse scattering, caused by short-range ordering, cannot be directly interpreted by known structural disorder theories^{1,2} which mainly deal with discrete satellite reflections. However, Monte Carlo methods in conjunction with optical or computer-based Fourier transforms yield information about deviations from the average structure. Besides this, high resolution electron microscopy (HREM) in combination with contrast simulations of predefined structure models is the most important real space method to achieve information about certain types of structural disorder on the atomic scale.

The above-mentioned methods have been applied to characterize the ordering phenomena of oxygen vacancies in the non-stoichiometric aluminosilicate mullite ($\text{Al}_2[\text{Al}_{2+2x}\text{Si}_{2-2x}]\text{O}_{10-x}$) which shows a complex scheme of satellite reflections and diffuse scattering throughout reciprocal space (Fig. 1).

HREM investigations of mullite mainly deal with beam directions parallel to $[001]$ ³⁻⁷ and $[010]$.⁸⁻¹⁰ Recently, Paulmann *et al.*¹¹ performed 200 kV and 300 kV HREM investigations along $[010]$ and $[100]$. They found preferred vacancy orientations in domains with higher vacancy concentrations, distributed in a matrix with minor degree of order.

Early investigations of the satellite reflections with optical Fourier transforms were performed by Saalfeld¹² for the $h01$ plane. Tokonami *et al.*¹³ examined the diffuse scattering in $hk\frac{1}{2}$ and $hk\frac{2}{9}$ planes and derived a model of the vacancy arrangement in large domains. Monte Carlo simulations of structural models together with their Fourier transforms were presented by Welberry

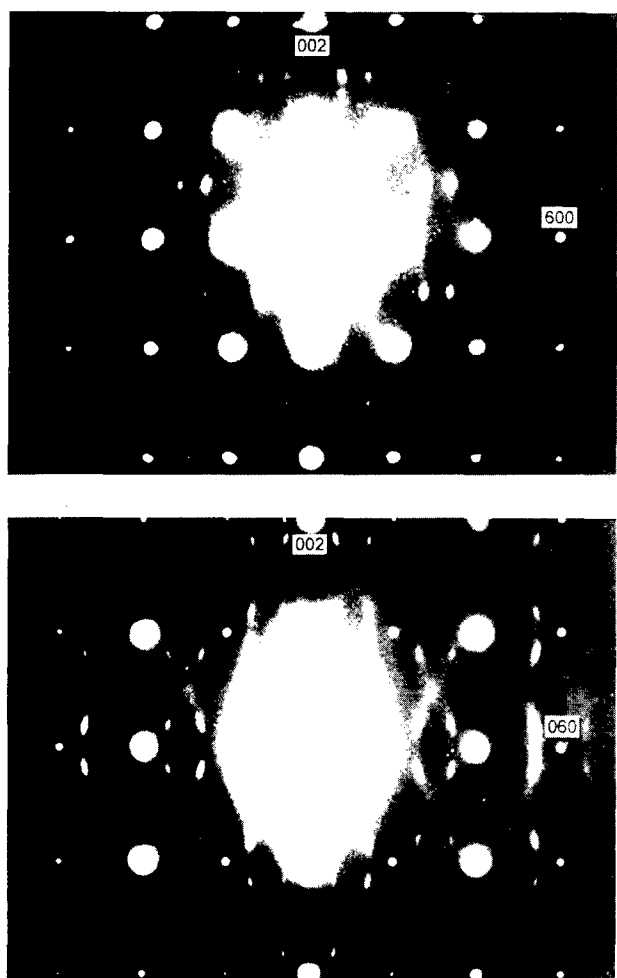


Fig. 1. Electron diffraction patterns of mullite: top, $h0l$; bottom, $0kl$.

and Withers¹⁴ to explain the diffuse scattering in $hk\frac{1}{6}$, $hk\frac{1}{4}$, $hk\frac{1}{3}$, $hk\frac{1}{2}$.

Taking the results of HREM investigations into consideration, a specific distribution scheme of inter-vacancy vectors in the (001) plane was presented by Rahman,^{15,16} Rahman and Paulmann,¹⁷ Paulmann *et al.*¹⁸ and Paulmann *et al.*¹¹ Butler *et al.*¹⁹ recently carried out a three-dimensional (3-D) real structure simulation by taking interaction pair energies into account, the latter having been obtained by Padlewski *et al.*²⁰ Variation and addition of pair energies led to relatively good agreement of Fourier transforms with the experimental diffraction patterns of the $hk\frac{1}{3}$ and $hk\frac{1}{2}$ reciprocal planes, whereas the Fourier transforms for $hk\frac{1}{6}$ and $hk\frac{1}{4}$ differed slightly from the experimental patterns.

Until now, Monte Carlo simulations of the mullite real structure have mostly dealt with the diffuse scattering in reciprocal planes from $hk0$ to $hk\frac{1}{2}$, taking neither the position of satellite reflections nor the diffuse scattering in $h0l$ and $0kl$ diffraction patterns into account. Additionally, no next nearest inter-vacancy correlation vectors were considered,²¹ although these vectors may play an important role in the exact interpretation of the

additional diffraction phenomena in the $h0l$ and $0kl$ planes.

Consequently, the aim of the present study is to combine results from a quantitative investigation of HREM images by contrast simulations and digital image processing methods with videographic real structure simulations²² to receive a 3-D description of the oxygen vacancy arrangement in mullite via inter-vacancy correlation vectors.

Experimental

The investigated specimens of 2:1 mullite grew as single crystals ($3 \times 3 \times 10$ mm) in ingots of commercially produced mullite bricks which were synthesized by heating a mixture of kaolinite and Al_2O_3 with an arc furnace and casting the melt at 2000°C. Several microprobe analyses of crystals with well-developed $\{110\}$ faces and growth direction along $[001]$ gave a chemical composition of 75.9 wt% Al_2O_3 and 23.8 wt% SiO_2 ($x = 0.39$), close to the ideal value of 0.40.

Electron microscope investigations (diffraction, HREM) were performed using Hitachi H-800 and H-9000 microscopes with LaB_6 cathodes, operating at 200 and 300 kV accelerating voltage, respectively.

Preparation of crystallites was carried out by conventional crushing with propanol in an agate mortar and transferring the suspension to carbon-coated copper grids.

The computer system for videographic real structure simulations comprised of an IBM-AT with a special array processor and graphic adaptor boards interconnected by a fast external port and to the host computer through the AT-bus interface. The configuration permitted calculation of fast Fourier transforms (FFT) of 1024×1024 pixels and 8-bit colour depth within 8 s.

HREM Investigations

HREM investigations of real structures require contrast simulations with predefined structure models to permit a correct interpretation of the contrast patterns. A detailed study with beam directions along $[010]$ and $[100]$ was recently carried out by Paulmann *et al.*¹¹ since the satellite reflections, indicating an incommensurate modulation of the mullite structure, are best visible in $h0l$ and $0kl$ diffraction patterns. A projection of the structure along these directions shows a dense packing of atoms with different scattering potentials. Nevertheless, extensive contrast simulations of supercells with more than 2000 atoms revealed

striking changes of the contrast pattern in the immediate vicinity of projected vacancy positions. This fact can be attributed to associated cation shifts near an oxygen vacancy which result in a remarkable change of the scattering potential. Both planes are characterized by contrast enhancements at vacancy positions, whereas in the (001) plane⁴ an intensity decrease of dots located clockwise next to a vacancy position is observed. Through-focus series of the (010) and (100) planes gave characteristic defect-induced contrast patterns at defocus values of -30, -65, -75 nm and -35, -45, -65, -75 nm, respectively. More details about the applied supercells and simulation parameters are given elsewhere.^{11,16} Special attention should be paid to a defocus range of -25 to -35 nm where dots in the contrast pattern directly coincide with the vacancy position (*ac*-plane) or cause an elongated and enhanced dot (*bc*-plane).

Figure 2 shows 200 kV HREM images along [010] and [100] at approximate defocus values of -30 nm. Closer inspection of the images reveals intensity variations of dots which can be attributed to higher vacancy concentrations along the incident beam.¹¹ Further investigations with different vacancy concentrations and different arrangements yield a linear dependence of defect-induced intensity enhancements and the concentration of oxygen vacancies along the beam direction. Furthermore, concentrations of only 20% still cause a detectable change of the contrast pattern.

In order to determine preferred vacancy arrangements in the (010) and (100) planes, digitized HREM images were investigated by image processing methods. After determining the greyscale area of the contrast patterns (8 bit) in Fig. 2, a progressive filtering procedure of selected greyscale areas was performed. As the stepwise filtering progresses, a continuous decrease of the observable maxima can be detected [Figs 3(a)-(e) and 4(a)-(e)], which enables the determination of O_c columns with different concentrations of vacancies and domains with specific ordering schemes. Detailed analyses were carried out for selected areas [rectangles in Figs 3(a) and 4(a)] and the results are presented in Figs 3(f) and 4(f), respectively.

A striking feature of (010) HREM images are linear arrangements of higher vacancy concentrations along [102] and [10-2] over two to four unit cells. In addition, ordered domains with higher amounts of vacancies exhibit a doubling of the *c*-axis which can already be seen in *h0l* diffraction patterns. Combining the arrangements along [102] and [10-2] and the twofold periodicity along [001] yields a centred pattern with columns of higher oxygen vacancy concentrations, frequently

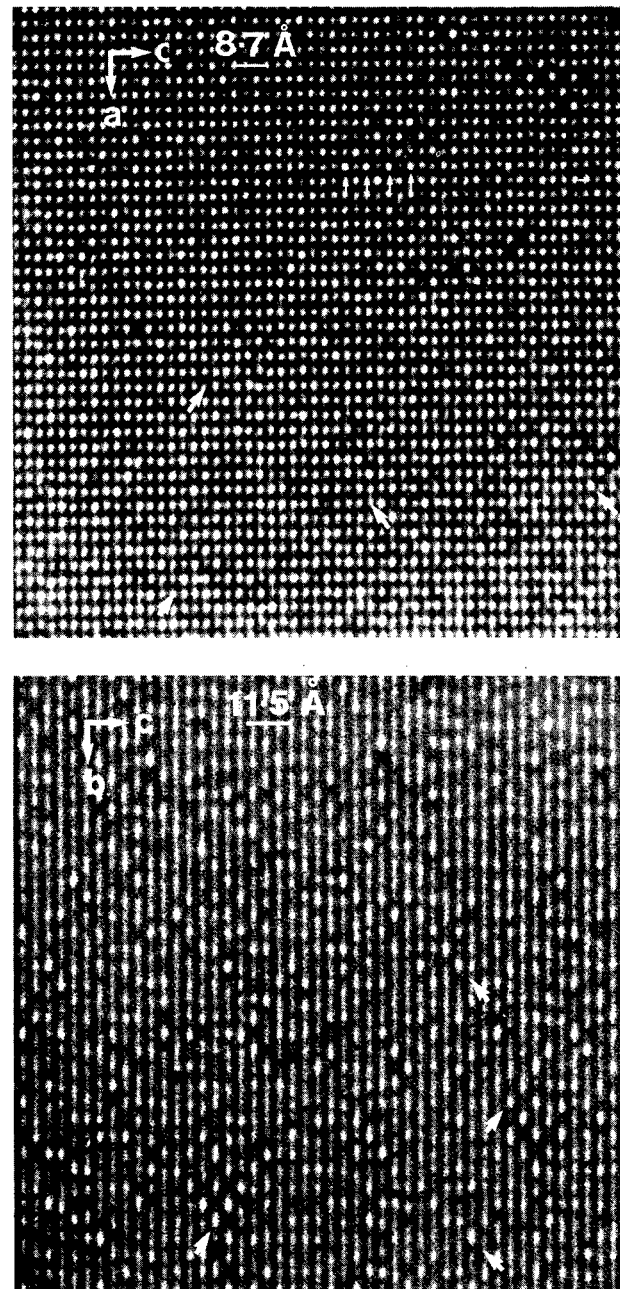


Fig. 2. 200 kV HREM images of 2:1 mullite: top, (010) plane; bottom, (100) plane.

building up an antiphase relationship. The pattern closely resembles those of Al-rich mullites ($x \geq 0.48$)⁹ but does not show long-range ordering. Vacancy arrangements in the (100) plane are characterized by preferred orientations along [012], [01-2] and [001], resulting in an average direction parallel to [013] and [01-3]. O_c columns with higher vacancy concentrations usually reveal distances of 1.5*b* and 5 to 6*c*.

Summarizing the HREM results, the oxygen vacancies in mullite form domains with higher defect concentrations and specific preferred directions. The domains are more or less statistically distributed in a disordered matrix. A schematic representation of the vacancy arrangements in the main crystallographic planes is presented in Fig. 5.

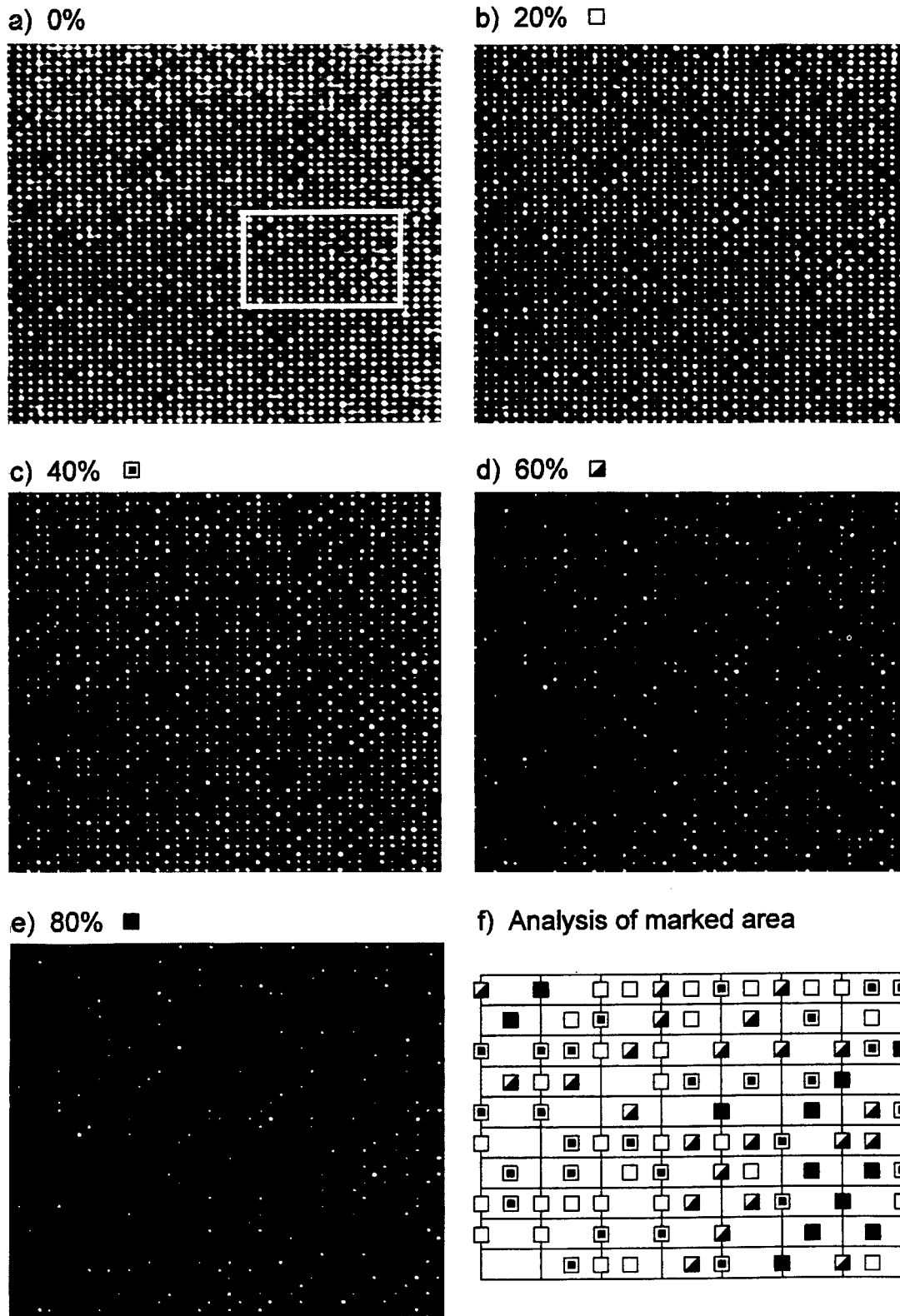


Fig. 3. Digital image processing of a 200 kV HREM image of the (0 1 0) plane. (a)–(e) Continuous filtering of dot greyscale in %. (f) Analysis of marked area in (a). *a*-Axis horizontal, *c*-axis vertical.

Although HREM investigations yield valuable information about preferred vacancy arrangements, one has to deal with some restrictions regarding the 3-D interpretation of the contrast patterns, since they are caused by a projection of the structure along the incident beam. However, the HREM results in the three main crystallographic directions give valuable parameters for

two-dimensional (2-D) and 3-D videographic real structure simulations.

2-D Videographic Real Structure Simulations

The videographic method is a procedure for the determination of real structures and employs a

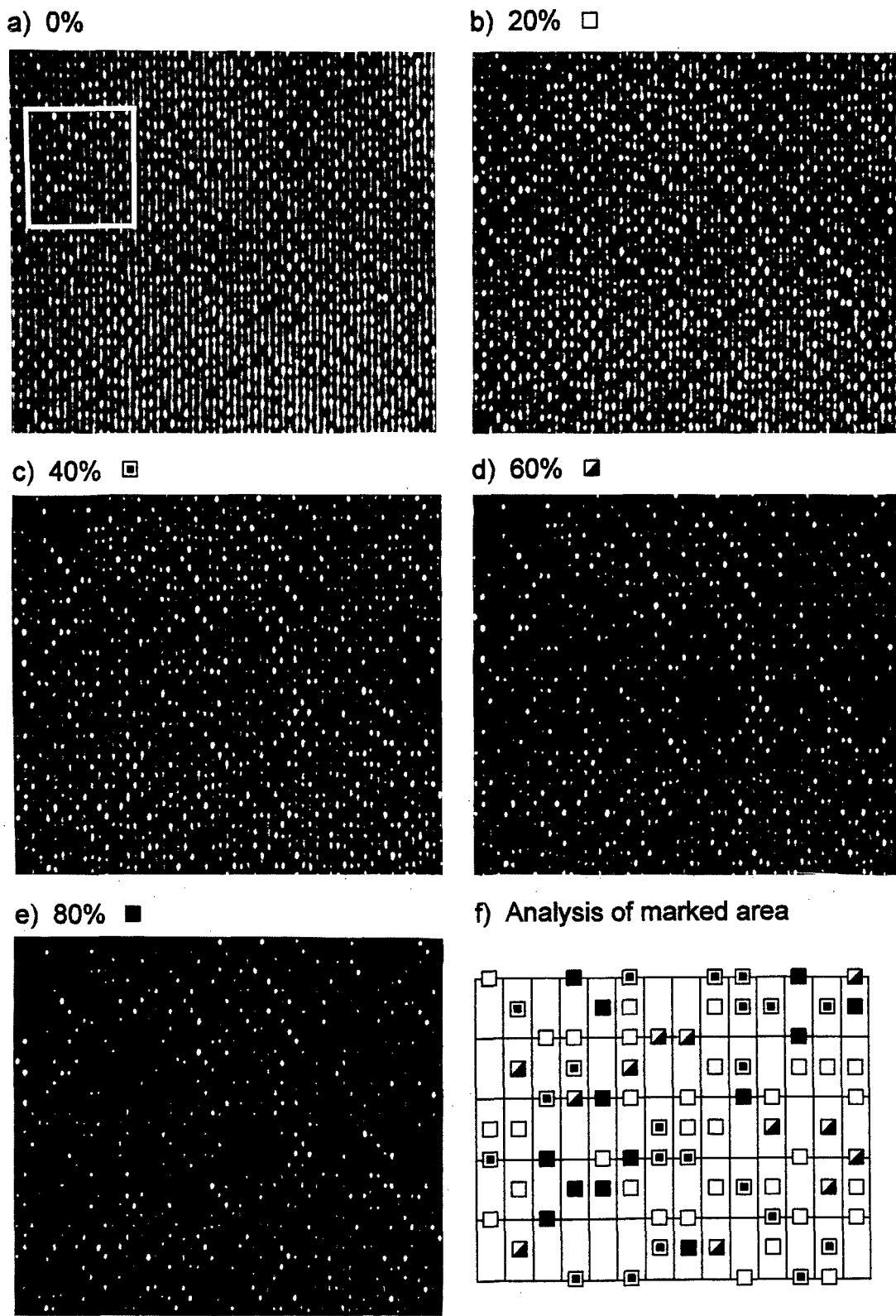


Fig. 4. Digital image processing of a 200 kV HREM image of the (100) plane. (a)–(e) Continuous filtering of dot greyscale in %. (f) Analysis of marked area in (a). *c*-Axis horizontal, *b*-axis vertical.

statistical mathematical approach and computer graphics to aid the interpretation of diffuse scattering from a disordered crystal.²² The video-graphic method replaces atoms of different scattering power by pixels with varying grey levels. Instead of calculating the diffraction pattern by a time-consuming real space summation, the method offers the opportunity of using the fast FFT

algorithm for Fourier transforming a real structure image (superstructure) which consists of structure variants, derived from the average structure.

Determinations of mullite average structure^{23–29} revealed the space group *Pbam* with chains of edge-sharing AlO_6 octahedra along [001] which are crosslinked by (Si, Al) tetrahedral double chains [Fig. 6(a)]. Introduction of oxygen vacancies on

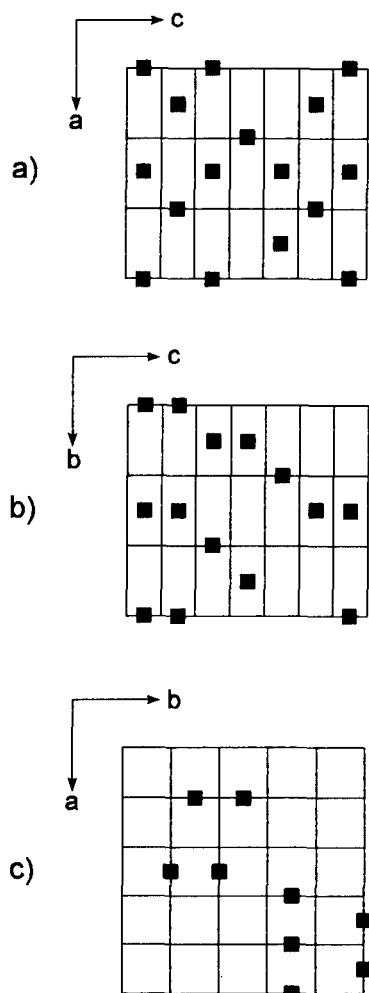


Fig. 5. Schematic representation of ordering schemes: (a) (010) plane; (b) (100) plane; (c) (001) plane.

O_c sites drives adjacent cations to occupy a new tetrahedral Al^{*} site to preserve a fourfold coordination. Additionally, neighboured O_c atoms shift towards a less symmetric O_c^{*} site [Fig. 6(b)]. According to Rahman,²² the average structure can be described as a superposition of a number of structure variants which are usually derived by taking crystal chemical rules into account. For a deconvolution of the mullite average structure the following arguments were applied.

$Si/Al-O_c$ bond lengths of 0.173 and 0.178 nm lead to a tetrahedral occupation by Al, whereas 0.167 nm for the $Si/Al-O_c$ bond gives an Si occupation of the tetrahedron in agreement with calculations of Padlewski *et al.*²⁰ Considering these rules and different O_c and O_c^{*} occupations, it is possible to derive 34 structure variants from the mullite average structure which are represented in Fig. 7. Each four variants (1–4, 5–8, 9–12, 13–16) exhibit an oxygen vacancy on the same cell edge and different O_c/O_c^{*} occupations on the remaining three edges. Numbers 17 to 32 are vacancy-free only with a variation on the O_c/O_c^{*} sites. Variants 33 and 34 represent the silica-free $\iota-Al_2O_3$ modification proposed by Saalfeld.³⁰ The distribution of

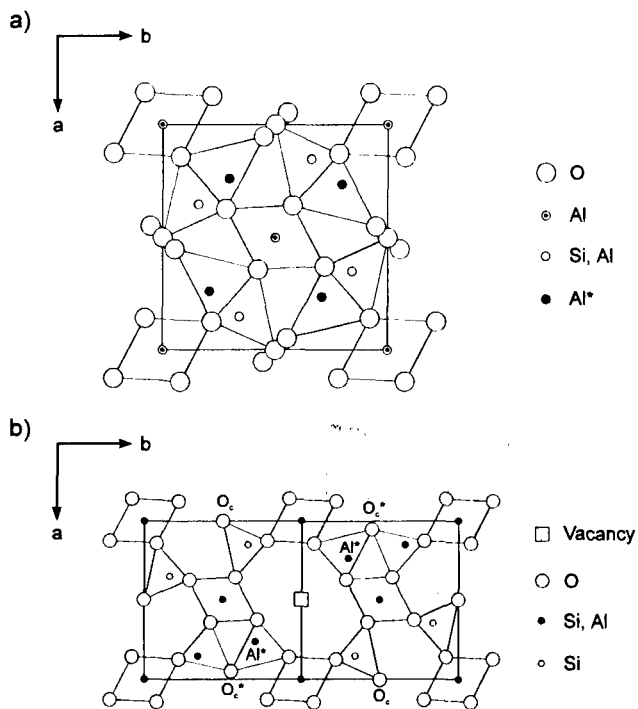


Fig. 6. (a) Average structure of mullite. (b) Atomic displacements around an oxygen vacancy.

the structure variants is performed using joint probabilities (nearest neighbours) and correlation vectors (next nearest neighbours, over next nearest) as described in more detail by Rahman²² and Rahman and Rodewald.³¹

For the 2-D videographic real structure simulations, the following preferred vacancy arrangements, obtained from HREM investigations and interpretation of diffraction patterns,¹¹ were taken into consideration.

(001) plane: Linear arrangements along [100] and [010] occasionally separated by 1.5b and 1.5a, respectively.

(010) plane: Arrangements along [102] and [10-2] with an incommensurate modulation of $\approx 1.5a$ and twofold periodicity along [001].

(100) plane: Arrangements along [012], [01-2] and [001] with an incommensurate modulation of $\approx 1.5b$ and approximate fivefold modulation along [001].

Extended videographic simulations³² with different structure variants represented by 8×8 and 16×16 pixel grids per structure variant yielded the preference of only a few correlation vectors to be responsible for the main features of the diffuse scattering in experimental X-ray diffraction patterns. The intensity distribution at higher scattering angles is mainly affected by an appropriate representation of the O_c/O_c^{*} shift in the videographic structure image, whereas the Al/Si occupation of the tetrahedral sites only plays a negligible role. Figure 8 (top) shows a diffraction

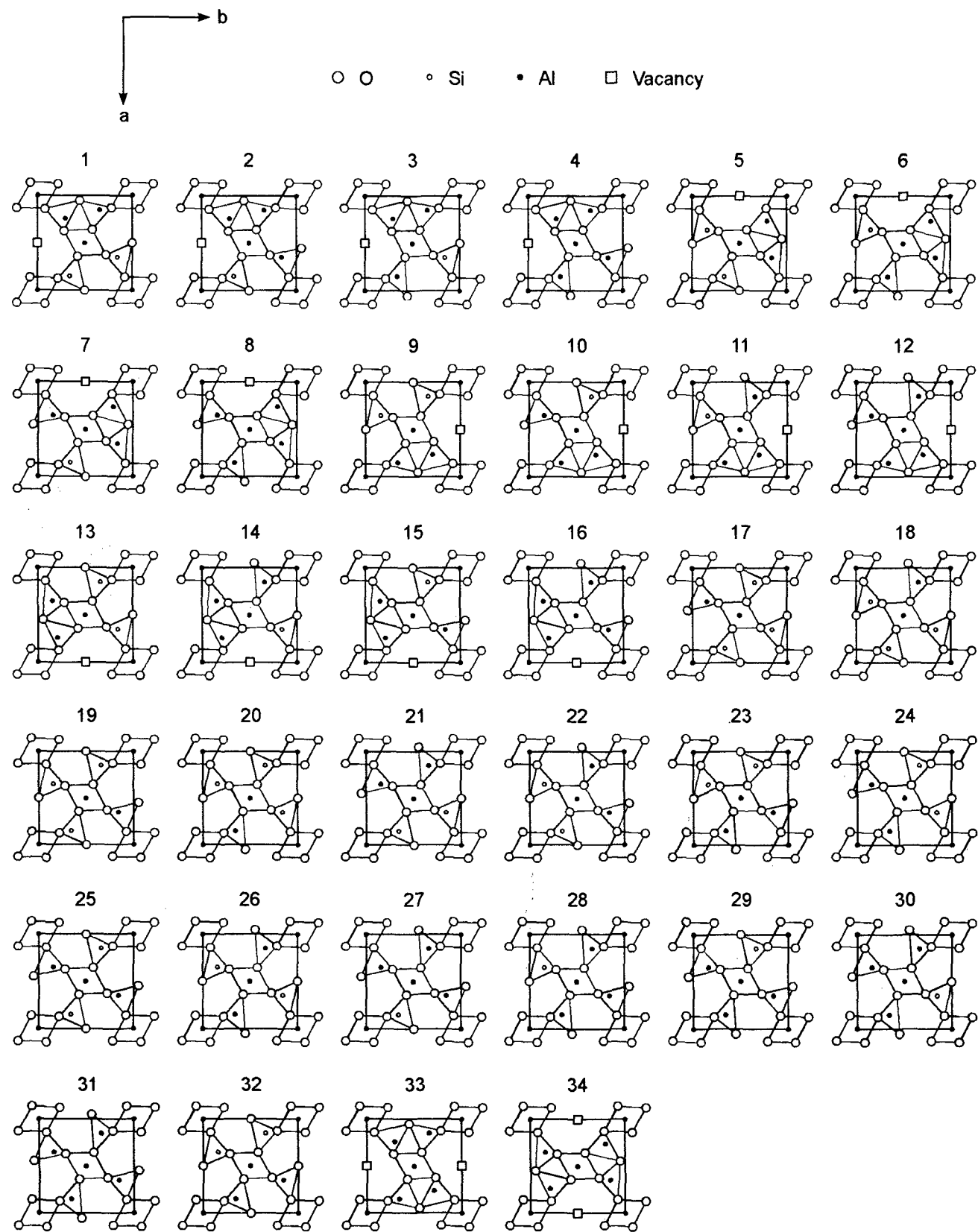


Fig. 7. 34 structure variants of mullite.

pattern of the $h k \frac{1}{4}$ plane which has been reconstructed from a digitized Weissenberg pattern with additional background correction and contrast enhancement of the weak diffuse scattering. Comparison with a Fourier transform [Fig. 8 (middle)] of the videographic structure image [Fig. 8 (bottom)] reveals good agreement because the application of

a 16×16 grid allows the representation of all atomic positions with sufficient accuracy.

For an analysis of the structure image, the unit lengths of the correlation vectors (lmn) were chosen to be $l = \frac{1}{2}a$, $m = \frac{1}{2}b$ and $n = c$. An analysis of the simulation field shows a higher frequency of $\langle 310 \rangle$, $\langle 130 \rangle$, $\langle 330 \rangle$, $\langle 020 \rangle$ and $\langle 200 \rangle$

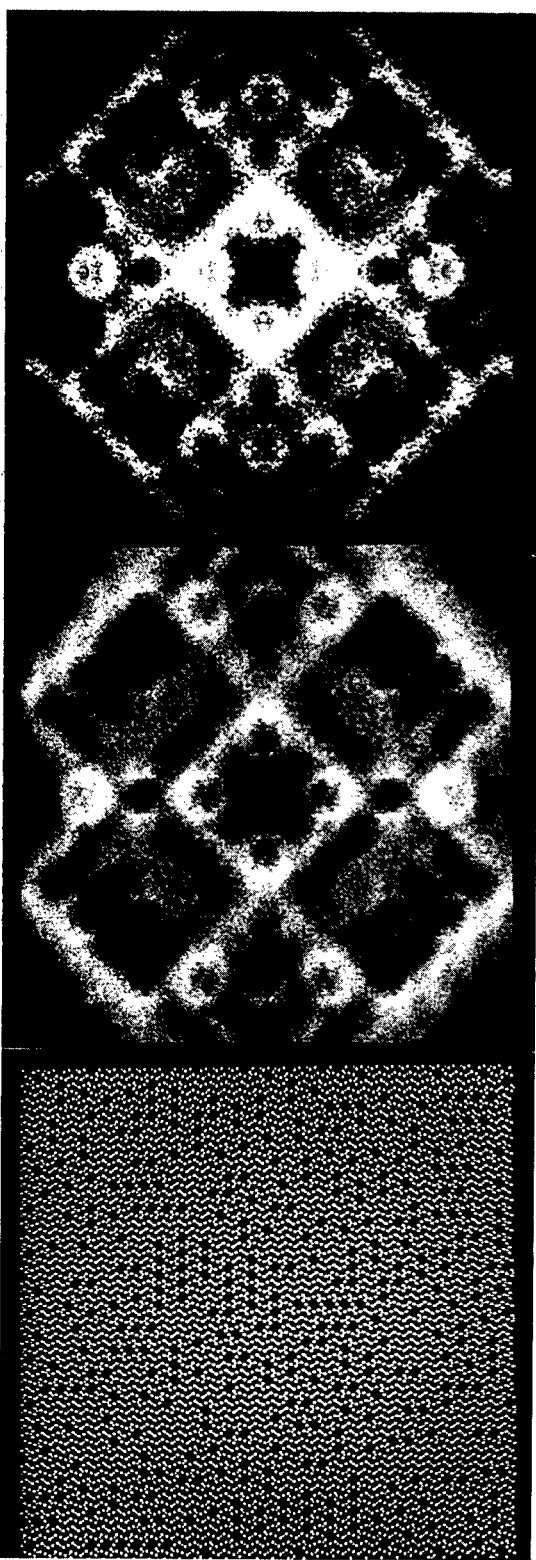


Fig. 8. 2-D videographic investigations of the $h k \frac{1}{4}$ plane: top, processed Weissenberg image; middle, Fourier transform of videographic structure image; bottom, small portion of videographic structure image. *b*-Axis horizontal, *a*-axis vertical.

short-range correlation vectors, where $\langle 330 \rangle$ results from a combination of $\langle 310 \rangle$ and $\langle 020 \rangle$ or $\langle 130 \rangle$ and $\langle 200 \rangle$.

Further investigations confirmed that $\langle 130 \rangle$ and $\langle 310 \rangle$ are mainly responsible for the diffuse circles at the 01 and 10 positions [Fig. 8 (middle)], whereas the exact shape is caused by longer corre-

lation vectors. Resulting from a combination of $\langle 130 \rangle$ and $\langle 310 \rangle$, an equal number of $\langle 240 \rangle$, $\langle 420 \rangle$, $\langle 440 \rangle$, $\langle 260 \rangle$, $\langle 620 \rangle$, $\langle 060 \rangle$ and $\langle 600 \rangle$ gives an exact circular shape of the diffuse scattering. In contrast, a higher frequency of $\langle 440 \rangle$ results in a rhombic form with edges along $\langle 110 \rangle^*$. Preferring $\langle 020 \rangle$ and $\langle 310 \rangle$ against $\langle 200 \rangle$ and $\langle 310 \rangle$ yields a diffraction pattern similar to the X-ray diffraction pattern of $h k \frac{1}{2}$.

Considering the above mentioned preferences, 2-D videographic real structure simulations were also performed for the (010) and (100) planes. By comparison, the satellite positions in the Fourier transforms of the videographic simulations are in close agreement with $h0l$ and $0kl$ electron diffraction patterns,³² respectively. Analysis of the 2-D simulations yielded most frequent correlation vectors of $\langle 002 \rangle$, $\langle 300 \rangle$, $\langle 101 \rangle$, $\langle 201 \rangle$, $\langle 501 \rangle$ and $\langle 302 \rangle$ for the (010) plane. The (100) plane revealed a higher frequency of $\langle 030 \rangle$, $\langle 022 \rangle$, $\langle 005 \rangle$, $\langle 023 \rangle$, $\langle 006 \rangle$ and $\langle 013 \rangle$ correlation vectors.

Before proceeding with 3-D videographic simulations, some valuable information about the ordering scheme can be already obtained from the 2-D investigations. The 1.5-fold modulations along [100] and [010] in $h0l$ and $0kl$ diffraction patterns are caused by a preference of $\langle 130 \rangle$, $\langle 310 \rangle$ and $\langle 330 \rangle$ correlation vectors. Furthermore, it can be assumed that the twofold period along [001] in $h0l$ patterns originates from more frequent $\langle 022 \rangle$ inter-vacancy correlation vectors which already appear in (100) HREM images as preferred arrangements along the $\langle 012 \rangle$ crystallographic directions (Fig. 2). Thus, a projection of the $\langle 022 \rangle$ vectors onto (010) results in a twofold period along [001].

3-D Videographic Real Structure Simulations

By comparing the frequencies of the correlation vectors in the 2-D simulations, a scheme of the 3-D vacancy distribution can be derived. The preferred vacancy arrangements along [102], [10-2], [012] and [01-2] (crystallographic directions) observed in HREM images can be achieved by a preference of the $\langle 111 \rangle$ correlation vector, in agreement with the 2-D simulation of the (010) plane with the high frequency of the $\langle 101 \rangle$. The preference of $\langle 201 \rangle$ in the 3-D simulation corresponds to the $\langle 201 \rangle$ in the 2-D simulation of the (010) plane and – in projection on (100) – to a vacancy arrangement along [001] which appears in (100) HREM images. In addition, the correlation vectors $\langle 312 \rangle$, $\langle 131 \rangle$, $\langle 113 \rangle$ and $\langle 223 \rangle$ are preferred in the 3-D simulations.

After projecting the 3-D videographic simulation field along the main crystallographic directions, the correctness of the simulated structure model was tested by comparing its Fourier transforms with experimental diffraction patterns (Fig. 1). The Fourier transforms of the (010) and (100) planes are given in Fig. 9. The positions and intensities of the satellites are in close agreement to the experimental diffraction patterns of the $h0l$ and $0kl$ planes. It can be concluded that the input parameters for the simulation field resemble the vacancy distribution in 2:1 mullite. The most frequent 15 inter-vacancy correlation vectors determined by analysing the simulation field are presented in Table 1 together with those measured by Butler and Welberry.²¹ Further calculations showed that slight changes in the frequencies and order of the correlation vectors do not influence the positions of the satellites but only have influence on the shape of the satellites and the

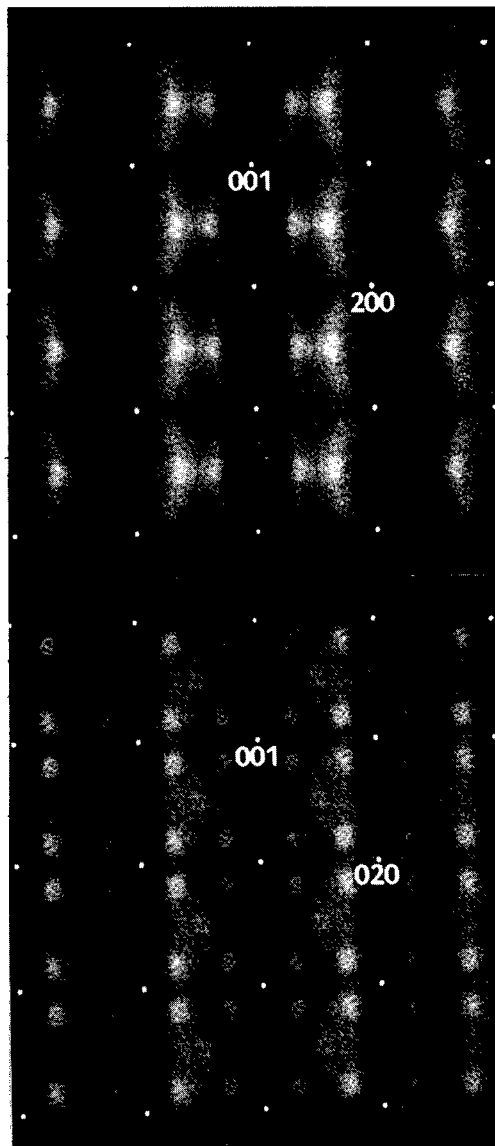


Fig. 9. Fourier transforms of the 3-D simulation field projected on (010) and (100).

Table 1. The most frequent 15 inter-vacancy vectors lmn ($l=a/2$, $m=b/2$, $n=c$) calculated from the 3-D simulation field [p = probability in %, a = short-range order parameter, a_{BW} = short-range order parameter determined by Butler & Welberry²¹]

lmn	p	a	a_{BW}
$<022>$	28.25	0.103	—
$<310>$	28.00	0.100	0.141
$<111>$	27.09	0.089	0.109
$<201>$	24.98	0.062	0.113
$<330>$	24.90	0.061	—
$<130>$	24.21	0.053	0.077
$<401>$	23.24	0.040	—
$<113>$	23.24	0.040	—
$<040>$	23.12	0.039	—
$<004>$	22.79	0.035	0.047
$<131>$	22.72	0.034	0.058
$<222>$	22.71	0.034	—
$<223>$	22.56	0.032	—
$<600>$	22.19	0.027	—
$<312>$	21.88	0.024	—

intensity of streaks. It must be noted that the most frequent inter-vacancy vector $<022>$ belongs to the second shell and plays an important role for the formation of the diffuse scattering in the $h0l$ and $0kl$ planes together with $<330>$, $<310>$ and $<130>$. The correlation vector $<022>$ can be obtained by a certain sequence of two $<111>$ vectors (e.g. $[111]$ followed by $[-111]$ or $[1-11]$ followed by $[-1-11]$, etc.) However, it is unlikely that the occurrence of $<022>$ is only caused by the combination of $<111>$ since the frequencies of $<111>$ and $<022>$ are nearly the same.

Short-range order parameters (correlation vectors) are usually used to describe the real structure of intermetallic alloys above the critical temperature, T_c . In most cases, the first three short-range order parameters are adequate to describe the short-range ordered state. In mullite, with T_c above the melting point, the three shortest correlation vectors are not sufficient to describe the oxygen vacancy ordering scheme. In this case, higher order inter-vacancy correlation vectors (Table 1) are important for complete interpretation of the real structure.

Acknowledgement

The authors gratefully acknowledge financial support of the Deutsche Forschungsgemeinschaft.

References

1. Korekawa, M., Theorie der Satellitenreflexe. Habilitationsschrift, Universität München, 1967.

2. Böhm, H., Eine erweiterte Theorie der Satellitenreflexe und die Bestimmung der modulierten Struktur des Natriumnitrits. Habilitationsschrift, Universität Münster, 1977.
3. Schryvers, D., Srikrishna, M. A. & Thomas, G., An electron microscopy study of the atomic structure of a mullite in a reaction-sintered composite. *J. Mater. Res.*, **3** (1988) 1355–66.
4. Rahman, S. H. & Weichert, H.-T., Interpretation of HREM images of mullite. *Acta Crystallogr.*, **B46** (1990) 139–49.
5. Epicier, T., O'Keefe, M. A. & Thomas, G., Atomic imaging of 3:2-mullite. *Acta Crystallogr.*, **A46** (1990) 948–62.
6. Epicier, T., Benefits of high-resolution electron microscopy for the structural characterization of mullites. *J. Am. Ceram. Soc.*, **74** (1991) 2359–66.
7. Rahman, S. H., Interpretation of mullite HREM images using the potential-exchange-method. *Z. Kristallogr.*, **203** (1993b) 67–72.
8. Nakajima, Y., Morimoto, M. & Watanabe, E., Direct observation of oxygen vacancy in mullite, $1.86\text{Al}_2\text{O}_3\cdot\text{SiO}_2$ by high resolution electron microscopy. *Proc. Jpn. Acad.*, **51** (1975) 173–8.
9. Ylä-Jääski, J. & Nissen, H.-U., Investigation of superstructures in mullite by high resolution electron microscopy and electron diffraction. *Phys. Chem. Minerals*, **10** (1983) 47–54.
10. Kahn-Harari, A., Abolhassani, S., Michel, D., Mazeilles, L., Portier, R. & Perez-Ramirez, J. G., Observation of ordering in silicon and germanium mullites. *J. Solid State Chem.*, **90** (1991) 234–48.
11. Paulmann, C., Rahman, S. H. & Strothenk, S., Interpretation of mullite HREM images along [010] and [100]. *Phys. Chem. Minerals*, **21** (1994) 546–54.
12. Saalfeld, H., The domain structure of 2:1-mullite. *N. Jb. Min. Abh.*, **134** (1979) 305–16.
13. Tokonami, M., Nakajima, Y. & Morimoto, N., The diffraction aspect and a structural model of mullite. *Acta Crystallogr.*, **A36** (1980) 270–6.
14. Welberry, T. & Withers, R. L., An optical transform and Monte Carlo study of the diffuse X-ray scattering in mullite $\text{Al}_2(\text{Al}_{2+2x}\text{Si}_{2-2x})\text{O}_{10-x}$. *Phys. Chem. Minerals*, **17** (1990) 117–24.
15. Rahman, S. H., Die Videographische Methode: Ein neues Verfahren zur Simulation und Rekonstruktion fehlgeordneter Kristallstrukturen. Habilitationsschrift, Universität Hannover, 1991.
16. Rahman, S. H., The real crystal structure of mullite. In *Mullite and Mullite Ceramics*, eds H. Schneider, K. Okada & J. A. Pask, Wiley and Sons, England, 1994, pp. 4–31.
17. Rahman, S. H. & Paulmann, C., Sauerstoffleerstellenverteilung in Mullit $\text{Al}_2[\text{Al}_{2+2x}\text{Si}_{2-2x}]\text{O}_{10-x}$. 25. DGE Tagung in Darmstadt, *Optik Supplement 4*, Vol. 88, 1991, Abstract 018.
18. Paulmann, C., Rahman, S. H. & Weichert, H.-T., Ordering scheme for oxygen vacancies in mullite. *Electron Microscopy EUREM92*, Granada, Spain, Vol. 2, 1992, pp. 445–6.
19. Butler, B. D., Welberry, T. R. & Withers, R. L., Oxygen vacancy ordering and the incommensurate structure of mullite. *Phys. Chem. Minerals*, **20** (1993) 323–32.
20. Padlewski, S., Heine, V. & Price, G. D., The energetics of interaction between oxygen vacancies in sillimanite: a model for the mullite structure. *Phys. Chem. Minerals*, **19** (1992) 196–202.
21. Butler, B. D. & Welberry, T. R., Analysis of diffuse scattering from the mineral mullite. *J. Appl. Crystallogr.*, **27** (1994) 742–54.
22. Rahman, S. H., The videographic method: a new procedure for the simulation and reconstruction of real structures. *Acta Crystallogr.*, **A49** (1993) 56–68.
23. Sadanaga, R., Tokonami, M. & Takeuchi, Y., The structure of mullite $2\text{Al}_2\text{O}_3\cdot\text{SiO}_2$ and relationship with the structures of sillimanite and andalusite. *Acta Crystallogr.*, **15** (1962) 65–8.
24. Burnham, C. W., The crystal structure of mullite. *Carn. I. Wash. Yb.*, **62** (1963) 158–62.
25. Burnham, C. W., Crystal structure of mullite. *Carn. I. Wash. Yb.*, **63** (1964) 223–7.
26. Durovic, S., Refinement of the crystal structure of mullite. *Chem. Zvesti*, **23** (1969) 113–28.
27. Angel, R. J. & Prewitt, C. T., Crystal structure of mullite a re-examination of the average structure. *Am. Mineral.*, **71** (1986) 1476–82.
28. Angel, R. J. & Prewitt, C. T., The incommensurate structure of mullite by Patterson synthesis. *Acta Crystallogr.*, **B43** (1987) 116–26.
29. Angel, R. J., McMullan, R. K. & Prewitt, C. T., Substructure and superstructure of mullite by neutron diffraction. *Am. Mineral.*, **76** (1991) 332–42.
30. Saalfeld, H., A modification of Al_2O_3 with sillimanite structure. *Transactions VIII International Ceramic Congress*, Copenhagen, (1962) pp. 71–4.
31. Rahman, S. H. & Rodewald, M., Simulation of short-range order in FCC-alloys. *Acta Crystallogr.*, **A51** (1995) 153–8.
32. Rahman, S. H., Strothenk, S. & Rodewald, M., Paper in preparation.

Local Structural Information of Mullite Obtained from Diffuse X-ray Scattering

T. R. Welberry & B. D. Butler*

Research School of Chemistry, Australian National University, Canberra, ACT 0200, Australia

(Accepted 22 July 1995)

Abstract

A full reciprocal space volume of diffuse scattering data from a single crystal of the mineral mullite, $Al_2(Al_{2+2x}Si_{2-2x})O_{10-x}$, $x = 0.4$, has been collected. These data were analysed using least-squares techniques by writing an equation for the diffuse scattering which involves only the local order between vacancies on specific oxygen sites in the material. The effect of the large, but predictable, cation shifts on the diffuse intensity was taken account of in the coefficients to the oxygen vacancy short-range order intensities. This analysis shows that in addition to the absence of defects separated by the vectors $\frac{1}{2}\langle 110 \rangle$ and $[110]$ (which results from the simplifying assumptions that were made), there is also a strong tendency to avoid defects separated by $\langle 001 \rangle$ and a moderately strong tendency to avoid pairs of defects separated by $\langle 003 \rangle$, $\langle 011 \rangle$, $[1-10]$ and $\frac{1}{2}\langle 312 \rangle$. The most common inter-defect vectors found were $\frac{1}{2}\langle 310 \rangle$, $\langle 101 \rangle$, $\frac{1}{2}\langle 112 \rangle$, $\langle 012 \rangle$, $\frac{1}{2}\langle 130 \rangle$, $\frac{1}{2}\langle 132 \rangle$ and $\langle 022 \rangle$.

Introduction

Conventional crystal structure determination involves measurement of the intensities of Bragg reflections – the sharp diffraction peaks that occur at integral points of reciprocal space. Analysis using this information leads to a description of the *average* structure of the material. For a disordered material such as mullite, this may include such information as the coordinates of different atomic sites in the average unit cell, site occupancies and mean-square atomic displacements. This latter information may result from the thermal motion of the atoms or may be related to a spatial average of a static distribution in which atoms in different unit cells lie on positions distributed about the mean.

Bragg-scattering thus provides only information about *single* site properties of the material. On the other hand, *diffuse X-ray scattering*, the much weaker broadly distributed scattering occurring at general points in reciprocal space, contains information concerning *pairs* of sites and is thus potentially a rich source of information regarding local chemical and displacement correlations and can be employed to aid the understanding of locally ordered materials such as mullite. Unfortunately, the extraction of correlation fields from diffuse diffraction data has proved to be a difficult task even for relatively simple systems and success in obtaining such information has mostly been limited to alloys and simple oxides (see, for example, Refs 1–3). At first sight mullite appears to be of such significantly greater complexity than these simple systems that success in extracting quantitative correlation information would seem unlikely. In this paper we describe how, by making certain simplifications based on chemical considerations, the diffuse X-ray scattering from mullite can be analysed to reveal a much more complete description of the structure than is possible from Bragg analysis.

The Average Structure

Details of the average structure of mullite of composition $Al_2(Al_{2+2x}Si_{2-2x})O_{10-x}$ where $x = 0.4$, as revealed by the Bragg scattering,⁴ are shown in Fig. 1. The structure is similar to that of sillimanite, $Al(AlSi)O_5$. Chains of edge-sharing AlO_6 octahedra, running parallel to the crystallographic c -axis, are crosslinked by $(Al, Si)O_4$ tetrahedra. In sillimanite the tetrahedrally coordinated cations are bridged by a single oxygen atom and are ordered in such a way that the bridging anion always connects an Si-containing tetrahedron with an Al-containing tetrahedron. In mullite some fraction, x , of these bridging oxygen sites are vacant. To preserve charge balance, each of the O^{2-} vacancies are accommodated by the exchange

*Current address: National Institute of Standards & Technology, A325 Broadway, Boulder, CO 80303, USA.

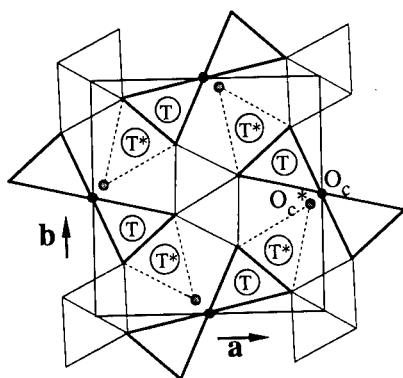


Fig. 1. The average structure of mullite seen in projection down the crystallographic c -axis. The sites labelled O_c and O_c^* contain oxygen atoms which bridge two or more tetrahedra. In an $x = 0.4$ mullite the T , T^* sites are disordered such that 80% of the T sites and 20% of the T^* sites are occupied by Al or Si. 40% of the O_c sites and 20% of the O_c^* sites are occupied.

of 2Al^{3+} for 2Si^{4+} . Because the tetrahedrally coordinated Al and Si are no longer present in the ratio of 1:1 these sites necessarily become chemically disordered. Furthermore, crystal structure analysis has identified the presence of a second tetrahedral site – displaced from the original by approximately 1.3 \AA – that is presumably occupied by cations which have lost bridging oxygen atoms. The bridging oxygen atom was also found to occasionally occupy a site displaced 0.5 \AA from its normal position and appears to be associated with the displaced tetrahedral site. In Fig. 1 the (Al, Si) tetrahedral sites are labelled T and T^* and the bridging anion sites are labelled O_c and O_c^* where $*$ indicates the displaced positions mentioned above. It should be stressed that it is only *presumed* that the T^* sites are occupied by cations which have lost bridging oxygen atoms and that the displaced O_c^* sites are directly associated with them. The Bragg experiment only reveals the overall average occupancies.

The Diffuse Diffraction Data

The diffuse intensity data were collected on an instrument specially designed for the rapid collection of planar sections of single crystal diffraction patterns. The apparatus is an electronic version of a Weissenberg camera utilizing flat-cone geometry in which a curved linear (gas filled) position sensitive detector (PSD) is used to collect data normal to the Weissenberg cylinder axis. A monochromated, sealed tube, $\text{Cu } K_\alpha$ source is employed. With this geometry a series of scans taken as the crystal is rotated through 360° produces a flat, two-dimensional section of the diffraction pattern normal to the crystal rotation axis. Several scans can be made using different goniometer settings to

construct a three-dimensional image of the diffraction space as a series of two-dimensional sections. Further details about the instrument can be found elsewhere.⁵

Although the data recorded in this way provide quantitative measurements at points in reciprocal space, it is convenient for display purposes to present the data as grey-scale images. We prefer this method to the often used practice of drawing contour plots. In Fig. 2 we show such plots of data from six different reciprocal sections. Each pattern consists of $\sim 180 \times 180$ pixels. Each pixel corresponds to an increment in the Miller indices Δh_1 , $\Delta h_2 = 0.05$. This resolution is rather poorer than the resolution that the instrument can provide, but the data were binned at this resolution to provide a manageable number of independent measurements. Eleven sections in $\Delta h_3 = 0.05$ increments from $h_3 = 0.5$ to 1.0 were measured, yielding in excess of 130000 independent measurements.

The plots of data in Fig. 2, which are all made on the same scale, demonstrate the rich detail that is present in the diffuse data. Many different features may be seen, varying from the relatively

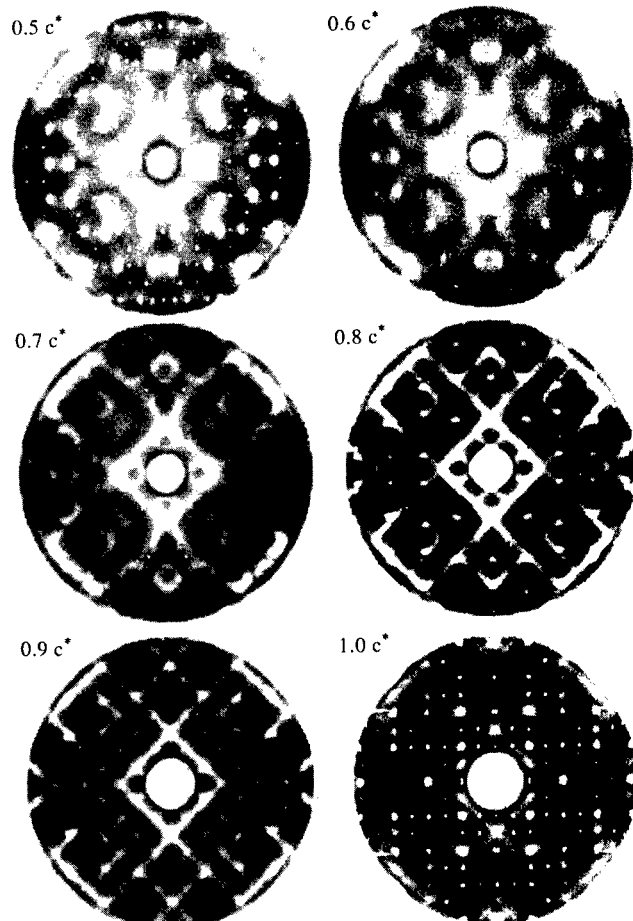


Fig. 2. Diffuse X-ray diffraction data. The data were collected digitally but are displayed on a grey scale so that the full range of diffuse features can be seen. Only six of the 11 diffuse planes that were used in the analysis are displayed. The small single pixel peaks seen in the $0.5c^*$ and $1.0c^*$ sections are Bragg peaks caused by $\lambda/2$ contamination of the beam.

sharp incommensurate peaks visible in the 0.5c* section to the more diffuse circular features in the 0.7c* section and the narrow lines of the 0.9c* section. Although in the past much interest has centred on the incommensurate peaks, these patterns reveal that these are just an integral part of the continuous diffuse distribution. The total integrated intensity in each of the different recorded sections is fairly constant.

Theory

A general description of diffuse scattering that allows for both short-range compositional (chemical) order and local atomic displacements can be obtained by expanding the exponential in the kinematic scattering equation in powers of displacement.

$$\begin{aligned}
 I &= \sum_{n=1}^N \sum_{m=1}^M f_m f_n \exp[i\mathbf{k} \cdot (\mathbf{R}_m + \mathbf{u}_m - \mathbf{R}_n - \mathbf{u}_n)] \\
 &\approx \sum_{n=1}^N \sum_{m=1}^M f_m f_n \exp[i\mathbf{k} \cdot (\mathbf{R}_m - \mathbf{R}_n)] \\
 &\quad \times \{1 + i\mathbf{k} \cdot (\mathbf{u}_m - \mathbf{u}_n) - \frac{1}{2} [\mathbf{k} \cdot (\mathbf{u}_m - \mathbf{u}_n)]^2 \\
 &\quad - \frac{i}{6} [\mathbf{k} \cdot (\mathbf{u}_m - \mathbf{u}_n)]^3 + \dots\}
 \end{aligned} \quad (1)$$

Here I is the scattered intensity and f_m is the scattering factor of the atom m associated with the lattice site at the location \mathbf{R}_m and which is displaced from its site by a small amount \mathbf{u}_m . $\mathbf{k} = h_1 \mathbf{a}^* + h_2 \mathbf{b}^* + h_3 \mathbf{c}^*$ is the scattering vector. Eqn (1) expresses the fact that the intensity distribution may be written as the sum of component intensities: the first term being independent of the displacements, the second term dependent on the first moment of displacements, the third term on the second moment, etc.

$$\mathbf{I}_{\text{Diffuse}} \approx \mathbf{I}_0 + \mathbf{I}_1 + \mathbf{I}_2 + \mathbf{I}_3 + \dots \quad (2)$$

It is usual in analyses of alloys and simple oxides to truncate this Taylor expansion at second order, although recently we have shown that for cubic-stabilized zirconias the third and higher order terms are also important. These components can be shown to have the following forms,

$$\mathbf{I}_0 = - \sum_{ij} \sum_{lmn} c_i c_j f_i f_j^* \alpha_{lmn}^{ij} \cos\{2\pi(h_1 l + h_2 m + h_3 n)\} \quad (3)$$

$$\begin{aligned}
 \mathbf{I}_1 &= -2\pi \sum_{ij} \sum_{lmn} c_i c_j f_i f_j^* (1 - \alpha_{lmn}^{ij}) [h_1 \langle X_{lmn}^{ij} \rangle \\
 &\quad + h_2 \langle Y_{lmn}^{ij} \rangle + h_3 \langle Z_{lmn}^{ij} \rangle] \\
 &\quad \times \sin\{2\pi(h_1 l + h_2 m + h_3 n)\}
 \end{aligned} \quad (4)$$

$$\begin{aligned}
 \mathbf{I}_2 &= -2\pi^2 \sum_{ij} \sum_{lmn} c_i c_j f_i f_j^* (1 - \alpha_{lmn}^{ij}) \\
 &\quad \times [h_1^2 \{ \langle (X_{lmn}^{ij})^2 \rangle - (1 - \alpha_{lmn}^{ij})^{-1} \langle (X_{\infty}^{ij})^2 \rangle \} \\
 &\quad + h_2^2 \{ \langle (Y_{lmn}^{ij})^2 \rangle - (1 - \alpha_{lmn}^{ij})^{-1} \langle (Y_{\infty}^{ij})^2 \rangle \} \\
 &\quad + h_3^2 \{ \langle (Z_{lmn}^{ij})^2 \rangle - (1 - \alpha_{lmn}^{ij})^{-1} \langle (Z_{\infty}^{ij})^2 \rangle \} \\
 &\quad + 2h_1 h_2 \{ \langle (X_{lmn}^{ij} Y_{lmn}^{ij}) \rangle + 2h_1 h_3 \langle (X_{lmn}^{ij} Z_{lmn}^{ij}) \rangle \\
 &\quad + 2h_2 h_3 \{ \langle (Y_{lmn}^{ij} Z_{lmn}^{ij}) \rangle \} \\
 &\quad \times \cos\{2\pi(h_1 l + h_2 m + h_3 n)\}
 \end{aligned} \quad (5)$$

The first term \mathbf{I}_0 is the intensity component due to short-range order and is not dependent on displacements. There is one term in this summation for every different interatomic vector lmn along which significant correlation may be present. Each term in the sum involves a short-range order parameter, α_{lmn}^{ij} , defined by

$$\alpha_{lmn}^{ij} = 1 - P_{lmn}^{ij}/c_j \quad (6)$$

where P_{lmn}^{ij} is the conditional probability of finding an atom with label j at the end of a vector \mathbf{r}_{lmn} given that there is an atom with label i at its origin. \mathbf{I}_1 and \mathbf{I}_2 , which involve displacements, similarly also have terms for every different interatomic vector. For a simple binary system \mathbf{I}_1 has six terms for each interatomic vector and \mathbf{I}_2 has 18. Fitting equations of this form with such large numbers of parameters is a formidable task even for simple systems, but for a system as complex as mullite it is quite prohibitive. Consequently we look for a means by which the problem may be simplified.

A Simplified Model

The simplification we adopt consists of making two assumptions. First we assume that only the distribution of oxygen vacancies is important, and that the shift of cations from the \mathbf{T} to the \mathbf{T}^* sites and the shift of the oxygens from \mathbf{O}_c to \mathbf{O}_c^* follow from these as a direct consequence [see Fig. 3(a)]. Secondly, we assume that certain local configurations, which are chemically implausible, do not occur at all in the structure. These are shown in Figs 3(b) and 3(c). In Fig. 3(b) the presence of two vacancies separated by $\langle \bar{1}10 \rangle$ causes the cation 'M' to have no bridging oxygen atom to bond with. In Fig. 3(c) the presence of two vacancies separated by $\langle 110 \rangle$ causes four tetrahedral cations to share the same bridging oxygen.

A description of the mullite structure based on the occupancy of the bridging oxygen sites alone can then be formulated as follows. When a bridging

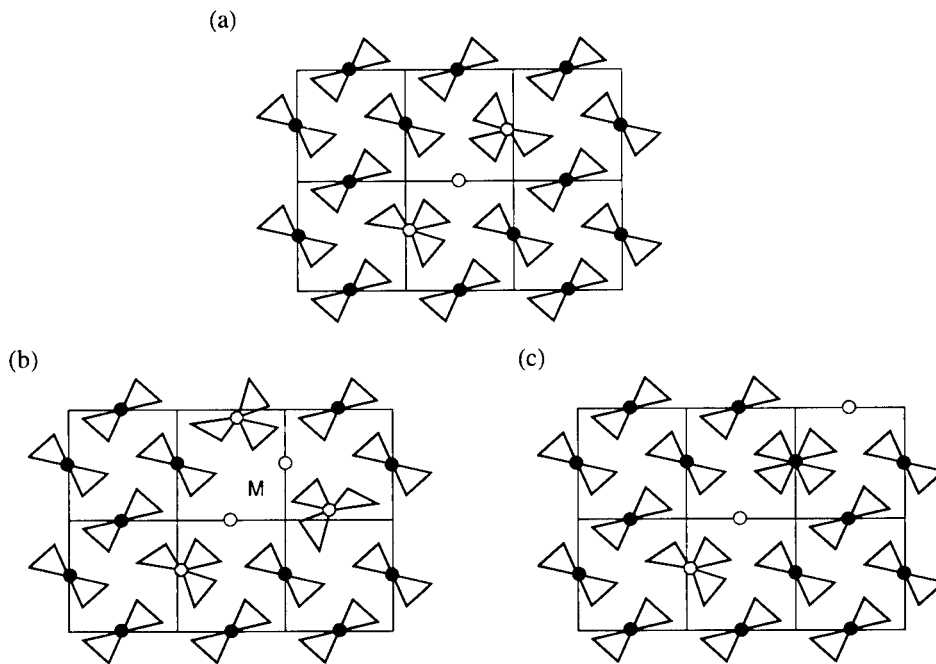


Fig. 3. In all the figures a black circle represents an oxygen atom on the \mathbf{O}_c site, a grey circle an oxygen atom on the \mathbf{O}_c^* site and an open circle represents a vacancy. (a) Shows the effect of introducing an oxygen vacancy into the mullite structure. Two nearby cations transfer from T sites to the alternative \mathbf{T}^* sites and the two \mathbf{O}_c oxygens, which now are bonded to three cations, move to the \mathbf{O}_c^* sites. (b) and (c) Show two configurations that are assumed never to occur in the disordered structure. In (b) the cation 'M' is left without a bridging \mathbf{O}_c atom to bond with. In (c) four cations are forced to share one bridging oxygen.

site is occupied by an oxygen atom we 'decorate' that site with one \mathbf{O}_c oxygen atom and two T cations. When the site is vacant we decorate with two \mathbf{T}^* cations, two neighbouring \mathbf{O}_c^* oxygen atoms and subtract two neighbouring \mathbf{O}_c oxygen atoms. Note that as long as the ordering rules stated above are obeyed and all the bridging sites have been 'filled' with either an oxygen atom or a vacancy, the positions of all tetrahedrally coordinated cations and all of the bridging oxygen atoms will have been specified. The 'negative' \mathbf{O}_c oxygen atoms that are included with an oxygen vacancy are used as a means to displace \mathbf{O}_c atoms from their normal positions to positions labelled \mathbf{O}_c^* while still preserving the total number of oxygen atoms in the crystal. Once the entire lattice has been decorated in this way there will be no remaining 'negative' oxygen atoms.

With this formulation we can discard the intensity components, \mathbf{I}_1 and \mathbf{I}_2 , and use only the short-range order (SRO) term \mathbf{I}_0 , in which we replace the atomic scattering factor by structure factors for the chemical motifs of an occupied or a vacant site. This simplification merely incorporates the displacements which would normally appear in \mathbf{I}_1 and \mathbf{I}_2 into \mathbf{I}_0 , but in doing so automatically dictates that the displacements when they occur are always of exactly the same magnitude. The scattering power of an occupied (O) and vacant (V) \mathbf{O}_c site can be calculated as a simple structure factor of the chemical motifs described above:

$$\begin{aligned} F_O^1 &= f_O + 2f_{Al}\cos\{2\pi(x_{T1}h_1 + y_{T1}h_2)\} \\ F_V^1 &= 2f_O \cos\{2\pi(x_{O_c^*}h_1 + y_{O_c^*}h_2)\} \\ &\quad + 2f_{Al}\cos\{2\pi(x_{T^*1}h_1 + y_{T^*1}h_2)\} \\ &\quad - 2f_O \cos\{2\pi(x_{O_c}h_1 + y_{O_c}h_2)\} \end{aligned} \quad (7)$$

Here, f_O , f_{Al} are the atomic scattering factors of O and Al; x_T , y_T etc. are the fractional coordinates of the T, \mathbf{T}^* , \mathbf{O}_c and \mathbf{O}_c^* sites measured relative to the \mathbf{O}_c site in question; h_1 , h_2 , h_3 are continuous reciprocal space coordinates; and the superscript on the structure factors indicates the sublattice upon which the oxygen atom or vacancy resides. Sublattice 1 refers to the \mathbf{O}_c site at $(\frac{1}{2}0\frac{1}{2})$ and translationally equivalent sites, while sublattice 2 refers to the \mathbf{O}_c site at $(0\frac{1}{2}\frac{1}{2})$. Equation (7) gives the expressions for motifs centred at sites on sublattice 1. Similar, symmetry-related, expressions may be written for motifs centred on sublattice 2.

Replacing the atomic scattering factors in Eqn (3) by the structure factors of the chemical motifs we obtain, after some manipulation (see Butler & Welberry⁶ for further details), the following expression for the SRO diffuse scattering in mullite:

$$I_{SRO}^{\text{mullite}} = \mu_1 I_1 + \mu_2 I_2 + \mu_{12} I_{12} \quad (8)$$

where

$$I_1 = \sum_{l, m, n \text{ integer}} \alpha_{lmn}^{O_1 V_1} \cos(h_1 l + h_2 m + h_3 n)$$

$$I_2 = \sum_{\substack{l, m, n \text{ integer} \\ lmn}} \alpha_{lmn}^{O_2 V_2} \cos(h_1 l + h_2 m + h_3 n)$$

$$I_{12} = \sum_{\substack{l, m, n \text{ integer} \\ l = \text{int} + 1/2 \\ m = \text{int} + 1/2 \\ n = \text{int}}} \alpha_{lmn}^{O_1 V_2} \cos(h_1 l + h_2 m + h_3 n) \quad (9)$$

and,

$$\begin{aligned} \mu_1 &= c_{Oc} c_V (F_{O_1} - F_{V_1})^2 \\ \mu_2 &= c_{Oc} c_V (F_{O_2} - F_{V_2})^2 \\ \mu_{12} &= 2c_{Oc} c_V \operatorname{Re}\{(F_{O_2} - F_{V_2})(F_{O_2} - F_{V_2})^*\} \end{aligned} \quad (10)$$

The three intensities, I_1 , I_2 , and I_{12} , are periodic functions in reciprocal space with a repeat that is commensurate with the first Brillouin zone and the coefficients μ_1 , μ_2 and μ_{12} are continuous functions in reciprocal space. I_1 and I_2 involve only correlations between sites on the same sublattice (1 and 2 respectively), while I_{12} involves cross-correlations between the two different sublattices. In Fig. 4 we show plots of the functions, μ_1 , μ_2 , μ_{12} , which are calculated from the fractional coordinates of the average structure obtained from the Bragg reflections. It should also be noted that since T , T^* , O_c and O_c^* all have the same z -coordinate in the structure, the functions μ_1 , μ_2 and μ_{12} are virtually independent of h_3 , the reciprocal coordinate in the c^* -direction. The variation of the intensity distribution with reciprocal section thus results entirely from the Warren short-range

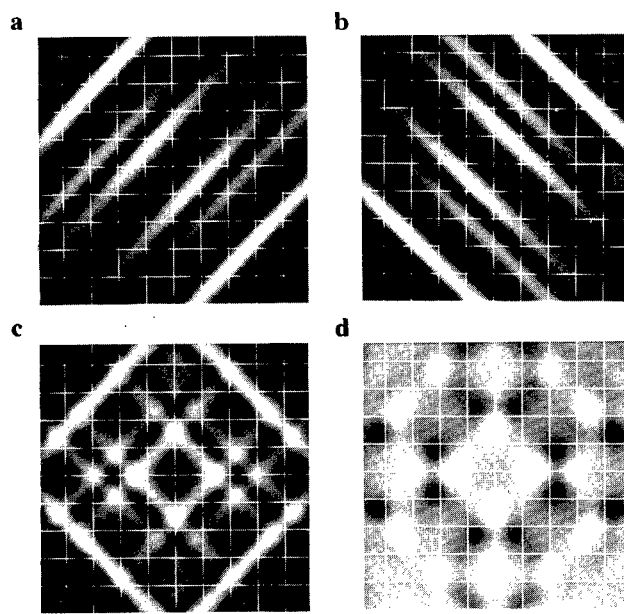


Fig. 4. Plots in the $(hk0)$ plane of the coefficients μ_1 , μ_2 and μ_{12} which occur in Eqn (8). These coefficients are constant functions calculated from the coordinates obtained from the average structure analysis. (a) μ_1 . (b) μ_2 . (c) $\mu_1 + \mu_2$. (d) μ_{12} . μ_1 and μ_2 are positive everywhere but μ_{12} varies from negative (black) to positive (white). The white lines drawn on the figures indicate where h_1 and h_2 are integral.

order parameters, α_{lmn} , appearing in the three intensity components I_1 , I_2 and I_{12} .

Results

A value for each of the three intensity components can be obtained for a given point inside the first Brillouin zone by gathering together several measurements of the diffuse intensity from points in the reciprocal space that are related by symmetry with this point. The set of measurements related by symmetry in this way is commonly referred to as an *associated set* and the point inside the minimum repeat volume is referred to as a *minimum volume point*.⁷ For example, if the point (h_1, h_2, h_3) , lies inside the first Brillouin zone, then the points $(1 - h_1, h_2, h_3)$, $(h_1, 2 + h_2, h_3)$, $(2 + h_1, 3 - h_2, 1 + h_3)$, etc. form the associated set of the minimum volume point (h_1, h_2, h_3) . Each of the intensity components I_1 , I_2 and I_{12} have the same numerical magnitude (but not necessarily sign) for all points inside a particular associated set but the coefficients μ_1 , μ_2 and μ_{12} vary predictably in a way that does not repeat commensurately with the underlying reciprocal lattice. Any collection of three or more measurements in an associated set can therefore be used to solve for the three intensity components at one minimum volume point. In the present case, upwards of 30–40 measurements were available in each associated set and with only three intensity components to solve for the problem is highly overdetermined. Standard least-squares procedures were used to solve for the three intensity components at each of 1331 points in the minimum volume.

When this had been done for every point in the minimum volume, the Warren short-range order parameters α_{lmn} were extracted from each of the three component intensities by simple Fourier inversion of Eqn (9). The most significant of these are given in Table 1. Assuming that the three SRO intensities derived this way are the only significant

Table 1. Local order parameters for mullite determined from the least-squares analysis

Interatomic vector, lmn	Short-range order parameter, α_{lmn}	Interatomic vector, lmn	Short-range order parameter, α_{lmn}
$\frac{1}{2}\langle 110 \rangle$	-0.250	$\langle 011 \rangle$	-0.122
[110]	-0.250	[111]	-0.079
[1-10]	-0.081	[1-11]	+0.000
$\langle 001 \rangle$	-0.227	$\frac{1}{2}\langle 112 \rangle$	+0.109
$\langle 100 \rangle$	-0.004	$\frac{1}{2}\langle 310 \rangle$	+0.141
$\langle 010 \rangle$	+0.015	$\frac{1}{2}\langle 130 \rangle$	+0.077
$\langle 002 \rangle$	-0.019	$\frac{1}{2}\langle 312 \rangle$	-0.092
$\langle 003 \rangle$	-0.124	$\frac{1}{2}\langle 132 \rangle$	+0.058
$\langle 004 \rangle$	+0.047	$\langle 012 \rangle$	+0.088
$\langle 101 \rangle$	+0.113	$\langle 022 \rangle$	+0.051

contributions to the total diffuse intensity in mullite, then the oxygen-vacancy SRO parameters obtained by this procedure will contain all the information that the diffuse part of the diffraction pattern can provide.

The intensity R factor

$$R = [\sum (I_{\text{obs}} - I_{\text{calc}})^2 / \sum I_{\text{calc}}^2]$$

for a typical least-squares solution of one of the 1331 minimum volume points was approximately 35%. This obvious quantitative discrepancy may seem very high by conventional crystallographical standards but the resulting least-squares fit is not as bad as this figure implies. When all 1331 independent solutions are used, together with the μ_1 , μ_2 , μ_{12} coefficients, to obtain a 'best-fit' calculated diffraction pattern for visual comparison with the observed patterns, the results are really rather convincing (see Fig. 5).

Both Figs 2 and 5 are reproduced on the same scale so that the grey shades can be compared to see how the two agree. There are a few obvious differences. For instance, in the $0.7c^*$ reciprocal layer the measured intensities near the origin and

at large scattering angles are noticeably higher than in the calculated pattern, whereas at intermediate angles this situation is reversed. There are also distinct diagonal dark bands visible in the $0.5c^*$ layer of the calculated pattern that are much less distinct in the data. These differences may indicate minor short-comings in the model used to derive Eqn (8) which does not allow for atom displacements other than those included in the simple chemical motifs described.

The most significant values for the Warren short-range order parameters, α_{lmn} , obtained from the analysis are shown in Table 1. For a vacancy concentration of 0.2 the most negative value of α_{lmn} feasible is $\alpha_{lmn} = -0.25$, which corresponds to complete avoidance of defect pairs separated by the vector lmn . Thus we see that, in addition to the absence of defects separated by the vectors $\frac{1}{2}\langle 110 \rangle$ and $\langle 110 \rangle$ (which results from the simplifying assumptions that were made), there is also a strong tendency to avoid defects separated by $\langle 001 \rangle$ and a moderately strong tendency to avoid pairs of defects separated by $\langle 003 \rangle$, $\langle 011 \rangle$, $\langle 1-10 \rangle$ and $\frac{1}{2}\langle 312 \rangle$. The most common inter-defect vectors found were $\langle 101 \rangle$, $\frac{1}{2}\langle 112 \rangle$ and $\frac{1}{2}\langle 310 \rangle$.

Conclusion

Comparison of Figs 2 and 5 demonstrates convincingly that, for this seemingly complicated mineral, the diffuse scattering can be described simply as the sum of three component short-range order diffuse intensities. Two of these components involve correlations between the basic defects on each of the two different sublattices (symmetry-related) and the third involves correlations between the two sublattices. Although there are quantitative discrepancies indicating some short-comings in the fine detail of the model, there is no doubt that the model is essentially correct.

The basic defect consists of a vacant \mathbf{O}_c site together with a transfer of its two neighbouring tetrahedral cations from a \mathbf{T} to a \mathbf{T}^* site. Each \mathbf{T}^* cation then shares a further bridging oxygen which shifts from \mathbf{O}_c to \mathbf{O}_c^* [see Fig 3(a)]. An integral part of the model was the necessity to assume that two chemically implausible configurations [shown in Figs 3(b) and 3(c)] were forbidden. If two defects were separated by $\frac{1}{2}\langle 110 \rangle$ the intervening cation would be left without a bridging \mathbf{O}_c atom, while if two defects were separated by $\langle 110 \rangle$ it would be necessary for four cations to share the same bridging \mathbf{O}_c atom. The analysis revealed that defect pairs separated by $\langle 001 \rangle$ were strongly avoided, and that defects separated by $\langle 003 \rangle$,

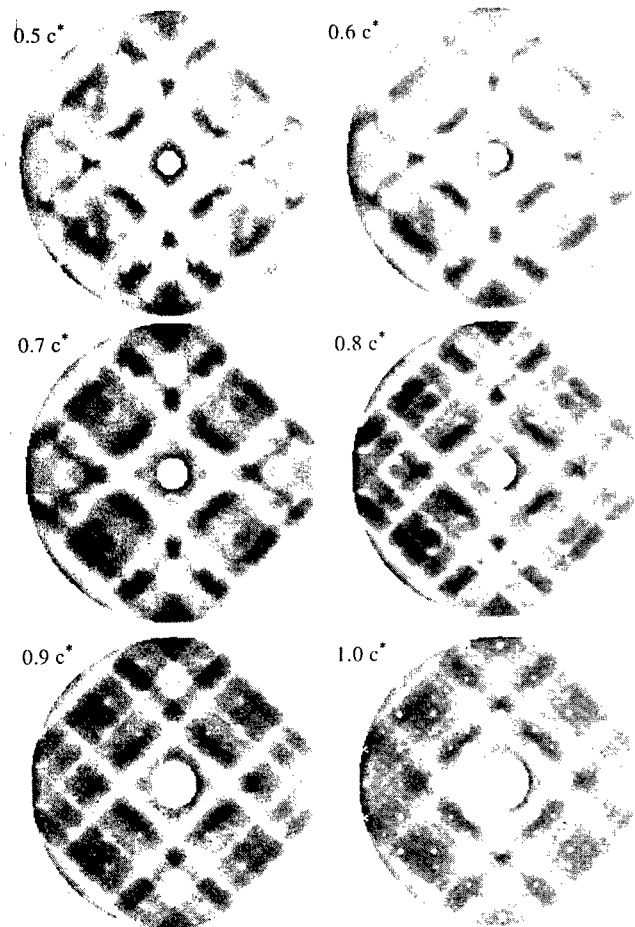


Fig. 5. Diffraction patterns calculated from the least-squares fit of the model to the observed data. The least-squares solution provided three intensity components at each of 1331 points inside the first Brillouin zone. The entire pattern was generated by multiplying these component intensities by the appropriate coefficients μ_1 , μ_2 , μ_{12} and adding.

$\langle 011 \rangle$, $\langle 1-10 \rangle$ or $\frac{1}{2}\langle 312 \rangle$ also tended to be avoided, although rather less strongly. The most common inter-defect vectors found were $\frac{1}{2}\langle 310 \rangle$, $\langle 101 \rangle$, $\frac{1}{2}\langle 112 \rangle$, $\langle 012 \rangle$, $\frac{1}{2}\langle 130 \rangle$, $\frac{1}{2}\langle 132 \rangle$ and $\langle 022 \rangle$.

References

1. Hayakawa, M. & Cohen, J. B., *Acta Crystallogr.*, **A31** (1975) 635-45.
2. Matsubara, E. & Cohen, J. B., *Acta Metall.*, **33** (1985) 1945-55.
3. Reinhard, L., Robertson, J. L., Moss, S. C., Ice, G. E., Zschack, P. & Sparks, C. J., *Phys. Rev. B*, **45** (1992) 2662-76.
4. Angel, R. J. & Prewitt, T., *Am. Mineral.*, **71** (1986) 1476-82.
5. Osborn, J. C. & Welberry, T. R., *J. Appl. Crystallogr.*, **23** (1990) 476-84.
6. Welberry, T. R. & Butler, B. D., *J. Appl. Crystallogr.*, **27** (1994) 742-54.
7. Wu, T. B., Matsubara, E. & Cohen, J. B., *J. Appl. Crystallogr.*, **16** (1983) 407-14.

Time-Resolved Fluorescence Spectroscopy of Cr^{3+} in Mullite

Bernard Piriou,^a Helmut Rager^b & Hartmut Schneider^c

^aPCM/URA 1907-CNRS, Ecole Centrale de Paris, F-92295 Châtenay-Malabry Cedex, France

^bInstitut für Mineralogie, Universität Marburg, D-35032 Marburg, Germany

^cGerman Aerospace Research Establishment, Institute for Materials Research, D-51140 Köln, Germany

(Accepted 22 July 1995)

Abstract

Mullites doped with Cr_2O_3 concentrations ranging from 2 to 10 wt% were investigated by both time-resolved emission spectroscopy and site-selective excitation. The emission decays are non-exponential. They depend on Cr concentration and emission frequency and, hence, it is possible to distinguish different kinds of Cr^{3+} sites: at least two different types of low field site, one type of high field site and one intermediate field site. The emission decay time for Cr^{3+} in intermediate field sites was found to be the longest. In Cr_2O_3 -poor mullites Cr^{3+} occurs dominantly at high field sites, i.e. at structural $M(1)$ positions replacing Al^{3+} , whereas in Cr_2O_3 -rich mullites the majority of Cr^{3+} is incorporated in interstitial sites.

1 Introduction

In recent years, mullite has attracted much interest because of its favourable high temperature properties such as low thermal expansion and conductivity, and because of its excellent creep resistance up to 1400°C.¹ Furthermore, chromium-doped mullite transparent glass-ceramics are promising compounds for tunable solid-state lasers. Mullite is able to incorporate a variety of transition metal cations into its structure. Among these ions Cr^{3+} is of special interest since it can be used as local probe for optical and electron paramagnetic resonance (EPR) investigations. Previous optical studies of chromium-doped mullite were carried out on glass-ceramics having Cr^{3+} concentrations between 0.1 and 0.05 wt% Cr_2O_3 .²⁻⁷

The energy levels of $\text{Cr}^{3+}(\text{d}^3)$ in an octahedral field are given by a Tanabe-Sugano diagram: some levels such as $^4\text{T}_2(\text{t}_2^2\text{e})$, $^4\text{T}_1(\text{t}_2^2\text{e})$ and $^4\text{T}_1(\text{t}_2\text{e}^2)$ depend strongly on the crystal field strength Dq . If Dq is larger than $\sim 1550 \text{ cm}^{-1}$ ($Dq/B = 2.1$) the low-

est excited state is $^2\text{E}(\text{t}_2^2\text{e})$ and Cr^{3+} is located in so-called high field sites (HFS). With $Dq < 1550 \text{ cm}^{-1}$, $^4\text{T}_2$ becomes the lowest state and Cr^{3+} is located in so-called low field sites (LFS). The ground state is $^4\text{A}_2(\text{t}_2^3)$. Depending on Dq , the HFS transition $^2\text{E} \Rightarrow ^4\text{A}_2$ and the LFS transition $^4\text{T}_2 \Rightarrow ^4\text{A}_2$ can be observed by emission spectroscopy. The LFS transition leads to a broad band decaying in a few μs . In crystalline phases the HFS transition exhibits two sharp R-lines with lifetime in the ms region. The intensity is low because the transition is spin-forbidden. The breaking of the selection rule is due to spin-orbit coupling and phonon-electron interaction which admixes the $^4\text{T}_2$ wave function into the ^2E state and vice versa. In aluminosilicates, glasses and in more or less ordered crystalline compounds this mixing is stressed because Dq lies in the crossing region of the $^4\text{T}_2$ and ^2E states, leading to a strong distortion of oscillator strength and of the lifetime of the excited levels.^{2,8-12}

Luminescence measurements of solids are helpful in the study of laser material and the search for new phosphors, because information is provided about the local structure of optically active ions in the host material, e.g. point group symmetry and crystal field strength can be inferred. In structurally disordered materials such as glasses and compounds with ion vacancies, the site-selective excitation technique is able to develop the individual response of optically different ions from an inhomogeneously broadened luminescence spectrum. Moreover, overlapping bands can often be discriminated by time-resolved spectroscopy provided the emitting levels have different decay times. In the investigation of ceramics, it was shown that the application of both techniques is suitable to follow the martensitic transformation in partially stabilized zirconia.¹³

This paper presents time-resolved fluorescence measurements of mullite with chromium concen-

trations between 2 and 10 wt% Cr_2O_3 using both these techniques, to determine structurally different Cr sites in mullite.

2 Experimental

2.1 Sample synthesis

Mullite samples were prepared by reaction sintering. Chemically pure powders of $\alpha\text{-Al}_2\text{O}_3$ (62 – x wt%), SiO_2 (38 wt%) and $x = 2, 5, 7.5$ and 10 wt% Cr_2O_3 were used for the syntheses. After grinding the starting powders with ethyl alcohol in an agate mortar, the mixture was annealed in a PtRh crucible at 1650°C for 10 days. The glass phase present after the reaction sintering process was leached with an HF/HCl acid solution. The chemical composition and the lattice parameters of the samples are compiled in Table 1. Samples are designated as CR2, CR5, CR7.5 and CR10, according to their bulk Cr_2O_3 contents. The acid-treated mullite powders are green in colour. Samples were checked prior to spectroscopic measurements with a polarizing microscope and by X-ray diffraction. Neither impurity minerals nor glass was observed in the samples. Therefore, the acid-treated material is considered to be single-phase mullite.

2.2 Luminescence measurements

The fluorescence spectra were measured with a 80 cm double grating spectrometer (Coderg Co., PhO model) equipped with an R 928 Hamamatsu photomultiplier. The signals were processed by a Tektronix 2430 digital oscilloscope and a BFM 187 personal computer. Time-resolved measurements were performed by ultraviolet (UV) pulsed excitation using a nitrogen laser (Jobin Yvon ISA, LAO4 model). Selected excitation in the visible region was performed by a dye laser (Jobin Yvon, EIT model) pumped by a nitrogen laser. Usual dyes, coumarins, rhodamines and blue nile, were used.

Each fluorescence decay, following the excitation pulse, was analysed in real time while simultaneously scanning the wavelength of the The signals were numerically integrated in different time gates, each one defined by a given delay and

width. Using up to six time gates the corresponding time-resolved emission spectra could be recorded during one scan. Each spectrum was normalized to its main band. The spectra were not corrected for the spectral sensitivity of the optical set-up. Since the cut-off of the spectrometer is near 11 000 cm^{-1} , the signals below 12 000 cm^{-1} did not have the true line shape. In order to reduce the energy transfer between chromium ions, most of the measurements were carried out at 77 K. Moreover, from this set-up, decay profiles were obtained by averaging over some hundred decay measurements.

3 Results

As reference for a Cr^{3+} high field site spectrum, the optical absorption of ruby was measured. The $^4\text{A}_2 \Rightarrow ^4\text{T}_2$ and $^4\text{A}_2 \Rightarrow ^4\text{T}_1$ transitions were observed as broad bands at 18 300 and 25 000 cm^{-1} , respectively. Weak narrow features in the spectrum correspond to spin-forbidden transitions from the ground state to the states ^2E , $^2\text{T}_1$ and $^2\text{T}_2$. In the absorption spectra of the samples investigated here two doublets can be distinguished. Their intensities correspond to the Cr concentration. The two doublets occur at 16 280/22 440 cm^{-1} and 18 520/24 520 cm^{-1} , respectively. By comparison with the ruby spectrum they were assigned to both low field site and high field site transitions.

Under UV pulsed excitation using a wavelength of 337 nm (29 674 cm^{-1}) all samples show a broad emission band designated as E (Fig. 1). The maximum lies at about 21 300 cm^{-1} and the line width is $\sim 5000 \text{ cm}^{-1}$. The time decay of band E is $< 50 \text{ ns}$. Below 15 000 cm^{-1} the intensity of the emission spectra depends slightly on the Cr concentration. This was not observed for sample CR2. Therefore, the concentration quenching seems to start with Cr_2O_3 contents $> 2 \text{ wt\%}$. Sample CR2 exhibits further an emission spectrum in the low energy range which differs in some details from the spectra of the samples with higher Cr content. For delay times ranging from 2 to 500 μs , two bands centred around 12 550 and 13 950 cm^{-1} , labelled as A and C respectively, were observed; band A exhibits the

Table 1. Chemical composition and lattice parameters of Cr_2O_3 -doped mullites

Sample	Chemical composition (wt%)			Lattice parameters (\AA)			
	Al_2O_3	SiO_2	Cr_2O_3	a	b	c	$v (\text{\AA}^3)$
CR2	68.8 (3)	28.9 (4)	2.3 (2)	7.5498 (7)	7.6951 (7)	2.8867 (2)	167.71 (1)
CR5	65.7 (4)	28.5 (4)	5.7 (2)	7.5561 (2)	7.7006 (2)	2.8921 (1)	168.281 (5)
CR7.5	62.8 (4)	28.4 (3)	8.6 (2)	7.5624 (4)	7.7067 (5)	2.8973 (2)	168.861 (1)
CR10	60.0 (4)	28.4 (3)	11.5 (2)	7.5674 (5)	7.7089 (7)	2.9010 (2)	169.23 (2)

The chemical composition refers to electron microprobe analyses. Values in parentheses are standard deviations. Data were taken from Rager *et al.*⁷

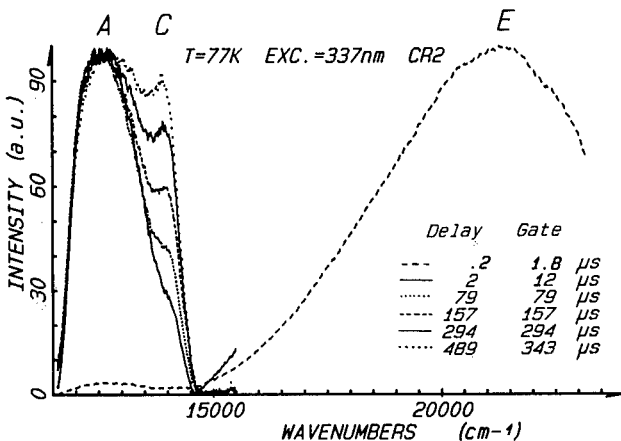


Fig. 1. Time-resolved emission spectra of sample CR2 at 77 K obtained with different delay and gate times. Excitation at 29674 cm^{-1} .

shorter decay time. Similar bands at 12500 and $14325/14300 \text{ cm}^{-1}$ were also reported from transparent mullite glass ceramics with Cr concentrations $< 0.1 \text{ wt\% Cr}_2\text{O}_3$.^{2,3,5}

Band A occurs in all our samples. Except for sample CR2, it is shifted towards lower energy by increasing the delay time from 0.1 to $\sim 20 \mu\text{s}$ (Fig. 2). The shift occurs mainly within the first $10 \mu\text{s}$. It depends also on the Cr concentration, i.e. it increases from sample CR5 to sample CR10. In the emission spectra of samples CR5 and CR7.5, additionally, a shoulder appeared at delay and gate times of $150 \mu\text{s}$. It corresponds probably to band C observed in sample CR2 (Fig. 1). On increasing the delay and gate times further, another shoulder designated as B appears at about 13600 cm^{-1} (Fig. 3). In the spectrum of sample CR10, however, no indication for the shoulders B and C could be observed when delay and gate times were $> 150 \mu\text{s}$.

The decay profiles of all samples were recorded at room and liquid nitrogen temperatures; decay profiles of sample CR2 were recorded also at 22 K . The decay profiles depended on Cr concentration, temperature and observation frequency

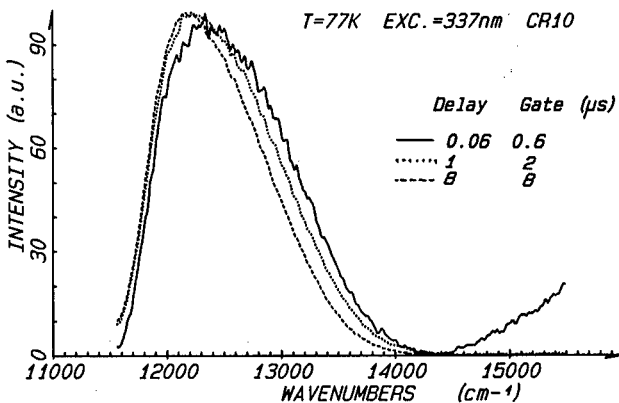


Fig. 2. Time-resolved emission spectra of band A in sample CR10 observed with short delay times. Excitation at 29674 cm^{-1} .

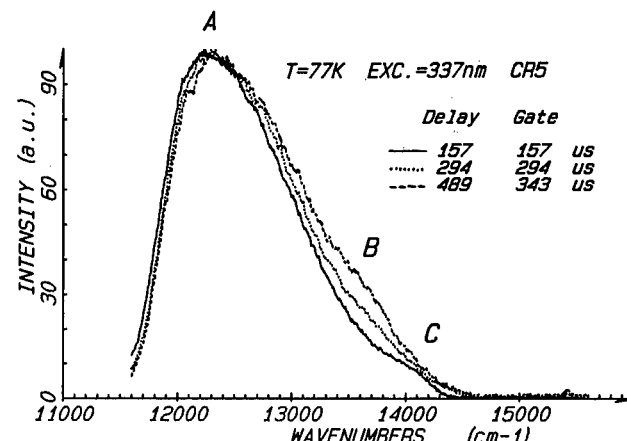


Fig. 3. Time-resolved emission spectra in sample CR5 observed with long delay times. Excitation at 29674 cm^{-1} .

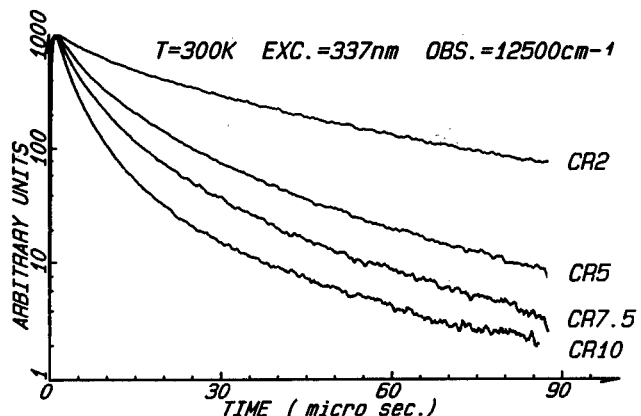


Fig. 4. Fluorescence decay profiles of band A in the different samples. Excitation at 29674 cm^{-1} ; observation at 12500 cm^{-1} .

(Figs 4 and 5) but only slightly on the excitation frequency. All decays are non-exponential and, hence, can be characterized by a short and a long lifetime component. The short component corresponds to an average lifetime in the first e-folding while the long-lived component governs the last recorded e-folding. Both lifetime components decrease with increasing Cr content and increase with decreasing temperature. For example, in samples

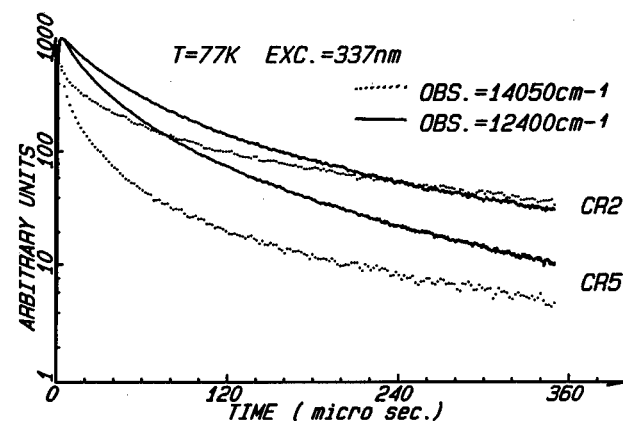


Fig. 5. Dependence of the fluorescence decay profiles on observation frequency and Cr³⁺ content at 77 K. Excitation at 29674 cm^{-1} ; observation at 14050 cm^{-1} (dotted lines) and 12400 cm^{-1} (solid lines).

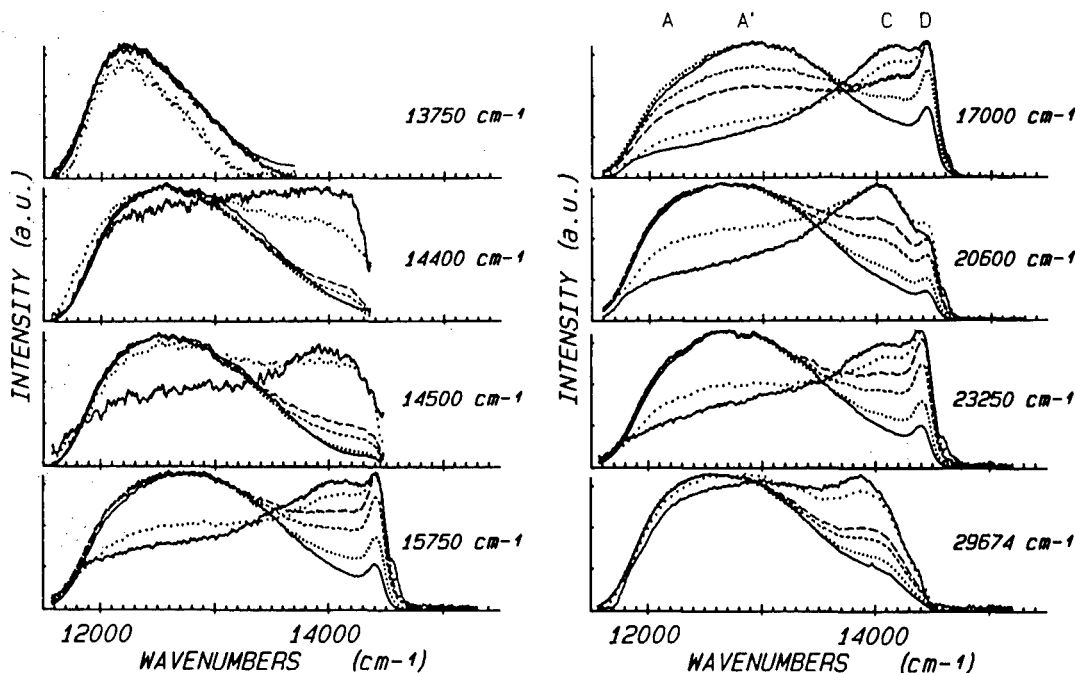


Fig. 6. Time-resolved emission spectra of sample CR2 as a function of the excitation frequency at 77 K. Gate/decay times in μ s are: —, 10/50; 50/100; - - - 100/170; - - - - 150/150; ○○○○○ 300/300; and —, 500/300.

CR2 and CR10 the short lifetime components of band A are ~ 15 and 3μ s, respectively, at 300 K, and 30 and 5μ s at 77 K. The long lifetime components for CR2 and CR10 are 45 and 35 μ s, respectively, at room temperature and 70 and 54 μ s at 77 K. The non-exponential behaviour of the decay profiles does not change very much with temperature and becomes almost constant below 100 K.

Below 15000 cm^{-1} the emission spectrum of sample CR2 is strongly time-dependent. Therefore, it was investigated in detail at 77 K varying the excitation energy from 29674 to 13750 cm^{-1} (Fig. 6). To compare the spectra the time-resolved emissions during each scan were recorded with the same set of delays and gates, i.e. with 10/50, 50/100, 100/170, 150/150, 300/300 and 500/350 μ s. Four bands centred at 12350 (A), 12800 (A'), 14100 (C) and 14480 (D) cm^{-1} could be resolved.

The intensity ratio of these bands depends on both the time elapsed after the excitation pulse and the excitation frequency. Due to the strong deviation from an exponential decay, the lifetimes could not be determined. The bands were, therefore, classified in the sequence A', A, D and C according to their increasing decay time. The decay times range from some hundred μ s to ms.

Band A could still be excited at 13700 cm^{-1} , which indicates a Stokes shift of $\sim 1500 \text{ cm}^{-1}$. The lowest excitation frequency for band A' was not determined since A and A' were not time-resolved under excitation in the $13700\text{--}15000 \text{ cm}^{-1}$ range. The width of the A-A' signal, however, is enlarged with increasing excitation energy. In contrast to the fast-decaying bands A and A', the Stokes shift of

Table 2. Summary of experimental data. Band frequencies are given in cm^{-1}

Material	$^2\text{E} \Rightarrow ^4\text{A}_2$ Emission	$^4\text{A}_2 \Leftrightarrow ^4\text{T}_2$ Emission	$^4\text{A}_2 \Leftrightarrow ^4\text{T}_1$ Absorption	Assignment	Reference	
Glasses*						
Mullites**	14280–14390	12000–12600 13300–13700 ⁺	15200–15900 16700–17200 ≈ 17150	22600 23300 ≈ 25000 ≈ 23900	LFS HFS HFS (A)	2, 3, 10, 14, 15 2, 3, 4, 5, 15 9
Kyanite	{ 14180 14210	13250 12400 12000	≈ 16240	≈ 23150	HFS (B) LFS (C) LFS	9 9 8
Sillimanite						
Ruby	14417–14446		18300	25000	HFS	This work
CR2	14480 (D)		18520	>21300 24520	HFS	This work
CR2		14000 (C)			IFS	This work
CR5, CR7.5		13600 (B)			IFS	This work
CR2		12350 (A)	16280	<21300 22440	LFS	This work
CR2		12800 (A')	16280		LFS	This work

*Silicate and other oxide glasses.

**Cr poor mullites originated in crystallization of aluminoborosilicate glasses.

⁺Band maximum depends on excitation frequency, attributed to IFS.

the two long-lived bands, C and D, was estimated to be $< 300 \text{ cm}^{-1}$ because these bands could still be excited at 14400 and 14500 cm^{-1} , respectively. The intensity of the long-lived and narrow band D runs through a minimum at the excitation frequency of 21000 cm^{-1} . It could not be excited at the energy of 29674 cm^{-1} . The spectroscopic data are listed in Table 2 and compared with literature data of some reference samples.

4 Discussion

The fast-decaying, high frequency emission band E was observed in all samples. It is assigned to the $^4\text{T}_1 \Rightarrow ^4\text{A}_2$ spin-allowed transition and corresponds to the main absorption band at 24520 cm^{-1} . The Stokes shift is $\sim 3000 \text{ cm}^{-1}$. This value is of the same order as observed for $^4\text{T}_2 \Rightarrow ^4\text{A}_2$ transitions in silicate glasses.¹³ For both these transitions, which occur between the t_2^3e and t_2^3 configurations, electron-phonon coupling has to be taken into account. The Stokes shift of 3000 cm^{-1} includes (i) twice the maximum frequency of the involved phonons (relevant to the Huang-Rhys parameter) and (ii) the inhomogeneous broadening of the zero phonon line due to a distribution of Cr sites for which the crystal field continuously varies. This interpretation is supported by the band width of 5000 cm^{-1} , which indicates a convolution of the state density of the involved phonons with the inhomogeneous zero phonon band. Moreover, both high and low field chromium sites may contribute to the unusual broadening of the zero phonon band. Because of the lack of spectral and time resolution inside the E band, the above-mentioned contributions cannot be separated. A similar band width for the $^4\text{A}_2 \Rightarrow ^4\text{T}_2$ absorption was reported for transparent mullite glass-ceramics.¹⁵

In sample CR10 only band A is observed. According to its low energy, this fast-decaying band is ascribed to $^4\text{T}_2 \Rightarrow ^4\text{A}_2$ transitions of Cr^{3+} in low field sites. The shoulder B, clearly observable only when the delay times were $> 500 \mu\text{s}$ and occurring only in the spectra of samples CR5 and CR7.5, is difficult to assign. The long decay time could be indicative of high field sites; however, the band width and the energy of the shoulder rules out this possibility. Band C appears at intermediate delay times of $\sim 150 \mu\text{s}$ and does not occur at other delay times. Regarding the intensities of the bands A, B and C, the dominant band A suggests that predominantly low field sites of Cr^{3+} exist in the samples CR5, CR7.5 and CR10.

In spite of the energy transfer due to different non-radiative relaxation processes, the emission spectra of CR2 show a significant degree of site

selection which is emphasized by the kinetic behaviour as shown in the spectra of Fig. 6. The time-resolved spectra reveal the presence of two bands, A and A', in the low energy range. The decay of A and A' is fast and, hence, they are assigned to $^4\text{T}_2 \Rightarrow ^4\text{A}_2$ transitions of two families of chromium low field sites. In previous investigations,^{3,5,15} only one band at about 12500 cm^{-1} was observed in this energy range. As for the E band this interconfigurational transition ($t_2^3e \Rightarrow t_2^3$) is phonon-assisted. The Stokes shift of 1500 cm^{-1} for band A was estimated from the limit of the site-selective excitation. It is significantly smaller than the Stokes shift of band E. This may be explained by assuming that only a small fraction of Cr^{3+} centres within a given distribution of low field sites was excited. In such a case the band width may be reduced to its homogeneous width. Furthermore, the excitation can still occur with low energy phonons, i.e. close to the zero phonon line.

The sharp long-lived band D at 14480 cm^{-1} is close to the ruby R-lines at 14417 and 14446 cm^{-1} . It is, therefore, attributed to transitions between the states ^2E and $^4\text{A}_2$ which belong to Cr^{3+} ions at high field sites. The transition $^2\text{E} \Rightarrow ^4\text{A}_2$ occurs within the t_2^3 configuration and is not vibronically broadened. Its inhomogeneous width of about 120 cm^{-1} indicates a certain variation of high field sites. The low fluorescence efficiency and the strong diffuse reflectance did not allow to observe resonantly this transition, but close to the excitation at 14500 cm^{-1} the emission band appears at 14400 cm^{-1} . Thus, the Stokes shift of $\sim 100 \text{ cm}^{-1}$ or even less indicates a weak phonon coupling.

The A/A' and D bands are usually encountered in silicate and aluminosilicate ceramics as well as in the corresponding glasses.^{2,4,5,14,15} They were identified without difficulty. In contrast, the origin of the C band around 14000 cm^{-1} is not clear. So far this band has not yet been mentioned in the literature, except for a band at 13700 cm^{-1} in a transparent glass-ceramic.¹⁴ The decay of C band is longer than the decay of high field site transitions between ^2E and $^4\text{A}_2$. The maximum frequency as well as the band width of about 800 cm^{-1} classify it just between LFS and HFS emissions. It is still present under a 14400 cm^{-1} excitation, which indicates a Stokes shift of $\sim 400 \text{ cm}^{-1}$. We ascribe it, therefore, to intermediate field sites (IFS) of Cr^{3+} for which the crystal field parameters lies in the crossing region of the $^4\text{T}_2$ and ^2E states. Nevertheless, the long decay and the small Stokes shift are not well understood. A distribution of Cr^{3+} at intermediate field sites was already mentioned by some authors^{5,15} and, hence, an emission from both $^4\text{T}_2$ and ^2E states may be expected. The intermediate field sites of Cr^{3+} are not restricted to

centres which obey the condition $\Delta E = {}^4T_2 - {}^2E = 0$. Cr³⁺ energy states which differ at 77 K from the above condition by less than ± 100 cm⁻¹ may be activated thermally to emit from the two levels. Further, the states 4T_2 and 2E should be in thermal equilibrium and, thus, emission from both levels should occur with the same decay. However, this consideration may not apply to bands D and C because they show a different time behaviour. Moreover, as pointed out by Andrews *et al.*,¹⁵ a two-level thermally equilibrated system could not be applied to the data obtained for Cr³⁺ in transparent glass-ceramics in the temperature range 77 to 298 K. A more sophisticated model,¹¹ with adequate parameters, and which includes spin-orbit and vibronic coupling effects in the crossing region, is needed to explain the nature of the C band. The admixture of wave functions with predominant 2E character, for example, could explain the long lifetime. Furthermore, a certain separation between the 2E and 4T_2 branches in the coupling region may explain the lowering of the emitting level with respect to the pure 2E level and the fact that no emission from the upper level occurs.

The intensity calibration of the time-resolved emission spectra was difficult because the intensities of the dye lasers are wavelength-dependent. Seven different dyes were required for the excitation beam to cover the range from 13 500 to 23 500 cm⁻¹. Further, reproducibility of the optical set-up was hard to achieve. Therefore, the selectivity of the spectra with respect to the individual chromium sites in mullite was estimated by the intensity ratios $(I_{14480}/I_{12900})_2$ and $(I_{14000}/I_{12900})_4$ of the bands D, C and A'. The subscripts 2 and 4 denote the second and fourth gates (see Fig. 6) through which bands D and C could best be resolved. The ratios (Fig. 7) reflect the spectral selectivity of the long-lived bands with respect to the fast-decaying bands, i.e. HFS/LFS ratios. The curves in Fig. 7 correspond roughly to the absorption spectrum of both high and low field chromium sites. Although the experimental accuracy of these plots is not high, two small dips at 14 600 and 14 800 cm⁻¹ should be noted. A similar fine structure also appeared in the ${}^4A_2 \Rightarrow {}^4T_2$ absorption band in Cr-doped glasses.^{10,14} The most probable interpretation is a Fano anti-resonance between the 4T_2 vibrational quasi-continuum and the 2T_1 and 2E discrete levels.

In the mullite sample with the lowest Cr₂O₃ content, bands D and C indicate high and intermediate field sites and bands A and A' two kinds of low field site. This corresponds to the observations in mullite glass-ceramics with low Cr contents which exhibit high and low field sites, though the major part of Cr³⁺ may occur in high

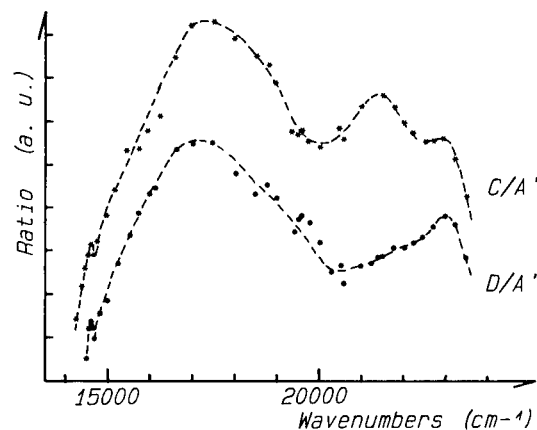


Fig. 7. Spectrum of the excitation ratios C/A' and D/A' bands in sample CR2 at 77 K.

field site domains.⁴ In mullites with intermediate and high Cr₂O₃ contents only the band A can be clearly observed. The results are interpreted in the following way: at low Cr₂O₃ contents the predominantly high field Cr sites are explained by Cr³⁺ at octahedral M(1) positions (position (2a) in the space group *Pbam* of mullite). With increasing Cr concentration in the mullite structure, low field Cr sites predominate which are described as distorted interstitial Cr sites. The fluorescence spectroscopic results presented here, i.e. the occurrence of at least two different structural Cr sites in mullite, agree well with spectroscopic investigations by electron paramagnetic resonance (EPR) and by optical absorption.^{1,7}

Finally, we would like to comment on the non-exponential behaviour of the band decays observed in all samples. This observation is not surprising because it was likewise reported for transparent mullite glass-ceramics.^{5,15} It is explained by an excitation transfer between the Cr³⁺ ions which increases with increasing Cr content and temperature. An energy transfer mechanism from HFS to LFS was proposed in the literature.³ However, other transfer mechanisms among Cr sites of the same kind cannot be excluded. Thus, for band A of sample CR10 (Fig. 2), which was identified as ${}^4T_2 \Rightarrow {}^4A_2$ transitions of low field chromium sites, a transfer from high to low energy sites within a distribution of low field sites could explain the observed shift towards lower energy as the delay time increases. Generally, excitation transfers are assumed to be responsible for the poor selectivity when applying site-selective excitations, as can be seen in Fig. 6.

5 Conclusion

In this work time-resolved fluorescence spectroscopy was applied in a wide time range to investi-

gate Cr sites in heavy doped mullite. ${}^4\text{T}_2 \Rightarrow {}^4\text{A}_2$, ${}^4\text{T}_2 \Rightarrow {}^4\text{A}_2$ and ${}^2\text{E} \Rightarrow {}^4\text{A}_2$ emissions were separated. As in low Cr content mullite glass-ceramics, high and low field chromium sites have been detected. The further findings are summarized as follows.

1. At least two types of low field chromium site occur in the mullite structure.
2. In addition to the 14480 cm^{-1} band which is attributed to high field chromium sites, another band at 14000 cm^{-1} with the longest observed decay time appears. It is assigned to intermediate field chromium sites. The ${}^2\text{E}$ character of the emitting level of this band is retained despite its unusual low energy.
3. In mullites containing high Cr_2O_3 contents, Cr^{3+} ions are mostly located in low field sites with a certain variation of their crystal fields. All sites have the ${}^4\text{T}_2$ state as the lowest level.
4. High field Cr sites are predominant in Cr_2O_3 -poor mullites. They are correlated with incorporation of Cr^{3+} at octahedral M(1) positions replacing Al^{3+} . Upon increasing the Cr_2O_3 content Cr^{3+} favourably enters the highly distorted low field sites, which are attributed to interstitial lattice positions in the mullite structure.
5. Strong deviation from an exponential decay is observed for all emission bands at room and low temperatures (22 K). This may be explained by an energy transfer between different Cr sites which occurs even at low temperatures.

References

1. Schneider, H., Okada, K. & Pask, J. A., *Mullite and Mullite ceramics*, John Wiley and Sons, Chichester, 1994.
2. Wojtowicz, A. J. & Lempicki, A., Luminescence of Cr^{3+} in mullite transparent glass ceramics (II). *J. Lumin.*, **39** (1988) 189–203.
3. Knutson, R., Liu, H., Yen, W. E. & Morgan, T. V., Spectroscopy of disordered low-field sites in Cr^{3+} : mullite glass ceramic. *Phys. Rev. B*, **40** (1989) 4264–70.
4. Liu, H., Knutson, R. & Yen, W. M., Saturation-resolved-fluorescence spectroscopy of Cr^{3+} mullite glass ceramic. *Phys. Rev. B*, **41** (1990) 8–14.
5. Liu, H., Knutson, R., Jia, W., Strauss, E. & Yen, W. M., Spectroscopic determination of the distribution of Cr^{3+} sites in mullite ceramics. *Phys. Rev. B*, **41** (1990) 12888–94.
6. Schneider, H., Transition metal distribution in mullite. *Ceram. Trans.*, **6** (1990) 135–58.
7. Rager, H., Schneider, H. & Graetsch, H., Chromium incorporation in mullite. *Am. Mineral.*, **75** (1990) 392–7.
8. Wojtowicz, A. J. & Lempicki, A., Luminescence of Cr^{3+} in sillimanite. *Phys. Rev. B*, **39** (1989) 8695–701.
9. Wojtowicz, A. J., Luminescence of Cr^{3+} in kyanite. *J. Lumin.*, **50** (1991) 221–30.
10. Brawer, S. A. & White, W. B., Optical properties of trivalent chromium in silicate glasses: a study of energy levels in the crossing region. *J. Chem. Phys.*, **67** (1977) 2043–55.
11. Donelly, C. J., Healy, S. M., Glynn, T. J., Imbush, G. F. & Morgan, G. P., Spectroscopic effects of small ${}^4\text{T}_2$ – ${}^2\text{E}$ energy separations in 3d^3 -ion systems. *J. Lumin.*, **42** (1988) 119–25.
12. Wojtowicz, A. J., Grinberg, M. & Lempicki, A., The coupling of ${}^4\text{T}_2$ and ${}^2\text{E}$ states of Cr^{3+} ion in solid state materials. *J. Lumin.*, **50** (1991) 231–42.
13. Piriou, B., Dexpert-Ghys, J., Bastide, B. & Odier, P., Martensitic transformation of TZP investigated by site selective spectroscopic method. *Proceedings of Zirconia 88*, 17 November 1988, Bologna.
14. Andrews, L. J., Lempicki, A. & McCollum, B. C., Spectroscopy and photokinetics of chromium (III) in glass. *J. Chem. Phys.*, **74** (1981) 5526–38.
15. Andrews, L. J., & Lempicki, A., Luminescence of Cr^{3+} in mullite transparent glass ceramics. *J. Lumin.*, **36** (1986) 65–74.

EXAFS Studies of Cr-doped Mullite

K. R. Bauchspieß^{a,*} H. Schneider^b & A. Kulikov^c

^aSchool of Mathematical and Physical Sciences, Murdoch University, Perth, WA 6150, Australia

^bGerman Aerospace Research Establishment (DLR), Institute for Materials Research, D-51140 Köln, Germany

^cInstitute of Chemistry, Russian Academy of Sciences, Vladivostok 690022, Russia

(Accepted 22 July 1995)

Abstract

Mullites doped with 7.3 (Cr 6) and 11.5 wt% Cr_2O_3 (Cr 10) were synthesized by reaction sintering of Al_2O_3 , SiO_2 and Cr_2O_3 powder compacts at 1650°C in air. Prior to the spectroscopic analyses, the powder samples were HF/HCl-washed in order to remove coexisting glassy phases. According to X-ray diffractometry all samples consisted of mullite only.

Measurements of the extended X-ray absorption fine structure (EXAFS) of the Cr K edge of mullite were performed at the Photon Factory, National Laboratory of High Energy Physics (KEK), in Tsukuba, Japan. The measured spectra were normalized by first subtracting a pre-edge background and then fitting a smoothly varying cubic-spline background in the region of the EXAFS. For all measured spectra the magnitude of the Fourier transform, which is related to the pair distribution function (PDF) and similar to it, is characterized by two pronounced peaks. The first peak is ascribed to oxygen making up the octahedra surrounding the Cr atoms and the second peak is assumed to be due to Al. It turned out that the second peak could not be fitted satisfactorily with one Al coordination shell alone. The discrepancy can be reduced by assuming that there is an additional contribution from Cr atoms that do not occupy regular lattice sites but are displaced by some amount. The existence of such displaced Cr atoms is known from EPR and crystal field spectroscopy experiments. Since these Cr atoms are not in the center of the Al coordination shell, the Al PDF seen by these Cr atoms is broadened and also slightly asymmetric. From our data analysis we find the displacement of the Cr atoms from the center of their surrounding aluminum coordination shell to be 0.50 Å.

1 Introduction

Mullite has the general composition $\text{Al}_{4+2x}\text{Si}_{2-2x}$

*To whom correspondence should be addressed.

O_{10-x} ($0.25 \leq x \leq 0.4$).¹ The orthorhombic crystal structure of mullite contains chains of edge sharing AlO_6 octahedra running parallel to the crystallographic *c*-axis. Octahedral columns are crosslinked by tetrahedra double chains with randomly distributed Al and Si atoms. Tetrahedra double chains also run parallel to *c*. Some O atoms bridging adjacent tetrahedra are removed and as a consequence a new tetrahedral site is formed, in which the bridging O atoms belong to three tetrahedra (e.g. Refs 2-4).

Earlier work on the doping of mullite with Cr was performed by Gelsdorf *et al.*,⁵ Murthy and Hummel,⁶ and Rager *et al.*⁷ It has been stated that up to 12 wt% Cr_2O_3 is incorporated in mullite. A detailed study of the crystal chemistry of Cr-doped mullites prepared by reaction sintering of Al_2O_3 , SiO_2 and Cr_2O_3 (0.5-11 wt%) powders, was performed by Rager *et al.*¹³ Rager *et al.* found a reciprocal and equimolar dependence between Cr_2O_3 and Al_2O_3 in mullite, but not between Cr_2O_3 and SiO_2 contents. They concluded that Cr^{3+} is incorporated by replacement of Al^{3+} . The structural state (*x*-value) of Cr-doped mullite, which corresponds to that of 3/2-type mullite, indicates that the variation of Cr incorporation is not correlated with a change of the amount of O(C) oxygen vacancies in mullite.

Electron paramagnetic resonance (EPR) studies provided information on the structural distribution of Cr in mullite:⁷ Cr-doped mullites exhibit two sharp EPR signals near $g_{\text{eff}} = 5$, and a broad signal near $g_{\text{eff}} = 2.2$. The peaks near $g_{\text{eff}} = 5$ were assigned to Cr^{3+} in slightly distorted octahedral Al chain positions in mullite. The broad, slightly asymmetric signal near $g_{\text{eff}} = 2.2$ may indicate coupling between localized magnetic moments, and was associated with interstitial Cr^{3+} incorporation in mullite. According to the EPR peak intensities the entry of Cr^{3+} into the regular AlO_6 octahedra is favoured at low bulk Cr_2O_3 contents of mullite, whereas interstitial incorporation with formation of Cr clusters becomes more important at higher Cr_2O_3 contents. Unpolarized crystal field spectra

measured by Ikeda *et al.*⁸ in the wavelength range from 340 to 1540 nm by reflection from mullite powders with about 8 wt% Cr₂O₃ yielded further evidence for the structural distribution model of Cr³⁺ developed by Rager *et al.*⁷

2 Sample Material

Samples were prepared from about 4 g of chemically pure Al₂O₃ (VAW, 302), SiO₂ (Ventron, 88316), and Cr₂O₃ (Merck, 2483) powders, with 62-x wt% Al₂O₃, 38 wt% SiO₂, and x wt% Cr₂O₃ (x = 6, 10; designated as samples Cr 6 and Cr 10). The mixtures were pressed into disks of 20 mm diameter and 5 mm thickness in a pressing mold using uniaxial pressure loading, in a laboratory furnace in air at 1650°C. Prior to the EXAFS measurements the samples were HF/HCl-washed in order to leach the coexisting glassy phase. According to X-ray diffractometry all HF/HCl-treated samples consisted of mullite only. The actual chemical compositions of acid washed mullites determined by microprobe analysis were: Cr 6: Al₂O₃: 64.1 wt%, SiO₂: 28.5 wt%, C₂O₃: 7.3 wt%, and Cr 10: Al₂O₃: 60.0 wt%, SiO₂: 28.4 wt%, Cr₂O₃: 11.5 wt% (see Ref. 7).

3 EXAFS Measurements

3.1 Basic considerations

EXAFS spectroscopy measures the pair distribution function with respect to the absorbing atom as center. The pair distribution function $P(R)$ about the X-ray absorbing atom is defined through

$$N(R) = 1 + \int_0^R P(\tilde{R}) d\tilde{R} \quad (1)$$

$N(R)$ is the number of atoms contained in a sphere of radius R centered at the X-ray absorbing atom. Hence, integrating $P(R)$ yields the number of atoms in the system. (The radial distribution function $g(R)$ is obtained via $g(R) = P(R)/(4\pi\nu R^2)$, where ν is the number density.) In a solid the atoms can be grouped in coordination shells about a given atom and $P(R)$ can be written as a sum over S coordination shells:

$$P(R) = \sum_{j=1}^S P_j(R) \quad (2)$$

The EXAFS function, $\chi(k)$, is given by the following expression:

$$\chi(k) = S_0^2 \cdot \sum_{j=1}^S \frac{1}{k_j} \int_0^\infty \frac{dR}{R^2} |f_{b,j}(k_j, R, \pi)| \cdot \exp(-2R/\lambda_j(k_j)) \cdot P_j(R) \cdot \sin(2k_j R + \delta_c(k_j) + \delta_{b,j}(k_j, R, \pi)) \quad (3)$$

$$R$$
 is the distance from the absorbing atom (Cr) and k_j is the magnitude of the wavevector of the photoelectron. The atoms of different coordination shells may experience different potentials and therefore the photoelectron wavevector k_j of a coordination shell must be adjusted. k_j is related to the wavevector k of the data by means of an adjustable energy shift ΔE :

$$k_j = \sqrt{k^2 - \Delta E/\gamma} \text{ with } \gamma = \frac{h^2}{8\pi^2 m_e} \cong 3.81 \text{ eV}\text{\AA}^2 \quad (4)$$

$|f_{b,j}(k_j, R, \pi)|$ and $\delta_{b,j}(k_j, R, \pi)$ are magnitude and phase of the complex backscattering amplitudes $f_{b,j}(k_j, R, \pi)$, and $\delta_c(k_j)$ is the central-atom phaseshift (of Cr) for K-shell absorption. $\lambda_j(k_j)$ is the inelastic mean free path of the photoelectron. S_0^2 is an overall amplitude reduction factor due to multi-electron excitations. Since the R -dependence of $f_{b,j}(k_j, R, \pi)$ is weak, R can be replaced by its average value R_j for shell j , as far as the backscattering amplitude is concerned, and eqn (3) becomes:

$$\chi(k) = S_0^2 \cdot \sum_{j=1}^S \frac{|f_{b,j}(k_j, R_j, \pi)|}{k_j} \int_0^\infty \frac{dR}{R^2} \exp$$

$$(-2R/\lambda_j(k_j)) \cdot P_j(R) \cdot \sin(2k_j R + \delta_c(k_j) + \delta_{b,j}(k_j, R_j, \pi)) \quad (5)$$

In the harmonic approximation it is assumed that the pair distribution functions $P_j(R)$ are Gaussians:

$$P_j(R) = \frac{N_j}{\sigma_j \sqrt{2\pi}} \exp(-(R-R_j)^2/2\sigma_j^2) \quad (6)$$

N_j is the number of atoms in shell j . Inserting eqn (6) into eqn (5) one obtains the standard EXAFS formula:

$$\chi(k) = S_0^2 \cdot \sum_{j=1}^S \frac{N_j}{k_j R_j^2} |f_{b,j}(k_j, R_j, \pi)| \cdot \exp(-2R_j/\lambda_j(k_j)) \cdot \exp(-2\sigma_j^2 k_j^2) \cdot \sin(2k_j R_j + \delta_c(k_j) + \delta_{b,j}(k_j, R_j, \pi)) \quad (7)$$

From the measured EXAFS data one can obtain a first guess at the pair distribution function by calculating the Fourier transform. This is done according to:

$$H(R) = \frac{1}{\sqrt{\pi}} \int_{-\infty}^{\infty} w(k) \chi(k) k^p e^{+i2kR} dk \quad (8)$$

Here the term k^p was introduced in order to compensate for the decrease of $\chi(k)$ with k . $w(k)$ is a Hamming window function⁹ and is applied in

order to suppress sidelobes in the Fourier transform. $w(k)$ vanishes everywhere except on the interval $k_{\min} \leq k \leq k_{\max}$ where it is given by:

$$w(k) = 0.54 + 0.46 \cos(2\pi k/\Delta k) \text{ with } \Delta k = k_{\max} - k_{\min} \quad (9)$$

$H(R)$ is a complex function whose magnitude is related, but not equal, to the pair distribution function. In order to extract quantitative information from the data one has to employ curve fitting techniques.

3.2 Experimental procedure

The EXAFS experiments were carried out at Beamline 7C of the Photon Factory, National Laboratory for High Energy Physics, Japan. The positron storage ring was operating at 2.5 GeV and had a beam lifetime of about 70 h. The average positron current during the measurements was 270 mA. Measurements of the Cr K edge EXAFS were performed on mullite samples doped with 7.3 and 11.5 wt% Cr_2O_3 (samples Cr 6 and Cr 10, see Section 2). Samples with an absorption thickness product of about 2 in the region just after the edge were mounted on Scotch Tape. The spectra were measured in transmission, with the first ion chamber filled with N_2 gas and the second filled with a mixture of 25% Ar and 75% N_2 . In order to suppress harmonics in the X-ray beam the Si(111) double-crystal monochromator was detuned from parallelism such that the output intensity decreased by at least 50%.

4 Results of EXAFS Data Analysis

The EXAFS was extracted from the measured X-ray absorption spectra by normalizing the spectra in the usual way. First, the pre-edge region was fitted to a Victoreen-type background: $A_0 + A_3/E^3 + A_4/E^4$. E is the X-ray energy. The background was then extended into the edge and post-edge region and subtracted from the whole spectrum.

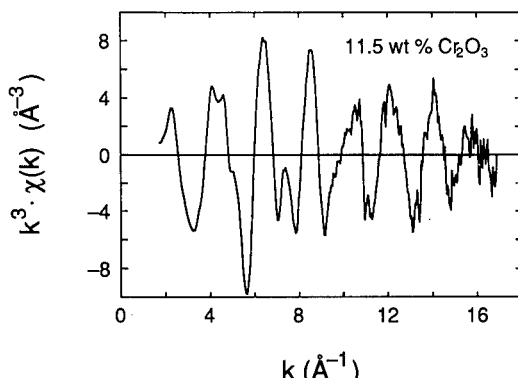


Fig. 1. k^3 -multiplied normalized EXAFS spectrum for the Cr 10 sample (~11.5 wt% Cr_2O_3) measured at 300 K.

After converting the spectrum above the energy E_{edge} of the absorption edge to the wavevector scale k according to $k = \sqrt{(E - E_{\text{edge}}) \cdot 8\pi^2 m_e / h^2}$ a second background was fitted to the EXAFS region of the spectrum. This background consisted of a smoothing spline $s(k)$ using cubic polynomials¹⁰. The EXAFS, $\chi(k)$ was then obtained by forming the difference between the data $y(k)$ and the background and dividing by the height D of the absorption step at the edge: $\chi(k) = (y(k) - s(k))/D$. One such normalized spectrum is shown in Fig. 1. The spectrum has been multiplied by k^3 in order to compensate for the decrease of the envelope with k . The data analysis is carried out using three different models, labelled 1, 2 and 3 and described below.

4.1 Model 1

For the samples investigated in this work, the magnitude of the Fourier transform, calculated according to eqn (8) and for $p = 3$, is dominated by two peaks (Fig. 2(a)). The first peak is due to the nearest-neighbour (NN) O atoms that surround the Cr atoms. The second peak is assumed

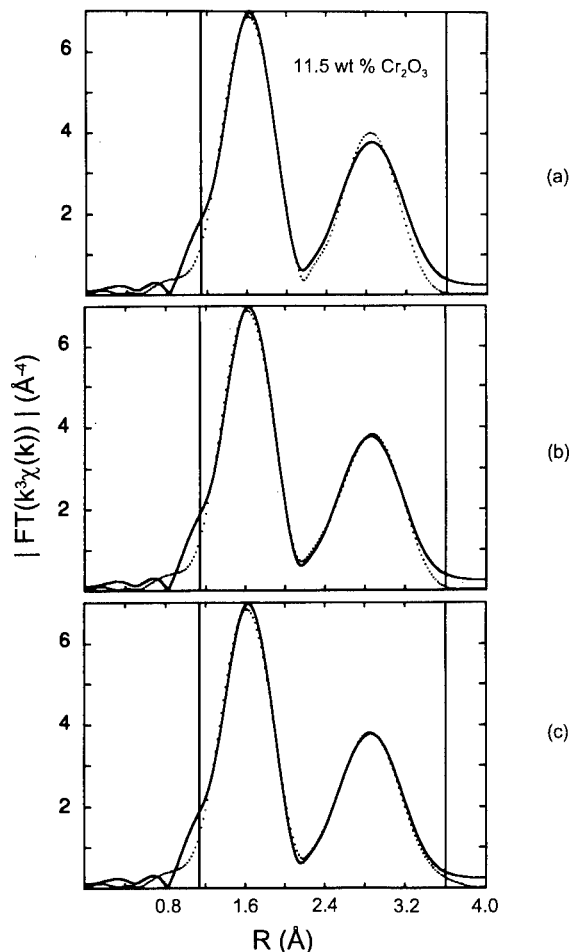


Fig. 2. Fourier transform magnitude for the Cr 10 sample (~11.5 wt% Cr_2O_3) measured at 300 K (solid line) and fit data (dotted line) from a simultaneous fit to three datasets: (a) with two coordination shells (O and Al) each; (b) with three coordination shells each; (c) with three coordination shells each, but taking the displacements of Cr atoms explicitly into account.

to be due to a next-nearest neighbour (NNN) coordination shell consisting of Al and/or Si atoms. It is impossible in EXAFS spectroscopy to distinguish between backscattering from Al and from Si atoms because Al and Si are too close in atomic number. Hence, it was assumed that the NNN coordination shell consisted of Al atoms only. In order to obtain quantitative information, the O and Al shells were curve fitted using a program developed by one of the authors.¹¹ The spectra were first fitted according to the standard EXAFS formula (eqn 7). Amplitudes and phases of the shells were calculated using the single-scattering version of the FEFF code (version 3.1.1).¹² In a fit using the harmonic approximation there are four parameters that can be varied for each coordination shell: ΔE_j , R_j , σ_j^2 and N_j . Least-squares fits to both coordination shells were carried out simultaneously to the real and imaginary parts of the Fourier transform. The Fourier transform of $k^3\chi(k)$, with $\chi(k)$ according to eqn (7), was fitted to the Fourier transform of the k^3 -multiplied data. The data that was fitted was for the Cr10 sample measured at 300 and at 150 K, and for the Cr 6 sample measured at 300 K. Three such datasets were fitted in real space simultaneously. By fitting multiple spectra one is able to include constraints on the fitting parameters and reduce the number of variable parameters per dataset. For example, one can exploit the fact that the energy corrections ΔE are identical for each atom type and that the coordination numbers are temperature independent. A typical fit carried out in this way is shown in Fig. 2. The fit interval is indicated by the vertical lines, and 16 variable fit parameters were employed for the simultaneous fit to three datasets with two shells each. There is a shoulder, which could not be fitted, at about 1 Å at the low R side of the oxygen peak. Assuming two oxygen shells could not reduce the discrepancy and thus only one O shell will be used.

The spectra had been fitted ignoring the amplitude reduction factor S_0^2 . Therefore, the coordination numbers had come out too low. From the absence of a peak just before the Cr K absorption edge one knows that the immediate Cr environment has inversion symmetry¹³ and one can thus assume that each Cr atom is octahedrally coordinated. With 6 oxygen atoms around each Cr atom, but only 4.3 atoms obtained from the data analysis, we conclude that for the data in Table 1 $S_0^2 = 0.72$. Values of S_0^2 are usually around 0.7. For Fe, which is near to Cr in the periodic table, a value of 0.69 is reported.¹⁴ Using $S_0^2 = 0.72$ one obtains for the Al coordination numbers $N_{Al} = 6.9$.

Special attention has been given to error estimation. Using a method outlined in Ref. 15, the

Table 1. Results of a simultaneous fit to three datasets with two coordination shells each

	R_O ΔR_O (Å)	σ_O^2 $\Delta\sigma_O^2$ (10^{-4} Å 2)	N_O ΔN_O	R_{Al} ΔR_{Al} (Å)	σ_{Al}^2 $\Delta\sigma_{Al}^2$ (10^{-4} Å 2)	N_{Al} ΔN_{Al}
7.3 wt%	1.985	34	6	3.258	42	6.9
300 K	±0.004	±4	±0	±0.007	±7	±0.6
11.5 wt%	1.984	33	6	3.261	47	6.9
300 K	±0.004	±4	±0	±0.007	±7	±0.6
Cr 10	1.984	28	6	3.258	36	6.9
150 K	±0.004	±4	±0	±0.006	±6	±0.6

$$\Delta E_O = 0.6 \text{ eV} \pm 1.0 \text{ eV}; \Delta E_{Al} = -10.4 \text{ eV} \pm 1.1 \text{ eV}; S_0^2 = 0.72 \pm 0.04.$$

error of a variable parameter in an n parameter fit was determined by giving this parameter fixed values around the optimum and for each given value performing an $n-1$ parameter fit with the remaining fit parameters. This method is computationally intensive but properly takes into account all parameter correlations. The error bars were obtained from the width of the minima of the residual sums of squares (χ^2) curves. In order determine up to which value χ^2_{max} along each χ^2 curve to go, it is assumed that the error for ΔE_O for the first coordination shell (O) is ± 1.0 eV. This determines χ^2_{max} and all other errors are then determined from the parameter values where χ^2 becomes equal to χ^2_{max} . For S_0^2 the error is determined from the fit error for the number N_O of atoms in the first coordination shell (O). All error bars were found to be approximately symmetric. The error bars given here do not include systematical deviations resulting from the procedure of calculating the scattering phases and amplitudes. Hence the EXAFS results are precise but not necessarily accurate. The methods described here to estimate S_0^2 and to determine the errors of the fit parameters are used throughout this work.

The PDF that is shown in Fig. 3(a) was calculated according to eqn (6) and corresponds to the fit shown in Fig. 2(a). The position of the Al peak (~3.26 Å) corresponds to Cr atoms occupying regular lattice sites in the mullite structure. Closer inspection of the data reveals that the second peak (Al) is not fitted very well. This is not because only Al, and not also Si, was considered here. Instead, the discrepancy might be due to asymmetry in the pair potential of Cr and Al atoms. A cumulant analysis,¹⁶ including C_3 for the phase and C_4 for the amplitude, was attempted. However, no conclusive results could be obtained because there was not enough EXAFS signal available at the high- k end of the spectrum (Fig. 1), which is important for determining any cumulant terms. Considering the possible presence of other Cr atoms in the vicinity of the Cr absorber could

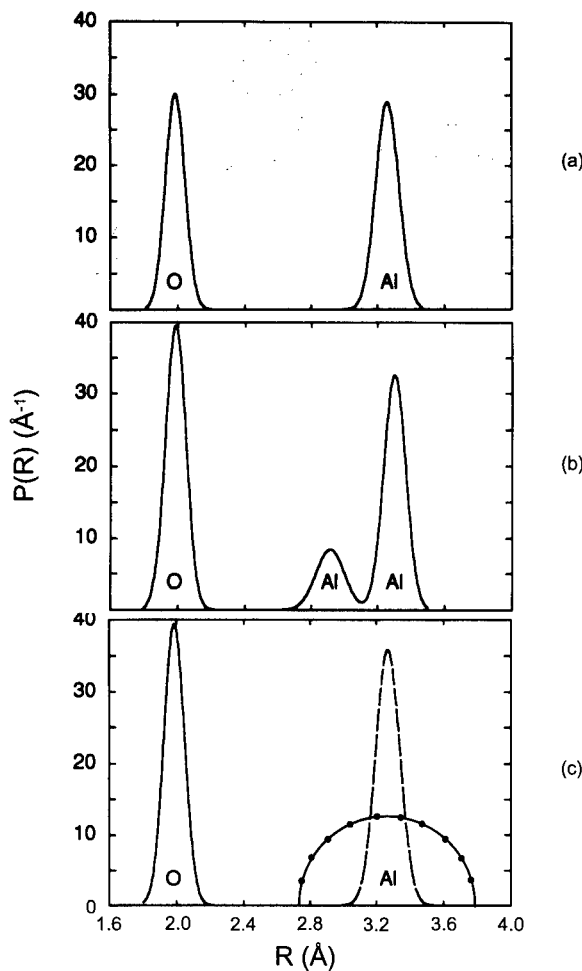


Fig. 3. Pair distribution function corresponding: (a) to the fit shown in Fig. 2(a); (b) to the fit shown in Fig. 2(b); (c) to the fit shown in Fig. 2(c); dashed line: Cr atoms in regular Al(1) sites, dotted line: Cr atoms in random interstitial sites.

not explain the discrepancy either and thus it had to be accounted for in other ways.

4.2 Model 2

The discrepancy can be reduced by including a third coordination shell, also consisting of Al atoms and close to the other Al shell. Again, three datasets were fitted simultaneously and the number of variable parameters is reduced by incorporating the constraints that all energy corrections ΔE are identical for each atom type and that the coordination numbers of each coordination shell

are the same for each dataset, that is, the coordination numbers are assumed to be independent of temperature and of Cr_2O_3 content. The simultaneous fit to three spectra, with three coordination shells each, had then 23 variable parameters for the 9 coordination shells. The fit for the Cr 10 sample measured at 300 K is shown in Fig. 2(b) and the fit results are listed in Table 2.

Comparing these results with those shown in Table 1 one finds that the total number of Al atoms about the absorbing Cr atoms is almost the same (7.2 compared to 6.9) except that they are now distributed over two coordination shells. Figure 3(b) shows the PDF corresponding to the fit of Fig. 2(b). The Al peak at ~ 2.9 Å probably describes the environment of the interstitial Cr atoms and the Al peak at ~ 3.3 Å describes the environment of the Cr atoms at the regular lattice sites. The asterisks in place of error bars for σ_{Al}^2 and N_{Al} for the coordination shell at ~ 2.9 Å indicate that the error was either very large or that it could not be determined because the minima of the χ^2 curves for σ_{Al}^2 and N_{Al} were too shallow. This means that σ_{Al}^2 and N_{Al} for the first Al coordination shell are not well defined.

For the 11.5 wt% Cr_2O_3 sample it can be seen from the table that the radius of the first Al shell decreases with increasing temperature. This anomalous behaviour could indicate an asymmetric PDF. However, taking asymmetry for this Al coordination shell into account is not practical because the correlation of the fit parameters becomes too large.

4.3 Model 3

In a third model, we now consider besides the Cr atoms occupying regular lattice sites, the effect of a large disorder of the interstitial Cr positions. These Cr atoms, with their NN oxygen octahedra, are assumed to be surrounded by an Al coordination shell of radius R_O but the average position of the Cr–O octahedra is off center by an amount ζ ($\zeta \geq 0$) as indicated in Fig. 4. The Al atoms are assumed to be continuously distributed over the coordination shell indicated in the figure. Neglecting atomic

Table 2. Results of a simultaneous fit to three datasets with three coordination shells each

	R_O ΔR_O (\AA)	σ_O^2 $\Delta \sigma_O^2$ (10^{-4}\AA^2)	N_O ΔN_O	R_{Al} ΔR_{Al} (\AA)	σ_{Al}^2 $\Delta \sigma_{\text{Al}}^2$ (10^{-4}\AA^2)	N_{Al} ΔN_{Al}	R_{Al} ΔR_{Al} (\AA)	σ_{Al}^2 $\Delta \sigma_{\text{Al}}^2$ (10^{-4}\AA^2)	N_{Al} ΔN_{Al}
7.3 wt%	1.985	37	6	2.92	64	1.8	3.30	40	5.4
300 K	± 0.004	± 4	± 0	± 0.04	*	*	± 0.02	± 20	± 1.6
11.5 wt%	1.984	37	6	2.91	73	1.8	3.30	40	5.4
300 K	± 0.004	± 4	± 0	± 0.04	*	*	± 0.02	± 20	± 1.6
11.5 wt%	1.984	31	6	2.93	54	1.8	3.29	35	5.4
150 K	± 0.004	± 4	± 0	± 0.03	*	*	± 0.02	± 15	± 1.6

$$\Delta E_O = 0.6 \text{ eV} \pm 1.0 \text{ eV}; \Delta E_{\text{Al}} = -3 \text{ eV} \pm 3 \text{ eV}; S_0^2 = 0.76 \pm 0.04.$$

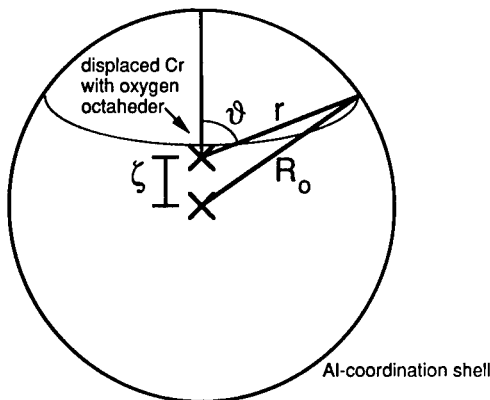


Fig. 4. Sketch of the displaced Cr atoms, octahedrally coordinated by six O atoms, but displaced from the center of the coordination sphere by the amount ζ . The Al atoms are assumed to be distributed continuously over the sphere.

vibrations for the moment, the distribution for the interstitial (displaced) Cr atoms ranges from $r = R_0 - \zeta$ to $r = R_0 + \zeta$. The number of Al atoms at distance r from a Cr atom displaced with its oxygen octahedra by ζ from the center of the Al coordination shell is proportional to the length $2\pi r \sin \vartheta(r)$ of the circle subtended by the angle ϑ (Fig. 4). The PDF for the Al atoms about the Cr atoms displaced by ζ is then:

$$P^*(r) = N_{\text{Al}} \frac{2\pi r \sin \vartheta(r)}{2\pi \int_{R_0 - \zeta}^{R_0 + \zeta} r \sin \vartheta(r) dr} \quad (10)$$

$; \quad R_0 - \zeta \leq r \leq R_0 + \zeta; \zeta \geq 0$

The denominator is a normalization constant so that the total number of Al atoms in the coordination shell is N_{Al} . By eliminating $\vartheta(r)$, $P^*(r)$ can be brought into the form:

$$P^*(r) = N_{\text{Al}} \cdot \frac{1}{C} \cdot \sqrt{[1 - (r - R_0)^2/\zeta^2] \cdot [(r + R_0)^2/\zeta^2 - 1]} \quad (11)$$

where the normalization constant C is given by:

$$C = \int_{R_0 - \zeta}^{R_0 + \zeta} \sqrt{[1 - (r - R_0)^2/\zeta^2] \cdot [(r + R_0)^2/\zeta^2 - 1]} dr \quad (12)$$

The function $P^*(r)$ looks like a slightly asymmetric semicircle and is very broad compared to Gaussian widths. No disorder of the Al atoms, which will modify $P^*(r)$, has been considered because its effect will only lead to a negligible broadening of $P^*(r)$. The same applies to the distribution of ζ values. This was confirmed by numerically convolving $P^*(r)$ with distributions for R_0 and ζ . Hence, $P^*(r)$ is employed as in eqns (11) and (12), without any convolution. Since $P^*(r)$ is not Gaussian the harmonic approximation cannot be used and eqn (5) is employed instead in order to calculate the EXAFS corresponding to $P^*(r)$. In addition to the constraints imposed for the previous model it is assumed that the ratio of ζ/R_0 is the same for the three datasets. This assumption is justified because it had turned out in preliminary fits, where ζ and R_0 had been varied independently, that ζ/R_0 was approximately the same for each of the three datasets. A fit to three datasets simultaneously has then 21 variable parameters. The fit result for the sample with a Cr_2O_3 content of 11.5 wt% and measured at 300 K is shown in Fig. 2(c) and numerical values are given in Table 3.

Now there are no problems with the estimation of the errors. We plot the PDFs for both types of Cr atoms separately using these results. Figure 3(c) shows the PDF corresponding to the Cr atoms at regular lattice sites. There are 6.5 Al atoms at $\sim 3.27 \text{ \AA}$ from the absorbing Cr atoms. The contribution from Cr atoms at random interstitial positions is also shown in Fig. 3(c) for the same sample. The Al peak is modified, according to the model presented here, and there are 10.1 Al atoms about the displaced Cr atoms. The average displacement is $\zeta = 0.50 \text{ \AA}$ and the ratio ζ/R_0 is 0.154 ± 0.007 . It is apparent that the radii of the Al coordination shell around the Cr–O octahedra are also about 3.27 \AA , just like the Al shell radii for the Cr atoms at regular sites. The number of Al atoms around the interstitial Cr atoms is now much higher than estimated in the previous model, where two Gaussian Al peaks were assumed (10.1 versus 1.8). This difference is possibly

Table 3. Results of a simultaneous fit to three datasets according to the third model

	R_0 ΔR_0 (\AA)	σ_O^2 $\Delta \sigma_O^2$ (10^{-4}\AA^2)	N_O ΔN_O	R_{Al} ΔR_{Al} (\AA)	σ_{Al}^2 $\Delta \sigma_{\text{Al}}^2$ (10^{-4}\AA^2)	N_{Al} ΔN_{Al}	$R_{\text{Al}} \equiv R_0$ ΔR_{Al} (\AA)	ζ $\Delta \zeta$ (\AA)	N_{Al} ΔN_{Al}
7.3 wt%	1.984	38	6	3.267	50	6.5	3.24	0.50	10.1
300 K	± 0.004	± 4	± 0	± 0.007	± 10	± 0.9	± 0.02	± 0.02	± 2.4
11.5 wt%	1.984	37	6	3.268	50	6.5	3.26	0.50	10.1
300 K	± 0.004	± 4	± 0	± 0.008	± 10	± 0.9	± 0.03	± 0.02	± 2.4
11.5 wt%	1.984	32	6	3.264	40	6.5	3.28	0.50	10.1
150 K	± 0.004	± 4	± 0	± 0.007	± 10	± 0.9	± 0.03	± 0.02	± 2.4

$$\Delta E_O = 0.4 \text{ eV} \pm 1.0 \text{ eV}; \Delta E_{\text{Al}} = -9.1 \text{ eV} \pm 1.1 \text{ eV}; S_0^2 = 0.76 \pm 0.04.$$

due in part to the uncertainty of N_{Al} in the previous model.

It should be noted that for the second and third model the small additional contributions to the Fourier transform is resulting from quite different PDFs. In the second model the additional Al coordination shell has only a few atoms (1.8) and therefore the contribution to the EXAFS or its Fourier transform is small. The third model results in a very broad distribution of Al atoms and the corresponding EXAFS is almost averaged out. However, due to the large number of Al atoms (10.1) a finite small contribution to the Fourier transform still remains.

5 Conclusions

The C-Al distances obtained using one Gaussian peak for the PDF of Al appear to be reasonable for Cr atoms located at regular octahedral lattice sites in the mullite structure (Model 1) though a simple fit with one coordination shell does not agree with the measured data sufficiently. In order to improve the fit, an additional Al coordination shell may be considered (Model 2). The error analysis for the data revealed, however, that σ_{Al}^2 and N_{Al} for the added coordination shell are not well defined, and therefore this model is not suitable. A better way of improving Model 1 is given by another model, where a displacement of Cr atoms is taken into account (Model 3). In this model, only 21, rather than 23, variable parameters are used, the residual sum of squares, χ^2 , is 25% smaller than in the second model, and the parameters are all well defined. We believe that these Cr atoms occur at distorted positions at interstitial lattice sites. For the Cr atoms an average displacement of $\zeta = 0.50 \text{ \AA}$ is obtained. This value is an approximation because the angular positions of the Al atoms, which influence the amount and direction of the deduced displacement, were not taken into account. A detailed evaluation of crystal structure data and using present EXAFS data of Cr-doped mullite may allow to define possible sites for the interstitial Cr atoms. Favourable sites for an interstitial incorporation of Cr^{3+} into the mullite structure may be O vacancies or the structure channels running parallel to the crystallographic *c*-axis.⁷

Acknowledgements

One of the authors (KRB) acknowledges with thanks the financial support by the Japan Society for the Promotion of Science (JSPS) through a fellowship during which some of this work was carried out. The work was also supported in part by grants from the Australian Research Council. Another author (AK) is grateful for a fellowship from the Japanese Ministry of Education (Monbusho).

References

1. Cameron, W. E., Mullite: a substituted alumina. *Am. Mineral.*, **62** (1977) 747.
2. Burnham, C. W., *Crystal structure of mullite*. Carnegie Inst., Washington Yearb., **63** (1964) 223.
3. Saalfeld, H. & Guse, W., *Structure refinement of 3:2-mullite ($3\text{Al}_2\text{O}_3\cdot 2\text{SiO}_2$)*. Neues Jahrb. Mineral. Monatsh., 1981, p. 145.
4. Angel, R. J. & Prewitt, C. T., Crystal structure of mullite: a re-examination of the average structure. *Am. Mineral.*, **71** (1986) 1476.
5. Gelsdorf, G., Müller-Hesse, H. & Schwiete, H. E., Einlagerungsversuche an synthetischem Mullit und Substitutionsversuche mit Galliumoxid und Germaniumoxid. *Teil II Arch. Eienhüttenwesen*, **29** (1958) 513.
6. Murthy, M. K. & Hummel, F. A., X-ray study of the solid solution of TiO_2 , Fe_2O_3 and Cr_2O_3 in mullite ($3\text{Al}_2\text{O}_3\cdot 2\text{SiO}_2$). *J. Am. Ceram. Soc.*, **43** (1960) 267.
7. Rager, H., Schneider, H. & Graetsch, H., Chromium incorporation in mullite. *Am. Mineral.*, **75** (1990) 392.
8. Ikeda, K., Schneider, H., Akasaka, M. & Rager, H., Crystal-field spectroscopic study of Cr-doped mullite. *Am. Mineral.*, **77** (1992) 251.
9. Harris, F. J., On the use of windows for harmonic analysis with the discrete Fourier transform. *Proceedings of the IEEE*, **66** (1978) 51.
10. Bauchspieß, K. R., EXAFS background subtraction using splines, *Physica B*, **208 & 209** (1995) 183.
11. Bauchspieß, K. R., EXAFIT: a curve-fitting program for EXAFS, *Jpn. J. Appl. Phys.*, **32** (Suppl. 32-2) (1993) 131.
12. Rehr, J. J., Albers, R. C. & Mustre de Leon, J., Single scattering curved wave XAFS code, *Physica B*, **158** (1989) 417.
13. Grunes, L. A., Study of the K edges of 3d transition metals in pure and oxide form by X-ray-absorption spectroscopy, *Phys. Rev.*, **B27** (1983) 2111.
14. Stern, E. A., Theory of EXAFS, in X-ray Absorption, In *Chemical Analysis*, Vol. 92, eds D. C. Koningsberger & R. Prins, Wiley, New York, 1988, Chap. 1, p. 40.
15. Bauchspieß, K. R., Alberding, N. & Crozier, E. D., Comment on simple method for the evaluation of bond length from data. *Phys. Rev. Lett.*, **60** (1988) 468.
16. Bunker, G., Application of the ratio method EXAFS analysis to disordered systems, *Nucl. Instr. and Meth.* **207** (1983) 437.

Electron Paramagnetic Resonance and Optical Absorption Studies on Cr-doped Mullite Precursors

H. Schneider,^a K. Ikeda,^b B. Saruhan^a & H. Rager^c

^aInstitute for Materials Research, German Aerospace Research Establishment, 51140 Köln, Germany

^bDepartment of Advanced Material Science and Engineering, Yamaguchi University, 755 Ube, Japan

^cDepartment of Geosciences, University of Marburg, 35032 Marburg, Germany

(Accepted 22 July 1995)

Abstract

Mullite precursors doped with 3 wt% Cr_2O_3 were investigated with X-ray diffractometry (XRD), electron paramagnetic resonance (EPR) and optical absorption spectroscopy. The development of phase assemblages occurs over three temperature ranges. In the first temperature field (450–600°C) the precursors are amorphous, and in the second field (800–1100°C) small amounts of γ - Al_2O_3 and crystalline Cr_2O_3 can be observed. Finally, in the third field ($\geq 1250^\circ C$) mullite forms, and simultaneously γ - Al_2O_3 and crystalline Cr_2O_3 disappear.

The EPR measurements reveal different temperature-controlled structural types of short-range order of Cr in the precursors, which go along with phase developments. Between 450 and 800°C EPR spectra appear with a main signal at $g_{eff} \approx 1.96$, most probably resulting from Cr^{5+} . Between 800 and 1250°C, the Cr EPR signal is similar to that of Cr-containing glasses, and above 1250°C the typical Cr^{3+} EPR spectrum of Cr-doped mullite appears.

Optical absorption spectroscopy yields evidence for the occurrence of Cr^{6+} , Cr^{5+} and Cr^{3+} in the mullite precursors, the concentrations of the different oxidation states being dependent on the calcination temperature: Cr^{6+} and Cr^{5+} contents are high at low temperatures (450°C), but gradually decrease with temperature. Simultaneously, increasing amounts of Cr^{3+} can be detected. At temperatures $> 1100^\circ C$, Cr^{6+} and Cr^{5+} cations completely disappear and optical absorption and EPR spectra of samples gradually approach to those of Cr-doped mullite. Although starting materials consist of Cr^{3+} , slow hydrolysis kinetics of Cr^{3+} causes formation of polyanions which contain Cr^{6+} . Deprotonation on heating results in reduction of $[Cr_2^{6+}O_7]^{2-}$ species to form $Cr_2^{3+}O_3$.

Introduction

Syntheses of high purity and ultra-reactive sol-gel mullite precursor powders have become important for the fabrication of advanced mullite ceramics.^{1,2} These materials exhibit outstanding mechanical, optical and electrical properties suitable for high temperature optical windows, for substrates in multilayer computer packaging, for high temperature insulating devices, and for high temperature structural applications in aircraft turbine engines and space vehicles.^{3,1}

Previous studies have shown that three different types of mullite formation processes can be distinguished in precursors of stoichiometric 3:2 mullite composition (72 wt% Al_2O_3 , 28 wt% SiO_2), designated as mullite precursor types I, II and III.⁴ Type I and type III precursors are amorphous at room temperature and remain so up to 900°C. Above this temperature, type I precursors crystallize to Al_2O_3 -rich mullite, while precursors of type III transform to γ -alumina and, consequently, mullite formation follows at temperatures $\geq 1200^\circ C$. Type II precursors consist of poorly crystalline pseudo-boehmite at room temperature which transforms to γ -alumina above $\sim 350^\circ C$. Mullite crystallization occurs at temperatures $\geq 1200^\circ C$.^{4,5} The different crystallization behaviours of mullite precursors were attributed to different structural short-range orders prior to mullite formation.

The aim of this study was to provide knowledge on the temperature-dependent development of the structural order of mullite precursors which are doped with paramagnetic and optically absorbant Cr ions. A specific goal was to investigate local structures of the precursors using Cr ions occurring in different oxidation states as probes. For that purpose X-ray diffractometry (XRD),

electron paramagnetic resonance (EPR) and optical absorption spectroscopy were applied.

Experimental Methods

Sample preparation

Cr-doped precursors were synthesized from purely organic starting materials. Tetraethoxysilane (TEOS) and aluminium-sec-butylate ($\text{Al}-(\text{OBu}^{\text{S}})_3$) were separately diluted with isopropanol and then admixed in proportions corresponding to 3:2 mullite (72 wt% Al_2O_3 , 28 wt% SiO_2). Chromium(III) acetate was dissolved in ethanol at $\sim 80^{\circ}\text{C}$. The solution was homogenized for 1 h using a magnetic stirrer and was added to the alcoholic mixed solution of TEOS and $\text{Al}-(\text{OBu}^{\text{S}})_3$. The addition of Cr corresponds to 3 wt% Cr_2O_3 in the final product. After further homogenization, hydrolysis was carried out by addition of deionized acidic water. Its pH was adjusted to 1.5 with HCl. Gelation took place immediately after hydrolysis. The gel was dried over several hours in a sandbath at 110°C and a very fine and greenish precursor powder was obtained. The precursor was calcined in a temperature range between 450 and 1750°C (Table 1).

X-ray diffractometry (XRD)

X-ray powder diffractometry studies were carried out with a computer-controlled Siemens D5000 powder diffractometer using Ni-filtered $\text{Cu} K_{\alpha}$ radia-

tion. Diffraction patterns were recorded in the 10 to $80^{\circ} 2\theta$ range, in the step scan mode (3 s/0.02°, 2θ).

Electron paramagnetic resonance spectroscopy (EPR)

EPR measurements were performed on powder samples at room temperature. The spectra were recorded at both X-band (9.5 GHz) and Q-band (35 GHz) frequency, using a magnetic modulation of 100 kHz and 5×10^{-4} T. Some selected samples were also measured at low temperatures down to 50 K in order to check unknown paramagnetic species in the precursor samples.

Optical absorption spectroscopy

Unpolarized diffuse reflectance spectra were recorded for the precursor series in the wavelength range 290 nm (34400 cm^{-1}) to 1538 nm (6500 cm^{-1}). A Hitachi 323S automatic recording spectrophotometer with an integrating globe was used. BaSO_4 was taken as reference material. Reading the original analogous spectra by a digitizer in 100 cm^{-1} intervals, digital spectra were obtained, and stored in a computer. The Kubelka–Munk function was applied. Before evaluation of the spectra a baseline correction in both the infra-red (IR) and ultraviolet (UV) region was carried out using Gaussian curves with centres around 3400 and 34000 cm^{-1} . Around these wavenumbers, vibronic bands of H_2O and M–O charge transfer bands occur. Overtone bands of adsorbed H_2O appearing around 6900 cm^{-1} were corrected by a smoothing procedure. On the basis of known crystal field absorption bands of Cr^{3+} in $\text{Cr}_2\text{O}_3\text{–SiO}_2$ gels and glasses,⁶ the obtained spectra were fitted with a Gaussian peak fitting procedure. Bands due to Fe^{2+} around 10000 cm^{-1} were included into the fitting procedure. High energy absorption bands of Cr^{3+} originating from the crystal field P term were also taken into account. These extra bands are labelled R, F, U, 9 and 10 (Table 2). All spectra fittings were carried out assuming a cubic crystal field.

Table 1. Heat treatments of Cr-doped mullite precursors

Sample key	Temperature (°C)	Duration (h)	Colour of powder
CR3-450	450	15	Yellow
CR3-600	600	15	Greenish yellow
CR3-800	800	15	Pale green
CR3-900	900	15	Greyish pale green
CR3-950	950	15	Greyish pale green
CR3-1100	1100	15	Greyish pale green
CR3-1650	1650	15	Grey
CR3-1750	1750	2	Grey

Table 2. Optical absorption band peak positions of Cr-doped mullite precursors heat-treated at different temperatures

Sample key	Absorption band (cm^{-1})													
	R	F	1	2	3	4	5	6	7	8	9	10	U	σ
CR3-450	3400	10 500	—	—	—	—	23 850	—	27 050	30 200	—	—	33 600	0.94
CR3-600	3400	10 500	—	—	—	—	23 850	—	27 050	30 200	—	—	33 700	0.99
CR3-800	3400	10 500	16 000	—	22 100	—	23 850	—	27 050	30 200	34 900	—	34 000	0.96
CR3-900	3400	10 600	14 800	17 000	20 100	22 450	—	26 000	27 050	30 200	32 000	36 300	34 000	1.62
CR3-950	3400	10 600	14 900	17 000	20 100	22 500	—	26 000	27 050	30 200	32 100	36 300	34 200	0.82
CR3-1100	3400	10 800	14 950	17 050	20 350	22 700	—	26 000	27 050	30 200	32 400	36 500	33 900	0.75
CR3-1650	3400	11 000	15 600	18 200	22 500	24 900	—	—	—	—	35 100	39 500	34 200	0.75
CR3-1750	3400	11 000	15 600	18 200	22 500	25 100	—	—	—	—	35 100	39 700	34 200	0.56

R, IR band of absorbed H_2O ; F, impurity ferrous; U, M–O charge transfer; 5, Cr^{5+} bands; 6, Fe^{3+} bands (impurities); 7 and 8, Cr^{6+} bands; 1, 3 and 9, low field Cr^{3+} bands; 2, 4 and 10, high-field Cr^{3+} bands. σ , standard deviation of fitting in %; all bands in cm^{-1} . For the sample key see Table 1.

Results

X-ray diffractometry (XRD)

The mullite precursors are amorphous up to 600°C (Fig. 1). Above this temperature, weak reflections appear in the XRD patterns which are due to some small amount of crystalline Cr_2O_3 . The Cr_2O_3 phase is present up to 1000°C. At 900°C, $\gamma\text{-Al}_2\text{O}_3$ forms, and becomes the only crystalline phase at 1100°C. The formation of mullite starts at 1250°C, as $\gamma\text{-Al}_2\text{O}_3$ disappears. XRD spectra taken from samples heat-treated above 1250°C show only the reflections of mullite. At 1750°C, besides mullite, a very low amount of $\alpha\text{-Al}_2\text{O}_3$ can be detected.

Electron paramagnetic resonance spectroscopy (EPR)

Precursors calcined in the temperature range between 450 and 800°C show a strong and sharp EPR signal at $g_{\text{eff}} \approx 1.96$ and a weak feature extending from $g \approx 5$ to $g \approx 2$ (Fig. 2), the former becoming anisotropic at Q-band frequencies. The

strong signal near $g_{\text{eff}} = 1.96$ disappears at calcination temperatures $> 800^\circ\text{C}$. Between 900 and 1000°C a glass-like Cr^{3+} EPR spectrum appears. Development of the typical Cr^{3+} EPR spectrum of mullite with characteristic features near $g_{\text{eff}} = 5$ is visible at higher temperatures ($\geq 1250^\circ\text{C}$).

In the temperature range between 800 and 1100°C, an isotropic and broad EPR signal centred at $g_{\text{eff}} \approx 2$ can be additionally detected (Fig. 2). The intensity of this signal increases, if the EPR spectra are recorded at temperatures $\geq 310\text{ K}$, due to the occurrence of crystalline Cr_2O_3 .⁷

No additional EPR signal was detected down to 50 K, indicating the absence of additional Cr-bearing phases in the mullite precursors.

Optical absorption spectroscopy

As shown in Fig. 3, the optical absorption spectra of the precursors calcined between 450 and 1650°C were fitted by Gaussian curves. The differentiated peaks were labelled with numbers from 1

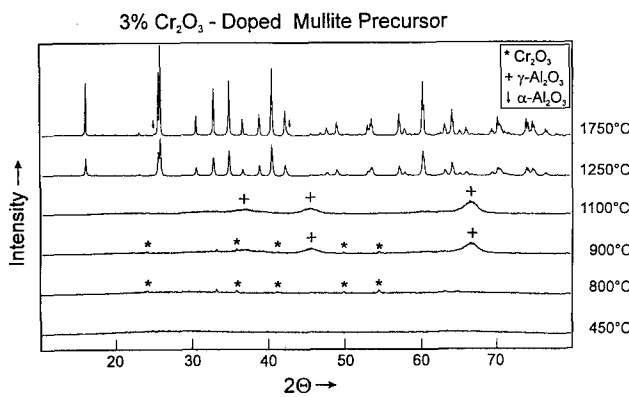


Fig. 1. Evolution of X-ray diffraction patterns of Cr-doped (3 wt%) mullite precursor with heat treatment temperature.

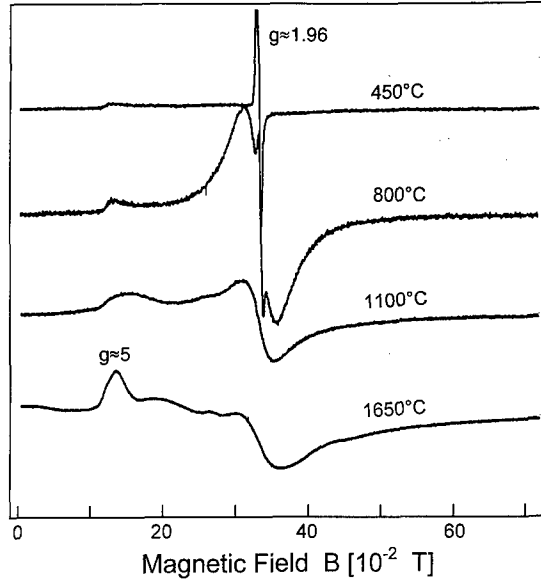


Fig. 2. Powder EPR spectra of Cr-doped (3 wt%) mullite precursors, heat-treated at 450, 800, 1100 and 1650°C. The spectra were taken at room temperature and 9.520 GHz.

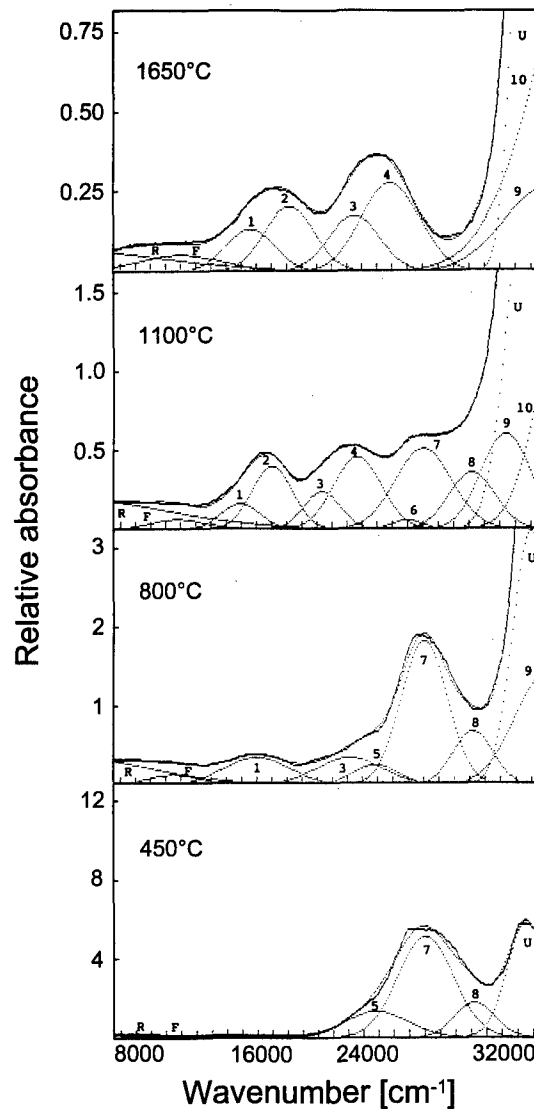


Fig. 3. Peak-fitted optical absorption spectra of Cr-doped (3 wt%) precursors, heat-treated at 450, 800, 1100 and 1650°C. For attribution of peak numbers see the text and Table 2.

to 10 (see the pattern of the 1100°C sample). They are listed in Table 2. Peaks 5, 7 and 8 are characteristic for the low temperature (450°C) sample, and are assumed to be the result of charge transfer transitions of Cr⁶⁺. The corresponding EPR spectrum at this temperature, however, shows the presence of Cr⁵⁺ in the precursor. The electron configuration of Cr⁶⁺ and Cr⁵⁺ ions are 3d⁰ and 3d¹, respectively. Cr⁵⁺ has an electron spin of $S = 1/2$ and is paramagnetic. It can therefore easily be detected by EPR. However, Cr⁶⁺ is diamagnetic and, hence, is not detectable by EPR. We believe that peak 5 belongs to Cr⁵⁺, and peaks 7 and 8 to Cr⁶⁺, which is in agreement with the yellow colour of the 450°C sample. The colour of precursors calcined at temperatures $\geq 800^\circ\text{C}$ turns to green due to the appearance of Cr³⁺. Above this temperature the intensities of optical absorption peaks 7 and 8, assigned to Cr⁶⁺, decrease as the intensity of peak 5, assigned to Cr⁵⁺, totally disappears.

Octahedrally coordinated Cr³⁺ generally displays two optical absorption peaks in the visible region due to the splitting of the F term. Sometimes an additional Cr³⁺ peak occurs in the UV region which results from the P term. This actually has been observed in the samples heat-treated at $\geq 800^\circ\text{C}$. The precursors calcined at 1650 and 1750°C have grey colour and their absorption spectra are equal to those of octahedrally coordinated Cr³⁺, occurring in high and low field sites.⁸ High and low field occupations of Cr³⁺ have also been observed in samples heat-treated between 900 and 1100°C, suggesting the evolution of a mullite-type short-range order in the precursors. However, Racah parameters (see below) show that this actually is not the case. Furthermore, peak 6 (Table 2) resolved in the spectra of these samples is believed to be due to impurity Fe³⁺ ions.⁹

Discussion

The EPR signal at $g_{\text{eff}} \approx 1.96$, appearing at calcination temperatures $\leq 1100^\circ\text{C}$, is connected with Cr doping, because it is not observed in undoped mullite precursors. The spin of the paramagnetic centre is assumed to be $S = 1/2$ and the g value indicates an electron centre. This signal is, therefore, assigned to Cr⁵⁺. A paramagnetic centre with $S > 1/2$, e.g. Cr³⁺ with $S = 3/2$, can be excluded, because the Cr³⁺ EPR should not display a single line spectrum around $g_{\text{eff}} \approx 2$. The Cr⁵⁺ signal at $g_{\text{eff}} \approx 1.96$ can be simulated at both 9.5 and 35 GHz using an axial g tensor with $g_{x,y} = 1.960$ and $g_z = 1.946$, an effective spin $S = 1/2$ and a constant line width of 25×10^{-4} T. The frequency-independent line width indicates that Cr⁵⁺ occurs in a non-random environment. According to the EPR data only one type of coordination exists for Cr⁵⁺.

Optical absorption spectra suggest that Cr⁵⁺ is present in larger amounts in the samples calcined at temperatures $< 900^\circ\text{C}$, while Cr⁶⁺ persists up to $\leq 1100^\circ\text{C}$. Taking into account the ionic radii of Cr⁶⁺ (0.38 Å) and Cr⁵⁺ (0.43 Å),¹⁰ both cations should be fourfold coordinated in these precursors. Substitution of Al³⁺ or Si⁴⁺ cations by Cr⁵⁺ or Cr⁶⁺ produces a charge surplus in the oxygen network which may be balanced by octahedral cation vacancies.

Although the Cr³⁺ EPR signal around $g_{\text{eff}} = 5$ is already present in the sample heat-treated at 450°C, its intensity is significant only at calcination temperatures $> 800^\circ\text{C}$. This is in accordance with optical absorption data. Furthermore, from the absorption spectra a certain variation of slightly different distorted octahedral Cr³⁺ sites in the precursors can be deduced as high and low field sites.

The crystal field parameters 10 Dq and B for Cr³⁺ and Cr⁵⁺ cations in the Cr-doped precursors (Table 3) are in general agreement with literature data.⁸ Racah parameters B of all samples are small, indicating a partly covalent bonding character of Cr³⁺ in the precursor matrix. The Racah parameter B of Cr³⁺ should be larger for high field and smaller for low field sites, respectively. This actually becomes true for samples heat-treated at 1650°C and at 1750°C, which comprise Cr-doped mullites. However, it does not hold for samples heat-treated in the temperature range between 900 and 1100°C where the formal application of the fitting procedure yielded high and low field sites with nearly the same Racah parameter ($\approx 518 \text{ cm}^{-1}$). Therefore, we assume that strongly distorted Cr³⁺ sites which do not allow a

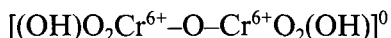
Table 3. Crystal field parameters 10 Dq and B of Cr-doped mullite precursors heat-treated at different temperatures

Sample key								
	CR3-450	CR3-600	CR3-800	CR3-900	CR3-950	CR3-1100	CR3-1650	CR3-1750
Oct. Cr ³⁺ 10 Dq	—	—	16 000	14 800/17 000	14 900/17 000	14 950/17 050	15 600/18 200	15 600/18 200
B	—	—	601	513/515	500/521	524/537	717/654	717/679
Tet. Cr ⁵⁺ 10 Dq	23 850	23 850	23 850	—	—	—	—	—

Slash indicating both of high-field and low-field in cm^{-1} . Oct. = octahedral, Tet. = tetrahedral.

differentiation between high and low field Cr³⁺ positions can explain the above observations.

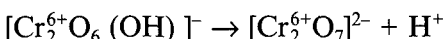
It is interesting to discuss the temperature-dependent mechanisms of Cr incorporation into the mullite precursors. The literature data on the hydrolysis behaviour of trivalent Cr³⁺ indicates that the kinetics of hydrolysis with Cr³⁺ are slow.¹¹ Slower kinetics facilitate occurrence of the gel network which results in the formation of polyanions by oxidation of Cr³⁺ to Cr⁶⁺.¹¹



On heating, deprotonation of the dimer occurs, yielding a gradual development of:



and



Reduction of [Cr₂⁶⁺O₇]²⁻ species at temperatures $\geq 800^\circ C$ may result in the formation of crystalline Cr₂³⁺O₃, as is observed by XRD of the calcined Cr-doped precursors.

Cr-doping of mullite precursors has a significant influence on the crystallization behaviour of the material. Undoped precursors prepared in exactly the same way as the Cr-doped precursors are amorphous up to $\approx 900^\circ C$. At this temperature they crystallize to mullite and some small amount of γ -Al₂O₃. The nearly exclusive formation of mullite indicates that a small degree of phase separation into Al₂O₃- and SiO₂-rich areas occurred before mullite crystallization. Addition of chromium acetate in alcoholic solution, how-

ever, promotes this phase separation to such an extent that intermediate phases of γ -Al₂O₃ and Cr₂O₃-rich non-crystalline SiO₂ form prior to mullitization, similar to the case of type III mullite precursors.⁴

References

1. Hoffman, D., Roy, R. & Komarneni, S., Diphasic xerogels, a new class of materials: phases in the Al₂O₃-SiO₂ system. *J. Am. Ceram. Soc.*, **67** (1984) 468-71.
2. Komarneni, S., Suwa, Y. & Roy, R., Application of compositionally diphasic xerogels for enhanced densification: the system Al₂O₃-SiO₂. *J. Am. Ceram. Soc.*, **69** (1986) C-155-C-156.
3. Schneider, H., Okada, K. & Pask, J. A., *Mullite and Mullite Ceramics*. John Wiley & Sons, Chichester, 1994.
4. Schneider, H., Saruhan, B., Voll, D., Merwin, L. & Sebald, A., Mullite precursor phases. *J. Eur. Ceram. Soc.*, **11** (1993) 87-95.
5. Schneider, H., Voll, D., Schmücker, M., Saruhan, B., Schaller, T. & Sebald, A., Constitution of the γ -alumina phase in chemically produced mullite precursors. *J. Eur. Ceram. Soc.*, **13** (1994) 441-8.
6. Tanaka, K. L. & Kamiya, K., Electron spin resonance and optical absorption spectra of chromium in silica gels and glasses prepared by the sol-gel method. *J. Mater. Sci. Lett.*, **10** (1991) 1095-7.
7. Rager, H., Schneider, H. & Graetsch, H., Chromium incorporation in mullite. *Am. Mineral.*, **75** (1990) 392-7.
8. Ikeda, K., Schneider, H., Akasaka, M. & Rager, H., Crystal-field spectroscopic study of Cr-doped mullite. *Am. Mineral.*, **77** (1992) 251-7.
9. Marfunin, A. S., *Spectroscopy, Luminescence and Radiation Centers in Minerals*. Springer, Berlin, 1979.
10. Whittaker, E. J. W. & Muntus, R., Ionic radii for use in geochemistry. *Geochim. Cosmochim. Acta*, **34** (1970) 945-56.
11. Brinker, C. J. & Scherer, G. W., *Sol-Gel Science*. Academic Press, San Diego, CA, 1990.

Mechanical Properties of Mullite Materials

M. I. Osendi & C. Baudín

Instituto de Cerámica y Vidrio (CSIC), E-28500, Arganda del Rey, Madrid, Spain

(Accepted 22 July 1995)

Abstract

The mechanical behaviour of two $3\text{Al}_2\text{O}_3\cdot2\text{SiO}_2$ dense mullite materials with the same level of impurities but different in nature has been studied. Microstructure has been characterized by SEM and TEM. Toughness, bend strength and Young's modulus have been determined from room temperature up to 1400°C. Dependence of toughness on strain rate has been investigated. Special attention has been paid to correlate the trend of the mechanical parameters to fractographic observations by SEM.

1 Introduction

Nowadays, highly reactive, homogeneous and pure mullite powders that allow us to obtain high density structural $3\text{Al}_2\text{O}_3\cdot2\text{SiO}_2$ mullite materials are available.¹ In these materials, the mullite phase is the 3:2 one. Even though the starting powders are highly pure, small amounts of impurities, whose nature depends on the synthesis route,² are always present. When powders are obtained by sol-gel methods the main contaminants come from the milling media, (eg. ZrO_2), whilst when mullite powders are fabricated from raw materials, the main impurities are alkalis and alkaline-earths. Some impurities, like iron oxide and titania,³ can enter in solid solution in mullite in rather large quantities or, like zirconia, remain mostly as isolated particles⁴ while others, like alkaline oxides can form liquids at rather low temperatures, (eg. $T \sim 1000^\circ\text{C}$ for Na_2O).⁵ After sintering of the mullite materials, a certain amount of liquid remains as glassy phases. Softening temperature and viscosity of these residual amorphous phases dramatically depend on their composition.^{6,7} Moreover, quantity and distribution of these glassy phases in the material should depend on sintering temperature, and content and nature of the impurities.

From a mechanical point of view, the most studied property of mullite materials at high temperature has been creep.⁸⁻¹² A variety of mechanisms, from solid-state diffusion to viscous flow,

and activation energies, ranging from 500 KJ/mol^{8,9} to 1300 KJ/mol,¹⁰ have been reported for mullite creep. This diversity in the data, in spite of the similar ranges of test temperatures and loads, could be attributed to slight differences in the impurity contents and their nature. In fact, small amounts of additives greatly change not only the viscosity of liquids⁶ but, certainly, their wetting characteristics. Distribution of remaining glassy phases, along grain boundaries or forming isolated pockets, will influence creep mechanisms at high temperatures.

On the other hand, probably due to its inherent brittleness, fracture properties of mullite have been analyzed less.^{13,14} In fact, most of the work has been devoted to establishing the relationships between mullite stoichiometry and parameters such as toughness and modulus of rupture.¹⁵⁻²⁰

In the present work, the mechanical behaviour of two mullite materials with the same level of impurities but different in nature has been studied. The selected parameters have been toughness, bend strength, and Young's modulus. Variations of these parameters with temperature and strain rate have been obtained. Special attention has been paid to correlate the parameter trends to the aspect of the fracture surfaces.

2 Experimental

Two kinds of mullite materials henceforth labelled as MS0 and MB0 have been prepared from commercial powders* as previously described.⁴ MS0 was processed from a commercial gel type mullite (1.5 μm of average particle size), that was spray dried, isostatically pressed and sintered at 1660°C for 2 h. MB0 powders were coarse grain commercial mullite, that were attrition milled with mullite balls down to 0.8 μm , before isostatically pressing and sintering at 1630°C for 4 h. Fundamental

*MS0: Chichibu Cement Co., supplied by Scimareck Ltd. Tokyo, Japan.

MB0: Baikowski Chimie, France.

Table 1. Main characteristics of the mullite materials

Material	Dynamic Young's Modulus (GPa)	Density (g/cm ³)	Average grain size (μm)	Al ₂ O ₃ /SiO ₂ ratio (wt%)
MS0	202 ± 2	3.05 ± 0.02	1.2 ± 0.9	2.66
MB0	195 ± 4	3.01 ± 0.02	0.7 ± 0.5	2.75

Table 2. Impurity contents in the mullite materials

Material	Fe ₂ O ₃ + TiO ₂ + Y ₂ O ₃ (wt%)	Na ₂ O + CaO + MgO + K ₂ O (wt%)	ZrO ₂ (wt%)
MS0	0.17	0.13	0.33
MB0	0.11	0.30	0.02

characteristics of the materials are collected in Table 1. Main impurities of these mullites are shown in Table 2.

Although the total level of impurities in both mullites is similar (<0.65 wt% in MS0 and <0.45 wt% in MB0) chemical compositions are quite different. The main impurity in MS0 is ZrO₂, followed far behind by TiO₂. Conversely, the more abundant impurities in MB0 are Na₂O and Fe₂O₃. The large amount of ZrO₂, found in MS0, is attributable to the powder milling procedure of the supplier.

Figure 1 shows representative microstructures (SEM) of the studied mullite materials. In MS0 some exaggerated grain growth and pore trapping have taken place whereas MB0 has a more uniform microstructure and mainly intergranular porosity.

In Fig. 2 the main characteristics of grain boundaries in MS0 samples are observed (TEM). Zirconia remains as particles (≈ 200 nm) located at triple points (Fig. 2(a)) while glassy pockets at grain junctions are scarcely observed (Fig. 2(b)). Figure 3 shows glassy pockets at triple points that are often present in MB0, where alkaline impurities concentrated as EDX analysis revealed. At the level of resolution employed no glassy phase films were observed along grain boundaries in any sample.

All mechanical and elastic tests were performed in an universal load testing machine with an electrically heated furnace, using 4-point bending fixtures made of SiC or Al₂O₃, with inner and outer spans of 20 and 40 mm.

Bend strength test measurements at temperatures ranging from RT to 1400°C were performed on $4 \times 3 \times 50$ mm bars that were diamond machined from the sintered compacts, polished and chamfered on the tension surface. At least 5 bars were tested at each temperature.

Static Young's modulus (RT–1400°C) was calculated from the central point deflection of bend bars measured using a SiC probe attached to a LVDT through an alumina tube. Three bars were tested at each temperature. For bend strength and Young's

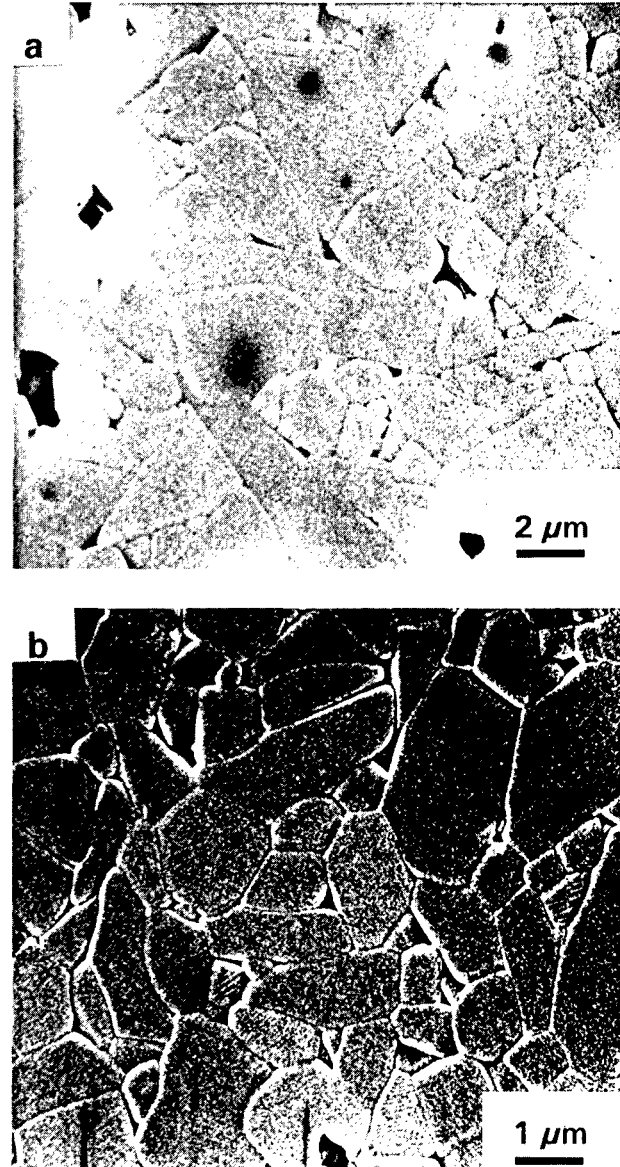


Fig. 1. Representative SEM microstructures of the studied mullite materials: (a) MS0; (b) MB0.

modulus measurements, load was applied at 1000 N/min.

Toughness was determined by the SENB method using five bars for each temperature. Bars of dimension $4 \times 6 \times 50$ mm were machined and

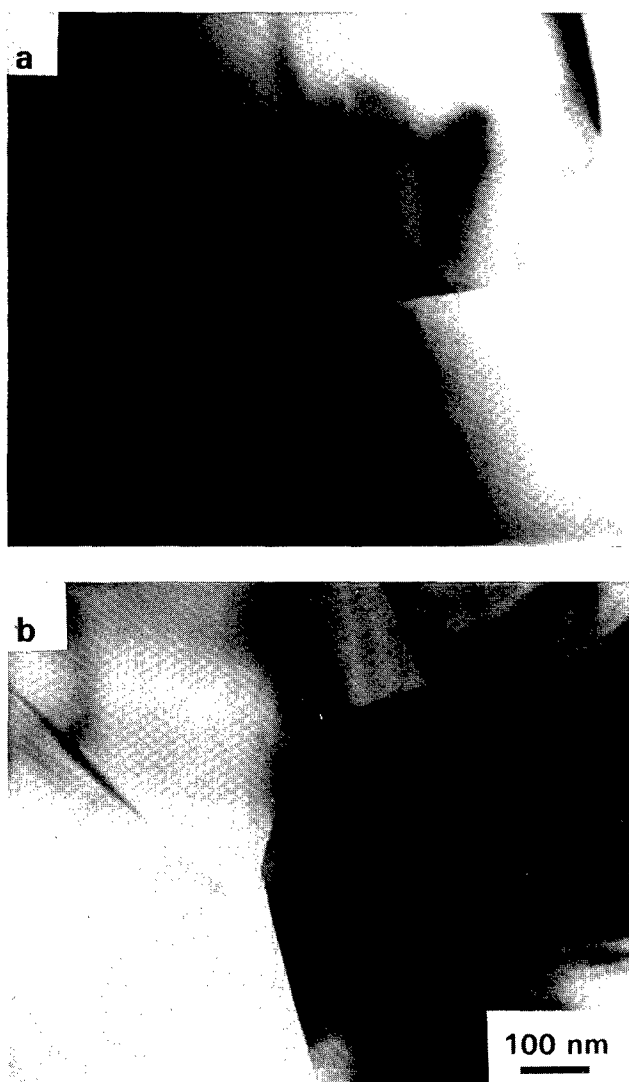


Fig. 2. TEM microstructures of MS0. The main characteristics of the grain boundaries are observed: (a) Zirconia located at triple points; (b) glassy pockets at grain junctions.

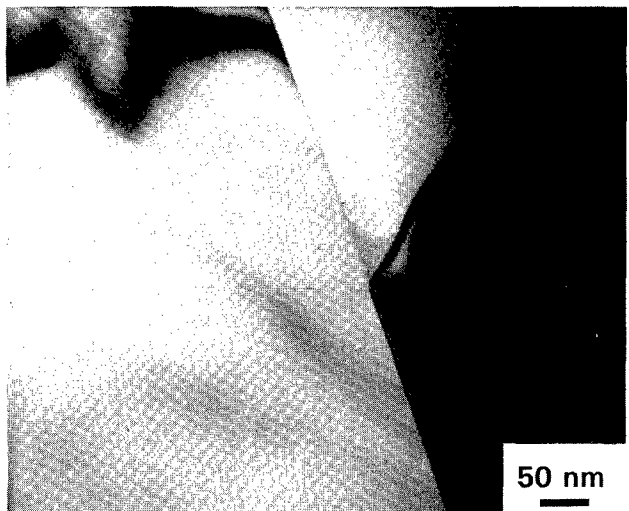


Fig. 3. TEM microstructure of MB0. Glassy pockets at triple points are observed.

notches were introduced with a thin diamond disc. Notches were 3 mm long and 200 μm width. The actuator rates ranged from 0.005 to 5 mm/min.

Polished and thermally etched (1500°C) samples

and 'as fractured' surfaces were observed by SEM. Specimens were thinned, dimpled and Ar milled in order to be analyzed by TEM.

3 Results

In Fig. 4 static Young's modulus versus temperature is depicted. Room temperature values are the same for both materials and a slight decrease with temperature is observed.

Bend strength as a function of temperature is shown in Fig. 5. Values are always lower for MS0 although data trends are the same for both mullites, showing peaks in strength at $T = 1200\text{--}1300^\circ\text{C}$.

Toughness values obtained using an actuator speed of 0.05 mm/min are represented in Fig. 6. Room temperature values are almost the same for

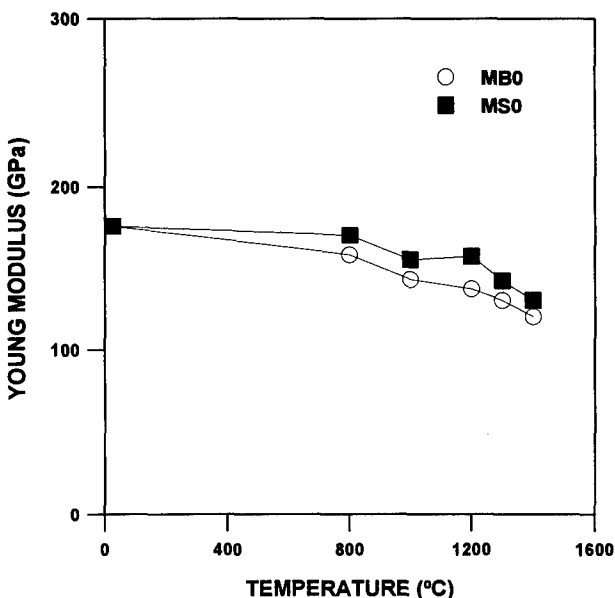


Fig. 4. Static Young's modulus versus temperature.

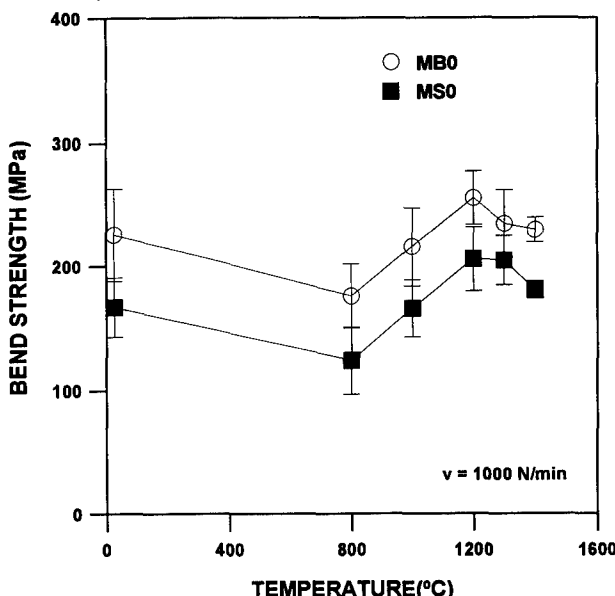


Fig. 5. Bend strength versus temperature.

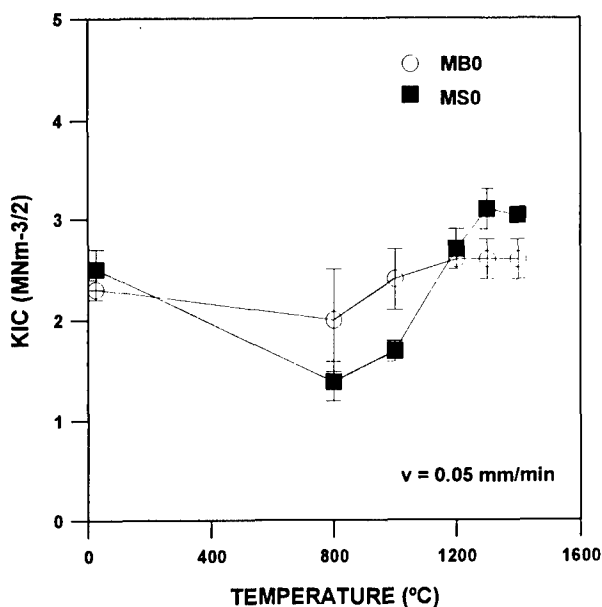


Fig. 6. Toughness values versus temperature obtained using an actuator speed of 0.05 mm/min.

both materials although toughness dependence on temperature is more marked for MS0, showing a decrease from room temperature up to 800 followed by a sudden increase.

Figures 7 and 8 show K_{IC} data as a function of the actuator speed for MS0 and MB0. Tests were performed at room temperature and 1300°C. At room temperature, K_{IC} increases with strain rate for MS0 whereas K_{IC} is practically constant for MB0. At 1300°C, toughness values diminish as strain rate increases for MS0. The dependence of toughness on strain rate is not monotonous for MB0: maximum values are obtained using the slowest strain rate (0.005 mm/min) and a minimum is found for a strain rate of 0.01 m/min.

In Fig. 9 room temperature fracture surfaces of

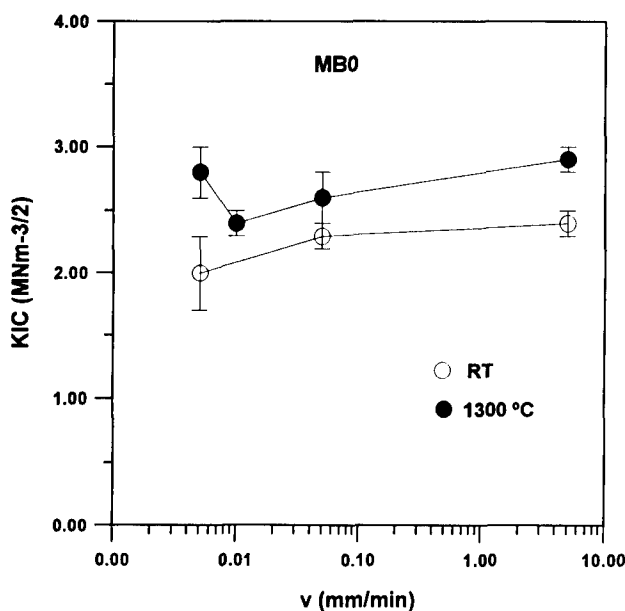


Fig. 8. K_{IC} data at room temperature and 1300°C as a function of the actuator speed for MB0.

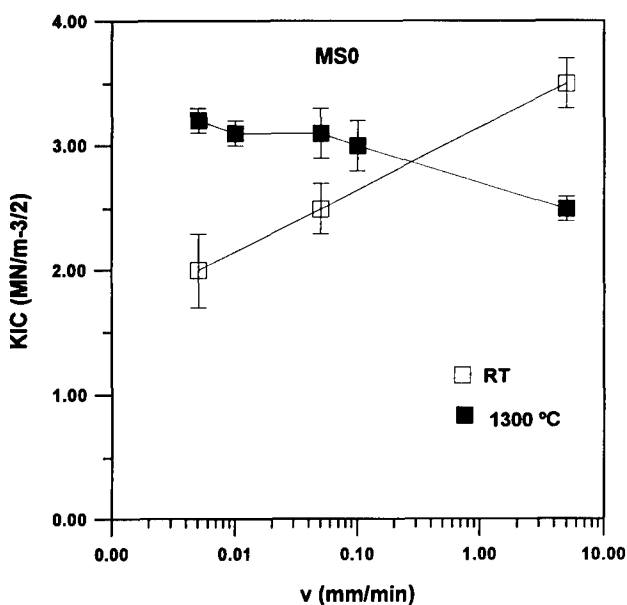


Fig. 7. K_{IC} data at room temperature and 1300°C as a function of the actuator speed for MS0.

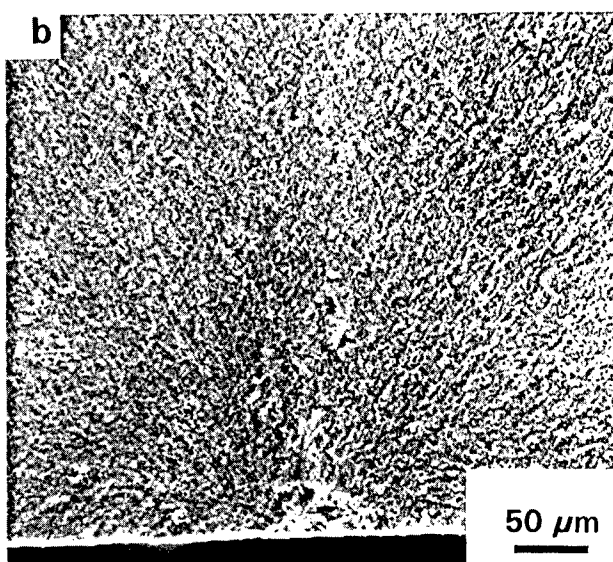
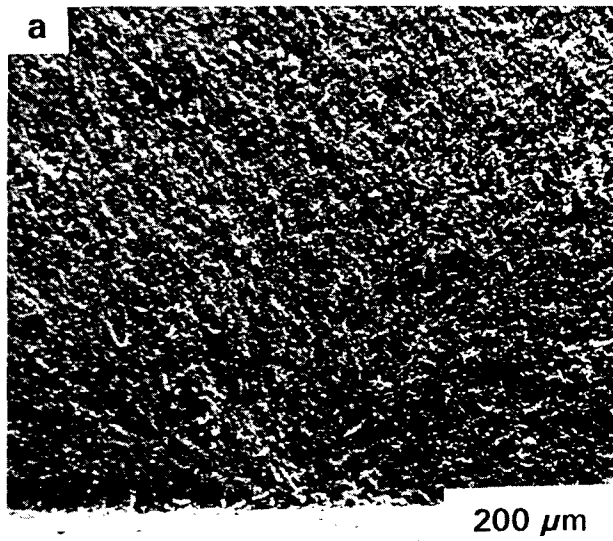


Fig. 9. Room temperature fracture surfaces of bend bars (SEM): (a) MS0; (b) MB0.

bend strength bars are displayed. In MS0, fracture origins are not well defined, but a characteristic semielliptical feature (diameter $\approx 150 \mu\text{m}$) close to the tension surface is usually detected (Fig. 9(a)). Most of fracture origins in MB0 samples are pores (diameter $\approx 30 \mu\text{m}$) as the one in Fig. 9(b).

Figure 10 shows typical fracture surfaces of MS0 notched bars after toughness testing. At room temperature, as well as at 1300°C, differentiated zones close to the notch exist (Fig. 10(a, b)). The size of these zones increased as strain rate decreased and as temperature increased. Higher magnification (Fig. 10(c)) shows that intergranular fracture predominates in these zones for tests done at room temperature. In parallel, in the samples tested at 1300°C the main features of the zone close to the notch are large areas ($d \approx 200 \mu\text{m}$ for the slowest strain rate) at both surfaces of the crack that have crept, sliding one against the other, coexisting with intergranular fracture (Fig. 10(d)).

Fracture surfaces of MB0 toughness specimens are collected in Fig. 11. No special features are

observed in the room temperature samples, being the fracture mainly transgranular through the whole specimen (Fig. 11(a, c)). Conversely, at 1300°C a differentiated zone close to the notch exist (Fig. 11(b)). Higher magnification (Fig. 11(d)) reveals a sharp transition from intergranular to transgranular fracture at the boundary of this zone. The size of this zone varies with loading rate and is minimum for samples tested at 0.005 mm/min.

4 Discussion

4.1 Room temperature mechanical behaviour

In order to explain the difference in the room temperature bend strength values, lower for MS0, whereas toughness values are about the same for both materials (Figs 5 and 6) the following equation should be considered:

$$\sigma_f = \frac{Z}{Y} \frac{K_{IC}}{\sqrt{c}}$$

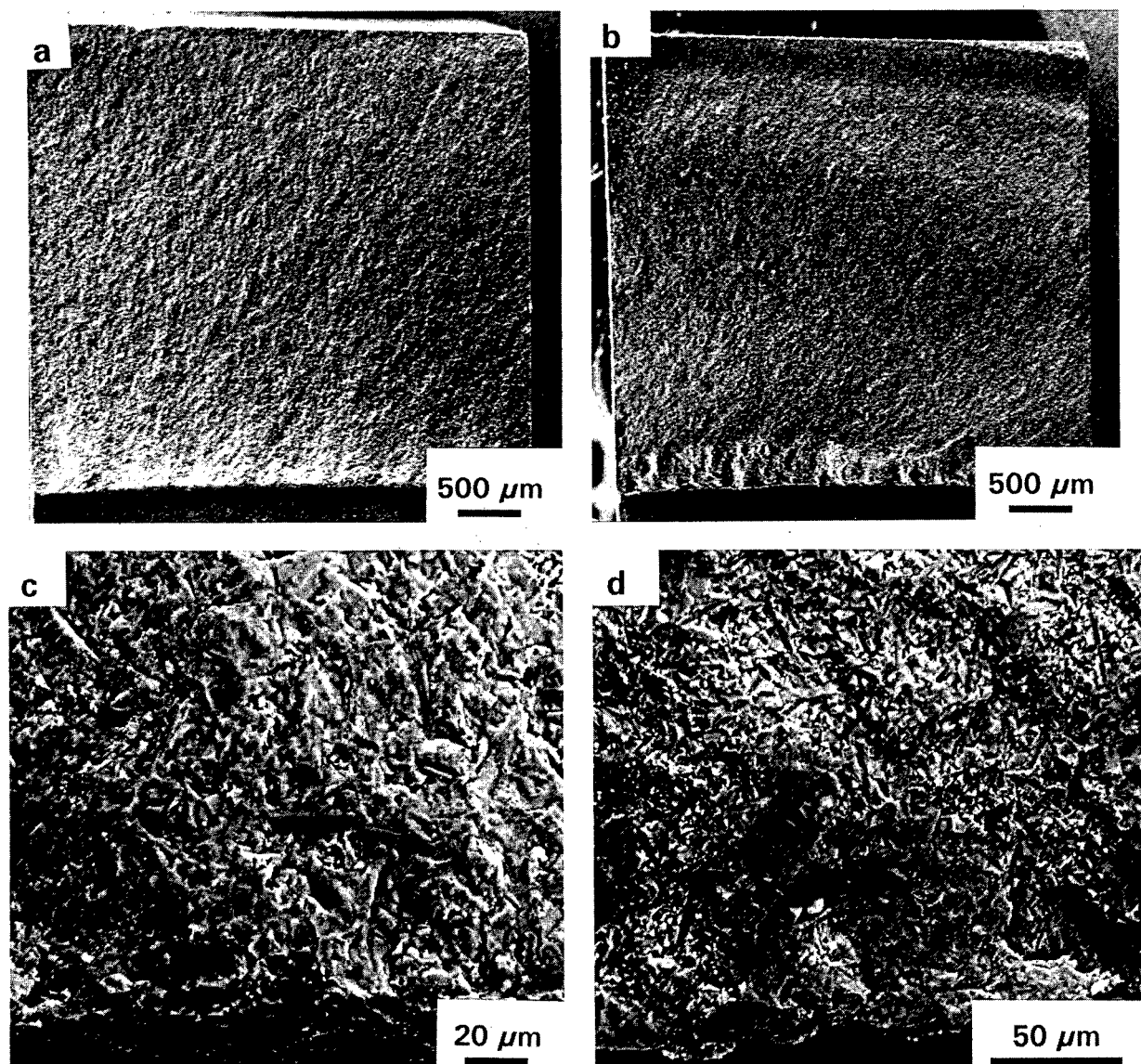


Fig. 10. Fracture surfaces of MS0 notched bars after toughness testing: (a) and (c) room temperature; (b) and (d) 1300°C.

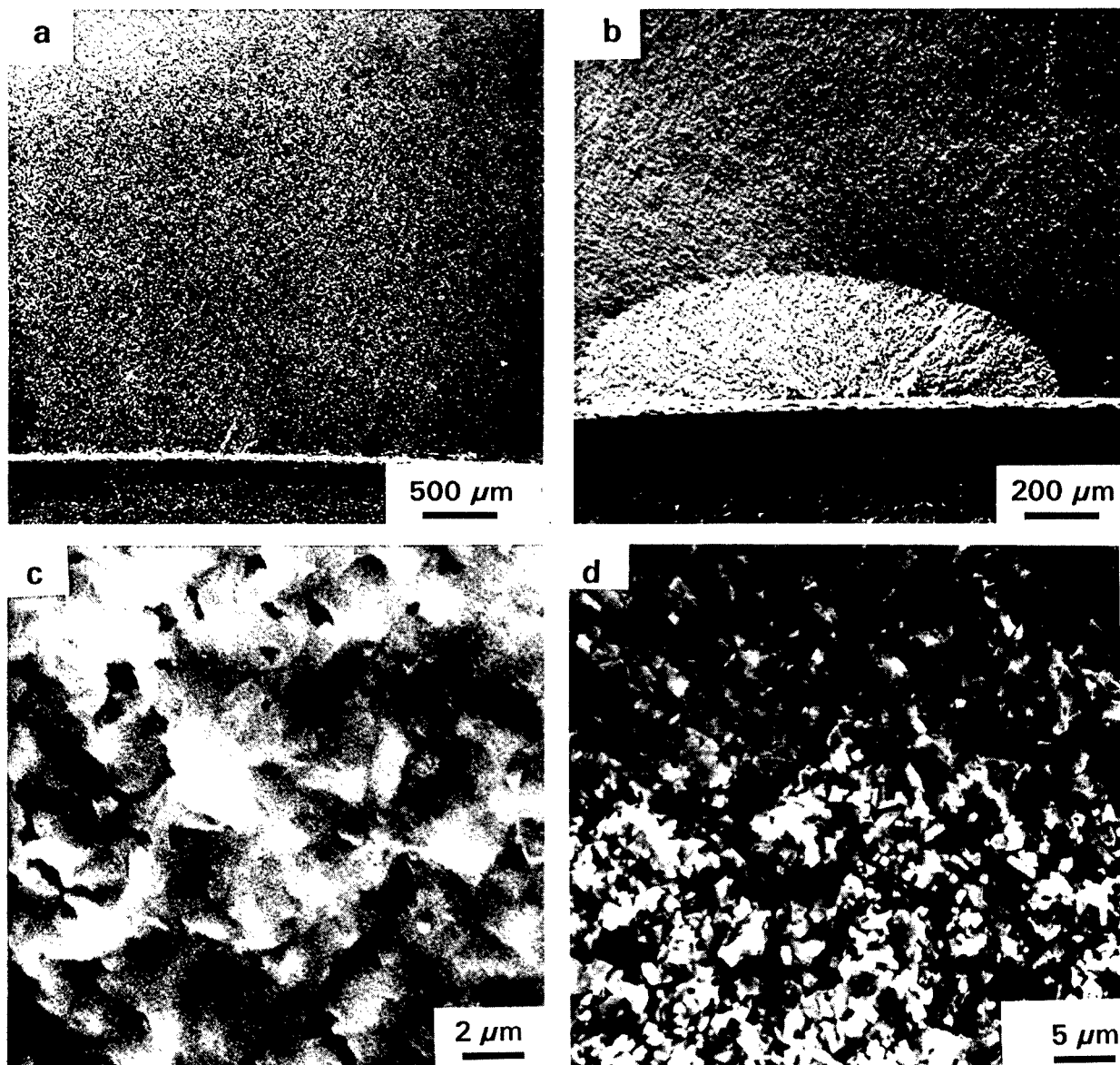


Fig. 11. Fracture surfaces of MB0 notched bars after toughness testing: (a) and (c) room temperature; (b) and (d) 1300°C.

Substituting the constant values for a semielliptical ($Z = 1.6$) surface ($Y = 2$) crack of radius c^{21} and introducing K_{IC} and σ_f limiting values into the expression, critical defect sizes ranging from 100 to 276 μm for MS0 and from 40 to 112 μm for MB0 are obtained.

In the case of MS0 specimens, these calculated critical flaw sizes agree well with the sizes of the semielliptical features observed close to the tension surfaces, as shown in Fig. 10(a). These semielliptical zones seem to develop from smaller processing defects by subcritical crack growth. Subcritical crack growth zones, defined by intergranular fracture mode, were also apparent on fracture surfaces of K_{IC} specimens tested at room temperature, as shown in Fig. 11(a,c). Moreover, toughness values determined using the slowest rate are much lower than those obtained at the fastest rate (Fig. 7). This trend of K_{IC} with loading rate also support subcritical crack growth in MS0.

Observing the fracture surfaces of MB0 specimens (Fig. 9(b)) fracture origin dimensions agree with the previous calculations. In fact, no dependence of room temperature K_{IC} values on loading rate occurs (Fig. 8) and no subcritical crack growth zone is observed close to the notch in toughness specimens (Fig. 11(a,c)). It is interesting to note that the range of loading rates that have been used is very large, thus apparently, no easy paths for crack growth exist in MB0.

The existence of subcritical crack growth at room temperature in MS0 and not in MB0 implies that grain boundaries are weaker in MS0 than in MB0. As mentioned in Section 2, no glassy films along grain boundaries were observed with the available techniques in neither mullite. Nevertheless, its presence in MS0 sample can be assumed considering the level of impurities and sintering temperatures. Furthermore, thin glassy films of ≈ 10 nm have been observed by other authors at

the mullite–mullite interfaces by HRTEM in the eutectic systems ZrO_2 –mullite²² and also in mullite materials doped with small amounts of ZrO_2 .²³ These facts support the evidence that the glassy phase is preferentially located along grain boundaries in MS0, in agreement with TEM observations in which triple point glassy pockets were scarcely observed in MS0. Conversely, large amounts of glassy pockets were observed in MB0 comparatively to MS0, which suggests that glassy phase is preferentially located at triple points in agreement to the lack of subcritical crack growth at room temperature in MB0 mullite.

4.2 Mechanical behaviour up to 1400°C

The decrease in Young's moduli with temperature for both mullites (Fig. 4) is the expected one considering the rather high loading rate used. At this rate, materials remain linear elastic through the load cycle at each testing temperature.

In terms of bend strength, both mullites present the usual behaviour of ceramic materials with small glassy phase amounts (Fig. 5). The initial decrease is related to elastic bond relaxation as temperature increases as discussed above. The increase at temperatures higher than 1000°C can be associated to the softening of the residual glassy phases in the range of testing temperatures, which could lead to healing of the critical flaws or an increase in apparent toughness.

For each mullite, toughness and bend strength dependences on temperature (Figs 5 and 6) show only slight differences that can be attributed to differences in strain rates between both tests. Both mullites experience K_{IC} and σ_f peak values in the interval 1200–1300°C. Therefore, the increase in bend strengths at high temperature can easily be associated to the toughness behaviour.

Most ceramics, like the mullites studied here, contain remaining glassy phases that have been formed during sintering. In materials such as alumina, silicon nitride and glass ceramics,^{24,25} peaks in strength and toughness with temperature have been associated with several phenomena derived from the softening of those remaining glassy phases.^{26,27} A variety of mechanisms, from blunting of critical flaws to grain boundary sliding, crack branching or formation of crack bridges by viscous flow during crack propagation have been proposed.²² Probably, not a single mechanism takes place but an interaction of several ones occurs depending on composition and distribution of the glass, testing temperature and strain rate.

In order to discern which of those mechanisms are predominant in the present mullite materials, K_{IC} data as a function of strain rate at two limiting temperatures RT and 1300°C were analyzed.

Considering first the MS0 samples, the increase in K_{IC} with strain rate at room temperature (Fig. 7) is due to subcritical crack growth through the easy paths provided by the glass phase as above discussed. The toughness behaviour at 1300°C is also attributed to the glassy phase, but the mechanism seems to be quite different. Actually, viscous flow at slow strain rates favors sliding between grains or agglomerates as can be observed on the micrographs of fracture surfaces at 1300°C (Fig. 10(b, d)). This grain boundary sliding phenomenon, and its related plastic deformation effect, produce higher apparent K_{IC} at slow strain rates, while at the very high strain rate it does not take place. Due to the lack of energy dissipative mechanisms at high strain rates, toughness values at high temperature are lower than at room temperature because of the decrease of the elastic modulus (Fig. 4), as experimentally observed in Fig. 7.

For MB0, K_{IC} values at 1300°C are always larger than at room temperature for each strain rate (Fig. 8) but, the energy absorbing mechanisms in this mullite are more complex than in MS0. In fact, the trend of K_{IC} values for MB0 samples with strain rate (Fig. 8) is opposite to that shown by MS0 and there is one point that does not follow the general trend ($v = 0.005$ mm/min). The K_{IC} fracture surfaces of MB0 samples (Fig. 1(b, d)) show process zones close to the notch, in which a total decohesion of the mullite grains is evident. This microstructural aspect could be due to migration of the low viscosity liquid phase during loading. The energy absorbing mechanisms associated to the liquid phase occur in MB0 through the whole range of strain rates, even at the very high one, but their effectiveness depend on time.

From post mortem observations of MB0 samples, the energy absorbing mechanism associated to the liquid can only be speculated. At medium-high loading rates, it might act as crack bridges, more effective for high loading rates due to its low viscosity (high alkaline content). For the lowest strain rate, microstructural changes such as solution-precipitation and/or crystallization phenomena at the crack tip could take place leading to an increase of toughness.

5 Conclusions

The mechanical behaviour of two structural mullites with the same levels of impurities but different nature strongly depends on strain rate. This dependence shows different trends at room temperature and at high temperatures (1300°C).

Fracture behaviour at room temperature is determined by the distribution of the residual glassy phase:

- (a) The glassy phase along grain boundaries leads to subcritical crack growth.
- (b) When the glassy phase remains at triple points no subcritical crack growth takes place.

Fracture behaviour at high temperature is determined by the nature of the residual glassy phase which softens during testing:

- (a) Decohesion of grains and liquid migration take place in mullite with higher alkali content (0.3%) due to the formation of low viscosity liquids.
- (b) Grain boundary sliding is the main mechanism in mullite with low alkali content (<0.1%) due to a higher viscosity of the liquids formed.

Acknowledgement

This work has been supported by CICYT, Project no. MAT 499-91.

References

1. Somiya, S. & Hirata, Y., Mullite Powder Technology and Applications in Japan. *Ceram. Bull.*, **70** (1991) 1624-32.
2. Sacks, M. D., Lee, H. W. & Pask, J. A., A Review of Powder Preparation Methods and Densification Procedures for Fabricating High Density Mullite. In *Mullite and Mullite Matrix Composites*, Ceramic Transactions, Vol. 6, The American Ceramic Society Inc., Ohio, 1990, pp. 167-213.
3. Baudín, C., Osendi, M. I. & Moya, J. S., Solid Solution of TiO_2 in Mullite. *J. Mater. Sci. Lett.*, **2** (1983) 185-7.
4. Baudín, C., Miranzo, P. & Osendi, M. I., High Temperature Mechanical Behaviour of $3Al_2O_3 \cdot 2SiO_2$ Mullite Based Materials. In *Third Euro-Ceramics V-3*, Faenza Editrice Ibérica S.L, Spain, 1993, pp. 369-75.
5. Osborn, E. F. & Muan, A., plate no. 501, *Phase Diagrams for Ceramists*, The Am. Ceram. Soc. Inc., Ohio, USA, 1964.
6. Urbain, G., Cambier, F., Deleter, M. & Anseau, M. R., Viscosity of Silicate Melts. *Trans. J. Br. Ceram. Soc.*, **80** (1981) 139-41.
7. Fernandez Navarro, J. M., *El Vidrio*, Consejo Superior de Investigaciones Científicas, Spain, 1991, pp. 337-50.
8. Lessing, P. A., Gordon, R. S. & Mazdiyasny, K. S., Creep of Polycrystalline Mullite. *J. Am. Ceram. Soc.*, **58** (1975) 149.
9. Dokko, P. C., Pask, J. A. & Mazdiyasny, K. S., High Temperature Mechanical Properties of Mullite under Compression. *J. Am. Ceram. Soc.*, **60** (1977) 150-5.
10. Okamoto, Y., Fukudome, H., Hayashi, K. & Nishikawa, T., Creep Deformation of Polycrystalline Mullite. *J. Eur. Ceram. Soc.*, **6** (1990) 161-8.
11. Hynes, A. P. & Doremus, R. H., High Temperature Compressive Creep of Polycrystalline Mullite. *J. Am. Ceram. Soc.*, **74** (1991) 2469-75.
12. Ashizuka, M., Honda, T. & Kubota, Y., Effects of Grain size on Creep of Mullite Ceramics. *J. Ceram. Soc. Jpn. Int. Edition*, **99** (1991) 282-5.
13. Mah, T. I., Mazdiyasny, K. S., Mechanical Properties of Mullite. *J. Am. Ceram. Soc.*, **66** (1983) 699-703.
14. Yamada, Y., Kawaguchi, Y., Takeda, N. & Kishi, T., *J. Ceram. Soc. Jpn. Int. Edition*, **99** (1991) 452-7.
15. Kanzaki, S., Tabata, H., Sintering and Mechanical Properties of Stoichiometric Mullite. *J. Am. Ceram. Soc.*, **68** (1985) C6-7.
16. Ismail, M. G. M. U., Nakai, Z. & Somiya, S., Microstructure and Mechanical Properties of Mullite Prepared by Sol-Gel Method. *J. Am. Ceram. Soc.*, **70** (1987) C7-8.
17. Ohnishi, H., Maeda, K., Nakamura, T. & Kawanami, T., High Temperature Mechanical Properties of Mullite Ceramics, in Ref. 2, pp. 605-12.
18. Mizuno, M., Shiraishi, M. & Saito, H., Microstructure and Bending Strength of Highly Pure Mullite Ceramics, in Ref. 2 pp. 413-24.
19. Mizuno, M., Microstructure, Microchemistry and Flexural Strength of Mullite Ceramics. *J. Am. Ceram. Soc.*, **74** (1991) 3017-22.
20. Kaumazawa, T., Ohta, S., Nagaoka, T., Yasuoka, M. & Kanzaki, S., Influence of Powder Characteristics on Sinterability and Mechanical Properties of Silica-Alumina Ceramics (74 wt% Al_2O_3). *J. Ceram. Soc. Jpn. Int. Edition*, **99** (1991) 1191-6.
21. Bansal, G. K., Effect of Flaw Shape on Strength of Ceramics. *J. Am. Ceram. Soc.*, **59** (1976) 87-8.
22. Notis, M. R., Dravid, V. P. & Lyman, C. E., AEM and HRTEM Studies of the Eutectic System Zirconia-Mullite, in Ref. 2, pp. 528-39.
23. Torrecillas, R., Comportamiento Mecánico de Mullita y Mullita-Circonia obtenida por sinterización reactiva, PhD Thesis. UNED, Madrid (Spain), 1990.
24. Cheeseman, C. R. & Groves, G. W., The Mechanism of Peak in Strength and Toughness at Elevated Temperatures in Alumina Containing a Glass Phase, *J. Mater. Sci.*, **20** (1985) 2614-22.
25. Rief, C. & Kromp, K., Fracture Toughness Testing. In *Mechanical Testing of Engineering Ceramics at High Temperatures*, Elsevier Applied Science, 1989, pp. 209-25.
26. Oda, I., Matui, M. & Sowa, T., High Temperature Fatigue Failure in Pressureless Sintered Silicon Nitride, In *Progress in Nitrogen Ceramics*, Martinus Nijhoff Publisher, The Netherlands 1983, pp. 501-6.
27. Kriz, K., Fracture Behaviour of Hot Pressed Silicon Nitride between Room Temperature and 1400°C, in Ref. 26 pp. 523-8.

Mechanical Properties of High Purity Mullite at Elevated Temperatures

H. Ohira,^a M. G. M. U. Ismail,^a Y. Yamamoto,^a T. Akiba^a & Shigeyuki Sōmiya^b

^aKumagaya Factory, Ceramics Business Div., Chichibu Onoda Cement Corp., 5310 Mikajiri, Kumagaya, Saitama 360, Japan

^bFaculty of Science and Engineering, The Nishi-Tokyo University, Uenohara, Yamanashi 409-01, Japan

(Accepted 22 July 1995)

Abstract

Microstructures and mechanical properties of stoichiometric mullite (71.8 wt% Al_2O_3 /28.2 wt% SiO_2) sintered at different temperatures (1650–1750°C) were studied. Maximum bulk density was obtained by sintering at 1675°C and the density slightly decreased with temperature above 1700°C. Grain size increased with sintering temperature from 1.8 μm at 1650°C to 4.0 μm at 1750°C, and a microstructure comprising a little glassy phase with large elongated grains was observed over 1725°C by scanning electron microscopy. Flexural strength measured below 1500°C decreased with sintering temperature, but creep resistance at 1550°C increased with sintering temperature. Plastic deformation was accompanied by fracture at elevated temperatures.

1 Introduction

High purity mullite is now considered as a prime candidate material for high temperature structural applications because of its excellent high temperature properties. Its flexural strength at room temperature is 300–400 MPa and it is maintained up to 1400°C.^{1,2} Excellent creep resistance is also reported.^{3–7} But it is reported that the existence of a glassy phase at the grain boundaries has a strong influence on its microstructure and mechanical properties.⁸

As for the stability of mullite at elevated temperature, Prochazka and Klug⁹ have suggested that stoichiometric mullite is not stable above a certain temperature. This implies that the microstructure and mechanical properties of stoichiometric mullite will be affected by the sintering temperature.

High purity stoichiometric mullite powder is now produced commercially via the sol–gel process.¹⁰ In the present investigation, the microstructures,

flexural strengths and creep resistance of high purity mullite bodies were studied as a function of sintering temperature.

2 Experimental Procedure

Commercial stoichiometric mullite powder (MP40, Chichibu Onoda Cement Corp., Japan) derived via the sol–gel process was used as starting material. Table 1 shows its standard characteristics and Fig. 1 presents a scanning electron micrograph of the as-received MP40. The powder was uniaxially pressed into 50 × 30 × 8 mm blocks and cold isostatically pressed under 200 MPa for 5 min. The blocks were then sintered at 1650, 1675, 1700, 1725 and 1750°C for 2 h in air. Bulk density of the sintered specimens was determined by the liquid displacement method. The sintered bodies were cut into 4 × 3 × 40 mm samples and polished for flexural strength and creep measurements.

Flexural strength and creep resistance were measured by the three-point bending method (Autograph DCS-5000, Shimadzu Corp., Japan) with span of 30 mm. Flexural strength was measured at room temperature, 1400, 1500 and 1600°C with crosshead speed of 0.5 mm min⁻¹ in air.

Creep resistance was measured at 1550°C and the strain rate, $\dot{\epsilon}$, and the stress exponent, n , were calculated by following equations:¹¹

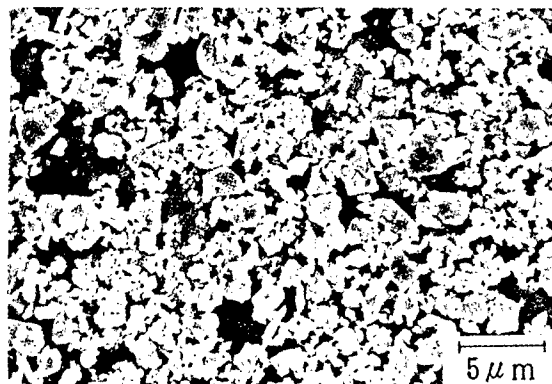
$$\sigma = \frac{3 P L}{2 b d^2} \cdot \frac{2 n + 1}{3 n} \quad (1)$$

$$\dot{\epsilon} = \frac{2 b (n + 2)}{L^2} \dot{y} \quad (2)$$

where σ is the maximum stress, P is the applied load, L is the span length, b is the width of the specimen, d is the thickness of the specimen and \dot{y} is the deflection rate at the load point.

Table 1. Standard characteristics of starting mullite powder (MP40)

Composition (wt%)	Al ₂ O ₃	71.8
	SiO ₂	28.2
Impurities (wt%)	TiO ₂	<0.1
	Fe ₂ O ₃	<0.01
	Na ₂ O	<0.01
Average particle size (μm)		1.4
Surface area (BET) (m ² g ⁻¹)		8

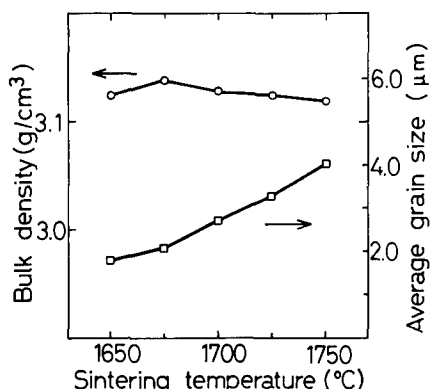
**Fig. 1.** Scanning electron micrograph of starting mullite powder (MP40).

The microstructure of the specimens was observed by scanning electron microscopy (SEM) (model SIGMA-V, Akashi Seisakusho Co., Ltd., Japan) after polishing and thermal etching. Average grain size was determined by the intercept method.¹²

3 Results and Discussion

3.1 Effects of sintering temperature on density and microstructure

Figure 2 shows the variation of bulk density and average grain size with respect to sintering temperature. Bulk density increased with sintering temperature, reaching a maximum value of 3.14 g cm⁻³ at 1675°C, and then decreased slightly with increase of sintering temperature above 1700°C. The average grain size was 1.8 μm in the 1650°C-sintered

**Fig. 2.** Variation of bulk density and average grain size of high purity mullite with sintering temperature (duration: 2 h).

specimen and gradually increased with sintering temperature, growing to 4.0 μm at 1750°C.

Representative microstructures of specimens sintered at different temperatures are shown in Fig. 3. In the 1650°C-sintered specimen, many small pores remained, the grains were relatively equiaxial and few elongated grains were observed. However, with the increase of sintering temperature above 1675°C, the grain morphology changed from equiaxial to elongated with the disappearance of the pores. Sintering above 1725°C caused the exaggerated growth of elongated grains, which reached 30 μm in certain cases. Also, small equiaxial grains grew gradually, and a phase separation resulting in the formation of a small amount of glassy phase was observed at the grain boundaries (Fig. 4). The exaggerated grain growth promoted the formation of large pores between the grains and small pores within the grains. The existence of glassy phase at the grain boundaries and the large elongated grain growth suggest that a phase may shift from stoichiometric mullite to high-Al₂O₃ mullite within the solid solution limit and that a liquid phase consisting mainly of SiO₂ may be formed by the phase separation. Prochazka and Klug⁹ suggested in their studies on the Al₂O₃–SiO₂ phase diagram that 3:2 mullite is not stable above a certain temperature, and that it forms high alumina mullite with a liquid phase. Thus our present results are consistent with theirs, even though the temperature at which phase separation was observed by SEM in this study was a little higher than the value reported by them.

3.2 Effects of sintering temperature on flexural strength

Figure 5 schematically illustrates load–displacement curves measured at different temperatures for the 1725°C-sintered specimens. The specimen tested at 1400°C showed brittle fracture and little plastic deformation prior to failure. At 1500°C, however, the fracture was brittle but evidence of slight plastic deformation was observed prior to failure. At 1600°C, the specimen fractured with considerable plastic deformation.

Figure 6 shows the variation of flexural strength at room and elevated temperatures as a function of sintering temperature. The data measured at 1600°C were excluded because of significant plastic deformation during the measurements, as shown in Fig. 5. It was evident that the flexural strength decreased with both testing temperature and sintering temperature. As for the relationship between flexural strength and sintering temperature, the strength at room temperature decreased from 400 MPa for the 1675°C-sintered specimen to 300 MPa for the 1750°C-sintered specimen. The

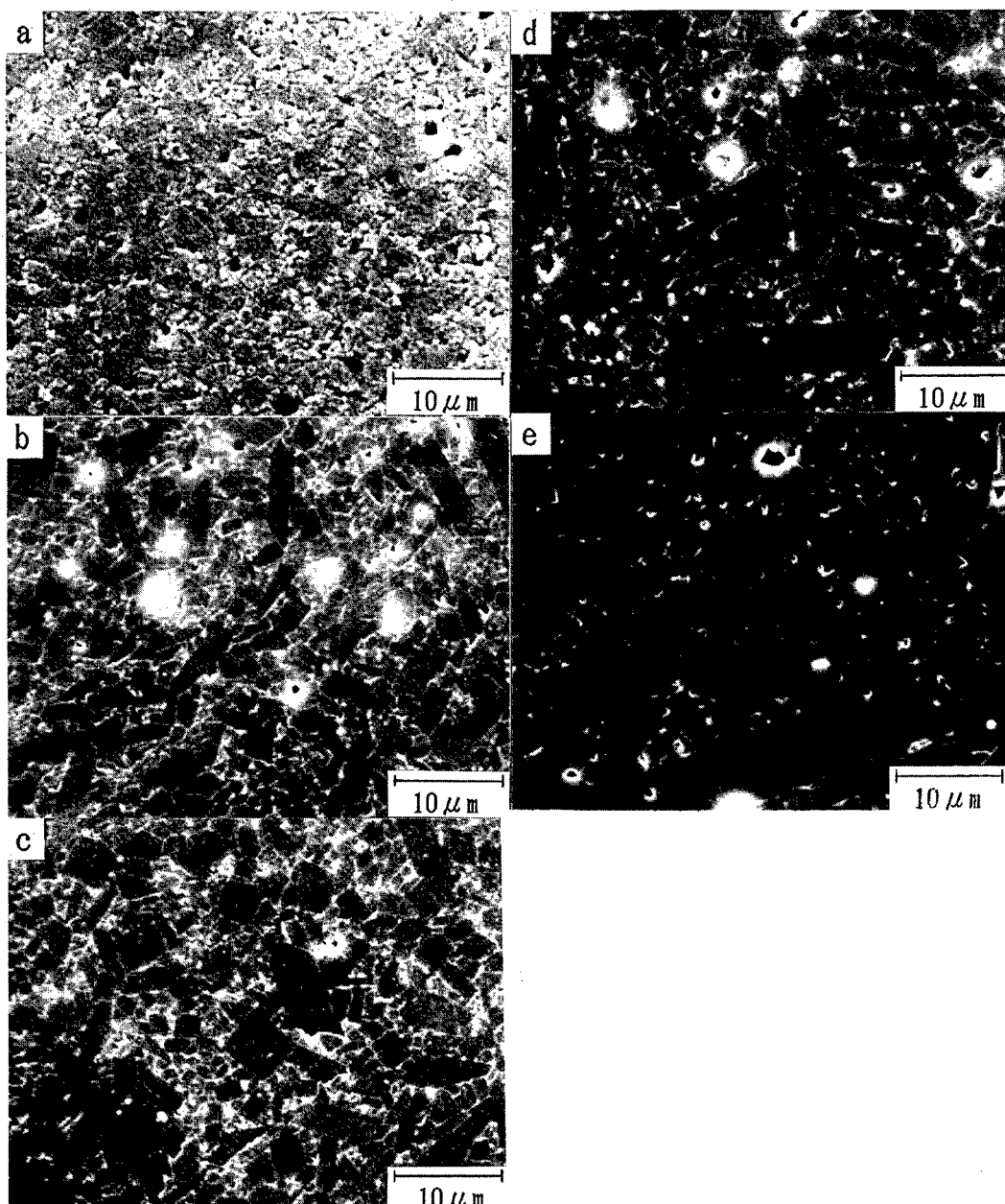


Fig. 3. Scanning electron micrographs of high purity mullite sintered at (a) 1650°C, (b) 1675°C, (c) 1700°C, (d) 1725°C and (e) 1750°C for 2 h (thermally etched at 1550°C).

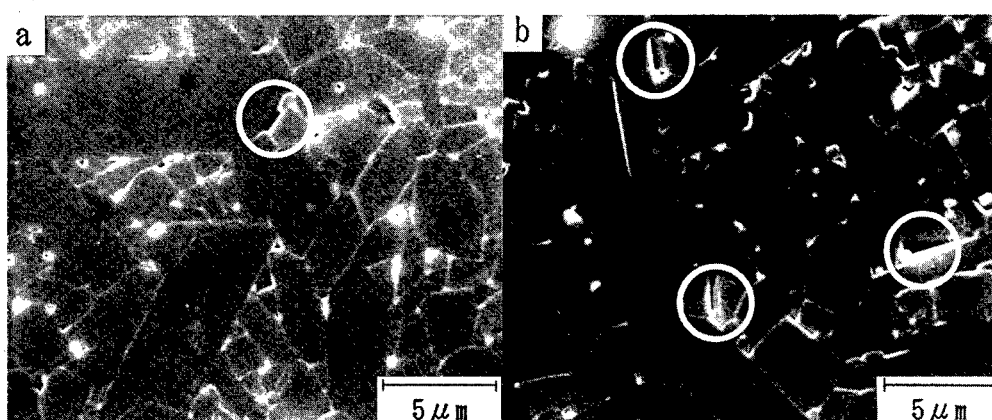


Fig. 4. Scanning electron micrographs of high purity mullite sintered at (a) 1725°C and (b) 1750°C, showing small glassy areas (thermally etched at 1550°C).

strength at 1400°C also decreased from 360 MPa for the 1650°C-sintered specimen to 280 MPa for the 1750°C-sintered specimen. The reason for this

strength degradation could be the grain growth, as discussed later. Strength degradation at 1500°C, however, became smaller than those of strength at

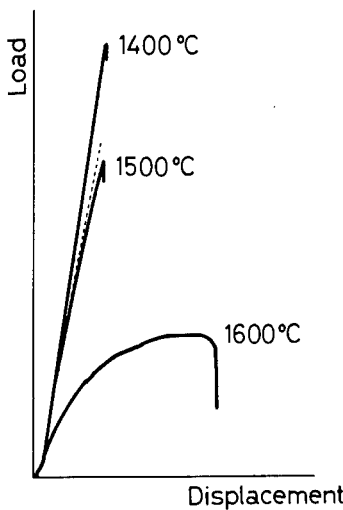


Fig. 5. Schematic illustration of load-displacement curves measured at elevated temperatures for the specimen sintered at 1725°C for 2 h (three-point bending, crosshead speed 0.5 mm min⁻¹).

room temperature and 1400°C. This observation could be explained by the relation between plastic deformation and the glassy phase. If glassy phase exists at the grain boundaries, plastic deformation at fracture will occur at elevated temperature and the calculated fracture stress will be higher than the real fracture stress. As previously shown in Figs 3 and 4, more glassy phase at grain boundaries was observed at higher sintering temperature. And also, more significant plastic deformation at fracture was observed at higher testing temperature as shown in Fig. 5. Therefore the effects of glassy phase on the fracture stress would be higher for the specimens sintered at higher temperature and, as a result, the strength degradation at 1500°C would become smaller.

Figure 7 shows the relationship between fracture stress and grain size. The relationship followed a Hall-Petch type equation,

$$\sigma_f = \sigma_0 + k d^{-1/2} \quad (3)$$

where σ_f is the fracture stress, σ_0 is the stress axis

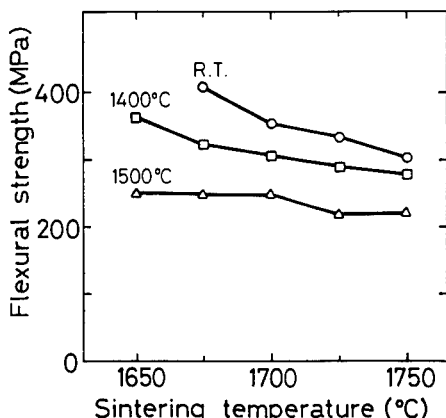


Fig. 6. Variation of flexural strength at different temperatures as a function of sintering temperature.

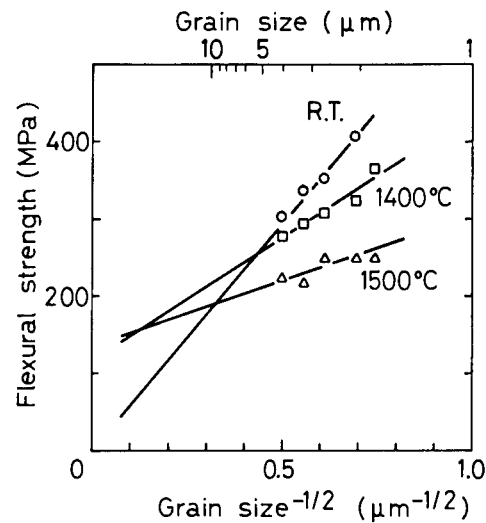


Fig. 7. Variation of flexural strength at different temperatures as a function of average grain size.

intercept, k is a constant and d is the grain size. Flexural strength at room and elevated temperatures obeyed a Hall-Petch relationship although the intercepts and gradients of the curves differed. The stress-axis intercept of the data at room temperature was close to zero and equation (1) can be expressed as,

$$\sigma_f = k' d^{-1/2} \quad (4)$$

where k' is a constant. Equation (4) is equivalent to the Griffith equation by assuming that the critical flaw size is proportional to the grain size, i.e.

$$c = \alpha d \quad (5)$$

where c is the critical flaw size and α is a constant. This implies that the specimens would fracture in the brittle manner at room temperature. On the other hand, the fracture stresses measured at 1400 and 1500°C follow Eqn (3) which has been confirmed for a variety of polycrystalline strength phenomena.¹³⁻¹⁵ This suggests that fracture at elevated temperatures could be accompanied by plastic flow, although little plastic deformation was observed from the load-displacement curves as shown in Fig. 5. That is, the stress at the crack tip becomes very high at fracture as a result of stress concentration, therefore plastic flow would occur even at 1400°C.

3.3 Effects of sintering temperature on creep

Figure 8 shows the steady-state creep rate vs. stress from 10 to 100 MPa at 1550°C as a function of sintering temperature. Creep resistance increased with sintering temperature, i.e. with the grain size. The stress exponent, n , of the 1675°C-sintered specimen was 1.3 and that of 1700°C-sintered specimen was 1.2. These similar values suggest that the same creep mechanism was operative in this tem-

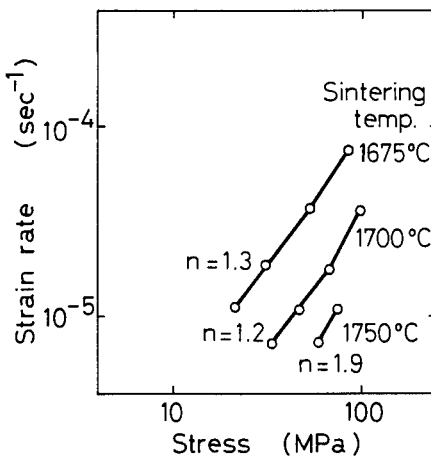


Fig. 8. Steady-state creep rate vs. stress at 1550°C by three-point bending as a function of sintering temperature.

perature region. Some researchers^{3,5,6} have reported that the stress exponents of stoichiometric mullite measured by the bending technique are 0.95–1.3 at 1400 and 1500°C, and that the deformation mechanism is diffusional creep. Results of the present study are similar to these reported values, therefore the deformation mechanism for the 1675°C and 1700°C-sintered specimens of this study may also be diffusional creep although the testing temperature was higher than in previous reports. For the specimen sintered at 1750°C, however, a higher n value of 1.9 was obtained, suggesting that a different creep mechanism was operative. As shown in Fig. 4, the microstructure of this specimen was a little different and a small amount of glassy phase was observed at grain boundaries by SEM observation. Therefore this glassy phase would have influenced the creep behaviour of this specimen.

4 Conclusions

Microstructures and mechanical properties of stoichiometric mullite (71.8 wt% Al_2O_3 /28.2 wt% SiO_2) sintered at different temperatures (1650–1750°C) have been studied and following results obtained.

1. Maximum bulk density is obtained by sintering at 1675°C and decreases slightly upon sintering above 1700°C. Grain size increases with sintering temperature from 1.8 μm at 1650°C to 4.0 μm at 1750°C, and a little glassy phase and large elongated grains are observed above 1725°C by SEM.
2. Flexural strength measured below 1500°C decreases with sintering temperature. Plastic

deformation is accompanied by fracture even at the temperature of 1400°C, although little plastic deformation prior to failure is observed in load-displacement curves.

3. Creep resistance increases with sintering temperature. The creep mechanism of specimens sintered at 1675 and 1700°C is considered to be diffusional creep, but a different creep mechanism may also be operative for the specimen sintered at 1750°C.

References

1. Kanzaki, S., Tabata, H., Kumazawa, T. & Ohta, S., Sintering and mechanical properties of stoichiometric mullite. *J. Am. Ceram. Soc.*, **68**(1) (1985) C-6–7.
2. Ismail, M. G. M. U., Nakai, Z., Ohira, H. & Sōmiya, S., Preparation and characterization of mullite containing materials. In *Ceramic Powder Science II B*, eds G. R. Messing, E. R. Fuller & H. Hausner, The American Ceramic Society, Inc., Westerville, OH, 1988, pp. 1108–14.
3. Lessing, P. A., Gordon, R. S. & Mazdiyasni, K. S., Creep of polycrystalline mullite. *J. Am. Ceram. Soc.*, **58**(3–4) (1975) 149.
4. Dokko, P. C., Pask, J. A. & Mazdiyasni, K. S., High temperature mechanical properties of mullite under compression. *J. Am. Ceram. Soc.*, **60**(3–4) (1977) 150–5.
5. Ohnishi, H., Maeda, K., Nakamura, T. & Kawanami, T., High temperature mechanical properties of mullite ceramics. In *Mullite and Matrix Composites*, eds S. Sōmiya, R. F. Davis & J. A. Pask, The American Ceramic Society, Inc., Westerville, OH, 1990, pp. 605–12.
6. Okamoto, Y., Fukudome, H., Hayashi, K. & Nishikawa, T., Creep deformation of polycrystalline mullite. *J. Eur. Ceram. Soc.*, **6** (1990) 161–8.
7. Ohira, H., Shiga, H., Ismail, M. G. M. U., Nakai, Z., Akiba, T. & Yasuda, E., Compressive creep of mullite ceramics. *J. Mater. Sci. Lett.*, **10**(14) (1991) 847–9.
8. Kumazawa, T., Kanzaki, S., Ohta, S. & Tabata, H., Influence of chemical composition on the mechanical properties of SiO_2 – Al_2O_3 ceramics. *Yogyo yokai-shi*, **96**(1) (1988) 85–91.
9. Prochazka, S. & Klug, F. J., Infrared-transparent mullite ceramic. *J. Am. Ceram. Soc.*, **66**(12) (1986) 874–80.
10. Ismail, M. G. M. U. & Nakai, Z., Properties of high-purity mullite prepared by the sol-gel method. In *Mullite II*, ed. S. Sōmiya, Uchida Rokakuho Publishing Co., Tokyo, Japan, 1987, pp. 69–80.
11. Hollenberg, G. W., Terwilliger, G. R. & Gordon, R. S., Calculation of stresses and strains in four-point bending creep tests. *J. Am. Ceram. Soc.*, **54**(4) (1971) 196–9.
12. Underwood, E. E., *Quantitative Stereology*. Addison-Wesley, 1970.
13. Sinha, M. N., Lloyd, D. J. & Tangri, K., Microyield and fracture in polycrystalline MgO . *J. Mater. Sci.*, **8** (1973) 116–22.
14. Tressler, R. E., Langensiepen, R. A. & Bradt, R. C., Surface-finish effects on strength-vs-grain-size relations in polycrystalline Al_2O_3 . *J. Am. Ceram. Soc.*, **57**(5) (1974) 226–7.
15. Bradt, R. C., Dulberg, J. L. & Tressler, R. E., Surface finish effects and the strength-grain size relationship in MgO . *Acta Metall.*, **24** (1976) 529–34.

Microstructure and Mechanical Properties of Mullite/Zirconia Composites Prepared from Alumina and Zircon under Various Firing Conditions

T. Koyama,^a S. Hayashi,^a A. Yasumori,^a K. Okada,^a
 M. Schmucker^b & H. Schneider^b

^aDepartment of Inorganic Materials, Tokyo Institute of Technology, O-Okayama, Meguro, Tokyo 152, Japan

^bGerman Aerospace Research Establishment (DLR), Institute for Materials Research, D-51140 Köln, Germany

(Accepted 22 July 1995)

Abstract

Zirconia-dispersed mullite composites were prepared by reaction sintering of alumina and zircon powders under various firing conditions. Mullite formed by firing at 1635°C apparently contained > 60 mol% Al_2O_3 and incorporated a small amount of zirconia. This transient mullite composition changed to the normal composition by treatments such as long firing time, annealing, two-step firing and/or seeding. Mullite/zirconia composites at room temperature showed good strength and fracture toughness, but these properties decreased significantly at high temperature because glassy phase in the grain boundaries. Mechanical strength at high temperature could be improved by those firing treatments which reduced the amount of glassy phase, especially by two-step firing and seeding methods.

1 Introduction

As a means to enhance the mechanical properties of mullite ceramics, mullite/zirconia composites have been investigated extensively by many workers.¹⁻⁵ Mullite/zirconia composites can be prepared via various methods: (1) sintering of mullite and zirconia, (2) reaction sintering of alumina and zircon, and (3) reaction sintering of alumina, silica and zirconia. We⁶ prepared mullite/zirconia composites by these methods and found that composites prepared by method (2) had some unique characteristic features compared with those by the other methods, e.g. higher fracture toughness. We considered that the reason could be attributed to the characteristic microstructure.⁶ We also found

that the chemical composition of mullite formed in the route (2) composites was richer in alumina than the expected composition of 60 mol%. The reason for these characteristic features of the composites are not clear yet.

In this work, we prepared mullite/zirconia composites from reaction sintering of alumina and zircon under various firing conditions and examined changes of the microstructure, the chemical composition of mullite and their mechanical properties.

2 Experimental Procedure

Fine and high purity alumina (TM-DAR, Taimei Chemicals), zircon (Tosoh) and mullite (MP-20, Chichibu Cement) powders were used for the experiments. The powders were mixed by wet ball milling in ethanol using a polyethylene pot and yttria-stabilized tetragonal zirconia balls of 2 mm in diameter. The mixtures were dried by stirring with a hot stirrer at 80°C. Pellets were compacted by uniaxial pressing at 400 MPa. They were fired under various firing schedules. The firing schedules are shown schematically in Fig. 1 and can be summarized as follows: (1) ordinary firing: fired with a heating rate of 15 K min⁻¹, firing temperature 1570–1635°C for 0–156 h and a cooling rate of 30 K min⁻¹; (2) annealing: fired in two steps, i.e. firing at 1635°C for 12 h and annealing at 1570°C for 12–144 h; (3) re-firing: fired in three steps, i.e. firing at 1635°C for 12–144 h, annealing at 1570°C for 12–144 h and re-firing at 1635°C for 12–144 h; (4) optimized firing: fired by a two-step firing profile at 1570°C for 2 h and subsequently at

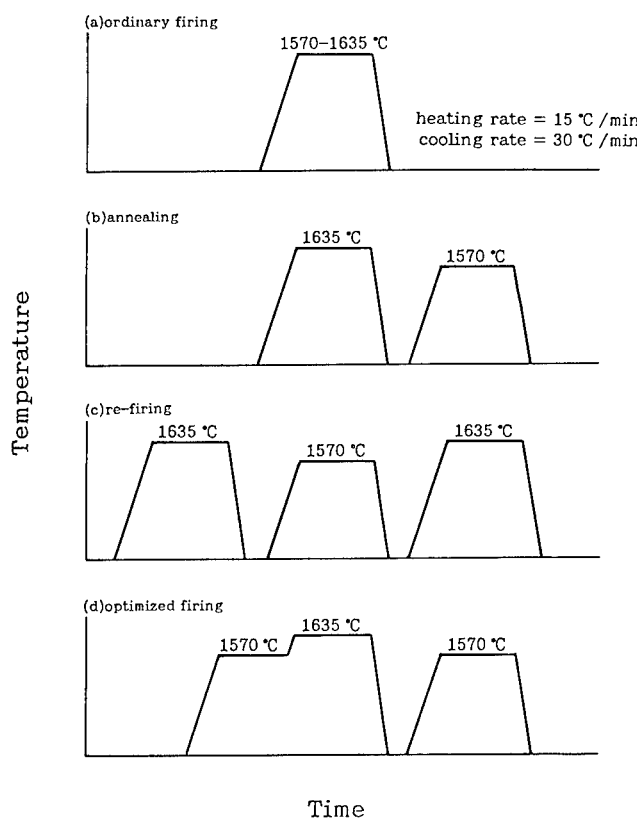


Fig. 1. Scheme of the firing schedules.

1635°C for 72 h, and then annealing at 1570°C for 72 h. Additionally, samples seeded with 5 and 20 vol% of mullite particles (average particle size 1.76 µm) were also prepared and fired with the optimized firing schedule.

X-ray diffraction (XRD) patterns of the samples were measured using a powder X-ray diffractometer (Geigerflex, Rigaku) with monochromated $\text{CuK}\alpha$ radiation. Seven mullite reflections in the powdered samples were precisely measured using an internal standard of Si powder. Lattice constants of mullite were calculated by the least-squares method. Microstructure of the fired samples was observed by transmission electron microscopy TEM (JEM 200CX, Jeol) using thin-sectioned samples. Chemical composition of mullite was analysed by EDX (Northern) with the TEM instrument and calculated by the *K*-factor method.

Four-point bending strengths of the samples were measured from room temperature to 1500°C using a testing instrument (Instron 4302) with a crosshead speed of 0.5 mm min⁻¹ for a test bar of 3 × 4 × 36 mm³ (JIS R 1601). The samples used for the measurements were > 98% of relative density and were polished by #800 diamond paste.

Table 1. Lattice parameters of mullite in the variously fired samples

Sample no.	Temp. (°C)/duration (h)	Lattice parameter (nm)		
		a-axis	b-axis	c-axis
(1) Ordinary firing				
1	1570/12	0.75609(10)	0.76877(14)	0.28853(05)
2	1600/12	0.75640(20)	0.76872(16)	0.28862(01)
3	1635/0	0.75619(13)	0.76890(05)	0.28850(05)
4	1635/6	0.75684(05)	0.76877(16)	0.28852(06)
5	1635/12	0.75701(11)	0.76876(04)	0.28863(01)
6	1635/18	0.75655(11)	0.76882(07)	0.28852(01)
7	1635/24	0.75648(11)	0.76882(12)	0.28861(03)
8	1635/84	0.75636(07)	0.76882(12)	0.28861(03)
(2) Annealing				
9 No. 5 →	1570/12	0.75643(18)	0.76876(05)	0.28853(02)
10 No. 5 →	1570/72	0.75592(07)	0.76879(07)	0.28855(07)
11 No. 5 →	1570/144	0.75533(07)	0.76892(05)	0.28846(02)
(3) Re-firing				
12 No. 9 →	1635/12	0.75622(03)	0.76870(01)	0.28856(04)
13 No. 10 →	1635/72	0.75512(02)	0.76906(05)	0.28850(04)
14 No. 11 →	1635/144	0.75486(11)	0.76907(01)	0.28851(04)
(4) Optimized firing				
15	1570/2, 1635/12, 1570/72	0.75472(06)	0.76911(04)	0.28839(03)
16	1570/12, 1635/12, 1570/12	0.75475(28)	0.76909(13)	0.28846(04)
5 Vol% mullite seeded				
17	1570/12	0.75602(07)	0.76909(05)	0.28844(07)
18	1600/12	0.75602(19)	0.76890(13)	0.28851(05)
19	1635/12	0.75607(18)	0.76893(16)	0.28853(04)
20 Vol% mullite seeded				
20	1570/12	0.75512(04)	0.76912(21)	0.28844(03)
21	1600/12	0.75504(08)	0.76910(19)	0.28852(04)
22	1635/12	0.75505(09)	0.76904(14)	0.28847(04)
23	1570/02, 1635/12, 1570/72	0.75456(09)	0.76911(06)	0.28846(03)

Standard derivations are in parentheses and refer to last decimal place.

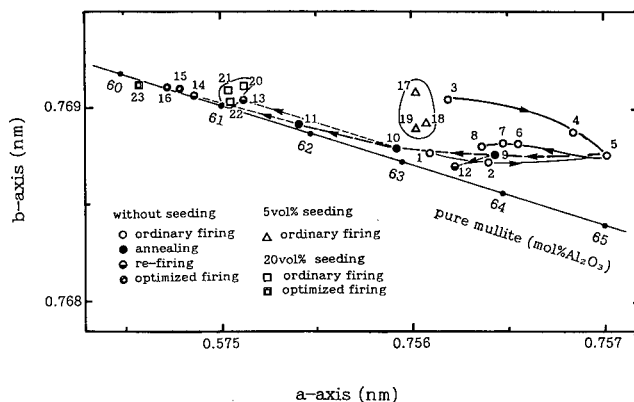


Fig. 2. Relation between the lengths of the *a*- and *b*-axes of mullite in the samples prepared under various conditions (see text and Table 1 for details).

Edges were chamfered with a diamond disc. Fracture toughness was determined using an indentation microcrack method⁷ with a load of 49 N.

3 Results and Discussion

3.1 Ordinary firing

In these experiments, the samples were prepared with two series of firing conditions. In the first series, the samples were fired for a constant duration of 12 h with firing temperatures from 1570 to 1635°C. In the second series, the samples were fired at a constant temperature of 1635°C with duration varying from 0 to 156 h. Lattice constants of mullite in these samples are listed in Table 1. The correlation between the lengths of the *a*- and *b*-axes is shown in Fig. 2. In the first series, the length of the *a*-axis of mullite increased with higher firing temperature while the lengths of the *b*- and *c*-axes did not change significantly (samples 1, 2, 5). The change was especially large between the mullite fired at 1600°C and that at 1635°C (samples 3–8). Due to this increase of the length of the *a*-axis, the lattice constant data of the mullite fired at 1635°C deviated from the relation reported for pure mullite, which is also depicted in Fig. 2. This deviation of the data

suggests incorporation of ZrO_2 into the mullite structure. A second series of experiments was, therefore, made in order to elucidate this phenomenon.

The lengths of the *a*- and *b*-axes for the second series samples (3–8) are also shown in Fig. 2. With longer firing time, the cell edges changed on a line parallel to the composition line of pure mullite, indicating increasing Al_2O_3 contents. This trend continued up to 12 h. Since this line runs parallel

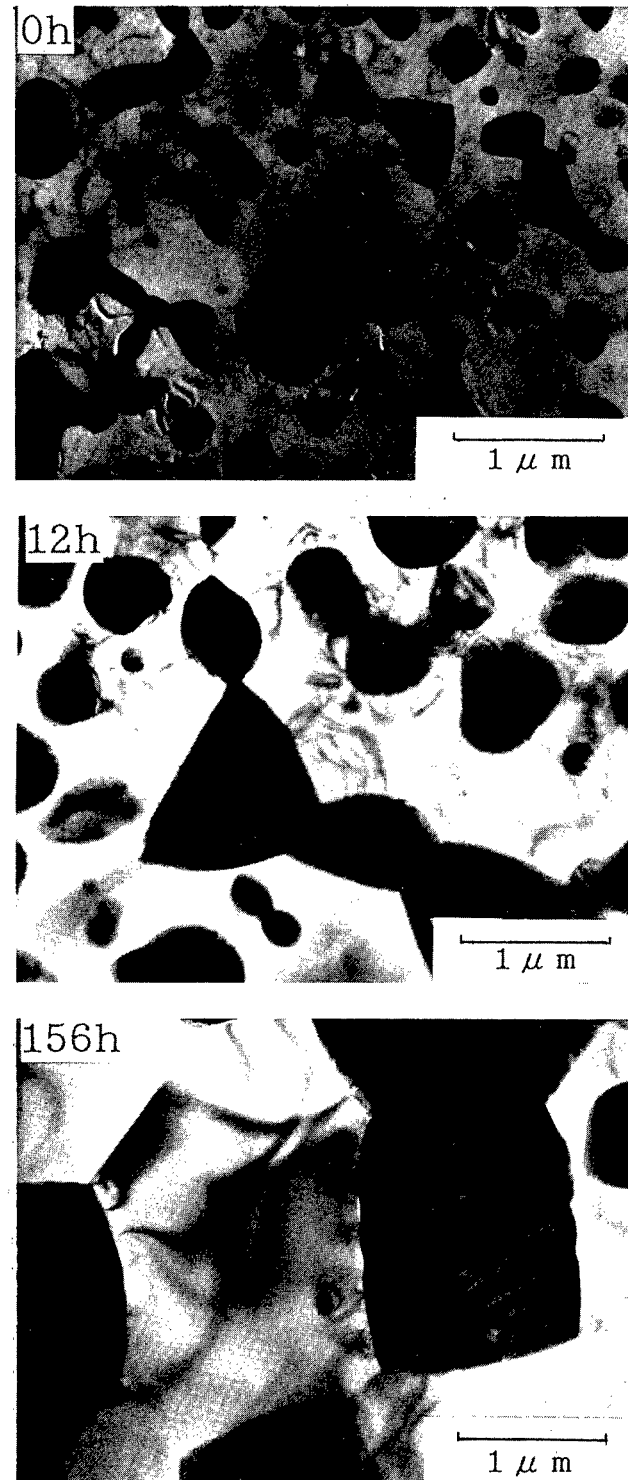


Fig. 3. TEM photographs of the 'ordinary firing' samples with various firing times.

Table 2. Chemical analysis of mullite by EDX

Sample no.	Chemical composition (mol %)			
	Al_2O_3	SiO_2	ZrO_2	Al_2O_3/SiO_2
3	61.3(13)	37.5(13)	1.2(04)	1.63
5	63.4(09)	35.5(09)	1.1(05)	1.79
8	63.8(10)	36.1(07)	1.1(04)	1.77
11	62.9(09)	36.5(09)	0.6(02)	1.73
21	60.7(07)	38.8(07)	0.5(02)	1.56

Standard deviations are in parentheses and refer to last decimal place.

to the pure mullite line, it is suggested that a small amount of zirconia is incorporated in these mullites. With firing times longer than 12 h, the *a*-axis became shorter again. This new trend approached the pure mullite line but stopped at a certain stage intermediate between pure mullite and the line given by samples 3, 4 and 5. Chemical compositions of some mullites were analysed by EDX and are listed in Table 2. From these data, it is confirmed that a small amount of zirconia was incorporated in the mullites (samples 3 and 5).

Figure 3 shows the microstructural changes in the samples fired at 1635°C for different times. With longer firing time, the grain size of the zirconia drastically increased and the thickness of a glassy grain boundary phase also increased. As the XRD and EDX results indicated, the mullites were richer in alumina than the expected composition of 60 mol%. Therefore, some excess silica should be exsolved and be present in the samples. Indeed, a thick amorphous film was observed in the grain boundaries as shown in Fig. 4. This amorphous film totally covered the mullite grains. The amorphous film was, therefore, considered to be silica-rich in composition. The liquid phase from which this amorphous film was formed is considered to have evolved transiently at high temperature because of the peculiar mullite formation reaction in this system, i.e. silica formed by the decomposition of zircon reacted with alumina to form mullite at high temperature. With higher firing temperature, the amount of the liquid phase

apparently increased. Therefore, the chemical composition of mullite changed transiently towards the $2\text{Al}_2\text{O}_3\text{:SiO}_2$ composition and incorporated some amount of zirconia due to the rapid mullitization in the presence of the liquid phase. However, this transient state then gradually changed to the apparently stable state at that temperature with longer firing time and the transiently formed mullite changed its chemical composition towards the apparently stable state and exsolved zirconia as a result. (This apparently stable state does not mean really equilibrium stable state.) Similar transient zirconia incorporation in mullite was also reported in the crystallization of mullite in rapidly quenched mullite/zirconia composites by Yoshimura *et al.*⁸

3.2 Annealing and re-firing

With longer firing times up to 156 h at 1635°C in the ordinary firing method described above, the chemical composition of mullite became almost constant at some intermediate state as reported in the previous section. Although the sample (5) showed a very high fracture toughness of 6.9 MPa $\text{m}^{1/2}$ and good four-point bending strength of 310 MPa at room temperature, the existence of a silica-rich amorphous phase in the grain boundaries was anticipated to be detrimental for high temperature mechanical properties of the composites. Hence, an annealing treatment was attempted at 1570°C in order to crystallize the grain boundary phase by a reaction between the amorphous phase and the alumina-rich mullite. This reaction should also

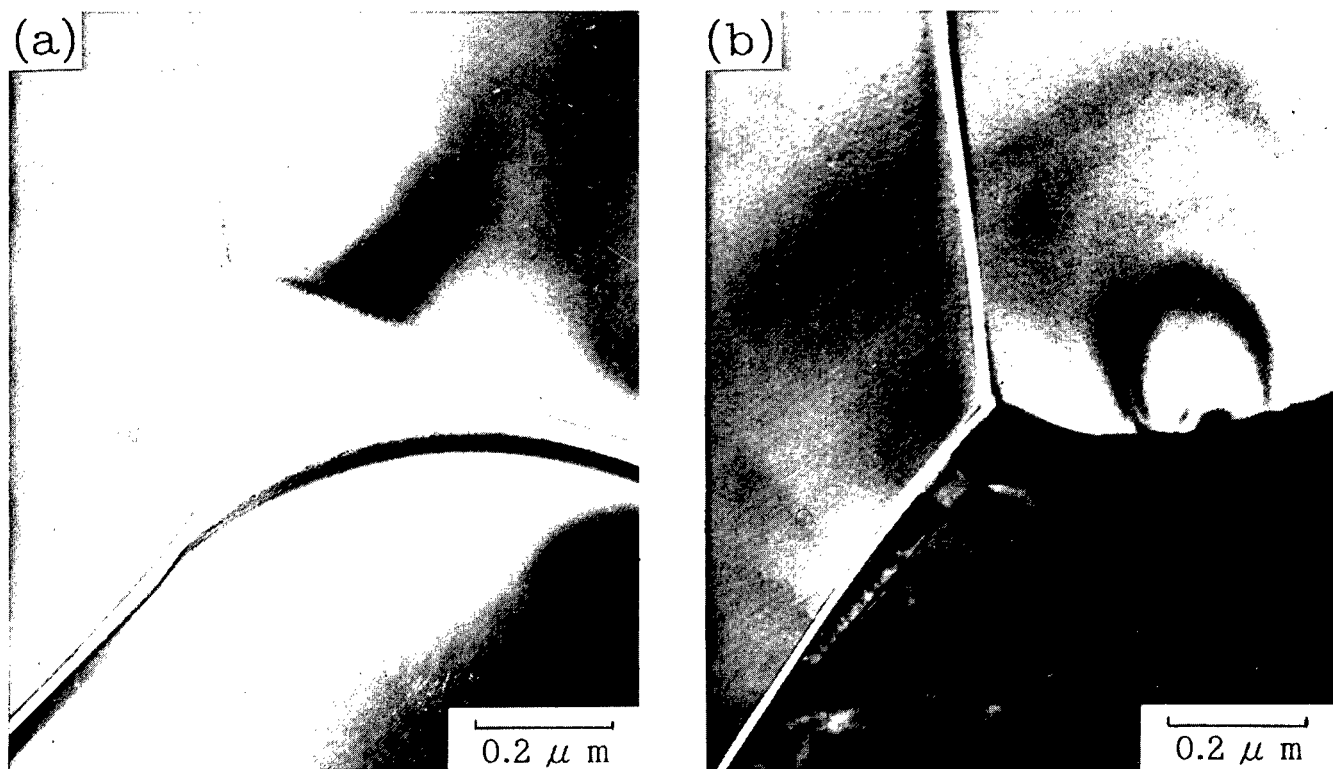


Fig. 4. TEM photographs of the grain boundaries of the 'ordinary firing' samples: (a) fired at 1635°C for 1 h; (b) for 156 h.

change the chemical composition of mullite to 60 mol% Al_2O_3 . The lattice parameter changes resulting from the annealing treatment are also shown in Fig. 2 (samples 9–11). With longer annealing time at 1570°C, the chemical composition of mullite indeed shifted and approached the expected value of 60 mol% Al_2O_3 . As is evident from Fig. 2, zirconia was mostly expelled from mullite by this treatment. This was also confirmed by EDX analysis listed in Table 2. The annealing treatment at 1570°C was found to be effective to change the chemical composition of mullite to the expected value. Further, annealing experiments were performed at 1520 and 1450°C but they were found to be less effective than those at 1570°C.

In the next step, we re-fired the annealed samples again at 1635°C. The lattice constants of mullite changed again upon this treatment, indicating that the chemical composition further approached 60 mol% Al_2O_3 . This implies that no liquid phase was formed during this re-firing even though it was fired at the same firing temperature as that of the 'ordinary firing', where a transient metastable liquid phase had formed. The reaction that occurred in the re-firing treatment was, therefore, considered to approach stable state at this temperature. In the case of the ordinary firing at 1635°C, the change of the lattice constants showed limitation and stopped at some intermediate stage even after long firing times. Comparing with this result, the change of the lattice constants of mullite was accelerated in the annealing and re-firing treatments. The driving force for this change is, however, uncertain at present.

3.3 Optimized firing

From the previous results, we found that the chemical composition of mullite formed by the ordinary firing was alumina-rich and yielded a silica-rich amorphous film in the grain boundaries. This type of microstructure is anticipated to lead to degradation of mechanical properties at high temperature. In order to avoid the formation of alumina-rich mullite, we considered two counterplans.

The first counterplan was firing the samples by a two-step firing schedule, which was first proposed by Claussen and Jahn.² The concept of this process was to separate the densification stage and the reaction stage. In the present study, we attempted to form mullite at a temperature lower than 1635°C to avoid alumina-rich mullite formation. Therefore, mullitization was done by holding at 1570°C for 2–12 h and then the samples were sintered at the higher temperature of 1635°C. Indeed, mullite formed by this firing schedule was much closer in composition to 60 mol% Al_2O_3

than in the samples made by the 'ordinary firing'. The samples were then further annealed at 1570°C as shown in Fig. 1. By this firing schedule (d), the chemical composition of mullite in the composites became very close to the expected composition of 60 mol% Al_2O_3 as shown in samples 15 and 16 of Fig. 2. The difference between the results of this firing schedule (samples 15 and 16) and the annealing schedule (samples 13 and 12) was quite considerable. This is attributed to the difference of their mullitization temperature. Apparently the chemical composition of firstly formed mullite is very important for the ability of the mullite to reach the final equilibrium composition close to 60 mol% Al_2O_3 .

Our second counterplan was the seeding method. Composites seeded with 5 and 20 vol% of mullite particles were prepared. As is apparent from the data of samples 17–22 in Fig. 2, the chemical composition of the mullite formed depended on the amount of seeding but was almost independent of the firing temperatures. Therefore, we combined the two counterplans of two-step firing and seeding methods and found that the mullite thus formed (sample 23 in Fig. 2) showed a composition very close to 60 mol% Al_2O_3 .

3.4 Temperature dependence of bending strength

Figure 5 shows the four-point bending strength of the mullite/zirconia composites from room temperature to 1500°C. The bending strength of the 'ordinary firing' sample (5) was fairly high (310

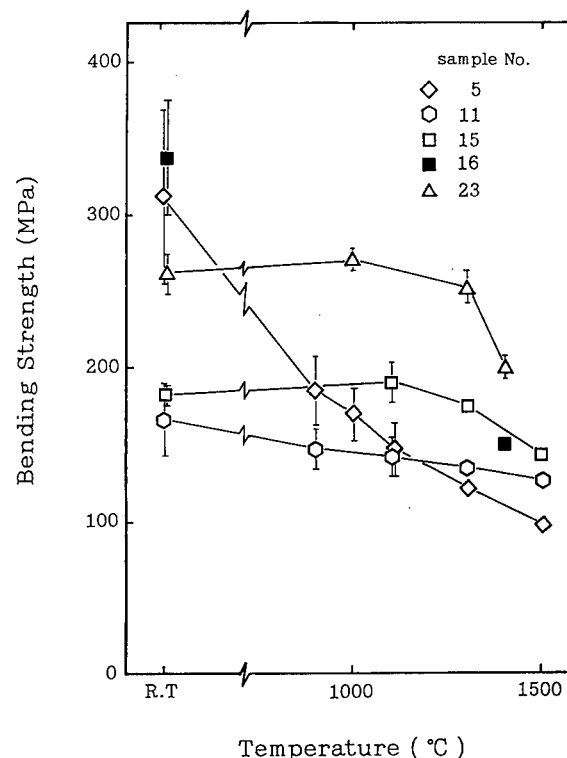


Fig. 5. Temperature dependence of the four-point bending strength different samples (see Table 1 for processing details).

MPa) at room temperature. However, it decreased linearly with temperature and was only 100 MPa at 1500°C. This large degradation of the strength was considered to be due to the presence of a thick and continuous silica-rich amorphous film in the grain boundaries as shown in Fig. 4. To avoid this degradation of strength at high temperature, the amorphous phase was crystallized by annealing at 1570°C for 144 h. The bending strength of the annealed sample (11) was, however, very low at room temperature. Since a jagged pattern was observed in the stress-strain curve of this sample, microcracking in the annealed sample was considered to be the main reason for the low bending strength. Many cracks along the grain boundaries were indeed observed by TEM. The cracks were considered to occur by the crystallization of mullite from the reaction of alumina-rich mullite and silica-rich amorphous phase in the grain boundaries. Therefore, crystallization of the grain boundaries was found not to be effective in these composites although this technique was reported to be effective to enhance the mechanical properties of silicon nitride.⁹

To avoid the formation of glassy phase and microcracks in the samples, we adopted the two-step firing and annealing treatments. Sample (15) showed a fair enhancement of the bending strength for the whole temperature range compared with the annealed sample (11). This enhancement of bending strength was considered to be due to the shorter firing time, that is, decreased grain size. However, the grain size of this sample was still much larger than that of the 'ordinary firing' and the bending strength at room temperature was also lower. With shorter annealing time, the bending strength (sample 16) was found to increase to around 340 MPa at room temperature but it was not improved at high temperature because of the residual glassy phase. On the other hand, the seeded sample (23) showed an improvement of high temperature strength compared with the previous sample (16). Since the firing schedule was the same for these two samples, the seeding with mullite particles was found to be effective to improve high temperature strength. This also confirms that seeding is very effective to control the chemical composition of mullite formed in the reaction sintering of alumina and zircon.

Torrecillas *et al.*¹⁰ and Kubota *et al.*¹¹ examined the high temperature mechanical properties of zirconia-dispersed mullite composites and also zirconia- and alumina-dispersed mullite composites prepared by reaction sintering of alumina and zircon. Torrecillas *et al.*¹⁰ considered the formation of liquid phase at high temperature. Recently,

Ebinuma *et al.*¹² showed direct evidence of liquid phase formation at high temperature in the reaction sintering of alumina and zircon. Torrecillas *et al.*¹⁰ and Kubota *et al.*¹¹ shifted the bulk chemical composition towards an alumina-rich composition to avoid the liquid phase formation. These composites showed little degradation of high temperature strength because of almost glass-free grain boundaries, but lowering of creep properties was inevitable due to co-existence of alumina. Comparing with their data, the bending strengths of the seeded sample in the present study were similar or a little higher for all temperatures from room temperature to high temperature.

4 Summary

Zircon-dispersed mullite composites were prepared via reaction sintering of alumina and zircon with various firing schedules. The following results were obtained.

In the 'ordinary firing' schedule, the chemical composition of the mullite formed was extraordinarily alumina-rich and a small amount of zirconia was incorporated. This caused continuous thick glassy films in the grain boundaries. Incorporation of zirconia was transient and expelled by longer firing time. By long duration of annealing at 1570°C, zirconia was also exsolved from mullite and some change was observed in the chemical composition of mullite by the crystallization of the glassy grain boundaries. However, it was insufficient for complete crystallizing of the glassy grain boundaries. Further progress was made by the re-firing treatment but this treatment was still insufficient for complete crystallization. The two-step firing treatment to form mullite at 1570°C was effective to avoid the formation of alumina-rich mullite. Seeding with 20 vol% of mullite particles accelerated the mullitization at that temperature. The 'ordinary firing' samples showed good four-point bending strength and fracture toughness at room temperature but showed degradation of the mechanical properties at high temperature. This was attributed to the continuous and thick glassy phase in the grain boundaries.

Four-point bending strength of the samples could not be improved when they were prepared by long firing time at high temperature because grain growth and microcracking occurred by these treatments. High temperature strength was improved, however, by reducing the silica-rich amorphous glassy phase in the grain boundaries. Seeding with mullite particles combined with two-step firing were most effective to obtain high strength from room temperature up to 1500°C.

Acknowledgements

We are grateful to Mr T. Mori of Tosoh Company, Japan for supplying the zircon powder and Dr C. Yamagishi of Nippon Cement Company, Japan for the measurement of bending strength.

References

1. Prochazka, S., Wallace J. S. & Claussen N., Microstructure of sintered mullite-zirconia composites. *J. Am. Ceram. Soc.*, **66**(8) (1983) c125-7.
2. Claussen, N. & Jahn J., Mechanical properties of sintered in-situ reacted mullite-zirconia composites. *J. Am. Ceram. Soc.*, **63**(3-4) (1980) 228-9.
3. Moya, J. S. & Osendi, M. I., Microstructure and mechanical properties of mullite/ZrO₂ composites. *J. Mater. Sci.*, **19** (1984) 2909-14.
4. Ismail, M. G. M. U., Nakai, Z. & Somiya, S., Properties of zirconia-toughened mullite synthesized by the sol-gel method. *Adv. Ceram.*, **24** (1988) 119-26.
5. Rundgren, K., Elfving, P., Tabata, H., Kanzaki, S. & Pompe, R., Microstructures and mechanical properties of mullite-zirconia composites made from inorganic sols and salts. *Ceram. Trans.*, **6** (1990) 553-66.
6. Koyama, T., Hayashi, S., Yasumori, A. & Okada, K., Contribution of microstructure to the toughness of mullite/zirconia composites. *Proc. Ceram. Process. Sci. Technol.*, in press.
7. Niihara, K., Evaluation of K_{IC} by indentation micro-fracture method. In *Abstracts 21st Symposium of Basic Science of Ceramics*, (1983) B-15.
8. Yoshimura, M., Hanaue, Y. & Somiya, S. Non-stoichiometric mullites from Al₂O₃-SiO₂-ZrO₂ amorphous materials by rapid quenching. *Ceram. Trans.*, **6** (1990) 449-56.
9. Hecht, N. L., McCullum, D. E. & Graves, G. A., In *Proc. 3rd Int. Symp. on Ceramic Materials and Components for Engines*, ed V. J. Tennery, Am. Ceram. Soc. Inc., 1989 pp. 806-17.
10. Torrecillas, R., Moya, J. S., De Aza, S., Gross H. & Fantozzi, G., Microstructure and mechanical properties of mullite-zirconia reaction-sintered composites. *Acta Metall. Mater.*, **41**(6) (1993) 1647-52.
11. Kubota, Y., Yamamoto, S., Mori, T., Yamamura, H. & Mitamura, T., Changes of microstructure and high-temperature strength of ceramic composite in the mullite-ZrO₂-Al₂O₃ system using an in-situ reaction between synthetic zircon and Al₂O₃. *J. Ceram. Soc. Jpn.*, **102**(1) (1994) 93-8.
12. Ebinuma, T., Hamano, K. & Okada, S., Preparation of alumina-zirconia-mullite composite on solid-phase reaction between alumina and zircon. In *Proc. 7th Autumn Symp.*, Sapporo, 1994, p. 66.

Phase Transformation and Grain Coarsening of Zirconia/Mullite Composites

Wen-Cheng J. Wei, H. C. Kao & M. H. Lo

Institute of Materials Science and Engineering, National Taiwan University, Taipei, Taiwan 106, Republic of China

(Accepted 22 July 1995)

Abstract

*ZrO₂/mullite composites (ZMC) with homogeneously dispersed ZrO₂ grains were prepared from colloidal or sol-gel processes of the precursors, which were a mixture of colloidal pseudo-boehmite (γ -AlOOH), zirconia and silicic acid gel, or prepared from dissociated zircon with alumina powder. After pressureless sintering of the ZMCs, their microstructure was examined by means of X-ray diffractometry, scanning electron microscopy and analytical transmission electron microscopy techniques. The microstructure of the ZMCs showed a difference in scale. ZrO₂ and mullite grains grown in the gel matrix were formed at temperatures as low as 1100 and 1300°C, respectively. Experimental results indicated that heat treatment from 1300 to 1600°C influences the growth of mullite and fine ZrO₂ grains in ZMCs, especially for the composite prepared from sol-gel methods in which the ZrO₂ grew from tens of nanometres to micrometre size. The effects of the presence of ultra-fine ZrO₂ on retarding the grain growth of mullite and the increase of metastable *t*-phase ZrO₂ are also discussed. The growth of fine ZrO₂ grains in a mullite matrix belongs to a mechanism of coalescence.*

1 Introduction

The appropriate selection of a matrix phase and the addition of various zirconia grains to form ceramic composites with better strength and toughness has become widely recognised as a method for producing materials for engineering applications. ZrO₂ in alumina,¹ Si₃N₄² and mullite³ have been reported to form composite systems that are effective in strengthening and toughening the ceramic matrix. Garvie⁴ also found that the addition of 10% tetragonal (*t*) zirconia enhanced the thermal shock resistance of zircon-zirconia composite. The retained strength of zirconia-zircon composites could be as high as 90% of the

original after quenching from 600°C. In addition, other advantages included less deterioration as a result of the tetragonal to monoclinic (*m*) phase transformation of zirconia grains at high temperature and in high humidity environment, and more economically feasible materials owing to lower costs. However, some disadvantages were also recognised: the zirconia particles coarsened in the alumina matrix⁵ as soon as the ceramic matrix densified. Also, thermal expansion mismatch of ZrO₂ with the ceramic matrix resulted in thermal stresses, either tensile or compressive, as the zirconia composite was cooled from sintering temperature. These would trigger the '*t*-to-*m*' transformation, thereby degrading mechanical properties.

High quality mullite can be made from various sources, alkoxides or other high purity chemicals, through the sol-gel or co-precipitation method.⁶ The method allows the addition of zirconia for making zirconia-toughened mullite (called ZMC in this paper) composites. In addition, the composites can also be made by the reaction sintering of zircon and alumina,^{7,8} by the co-sintering of fine zirconia/mullite mixture,⁹ or by directly sintering the mixture of alumina, silica and zirconia.

High temperature densification above 1450°C with sintering aids is currently used to densify the zirconia-mullite composite. TiO₂,³ MgO^{10,11} and Ca¹² can facilitate the formation of a liquid phase to achieve viscous sintering. These additives were reported to have a profound influence on the high temperature properties of ZMC⁸ and on the formation of glassy and grain boundary phases.¹⁰

The additives, including ZrO₂ and sintering aids, may dissolve in the mullite matrix to some extent. A microanalysis experiment to determine the ZrO₂ content in mullite grains was conducted by Dinger *et al.*,¹³ who found the presence of an apparent solid solution on the crust of mullite grains. This gave a grain boundary of mullite in a state of expansion, thereby improving the toughness of the composite. Other oxide dopants, including Ti, V, Mn, Fe and Co oxides,¹⁴ incorporated into

the mullite structure were determined as being preferentially located in oxygen octahedral sites. The upper limit of solubility is controlled by cation radii and the valence state of cations. This work was partially motivated by the report that the amount of ZrO_2 solid solution in mullite composites was of the order of few per cent up to 20%,¹³ which was thought to be quite influential in determining the grain growth mechanism of ZrO_2 .

Since the toughness and high temperature stability of ZMC are dependent upon the reactions between zirconia and mullite phases, gel-derived precursors and high purity zircon reacted with alumina are used here with and without sintering additives. This research attempts to characterize the transformation of ZrO_2 and the microstructural features, as well as determine the coarsening phenomenon of zirconia and mullite. Thus, rationalizing the parameters which govern the grain growth phenomenon is of interest, thereby permitting the development of an appropriate quantitative model.

2 Experimental

2.1 Sample preparation

2.1.1 Gel-derived (GD-) ZMC

The solution prepared for gelation included 50 wt% tetraethyl orthosilicate (TEOS; Merck Chemical Co., Germany), 30 wt% dry alcohol (reagent grade; Showa Chemicals Co., Ltd, Tokyo, Japan) and 20 wt% 0.018 N HCl (diluted from reagent grade 0.1 N HCl; Merck Chemical Co., Germany). The three chemicals were first mixed and then maintained in a water bath at 50°C for 3 h, so as to obtain a well-mixed silicic acid solution.⁶ Next, pseudo-boehmite sol (Remet Co., NY, USA) and ZrO_2 sol (Johnson Matthey Co., MA, USA) were slowly added to the solution. After mixing for 30 min, the viscosity of the solution increased until gelation. The gel was dried at 80°C for several days until no further weight loss was measured. The aerogel was crushed and sieved through 325 mesh. The Al_2O_3 and SiO_2 ratio was at the mullite stoichiometry and the volume fraction of added ZrO_2 was 24, 9 or 3 vol%. ZMC powders were die-pressed at a pressure of 160 MPa. Sintering of the specimens was conducted at 800 to 1600°C for 2 to 6 h.

2.1.2 Reaction-sintered (RS-) ZMC

Two types of RS-ZMC mixture were selected as comparative cases.¹⁵ One was a mixture of dissociated zircon (supplied by Z-Tech Corp.; impurities included 0.36% Al_2O_3 , 0.08% TiO_2 , 0.03% Fe_2O_3 , and 0.11% free SiO_2) and alumina (A-16SG; Alcoa

Corp., USA) powders. The other consisted of ground zircon sand, alumina and 4 wt% CeO_2 as a sintering aid. They are named DZ-ZMC and RS(CeO_2)-ZMC, respectively. The zircon/alumina mixtures were in a molar ratio of 2:3, subsequently yielding 24 vol% ZrO_2 . These powders were initially dispersed in distilled water with 1 wt% dispersant (based on solid phase; Darvan C, supplied by R.T. Vanderbilt Co., USA), then turbo-mixed for 2 h. The solid fraction of the slurry was 30 vol%. After being cast and dried on a plaster mould, the CeO_2 -doped RS-ZMC was sintered between 1400 to 1550°C for 2 h; however, the DZ-ZMC was sintered at higher temperatures, from 1400 to 1700°C (which is higher than the dissociation temperature of zircon) for 30 min. The heating rate of the sintering was 10°C min⁻¹. Nearly fully-dense DZ-ZMC and RS-ZMC samples were obtained, then heat-treated at temperatures from 1400 to 1700°C.

2.2 Characterization

Densification of the ZMCs was examined by a dilatometer (Theta Industries, Inc., USA) up to 1500°C. Crystalline phases were determined by X-ray diffractometry (XRD; PW 1729, Philips Electronics Instruments, Inc., USA). Microstructural and micro-chemical analyses were performed by using scanning electron microscopy (SEM; Philips 515) and transmission electron microscopy (TEM; JEOL 100CXII and 2000FX, JEOL Inc., Japan), the latter equipped with EDAX (Tracer Northan Co., USA). The densities of the sintered specimens were obtained by Archimedes' method.

3 Results and Discussion

3.1 Transformation sequence

The XRD patterns of three ZMC powders were analysed and are summarized in Table 1. GD-ZMC appeared to have no crystalline phases when sintered at 800°C for 2 h. Tetragonal- ZrO_2 and mullite phases appeared at 1100 and 1300°C, respectively. The peak width of the *t*-phase ZrO_2 at 1100°C in Fig. 1 is apparently broader than the diffraction peaks of *t*- ZrO_2 at temperatures $\geq 1200^\circ\text{C}$. This implies that the zirconia has a fine grain size. After sintering at temperatures of 1600°C or above, a large portion of ZrO_2 transforms to *m*-phase in the GD-ZMC. As for the RB-ZMC, only about one-third of the ZrO_2 was found to be the tetragonal phase at sintering temperatures above 1450°C, but this quantity decreased with increasing sintering temperature and CeO_2 additive, as shown in Fig. 2. This decrease could be due to grain growth of the

Table 1. Phases detected in ZMCs prepared from three different sources and sintered at temperature shown for 2 h

GD-ZMC							
phase/temp.	1000	1100	1200	1300	1400	1500	1600 (°C)
Zircon	—	—	*	*	*	—	—
Mullite	—	—	—	*	*	*	*
<i>t</i> -ZrO ₂	**	**	**	**	**	*	*
<i>m</i> -ZrO ₂	—	—	—	—	—	*	**
RS-ZMC (without additive)							
phase/temp.	1400	1450	1500	1550 (°C)	—	—	—
Zircon	**	**	*	*	—	—	—
Mullite	—	—	*	*	—	—	—
<i>t</i> -ZrO ₂	—	—	*	*	—	—	—
<i>m</i> -ZrO ₂	—	—	*	**	—	—	—
RS-ZMC (with 4 wt% CeO ₂ additive)							
phase/temp.	1400	1450	1500	1550 (°C)	—	—	—
Zircon	**	*	*	*	—	—	—
Mullite	—	*	*	*	—	—	—
<i>t</i> -ZrO ₂	—	—	*	—	—	—	—
<i>m</i> -ZrO ₂	—	*	*	**	—	—	—

Note –, * and ** means that the X-ray diffraction intensity of the phase is not detectable, detectable and in large quantity, respectively.

ZrO₂, lack of phase stabilizer such as CaO or MgO, and thermal stress induced transformation. However, the amount of *t*-ZrO₂ finally became stable at a level of 20% (Fig. 2) when the heat treatment was extended up to 4 h at 1450°C. This occurrence is explained later by means of microstructural observations (in Section 3.3), in which the *t*-ZrO₂ is possibly intragranular and holds a submicrometre size.

The formation temperatures of these zirconia and mullite phases in GD-ZMC are apparently lower than the RS-ZMCs, as shown in Table 1, and are also lower than those reported by Low and McPersonal.¹⁶ GD-ZMC underwent this transformation at a temperature 200°C lower than that for RS-ZMC.¹⁷ This lower transformation is due to the reaction kinetics, enhanced by the fact of the diminutive gel structure in GD-ZMC.

Zircon, as a reaction product of zirconia and silica, forms as a transition phase in the gel-

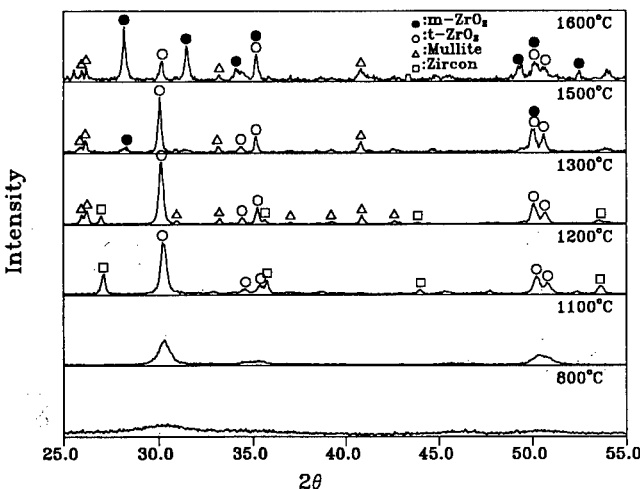


Fig. 1. XRD patterns for GD-ZMC samples after sintering at 800 to 1600°C for 2 h.

derived ZMC in the range between 1200 and 1500°C. If the temperature increases, the amount of zircon phase decreases and is accompanied by the appearance of mullite phase. The formation and diminishing of zircon phase in a similar ZMC

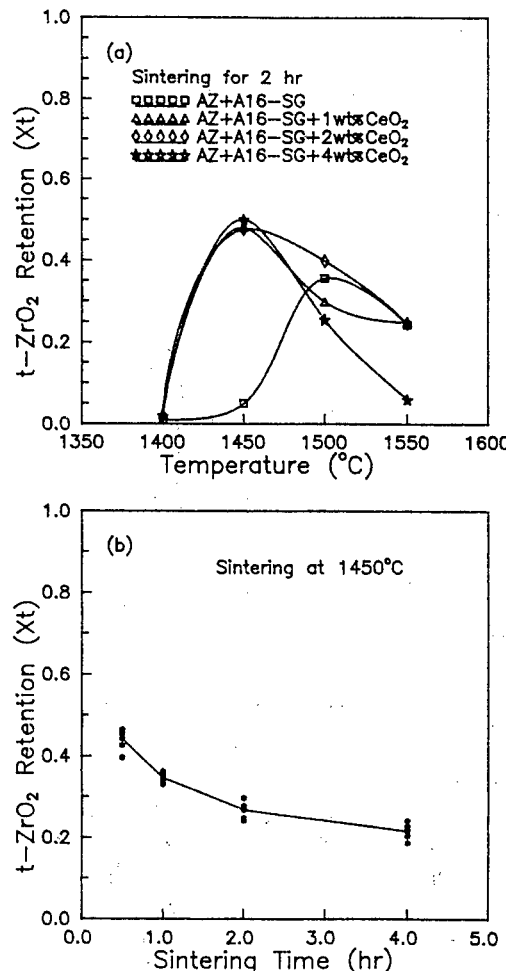


Fig. 2. Weight fraction of *t*-phase zirconia in reaction-sintered RS-(CeO₂)-ZMC as a function of (a) sintering temperature and (b) sintering time at 1450°C.

was also reported by Holmstrom *et al.*,¹⁸ who used Al_2O_3 , SiO_2 and ZrO_2 as raw materials to prepare a reaction-sintered ZMC. The zircon appeared at temperatures between 1450–1560°C when the ZrO_2 content was >15 vol%. In this study, the spray-dried powders were found to have phase transformation sequences similar to those of the powders prepared from grinding.

3.2 Densification of ZMCs

Dilatometric data of the ZMCs are shown in Fig. 3 plotted as a function of sintering temperature up to 1500°C. The changes in the dimensions of die-pressed GD-ZMC at temperatures around 300 and 550°C correspond to the sintering of extremely fine pores, in which the contained volatile species evaporate readily. Those nm size pores are densified at 600°C or lower temperatures, as reported previously.⁶ Testing at higher temperature unveils that the next densification of GD-ZMC starts at 900°C and exhibits the fastest densification rate at 1200°C. In comparison, DZ- or RS-ZMC specimens undergo less densification and at higher temperature starting from 1100°C. The densification rate of RS-ZMC can be enhanced by the addition of CeO_2 , as revealed by the densification curve of the RS(CeO_2)-ZMC in Fig. 3. The GD-ZMC shows a lower sintering temperature and more shrinkage than the other two ZMCs.

3.3 Microstructural evolution

Figure 4 shows SEM micrographs of polished and thermally-etched RS- and DZ-ZMC samples. The micrographs show dense and well reacted ZMCs, which have a relative density of >95% TD (theoretical density). The densified ZMCs show very stable microstructural features, most of the intergranular ZrO_2 being 3 μm in size (Fig. 5), as they are post-annealed at temperatures of 1400 to

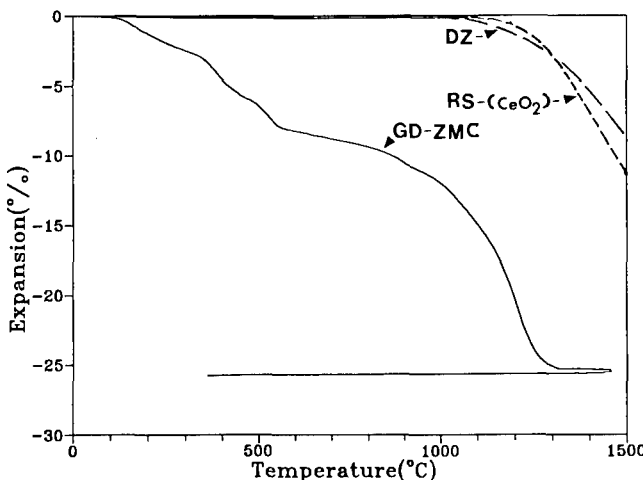


Fig. 3. Dilatometric curves of gel-derived (GD), reaction-sintering with 4 wt% CeO_2 (RS-(CeO_2)-) and DZ-ZMC specimens plotted as a function of temperature.

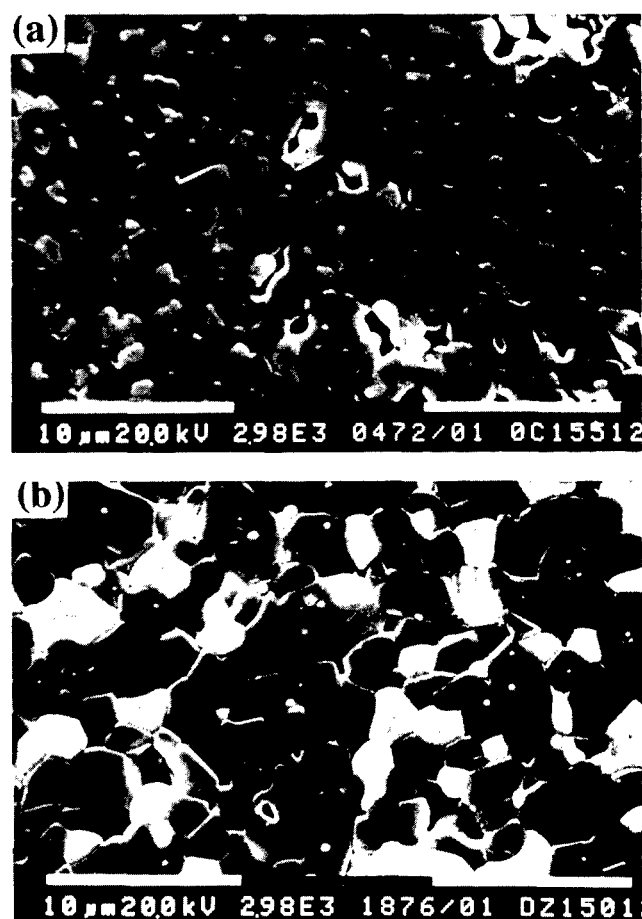


Fig. 4. SEM micrographs of (a) RS-ZMC without doping additive sintered at 1550°C for 12 h; (b) DZ-ZMC sintered at 1700°C for 30 min, then annealed at 1500°C for 12 h. The samples were all polished and thermally etched.

1600°C for up to 24 h. The grain sizes of mullite and ZrO_2 change within the range of experimental error, so that their grains are considered not to coarsen during the heat treatment. Some fine and submicrometre-sized zirconia grains are observed

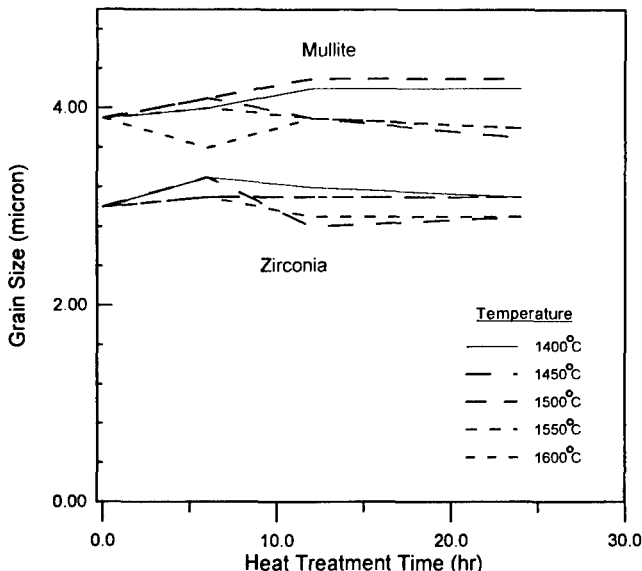


Fig. 5. Average grain sizes (μm) of intergranular zirconia and mullite grains of DZ-ZMC samples with 24 vol% ZrO_2 sintered at 1700°C for 30 min following various heat treatments.

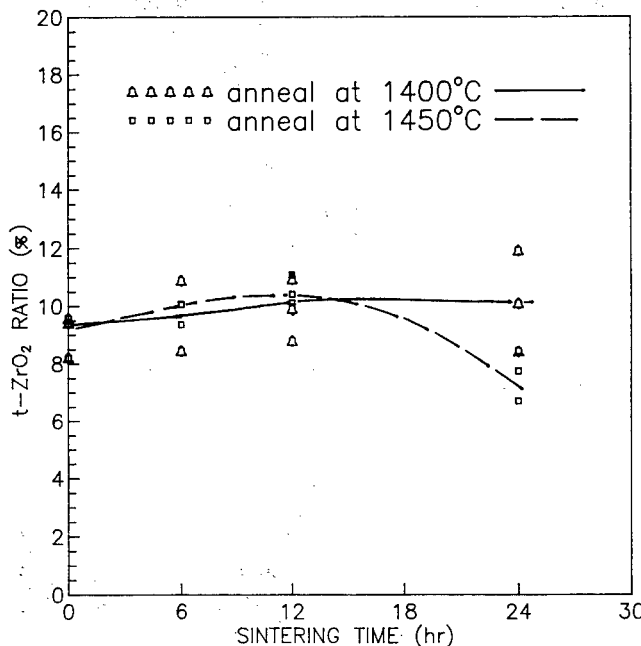


Fig. 6. Weight percentage of *t*-ZrO₂ phase to all ZrO₂ in DZ-ZMC vs. annealing period at 1400 or 1450°C.

that are nearly spherical and engulfed in mullite grains (Fig. 4). These intragranular ZrO₂ grains are the major part of *t*-phase ZrO₂ which is not transformable even following the same post-annealing at 1400 or 1450°C as long as 24 h (Fig. 6). The microstructures of the RB-ZMCs are stable at high temperatures (>1400°C). However, the reaction-sintering process for the preparation of ZMC cannot offer the microstructure with finer ZrO₂ and submicrometre-sized mullite grains.

GD-ZMC samples sintered at 1400, 1500 or 1600°C for 2 h were carefully polished and thermally-etched at the conditions 1350°C for 2 h, 1475°C or 1500°C for 30 min, respectively. The GD-ZMC sample sintered at 1600°C [Fig. 7(c)] has a similar microstructure to the previous RS-ZMCs. A small fraction of fine-grained zirconia is enclosed in the mullite grains, which are of the order of a few micrometres in size. Figures 7(b) and (c) clearly show that ZrO₂ grains are either intergranular or intragranular; the grain size of intergranular ZrO₂ increasing with sintering temperature. The intragranular ZrO₂ in the 1400°C and 2 h sintered sample is <0.1 μm. If sintered at 1600°C for 2 h, it grows to 2.3 μm and becomes intergranular. Increasing the size of ZrO₂ grains has been shown previously to instantly transform ZrO₂ to *m*-phase.⁵ The analysis of XRD patterns in Fig. 1 reveals several strong diffraction peaks of the *m*-phase in the pattern of the 1600°C sintered samples; however, the *m*-phase is rarely detected in the GD-ZMC processed at 1500°C or lower temperatures.

It is noted that the amount of intragranular ZrO₂ decreases with increasing sintering tempera-

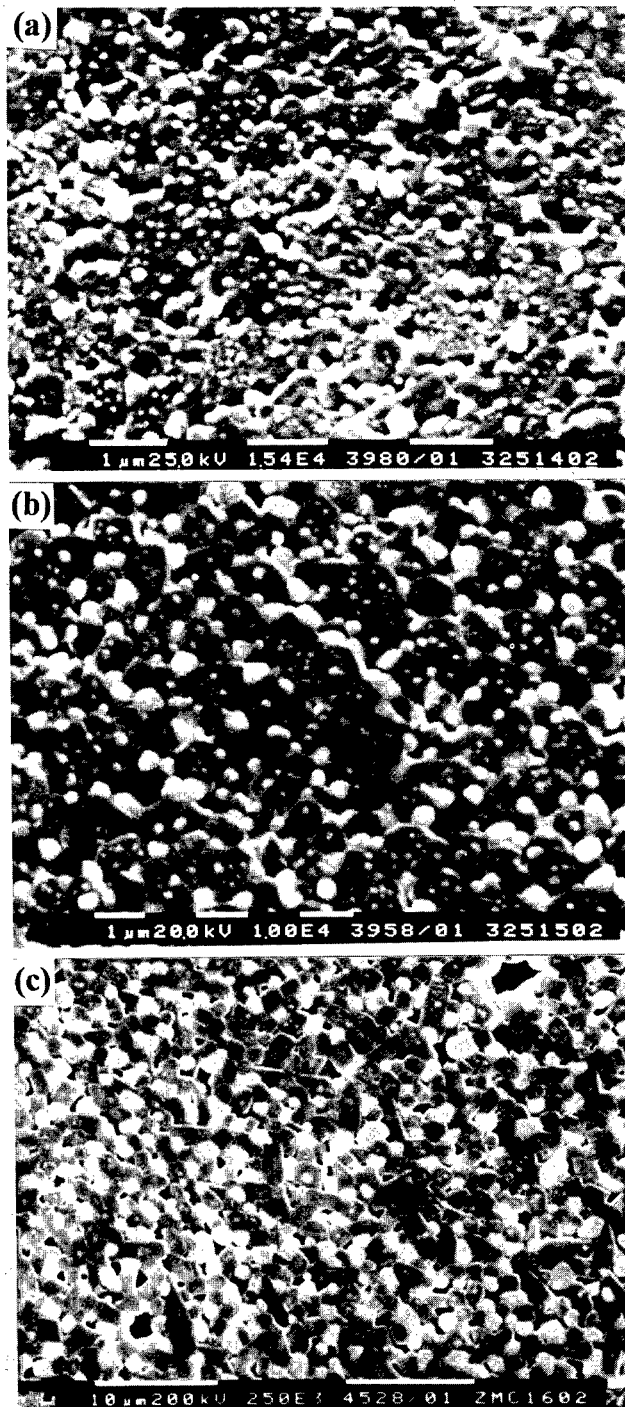


Fig. 7. SEM micrographs of polished and thermally etched GD-ZMC specimens sintered at (a) 1400°C, (b) 1500°C and (c) 1600°C for 2 h.

ture. Meanwhile, the average grain sizes of the intergranular ZrO₂ and matrix mullite grow larger. The grain size data, obtained from SEM and TEM micrographs, reveal that the intergranular ZrO₂ and matrix mullite grains scarcely grow from 1300 to 1500°C. However, both phases grow rapidly in size when the sintering temperature rises from 1500 to 1600°C.

TEM bright-field (BF) and centred-dark-field (CDF) micrographs of a GD-ZMC sample sintered at 1300°C for 2 h are shown in Fig. 8. The BF image shows that the ZrO₂ grains in dark

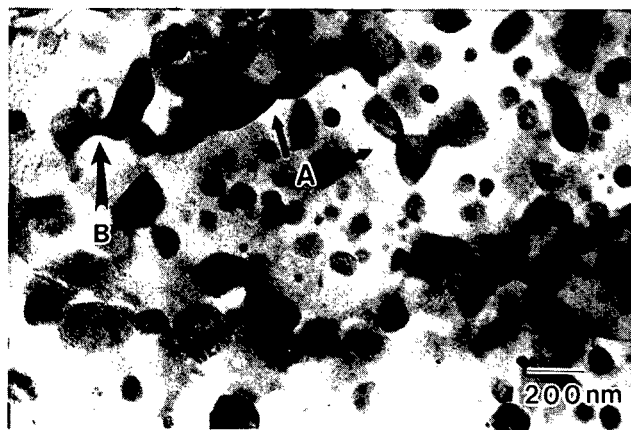


Fig. 8. TEM BF micrograph of GD-ZMC (with 24 vol% ZrO_2) sintered at 1300°C for 2 h.

contrast are uniformly dispersed within the mullite matrix. For sintering at higher temperature, a few large (0.3 μm or larger) intergranular ZrO_2 grains are occasionally found in the 1400°C sintered GD-ZMC. The twinning features of these grains (Fig. 9) are characteristic of *m*-phase ZrO_2 . The boundaries of each ZrO_2 lath in the large *m*- ZrO_2 grains exhibit interfacial microcracks, as denoted by arrows A and B in Fig. 9. In addition to the microcracks, strain fringes (arrow C) occurring next to large ZrO_2 grains are produced by thermal mismatch, and represent internal stresses.¹⁹ These features, i.e. microcracks and strain fringes, are possibly caused by the phase transformation of *t*- ZrO_2 to *m*- ZrO_2 and thermal expansion mismatch between mullite and ZrO_2 .

SEM and TEM analyses indicate that GD-ZMC has a smaller grain size than DZ- or RS-ZMC when sintering at the same temperature. For 24 vol% ZrO_2 samples, the average grain size of the intergranular ZrO_2 in GD-ZMC is 98 nm and the size of the mullite grains is 600 nm, which is

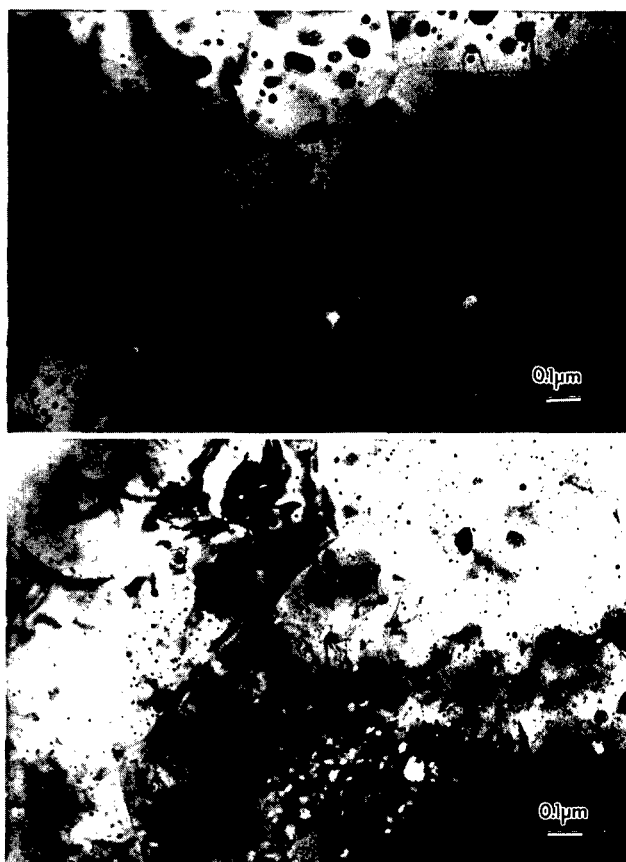


Fig. 10. TEM micrographs of GD-ZMC samples with (a) 9 vol% and (b) 3 vol% of ZrO_2 sintered at 1400°C for 2 h.

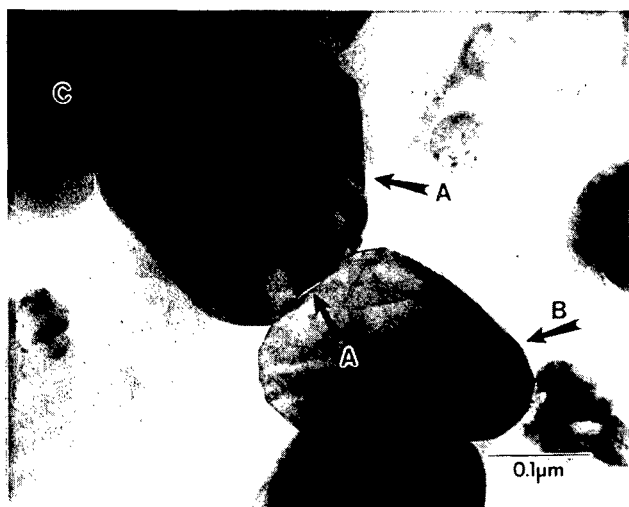


Fig. 9. Microcracks (A and B) and strain fringes (C) around two overgrowth *m*- ZrO_2 grains, imaged with TEM BF conditions. The GD-ZMC was sintered at 1400°C for 2 h.

several times less than the size of mullite grains measured in a pure aluminosilicate gel system.⁶ However, the mullite grows to a larger size if sintered at a higher temperature or the composition contains less ZrO_2 . Figure 10 presents TEM micrographs of GD-ZMC samples containing either 9 or 3 vol% ZrO_2 . Their ZrO_2 grains are mostly intragranular, and have an average grain size, 30 or 9 nm, which is several times less than that of GD-ZMC with 24 vol% ZrO_2 . The mullite grains in Fig. 10 grew to larger size, near 1 μm , and had straight grain boundaries. The dragging of mullite grain boundaries by ZrO_2 grains is apparently dependent upon the volume fraction and size of the ZrO_2 , which is similar to the behaviour reported by Lange and Hirlinger²⁰ and Prochazka *et al.*⁹ An illustrative example, i.e. the 1300°C-sintered GD-ZMC sample, is given in Fig. 8; the mullite grains exhibit crooked boundaries which trap several larger ZrO_2 grains (larger than the average size of intragranular ZrO_2). This demonstrates the likelihood that the growth of mullite grains is inhibited by ZrO_2 grains.

3.4 Grain growth of zirconia and mullite

The results of previous SEM and TEM micrographs are reported in Fig. 11, from which it can be seen that the grain sizes of mullite and ZrO_2 in

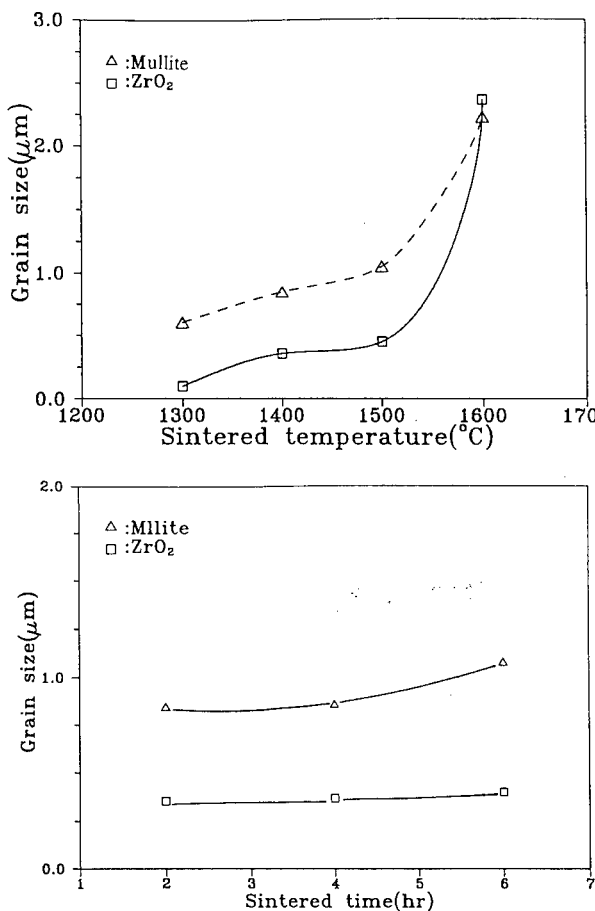


Fig. 11. Grain sizes of mullite and intergranular ZrO_2 in various GD-ZMC samples with 24 vol% ZrO_2 : (a) sintered at 1300 to 1600°C for 2 h; (b) sintered at 1400°C for 2 to 6 h.

various gel-derived ZMCs increase as the sintering temperature and sintering time increase. The application of Zener's relationship²¹ to the above cases illustrates the relationship between the mean grain radius (R) of the mullite matrix, the mean radius (r) of the ZrO_2 inclusions and the volume fraction (f) of the inclusion:

$$R = 4r/(3f) \quad (1)$$

This relationship provides a calculated R value for the 1400°C-sintered GD-ZMC that is comparable with the measured R (Table 2). However, the measured mullite grain size increases as the amount of zirconia decreases, and the zirconia inclusions are not all spherical and uniformly distributed (Fig. 10), leading to differences between measured and calculated R values. In addition, the relationship does not hold true for mullite grains in the GD-

Table 2. Calculated and measured mean radius (R) of mullite in GD-ZMC determined from the volume fraction (f) and grain radius (r) of zirconia phase

f	r (nm)	Calculated R (nm)	Measured R (nm)
0.24	49	272	300
0.09	15	222	~600
0.03	4.5	200	~750
Pure mullite ²²	—	—	~1250

ZMC sintered at temperatures $>1500^\circ\text{C}$ [Fig. 11(a)]. The growth of the mullite grains is accompanied by the coarsening of ZrO_2 inclusions. Two phases are growing inter-affected.

The second-phase ZrO_2 in the mullite matrix can ripen either by Ostwald ripening or by coalescence. The processes are well documented in a similar ceramic composite system,⁵ in which Ostwald ripening is driven by the variation of solubility of ZrO_2 with various particle sizes, and the composite grows larger ZrO_2 particles at the expense of smaller ZrO_2 particles. Coalescence of ZrO_2 particles occurs by the dragging of matrix mullite boundaries. The phenomenological evidence for the former process was a particle-free zone at matrix grain boundaries despite the fact that the diffusion rate along the mullite grain boundaries is faster than that in the mullite lattice. Alternatively, the latter case is particle clustering at grain boundaries. In this study, the micrographs revealed no grain boundary particle-free zone.

It was reported by Dinger *et al.*¹³ that a 2% solid solution of ZrO_2 near interface grain boundaries of mullite has been detected. They sintered the sample at 1570°C for 2 to 16 h. Mullite with an extensive amount of zirconia solid solution should be expected at temperature $>1570^\circ\text{C}$. But a quite controversial result was reported later by the same research group,¹⁰ that >20 wt% of ZrO_2 was found in the mullite grains. This seems *not to be the case* for our ZMC. Figure 12 shows a DZ-ZMC sample that has been sintered at 1700°C for 30 min. The zirconia grains either intergranularly or intragranularly are of size 50 nm to 3.5 μm , as shown in Fig. 12. Scanning transmission electron microscopy with micro-beam EDS analysis reveals that the ZMC has a non-detectable zirconia concentration in the mullite grains, as shown in the EDS spectra obtained from spots 2 and 4. That implies that *no zirconium forms a solid solution in mullite*. This finding is consistent with the recent measurement given by Moya²³ that <0.1 wt% zirconia solid solution is measured in zirconia-toughened mullite. This implies that ripening through grain boundary diffusion was not occurring in ZMC. Many intergranular ZrO_2 particles are actually in the form of clustering at triple grain boundaries, and exhibit larger grain size. We believe that such particle clustering is good evidence for coarsening by the coalescence of ZrO_2 . The zirconia in GD-ZMC is apparently ripening intergranularly while being treated above 1300°C in this experiment.

4 Summary

Three types of ZMC prepared either from gel

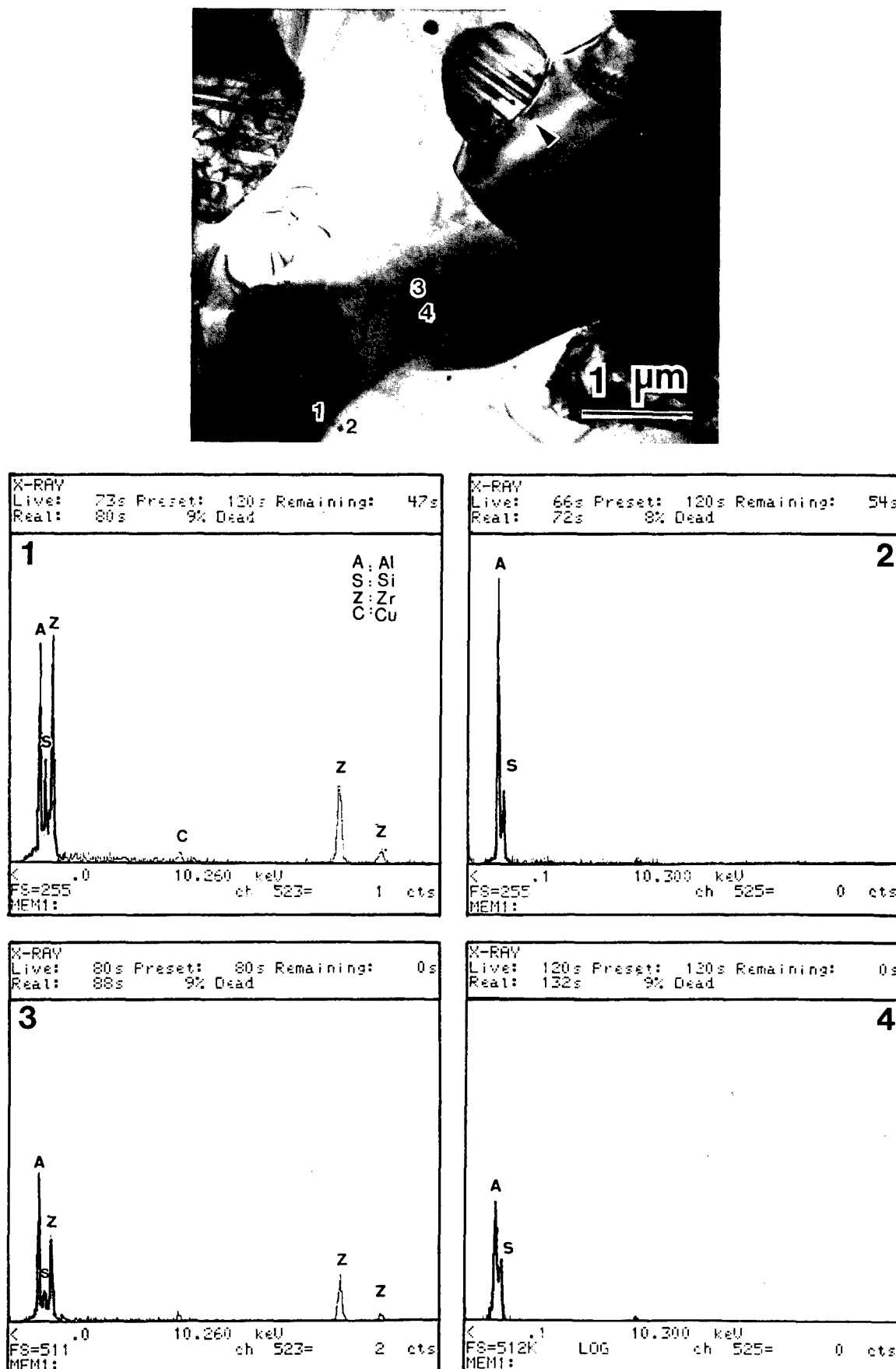


Fig. 12. TEM BF micrograph and EDX results of the intergranular and intragranular zirconia grains (1 and 3) and their mullite neighbourhood (2 and 4). The DZ-ZMC was sintered at 1700°C for 30 min.

precursors or solid powder mixtures were investigated in this study. Quantitative analysis on the micro-structural evolution of ZrO_2 and mullite

matrix grains was conducted, and correlated with the processing temperature and the content of ZrO_2 .

The solid solution of ZrO_2 in the mullite matrix was undetected and ZrO_2 particle-free zones were not observed in the GD- and DZ-ZMC samples, including the one with the longest heat treatment (1600°C for 24 h). This implies that the growth of ZrO_2 grains in mullite matrix cannot proceed via the process of Ostwald ripening. Grain clustering of intergranular ZrO_2 was observed, suggesting the coalescence of the ZrO_2 can occur at temperatures above 1300°C. Coarsening of intergranular and intragranular ZrO_2 particles in the mullite matrix is triggered by the mullite grain growth. The dragging of mullite grain boundaries by ZrO_2 is apparent for samples sintered at temperatures of 1400°C and above. The relationship between the grain growth of mullite and the volume fraction and size of ZrO_2 inclusions can be verified, but not well described by Zener's equation.

The advantages of the gel-process over reaction-sintering to prepare ZMCs with fine microstructure are clearly revealed in this work. A lower sintering temperature offers a higher densification rate and smaller grain size, thereby resulting in more *t*-phase zirconia and smaller grain size of mullite.

Acknowledgement

This work was supported by National Science Council in Taiwan under contract numbers NSC 81-0405-E002-25 and 82-0405-E002-245.

References

1. Claussen, N. & Ruhle, M., Design of transformation-toughened ceramics. In *Science and Technology of Zirconia III*, Advances in Ceramics, Vol. 24, eds S. Somiya, N. Yamamoto & H. Yanagida, The American Ceramics Society, Westerville, OH, 1988, p. 137.
2. Lange, F. F., Low thermal conductivity silicon nitride/zirconia composite ceramics. US Patent 4 640 902, 3 Feb. 1987.
3. Rincon, J. M. & Moya, J. S., Microstructural study of toughened ZrO_2 /mullite ceramic composition obtained by reaction sintering with TiO_2 . *Br. Ceram. Trans. J.*, **85** (1986) 201-6.
4. Garvie, R. C., Improved thermal shock resistant refractories from plasma-dissociated zircon. *J. Mater. Sci.*, **14** (1979) 817-22.
5. Kibbel, B. W. & Heuer, A. H., Ripening of inter- and intragranular ZrO_2 particles ZrO_2 -toughened Al_2O_3 . In *Science and Technology of Zirconia II*, Advances in Ceramics, Vol. 12, The American Ceramics Society, Westerville, OH, 1984, pp. 415-24.
6. Wei, W., Ph. D. Thesis, Case Western Reserve University, July 1986.
7. Wallace, J. S., Petzow, G. & Claussen, N., Microstructure and property development of in situ-reacted mullite- ZrO_2 composites. In *Science and Technology of Zirconia II*, Advances in Ceramics, Vol. 12, The American Ceramics Society, Westerville, OH, 1984, pp. 436-42.
8. Descamps, P., Sakaguchi, S., Poorteman, M. & Cambier, F., High-temperature characterization of reaction-sintered mullite-zirconia composites. *J. Am. Ceram. Soc.*, **74**(10) (1991) 2476-81.
9. Prochazka, S., Wallace, J. S. & Claussen, N., Microstructure of sintered mullite-zirconia composites. *J. Am. Ceram. Soc.*, **66** (1983) C125-7.
10. Miranzo, P., Pena, P., de Aza, S., Moya, J. S., Ma Rinco, J. & Thomas, G., TEM study of reaction-sintered zirconia-mullite composites with CaO and MgO additions. *J. Mater. Sci.*, **22** (1987) 2987-92.
11. Leriche, A., Mechanical properties and microstructures of mullite-zirconia composites. In *Mullite and Mullite Matrix Composites*. Ceramic Transactions, Vol. 6, eds S. Somiya, R. F. Davis & J. A. Pask, The American Ceramics Society, Westerville, OH, 1990, pp. 541-52.
12. Pena, P., Miranzo, P., Moya, J. S. & de Aza, S., Multi-component toughened ceramic materials obtained by reaction sintering, Part I-System ZrO_2 - Al_2O_3 - SiO_2 - CaO . *J. Mater. Sci.*, **20** (1985) 2011-22.
13. Dinger, T. R., Krishnan, K. M., Thomas, G., Osendi, M. I. & Moya, J. S., Investigation of ZrO_2 /mullite solid solution by energy dispersive X-ray spectroscopy and electron diffraction. *Acta. Metall.*, **32**(10) (1984) 1601-7.
14. Schneider, H., Transition metal distribution in mullite. In *Mullite and Mullite Matrix Composites*, Ceramic Transactions, Vol. 6, eds S. Somiya, R. F. Davis & J. A. Pask, The American Ceramics Society, Westerville, OH, 1990, pp. 135-58.
15. Ho, Y. F. & Wei, W. J., Reaction sintering of zirconia-mullite composites. In *Proc. 1992 Annual Conf. Chinese Soc. for Mater. Sci.*, 24-26 April 1992, pp. 470-1.
16. Low, I. M. & McPersonal, R., Crystallization of gel-derived mullite-zirconia composites. *J. Mater. Sci.*, **24** (1989) 951-8.
17. Shiga, H., Katayama, K., Tsunatori, H. & Ismail, G. M. U., Sol gel synthesis and sintering of oxide-doped mullite- ZrO_2 composite powders. *Ceram. Powder Sci. IV*, (1990) 457-62.
18. Holmstrom, M., Chartier, T. & Boch, P., Reaction-sintered ZrO_2 -mullite composites. *Mater. Sci. Eng.*, **A109** (1989) 105-9.
19. Mader, W., On the electron diffraction contrast caused by large inclusions. *Phil. Mag. A*, **55**(1) (1987) 59-83.
20. Lange, F. F. & Hirlinger, M. M., Hindrance of grain growth in Al_2O_3 by ZrO_2 inclusion. *J. Am. Ceram. Soc.*, **67**(3) (1984) 164-8.
21. Reed-Hill, R. E., *Physical Metallurgy Principles*, Van Nostrand, Princeton, NJ, 1973, p. 138.
22. Wei, W. & Halloran, J. W., Transformation kinetics of diphasic aluminosilicate gels. *J. Am. Ceram. Soc.*, **71**(7) (1988) 581-7.
23. Moya, J. S., Private communication, September 1994.

Mullite-Aluminosilicate Glassy Matrix Substrates Obtained by Reactive Coating

J. Requena,^a J. F. Bartolomé,^a J. S. Moya,^a S. de Aza,^a F. Guitian^b & G. Thomas^c

^aInstituto de Cerámica y Vidrio (CSIC), Arganda del Rey, Madrid, Spain

^bInstituto de Cerámica, Universidad de Santiago, Spain

^cDepartment of Materials Science and Mineral Engineering, University of California, Berkeley, CA 94720, USA

(Accepted 22 July 1995)

Abstract

Layered kaolinite-alumina composites have been obtained by a sequential slip casting technique. The interfacial reaction as well as the microstructure of different layers have been studied in laminates fired at 1650°C. The results are discussed on the basis of the SiO₂-Al₂O₃-K₂O equilibrium diagram. Taking into account these results, a new low-cost ceramic substrate for electronic applications — reinforced by mullite whiskers and with controlled closed porosity, low permittivity value ($\epsilon \approx 4$ at 1 MHz) and thermal expansion coefficient close to that of silicon ($3.8 \times 10^{-6} \text{ }^{\circ}\text{C}^{-1}$) — has been developed starting from conventional kaolinite powder.

Introduction

Recently, Liu *et al.*^{1,2} have studied mullite formation in the alumina-kaolinite system. By X-ray diffraction (XRD) and transmission electron microscopy (TEM) analysis, they have clearly shown the formation of monosized primary mullite in plate-like kaolinite at 1300°C. At higher temperatures bimodal mullite crystals were detected, indicating formation of secondary mullite by nucleation and primary mullite growth. This secondary mullite is formed mainly by a solution-precipitation mechanism. Both types of mullite have a different composition and different morphologies. Primary mullite is needle-like with [001] being the crystallographic growth direction.³ The secondary mullite has a higher content of alumina and no preferential growth direction.

In the present work kaolinite has been spatially separated from alumina by means of a layered structure obtained by sequential slip casting. In this configuration, the interfacial reaction, microstructure development into the layers and morphological

aspects of the fired composites have been studied. On the basis of the results obtained, a new substrate with low permittivity value is proposed for electronic applications.

Experimental

The following starting materials have been used: (1) high-purity kaolinite (Caobar S.A., Spain) with an average particle size of 3 μm and a specific surface area of 9.2 $\text{m}^2 \text{ g}^{-1}$, with mica and quartz as minor constituents; and (2) commercial submicronic alumina (Alcoa CT 3000 SG) with an average particle size of 0.5 μm and a specific surface area of 8.0 $\text{m}^2 \text{ g}^{-1}$. The results of wet chemical analysis (wt%) of both materials are (1) Caobar kaolinite: SiO₂ (48.4), Al₂O₃ (37.0), Fe₂O₃ (0.25), TiO₂ (0.002), Na₂O (0.13), K₂O (0.46), CaO (0.31), MgO (0.05) and (2) α -alumina: Al₂O₃ (99.2), Na₂O (0.12), SiO₂ (0.08), MgO (0.1) and Fe₂O₃ (0.03). Aqueous suspensions were prepared of alumina and kaolinite, using an alkali-free organic polyelectrolyte in the case of alumina and sodium silicate and sodium carbonate in the case of kaolinite. Both suspensions were dispersed in alumina ball mills for 4 h. The suspensions showed Newtonian flow behaviour and low viscosity values (i.e. 11 and 15 mPa s^{-1} for Al₂O₃ and kaolinite, respectively).

Multilayer alumina-kaolinite composites were obtained by alternately casting alumina and kaolinite suspensions in plaster of Paris moulds according to the flow chart shown in Fig. 1.

Microstructural analysis was performed on polished cross-sections with and without chemical etching (10% HF solution) using optical microscopy (Zeiss Axiophot, Germany) with an image analyser, and scanning electron microscopy (SEM) with EDS and WDS (Jeol JMS-6400, Japan).

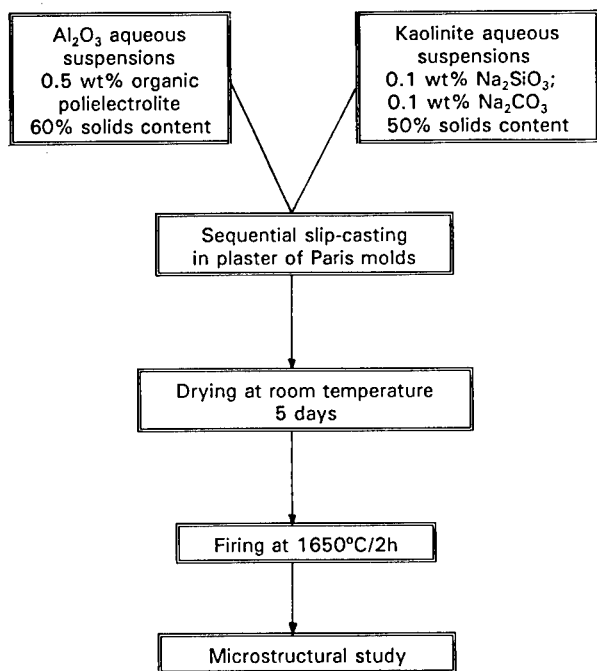


Fig. 1. Processing flow chart for layered composites.

Results and Discussion

Layered composites

The cross-section of a layered composite after firing is shown in Fig. 2. As observed, the morphology of the laminate is built up of dense alumina layers and porous aluminosilicate (original kaolinite) layers. Cracks due to the thermal expansion mismatch are visible.

SEM micrographs of polished and chemically etched surfaces are shown in Fig. 3. It is seen that the interface is formed by a $\sim 5 \mu\text{m}$ layer of secondary mullite which penetrates into the alumina

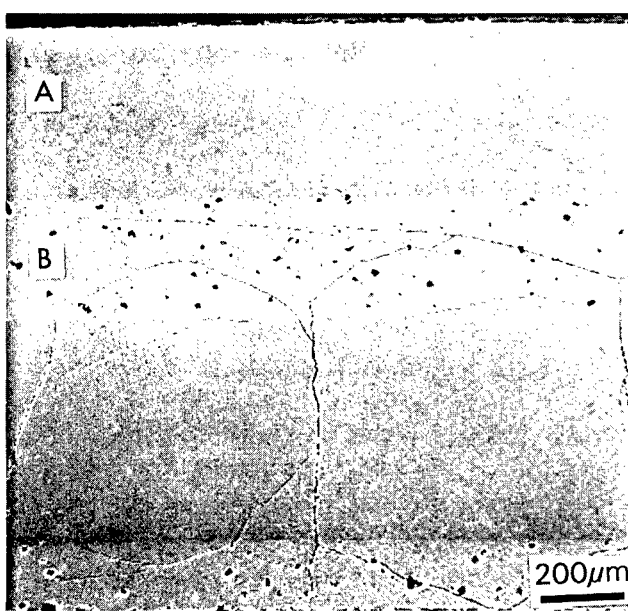


Fig. 2. SEM micrographs of the alumina-kaolinite multilayer composite fired at 1650°C: (A) alumina layer; (B) original kaolinite layer.

Table 1. Quantitative microprobe (WDX) analysis (wt%)

	Al ₂ O ₃	SiO ₂	K ₂ O
Primary mullite	72.0 \pm 0.5	26.6 \pm 0.3	—
Secondary mullite	73.5 \pm 0.3	27.8 \pm 0.3	—
Glassy matrix*	26.4 \pm 0.7	73.88 \pm 0.56	1.47 \pm 0.05

*CaO and Fe₂O₃ impurities have not been considered.

layer, entrapping alumina grains. The original kaolinite layer transforms into a silica-rich glassy matrix containing aluminium, potassium, calcium and iron, as can be seen in the corresponding EDS pattern, and prismatic primary mullite crystals. EDS spectra corresponding to primary and secondary mullite are also shown.

This particular microstructure can be explained by means of the SiO₂-Al₂O₃-K₂O equilibrium phase diagram.⁴ In Fig. 4 the silica-alumina-rich portion of this diagram is plotted. The theoretical composition of metakaolinite as well as the composition of the calcined Caobar kaolinite have also been plotted. In this plot only the K₂O impurity has been taken into account. According to this equilibrium diagram, on heating, Caobar kaolinite will develop a liquid phase at the eutectic temperature (985°C) which corresponds to the invariant point of the subsystem silica-mullite-potash feldspar. As the temperature increases, the composition of the glassy phase will move along the cristobalite-mullite boundary until reaching a temperature close to 1470°C. Then the cristobalite disappears and the liquid phase moves away from the binary boundary following the tie-line which joins the Caobar kaolinite composition with the silica-rich mullite composition, until reaching the isothermal line corresponding to 1650°C, the final firing temperature. This liquid is in equilibrium with primary mullite. In a subsequent step this liquid will react with the alumina layer, giving alumina saturated with secondary mullite.

Quantitative microprobe analysis (WDS) of the primary mullite, secondary mullite and glassy matrix corresponding to the layered composites fired at 1650°C is reported in Table 1. As can be observed, these data are in good agreement with the previous synopsis.

Layered substrates for electronics

One basic requirement for electronic ceramics that support high frequency circuitry,⁵ is to have a low permittivity value (ϵ), to provide short signal transmission delay time (t_d):

$$t_d = \frac{\sqrt{\epsilon s}}{c}$$

where s = signal pass length and c = velocity of light.

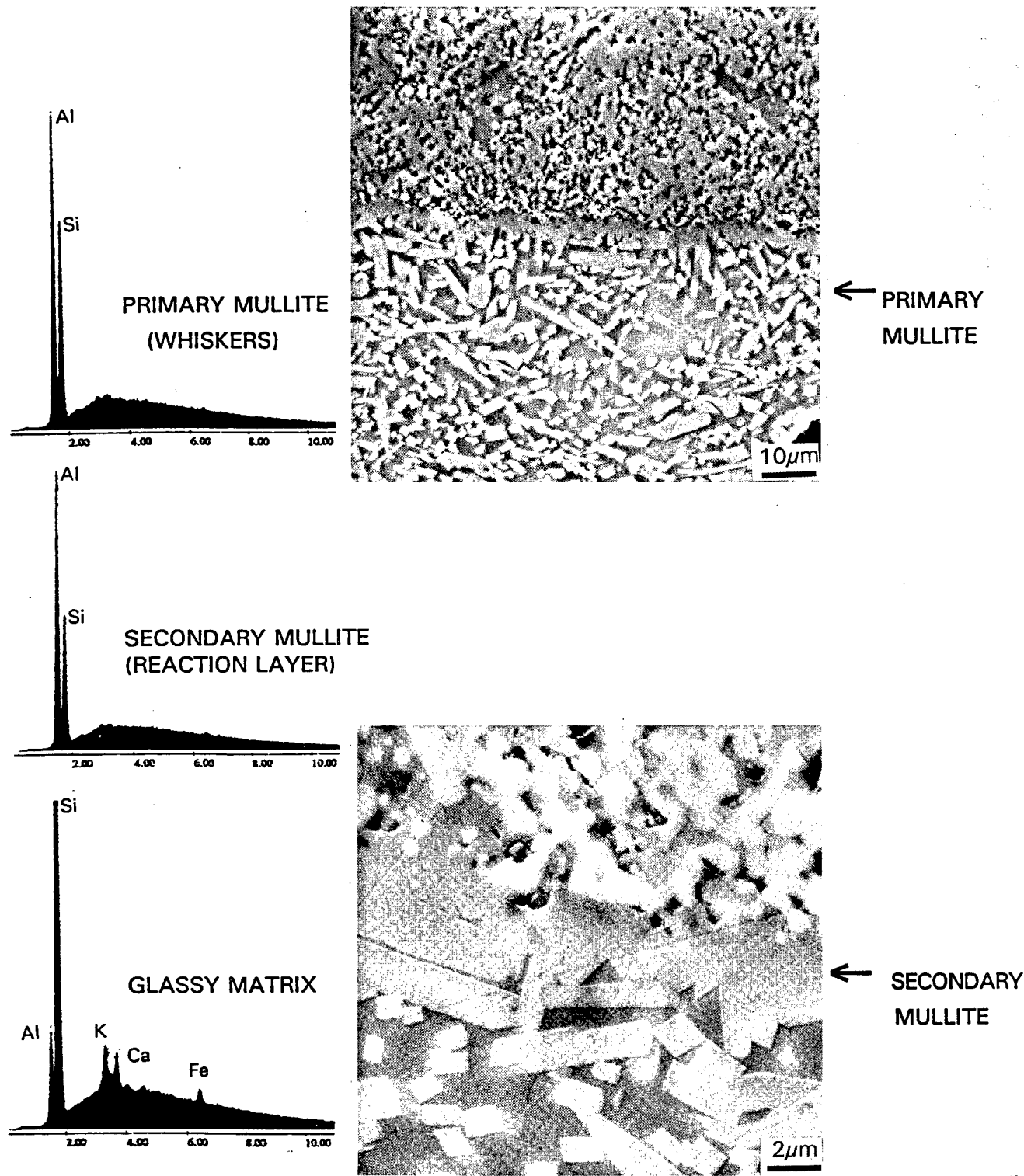


Fig. 3. SEM micrograph of polished and HF-etched cross-section of the alumina-kaolinite layered composite. The EDS spectra corresponding to primary mullite, secondary mullite and glassy matrix are also shown.

The major problems for large-scale production of mullite silica glass substrate are:^{6,7}

- high cost of starting materials;
- porosity control;
- formation of cristobalite;
- low mechanical properties.

Taking into account the results obtained in the layered composites as previously reported, it should be possible to design a silicoaluminate

glassy matrix reinforced with mullite whiskers and with controlled porosity starting from low-cost kaolinite raw materials.

The idea consists of coating a prefired kaolinite block with a sufficiently thin layer of alumina in order to develop, during final firing (at 1650°C), an electrical insulator layer of secondary mullite, avoiding the cracks formed because of the thermal expansion mismatch between alumina and silicoaluminate layers (Fig. 2).

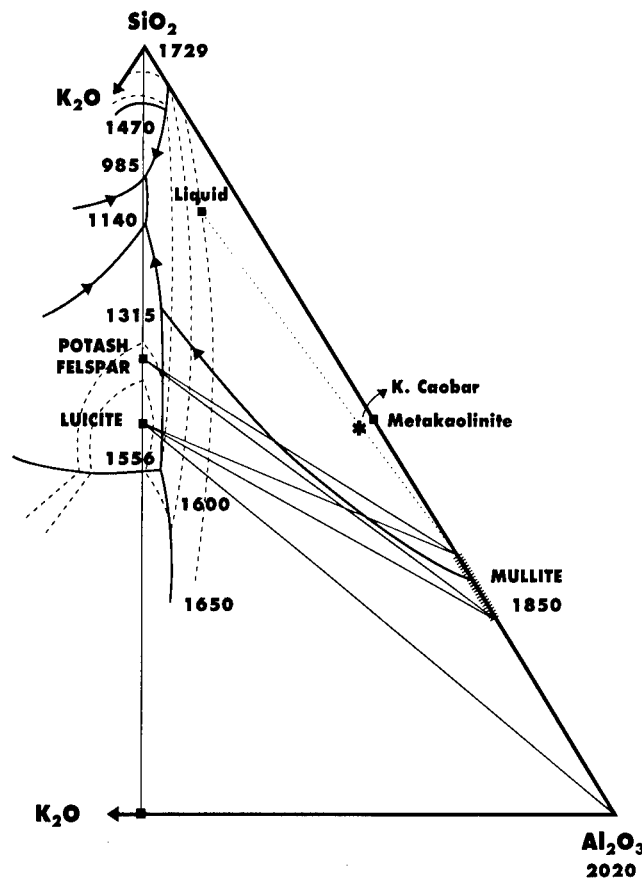


Fig. 4. The SiO_2 – Al_2O_3 – K_2O equilibrium diagram.

According to the equilibrium diagram plotted in Fig. 4 as well as the time–temperature–transformation curves reported by Liu *et al.*² for Caobar kaolinite (Fig. 5), if firing is made at $T > 1470^\circ\text{C}$ no cristobalite is present. In this case only mullite and glassy phases are formed, as has been observed in the present case. In this sense, a processing-flow chart, as shown schematically in Fig. 6, has been followed.

Figure 7 shows an optical micrograph of the cross-section of the fired substrate. As observed, closed pores $< 40 \mu\text{m}$ are present. The total porosity has been determined by image analysis on micrographs and found to be $8 \pm 1 \text{ vol\%}$.

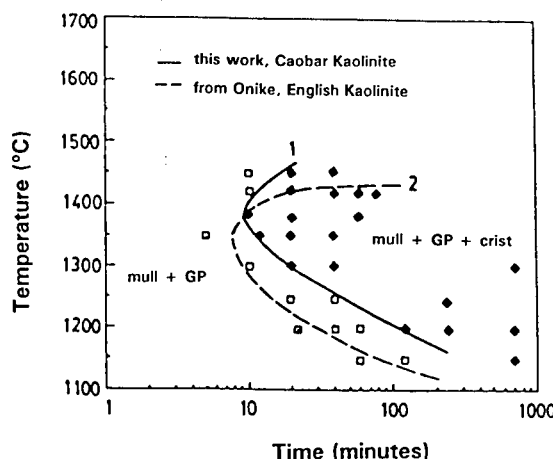


Fig. 5. Time–temperature–transformation curves of cristobalite nucleation for Caobar Kaolinite and English Kaolinite.

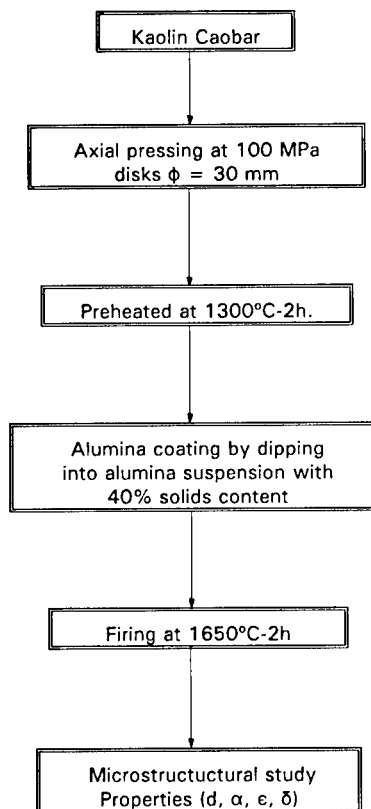


Fig. 6. Substrates processing flow chart.

The micrograph of an HF etched polished cross-section shows the presence of $5 \mu\text{m}$ thick coating of a secondary mullite layer and a bulk formed by continuous glassy matrix reinforced by primary mullite whiskers. These are of length $20 \pm 5 \mu\text{m}$ and width $2 \pm 0.5 \mu\text{m}$, having an aspect ratio of 10 ± 2 (Fig. 8). The content of the primary mullite needle-like single crystals has been determined by quantitative XRD analysis and found to be 60 wt%. These data are in agreement with that calculated from Fig. 4 at 1650°C ($60 \pm 5\%$).

The specific gravity of the fired substrate has

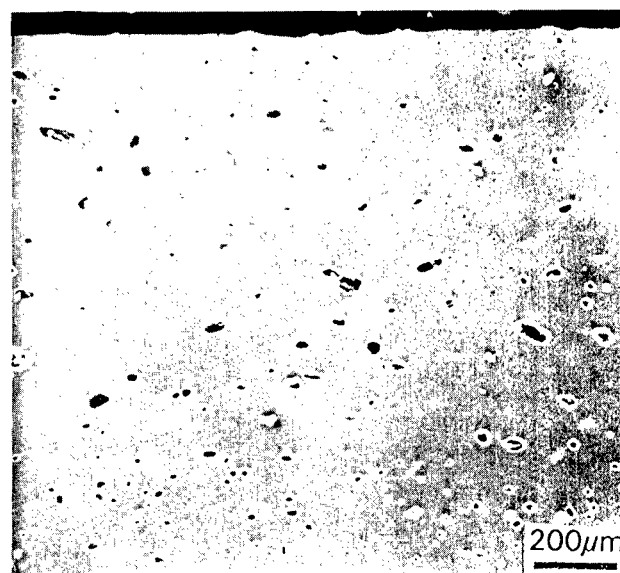


Fig. 7. Optical micrograph of the cross-section of a substrate, showing closed porosity.

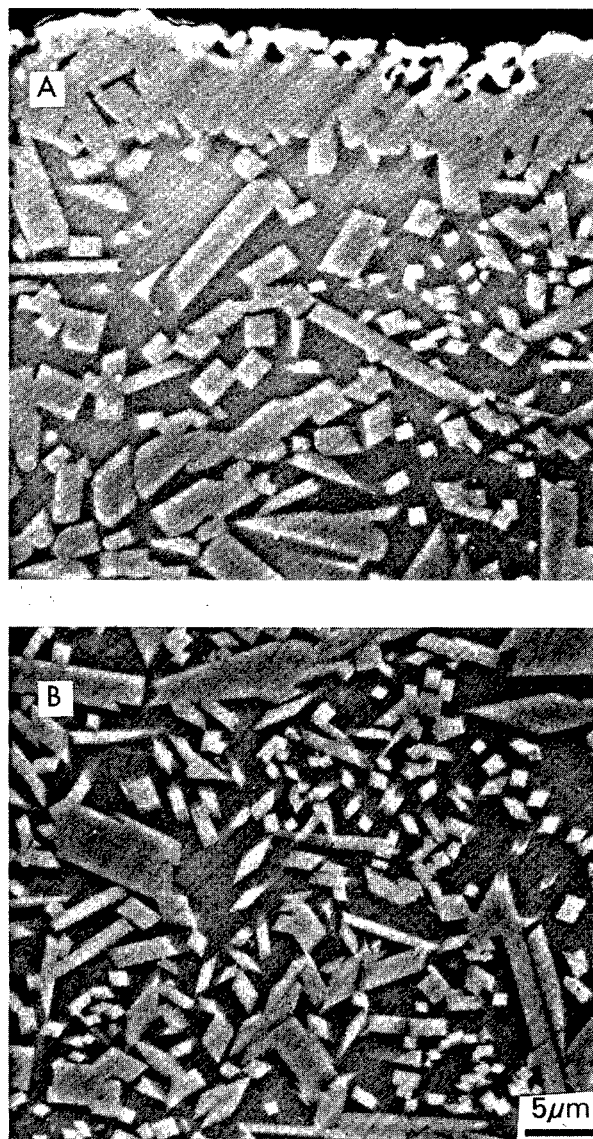


Fig. 8. SEM micrographs of the cross-section of a substrate fired at 1650°C: (A) secondary mullite top layer; (B) glassy matrix reinforced with primary mullite whiskers.

been determined using Archimedes' method in Hg and has been found to be $2.75 \pm 0.06 \text{ g cm}^{-3}$.

The thermal expansion of the substrate has been determined by dilatometry using a sample of 1 cm length, giving $\alpha_{20-500} = 3.8 \times 10^{-6} \text{ }^{\circ}\text{C}^{-1}$. As can be observed in Fig. 9, the thermal expansion of the substrate matches that of silicon in the temperature interval ranging from 20 to 600°C.

The dielectric constant and dielectric loss were determined on discs 25 mm in diameter and 2 mm height with parallel flat surfaces coated by Ag (70 wt%) + Pd (30 wt%), the discs being heated at 200°C for 30 min prior to measurements. A Hewlett-Packard 4192 ALF impedance analyser at 1 kHz to 10 MHz at 0.1–0.2 mV was used. The results obtained were: $\epsilon = 4$ at 1 MHz; $\delta = 0.01$ at 1 MHz.

Tummala⁸ has pointed out that for high performance ceramic packaging, the two main requirements are: (i) less interconnect delay and (ii) larger chip. To meet the first requirement ceramic

SECONDARY MULLITE LAYER

PRIMARY MULLITE WHISKERS REINFORCE GLASSY MATRIX

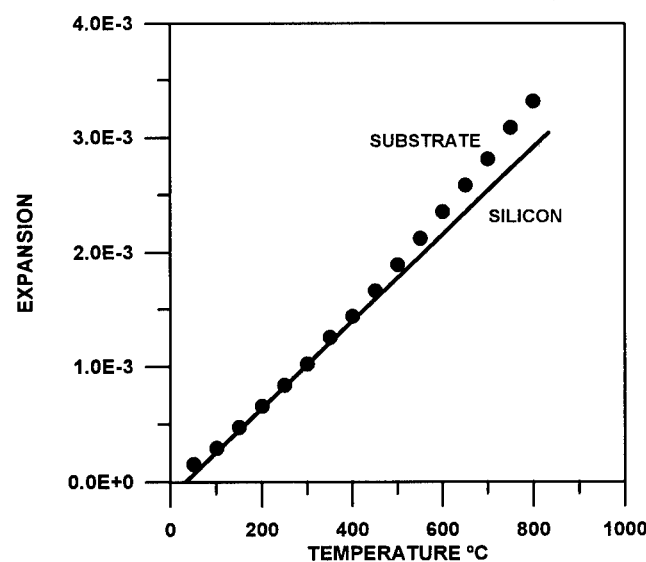


Fig. 9. Thermal expansion curve of the substrate. That of silicon is also shown for comparison purposes.

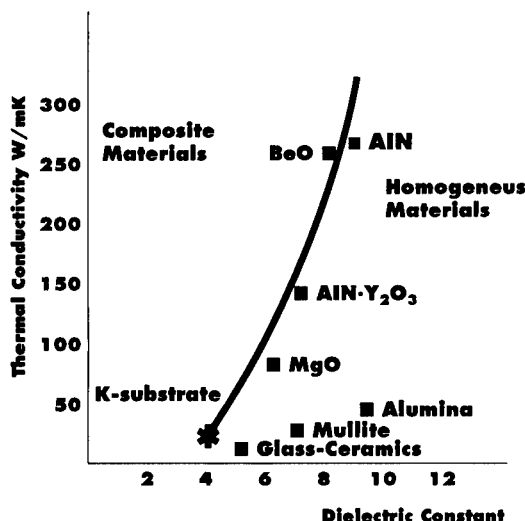


Fig. 10. Thermal conductivity versus dielectric constant for several materials used in electronic packaging. The value corresponding to the kaolinite-based substrate is also plotted (*).

substrates with lower dielectric constant and higher packaging density are necessary. The second one is met by decreasing the thermal expansion mismatch between substrate and silicon.

The kaolinite substrate prepared as described in this paper, has the lowest permittivity value obtained to date (Fig. 10) and a thermal expansion very close to that of silicon (Fig. 9). Because of these facts and the low cost of the starting raw materials, this substrate may be of potential interest for the electric and electronic industries.

Conclusions

Layered kaolinite–alumina ceramics obtained by

sequential slip casting have proved to be a useful model to design new ceramic materials.

A new low-cost ceramic substrate for electronic applications, reinforced by mullite whiskers and with controlled closed porosity, low permittivity value ($\epsilon \approx 4$ at 1 MHz) and thermal expansion coefficient close to that of silicon ($3.8 \times 10^{-6} \text{ }^{\circ}\text{C}^{-1}$), has been developed starting from conventional kaolinite powder.

Acknowledgement

This work was supported by CYCIT Spain under contract MAT-94-0974.

References

1. Lui, K. C., Thomas, G., Caballero, A., Moya, J. S. & de Aza, S., Mullite formation in kaolinite– Al_2O_3 . *Acta Metall. Mater.*, **42**(2) (1994) 489–95.
2. Lui, K. C., Thomas, G., Caballero, A., Moya, J. S. & de Aza, S., Time–temperature–transformation curves for kaolinite– α -alumina. *J. Am. Ceram. Soc.*, **77** (1994) 1545–52.
3. Katsuki, H., Furuta, S., Ichinose, H. & Nakao, H., Preparation and some properties of porous ceramics sheet composed of needle-like mullite. *J. Ceram. Soc. Jpn. Int.*, **96** (1988) 1056–61.
4. Leving, E. M., Robbins, C. R. H. & McMurdie, H. F., in *Phase Diagrams for Ceramists*, ed. R. K. Reser, American Ceramics Society, Columbus, OH, 1964, Fig 407.
5. Tummala, R. R., & Rymaszewski, E. J., *Microelectronics Packaging Handbook*, Van Nostrand Reinhold, New York, 1989.
6. Kanzaki, S., Ohashi, M. & Tabata, H., Mullite ceramics for insulating substrates. *Ceram. Trans.*, **6** (1990) 389–99.
7. Giess, E. A., Roldan, J. M., Bailey, Ph. J. & Goo, E., Microstructure and dielectric properties of mullite ceramics. *Ceram. Trans.*, **15** (1990) 167–77.
8. Tummala, R. R., Ceramics in microelectronic packaging. *Am. Ceram. Soc. Bull.* **64**(4) (1988) 752–8.

Fabrication of Low-to-Zero Shrinkage Reaction-Bonded Mullite Composites

Dietmar Holz,^a Sonja Pagel,^a Chris Bowen,^b Suxing Wu^c & Nils Claussen^d

^aPhilips WEB, 22419 Hamburg, Germany

^bUniversity of Leeds, School of Materials, Leeds, UK

^cLehigh University, Materials Research Center, Bethlehem, USA

^dTechnische Universität Hamburg-Harburg, Advanced Ceramics Group, 21071 Hamburg, Germany

(Accepted 22 July 1995)

Abstract

The technology of reaction bonding Al_2O_3 (RBAO) can be modified by the use of Si-containing additives to yield low-to-zero shrinkage mullite composites. In the present work, SiC particles were added to the Al/Al_2O_3 precursor mixture. During air heat-treatment, first Al oxidizes to Al_2O_3 at 300–900°C, thereafter SiC converts to SiO_2 (900–1200°C). Both phases form mullite ($3Al_2O_3 \cdot SiO_2$) at temperatures >1400°C. Depending on the hold time at 900–1200°C, the extent of SiC oxidation, hence the ratio of mullite to dispersed SiC can be controlled. Since both oxidation reactions and the mullitization are associated with volume expansions, the sintering shrinkage can either be fully or partially compensated for. The process parameters amount of Al and SiC, green density and degree of SiC oxidation can be utilized to fabricate low-to-zero shrinkage mullite composites.

1 Introduction

In recent years, the development of high-strength mullite for engineering and electronic applications has become a new area of ceramic research. This is due to many advantageous properties like high melting point, good creep resistance, low thermal expansion, low dielectric constant, and good corrosion resistance.¹ However, the mechanical properties of plain mullite are low (bending strength: ≈250 MPa, fracture toughness: ≈2.5 MPa m^{1/2}) when compared to other ceramics.² Therefore, several mullite composites have been fabricated to improve the mechanical properties, e.g. by adding ZrO_2 as well as platelets, whisker, or fibers.^{3–7} The

fabrication of these improved mullite composites often requires new processing routes, such as sol–gel techniques combined with hot pressing, which limits the shape and size of the product and reduces the economy of the process.

The Reaction Bonding of Aluminum Oxide (RBAO) technology,^{8–10} provides a new processing route to fabricate low-to-zero shrinkage high-strength mullite composites.^{11–13} The plain RBAO process, which results in a product consisting only of Al_2O_3 , starts from intensively milled Al/Al_2O_3 precursor powder mixtures. Heating powder compacts in oxidizing atmosphere (usually air) up to temperatures of ~900°C results in complete oxidation of Al to Al_2O_3 . Due to very small ‘new’ Al_2O_3 crystallites, sintering starts at ~1100°C. The Al oxidation results in a 28% volume expansion partially compensating for the sintering shrinkage. Therefore, low shrinkage (5–15%) Al_2O_3 ceramics are readily fabricated. In order to further reduce the shrinkage even to zero, the RBAO process can be modified in various ways by incorporating other metal or ceramic additives that exhibit volume expansions on oxidation which further compensate for the sintering shrinkage.

In this work, SiC additions are utilized to form mullite ceramics. Because of the large volume expansion associated with both the oxidation of SiC to SiO_2 (108%) and with the mullite ($3Al_2O_3 \cdot SiO_2$) formation (4.2%), the sintering shrinkage is effectively compensated. In this respect, 26 vol.% in the precursor powder composition is necessary to fabricate pure mullite.¹¹ Therefore, the heat treatment should be set ensuring complete oxidation of SiC. If the heat treatment is selected such that the SiC particles are not completely oxidized, various mullite/ Al_2O_3 /SiC composites result. The aim of this paper is to describe and to discuss the formation of low-to-zero shrinkage mullite composites obtained by the RBAO technology.

Dedicated to Professor Heinz Mecking on the occasion of his 65th birthday.

2 Experimental

Powder compositions and sources of raw materials used are listed in Table 1. The notations for the compositions contain the SiC content in vol.% in the precursor composition and a small letter defining the SiC particle size (c for coarse and f for fine). The powder mixtures were attrition-milled in acetone for 7 h with TZP (3Y-ZrO₂) milling media. The amount of ZrO₂ introduced into the powder was estimated from qualitative phase analyses of the reaction-bonded samples. After milling, the powder was dried and sieved with a 200 µm mesh. Green bodies were produced by uniaxial pressing at 50 MPa followed by cold isostatic compaction (CIP) at pressures of 300 and 900 MPa. Oxidation and sintering was carried out in a box furnace in air using the heating cycle shown in Fig. 1. At 1150°C, a dwell time of 15 h (coarse SiC) and 10 h (fine SiC) was selected to ensure complete oxidation of SiC. This temperature was chosen because sintering is not yet significant, hence the powder compacts still contain open porosity. Therefore, the carbon monoxide produced by the SiC oxidation can diffuse outwards. Sintering was carried out at 1550°C for 1 h. The density of the final products was measured by the Archimedes method. Reaction products were identified by X-ray diffraction (XRD). Qualitative phase compositions were determined by Rietveld analysis. Microstructures were investigated by transmission electron microscopy (TEM).

Table 1. RBAO precursor powder compositions

	SC30c	SC30f	SC45f
¹ Al	40	40	40
² Al ₂ O ₃	30	30	15
SiC	³ 30	⁴ 30	⁴ 45

¹Alcan 105, <50 µm, globular, Alcan International, Canada.

²Ceralox HPA-0.5, ≈0.8 µm, Condea Chemie GmbH, Brunsbüttel, Germany.

³F1000, 2.5–3.5 µm, Norton AS, Lillesand, Norway.

⁴Ultra-fine, 0.27 µm, Ibiden Co., Ogaki, Japan.

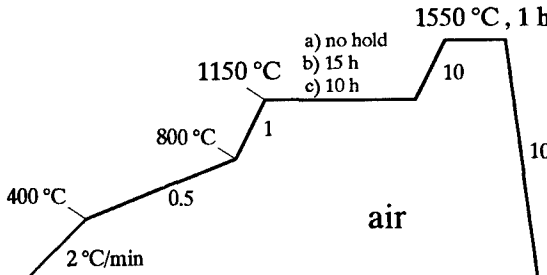


Fig. 1. Heat treatment cycles: (a) without and (b, c) with oxidation holds for SiC.

3 Results and Discussion

3.1 Phase development

The XRD diagrams (Fig. 2) of composition SC30c at 1150°C without and with 15 h hold show that, for both temperature cycles, all Al has been completely oxidized, and that a large amount of ZrO₂ is introduced (12–15%) during milling. It originates from wear debris of the TZP balls and discs. Composition SC30f (fine SiC) contains somewhat less ZrO₂ (~10%) which is due to the reduced aggressiveness of the smaller SiC particles. When using coarse SiC, it is impossible to get complete oxidation, even after 15 h hold, while with finer SiC (SC30f), even 10 h at 1150°C are sufficient. The oxidation product is amorphous SiO₂ not detectable by XRD. It has been shown previously¹¹ that crystalline SiO₂ (α -cristobalite) does not form until ~1200°C.

Phase compositions of samples SC30c and SC30f after sintering at 1550°C for 1 h are shown in Fig. 3. Sample SC30c without holding at 1150°C (SC30c1550/0, left bar) consists of mullite/Al₂O₃/SiC/

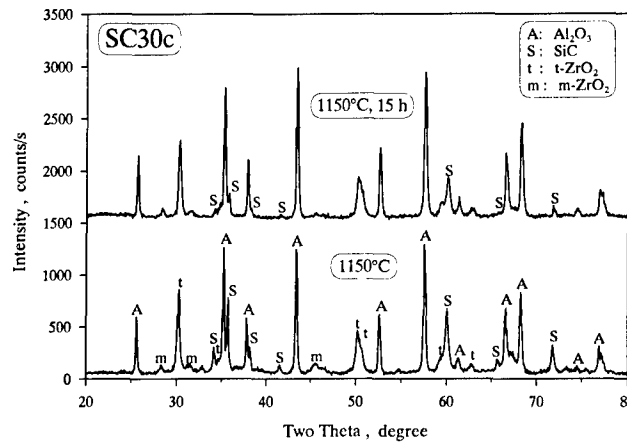


Fig. 2. XRD diagrams of sample SC30c without and with hold for 15 h at 1150°C.

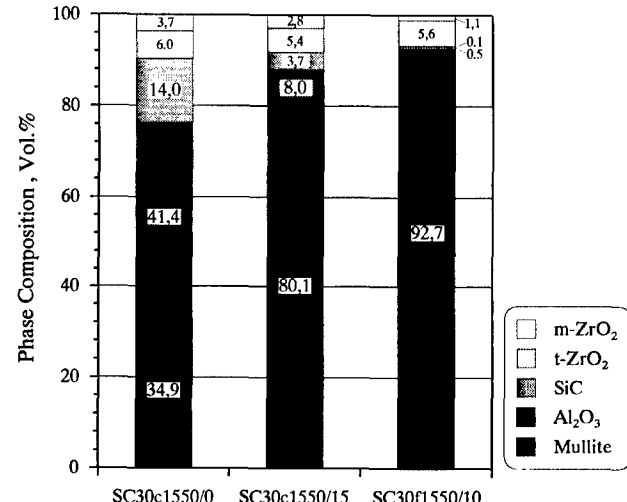


Fig. 3. Phase compositions of samples SC30c and SC30f after sintering at 1550°C for 1 h.

$t\text{-ZrO}_2/m\text{-ZrO}_2$ (34.9/41.4/14.0/6.0/3.7 vol.%). After holding at 1150°C for 15 h (SC30c1550/15) before sintering, the sample still contains mullite/ $\text{Al}_2\text{O}_3/\text{SiC}/t\text{-ZrO}_2/m\text{-ZrO}_2$ (80.1/8.0/3.7/5.4/2.8 vol.%). Due to the higher degree of SiC oxidation though, the amount of mullite is strongly increased and correspondingly the content of Al_2O_3 and SiC is lower. When coarse SiC is used neither dwell time nor heat-up time to the sintering temperature (heating rate is 10°C/min) are sufficient to allow complete SiC oxidation. However, sample SC30f after holding at 1150°C for 10 h before sintering (SC30f1550/10, Fig. 3 right bar) consists mainly of mullite and ZrO_2 (92.7/6.7 vol.%). Only traces of Al_2O_3 and SiC are left (<0.5 / <0.1 vol.%).

It is interesting to note that, at temperatures >1400°C in air, samples with non-completely oxidized SiC always have a white outer layer consisting of mullite and Zircon (ZrSiO_4). This effect is attributed to preferred densification in the surface region due to oxidation of SiC and mullite formation. These reactions are associated with a volume increase enhancing surface layer densification and thus hindering oxygen diffusion inwards thereby preventing further oxidation in the interior. The formation of Zircon can be explained by an excess of SiC leading to a reaction of SiO_2 with ZrO_2 . With progressing densification, the trapped gas inside of the sample, due to further SiC oxidation, diffuses outwards resulting in a higher porosity of the outer layer which remains even after sintering. Prevention of this layer can be achieved by initially oxidizing the SiC and Al in air and sintering the body in an inert atmosphere.

3.2 Microstructural development

The TEM micrograph (Fig. 4) of sample SC30c after holding at 1150°C for 15 h demonstrates that, when using coarse SiC particles, the heat treatment used is not sufficient for complete oxidation of all SiC particles. For this heating schedule, the critical SiC particle size after milling for complete oxidation is ~0.3–0.4 μm . The amorphous oxide layer thickness around SiC particles larger than this critical size is ~0.15–0.2 μm .

Figure 5 shows microstructures of samples SC30f after sintering at 1550°C for 1 h (a) without and (b) with hold at 1150°C for 10 h. The microstructure of the sample without hold (Fig. 5(a)) consists of mullite, Al_2O_3 , SiC, and ZrO_2 (cf. Section 3.1). The grain sizes of all phases are $\leq 1 \mu\text{m}$. Mullite and Al_2O_3 grains cannot be distinguished optically, only by EDX. SiC as well as ZrO_2 particles are mostly located at mullite or Al_2O_3 grain boundaries. SiC show the typical polypeptide structure. Some small SiC particles are located within the mullite grains. In contrast to XRD

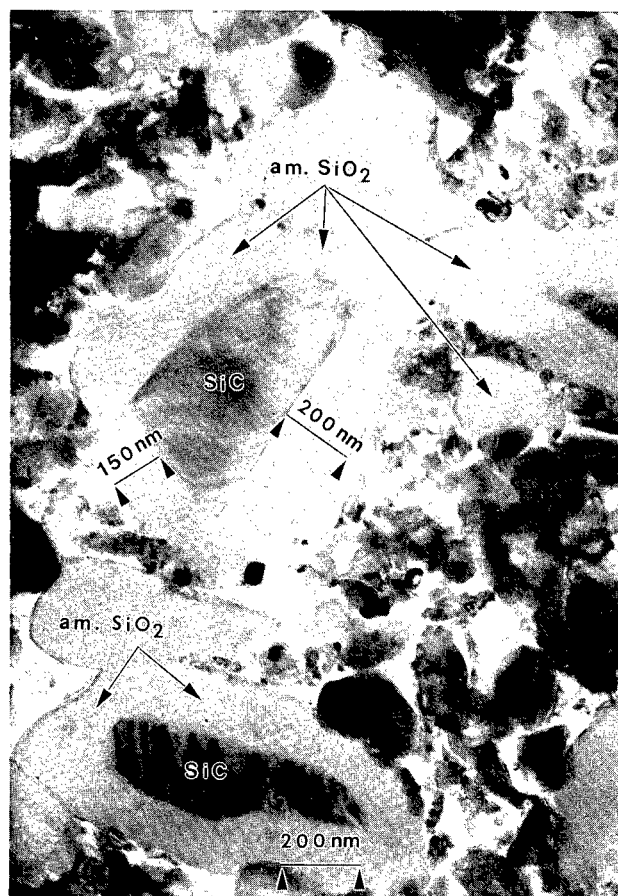


Fig. 4. TEM micrograph demonstrating the effect of SiC oxidation at 1150°C for 15 h.

results, ZrO_2 is in monoclinic crystal symmetry. The tetragonal-to-monoclinic phase transformation is attributed to TEM sample preparation.

The microstructure of SC30f in Fig. 5(b) after sintering at 1550°C with hold at 1150°C for 10 h (complete SiC oxidation) is characterized by a dense and homogeneous mullite matrix with ZrO_2 dispersions at grain boundaries and Al_2O_3 particles inside mullite grains. Some tiny SiC particles are also found within mullite grains. The survival of these SiC particles can be explained by reduced oxygen access in the final state of densification. Consequently, also some small Al_2O_3 particles survive embedded in mullite during grain growth. The density of this mullite/ ZrO_2 sample is somewhat higher (96%) than that shown in Fig. 5(a) (94.5%). This is due to the increased SiC content which is known to hinder densification of Al_2O_3 .^{14,15}

3.3 Zero-shrinkage conditions

The shrinkage calculation of mullite composites requires the knowledge of: (a) the fraction of Al oxidized during milling (f); (b) the fraction of ZrO_2 introduced by milling wear (V_{ZrO_2}); (c) the degree of SiC oxidation during reaction bonding (Ψ) and (d) green (ρ_0) and final density (ρ). The

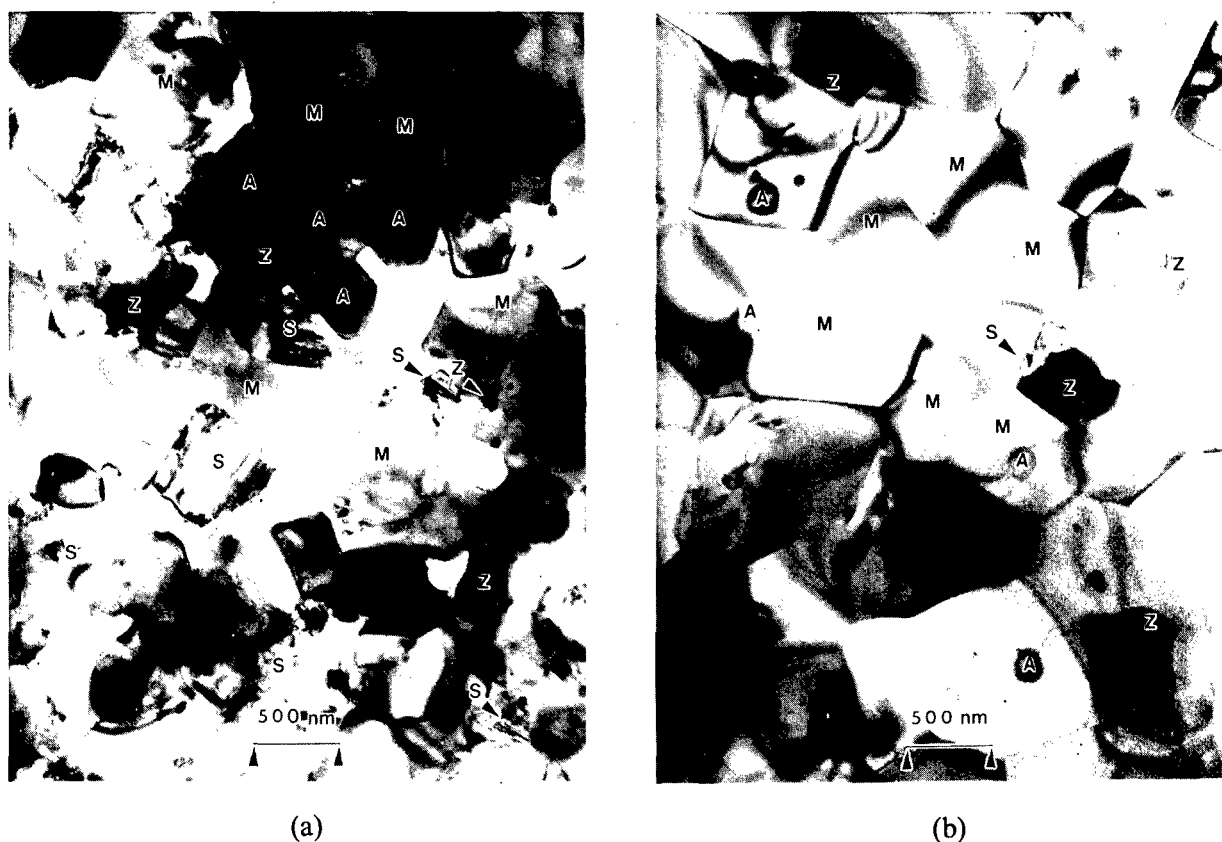


Fig. 5. TEM micrographs showing composition SC30f after sintering at 1550°C for 1 h: (a) without and (b) with hold at 1150°C for 10 h (M: Mullite, A: Al_2O_3 , S: SiC , Z: ZrO_2).

determination of f has been described elsewhere⁹ and can be done by quantitative X-ray or thermogravimetric analyses. Typical values for f are 0.3–0.5. V_{ZrO_2} can be determined by different methods: (a) XRD analysis of the milled powder (difficult because of the amorphous Al_2O_3); (b) weighing the milling discs and balls before and after milling (not very accurate), and (c) quantitative XRD phase analysis of reaction-bonded bodies. Method (c), e.g. Rietveld analysis, enables the exact determination of phase composition after reaction bonding, however, phase composition depends strongly on the degree of SiC oxidation. Therefore, exact calculation of V_{ZrO_2} requires the determination of the ZrO_2 content of a sample with completely oxidized SiC ($\Psi = 1$). V_{ZrO_2} can then be calculated considering the ZrO_2 volume fraction in the final composition ($V_{\text{ZrO}_2}^{\#}$) and the volume expansion during reaction bonding.¹⁰

$$V_{\text{ZrO}_2} = \frac{\left(\frac{1 + 0.28V_{\text{Al}} + 1.125V_{\text{SiC}}}{1 + 0.60fV_{\text{Al}}} \right) \cdot V_{\text{ZrO}_2}^{\#}}{1 - V_{\text{ZrO}_2}^{\#}} \quad (1)$$

Thereby, 0.28 and 1.125 are the volume expansions associated with the Al oxidation (0.28) and the combination of SiC oxidation (1.08) and mullite formation (0.042), and V_{Al} and V_{SiC} the respective volume fractions. 0.60 is the volume expansion

associated with the oxidation of Al to amorphous Al_2O_3 (density $\sim 3.2 \text{ g/cm}^3$) during milling.¹⁰

Exact shrinkage calculations require the reevaluation of the true volume fractions of each phase after milling (V_i^*). The true volume fraction is given by the ratio of volume fraction before milling (V_i^*) to increased total volume after milling (formation of amorphous Al_2O_3 and ZrO_2 wear debris).

$$V_i^* = \frac{V_i}{1 + 0.60fV_{\text{Al}} + V_{\text{ZrO}_2}} \quad (2)$$

Equation (2) also enables the differentiation between the volume fraction of Al left after milling (V_{Al}^*) and the volume fraction of Al oxidized to amorphous Al_2O_3 ($V_{\text{Al}}^{\text{amorph}}$). In this case, V_i for Al is equal to $(1-f)V_{\text{Al}}$ and for amorphous Al_2O_3 equal to $1.60fV_{\text{Al}}$, respectively. Generally speaking, the volume increase during reaction bonding due to oxidation of Al can be calculated either by considering V_{Al} and f (see also Ref. 10) or by the real volume fractions, as demonstrated in eqn (3). Thereby, -0.20 is the volume decrease associated with the phase transformation of amorphous Al_2O_3 to α -modification. However, in case when for shrinkage calculations also wear debris has to be considered always the real volume fractions have to be determined.

$$\frac{1 + 0.28V_{\text{Al}}}{1 + 0.60fV_{\text{Al}}} = 1 + 0.28V_{\text{Al}}^* + 0.20V_{\text{amorph}}^* \quad (3)$$

To determine the degree of SiC oxidation during reaction bonding (ψ), the SiC phase content after reaction bonding (V_{SiC}^*) has to be measured, e.g. by Rietveld analysis. V_{SiC}^* is also given by the volume ratio of non-oxidized SiC ($1 - \psi$) V_{SiC}^* to total volume after reaction bonding.

$$V_{\text{SiC}}^* = \frac{(1 - \psi) V_{\text{SiC}}^*}{1 + 0.28V_{\text{Al}}^* - 0.20V_{\text{amorph}}^* + 1.125\psi V_{\text{SiC}}^*} \quad (4)$$

Rearranging eqn (4) gives:

$$\psi = \frac{1 - \frac{V_{\text{SiC}}^*}{V_{\text{SiC}}^*} (1 + 0.28V_{\text{Al}}^* - 0.20V_{\text{amorph}}^*)}{1 + 1.125V_{\text{SiC}}} \quad (5)$$

The shrinkage calculation also requires the knowledge of relative green (ρ_0) and final (ρ) density. Therefore, theoretical green and final density have to be calculated considering the true volume fractions. A modified equation predicting the total dimensional linear change, S , during reaction bonding of SiC-containing RBAO ceramics is then given by

$$S = \left[(1 + 0.28V_{\text{Al}}^* - 0.20V_{\text{amorph}}^* + 1.125\psi V_{\text{SiC}}^*) \frac{\rho_0}{\rho} \right]^{-\frac{1}{3}} - 1 \quad (6)$$

Following eqn (6), the conditions for low-to-zero shrinkage are high Al and SiC contents, complete oxidation ($\psi = 1$), low fraction of Al oxidized during milling (V_{amorph}^* small), and high green and

low final densities. In composition SC30, the Al and SiC content is given with 40 and 30 vol.% in the precursor powder. Calculations according to eqn (6) for low-to-zero shrinkage conditions assuming $\psi = 1$ (complete SiC oxidation) and $V_{\text{ZrO}_2}^* = 10$ vol.% together with general trends mentioned before are given in Fig. 6. A low-to-zero shrinkage range can be defined for samples with 90% final density and $f = 0$ as an upper limit and with 100% final density and $f = 0.5$ as a lower limit. The dashed line represents samples with 100% final density and $f = 0$.

A green machined sample of composition SC30 was fabricated with a linear shrinkage of 0.6%, 96% TD final density, and a ZrO_2 content of 6.7 vol.% (see Fig. 7). The green density was 68% TD (CIP pressure: 900 MPa), $f \sim 0.3$, and SiC completely oxidized. According to eqns (1) and (2), the phase composition in the powder mixture after milling has been calculated to be 23.7/16.2/25.2/25.2/19.7 vol.% (Al, amorphous Al_2O_3 , Al_2O_3 , SiC, and ZrO_2), respectively. Calculating the linear dimensional change according to eqn (6) and considering the true phase composition gives a shrinkage of 2.1% which is higher than the experimental value. This can be explained by an increased volume of the porous outer layer consisting of mullite and Zircon (see Section 3.1). Neglecting the change of phase composition due to ZrO_2 wear debris gives a linear shrinkage of 1.4% which is similar to that considering V_{ZrO_2} . The calculated and experimentally determined shrinkage values are also presented in Fig. 6.

In order to reduce the required green density for zero-shrinkage behavior, SiC contents > 26 vol.% may be used to further increase the oxidation expansion. However, when more than 26 vol.% SiC is used, an excess of SiO_2 remains. Therefore, the volume expansion due to SiC oxidation (ΔV_{SiC}) has to be modified considering the

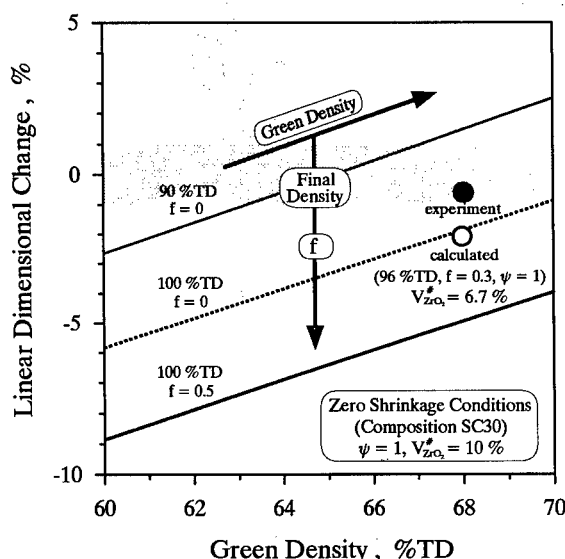


Fig. 6. Calculated linear dimensional change (according to eqn (1)) of composition SC30 for 90 and 100% final density. Experimental and calculated data points for composition SC30 (68 and 96% green and final density, $f = 0.3$) are also given.

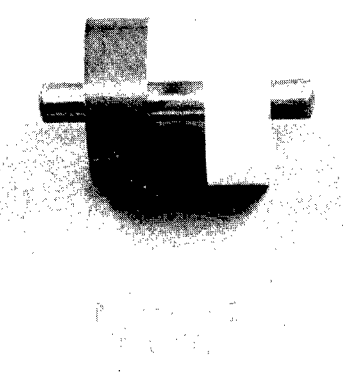


Fig. 7. Photograph demonstrating zero-shrinkage of a part made from composition SC30. The inner diameter of the green (dark) and reaction-bonded part (white) did not change.

amount of remaining SiO_2 . ΔV_{SiC} is then a combination of only SiC oxidation ($\Delta V_{\text{SiC} \rightarrow \text{SiO}_2} = 1.08$) and SiC oxidation plus mullitization ($\Delta V_{\text{SiC} \rightarrow \text{mullite}} = 1.125$). A composition consisting of 40/15/45 vol.% Al/ Al_2O_3 /SiC (SC45) was fabricated and a shrinkage of 1% (97% final density) was observed using a CIP pressure of only 300 MPa. The presence of SiO_2 would possibly reduce the high temperature strength of the composite.

4 Conclusions

- (1) The RBAO process can be modified by adding SiC to the precursor powder mixture to fabricate low-to-zero shrinkage mullite/ Al_2O_3 /SiC/ ZrO_2 composites. Attrition-milling of RBAO precursor powders is normally carried out with TZP balls and discs which introduces, when SiC is present, a substantial amount of ZrO_2 wear debris into the mixture (10–15%). ZrO_2 is not necessary for the RBAO process, however, it improves the microstructural development.⁸
- (2) The phase ratio of mullite to SiC in the final composition can be varied by adjusting the degree of SiC oxidation.
- (3) The exact calculation of the linear dimensional change during reaction bonding requires the determination of the true volume fractions of each phase in the green and sintered state considering the fraction of Al oxidized during milling, the ZrO_2 wear debris, and the degree of SiC oxidation.
- (4) To achieve zero shrinkage, high SiC contents (>26%), high green densities (>65%) and complete SiC oxidation are required. Therefore, small SiC powders (<1 μm) and intensive milling are recommended.
- (5) In order to reduce the required green density for zero shrinkage, SiC contents >30% should be used to further increase the oxidation expansion. However, when >26% SiC is used, excess SiO_2 remain in the body.
- (6) At temperatures >1400°C, a white porous outer layer consisting of mullite and Zircon (ZrSiO_4) is produced. Prevention of this layer can be achieved by initially oxidizing the SiC and Al in air and sintering the body in an inert atmosphere.
- (7) Reaction-bonded mullite/ Al_2O_3 /SiC/ ZrO_2 com-

posites exhibit superior mechanical properties. These results are published elsewhere.¹²

Acknowledgements

The authors thank Deutsche Forschungsgemeinschaft (DFG) for financial support under contracts No. Cl 52/12-2 and Cl 52/23-1. Thanks are also due to D. Thiele for Rietveld analyses.

References

1. Schneider, H., Okada, K. & Pask, J. A., *Mullite and Mullite Ceramics*, John Wiley & Sons, Chichester, 1994.
2. Kanzaki, S., Tabata, H., Kumazawa, T. & Ohta, S., Sintering and mechanical properties of stoichiometric mullite. *J. Am. Ceram. Soc.*, **68** (1985) C6–7.
3. Claussen, N. & Jahn, J., Mechanical properties of sintered *in situ*-reacted mullite/ ZrO_2 composites. *J. Am. Ceram. Soc.*, **63** (1980) 229.
4. Wei, G. C. & Becher, P. F., Development of SiC-whisker-reinforced ceramics. *Am. Ceram. Soc. Bull.*, **64** (1985) 298–304.
5. Liu, H. Y., Claussen, N., Hoffmann, M. J. & Petzow, G., Fracture sources and processing improvements of SiC-whisker-reinforced mullite (ZrO_2) composites. *J. Eur. Ceram. Soc.*, **7** (1991) 41–7.
6. Nischik, C., Seibold, M., Travitzky, N. A & Claussen, N., Effect of processing on mechanical properties of platelet-reinforced mullite composites. *J. Am. Ceram. Soc.*, **74** (1991) 2464–8.
7. Niihara, K., New design concept of structural ceramics-ceramic nanocomposites. *J. Ceram. Soc. Japan, In. Edt.*, **99** (1991) 945–52.
8. Wu, S., Holz, D. & Claussen, N., Mechanisms and kinetics of reaction-bonding Al_2O_3 (RBAO) ceramics. *J. Am. Ceram. Soc.*, **76** (1993) 970–80.
9. Holz, D., Wu, S., Scheppokat, S. & Claussen, N., Effect of processing parameters on phase and microstructure evolution in RBAO ceramics. *J. Am. Ceram. Soc.*, **77** (1994) 2509–17.
10. Claussen, N., Wu, S. & Holz, D., Reaction bonding of aluminum oxide (RBAO) composites: Processing, reaction mechanisms, and properties. *J. Eur. Ceram. Soc.*, **14** (1994) 97–109.
11. Wu, S. & Claussen, N., Fabrication and properties of low-shrinkage reaction-bonded mullite. *J. Am. Ceram. Soc.*, **74** (1991) 2460–3.
12. Wu, S. & Claussen, N., Reaction bonding and mechanical properties of Mullite/SiC composites. *J. Am. Ceram. Soc.*, **77** (1994) 2898–904.
13. Brandt, J. & Lundberg, R., Processing of mullite-based long-fiber composites via slurry routes and by oxidation of an Al:Si alloy powder. *J. Eur. Ceram. Soc.*, **16** (1996).
14. Nakahira, A. & Niihara, K., Sintering behaviors and consolidation process for Al_2O_3 /SiC nanocomposites. *J. Ceram. Soc. Japan, Int. Edt.*, **100** (1992) 448–53.
15. Stearns, L. C., Zhao, J. & Harmer, M. P., Processing and microstructure development in Al_2O_3 -SiC 'nanocomposites'. *J. Eur. Ceram. Soc.*, **10** (1992) 473–7.

Processing of Mullite-based Long-fibre Composites via Slurry Routes and by Oxidation of an Al-Si Alloy Powder

J. Brandt^a & R. Lundberg^b

^aSwedish Ceramic Institute, Box 5403, S-402 29 Göteborg, Sweden

^bVolvo Aero Corporation, S-461 81 Trollhättan, Sweden

(Accepted 22 July 1995)

Abstract

A novel technique to synthesize mullite by the oxidation of Al-Si alloy powder was used for the manufacture of Al_2O_3 long-fibre reinforced mullite composites. It included (1) slurry infiltration/fibre winding of continuous Al_2O_3 yarns (ALMAX) and (2) slurry infiltration/slip casting of sapphire fibres (Saphikon). The nonaqueous slurry used consisted of an Al-Si alloy, mullite and additives. During reaction-bonding of green matrices, the Al-Si alloy oxidized and was fully converted to mullite after 1 h at 1430°C in air. The oxidation caused an internal volume expansion, resulting in reduced fibre/matrix shrinkage stresses during reaction-bonding of composites, which minimized the sensitivity to crack formations. For the ALMAX-based composites, the fracture was non-catastrophic. Regarding the sapphire-based composites, an interfacial space between the fibres and the matrix gave the desired fibre pull-out.

1 Introduction

Ceramic long-fibre reinforced composites are being considered as future materials for gas turbine hot parts.¹ However, there are still some obstacles to overcome before this group of materials are mature enough for turbine applications, where there are high demands on long-term, high-temperature stability in the oxidizing environment. For instance, it has been difficult to produce dense ceramic long-fibre composites with adequate high temperature properties, including good oxidation resistance, for use at over 1400°C. This is especially true for nonoxide materials, where both fibres, matrix and interface material are nonoxides and consequently oxidize to form a strong fibre/matrix bond leading to brittle fracture behaviour.²

One possible solution is to develop composites consisting of high temperature *oxide* matrices and fibres and maybe even allow some open porosity in the final material.³

Mullite ($Al_6Si_2O_{13}$) is of particular interest as matrix material among the binary metal oxide ceramics.⁴ This refractory possesses good creep resistance and excellent oxidation resistance.⁵ However, the drawbacks of mullite are the low fracture toughness ($K_{Ic} = 2-3 \text{ MPa}\cdot\text{m}^{1/2}$) and the poor sinterability, mainly due to the low interdiffusion rates of silicon and aluminium ions in crystalline mullite.⁶ However, if this material is reinforced with high-temperature oxide long-fibres, and if some porosity could be accepted, then mullite could definitely be a competitive, moderate cost material for high-temperature structural applications. The fibres also facilitate the production of large thin-walled, complex-shaped components.⁷

A new technique to synthesize mullite has been developed, particularly, in view of the manufacture of mullite-based long-fibre composites.⁸ The technique is described in this paper. In short, a mixture of an Al-Si alloy and oxide powders is milled and formed into a powder compact, after which the alloy is oxidized and reaction-bonded to its corresponding ceramic composition, i.e. mullite. The brittle Al-Si is effectively comminuted during milling, avoiding the formation of undesired large, flat agglomerates by cold welding, as is the case with pure Al powder.^{9,10} Consequently, when long-fibre composites are processed, fibre tows are more easily infiltrated. Because of the fine metal distribution in the alloy, the transformation to mullite, during oxidation and reaction-bonding, is favoured. Another advantage is that the oxidation causes an internal volume expansion of the matrix.¹¹ This minimizes the sensitivity to crack formation due to reduced shrinkage stresses between the fibres and the matrix.^{12,13}

2 Experimental

2.1 Materials

A commercially available, gas-atomized Al-Si alloy with a weight-ratio of 75:25 (Al75/Si25 (hypereutectic compound)), particle size <150 µm, (AL146010, GoodFellow, UK) was selected. The Al-Si ratio is close to the one necessary for the formation of stoichiometric mullite ($3\text{Al}_2\text{O}_3\text{:}2\text{SiO}_2$) during reaction-bonding. Between 577 and 760°C, the Al75/Si25 alloy is melted to a liquid phase of a eutectic composition (Al88/Si18) plus a solid phase of large Si grains.¹⁴ On oxidation, the theoretical weight increase is 95%. If full conversion to mullite is achieved (including some excess Al_2O_3), the volume expansion is 59%. In addition to the alloy, the oxide powders used were mullite (SACR193, Baikowski Chimie, France), Al_2O_3 (AKP-30, Sumitomo, Japan) and MgO (Merck, Germany) as an oxidation catalyst. Extra Al_2O_3 was added to form mullite of otherwise unreacted, free SiO_2 — an excess of Al_2O_3 was preferred in the final material.

Two kinds of ceramic long fibres were used for the manufacture of the composites: (1) polycrystalline, continuous $\alpha\text{-Al}_2\text{O}_3$ yarn with 1000 filaments per yarn (filament diameter 10 µm) and without any sizing (ALMAX Y-1010S-N, Mitsui Mining Material, Japan) and (2) single crystal, continuous $\alpha\text{-Al}_2\text{O}_3$ sapphire fibres with a diameter of 130 µm (Saphikon, USA). Whereas the ALMAX polycrystalline fibres showed limited resistance to heat in earlier experiments, the sapphire fibres have excellent high temperature properties.^{15,16} The ALMAX fibres should thus be considered as a model material.

For the preparation of the slurry, an organic, non-polar solvent, with a high boiling point, and a suitable dispersant, KD-3 (ICI, USA), were used.

2.2 Specimen preparation

One master slurry was prepared for all the experiments. A batch with a composition by weight of 30% Al75/Si25, 63% mullite, 5% Al_2O_3 and 2% MgO was mixed in the organic solvent with 3% KD-3 (on powder), resulting in a solid loading of 73.0 wt% (40.3 vol%). After prolonged ball milling, the slurry was wet-sieved through a 20 µm cloth.

Bars with the dimensions 60 × 9 × 8 mm³ were slip cast onto a plaster mould, both with and without a few sapphire fibres suspended parallel in the middle of the mould. In addition, long-fibre composites with the ALMAX fibre yarn were prepared by slurry infiltration/fibre winding. To keep the filament together during the fibre winding procedure, the fibre yarn bobbin was soaked with

organic solvent. The yarn was then passed through the slurry, with a thread tension of 0.08 N and a speed of 2 m/min, and wound on a quadrangular take-up spool (65 × 65 mm²). When the soaked yarn came into contact with the slurry, the organic solvent had evaporated enough for the yarn, via capillary forces, to become fully impregnated by the slurry. In fact, the solvent residue improved the wettability of the yarn. All specimens were carefully dried, burned out in nitrogen at 500°C and subsequently stored in a dry atmosphere.

The specimens were reaction-bonded and partly densified in flowing air with heating rates of 10°C/min to 450°C and 2°C/min to maximum temperatures of 1430–1600°C with dwelling periods of 5–240 min.

2.3 Evaluation

The effect of ball milling was verified by means of specific surface area (BET) measurements and micrographs of the particles, before and after milling. The weight and the dimensional changes during the reaction-bonding process were recorded with a thermobalance (TGA) and a dilatometer (TDA). Phase compositions were determined by X-ray diffractometry (XRD), and microstructures were studied by scanning electron microscopy (SEM). Densities of reaction-bonded specimens were estimated by Archimedes' principle of volume displacement. Fracture strength and Young's modulus were measured at room temperature in a universal testing machine in four-point bending (20/40 mm span). Only a few test specimens (dimensions: 55 × 6 × 2 mm³) were prepared.

3 Results and Discussion

3.1 Specimen preparation

As can be seen in Fig. 1, the particle size was considerably reduced after milling and there are no large, flat agglomerates present. These micron-sized, round-shaped particles favour a more homogeneous particle distribution in the powder compacts and facilitate the infiltration of fibre tows. A number of as-received, spherical Al-Si alloy particles are shown in the left micrograph.

The milling result was also checked by BET specific surface area measurements, which gave 2.7 m²/g before milling and 8.8 m²/g after milling.

The bulk density of the slip cast green bodies was 58.0% of theoretical density (TD). Presumably, the green density of the matrix in the fibre wound composites was slightly less, due to non-optimized particle packing. By light microscope studies, no cracks could be found in the green composites.

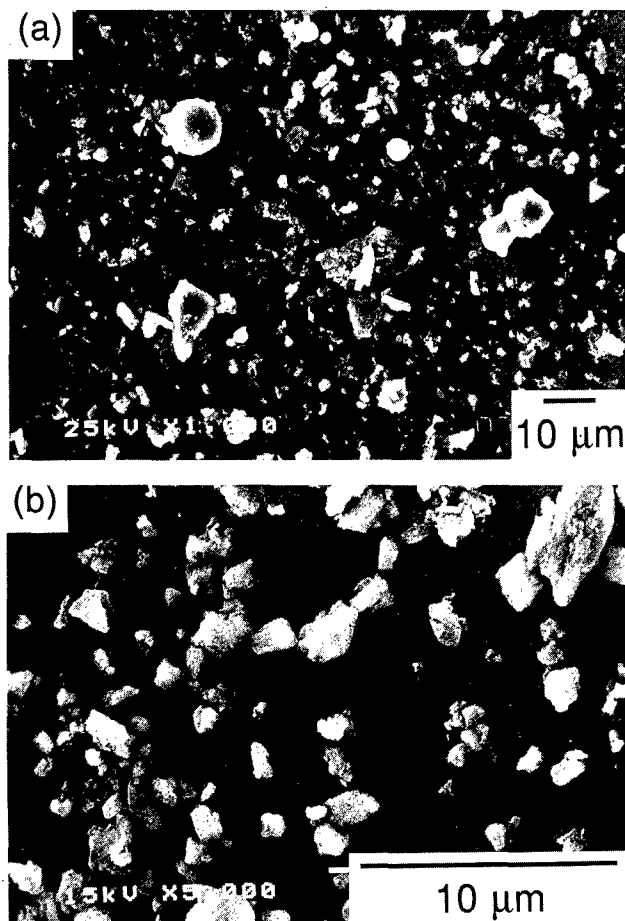


Fig. 1. Scanning electron micrographs of particles from the batch before (a) and after milling (b).

3.2 Oxidation/reaction-bonding behaviour

Thermogravimetry (TGA) and dilatometry (TDA) were used to determine the oxidation and reaction-bonding behaviour of slip cast, green bodies. In Fig. 2, the dimensional change, degree of

oxidation and oxidation rate during the reaction-bonding cycle are shown.

The oxidation rate curve in Fig. 2, shows a sharp oxidation peak at 528°C, where surface oxidation of solid Al particles takes place. This reaction is strongly exothermal and probably causes local temperature increase. Since the alloy starts to melt at 577°C, this intermittent increase is expected to be high enough to partly melt the alloy, enabling a certain particle rearrangement. This may explain the minor shrinkage in the TDA at 530°C. In addition, the fine-grained Al_2O_3 that is formed reacts with the added MgO to form spinel (MgAl_2O_4), which presumably further favours the oxidation of Al in this temperature region.¹⁷ Approximately 15% of the Al in the alloy appears to oxidize by solid state/gas reaction.

After further heating, the oxidation of Al slows down considerably. At about 680°C, though, the process accelerates, with an oxidation rate maximum at 797°C. The thermal expansion of the melt presumably results in a rupture of the oxide shell so that the melt leaks out, resulting in a more rapid oxidation.^{12,18} This causes, once again, a shrinkage of the powder compact because of the particle rearrangement. This is consistent with the dilatometer analysis, with the shrinkage starting at 680°C, followed by an intermediary expansion peak at 805°C, then a small drop, before the expansion continues.

As the Al in the melt is consumed, the phase composition of the alloy is shifted towards the Si corner.¹⁴ The liquidus temperature (when also the Si grains melt) increases gradually. An oxidation rate of 0.2 %/min (based on TGA) for the Al corresponds to an increase in the liquidus temperature of approximately 1°C/min. The Si will thus be supersaturated and precipitate, which has been verified by calculations. Consequently, the primary solid Si grains will not dissolve at the liquidus temperature of A175/Si25 of 760°C.

The increasing oxidation rate at ~1180°C indicates that Si begins to oxidize in order to form α -cristobalite (SiO_2). In spite of the fact that there is a large volume increase involved when Si oxidizes (114%), the TDA shows no expansion from 1200 up to 1240°C. One possible explanation is that the previously formed, fine α - Al_2O_3 crystals to some extent sinter. Above 1240°C, however, the oxidation of Si prevails and the expansion curve rises steeply as expected until all the Si has been oxidized. The small oxidation rate peak at 1395°C is related to the melting temperature of Si (1410°C), which may be lowered due to impurities. It is interesting to note the high degree of conversion (85.5% of the theoretical weight gain), implying that less than 15% of the alloy was

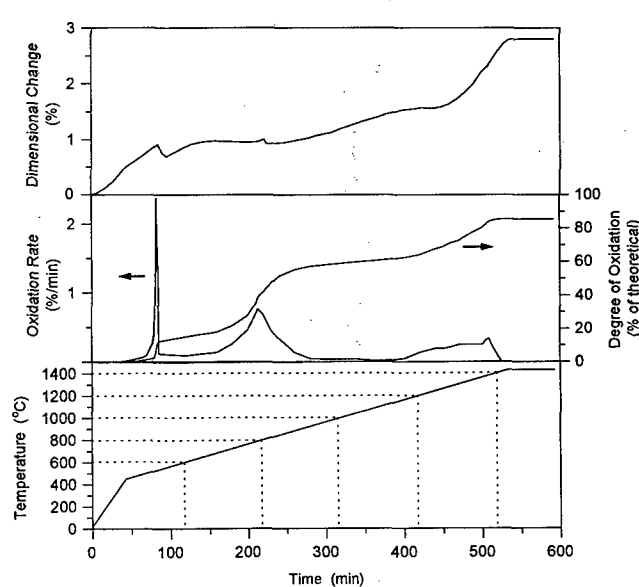


Fig. 2. Dimensional change, degree of oxidation and oxidation rate of a slip cast and burned out powder compact (without fibres) as a function of the reaction-bonding cycle, in flowing air. The total cycle time, including cooling, was 10 h.

oxidized during milling. This is one of the significant advantages when employing an alloy instead of pure Al (for which up to 40 wt% premature oxidation has been reported^{11,18}). There is another advantage during reaction-bonding due to the sluggish oxidation of Si: The homogeneously distributed Si in the alloy, which encloses the reactive Al, improves the oxidation controllability and the oxidation rate can thus be increased.

All oxidation experiments were carried out in air. During this process a large amount of oxygen is consumed. According to a rough estimate (assumptions: an average pore volume of 40% in the green bodies, pores filled with oxygen batchwise at an average oxidation temperature of 800°C), the pore network has to be refilled 17000 times with oxygen from the surrounding air to completely oxidize the specimens. This leads to a substantial reduction of the partial oxygen pressure, especially in the interior part, since the surface layer reacts with most of the inflowing oxygen. However, to avoid a runaway oxidation because of the strongly exothermal nature of the oxidation reaction, low partial oxygen pressure is necessary.

The conversion to mullite ($3\text{Al}_2\text{O}_3 + 2\text{SiO}_2 \rightarrow \text{Al}_6\text{Si}_2\text{O}_{13}$) begins below 1400°C. Table 1 shows the resulting crystalline phases before and after oxidation at 1430°C in flowing air.

Practically all Si and SiO_2 have reacted with Al_2O_3 to form mullite already after 5 min at 1430°C. In addition, an intermediate phase of cordierite ($2\text{MgO} \cdot 2\text{Al}_2\text{O}_3 \cdot 5\text{SiO}_2$) has formed. Cordierite is an undesirable final product, since two of the ternary eutectic compositions including cordierite in the $\text{MgO}-\text{Al}_2\text{O}_3-\text{SiO}_2$ system melt at 1345 and 1360°C, respectively. Fortunately, the cordierite turns into mullite and a Mg-, Al-spinel during extended heating at 1430°C. Yet to be explored is if cordierite favours the mullitization process.

According to Table 1, after oxidation/reaction-bonding at 1430°C for 60 min in flowing air, the predominant phase was mullite, but there was also some Al_2O_3 , due to the surplus alumina added, together with traces of cordierite. The total linear dimensional change for the specimen above was 2% in expansion.

Table 1. Crystalline phases of the green and the reaction-bonded matrices, by X-ray diffraction.

Temp. (°C)	Time (min)	$\text{Al}_6\text{Si}_2\text{O}_{13}$ (mullite)	Al_2O_3	Al	Si	SiO_2	MgO	$2\text{MgO} \cdot 2\text{Al}_2\text{O}_3 \cdot 5\text{SiO}_2$ (cordierite)
Green body		m	w	s	s	w	vw	—
1430	5	s	w/m	—	—	vw	—	w
1430	60	s	w	—	—	—	—	vw

s = strong; m = medium; w = weak; vw = very weak.

3.3 Microstructure and mechanical properties of composites

Figure 3 shows micrographs of sapphire fibre reinforced mullite, reaction-bonded at three different temperatures. The effect of increasing the maximum reaction temperature can clearly be observed. First, the obvious increase of the density of the matrices: the density was after reaction-bonding at 1430°C (5 min) 65.6%, 1430°C (60 min) 66.5%, 1500°C (60 min) 80.2% and at 1600°C (60 min) 94.1% of theoretical density. The 1600°C matrix had only closed porosity. This can also be seen by comparing the SEM micrographs, where the open, fine-distributed pore network in Figs 3(a-d) have changed into enlarged close pores in Figs 3(e,f).

Images of the sapphire fibre/matrix interfaces in Fig. 3(b,d) indicate that there are spaces between the fibres and the matrices, whereas in Fig. 3(f), no space can be observed. Instead, surrounding cracks in the matrix are seen. These phenomena are due to the expansion coefficient mismatch of alumina ($8.8 \times 10^{-6} \text{ K}^{-1}$) and mullite ($5.3 \times 10^{-6} \text{ K}^{-1}$). Thus, during cooling, the sapphire fibres shrink more than the mullite matrices, causing a widening of the interface spaces. According to calculations, the space width should theoretically be $0.35 \mu\text{m}$. At the higher temperature (Fig. 3(f)), the matrix may react with the fibres to form a strong bond. The cooling stresses then lead to cracking of the adjacent matrix and even of the fibres.

One role of the fibres is to increase the fracture toughness of the material.¹⁹ As suggested by Davis *et al.*,²⁰ the interfacial debonding energy should be about one quarter of the fibre fracture energy, resulting in high-energy sliding when the fibres are pulled out. Figure 4 shows a sapphire fibre pull-out in a matrix of mullite, but whether this composite, reaction-bonded at 1430°C for 60 min, has the appropriate energy ratio has not yet been examined. A possibility is to coat the fibres with an interfacial, debonding layer, for instance ZrO_2 ,^{20,21} and thus enable sintering of the composite at higher temperatures.

In Fig. 5, an ALMAX fibre reinforced mullite composite is shown. For all composites based on ALMAX fibres, the reaction-bonding cycle was

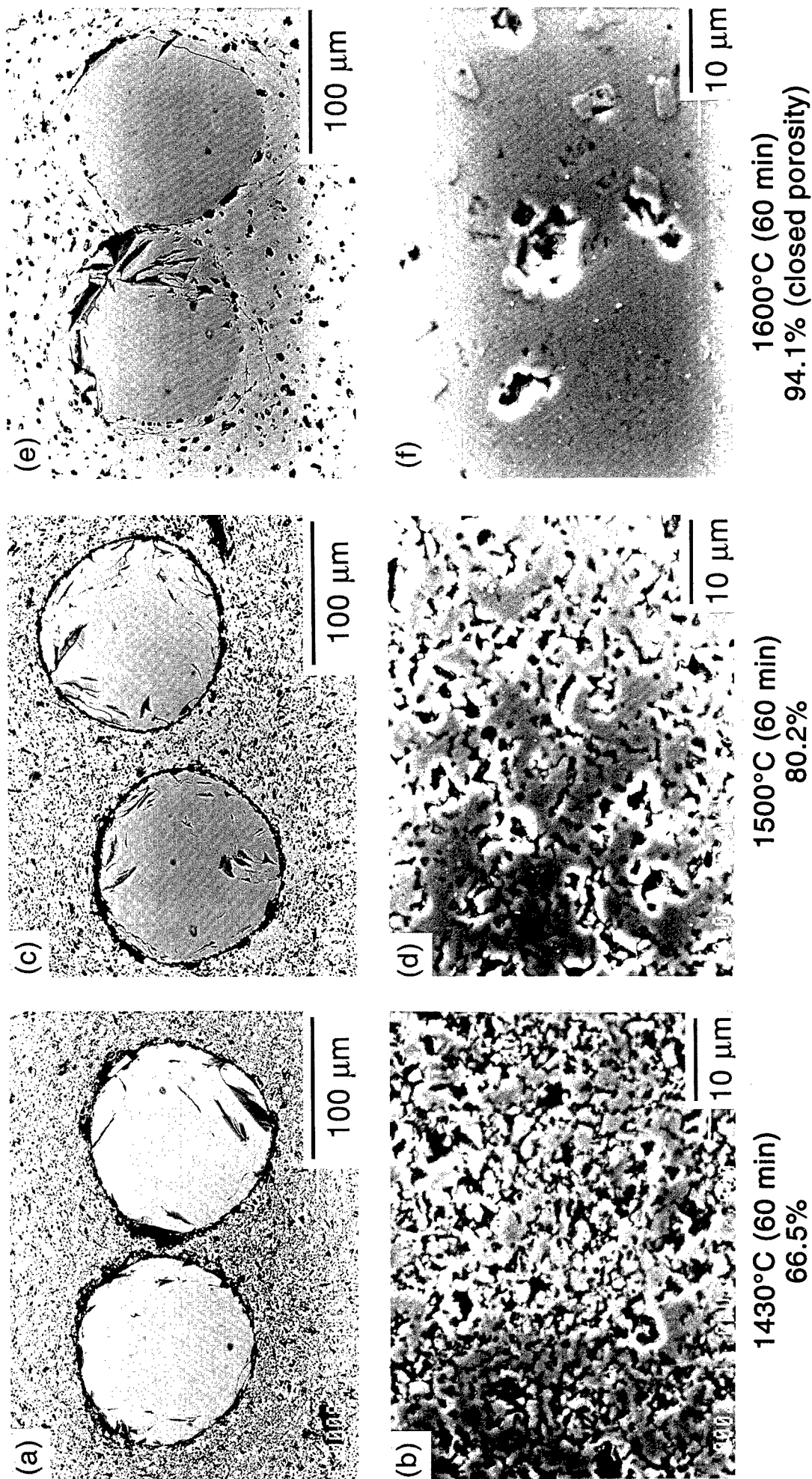


Fig. 3. Scanning electron micrographs of sapphire fibre reinforced mullite, reaction-bonded at 1430 (a, b), 1500 (c, d) and 1600°C (e, f), respectively, for 60 min. The graphs underneath are close-ups of the matrices above.

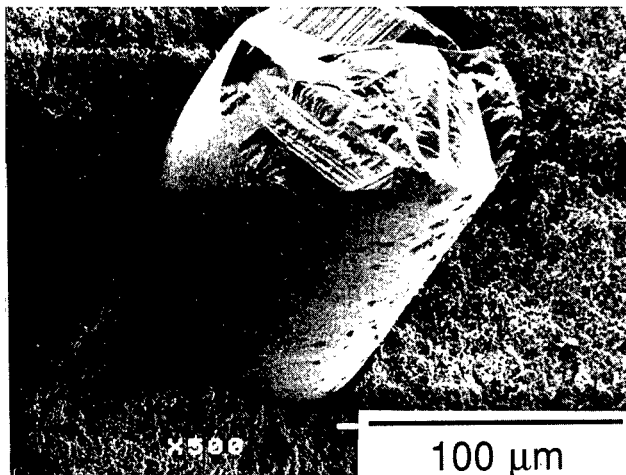


Fig. 4. Scanning electron micrograph of the fracture of a sapphire fibre reinforced mullite specimen, reaction-bonded at 1430°C for 60 min, showing a fibre pull-out.

limited to 1430°C for 5 min. This because the polycrystalline ALMAX fibres may degrade at elevated temperatures, as mentioned previously.

From the close-up (Fig. 5(b)), it is clear that the slurry has properly infiltrated the fibre tows and no fibres are in contact with each other. In addition, no cracks can be detected. The absence of cracks is probably due to the internal volume

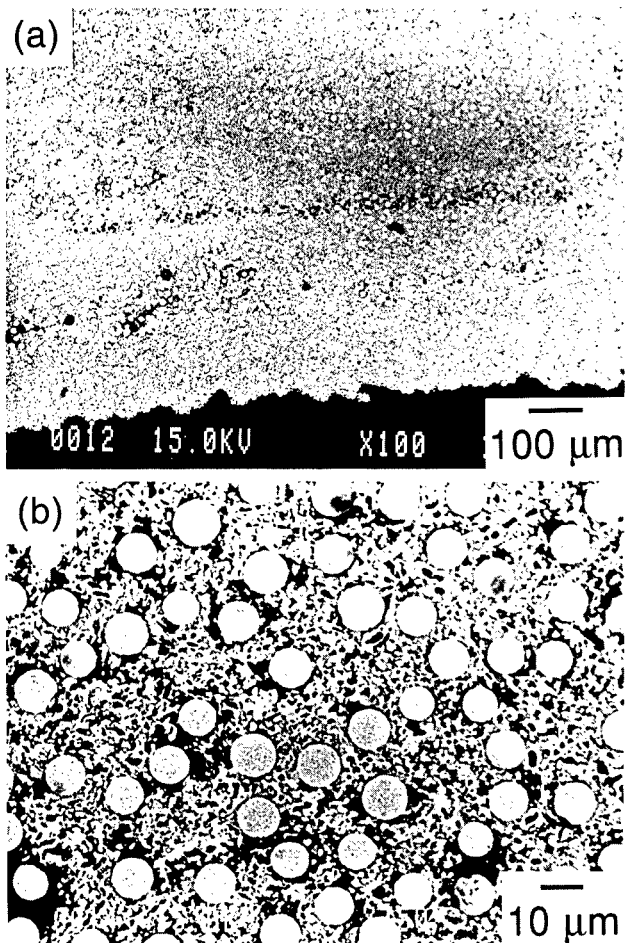


Fig. 5. Scanning electron micrographs of ALMAX fibre reinforced mullite, prepared by slurry infiltration/fibre winding followed by reaction-bonding at 1430°C for 5 min. The fibres are approximately 10 μm in diameter.

expansion of the matrix on oxidation, which reduces the fibre/matrix stresses. Unfortunately, the overview graph shows regions where there are almost no fibres present, indicating that too much slurry has covered the tows during winding and hence obstructed a homogeneous fibre distribution.

The fracture behaviour of an as-reaction bonded ALMAX fibre/mullite matrix composite is illustrated in Fig. 6. As the test specimens were not machined, this test only gives an indication of the strength potential for these composites. For the charted one, which was reaction-bonded at 1430°C for 5 min, the strength was 120 MPa. As can be seen, there was no catastrophic failure; on the contrary, a partial load-transfer took place. Even after testing, the broken parts held together. The Young's modulus was calculated for the first straight slope; with a thickness of the specimen of 2 mm it was roughly 90 GPa.

4 Conclusion

Composites of reaction-bonded long-fibre reinforced mullite were prepared by means of a new reaction-bonding technique. Both the technique, in which an Al–Si alloy in a powder compact during oxidation converts to mullite, as well as the preparation of the composites via a slurry route were demonstrated.

Starting with an Al–Si alloy, instead of Al and Si as separate components, resulted in a more effective milling, a better distribution of the two reactants, less undesired oxidation during milling and improved control of the oxidation during the reaction-bonding cycle. Furthermore, there was neither Si nor SiO_2 in the final matrix material, reaction-bonded at 1430°C for 1 h.

The long-fibres, including also fibre tows, were properly infiltrated by the Al–Si-based slurry. After reaction-bonding at 1430°C for 5 min, the

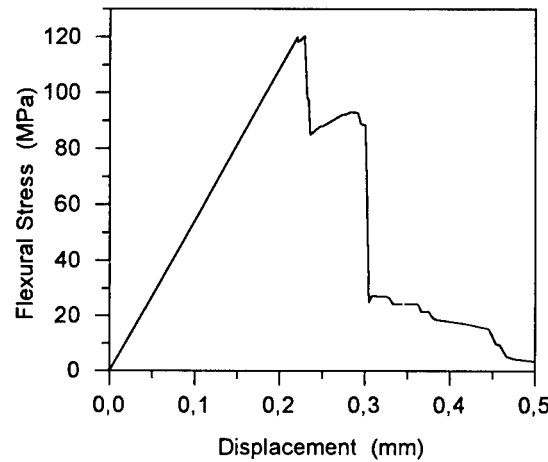


Fig. 6. Plot of the flexural stress at room temperature as a function of the displacement of an ALMAX fibre reinforced mullite test specimen, reaction-bonded at 1430°C for 5 min.

ALMAX-based composites showed no matrix cracks. The flexural test gave non-catastrophic failure characteristics. For the sapphire-based composites, reaction-bonded at 1430 and 1500°C, for 1 h, there were void spaces between the fibres and the mullite, due to a thermal expansion mismatch on cooling.

Acknowledgements

We wish to thank Lars Eklund for all SEM micrographs, Annika Kristoffersson for assistance in fibre winding and Robert Pompe for valuable discussions and constructive criticism of this paper.

References

1. Butler, E. G. & Lewis, M. H., Prospects for ceramics in airborne gas turbine engines. In *Proceedings of the 4th International Symposium on Ceramic Materials and Components for Engines*, eds R. Carlsson, T. Johansson & L. Kahlman, Elsevier Applied Science, London, 1991, pp. 32-49.
2. Brandt, J., Rundgren, K., Pompe, R., Swan, H., O'Meara, C., Lundberg, R. & Pejryd, L., SiC continuous fiber-reinforced Si_3N_4 by infiltration and reaction bonding. *Ceram. Eng. Sci. Proc.*, **13** (1992) 622-31.
3. Kristoffersson, A., Warren, A., Brandt, J. & Lundberg, R., Reaction bonded oxide composites. In *Proceedings of the 6th European Conference on Composite Materials (EACM), High Temperature Ceramic Matrix Composites*, eds R. Naslain, J. Lamon & D. Doumeingts, Woodhead Publishing Ltd, Abington Cambridge, UK, 1993, pp. 151-9.
4. Aksay, I. A., Dabbs, D. M. & Sarikaya, M., Mullite for structural, electronic, and optical applications. *J. Am. Ceram. Soc.*, **74** (1991) 2343-58.
5. Dokko, P. C., Pask, J. A. & Mazdiyasni, K. S., High-temperature mechanical properties of mullite under compression. *J. Am. Ceram. Soc.*, **60** (1977) 150-5.
6. Sacks, M. D., Lee, H. & Pask, J. A., A review of powder preparation methods and densification procedures for fabricating high density mullite. In *Proceedings of the International Conference on Mullite*, Vol. 6, American Ceramic Society, Westerville, OH, USA, 1990, pp. 167-207.
7. Ko, F. K., Preform fiber architecture for ceramic-matrix composites. *Am. Ceram. Soc. Bull.*, **68** (1989) 401-14.
8. Brandt, J. & Lundberg, R., Synthesis of mullite materials by oxidation of metal alloy powder compacts. In *Third Euro-Ceramics, Vol. 1 Processing of Ceramics*, eds P. Duran & J. F. Fernández, Faenza Editrice Ibérica S.L., Spain, 1993, pp. 169-76.
9. Milling of brittle and ductile materials. *Metals Handbook*, Vol 7, 9th Edition, ASM International, Materials Park, OH, 1984, 56-70.
10. Claussen, N., Le, T. & Wu, S., Low-shrinkage reaction-bonded alumina. *J. Eur. Ceram. Soc.*, **5** (1989) 29-35.
11. Wu, S. & Claussen, N., Fabrication and properties of low-shrinkage reaction-bonded mullite. *J. Am. Ceram. Soc.*, **74** (1991) 2460-3.
12. Claussen, N., Wu, S. & Holz, D., Reaction bonding of aluminium oxide (RBAO) composites: processing, reaction mechanisms and properties. *J. Eur. Ceram. Soc.*, **14** (1994) 97-109.
13. Thompson, I. & Witt, M. C., Fabrication of continuous fibre ceramic matrix composites via slurry routes. In *British Ceramic Proceedings No. 49, Special Ceramics 9*, The Institute of Ceramics, Stoke-on-Trent, 1992, pp. 269-78.
14. Specific metals and alloys. *Metals Handbook*, Vol 2, 10th Edition, ASM International, Materials Park, OH, 1990, pp. 124.
15. Corman, G. S., High-temperature creep of some single crystal oxides. *Ceram. Eng. Sci. Proc.*, **12** (1991) 1745-66.
16. Haggerty, J. S., Wills, K. C. & Sheehan, J. E., Growth and properties of single crystal oxide fibres. *Ceram. Eng. Sci. Proc.*, **12** (1991) 1785-801.
17. Newkirk, M. S., Urquhart, A. W. & Zwicker, H. R., Formation of LanxideTM ceramic composite materials. *J. Mater. Sci.*, **1** (1986) 81-9.
18. Wu, S., Holz, D. & Claussen, N., Mechanism and kinetics of reaction-bonded aluminium oxide ceramics. *J. Am. Ceram. Soc.*, **76** (1993) 970-80.
19. *International Encyclopedia of Composites*. Vol. 1, eds Lee, S. M., VCH Publishers, Inc., New York, 1990, pp. 267-77 and 297-318.
20. Davis, J. B., Löfvander, J. P. A. & Evans, A. G., Fiber coating concepts for brittle-matrix composites. *J. Am. Ceram. Soc.*, **76** (1993) 1249-57.
21. Hay, R., Fiber-matrix interfaces for oxide fiber-oxide matrix composites. In *Proceedings of the 6th European Conference on Composite Materials, High Temperature Ceramic Matrix Composites*, eds R. Naslain, J. Lamon & D. Doumeingts, Woodhead Publishing Ltd, Abington Cambridge, UK, 1993, pp. 385-9.

Preliminary Results on a Novel Fabrication Route for α -Al₂O₃ Single Crystal Monofilament-reinforced Reaction-bonded Mullite (RBM)

B. Saruhan, W. Luxem & H. Schneider

German Aerospace Research Establishment (DLR), Institute for Materials Research, D-51140 Köln, Germany

(Accepted 22 July 1995)

Abstract

Owing to their excellent properties, continuous-fibre reinforced mullite-matrix composites are good candidates for applications in which oxidation resistance and damage tolerance at high temperatures ($>1000^\circ\text{C}$) are required. To avoid fibre damage, near net-shape fabrication techniques of the composite are required. This has been achieved by using the reaction-bonding process which benefits the oxidation of metal powders producing volume expansion, and hence fully or partially compensating for the sintering-induced shrinkage. Starting materials include Al-Si alloy (80:20), Si metal, α -Al₂O₃ and mullite precursor powders. Due to the variety of starting compounds with different reaction and sintering kinetics, composite fabrication becomes a complex process. Differential scanning calorimetry (DSC) measurements, scanning electron microscopy (SEM) observations, and X-ray diffractometry (XRD) data show that effective milling of metal powder leads to a high degree of mullite formation ($\approx 84\%$) at temperatures as low as 1500°C , although densification of the ceramic compacts remains rather low ($\approx 45\%$ of theoretical density).

Single crystal α -Al₂O₃ monofilaments were used to reinforce the reaction-bonded mullite (RBM) matrix. Although no intense reaction between the matrix and the fibres was observed at process temperature, strong bonding develops between uncoated fibres and the matrix. In order to produce a weaker fibre-matrix interface, which is necessary for improvement of the damage tolerance, the fibres were coated with ZrO₂ by means of high frequency sputtering. Microstructural observations of the fibre surfaces before and after the reaction-bonding process indicate that thick coatings ($>10\ \mu\text{m}$) produce very weak bonding, insufficient for matrix-fibre load transfer due to shrinkage of the low density ZrO₂ layers. Thinner layers ($1\ \mu\text{m}$) produce a better interfacial relation with suitable pull-out of fibres.

1 Introduction

Mullite is an excellent candidate for ceramic components requiring high temperature oxidation resistance.^{1,2} However, due to the low strength and fracture toughness of mullite, continuous-fibre reinforcement is required if the material should be damage tolerant under cycling temperature conditions.

Fabrication of ceramic composites with continuous fibres is a complicated process, since volume shrinkage of the matrix during processing can give rise to fibre damage. Reaction bonding of metal powders has been suggested to be a suitable method to acquire near net-shape production of ceramics. Reaction-bonded silicon nitride (RBSN) and aluminium oxide (RBAO) are the best known examples of such materials, in which sintering-induced shrinkage is at least partially compensated by nitridation or oxidation yielding volume expansion of the starting metals and alloys.^{3,4} Recently, some studies were devoted to fabricating mullite ceramics with this method (reaction bonded mullite; RBM), using Al-Si alloys or Al and Si metal and SiC powders as starting compounds.^{3,4,7}

The aim of the present study was to produce continuous-fibre reinforced mullite matrix composites with long-term oxidation resistance, good high-temperature stability ($\geq 1250^\circ\text{C}$), good thermal shock behaviour, and low creep rate. As a matrix, mullite meets these requirements. One possible way to increase the damage tolerance of the brittle mullite matrix is to use polymer-derived oxide-based fibres. However, most of the commercially available fibres are stable only up to 1250°C for long-term and up to 1400°C for short-term use.⁵ Another approach to solve this problem is to use single crystal fibres. The present paper presents preliminary results on the fabrication of α -Al₂O₃ single crystal monofilament-reinforced mullite composites, making use of a modified reaction-bonding technique.

2 Materials and Experimental Methods

2.1 Processing of composites

2.1.1 Starting materials

Starting materials for mullite reaction bonding were Al–Si (80:20) alloy (24 wt%), mullite precursor (60 wt%), α -Al₂O₃ (14 wt%) and Si metal powders (2 wt%). The laboratory produced (nitrogen-atomized) Al–Si metal powder (Toyal, Osaka, Japan) had a particle size of $d_{av} = 60 \mu\text{m}$. To decrease the mullitization temperature of the system, a commercial mullite precursor produced from colloidal starting materials (Siral, Condea Chemie, Hamburg, Germany) was added. The as-received precursor was a nanometre-sized powder. It was calcined at 400°C in order to burn out the organic species and thereby reduce weight loss during composite processing. α -Al₂O₃ was a sub-micrometre-sized powder (99.995% Al₂O₃, AKP-50, Sumitomo, Tokyo, Japan), while the Si powder had an average particle size of 3 μm (Starck, Goslar, Germany).

For reinforcement of the composite, commercial single crystal corundum (α -Al₂O₃) continuous monofilaments ($d = 125 \mu\text{m}$), with the fibre axis being parallel to the crystallographic *c*-axis of α -Al₂O₃, were used (Saphikon, Milford, USA).

2.1.2 Coating of fibres

Fibres were coated with ZrO₂. Coatings were produced in argon atmosphere at about 150°C by using commercial ZrO₂ (+ 3% HfO₂) targets in a high frequency sputtering equipment (Balzers, Lichtenstein, Germany). For the coating procedure fibres were mounted between metal grids and were rotated (50 rev min⁻¹). Two types of coating experiment were carried out on the α -Al₂O₃ fibres, one having a duration of 15 min and the other a duration of 4 h. After a coating time of 15 min, the layer thickness was about 1 μm ; it reached about 12–15 μm after 4 h of sputtering.

2.1.3 Composite fabrication

The principles of mullite matrix development and composite fabrication are given in Fig. 1. Mullite precursor, α -Al₂O₃ and Si metal powders were mixed with organic pressing aids in alcohol and wet-milled overnight. The Al–Si alloy powder was milled separately according to three different schedules in order to achieve a high degree of oxidation of the Al–Si metal powder at low temperature during reaction bonding:

- wet-planetary milling of the Al–Si alloy powder together with the other reactants;
- separate dry ball-milling of the Al–Si alloy

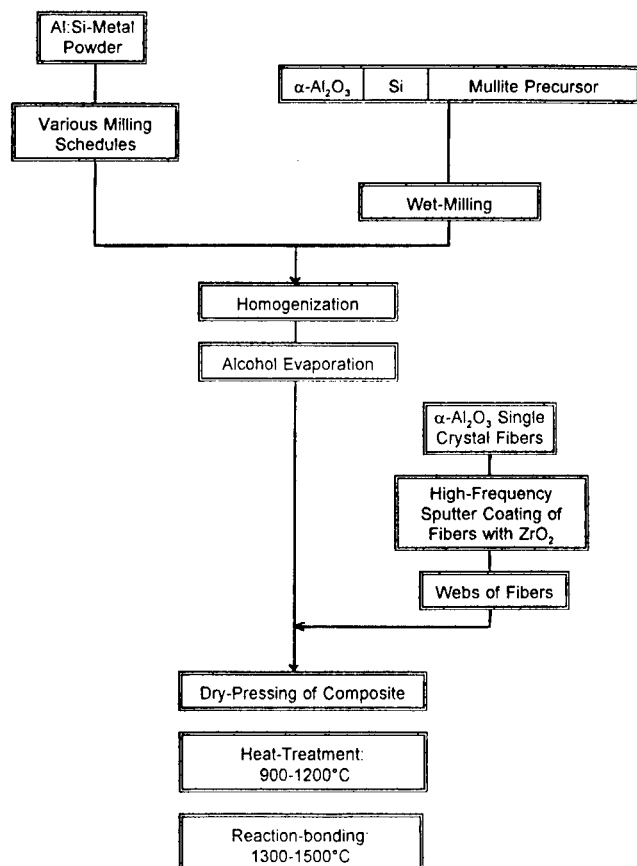


Fig. 1. Processing flow chart of reaction-bonded mullite matrix composites.

powder, prior to mixing with the other reactants. To avoid the danger of flaming, the alloy powder was previously calcined in air at 350°C;

- dry ball-milling of the calcined Al–Si alloy powder as described above but after an attrition milling step in alcohol.

After homogenization of the powder mixtures, alcohol was evaporated in each case by a rotary evaporator. Fibres were arranged in webs by using a fixture which consisted of fine grooves of 100 μm . The fibre webs were fixed with glue at the fibre ends. Composite samples were prepared by uniaxial pressing of the fibre webs, which had been filled with the powder mixtures.

Composite powder compacts were heat-treated (300°C h⁻¹) at 900 and 1200°C for 5 h to promote volume oxidation of Al and Si particles. Reaction-bonding was performed at 1500°C (60°C h⁻¹) for 1 h.

2.2 Characterization methods

2.2.1 X-ray diffractometry (XRD)

X-ray powder diffraction studies were carried out at room temperature with a computer-controlled Siemens D5000 powder diffractometer using Cu $K\alpha$ radiation. Diffraction patterns were recorded in the 2 θ range of 10 to 80°, in a step scan mode (3 s / 0.02°, 2 θ).

2.2.2 Differential scanning calorimetry (DSC)

DSC data were collected by a computer-controlled Netsch DSC 404 equipment with respect to a sapphire reference material considering baseline corrections of the DSC curves. Measurements were carried out in air up to 1400°C, with a heating rate of 10°C min⁻¹.

2.2.3 Microstructural investigations

Microstructural investigations were performed with a Philips 525M scanning electron microscope (SEM) on fracture surfaces of uncoated and ZrO₂-coated α -Al₂O₃ fibres and composites.

3 Results and Discussion

The investigation on the fabrication of α -Al₂O₃ single crystal monofilament-reinforced mullite composites was focused on two main activities: (i) development of the reaction-bonded mullite matrix and (ii) coating of α -Al₂O₃ single crystal monofilaments and subsequent fabrication of composites.

3.1 Development of the reaction-bonded mullite matrix

The main aims of matrix development were to achieve near net-shape production, low Al-Si alloy oxidation and low mullitization temperatures, homogeneous microstructures, and suitable densities. Near net-shape production requires compensation of the sintering-induced shrinkage of the green body by volume expansion of the starting metal powder caused by oxidation of the alloy and subsequent reaction of Al₂O₃ and SiO₂ to mullite.

The present study used an Al-Si metal alloy with an Al:Si ratio of 80:20, which is near to that of mullite (75:25). DSC measurements showed that the as-received Al-Si alloy powder melts at 584°C, whereas surface oxidation of particles starts immediately after melting and reaches to maximum at about 620°C. The sudden oxidation

results in the formation of an oxide layer which slows down further oxidation of the Al-Si alloy particles. Volume oxidation of the Al-Si alloy takes place at about 900°C (Fig. 2). Si oxidizes in turn above 1200°C.⁴

Microstructural observations show that the melting of Al-Si alloy particles prior to oxidation is highly unfavourable, since this produces large, channel-like pores. We believe that the initial exothermal surface oxidation primarily forms a shell structure around the Al-Si alloy particles and consequently causes local temperature increase and melting of the Al-Si alloy left in the core. The melt diffuses out of the oxidized shell through grain boundaries and microcracks and wets the other existing particles, causing large voids in the shell centres. This may be prevented by achievement of complete oxidation of Al-Si particles prior to melting. Literature data report that this is possible if very fine ($\leq 1 \mu\text{m}$) metal powders are used.⁷ Furthermore, addition of α -Al₂O₃ enhances oxidation of metal powders probably due to an increased oxygen partial pressure provided by alumina.³

DSC and XRD investigations showed that the milling procedure of the Al-Si alloy powders has a significant influence on the oxidation behaviour and on reaction processes. According to DSC measurements, wet-milling of the metal powder together with the other reactants has no significant effect on the oxidation behaviour (Fig. 2). Dry-milling of the precalcined metal powders prior to mixing with the other reactants results in an increase of particle surface area. In this case, the rates of surface and volume oxidation are similar (Fig. 3). Surface oxidation becomes more significant if metal powder is attrition-milled. Thereby, the melting and oxidation temperatures of the alloy have also been reduced to 578°C and 600°C, respectively (Fig. 3).

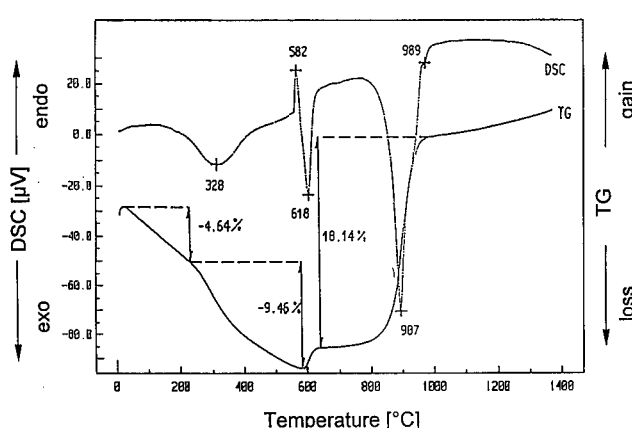


Fig. 2. DSC measurement and thermal gravimetry analysis (TGA) on powder wet-milled in air up to 1400°C (10°C min⁻¹) mixtures.

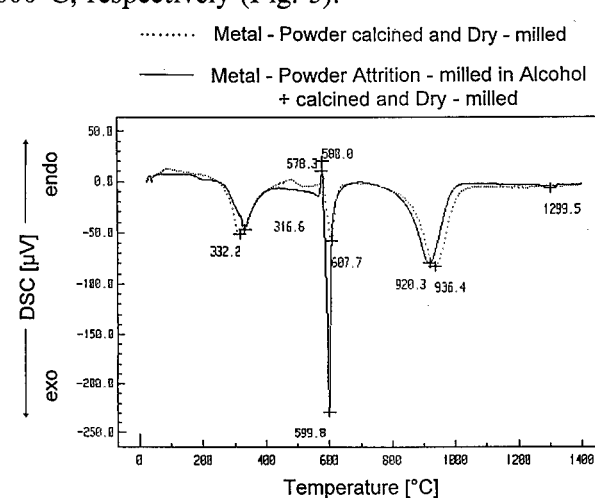


Fig. 3. DSC measurement on metal alloy, ceramic, precursor powder mixtures in air up to 1400°C (10°C min⁻¹), after dry-planetery and attrition-milling of metal powders.

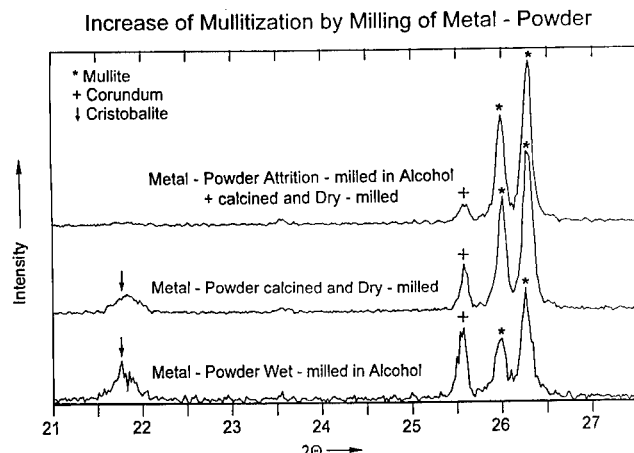


Fig. 4. XRD traces of metal alloy, ceramic and precursor powder compacts after various milling schedules and reaction-bonding processes at 1500°C.

XRD data show that the milling of Al-Si alloy powders greatly affects the rate of mullitization. Best results were obtained by attrition-milled metal powders (Fig. 4). Powder compacts, prepared by attrition-milling and subsequent reaction bonding at 1500°C, contain high mullite (84%) and low corundum (16%) contents. Dry- and wet-milled powders have lower mullite-to-corundum ratios and contain same cristobalite (Fig. 4).

Non-crystalline mullite precursors, transforming to mullite at temperatures above about 1200°C, were added to the starting powders. These low temperature-produced mullite crystals may act as nuclei for reaction-bonding induced mullitization, thus increasing the mullite formation rate at a given temperature with respect to samples without precursor addition in the starting material. Precursor additions to the green bodies also have a strong influence on the volume stability during processing. Precursor additions of 40 wt% led to a slight total volume expansion of the sintered samples (2–15 vol%). Precursor additions of >60 wt% produce volume shrinkages (~10–16 vol%). In order to achieve a near-zero volume shrinkage, precursor contents between 45 and 55 wt% may be considered. The experiments also showed that the processing temperature of the RBM compacts can be reduced by more than 100°C, by addition of ~40 wt% mullite precursor. This may be an essential point, if polycrystalline fibres are used for the reinforcement instead of α -Al₂O₃ single crystal fibres, since the former are unstable at processing temperatures \geq 1300°C.

3.2 Coating of α -Al₂O₃ single crystal fibres and fabrication of composites

Preliminary experiments were carried out to identify the fibre stability, during processing, and to develop suitable fibre coatings. Fibre coatings are essential to produce the necessary fibre-matrix

interaction which on the one hand enables load transfer from the matrix to the fibre, and on the other gives rise to energy-consuming crack deflection and pull-out effects. Frequently used coating materials are SiC, C or graphite-type BN, which may initiate favourable fibre debonding by sliding processes parallel to the respective {001} crystallographic planes.⁸ However, due to poor oxidation resistance, these coatings are not suitable for long-term use in oxidizing atmospheres.

In this study α -Al₂O₃ fibres were coated with ZrO₂ by using high frequency sputtering technique. After 4 h of high frequency sputtering, the thickness of the ZrO₂ layers on the fibres was ~12–15 μ m. The layers exhibit columnar microstructure with ZrO₂ growing perpendicular to the fibre surface (Fig. 5). Between individual ZrO₂ columns small pore-like channels occur. The webs of coated fibres were compacted with matrix powder mixture and die-pressed prior to reaction bonding at 1500°C. After processing the thickness of ZrO₂ layers was reduced to 7 to 8 μ m, due to sintering of the low density ZrO₂ coatings. This

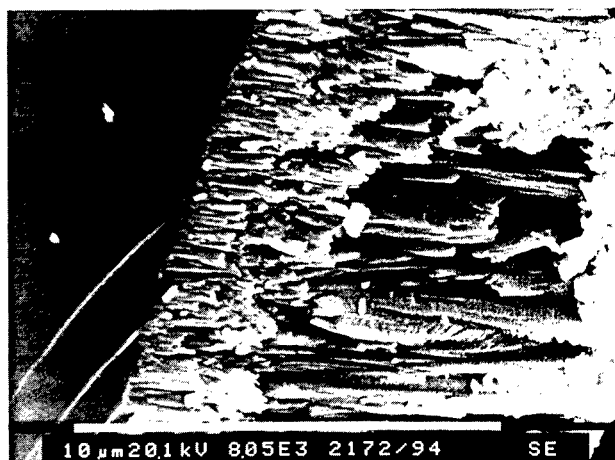


Fig. 5. High frequency sputtered ZrO₂ layer (4 h) on single crystal α -Al₂O₃ fibres, before reaction bonding.



Fig. 6. High frequency sputtered ZrO₂ layer (4 h) on single crystal α -Al₂O₃ fibre, after reaction bonding at 1500°C.

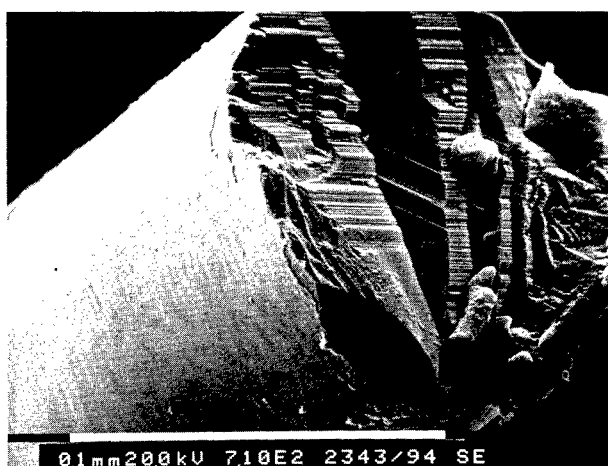


Fig. 7. High frequency sputtered ZrO_2 layer (15 min) on single crystal α - Al_2O_3 fibre, before reaction-bonding process.

effect is reinforced by the strong thermal contraction of ZrO_2 (higher expansion coefficient), caused by cooling down the composite from processing to room temperature (Fig. 6). Thereby, gaps up to 5 μm wide are formed between the fibres and matrix, producing low or even insufficient interfacial fibre–matrix bonding at room temperature.

Short time high frequency sputtering experiments (15 min) deposit thin ZrO_2 layers ($\approx 1 \mu m$) on the α - Al_2O_3 fibres (Fig. 7). The interfacial gaps produced by shrinkage of the ZrO_2 coating after processing in this case are almost negligible. In spite of the very thin ZrO_2 layers on the fibres, no reaction between the fibres and the matrix has been observed.

Our preliminary study on the fabrication of the ZrO_2 -coated α - Al_2O_3 single crystal monofilament-reinforced mullite composite stresses its potential as a high temperature oxidation resistant, damage tolerant material. However, further intensive work

is needed in order to improve RBM matrices, fibre coatings and related fibre–matrix interactions, and the fabrication of composites. These investigations should include a careful mechanical characterization of the composites, extending to strength measurements, damage tolerance studies and fibre push-out tests at room temperature and at high temperatures.

Acknowledgements

The authors gratefully thank Ms G. Paul for DSC measurements and Mr H. Gedanitz for high frequency sputtering of fibres.

References

1. Aksay, A., Dabbs, D. M. & Sarikaya, M., Mullite for structural, electronic and optical applications. *J. Am. Ceram. Soc.*, **75**(10) (1991) 2343–58.
2. Schneider, H., Okada, K. & Pask, J. A., *Mullite and Mullite Ceramics*, John Wiley and Sons, Chichester, 1994.
3. Wu, S. & Claussen, N., Fabrication and properties of low-shrinkage reaction-bonded mullite. *J. Am. Ceram. Soc.*, **74** (1991) 2460–3.
4. Brandt, J. & Lundberg, R., Synthesis of mullite materials by oxidation of metal alloy powder compacts. *Third Euro Ceramics, Vol. 1*, eds P. Durán & J. F. Fernández, Faenza Editrice Ibérica S.L., 1993, pp. 169–76.
5. Schmücker, M., Flucht, F. & Schneider, H., High temperature behaviour of polycrystalline aluminium silicate fibres with mullite bulk composition. I. Microstructure and strength properties. *J. Eur. Ceram. Soc.*, **16** (1996) 281–5.
6. Schneider, H., Saruhan, B., Voll, D., Merwin, L. & Sebald, A., Mullite precursor phases. *J. Eur. Ceram. Soc.*, **11** (1993) 87–94.
7. Claussen, N., Private communication.
8. Ha, J.-S., Chawla, K. K. & Engdahl, R. E., Effect of processing and fibre coating on fibre–matrix interaction in mullite fibre–mullite matrix composites. *Mater. Sci. Eng.*, **A161** (1993) 303–8.

Effects of Composition and Atmosphere on Reactive Metal Penetration of Aluminium in Mullite

Eduardo Saiz,^a Antoni P. Tomsia,^a Ronald E. Loehman^b & Kevin Ewsuk^b

^aCenter for Advanced Materials, Lawrence Berkeley Laboratory, Berkeley, CA, USA

^bSandia National Laboratories, Albuquerque, NM, USA

(Accepted 22 July 1995)

Abstract

Ceramic–metal composites can be made by reactive penetration of dense ceramic preforms by molten Al. Molten Al will reduce mullite to produce a composite of Al_2O_3 , Si and Al. The reaction can be written as $3Al_6Si_2O_{13} + (8 + x)Al \rightarrow 13Al_2O_3 + Al_xSi_y + (6 - y)Si$. The penetration is driven by the strongly negative Gibbs free energy for reaction. In order to assess the influence of atmosphere and temperature in the penetration process, reaction couples of molten Al on mullite were heated at temperatures from 950 to 1150°C, and at $p(O_2)$ from $\sim 10^{-10}$ to $\sim 10^{-20}$ atm. In this range $p(O_2)$ has little influence on reaction kinetics; the reaction rate is controlled by the rate of Si diffusion out of the preform to the external Al source.

Introduction

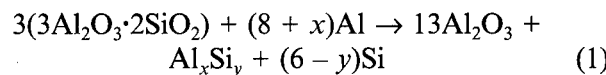
The development of ceramic/metal composites offers an opportunity to produce ceramics with significantly improved properties. Advanced ceramic composites are potential structural materials with improved strength, stiffness and toughness, and thus are more resistant to failure.^{1,2}

Techniques for making ceramic/metal composites by reactive synthesis have been under development for a number of years. Processes that involve a gas-phase reactant include chemical vapour infiltration (CVI), gas-phase reaction bonding and the direct oxidation of molten metal.^{3,4} Reactive processing of condensed phases to make composites include infiltration of reactive liquids into porous preforms, self-propagating high temperature synthesis (SHS) and *in situ* displacement reactions.^{3–5}

Recently, several research groups have reported techniques for making ceramic/metal composites by reaction between molten metals and dense glass or ceramic preforms.^{6–8} In these techniques, a dense oxide preform is converted to a composite

as an oxidation–reduction reaction front moves into the preform. For example, reaction synthesis of composites in the SiO_2/Al system has recently been reported by Matsuo and Inabe⁶ and by Breslin *et al.*^{7,8} Matsuo and Inabe⁶ made $Al_2O_3/Al/Si$ composite bodies by reacting amorphous silica and molten aluminium at 900–1000°C. The reaction product was a mutually interpenetrating structure of ~70 wt% alumina and ~25 wt% Al with reported improvements on bend strength and other physical properties. Breslin *et al.*^{7,8} also reacted amorphous silica with molten aluminium to give similar composites.

In contrast to the work just cited, the ceramic–metal composites discussed in this paper are synthesized from dense ceramic preforms rather than from amorphous silica. Al reacts and penetrates dense ceramic mullite preforms according to the reaction:



The reaction product has the form of an interpenetrating diphasic composite of alumina and an Al/Si alloy (Fig. 1). The reactive metal penetration technique has the advantage of producing complex ceramic parts with near net-shape and very low porosity. It appears that the mechanism for reactive penetration of polycrystalline ceramics such as mullite^{9,10} is completely different from that for the glass preforms described above.^{6–8} Thus the method discussed in this paper can be expected to have its own specific advantages for synthesis of ceramic/metal composites.

If reactive metal penetration is to be a commercially useful way of composite fabrication, it must be economical, reliable and designed to produce the adequate microstructures that will optimize critical properties. The main objective of this work was to study the processing variables that affect Al wetting and reaction with mullite substrates, with particular emphasis on the effects of temperature and $p(O_2)$.

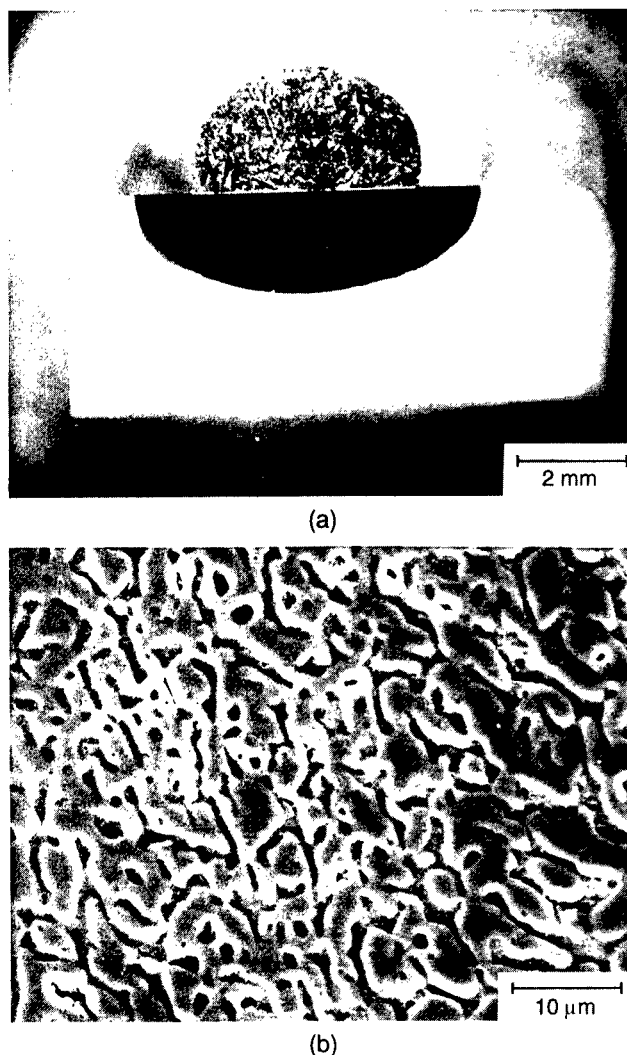


Fig. 1. (a) Al drop on mullite substrate after reaction for 60 min at 1100°C. The reaction zone under the Al drop is a composite of Al and Al_2O_3 . (b) Micrograph of the composite reaction zone showing the interpenetrating Al/ Al_2O_3 microstructure.

Experimental

Mullite substrates for the wetting and infiltration experiments were made using Chichibu MP40 mullite powder (Scimarec Co., Ltd., Tokyo, Japan). Mullite ceramic pellets were formed by cold isostatic pressing at ~ 200 MPa and sintering in vacuum ($\sim 6.7 \times 10^{-4}$ Pa) at 1600–1650°C for 2 h. The final compacts (~ 200 g) had a density $\rho \geq 95\%$ theoretical. Mullite substrates ($\sim 2 \times 2 \times 0.5$ mm) were cut using a diamond saw and were subsequently surface finished using a 800 grit resin-bonded diamond wheel.

Contact angle measurements of molten Al on mullite were made by placing Al cylinders (0.2–0.3 g) on the substrates, and the assemblies were heated in 30 min to the test temperature (950–1150°C) in a furnace with a tubular metal resistance heating element. The contact angle was monitored through a porthole in the furnace and recorded as a function of time using a telegoniometer. The tempera-

ture was recorded with a calibrated Pt–Pt10Rh thermocouple. After the test, the sample was cooled in 10 min to 900°C and in 300 min from 900°C to room temperature. Al/Si alloys for wetting studies were made *in situ* by placing Si chips over the Al cylinders.

The tests were performed in two kinds of atmospheres.

- (a) High $p(\text{O}_2)$: Ar (99.998%) flow (0.5 l min^{-1}) with a Pt tube resistance heating element, $p(\text{O}_2) \sim 10^{-10}$ atm.
- (b) Low $p(\text{O}_2)$: Ar (99.998%) gettered with Ti/Zr chips at 900°C, flowing (0.5 l min^{-1}) with a Ta tube resistance heating element lined inside with Zr foil, $p(\text{O}_2) \sim 10^{-20}$ atm.

In both cases the $p(\text{Ar})$ was kept slightly higher than 1 atm.

After the tests, the samples were mounted in an epoxy resin and cut perpendicular to the metal/ceramic interface. The cross-sections were then polished to $1/4 \mu\text{m}$ diamond finish. The thickness and volume of the reaction layer and its microstructure were measured using reflected light optical microscopy (RLOM) and scanning electron microscopy (SEM). Elemental analysis and X-ray mapping were performed both by energy dispersive (EDS) and wavelength dispersive (WDS) methods.

Results and Discussion

Figure 2 shows the contact angles and reaction layer thicknesses vs. time for wetting experiments carried out at 1100°C, for times up to 150 min in both high and low $p(\text{O}_2)$ atmospheres. In the high $p(\text{O}_2)$ atmosphere ($\sim 10^{-10}$ atm) a thick oxide layer developed on the surface of the Al drop, making the contact angle measurement unreliable. In low $p(\text{O}_2)$ ($\sim 10^{-20}$ atm) the drop surface was shinier and measurements were reproducible. Even after 150 min an equilibrium contact angle was not reached. Despite the differences in contact angles, the microstructures and thicknesses of the reaction layers were practically the same for both atmospheres. The microstructure is that of an Al_2O_3 –Al/Si (alloy) composite. The reaction layer thickness did not follow a $t^{1/2}$ law as would be expected for a diffusion driven process (Fig. 2).

Contact angle measurements carried out for 60 min at temperatures ranging from 950 to 1150°C in low $p(\text{O}_2)$, Fig. 3, show an equilibrium contact angle value of 140° at 950°C. At 1000°C there is a sudden decrease, from $\sim 140^\circ$ to $\sim 110^\circ$, after 25–30 min. For higher temperatures the contact angle decreases with time to values down to $\sim 90^\circ$. Measurements of the reaction layer thickness after

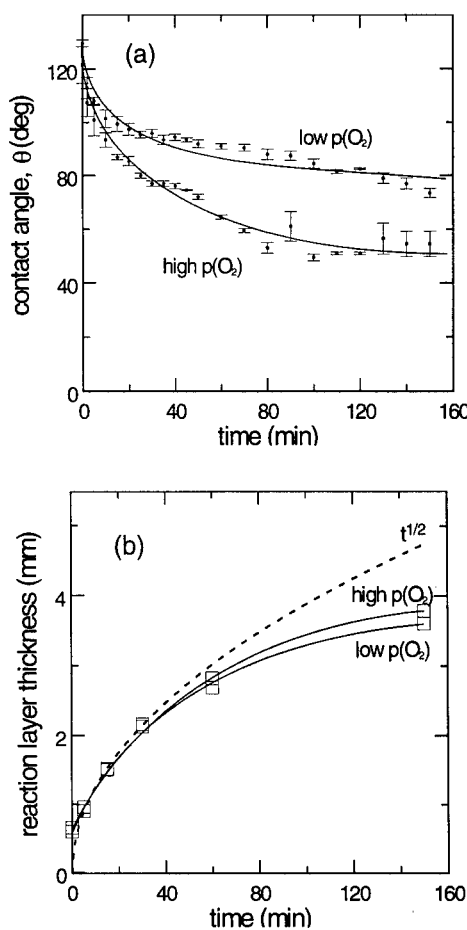


Fig. 2. (a) Contact angle vs. time for aluminium on mullite in different atmospheres ($T = 1100^\circ\text{C}$). (b) Reaction layer thickness vs. time after the wetting experiments ($T = 1100^\circ\text{C}$).

the experiments show a maximum around 1100°C (Fig. 3).

Si mapping and EDS analysis in the reaction layer revealed a lower Si content than that corresponding to the original mullite substrate (Fig. 4). This decrease is due to Al–Si interdiffusion during the test. Large silicon crystals can be observed in the drop (darker crystals in Fig. 5) and metallic Al/Si alloy in the reaction layer after the experiment. There is a small gradient in the Si content in the reaction layer, reaching a maximum at the interface between reaction layer and mullite. The Si content at that interface increases with time at the reaction temperature (Fig. 4).

Wetting experiments between pure Al and mullite were also performed using larger Al drops. In Fig. 6 it can be observed that when the test is done using a 1.43 g drop the contact angle is larger than the one corresponding to the small drops (0.2–0.3 g), and the reaction layer is thicker with the larger Al drop. The thicknesses corresponding to reactions for 0, 5 and 15 min with the small drop and 150 min with the big one fit to a $t^{1/2}$ law.

In order to further assess the role of Al–Si interdiffusion and Si dissolution into Al, a wetting

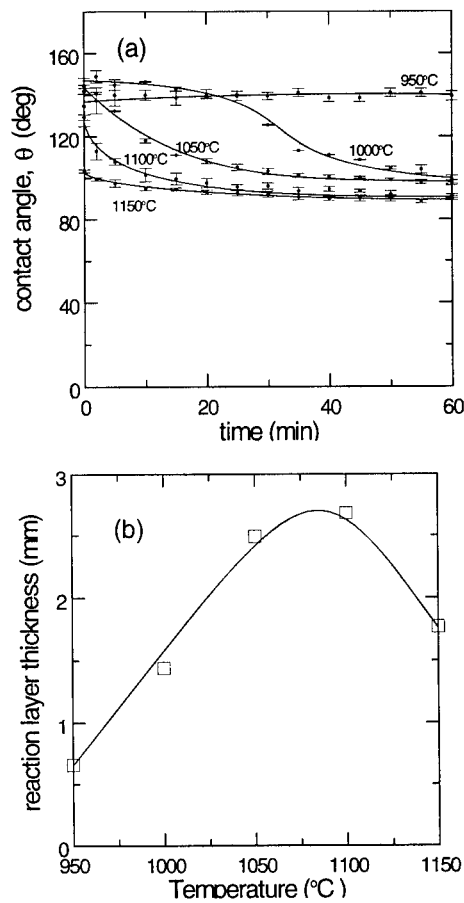


Fig. 3. (a) Contact angle vs. time at different temperatures for Al on mullite at low $p(O_2)$. (b) Reaction layer thickness after wetting experiments at different temperatures in a low $p(O_2)$ atmosphere.

experiment was carried out at 1100°C in a low $p(O_2)$ atmosphere using a Al/Si (40/60 wt%) liquid alloy already saturated with silicon at the test temperature (saturation value at 1100°C is 56 wt% Si¹¹). The contact angle of the Al/Si alloy reached an equilibrium value of 55° (Fig. 6) and the corresponding reaction layer thickness is $180 \mu\text{m}$ (~ 20 times smaller than for pure Al).

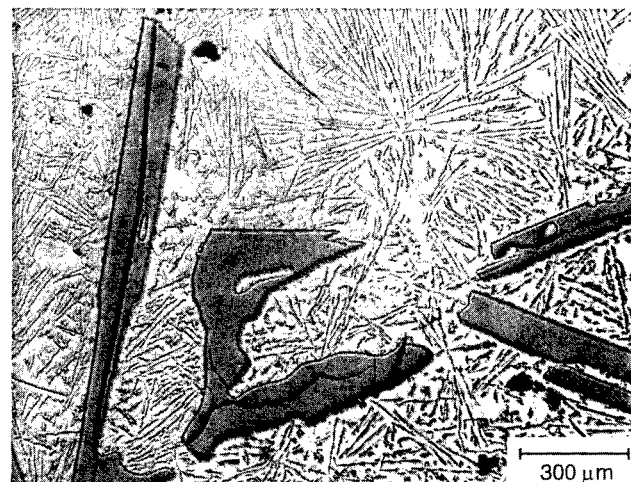


Fig. 4. Micrograph of Al drop after reacting with mullite substrate for 60 min at 1100°C . The needle-like crystals are from Si that diffuses into the molten Al drop during reaction.

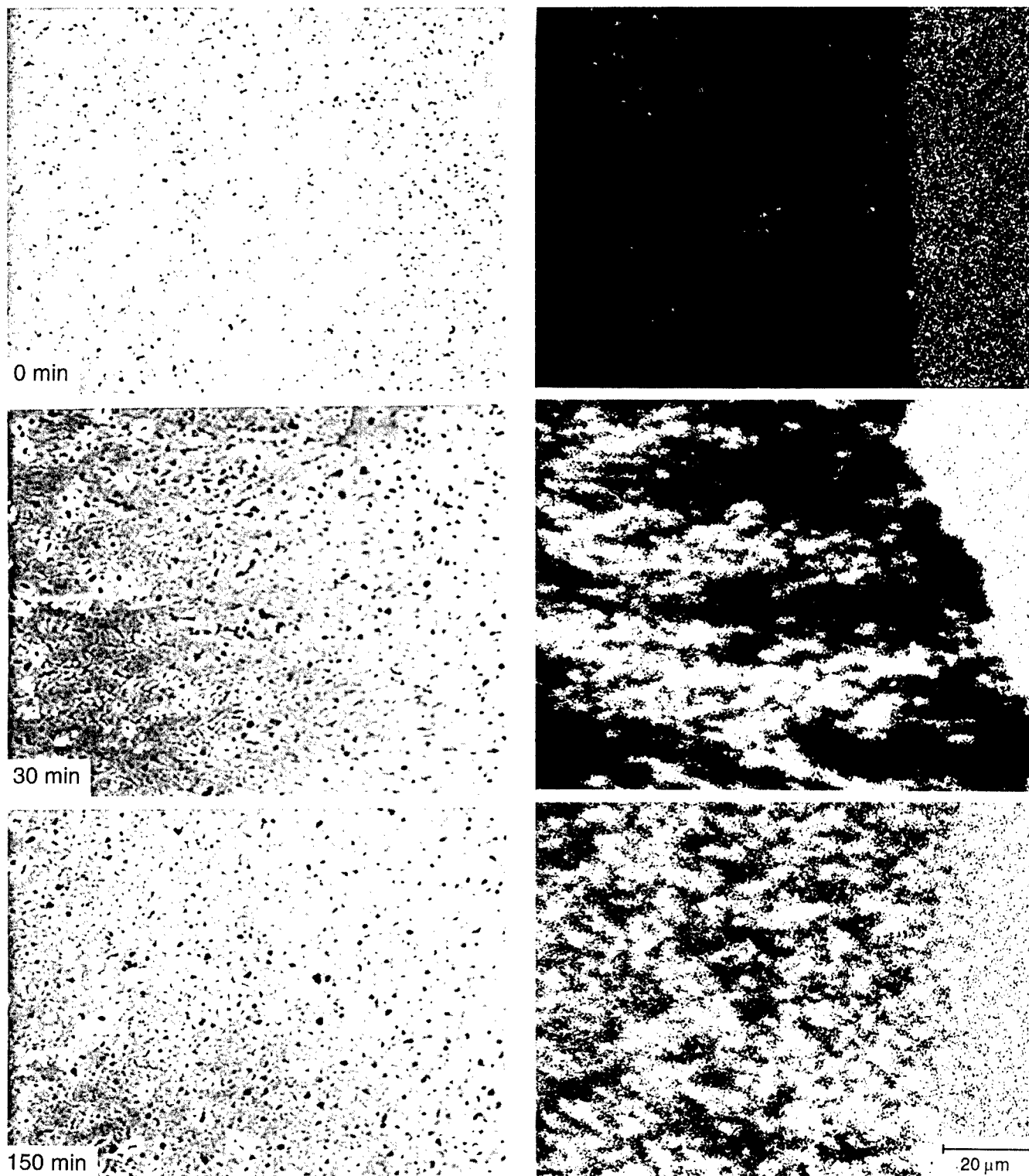


Fig. 5. Micrographs of interface between Al/Al₂O₃ composite and unreacted mullite after 0, 30 and 150 min at 1100°C. The right-hand photos are X-ray compositional maps of Si.

Table 1. Free energy values corresponding to Eqns (3) and (5), y (wt%) value corresponds to Si saturation at each temperature, ΔG_2 is calculated taking $N = 6/y$ (Refs 13 and 14).

Temperature (°C)	ΔG_1 (kJ)	y (Si solubility in Al) ¹¹	ΔG_2 (kJ)	ΔG_R (kJ)
950	-952	0.42	-46	-998
1000	-933	0.46	-44	-977
1050	-914	0.52	-39	-953
1100	-895	0.56	-35	-930
1150	-876	0.62	-29	-905

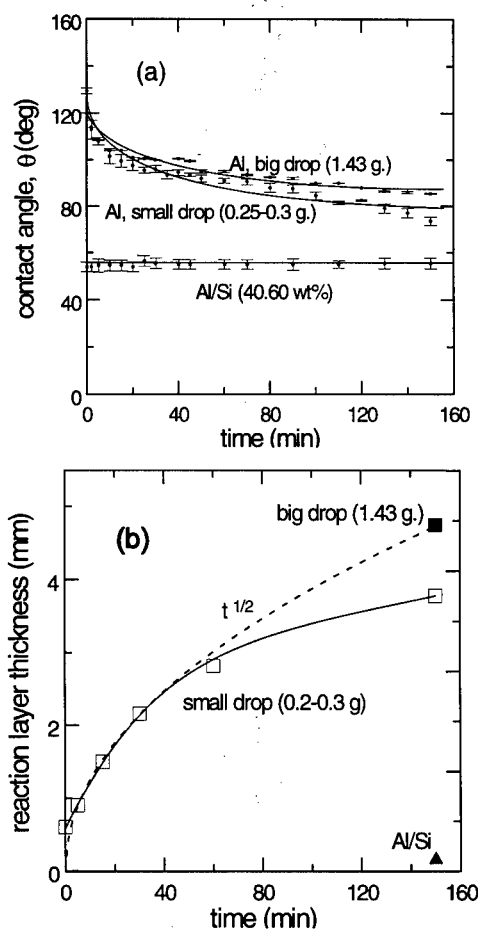
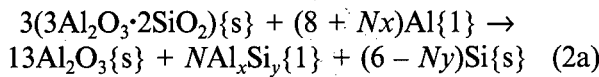


Fig. 6. (a) Contact angle vs. time for different sizes of Al drop and Al/Si alloy on mullite. (b) Corresponding reaction layer thicknesses.

As has been reported by Brennan and Pask,¹² under most conditions there is always an Al_2O_3 layer present on the surface of aluminium. Those authors report that temperatures higher than 950–1000°C are necessary to break that layer and expose fresh Al to the furnace atmosphere. This effect could explain the invariant contact angle of Al on mullite at 950°C in low $p(\text{O}_2)$, see Fig. 3. The sudden decrease in contact angle at 1000°C is probably related to the breakup of this alumina layer.

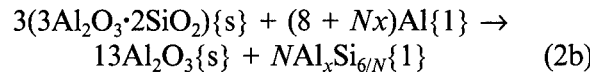
At $T \leq 1000^\circ\text{C}$ the presence of an Al_2O_3 passivating layer on the metal drop surface inhibits the contact of fresh Al and the mullite substrate, consequently reduced reaction rates are observed (Fig. 3). At $T > 1000^\circ\text{C}$, and once the passivating layer breaks, fresh Al is in contact with the ceramic; the reaction front seems isolated from the furnace atmosphere and reaction kinetics together with reaction layer microstructure and composition do not depend on $p(\text{O}_2)$ (Figs 3 and 4).

At the test temperature, the net reaction (1) between mullite and Al can be rewritten to show the effect of the starting amount of Al on Si precipitation:



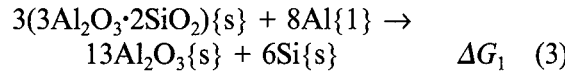
where $x + y = 1$ and where y , the solubility of Si in Al, depends on temperature. Nx represents the excess of Al with respect to the amount necessary for mullite reduction.

With an excess of Al (no Si precipitates, $N > 6/y$):

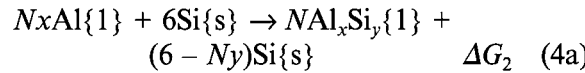


ΔG_R , the change in free energy corresponding to the reactions (2a) and (2b), must be negative in order for the reactions to proceed as written.

The reactions (2a) and (2b) are made up of two partial reactions, Eqns (3) and (4a), (4b):



The second partial reaction can be written in two ways, depending on whether the Si concentration is high enough to give precipitates. For $N \leq 6/y$ [Eqn (2a)], Si precipitates:



For $N > 6/y$ [Eqn (2b)], no Si precipitates:



Then, depending on whether the concentration of Si exceeds the solubility limit at the processing temperature or not:

$$\Delta G_R = \Delta G_1 + \Delta G_2 \quad \text{or} \quad \Delta G_R = \Delta G_1 + \Delta G_3 \quad (5)$$

Table 1 shows some of the ΔG_R , ΔG_1 , ΔG_2 and y values at different temperatures. It can be seen that the contribution of Si dissolution to the total free energy of the reaction is relatively low.

The corresponding change in the volume of solids at the test temperature is:

$$\% \Delta V = [13V_{\text{Al}_2\text{O}_3} + (6 - Ny)V_{\text{Si}} - 3V_{3\text{Al}_2\text{O}_3 \cdot 2\text{SiO}_2}] \times 100/3V_{3\text{Al}_2\text{O}_3 \cdot 2\text{SiO}_2} \quad (6)$$

where $V_{\text{Al}_2\text{O}_3}$ (25.7 cm³ mol⁻¹), V_{Si} (12.1 cm³ mol⁻¹) and $V_{3\text{Al}_2\text{O}_3 \cdot 2\text{SiO}_2}$ (135 cm³ mol⁻¹) are correspondingly the molar volumes of alumina, silicon and mullite. If the liquid does not dissolve any of the Si that originates from the mullite reduction, $y = 0$ and $\% \Delta V \approx 0$, Al and mullite must then react by solid-state diffusion through an $\text{Al}_2\text{O}_3/\text{Si}$ layer. On the other hand, if there is a Si dissolution, $y > 0$ and $\% \Delta V < 0$ ($\% \Delta V = -17\%$ for $y = 6/N$), space is created through which the Al/Si liquid can penetrate into the reaction front and the reaction can progress at a faster pace than the one corresponding to solid-state diffusion driven processes. When the experiment is performed using Al/Si alloy already saturated in Si, the liquid does not dissolve any silicon coming from mullite reduction; then, on one hand, there is a reduction in the total free energy of the reaction because the inverse of Eqn

(4a), for $N = 6/y$, takes place, while on the other hand, the liquid does not dissolve Si and does not create space to penetrate fast into the reaction front. These can explain the lower reaction rate observed for the Al saturated with Si at the test temperature (Fig. 6).

In the case of the small drop, the concentration of Si in the Al drop increases noticeably after 30–60 min, consequently the diffusion rate of Si decreases and so does the reaction rate. In the case of the large drop the Si concentration remains low and the diffusion rate of Si remains constant, consequently the reaction rate is higher and exhibits a $t^{1/2}$ law corresponding to a diffusion-driven process. The calculated diffusion coefficient, $D \approx 2 \times 10^{-5} \text{ cm}^2 \text{ s}^{-1}$, is in the order of diffusion coefficients observed in liquid metals.¹⁵

These results indicate that Si/Al interdiffusion is the kinetic limiting step for the reaction/penetration of molten Al into dense mullite ceramics.

It can also be observed that the contact angle does not decrease when the reaction layer thickness increases (the bigger drop has a bigger reaction layer). It seems that the decrease in contact angle as the reaction goes on is more related to the increase in Si concentration in the drop.

Conclusions

The results presented in this paper indicate that the kinetic limiting step for the reactive penetration of molten Al into dense mullite substrates is the diffusion of Si out of the composite. In the range of $p(\text{O}_2)$ studied the oxygen partial pressure does not affect appreciably either the penetration rate or the microstructure of the reaction layer.

These data suggest that processing conditions can be adjusted to make this a practical system for

the fabrication of metal/ceramic composites by reactive metal penetration.

Acknowledgements

This work was supported by the US DOE Office of Industrial Technologies and the US DOE under contract No. DE-AC04-94AL85000. E. Saiz wishes to acknowledge Fulbright Foundation and MEC (Spain) for financial support.

References

1. Harrigan, W. C. Jr, in *Metal Matrix Composites Processing and Interfaces*, eds R. K. Everett & R. J. Arsenault, Academic Press, New York, 1991, Vol. 1.
2. Ashby, M. F., *Acta Metall. Mater.*, **41**[5] (1993) 1313.
3. Chiang, Y., Haggerty, J. S., Messner, R. P. & Demetry, C., *Ceram. Bull.*, **68**[2] (1989) 420.
4. Claussen, N., *J. de Physique IV, Colloque C7*, **3** (1993) 1327.
5. Hilling, W. B., *Ceram. Bull.*, **73**[4] (1994) 56.
6. Matsuo, S. & Inabe, T., *Tokyo Ceramics*, (1991) 222.
7. Breslin, M. C., Rignalda, J., Seeger, J., Marasco, A. L., Daehn, G. S. & Fraser, H. L., *Ceram. Eng. Sci. Proc.*, **15**[4] (1994) 104.
8. Breslin, M. C., US Pat. No 5 214 011, 25 May 1993.
9. Tomsia, A. P., Loehman, R. E. & Ewsuk, K., *J. Am. Ceram. Soc.*, submitted.
10. Fahrenholtz, W. G., Ewsuk, K. G., Loehman, R. L. & Tomsia, A. P., in *In Situ Reactions for Synthesis of Composites, Ceramics and Intermetallics*, eds E. B. Berrera, F. D. S. Marquis, W. E. Frazier, S. G. Fishman, N. N. Thadhani & Z. A. Munir, The Minerals, Metals and Materials Society, Warrendale, PA, 1995.
11. *Binary Alloy Phase Diagrams*, ed. T. B. Massalski, ASM International, Metals Park, OH, 1990.
12. Brennan, J. J. & Pask, J. A., *J. Am. Ceram. Soc.*, **51**[10] (1968) 569.
13. Kubachesky, O. & Alcock, C. B. (eds), *Principles of Metallurgical Thermodynamics*, 5th Edn, Pergamon Press, New York, 1979.
14. HSC Chemistry for Windows, Outokumpu Research.
15. Smithells, C. J. (ed.), *Metals Reference Book*, Butterworth & Co, London, 1976.

High Temperature Behaviour of Polycrystalline Aluminosilicate Fibres with Mullite Bulk Composition. I. Microstructure and Strength Properties

M. Schmücker, F. Flucht & H. Schneider

German Aerospace Research Establishment (DLR), Institute for Materials Research, D-51140 Köln, Germany

(Accepted 22 July 1995)

Abstract

Temperature-dependent microstructure/strength relations of commercial aluminosilicate fibres with near-stoichiometric mullite bulk composition are investigated.

As-received Nextel 440TM fibres (70 wt% Al₂O₃, 28 wt% SiO₂, 2 wt% B₂O₃), consisting of nanometre-sized γ -Al₂O₃ and a minor amount of amorphous phase, have tensile strength of 2100 MPa. Heat treatment at 1200°C causes transformation into fine-grained mullite (mean grain size: 80 nm). The remaining tensile strength is 1600 MPa. Heat treatment at higher temperatures leads to considerable reduction of strength (1100 MPa after firing at 1400°C) attributed to mullite grain coarsening (mean grain size at 1400°C: 135 nm).

Altex 2K fibres (72 wt% Al₂O₃, 28 wt% SiO₂) consist of single-phase mullite with a mean grain size of 115 nm. Tensile strength is comparatively low (1250 MPa). Annealing at 1000°C causes a significant increase in strength (1600 MPa). Above 1200°C mullite coarsening and strength reduction are similar to those of Nextel 440 fibres.

1 Introduction

Aluminosilicate fibres are used in a wide variety of high temperature applications, e.g. for thermo-couple insulations, furnace seals and filter bags.¹ Another promising application of aluminosilicate fibres is the reinforcement of ceramic matrices in composites (see, for example, Ref. 2). Aluminosilicate fibres of mullite bulk composition may consist of non-crystalline precursor states, of nanocrystalline γ -Al₂O₃ plus SiO₂ phase assemblages or of microcrystalline mullite. Due to their phase compositions and/or small crystal sizes, the microstructures of these fibres are not stable thermodynamically: by heat treatment at sufficiently high temperature, phase transformations and grain

coarsening occur which in most cases are harmful for the mechanical properties of the fibres. Detailed knowledge of the temperature-dependent microstructures and strengths is therefore essential for the prediction of possible applications of the fibres in high temperature composites.

2 Experimental

2.1 Sample material

Two types of technical aluminosilicate fibres were investigated: Nextel 440TM (3M, St. Paul, MN, USA) with 70 wt% Al₂O₃, 28 wt% SiO₂, 2 wt% B₂O₃¹ and Altex 2K (Sumitomo Chemical Inc., Osaka, Japan) with 72 wt% Al₂O₃ and 28 wt% SiO₂. Nextel 440 fibres have elliptical cross-sections with 7 and 12 μ m diameters and consist of transition alumina (designated as γ -Al₂O₃ in the following) and silica-rich glassy phase. Sumitomo Altex 2K fibres have circular cross-sections with a mean diameter of 12 μ m, and consist of single-phase mullite. Both fibre materials were annealed in air in an induction heated laboratory furnace at 1000, 1100, 1150, 1200, 1300, 1400, 1500, 1600°C for 4 h in each case.

2.2 Single fibre tensile strength measurements

Room temperature strengths of the fibres annealed for 4 h at various temperatures were determined, based on at least 30 individual measurements in each case. Single fibres were glued on a paper bridging the centre of a circular hole (diameter \approx 5 mm). On both sides of the hole the paper was separated and bridged by a polymer fibre. The arrangement was installed in a tensile testing equipment with a load cell for very small loads. After fixing the holder the polymer fibres were melted and special care was taken that the test fibre was not damaged by this procedure. Tensile tests were performed under a constant crosshead speed of 0.2 mm min⁻¹. Actual tensile strength

values of fibres were then calculated considering individual fibre cross-sections measured by scanning electron microscopy. Elliptical cross-section areas of Nextel fibres were determined according to the procedure described by Fernando *et al.*³

2.3 Microstructural characterization of fibres

Due to the small grains occurring in all fibres, microstructures were examined by transmission electron microscopy (TEM, Philips EM 430) with an accelerating voltage of 300 kV. Electron transparent areas in long sections of the fibres were achieved by Ar-ion beam milling. Based on TEM photographs, grain area distributions of starting materials and of heat-treated fibres were calculated by means of a Synoptics-Semper 6 image processing system using at least 100 grain area values. Diameter distributions and mean grain sizes for each sample were calculated neglecting intersectional effects.

Information on the temperature-dependent phase compositions were obtained by X-ray powder diffractometry. Studies were carried out with a computer-controlled Siemens D 5000 powder diffractometer using Ni-filtered CuK_α radiation. Diffraction patterns were recorded in the 2θ range from 10 to 80°, in step scan mode.

3 Results

3.1 Tensile strengths of fibres

Tensile strengths of Nextel and Altex fibres as-received and heat-treated at 1000, 1200 and 1400°C are given in Table 1 and Fig. 1. The tensile strength of Nextel fibres in the as-received state is >2 GPa. This value remains nearly constant up to 1000°C heat treatment. At higher annealing temperatures, however, the tensile strength decreases. Tensile strength of as-received Altex 2K fibres is significantly lower than that of Nextel 440 fibres. The strength of the Altex fibres annealed at 1000°C significantly increases with respect to the starting material, whereas the value of the 1200°C sample is similar to that of the as-received material. Distinct strength reduction is observed in Altex 2K fibres heat-treated at 1400°C. Above 1400°C, both fibres become so brittle that handling with regard to the testing facilities was not possible, which indicates drastic decrease in strength.

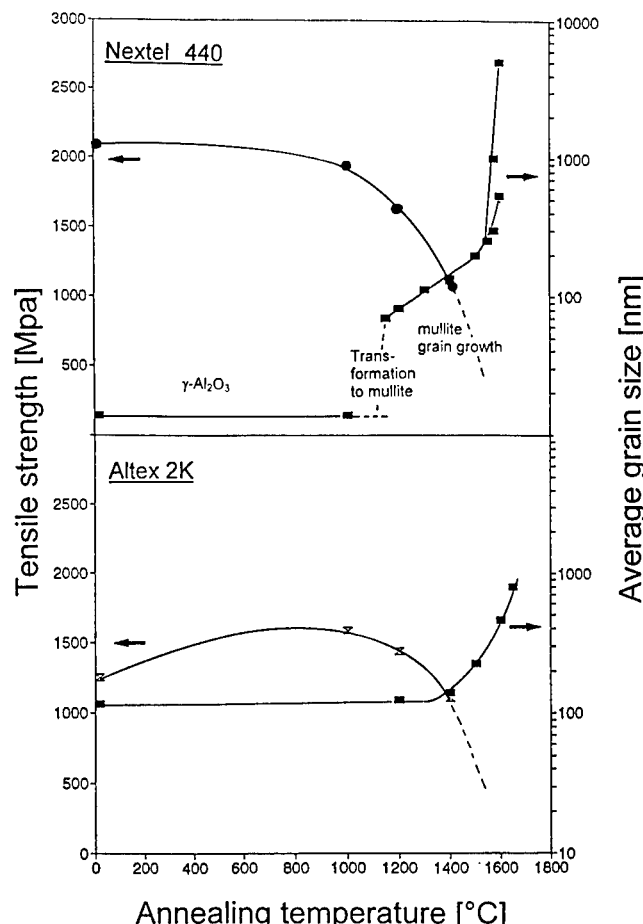


Fig. 1. Grain size and strength of Nextel 440 and Altex 2K fibres heat-treated between 1000 and 1600°C.

3.2 Phase content and microstructural development of fibres

3.2.1 Nextel 440 fibres

According to phase content and microstructure, the temperature-dependent development of the Nextel 440 fibres can be subdivided into three stages (Fig. 1): 'γ-Al₂O₃ + SiO₂ stage'; 'γ-Al₂O₃ + SiO₂ to mullite transformation stage'; and 'mullite grain growth stage'.

(a) $\gamma\text{-Al}_2\text{O}_3 + \text{SiO}_2$ stage. The $\gamma\text{-Al}_2\text{O}_3 + \text{SiO}_2$ region extends from the as-received state up to ≈1100°C. A typical microstructure of this stage is given in Fig. 2, showing equiaxed $\gamma\text{-Al}_2\text{O}_3$ crystallites with an average grain size of 15 nm. Annealing up to 1100°C causes no coarsening of the $\gamma\text{-Al}_2\text{O}_3$ nanocrystals.

Table 1. Tensile strength of Nextel and Altex 2K fibres as-received and heat-treated at different temperatures

	as-received		1000°C		1200°C		1400°C	
	Nextel	Altex	Nextel	Altex	Nextel	Altex	Nextel	Altex
σ_m (MPa)	2086	1253	1954	1594	1635	1439	1117	1108
Weibull parameter, m	4.9	6.1	6.0	5.8	4.6	5.1	6.1	5.7

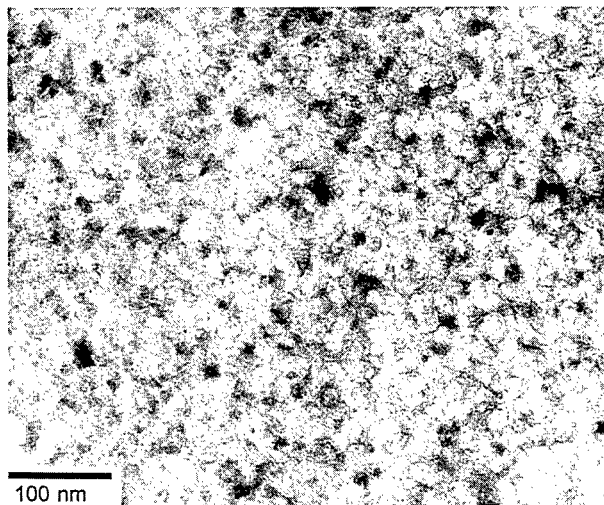


Fig. 2. Micrograph (TEM) of as-received Nextel 440 fibres: nanosized $\gamma\text{-Al}_2\text{O}_3$ crystals.

(b) $\gamma\text{-Al}_2\text{O}_3 + \text{SiO}_2$ to mullite transformation stage. The $\gamma\text{-Al}_2\text{O}_3 + \text{SiO}_2$ to mullite transformation region extends from ≈ 1100 to 1200°C . In samples heat-treated at 1100°C small mullite crystals are occasionally detected by means of convergent beam diffraction or lattice fringe imaging (Fig. 3). With increasing temperature the mullite content gradually increases. A detailed analysis of the $\gamma\text{-Al}_2\text{O}_3 + \text{SiO}_2$ to mullite transformation behaviour is presented in the second part of this study.⁴

(c) Mullite grain growth stage. This region refers to annealing temperatures $> 1200^\circ\text{C}$, where distinct mullite grain coarsening occurs. Microstructures of Nextel 440 fibres completely transformed to mullite by heat treatments at 1200 , 1400 and 1600°C are shown in Figs 4 to 6. Firing at 1200°C leads to irregular-shaped mullite crystals with an average grain size of 80 nm (Fig. 4). After firing at 1400°C the mean grain size of mullite has increased to 135 nm and the crystals develop more

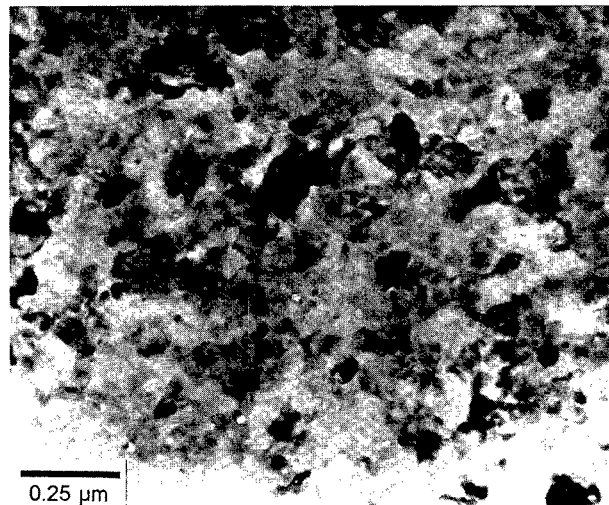
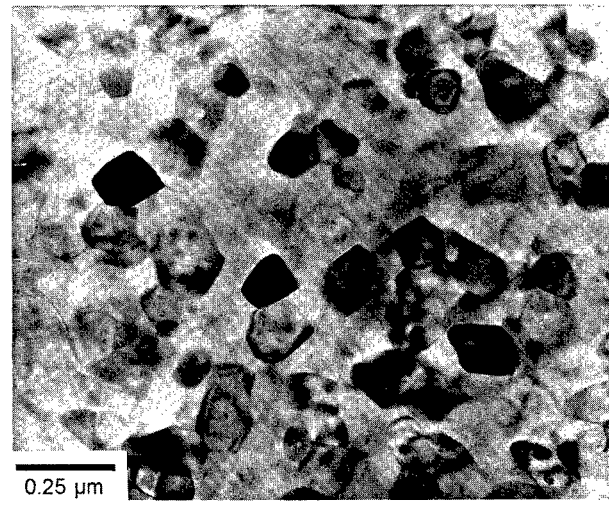
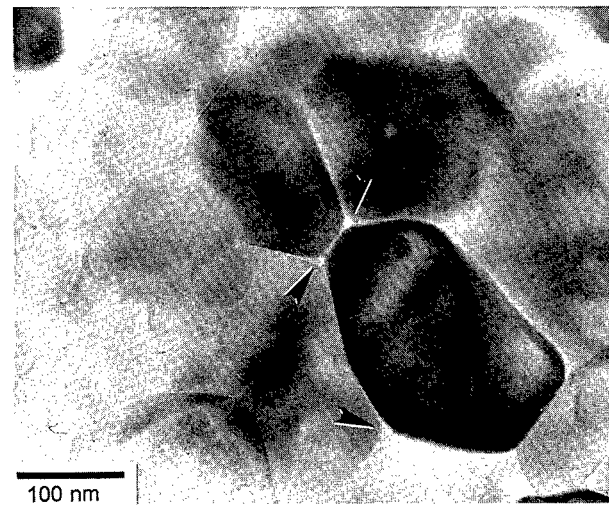


Fig. 4. Micrograph (TEM) of Nextel 440 fibres heat-treated at 1200°C , 4 h: irregular-shaped mullite grains.

regular polygonic shapes [Fig. 5(a)]. At triple grain junctions glassy phase is detected [Fig. 5(b)]. Above 1550°C exaggerated grown mullite crystals



(a)



(b)

Fig. 5. Micrographs (TEM) of Nextel 440 fibres heat-treated at 1400°C , 4 h: (a) coarsened polygonic mullite grains; (b) glassphase at triple grain junctions (arrows).

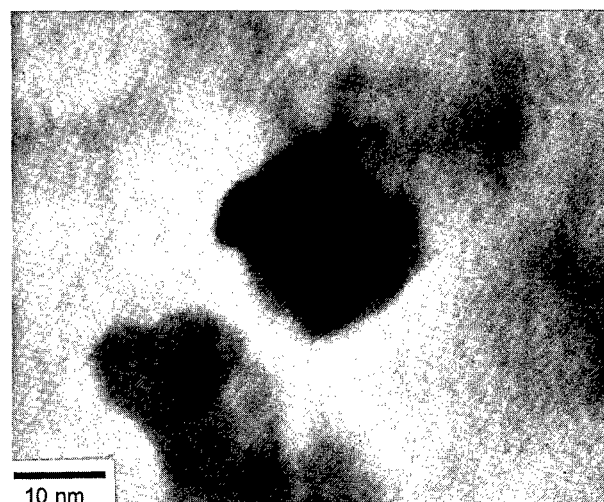


Fig. 3. Micrograph (TEM) of Nextel 440 fibres heat-treated at 1100°C , 4 h: small mullite crystal with (100) lattice fringes.

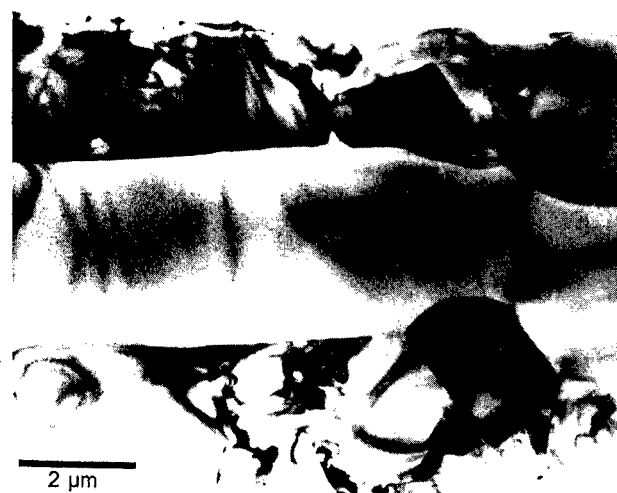


Fig. 6. Micrograph (TEM) of Nextel 440 fibres heat-treated at 1600°C, 4 h: secondary grain growth of mullite.

are observed which are embedded in a finer grained matrix (Fig. 6). The bimodal grain size distribution leads to the split grain size curve at $\geq 1550^{\circ}\text{C}$ (Fig. 1): the upper branch corresponds to the large secondary mullite grains, while the lower one represents the unconsumed primaries.

3.2.2 Altex 2K fibres

The microstructure of the as-received Altex 2K fibres is similar to that of Nextel 440 heat-treated at 1200°C , i.e. containing irregular-shaped mullite grains with a mean grain size of ≈ 115 nm. Heat treatments at 1000°C and 1200°C cause no distinct microstructural change, but above 1200°C moderate grain coarsening occurs (Fig. 1). The average grain sizes and strengths of Altex fibres fired at 1400°C are very similar to those of Nextel 440 fibre heat-treated under the same conditions. However, secondary growth of mullite grains does not occur in Altex 2K fibres even at 1650°C .

4 Discussion

Only $\gamma\text{-Al}_2\text{O}_3$ could be detected by TEM in the as-received Nextel 440 fibres, although, according to the bulk composition, SiO_2 is present at 28 wt%. Though a certain amount of SiO_2 is known to be incorporated in the alumina phase,⁵ a remaining fraction must occur, presumably as very thin (~ 1 nm) non-crystalline layers which are not detectable by our TEM analyses of the nanocrystalline material.

These amorphous films surrounding the transition alumina grains may explain the stability of the nanocrystalline microstructure up to 1100°C : obviously the high Si-O bond strength⁶ within the SiO_2 films may cause them to act as diffusion barriers, thus preventing crystal coarsening. On the other hand, the occurrence of amorphous films

enveloping $\gamma\text{-Al}_2\text{O}_3$ crystallites considerably reduces the mechanical strength and creep resistance at elevated temperature by viscous flow mechanisms.

Between about 1100 and 1200°C the nanometre-sized $\gamma\text{-Al}_2\text{O}_3 + \text{SiO}_2$ phase assemblage transforms to mullite. The phase transformation is associated with a strong increase of mean grain size and leads to a distinct reduction of tensile strength. Heat treatments of Nextel 440 fibres between 1200 and 1400°C cause a drastic decrease in strength, attributed to grain coarsening. According to the reciprocal relationship between grain size and strength:⁷

$$\sigma \propto d^{-p}$$

(where σ is strength, d is grain size and $p \approx 0.5$), it turns out that the coarsening of small grains in particular has a strong influence on strength. A strength reduction of 23% (380 MPa) is estimated considering Nextel grain growth data between 1200 and 1400°C . The slightly higher strength loss of 31% (520 MPa) found experimentally may be caused by changes in grain morphology. Strong agglomerations of micropores or glassy phase are assumed if the irregular-shaped mullite crystals develop planar interfaces at high temperature. Obviously the increasing flaw density reduces the mechanical strength.

Above 1550°C exaggerated grain growth takes place in Nextel 440 fibres. Presumably secondary grain growth is assisted by the existence of grain boundary glassy phase separating the surfaces of the small and large grains.⁸ Low viscosity glassy phase occurring at high temperature is related with the B_2O_3 content of the fibres. Retention of B_2O_3 in fired Nextel 440 fibres is deduced from very small weight loss ($< 1\%$) after heat treatment at 1600°C .¹

As-received Altex 2K fibres exhibit similar microstructures to Nextel 440 fibres in the temperature range just beyond the $\gamma\text{-Al}_2\text{O}_3 + \text{SiO}_2$ to mullite transformation (1200°C). We assume therefore that the Altex fibres were produced in this temperature range. This suggestion fits well with the observation that there is no significant change of the microstructure up to 1200°C . Moreover, no glassy phase is detected, probably due to the lack of B_2O_3 flux in Altex 2K fibres. The probable lack of a grain boundary glass phase accounts for the better creep resistance of Altex 2K fibres than of Nextel 440, although the room temperature strength of Altex 2K is comparatively low. The increase of tensile strength of Altex 2K fibres after annealing at 1000°C is attributed to the reduction of residual stresses. Residual stresses may be caused by rapid cooling of the fibres during the fabrication process, due to anisotropy of the thermal expansion coefficients of mullite ($\sim 3.9 \times 10^{-6} \text{ K}^{-1} \parallel a\text{-axis}$ and $\sim 7 \times 10^{-6} \text{ K}^{-1} \parallel b\text{-axis}$)⁹.

The present study of the two commercial polycrystalline aluminosilicate fibres with near-stoichiometric mullite composition shows that fibres consisting of nanocrystalline γ - Al_2O_3 + SiO_2 in the as-received state are suitable for high strength applications at low or moderate temperatures. For applications at higher temperatures ($> 1100^\circ\text{C}$), fibres consisting of polycrystalline mullite without any coexisting glass phase will be more favourable due to the higher creep resistance and resistance against creep-induced fracture.

Moreover, it has been shown that suitable mechanical properties for high temperature applications of the fibres demand homogeneous and extremely fine-grained microstructures and that the content of non-crystalline grain boundary phase should be as low as possible. However, fulfilment of both requirements simultaneously is difficult. For instance, addition of B_2O_3 to a diphasic aluminosilicate starting material causes high nucleation density of mullite, leading to a favourable fine-grained microstructure.⁴ On the other hand, due to B_2O_3 addition, the tendency of forming amorphous grain boundary phases is increased which has a negative influence on the high temperature mechanical properties.

Another result of the investigation is that grain coarsening at elevated temperatures does reduce the strength of the fibres drastically. Therefore

further developments of mullite fibre should have the aim of grain growth reduction. A possible way to be successful is doping the starting materials with vanadium or chromium, both of which have a negative influence on the mullite grain growth rate.¹⁰

References

1. *Nextel Keramische Fasern*, 3M technical data, 1989.
2. Schneider, H., Okada, K. & Pask, J., *Mullite and Mullite Ceramics*. John Wiley & Sons, Chichester, 1994, p. 186.
3. Fernando, J. A., Chawla, K. K., Ferber, M. K. & Coffey, D., Effect of boron nitride coating on the tensile strength of Nextel 480TM fibre. *Mater. Sci. Eng.*, **A154** (1992) 103–8.
4. Hildmann, B. O., Schneider, H. & Schmücker, M., High temperature behaviour of polycrystalline aluminosilicate fibres with mullite bulk composition. II. Kinetics of mullite transformation. *J. Eur. Ceram. Soc.*, **16** (1996) 287–92.
5. Schneider, H., Voll, D., Saruhan, B., Schmücker, M., Schaller, T. & Sebald, A., Constitution of the γ -alumina phase in chemically produced mullite precursors. *J. Eur. Ceram. Soc.*, **13** (1993) 441–8.
6. *Ullmann's Encyclopedia of Industrial Chemistry*, Vol. 23A. VCH Publishers, Inc., Weinheim, 1993, p. 586.
7. Kingery, W. D., Bowen, H. K. & Uhlmann, D. R., *Introduction to Ceramics*, 2nd edn. John Wiley & Sons, New York, 1976, p. 794.
8. Kingery, W. D., Bowen, H. K. & Uhlmann, D. R., *Introduction to Ceramics*, 2nd edn. John Wiley & Sons, New York, 1976, p. 465.
9. Schneider, H. & Eberhard, E., Thermal expansion of mullite. *J. Am. Ceram. Soc.*, **73** (1990) 2073–6.
10. Schneider, H., Transition metal distribution in mullite. *Ceram. Trans.*, **6** (1990) 135–58.

High Temperature Behaviour of Polycrystalline Aluminosilicate Fibres with Mullite Bulk Composition. II. Kinetics of Mullite Formation

B. O. Hildmann, H. Schneider & M. Schmücker

German Aerospace Research Establishment (DLR), Institute for Materials Research, D-51140 Köln, Germany

(Accepted 22 July 1995)

Abstract

Kinetics and mechanisms of mullite formation in technical diphasic aluminosilicate fibres (NextelTM 440), consisting of transition alumina and a non-crystalline silica-rich phase, were studied by quantitative X-ray phase analysis. The as-received fibres were heat-treated in the temperature and time ranges from 1130 to 1215°C and from 7.5 min to 32 h. The overall mullitization process can be described by an Avrami reaction law, or alternatively, by a simple exponential reaction law with a temperature-dependent induction period. Early stages of mullite formation with a low mullitization degree ($\alpha = 0.02$) are characterized by an activation energy of $\sim 650 \text{ kJ mol}^{-1}$, whereas the apparent activation energy of the overall transformation reaction is $\sim 900 \text{ kJ mol}^{-1}$. Both activation energies are significantly lower than those described in the literature for other diphasic aluminosilicate gels. The relatively low activation energies of mullite formation in Nextel 440 fibres are attributed to the small B_2O_3 content of the as-received fibres. The presence of B_2O_3 may be responsible for the decrease of viscosity of the coexisting non-crystalline SiO_2 -rich phase, by which diffusion, and mullite nucleation and growth is accelerated.

1 Introduction

NextelTM 440 aluminosilicate fibres in the as-received state are diphasic and consist of nanocrystalline transition alumina ($\gamma\text{-Al}_2\text{O}_3$) and a non-crystalline silica-rich phase, which contains 2 wt% B_2O_3 . Above 1100°C these fibres transform into mullite which is associated with a distinct drop of tensile strength from about 2.0 to 1.6 GPa. A detailed description of the temperature-dependent microstructural development and related mechanical properties is presented in Part I of this study.¹

Mullite formation processes from diphasic gels in the system $\text{Al}_2\text{O}_3\text{-SiO}_2$ have been investigated by several groups (e.g. Refs 1-7). Wei and Halloran⁴ studied reaction kinetics and phase transformation mechanisms of a diphasic gel by quantitative X-ray diffraction of annealed samples and described the kinetics by an Avrami equation with an average time exponent $\langle n \rangle = 1.3(2)$ and a temperature-dependent induction period. Li and Thomson⁵ analysed the kinetic mechanisms from different sol-gel precursors using dynamic X-ray diffraction and differential thermal analysis (DTA) methods and found a significant change in the Avrami exponent n . Huling and Messing⁶ investigated 'hybrid' gels and analysed the influence of various seedings on the crystallization of aluminosilicate phases. However, no information is available so far on phase transformations in technical Nextel 440 fibres containing some B_2O_3 . Information on transformation kinetics and mechanisms is valuable for evaluation of the temperature application range of the fibres, and may also help to understand the microstructural developments of the fibres.

2 Experimental

2.1 Sample material

Continuous Nextel 440 fibre bundles (3M Inc., St. Paul, MN, USA) were used for this study. The chemical composition of the fibres is 70 wt% Al_2O_3 , 28 wt% SiO_2 and 2 wt% B_2O_3 .⁸ The as-received fibres have elliptical cross-sections (mean diameters are 7 and 12 μm), and consist of transition alumina (designated as ' $\gamma\text{-Al}_2\text{O}_3$ ' in the following) and a coexisting silica-rich, non-crystalline phase.

2.2 Annealing experiments

Annealing experiments were performed in an induction heated laboratory furnace with SiC

susceptor tube at 1128, 1148, 1166, 1183, 1192 and 1215°C under normal air atmosphere conditions. The annealing times ranged between 7.5 min and 32 h with about six different time intervals for each temperature. Furnace temperatures were controlled using a conventional PID controller and a Pt₁₀₀/Pt₉₀Rh₁₀ thermocouple located close to the sample. By means of an additional reference thermocouple, the accuracy of measurements was estimated to be better than $\pm 3^\circ\text{C}$. For the annealing experiments a sample of ~ 1 g fibre was loaded in a small Al₂O₃ crucible and placed into the hot induction furnace. Special care was taken to bring the samples immediately to the annealing temperatures and to quench to room conditions at the end of annealing time.

2.3 X-ray diffraction (XRD)

XRD studies were performed with a computer-controlled Siemens D 5000 diffractometer, equipped with a graphite monochromator in front of the counter. Diffraction patterns were recorded at room temperature with CuK_α radiation in the 2θ range between 25 and 71°. To reduce scattered background intensity, flat silicon single crystal sample holders were used, orientated in such a way that no Si reflection appeared over the 2θ scan region. Following standard procedures in quantitative X-ray analysis^{9,10} for determining weight fractions of transformed mullite, calibration XRD reference measurements were recorded from defined mixtures of as-received fibres (not transformed) and fibres that had been heat-treated at 1230°C (completely transformed into the mullite phase). Calibration curves were obtained from integrated intensities of the mullite reflection doublets 120/210, 121/211, 230/320 and from the integrated diffraction intensity of the 400 reflection of transition alumina (γ -Al₂O₃). Based on these calibration curves, the degree of transformation could be determined with an estimated error of $\pm 1\%$.

3 Results and Discussion

According to X-ray diffraction spectra and transmission electron microscopic observations, the as-received fibres consist of transition alumina (γ -Al₂O₃) and a non-crystalline SiO₂-rich phase, containing 2 wt% B₂O₃. The phase assemblage directly transforms to mullite in a temperature interval extending from ~ 1100 to $\sim 1230^\circ\text{C}$ without forming any other transient crystalline phase. The experimentally determined transformation levels α (α = weight fraction of newly formed mullite) are plotted vs. annealing time at different annealing

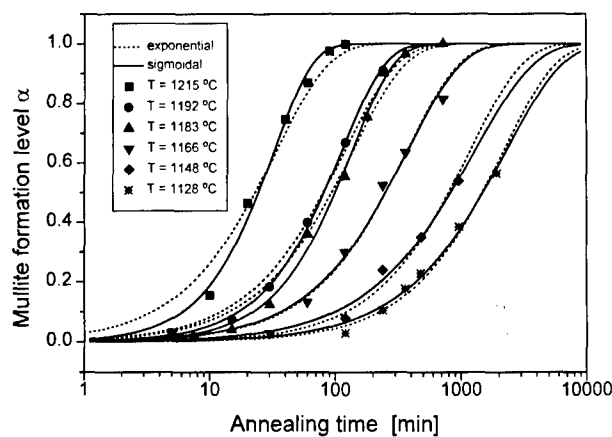


Fig. 1. Experimentally determined mullite formation levels α (weight fraction) plotted as function of annealing time on a logarithmic time scale. Dotted and solid lines correspond to exponential and sigmoidal approximations, respectively, assuming no induction periods ($\tau = 0$) (see Section 3.2).

temperatures in Fig. 1 in a semi-logarithmic scale. The fitted curves represent both simple exponential and sigmoidal functions and will be discussed in Section 3.2.

3.1 Early stages of reaction

Independent from any particular kinetic law, early reaction stages of mullite formation were evaluated by analysing time intervals τ required to attain small, but definite transformation levels α . Though being of major interest, precise determination of formation time intervals τ for very small conversion levels ($\alpha < 0.02$) turned out to be difficult, due to the lack of precisely measured data at the very beginning of the transformation processes. Therefore reaction time intervals necessary for the formation of 2, 5 and 10 wt% mullite ($\alpha = 0.02$, 0.05 and 0.10) were determined from isothermal data sets by interpolating between zero and the first measured data points using linear, polynomial and sigmoidal interpolation functions. Transformation time intervals $\tau_{\alpha=0.02}(T)$, $\tau_{\alpha=0.05}(T)$ and $\tau_{\alpha=0.10}(T)$ belonging to mullite formation levels $\alpha = 0.02$, 0.05 and 0.10, respectively, are plotted in an Arrhenius diagram in Fig. 2. From the slopes of the fitted straight lines slightly increasing activation energies are obtained with the increase of the transformation level: $\Delta E(\tau_{\alpha=0.02}) = 644(18)$ kJ mol⁻¹, $\Delta E(\tau_{\alpha=0.05}) = 679(12)$ kJ mol⁻¹, and $\Delta E(\tau_{\alpha=0.10}) = 696(17)$ kJ mol⁻¹.

Formation time intervals $\tau_{\alpha=0.02}(T)$ certainly cover the early (induction) stages of the transformation processes, including the period of stable nuclei formation and beginning of grain growth. The activation energy of initial mullite formation in Nextel 440 fibres at transformation level $\alpha = 0.02$ [$\Delta E(\tau_{\alpha=0.02}) = 644(18)$ kJ mol⁻¹] is significantly lower than the corresponding value

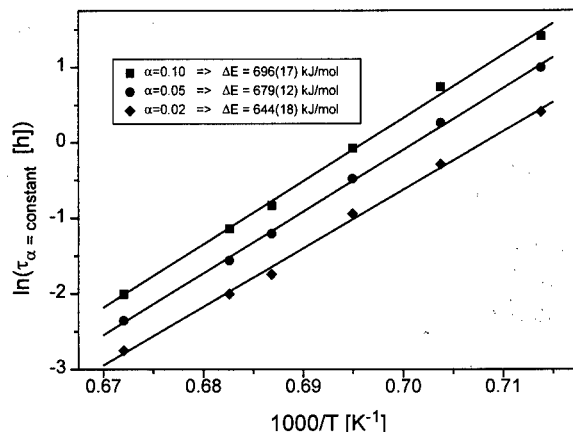


Fig. 2. Arrhenius plot of mullite formation times $\tau_{\alpha=0.02}(T)$, $\tau_{\alpha=0.05}(T)$ and $\tau_{\alpha=0.10}(T)$ required to attain mullite formation levels $\alpha = 0.02$, 0.05 and 0.10 , respectively. An activation energy of ~ 650 kJ mol $^{-1}$ is determined for the early mullite formation stages.

obtained under the same conditions by Wei and Halloran [$\Delta E(\tau_{\alpha=0.02}) = 987(15)$ kJ mol $^{-1}$]⁴ for the transformation of diphasic aluminosilicate gels to mullite. The large difference of almost 350 kJ mol $^{-1}$ between both ΔE values can be explained by different nucleation characteristics: a very high nucleation density of about 2×10^{15} cm $^{-3}$ is observed in Nextel 440 fibres,¹ which is four orders of magnitude higher than that in diphasic gels, $\sim 2 \times 10^{11}$ cm $^{-3}$.⁴ The high nucleation density in the Nextel 440 fibres may be caused by the occurrence of a non-crystalline silicate phase of low viscosity in the transformation interval due to the presence of ~ 2 wt% B₂O₃. Thereby diffusion processes are accelerated by liquid phase assisted mechanisms.

Aksay¹¹ investigated the diffusion of Si and Al in mullite (and other aluminosilicates) and found that the activation energy for the diffusion of Si and Al species alone amounts to ~ 700 kJ mol $^{-1}$ which is slightly higher than our experimentally obtained value for the initial processes in Nextel 440 fibres. A conclusion is either that in our case

(1) the additional activation energy term for nuclei formation is negligibly small, or (2) diffusion barriers play a less important role than they do usually in the initial stages of mullite formation, due to the presence of B₂O₃.

3.2 Overall transformation laws

In the discussion of the kinetics of the overall mullite formation processes, we used rate equations of the general form:¹²

$$K(T) \cdot (t - \tau) = f(\alpha) \quad (1)$$

with α = transformation level (weight fraction of newly formed mullite), K = reaction rate parameter, t = annealing time and τ = induction period.

In a first approach the kinetic data were fitted using a simple exponential function (index e). Such transformation laws are characteristic for chemical first-order reactions and have often been used to describe diffusion controlled grain growth processes:

$$K_e(T) \cdot (t - \tau) = -\ln(1 - \alpha) \quad (2)$$

The dashed curves in Fig. 1 are least-squares fits using Eqn (2), but without considering any induction period ($\tau = 0$). In a $\ln(1 - \alpha)$ vs. t diagram, not shown here, linear regression lines are obtained documenting a reasonable fit of measured and calculated data. Refined values for K_e are summarized in Table 1.

A closer look at the kinetic data shows that the transformation curves do not really follow the simple kinetic law of Eqn (2) with $\tau = 0$, but display sigmoidal shapes (index s). Transformation curves of this type are described by a modified Avrami kinetic law:¹²

$$K_s(T) \cdot (t - \tau) = [-\ln(1 - \alpha)]^{1/n} \quad (3)$$

Compared with Eqn (2), Eqn (3) has a time exponent n (real number) as an additional freely

Table 1. Kinetic data evaluation of the overall mullite formation: reaction rate coefficients K and exponents n for one exponential and two sigmoidal approximations of the kinetic Avrami law in the general form $K \cdot (t - \tau) = [-\ln(1 - \alpha)]^{1/n}$. In one sigmoidal approximation induction periods $\tau = \tau_{\alpha=0.02}$ were assumed. The numbers in parenthesis represent standard deviations from least-squares refinements and refer to the last digits.

Annealing temperature, T (°C)	Exponential approximation (n = 1):		Sigmoidal approximations (n ≠ 1):					
	$\ln(1 - \alpha) = -K_e \cdot t$		$\ln[-\ln(1 - \alpha)] = n \cdot \ln(K_s) + n \cdot \ln(t - \tau)$					
	No induction period, $\tau = 0$	K_e	$\ln(K_e)$	$n \cdot \ln(K_s)$	n	$n \cdot \ln(K_{s\tau})$	n_τ	$\tau_{\alpha=0.02}$ (h)
1215	2.27(10)	0.82	0.87(18)	1.59(13)	0.869(52)	1.11(3)	0.064	
1192	0.585(15)	-0.54	-0.83(10)	1.373(84)	-0.502(36)	0.98(3)	0.135	
1183	0.539(21)	-0.62	-1.113(63)	1.367(63)	-0.671(56)	1.03(4)	0.175	
1166	0.1498(64)	-1.90	-2.20(19)	1.23(13)	-1.511(36)	0.88(2)	0.39	
1148	0.0504(23)	-2.99	-3.00(31)	1.03(16)	-2.46(12)	0.82(7)	0.75	
1128	0.02727(95)	-3.60	-3.94(27)	1.15(12)	-2.907(31)	0.81(2)	1.5	
mean of n				1.29(20)			0.94(12)	

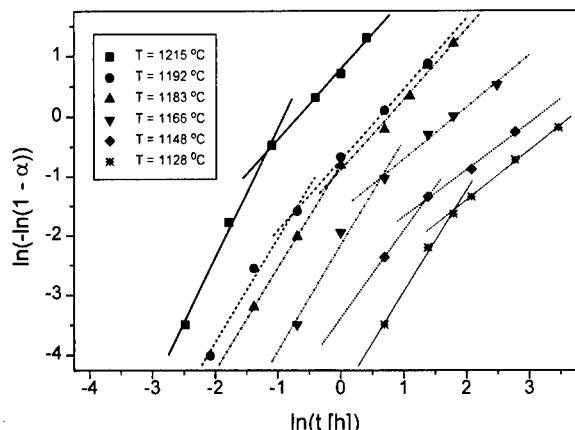


Fig. 3. Mullite formation levels α plotted in the form $\ln[-\ln(1 - \alpha)]$ vs. $\ln(t)$ without considering any induction period [$\tau = 0$]. It is obvious that the measured data is not well fitted by one straight line, but 'initial' and 'final' regions can be distinguished.

refined parameter, and an induction period τ . The solid lines in Fig. 1 are least-squares fits using Eqn (3), again without considering any induction period ($\tau = 0$). Compared with the exponential approach the sigmoidal functions represent better numerical approximations. Refined values for n [average $\langle n \rangle = 1.3(2)$] and $n \cdot K_s(T)$ are listed in Table 1.

If the measured raw data are plotted in double logarithmic plots, $\ln[-\ln(1 - \alpha)]$ vs. $\ln(t)$, it becomes obvious that one single straight line for each isothermal data set does not fit the data well (see Fig. 3). Instead, two straight lines with significantly different slopes n referring to an 'initial' (index 1) and a 'final' (index 2) transformation region* can be distinguished ('split model'). Linear regression fits for the two transformation regions lead to values $n_1 \cdot \ln(K_1)$ and n_1 [average $\langle n_1 \rangle = 1.81(18)$] and to $n_2 \cdot \ln(K_2)$ and n_2 [average $\langle n_2 \rangle = 1.00(20)$], respectively.

Several possible explanations for the change of slopes n were discussed in the literature. Arguments are based on the ideas that (1) nucleation sites are consumed in the 'initial' region,¹³ (2) variable nucleation and growth rates occur in different grains,¹⁴ and (3) impingement of growing grains takes place in the 'final' region.¹⁵ Li and Thomson described a significant change in the Avrami slope for a diphasic gel⁵ (from $\langle n_1 \rangle = 2$ to $\langle n_2 \rangle = 0.5$) and a somewhat smaller change for a single-phase gel¹⁶ (from $\langle n_1 \rangle = 1$ to $\langle n_2 \rangle < 0.4$). Li and Thomson⁵ explained the change of n in the diphasic gel by impingement of grains in the 'final' region using the model of Rosen *et al.*,¹⁵ who analysed the recrystallization of pure iron and

suggested preferred impingement of grains in the axial direction causing the grains to grow only in the transverse direction. Impingement of grains effectively leads to a reduction of growth dimensionality, and thus of slope n , due to restrictions in normal growth directions. Huling and Messing⁶ also attributed lower n values to effectively lower dimensional growth, e.g. due to combinations of growth along and normal to the interfaces in diphasic 'hybrid' 75M₁ gels. In Nextel 440 fibres reduction of growth dimensionality may also take place due to impingement of grains and, thus, explain the change of n . Here, however, the difference of n values between 'initial' and 'final' region [$\langle n_1 \rangle = 1.81(18)$ and $\langle n_2 \rangle = 1.00(20)$] is smaller than the values reported in the literature.

Another way to treat the change of slopes n is based on the consideration of induction periods $\tau(T)$, which have not been taken into account in our data analyses up to this point and have also not been considered by Li and Thomson.^{5,16} In order to check for linearity in $\ln[-\ln(1 - \alpha)]$ vs. $\ln(t)$ plots, induction periods $\tau(T)$ were introduced prior to numerical data evaluation. It should be kept in mind that precise estimations of $\tau(T)$ values are required, and that slight variations of τ sensitively influence the shape of the reaction curves. Such a precise determination of τ from the measured raw data at early reaction stages is difficult (see also Section 3.1). Following the procedure of Wei and Halloran,⁴ formation time periods $\tau_{\alpha=0.02}(T)$, required to attain a mullite formation level $\alpha = 0.02$, were arbitrarily considered as induction periods τ to correct the time axis of the measured isothermal raw data before subsequent calculations. Starting from this point, data sets of $\alpha(T)$ were numerically approximated via least-squares techniques using Eqn (3) in the form

$$\ln[-\ln(1 - \alpha)] = n(T) \cdot \ln[K_s(T)] + n(T) \cdot \ln[t - \tau_{\alpha=0.02}(T)] \quad (4)$$

Induction time periods $\tau_{\alpha=0.02}(T)$ and freely refined parameters $n \cdot K_s$ and n are listed in Table 1. Mullite formation levels α presented in double logarithmic plots now yield straight lines. The lines have slightly different slopes $n(T)$ ranging around a mean value of $\langle n \rangle = 0.94(12)$ (see Fig. 4). Since n is close to 1 in each case mullite formation can be equally well described by a first-order reaction ($n = 1$), if correct temperature-dependent induction periods $\tau_0(T)$ are taken into account. Finally, refinements with fixed $n = 1$ and slightly changed induction periods $\tau_0(T)$ confirm this conclusion. We believe that this simple kinetic model is best suited to describe the mullite formation processes in Nextel 440 fibres.

Arrhenius plots fitted on the basis of least-squares regressions of experimentally determined

*The 'initial region' extends up to a transformation level of 20 to 35 wt%. It should not be mixed up with the term 'induction period', which characterizes the early beginning of the reaction ($\alpha < 0.02$).

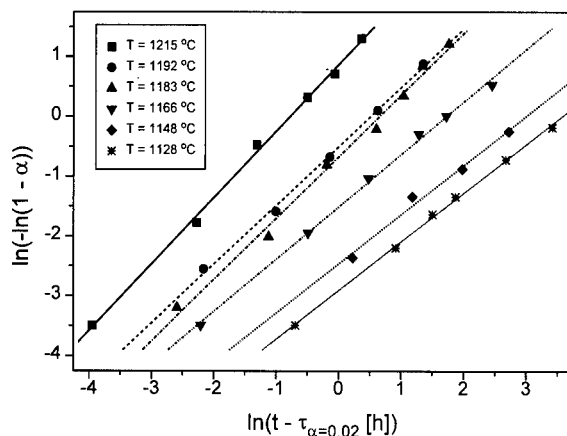


Fig. 4. Mullite formation levels α plotted in the form $\ln[-\ln(1 - \alpha)]$ vs. $\ln(t - \tau)$. Induction times $\tau = \tau_{\alpha=0.02}(T)$ were used to correct the time axis prior to numerical fitting. Linear regression fits yield values $n_{\tau} \ln(K_{s\tau})$ and n_{τ} listed in Table 1 (compare with Fig. 3).

rate coefficients $\ln(K_e)$ and $\ln(K_{s\tau})$ are shown in Fig. 5 (see Table 1). From the slopes of the straight lines apparent activation energies of the overall mullite formation processes can be derived. Based on reaction rate coefficients K_e and $K_{s\tau}$, the values $\Delta E_e = 914(56)$ kJ mol $^{-1}$ and $\Delta E_{s\tau} = 903(54)$ kJ mol $^{-1}$ are obtained, respectively. An Arrhenius plot of $n \cdot \ln(K_s)$ leads to the energy value 939(56) kJ mol $^{-1}$. From Arrhenius plots of $\ln(K_1)$ and $\ln(K_2)$ of the 'split model', apparent activation energies $\Delta E_1 = 727(59)$ kJ mol $^{-1}$ and $\Delta E_2 = 908(64)$ kJ mol $^{-1}$ were calculated. Compared with the activation energy of the initial stages of reaction (derived from Arrhenius plots of formation times $\tau_{\alpha=0.02}$, see Section 3.1), the apparent activation energies for the overall mullite forming processes [derived from Arrhenius plots of the reaction coefficients $\ln(K)$] are clearly higher. This indicates that processes associated with initial nucleation

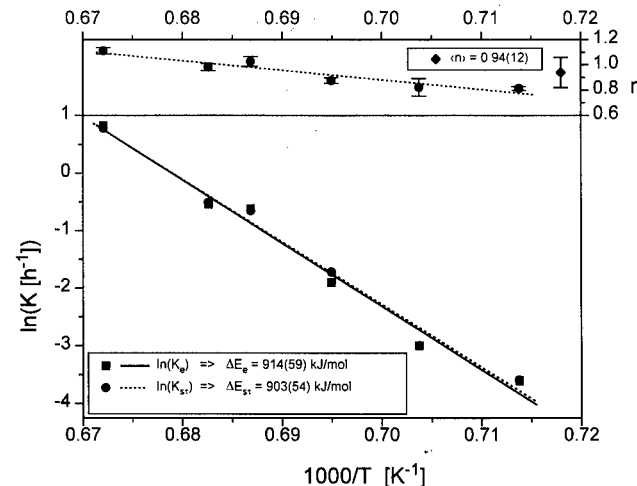


Fig. 5. Arrhenius plot of $\ln(K_e)$ (exponential approximation) and $\ln(K_{s\tau})$ (sigmoidal approximation considering induction periods $\tau = \tau_{\alpha=0.02}$) for the overall mullite transformation. The different slopes give apparent activation energies of $\Delta E_e = 914(56)$ kJ mol $^{-1}$ and $\Delta E_{s\tau} = 903(54)$ kJ mol $^{-1}$. The average value of the exponent n is 0.94(12).

and grain growth are characterized by smaller energy barriers than those related to final formation and grain growth.

The mean values of the apparent mullite activation energies of Nextel 440 fibres are lower than the mean values of diphasic gels reported in the literature (e.g. Wei and Halloran:⁴ $\Delta E = 1070(200)$ kJ mol $^{-1}$; Li and Thomson:⁵ $\Delta E = 1028(37)$ kJ mol $^{-1}$; and Huling and Messing:⁶ $\Delta E = 987(71)$ kJ mol $^{-1}$ for the hybrid gel 25M₁). It must be emphasized that Wei and Halloran obtained their value from an Arrhenius plot of $n \cdot \ln(K_s)$ considering induction periods $\tau = \tau_{\alpha=0.02}$ before data evaluation, whereas Huling and Messing obtained theirs from an Arrhenius plot of $\ln(K_s)$ without considering an induction period. Li and Thomson obtained their value from DTA measurements. The differences between apparent activation energies of mullitization between the present study and literature data may have similar reasons as already discussed for the initial stages of reaction (see Section 3.1). A suitable explanation is that atomic diffusion, which is the rate-controlling process for both nucleation and growth, is enhanced in Nextel 440 fibres by the presence of the viscous glassy phase containing B₂O₃, which, according to our observations, is retained in the bulk of the fibres at least up to 1400°C. Our own preliminary studies have also shown that diphasic fibres without B₂O₃ (NextelTM 550, Altex from Sumitomo Chemical Inc.) transform into mullite in a similar way as do, for example, Wei and Halloran's diphasic (but B₂O₃-free) gels, thus supporting the suggestion that B₂O₃ content has a transformation-controlling influence.

References

1. Schmücker, M., Flucht, F. & Schneider, H., High temperature behaviour of polycrystalline aluminosilicate fibres with mullite bulk composition, I. Microstructure and strength properties. *J. Eur. Ceram. Soc.*, **16** (1996) 281–5.
2. Hoffmann, D. W., Roy, R. & Komarneni, S., Diphasic xerogels, a new class of materials in the system Al₂O₃–SiO₂. *J. Am. Ceram. Soc.*, **67** (1984) 468–71.
3. Wei, W. & Halloran, J. W., Phase transformation of diphasic aluminosilicate gels. *J. Am. Ceram. Soc.*, **71** (1988) 166–72.
4. Wei, W. & Halloran, J. W., Transformation kinetics of diphasic aluminosilicate gels. *J. Am. Ceram. Soc.*, **71** (1988) 581–7.
5. Li, D.X. & Thomson, W. J., Kinetic mechanisms for mullite formation from sol–gel precursors. *J. Mater. Res.*, **5** (1990) 1963–9.
6. Huling, J. C. & Messing, G. L., Epitactic nucleation of spinel in aluminosilicate gels and its effect on mullite crystallization. *J. Am. Ceram. Soc.*, **74** (1991) 2374–81.
7. Voll, D., Mullitprecursoren: Synthese, temperaturabhängige Entwicklung der strukturellen Ordnung und Kristallisationsverhalten. PhD thesis, University of Hannover, 1994.

8. 3M Company, *Properties of NextelTM 440 ceramic fibers*. Technical data, 3M Ceramic Materials Department, 1993.
9. Klug, H. P. & Alexander, L. E., *X-ray Diffraction Procedures*. John Wiley, New York, 1954.
10. Cullity, B. D., *Elements of X-ray Diffraction*. Addison-Wesley, London, 1956.
11. Aksay, I. A., Diffusion and phase relationship studies in the alumina silica system. PhD Thesis, University of California, Berkeley, CA, 1973.
12. Bamford, C. H. & Tipper, C. F. H., *Chemical Kinetics-Reactions in the Solid State*. Elsevier Scientific, Amsterdam, 1980, Vol. 22.
13. Avrami, M., Kinetics of Phase Changes II. Transformation-time relations for random distribution of nuclei. *J. Chem. Phys.*, **8** (1940) 212-24.
14. Rollet, A. D., Srolovitz, D. J., Doherty, R. D. & Anderson, M. P., Computer simulation of recrystallization in non-uniformly deformed metals. *Acta Metall.*, **37** (1989) 627-39.
15. Rosen, A., Burton, M. S. & Smith, G. V., Recrystallization of high-purity iron. *Trans. AIME*, **230** (1964) 205-15.
16. Li, D. X. & Thomson, W. J., Mullite formation kinetics of a single-phase gel. *J. Am. Ceram. Soc.*, **73** (1990) 964-9.

Processing, Structure, and Properties of Mullite Fiber/Mullite Matrix Composites

K. K. Chawla, Z. R. Xu & J.-S. Ha

Department of Materials and Metallurgical Engineering, New Mexico Institute of Mining and Technology, Socorro, New Mexico 87801, USA

(Accepted 22 July 1995)

Abstract

Oxide fiber/oxide matrix composites form an important and very attractive subpart of ceramic matrix composites because of their inherent stability in oxidizing atmospheres at high temperature. In particular, mullite fiber/mullite matrix composites have the potential of high temperature usage in oxidizing atmospheres.

The interface in mullite fiber/mullite matrix was engineered by using thick BN (1 μm) or BN/SiC double coating on mullite fibers, such that deformation mechanisms conducive to toughness enhancement could be brought to play. Significant improvements in the room temperature mechanical properties of these mullite fiber/mullite matrix composites could be achieved by incorporation of these interfacial coatings and by using a colloidal processing route to make dense mullite matrix.

Introduction

Ceramic matrix composites (CMCs) capable of maintaining excellent strength and fracture toughness are required for high temperature structural applications. Many of these applications require exposure to an oxidizing environment, as such the thermodynamic stability and oxidation resistance of CMCs become important issues. Nonoxide fiber/nonoxide matrix composites generally show good low temperature strength, but oxidation resistance is a major limitation.^{1,2} Nonoxide fiber/oxide matrix composites or oxide fiber/nonoxide matrix composites do not have high oxidation resistance because the permeability constant for the diffusion of oxygen is high, resulting in rapid oxygen permeation through the oxide matrix.³ It would thus appear that in applications where stability in air at high temperature is a prime objective, oxide fiber/oxide matrix composites should be considered because they are inherently stable in air.

Some oxide/oxide matrix composite systems have been investigated.⁴⁻⁷ A strong fiber/matrix bond forms in the oxide matrix reinforced with uncoated oxide fibers, such as in the like/like systems, (e.g. mullite/mullite)^{4,5} or in the mixed systems, (e.g. $\text{Al}_2\text{O}_3/\text{SiO}_2$)⁶ where additional compound(s) could form at the interface, and the overall mechanical properties of those composites were not much improved. As a consequence, a barrier layer is generally introduced to prevent fiber/matrix interaction, and thus, prevent strong interfacial chemical bonding. Carbon barrier coating has been frequently used in oxide/oxide composites.⁸ In this work on mullite/mullite composites, we have used BN and BN/SiC duplex coatings as interphase materials. We recognize that both BN and SiC are nonoxides, but are more oxidation resistant than carbon. Ideally, one would like to incorporate an oxide coating, but in this preliminary work we wish to explore the basic idea of mullite/mullite composites. If we can produce such composites with a BN or BN/SiC interphase without surface cracks, then oxygen ingress will be inhibited. The use of a BN coating is desirable because of its ease of sliding along the basal planes.⁹

Objective

The objectives of this work were to use an interface engineering approach, involving fiber coating, microstructure characterization of the interface, mechanical test and fractography study, in mullite/mullite systems to weaken the interfacial bond in order to achieve oxide/oxide composites with high work of fracture and a noncatastrophic failure mode.

Materials and Experimental Procedure

Mullite fibers, Nextel 480 and Nextel 550, both of 3M Co., were used in mullite matrix composites.

Table 1. Properties of fibers, mullite matrix, and fiber coatings

Properties	Nextel 480	Nextel 550	Mullite matrix ($3Al_2O_3-2SiO_2$)	Boron nitride (<i>h</i> -BN)	Silicon carbide (β -SiC)
Composition	70wt% Al_2O_3 28wt% SiO_2 2wt% B_2O_3	73wt% Al_2O_3 27wt% SiO_2	—	—	—
Melting point (°C)	1850	1850	1850	3000	2220
Density (g/cm ³)	3.03	3.03	3.17	2.27	3.21
Strength [†] (MPa)	1900 [#] (Tensile)	2000 [#] (Tensile)	128–185	80–110	255–465*
Young's Modulus (GPa)	220	193	181	60–80*	440–470*
Coefficient of thermal expansion (10 ⁻⁶ /°C)	4.5	4.5	4.5	5	4.8
Diameter (μm)	8 × 12	8 × 12	—	—	—
Reference	10	11	12–14	15–17	12, 18

[†]: At room temperature.

[#]: 51 mm gauge length.

*: Data of CVD materials.

Nextel 480 is a polycrystalline mullite fiber, while the as-received Nextel 550 is not crystalline mullite but a mixture of α -alumina and amorphous silica with mullite composition, which can be transformed to mullite when heated above 1200°C. Fiber coating of BN on Nextel 480 was applied by Synterials Co. (Herndon, VA) using a proprietary CVD technique, and the double coating of BN/SiC on Nextel 550 was applied by 3M Co. (St. Paul, MN) via a proprietary CVD technique. In the double coating, the outer layer was SiC.¹⁰ The nominal compositions and some properties of the materials used are summarized in Table 1.^{11–19}

Conventional mullite powders need temperatures above 1500°C for considerable densification because of the low interdiffusion rates of silicon

and aluminum ions in crystalline mullite.^{18,19} Such high processing temperatures could cause severe damage on the fibers.⁴ The composite fabricated from the commercial mullite powder with uncoated Nextel 480 fiber showed fiber deformation and extensive interaction between the fiber and matrix, see Fig. 1. Note that large matrix grains had grown into the fiber due to the high processing temperature and pressure required for densification of the commercial mullite powders. The mullite matrix used in this work was obtained via a powder synthesized in our laboratory by a diphasic gel route using a boehmite ($AlOOH$) powder (Dispal 11N7, Remet Chemical Corp., Chadwicks, NY) and an amorphous silica sol (SP-30, Remet Chemical Corp.) as precursors. The gel was prepared by dispersing the boehmite powder in distilled water to get a boehmite sol, which was then mixed with the silica sol to have the stoichiometric mullite composition (71.8 wt.% Al_2O_3 and 28.2 wt.% SiO_2), followed by gelling at room temperature. The gel obtained was dried at 70°C and ground into powder form. All the composites were fabricated by slurry impregnation method.²² Consolidation of composites was done by hot-pressing. The composites were fabricated by infiltrating uncoated and coated fibers, Nextel 480, with a slurry of the matrix powder prepared with isopropanol and an organic binder, and unidirectionally laying the infiltrated fibers on mylar tapes. After drying, the prepared tapes were cut, stacked, and heated at 700°C for 2 h in air to remove the binder and the hydroxyl in the boehmite. Consolidation of composites was done by hot-pressing at 1300°C and 35 MPa for 1 h in vacuum. A part of the hot-

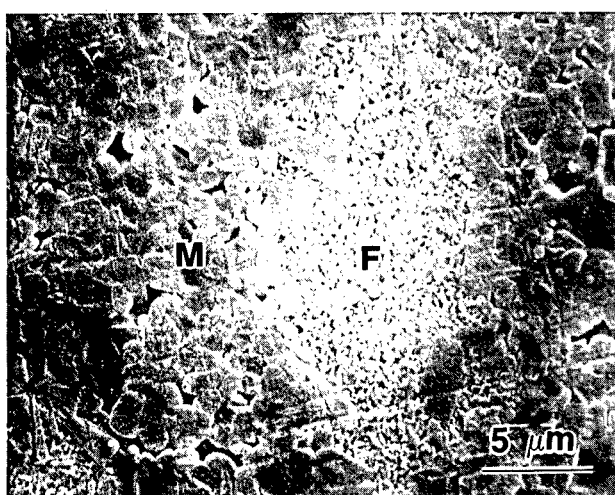


Fig. 1. Etched surface of uncoated Nextel 480/mullite composite fabricated with a commercial mullite powder as the matrix material. Note the extensive fiber (F)/matrix (M) interaction and fiber deformation.

pressed composite was cut and heat treated at 1320°C for 1 h in N₂, to cause produce complete crystallization of the mullite matrix, since it was found that the matrix in the as-hot-pressed composite did not crystallize. The details of processing have been reported elsewhere.^{23,24}

Optical and scanning electron microscopes were used for general characterization of the microstructure of the composites. Secondary ion mass spectrometry (SIMS) was used to identify the coatings in composites. Strength of composites was measured in three-point bend tests at room temperature using rectangular bar-shaped specimens with fiber direction parallel to the length of the specimen. Work of fracture (WOF) and the critical stress intensity factor of the composites were measured at room temperature using Chevron-notched bar specimen in three-point bend tests. The frictional shear stress in the BN coated Nextel 480/mullite composite was measured using an interfacial testing system (ITS). The details of this method have been published in Ref. 25.

Results and Discussion

Characterization of the interface

Figure 2(a) shows the cross-section of the BN coated Nextel 480 fiber, with coating thickness being about 1 μm . SIMS characterization verified that there was boron present, see Fig. 2(b). BN structure was turbostratic.²⁶ The microstructure of the BN/SiC coated Nextel 550 fiber, Fig. 3(a), shows that the fiber was fairly uniformly coated with two layers, BN and SiC, with thickness of about 0.1 and 0.2 μm , respectively. SIMS characterization also illustrated the presence of the double coating in the composites, Fig. 3(b and c). Such a thick (1 μm) BN coating was used to survive the processing conditions in order to provide a desired weak interface. By the same token, the outer SiC coating was used to protect the BN inner layer from oxidation during composite fabrication.

Typical raw load versus fiber-end displacement curves from single fiber pushout tests are shown in Fig. 4 (a and b). Note that after fiber pushout, which coincides with load drop, the curve rises with upward concavity. This is because the 10 μm flat-bottomed indenter is very close in dimension to the minor axis of the fiber and soon after fiber pushout the indenter starts loading the matrix. Figure 5 shows the stress versus fiber-end displacement curve after correcting for the contribution of the load train compliance to the total measured displacement. The load train compliance is determined from load versus displacement curves

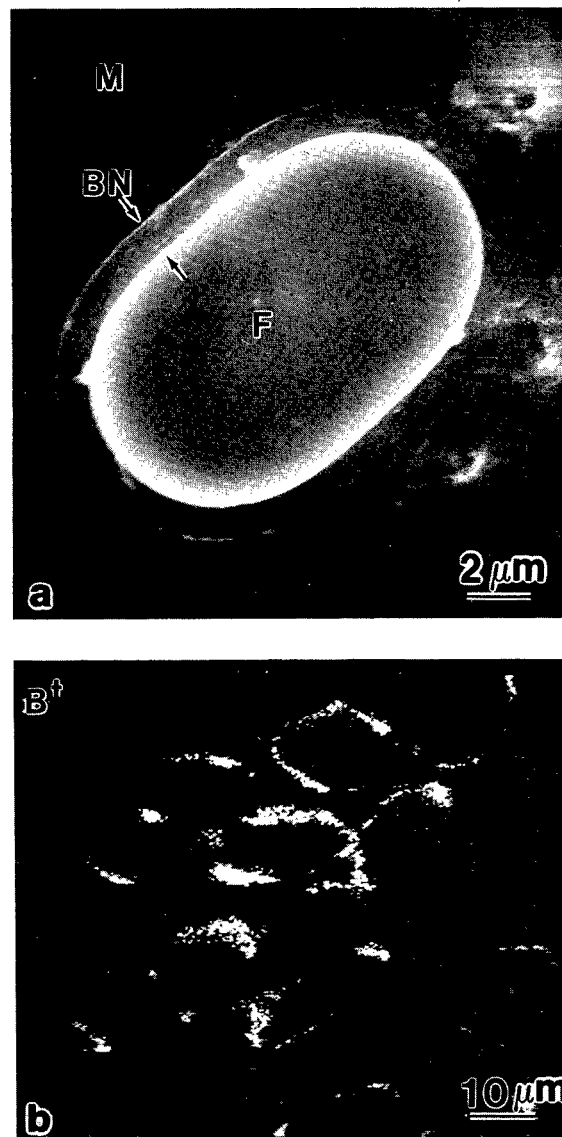


Fig. 2. (a) Cross-section of a BN-coated Nextel 480 fiber, showing the coating thickness 1 μm , (M: matrix, F: fiber); (b) B⁺ mapping by SIMS in a BN-coated Nextel 480/mullite composite.

obtained by subjecting the sample to compression at various points along the wedge by means of a 500 μm diameter stainless steel rod. Typical values for the compliance of the ITS system and wedged continuous fiber reinforced ceramic composite sample are between 4 and 6 $\mu\text{m}/\text{N}$.²⁷ Also shown is the best fit of the data (from the initiation of debonding to the point of fiber pushout) using the progressive fiber debonding and sliding model of Hsueh.²⁸ It should be pointed out that the predictions of the strength-based model of Hsueh are equivalent to those of the energy-based model of Kerans and Parthasarathy.^{27,29} The frictional shear stress in the present system was about 50 MPa.

Mechanical properties

The density, fiber volume fraction, and phases of the composites are listed in Table 2. It can be seen from this table that the matrix in the as-hot-

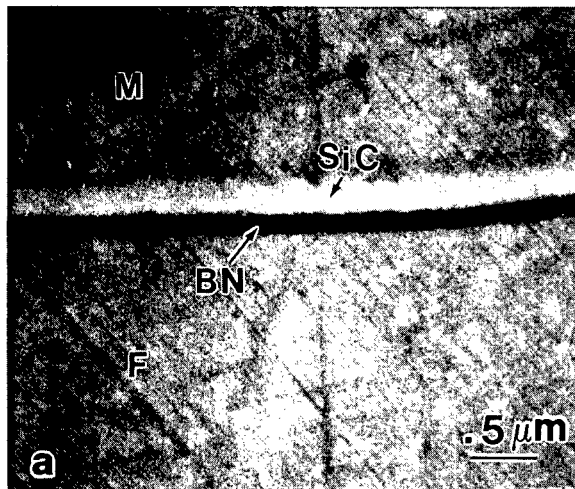


Fig. 3. (a) Cross-section of a SiC/BN coating Nextel 550 fiber, showing the double coating. (M: matrix, F: fiber); (b and c) SIMS analysis of the surface of a SiC/BN-coated Nextel 550/mullite composite, showing the presence of boron and silicon.

pressed composites did not transform to crystallize mullite at the hot pressing temperature. However, a complete mullite crystallization of the mullite matrix was achieved after the heat treatment (see the section on Materials and Experimental Procedure).

The bend strength, work of fracture, and criti-

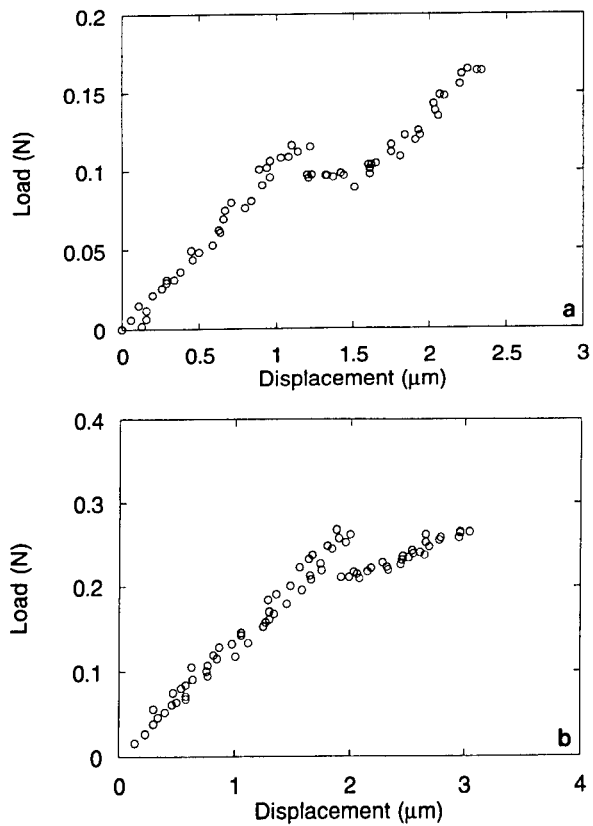


Fig. 4. (a and b) Typical raw load versus fiber-end displacement curves from single fiber pushout tests. Note that after the fiber pushout, which coincides with load drop, the curve rises with upward concavity. This is because soon after debonding the indenter starts loading the matrix.

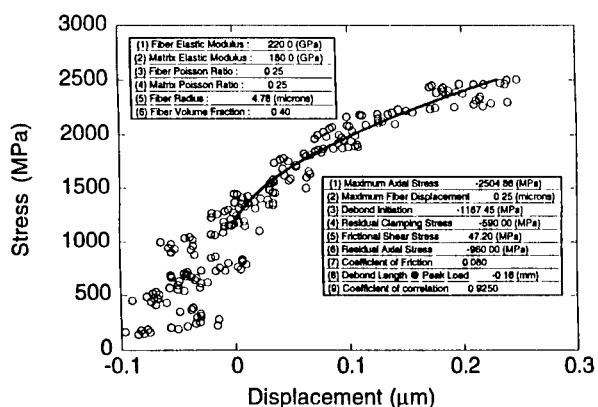


Fig. 5. Stress versus fiber-end displacement curve after correcting for the contribution of the load train compliance to the total measured displacement. Also shown is the best fit of the data (from the initiation of debonding to the point of fiber pushout) using the progressive fiber debonding and sliding model of Hsueh.²⁵

cal stress intensity factors for mullite/mullite composites are listed in Table 3. As can be seen, significant improvements, especially in fracture toughness, were obtained in the interface engineered mullite/mullite composites.

The composite with 1 μm BN coated Nextel 480 exhibited damage tolerant characteristics with a load-bearing capacity even beyond the maximum load, as indicated by a gradual load drop which continued up to a significant amount of displace-

Table 2. Density, fiber volume fraction, and phases of the composites

	Nextel 480/BN/mullite	Nextel 550/BN/SiC/mullite
Density(%) [#]	90	85
Fiber volume fraction, V_f	0.41	0.33
Phase		
As-HP [†]	$\alpha + s + m^*$	$\alpha + s^*$
HP+HT [‡]	Mullite	Mullite

[#]Relative densities to the theoretical composite densities calculated using a rule of mixture.

[†]As hot pressed.

[‡]As hot pressed and heat treated.

* α , s and m denote δ -alumina, amorphous silica, and mullite, respectively.

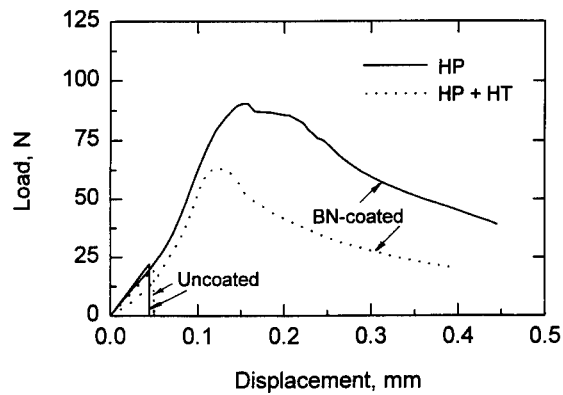


Fig. 6. Load-displacement curves obtained in Chevron-notch tests for Nextel 480/BN/mullite composites in as hot-pressed and hot-pressed + heat-treated conditions.

ment without complete failure during the test, as seen in Fig. 6. After heat treatment leading to complete mullite crystallization of the matrix, this composite still showed a non-catastrophic failure, also shown in Fig. 6. The loss of fiber strength resulted from the heat treatment was responsible for the load drop to a certain level after heat treatment.

Similar to the composite with 1 μm BN coated Nextel 480 fibers, the composite with SiC/BN

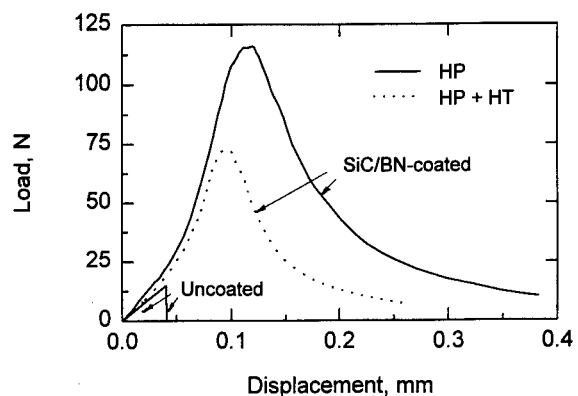


Fig. 7. Load-displacement curves obtained in Chevron-notch tests for Nextel 550/BN/SiC/mullite composites in as hot-pressed and hot-pressed + heat-treated conditions.

double coated Nextel 550 fibers showed a non-brittle failure, see Fig. 7.

Scanning electron micrographs of the fracture surfaces obtained in three-point bend test of the mullite/mullite composites are shown in Figs 8, 9 and 10. The BN coating in Nextel 480/mullite was found on the pulled-out fiber surface with some peeling-off or separation from the fiber, see Fig. 8. This indicates that both the interfaces of matrix/coating and coating/fiber were weakly bonded. This is not surprising inasmuch as hexagonal BN shears easily. The pulled-out fiber surfaces in the BN/SiC coated Nextel 550/mullite composite were mostly clean and smooth, see Fig. 9. An SEM picture, Fig. 10, showing one of the holes formed in the matrix of Nextel 550/mullite composite as a result of the fiber pullout, reveals that the SiC and BN layers were intact in the matrix and a strong bonding was formed between the matrix and the SiC coating. This can be attributed to a relative strong bonding between SiC and matrix. Also, the BN thickness in double coating is very thin (~0.1 μm). This indicates that, unlike Nextel 480/BN/mullite in which the fiber pullout could occur at

Table 3. Mechanical properties of the composites

Composite	V_f	$\sigma_{max}(\text{MPa})$	$WOF(\text{J/m}^2)$	$K_{IC}(\text{MPa m}^{1/2})$
Nextel 480/mullite:				
Uncoated	As-HP	0.45	104	56
	HP+HT	0.45	106	47
BN-coated	As-HP	0.41	322	2410
	AP+HT	0.41	258	1630
Nextel 550/mullite:				
Uncoated	As-HP	0.47	87	18
	HP+HT	0.47	71	12
BN-coated	As-HP	0.33	182	733
	HP + HT	0.33	223	308

As-HP: as hot pressed; HP+HT: as hot pressed and heat treated.

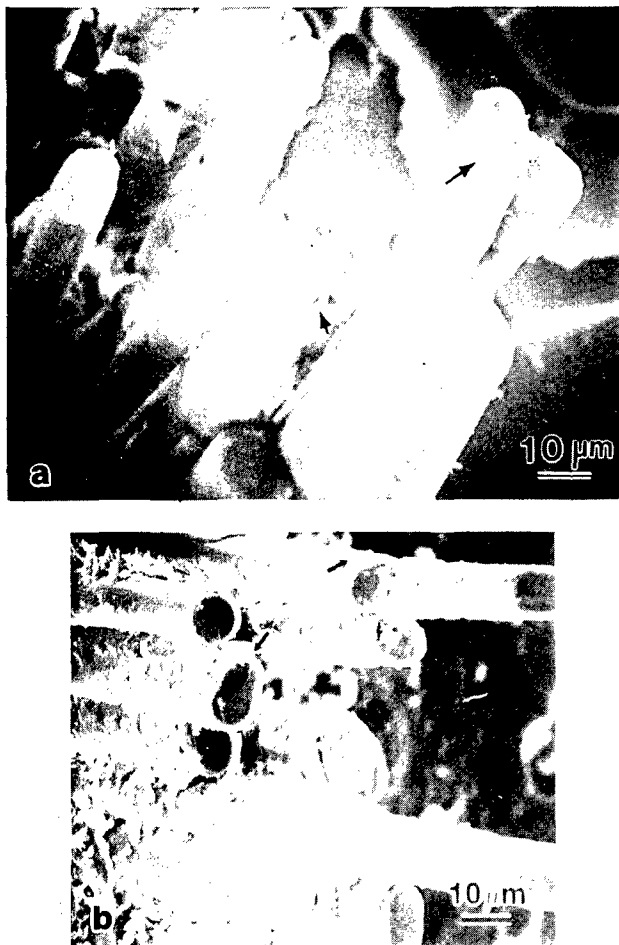


Fig. 8. Fracture surface of BN-coated Nextel 480/mullite composites: (a) hot-pressed and (b) hot-pressed + heat-treated, arrows showing the separation or peeling off of the BN coating.

the interfaces of either matrix/coating or coating/fiber, the fiber pullout occurred along the interface of the fiber and BN coating only.

Conclusions

The fiber/matrix interaction in mullite fiber/mullite matrix composites during processing can be effectively controlled by interface engineering approach. These engineered interfaces consisting of thick BN or a double BN/SiC coating coupled with the colloidal processing to consolidate the mullite matrix at a relatively low temperature, allowed us to make mullite fiber/mullite matrix composites showing high work of fracture and a noncatastrophic failure mode at room temperature.

Acknowledgements

This work was supported by the office of Naval Research, Contract No. N0014-89-J1459 and was monitored by Dr S. G. Fishman.

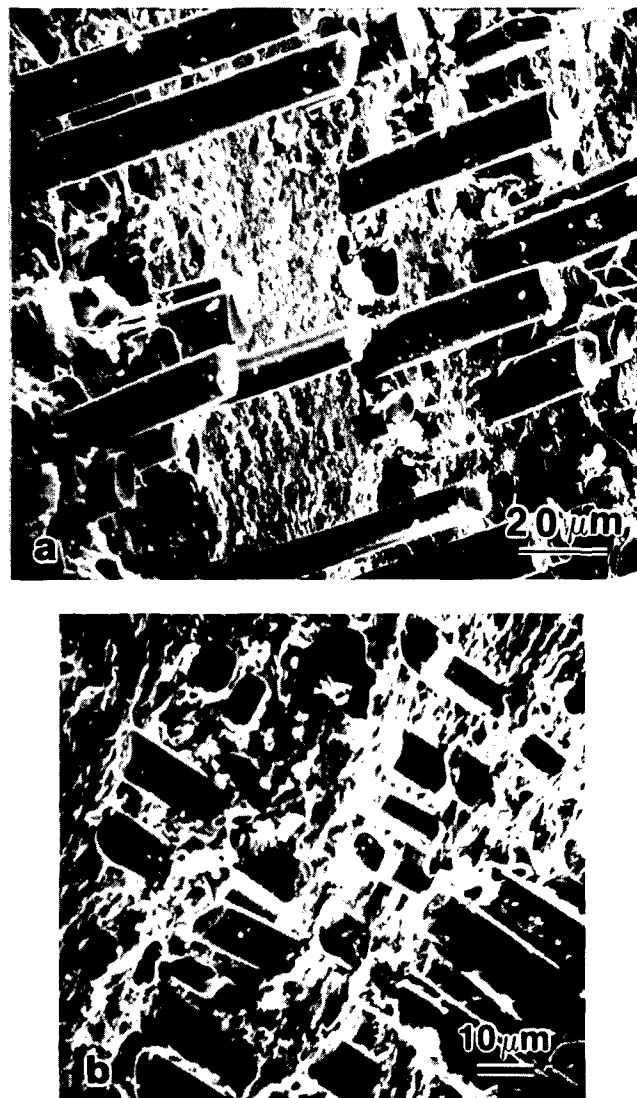


Fig. 9. Fracture surface of BN/SiC coated Nextel 550/mullite composites: (a) hot-pressed and (b) hot-pressed + heat-treated.

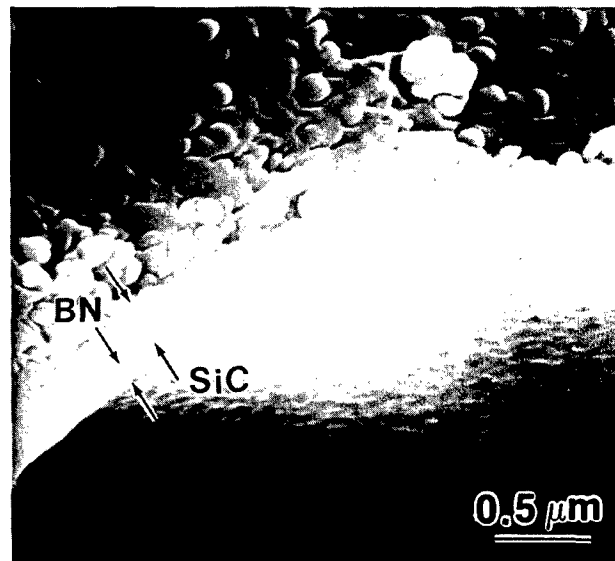


Fig. 10. Fracture surface of SiC/BN coated Nextel 550/mullite composite showing a hole formed in the matrix as a result of fiber pullout. Note the double coating left in the matrix during fiber pullout and the strong bonding between the matrix and the SiC coating.

References

1. Prewo, K. M. & Batt, J. A., The oxidative stability of carbon fibre reinforced glass-matrix composites. *J. Mater. Sci.*, **23** (1988) 523-7.
2. Mah, T., Hecht, N. L., McCullum, D. E., Hoenigman, J. R., Kim, H. M., Katz, A. P. & Lipsitt, H. A., Thermal stability of SiC fibres (Nicalon). *J. Mater. Sci.*, **19** (1984) 1191-201.
3. Hermes, E. E. & Kerans, R. J., Degradation of non-oxide reinforcement and oxide matrix composites. *Mat. Res. Soc. Symposium Proceedings*, **125** (1988) 73-8.
4. Singh, R. N. & Brun, M. K., Effect of boron nitride coating on fiber-matrix interactions. *Ceram. Eng. Sci. Proc.*, **8** (1987) 636-43.
5. Yeheskel, O., Balmer, M. L. & Cranmer, D. C., Interfacial chemistry of mullite/mullite composites. *Ceram. Eng. Sci. Proc.*, **9** (1988) 687-94.
6. Michalske, T. A. & Hellmann, J. R., Strength and toughness of continuous-alumina-fiber-reinforced glass-matrix composites. *J. Am. Ceram. Soc.*, **71** (1988) 725-31.
7. Fitzer, E. & Schlichting, J., Fiber-reinforced refractory oxides. *High Temperature SiC*, **13** (1980) 149-72.
8. Lehman, R. L. & Doughan, C. A., Carbon coated alumina fiber/glass matrix composites. *Comp. Sci. & Tech.*, **37** (1990) 149-64.
9. Rice, R. W., BN coating of ceramic fibers for ceramic matrix composites. *US Patent*, **4, 642,271**, Feb. 10, 1987.
10. Ha, J.-S., Chawla, K. K. & Engdahl, R. E., Effect of processing and fiber coating on fiber-matrix interaction in mullite fiber-mullite matrix composites. *Mater. Sci. & Eng.*, **A161** (1993) 303-8.
11. Johnson, D. D., Hiltz, A. R. & Grether, M. F., Properties of Nextel 480 ceramic fibers. *Ceram. Eng. Sci. Proc.*, **8** (1987) 744-54.
12. Experimental Product Data Sheet, Ceramic Materials Department, 3M Co., St. Paul, Minnesota.
13. Ceramic Sources, Vol. 1, American Ceramic Society, 1985 pp. 336 and 350.
14. Skoog, A. & Moore, R., Refractory of the past for the future: mullite and its use as a bonding phase. *Am. Ceram. Soc. Bull.*, **67** (1988) 1180-5.
15. Kumazawa, T., Ohta, S., Kanzaki, S., Sakaguchi, S and Tabata, H., Elastic properties of mullite ceramics at elevated temperature. *J. Mater. Sci.*, **8** (1989) 47-8.
16. Blocher, Jr, J. M., Nitrides. In *High-Temperature Materials and Technology*, Chap. 11, eds I. E. Campbell & E. M. Sherwood, John Wiley & Sons, New York, 1967, p. 379.
17. Williams, D. S., Elastic stiffness and thermal expansion coefficient of boron nitride films. *J. Appl. Phys.*, **57** (1985) 2340-2.
18. Hampshire, S., Engineering properties of nitrides. In *Engineered Materials Handbook*, Vol. 4: Ceramics and Glasses, ed. S. J. Schneider, ASM International, 1991, p. 819.
19. Shaffer, P. T. B., Engineering properties of carbides. In *Engineered Materials Handbook*, Vol. 4: Ceramics and Glasses, ed. S. J. Schneider, ASM International, 1991, p. 808.
20. Sacks, M. D., Lee, H.-W. & Pask, J. A., A review of powder preparation methods and densification procedures for fabricating high density mullite. In *Ceramic Transactions*, Vol. 6: Mullite and Mullite Matrix Composites, Eds S. Somiya, R. F. Davis and J. A. Pask, American Ceramic Society, Westerville, OH, 1990, p. 167.
21. Aksay, A., Dabbs, D. M. & Sarikaya, M., Mullite for structural, electronic and optical applications. *J. Am. Ceram. Soc.*, **74** (1991) 2343-58.
22. Chawla, K. K., *Ceramic Matrix Composites*, Chapman & Hall, London, 1993, p. 128.
23. Ha, J.-S. & Chawla, K. K., The effect of precursor characteristics on the crystallization and densification of diphasic mullite gels. *Ceramics International*, **19** (1993) 299-305.
24. Ha, J.-S. & Chawla, K. K., Effect of SiC/BN double coating on fibre pullout in mullite fibre/mullite matrix composites. *J. Mater. Sci. Lett.*, **12** (1993) 84-6.
25. Chawla, K. K., Xu, Z. R., Ha, J.-S., Lara-Curzio, E., Ferber, M. K. & Russ, S., Interfacial characteristics of mullite fiber/BN/coating/mullite matrix composites. In *Pro. Advanced Ceramic Matrix Composites*, ed. J. P. Singh, Amer. Ceram. Soc., 1994, p. 779.
26. Chawla, K. K., *Ceramic Matrix Composites*, Chapman & Hall, London, 1993, p. 325.
27. Lara-Curzio, E. & Ferber, M. K., *J. Mater. Sci.*, 1994, in press.
28. Hsueh, C.-H., Evaluation of interfacial properties of fiber-reinforced ceramic composites using a mechanical properties microprobe. *J. Am. Ceram. Soc.*, **76** (1993) 3041-50.
29. Kerans, R. J. & Parathasarathy, T. A., Theoretical analysis of the fiber pullout and pushout tests. *J. Am. Ceram. Soc.*, **74** (1991) 1585-96.

Sol-gel Mullite Matrix-SiC and -Mullite 2D Woven Fabric Composites with or without Zirconia Containing Interphase: Elaboration and Properties

Ph. Colombar,^{a*} E. Bruneton,^{a,b} J. L. Lagrange^a & E. Mouchon^a

^aONERA-OM, BP 72, 92322 Chatillon, France

^bCNRS-CECM, 15 rue G. Urbain, 94407 Vitry-sur-Seine, France

(Received September 1994; accepted 30 October 1995)

Abstract

The properties of composites made with fabrics of Nicalon® NLM202 SiC or Nextel® 440 mullite fibers are reported. The method used to make composites is a three stages sol-gel process: (i) in situ gelation of a mixture of alkoxides in a ceramic fiber fabric; (ii) the deposit of a matrix precursor onto the impregnated fabrics and (iii) hot-pressing of the stacked fabrics in a carbon mold. The composites have been studied by SEM and TEM. Three point flexural strength has been measured at room temperature and at 900°C in air. Local Young's modulus, microhardness and interfacial shear stress have been determined at RT. Micro-Raman spectra and X-ray microanalysis have been used to study the fiber-interface reactions. Using a mixture of aluminium–silicon ester and tributylborate as interface precursor, we obtained a carbon film free SiC-mullite sliding interface. The use of a complementary ZrO_2 – GeO_2 gel interface precursor allows us to obtain dense composites at a low temperature exhibiting good mechanical properties (linear behaviour up to ~180 MPa, even after annealing in air). The effects of a zirconia interphase on the mechanical properties of mullite–mullite composite are also discussed.

Introduction

Many advanced aerospace systems require or would benefit from new low density materials for structural applications. Ceramic materials could replace existing metals and alloys, especially in corrosive environments. This is particularly true of those applications requiring materials working

at temperatures above 800°C, e.g. aircraft engine parts. For these applications the most promising class of new materials is ceramic woven fabric-reinforced ceramic matrix composites. The use of monolithic ceramics is limited by their intrinsic inability to tolerate mechanical damage without brittle rupture due to their polycrystalline state and the nature of the chemical bonds existing in these compounds. The use of long, continuous ceramic fibers embedded in a refractory ceramic matrix results in a composite material exhibiting enhanced toughness through a specific micromechanism at the fiber–matrix interface: the cracks appearing in the matrix are deflected, dissociated and then stopped at the fiber–matrix interface. Thus the composite materials exhibit a pseudo-plastic fracture easily observed in the load–strain plots. Calculations with safety coefficients would thus be possible for parts made of ceramic matrix composites as well the manufacture of complex architectures. For aerospace applications requiring high reliability, it is necessary to use woven ceramic fibers as reinforcement. At present, Nicalon® NLM202 SiC fibers are considered to be the most convenient fibers but mullite fibers such as Nextel® 440 also present some potential advantages in the preparation of composites exhibiting both good thermomechanical properties and oxidation resistance. One of the most interesting matrices is mullite. The interest in the mullite matrix arises from its superb thermal and chemical stability and from its relatively low temperature expansion, comparable with that of the fibers. Furthermore, its mechanical properties, up to 1300–1500°C are retained. Also, its low toughness and Young's modulus can be improved by zirconia dispersion.

Improvements can be made using the sol-gel method, which allows refractory oxide matrices such as mullite, alumina, zirconia^{1,2} to be processed

*To whom correspondence should be addressed. Also at CNRS-LASIR, 2 rue Henry Dunant, 94320 Thiais, France.

at relatively low temperatures (1000–1300°C) and fine grained ceramics to be produced with regular submicronic zirconia dispersion.³ Finally, as these matrices are free of alkali- or alkaline-earth ions, there is no formation of a carbon rich interface at the boundary of the Nicalon SiC fiber.⁴ This absence of a carbon film prevents rapid thermal degradation in oxidizing atmospheres. The reaction between the oxide fiber and the matrix has to be controlled in order to prevent the formation of a strong interfacial bond. In spite of the potential interest of mullite as a matrix for use in more or less oxidizing atmospheres, attempts to prepare long fiber reinforced mullite matrix composites remain limited. Jones *et al.*⁵ and Qui & Pantano⁶ have prepared mullite matrix composites using long SiC and carbon fibers. To date no work has been reported on the preparation and properties of woven fabric reinforced mullite matrix composites, except our preliminary reports of Refs 4 and 7.

In this paper we compare the properties of ceramic composites consisting of Nicalon® NLM202 (Nippon Carbon) SiC or with Nextel® 440 (3M) mullite fibers in mullite matrices, before and after annealing in air at temperatures between 900 and 1300°C. Emphasis is given on understanding the mechanical behaviour of each composite component: the fiber, the matrix and the fiber/matrix interface and interphases.

Experimental

Composite preparation

Our preparation process of two-dimensional (2D) woven fabric reinforced composites is based on the hydrolysis–polycondensation of alkoxides according to the following reaction



The resulting material is a gel (composition: $\text{MO}_{n-2x}(\text{OH})_x \cdot m\text{H}_2\text{O}$) which is converted by thermal treatment into a meso/microporous ‘glass’ and then, after the departure of the last OH^- , densification leads to a glass, a glass-ceramic or a ceramic depending on composition.^{1,2,8} The CMC’s preparation process takes place in three stages (Fig. 1):

- (i) impregnation of the fiber yarn of the fabrics with an interface fiber–matrix precursor (a liquid alkoxide mixture which slowly hydrolyses and polycondenses, *in situ* by reaction with air moisture into a gel);
- (ii) deposition of the fine amorphous and reactive–matrix precursor (a gel powder which has been converted by thermal treatment at ca. 600–800°C in a mesoporous xerogel in order to evacuate most of the water in the polymeric network and hence to reduce the shrinkage). This powder precursor is deposited onto the interface precursor impregnated fabric in the form of a suspension in chlorobenzene, with addition of PMMA;

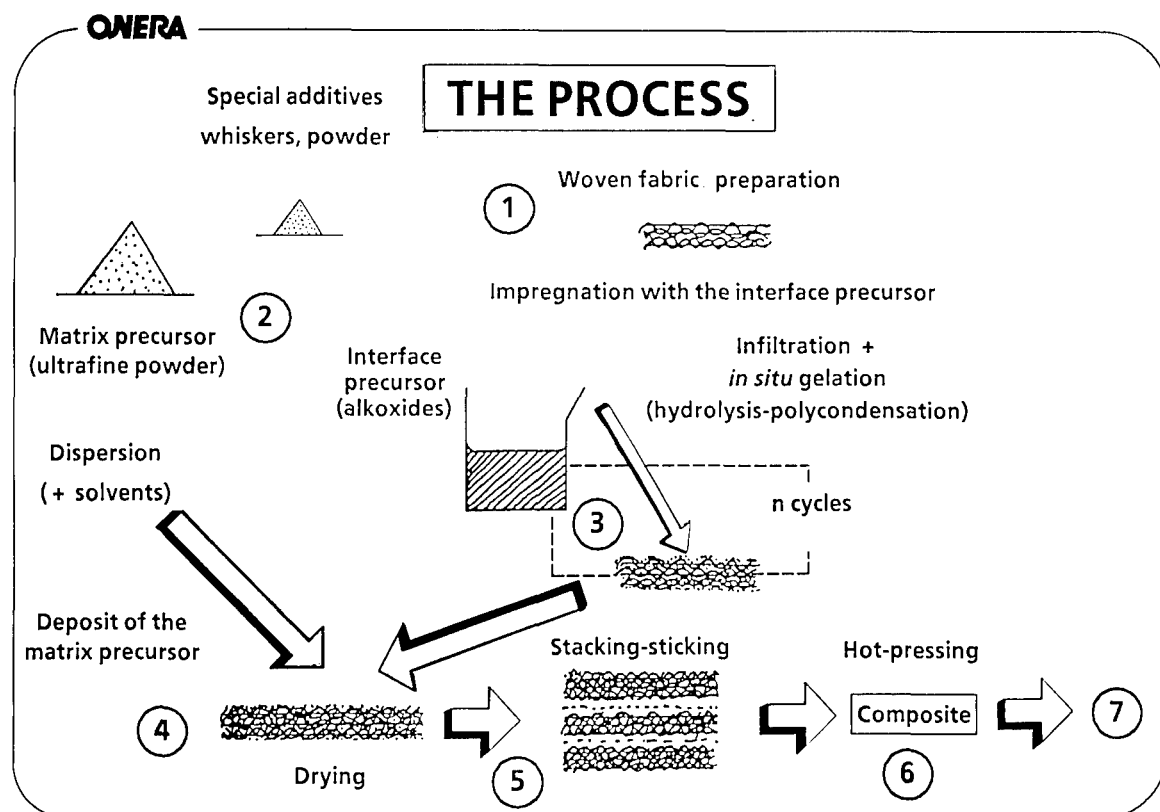


Fig. 1. Flowchart of the sol-gel route for the manufacture of ceramic fiber woven fabric–ceramic matrix composites.

- (iii) hot pressing of the impregnated and stacked fabrics in a graphite mold at a temperature between 1000 and 1400°C.

Details on the manufacturing technology are given in Ref. 9.

The problems arising in the preparation of refractory matrix dense composites leads to the difficulty of achieving an open porosity below 8–10%. The fiber must be thoroughly embedded in the matrix and the matrix must be incorporated through the voids between fibers (a few microns or less, in size). This is possible by infiltration of liquid or gaseous precursors for which the ceramic yield is necessarily low. It results in considerable shrinkage which generates new voids: the presence of the woven fabrics inhibits the coherent shrinkage of the matrix. The ceramic precursor can infiltrate the yarns reducing the porosity and the shrinkage creates voids. In the case of two-dimensional reinforcement: this dilemma is solved by the use of a very reactive matrix precursor in association with a liquid interface precursor which polycondenses within the fiber yarns into a gel. On heating, the gel is converted in glass-ceramic and gives rise to a temporary liquid sintering aid at the same temperature at which the matrix densification occurs.⁸ The liquid phase contributes to the densification by mass transport (liquid assisted sintering) but also helps to lubricate the powder rearrangement under pressure and to achieve a good contact between the grains coming from the matrix precursor and/or from the interface precursor despite the presence of a fiber network (Fiber volume: ~30–40%).

The matrix precursor is prepared by rapid hydrolysis of an alkoxide mixture diluted in propanol with very strong stirring.¹ The resulting gel is dried under IR bulbs and heated up to 750°C to reach the amorphous state. Densification occurs at about 1000°C for mullite with the dehydroxylation–nucleation–densification reaction.^{8,10,11}

Woven fabrics

Nicalon® NLM202 fibers (Nippon Carbon Co.) were woven by CRST (21350 Gissey, France) along four directions in the plane to give a ~1 mm thick fabric (surface mass: 76×10^{-3} g/cm²). The SiC fiber diameter is ~15 μm and the thermal expansion of fiber is about $3-3.5 \times 10^{-6}$ K⁻¹.¹⁰ Yarns contain ~500 fibers.

Nextel® 440 mullite fiber (3M Co) were woven by Ets Cotton Frères (France) along two directions, within the plane to give a ~0.4 mm thick satin (surface mass: 22×10^{-3} /cm²). The mullite fiber diameter is about 11 μm and a yarn contains 390 fibers. The thermal expansion is about 5×10^{-6} K⁻¹.

Interface precursors

Different kinds of interface precursors (so-called because the fiber–matrix interface will result from the reaction between the fibers and the precursor) may be used, solely or in combination, depending on the matrix and the fibers.^{9,12} In the case of mullite matrix composites three different precursors are used:

- (i) a mixture of (OBu)₂–Al–O–Si(OEt)₂ ester (ref. SiAl084 Dynasyl, from formerly Dynamit Nobel, now Hüls-France) and tributylborate (TBB, from Alfa-Ventron, ref. 10691), or tributylphosphate PO(O₂C₄H₉)₃ (TBP from Fluka, ref. 10138);
- (ii) pure zirconium i-propoxide (ZP, ref. 88733 from Fluka);
- (iii) a mixture of ZP and tetra-ethoxy-germane (TEOG, prepared at the laboratory).

The transient liquid sintering aid results from the melting of B₂O₃ (~600°C), Ge and of GeO₂ (~1100°C), both liquids being eliminated by volatilization during the hot-pressing cycle or incorporated in the matrix. It is important that no traces remain present at the grain boundaries in order to maintain good mechanical properties at high temperatures or in water-rich atmospheres.

Mullite matrix

A mullite matrix reinforced with a dispersion of zirconia is prepared by instant hydrolysis of a mixture of ZP and aluminum isobutoxide and silicon methoxide diluted in propanol as described in Ref. 13. A submicronic dispersion of tetragonal zirconia is obtained, (Fig. 2). The great advantage of the alkoxide route is that it blends the liquid gel-formers very homogeneously and keeps this homogeneity up to the nucleation at about 1000°C.^{1,3} The steady size of the precipitates whatever the thermal treatment time is due to the low diffusion coefficient in the mullite glass-ceramic below 1400°C. The equilibrium between the crystallites and the host amorphous or spinel-like matrix depends only on temperature and composition.^{3,11,14}

Hot pressing

Pressure sintering is performed under vacuum up to 400°C, a N₂ atmosphere (1 atm) being applied above 400°C. The heating rate is 250°C/h up to 600°C and increased to 350°C/h up to the dwell temperature. A pressure of 2.5 MPa is applied at the beginning of the hot-pressing cycle in order to get a good contact between the fiber yarns and the interphase and matrix precursors. The applied pressure is then raised to 20 MPa between 600 and 900°C, this maximum value being reached before the beginning of the mullite intrinsic shrinkage (~850°C), related to the dehydroxylation–

nucleation reaction;^{8,11} the pressure is removed just before the end of the dwelling time. Cooling is complete after 5 h.

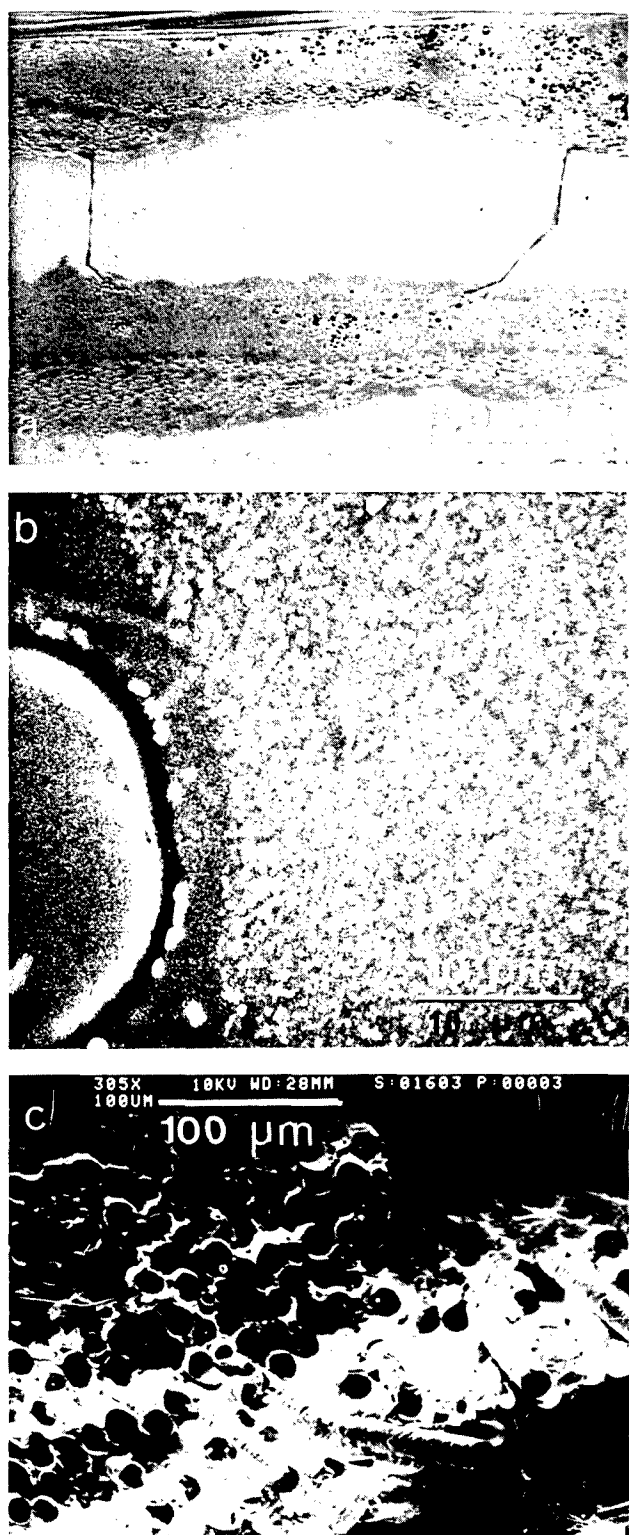


Fig. 2. Photomicrograph of a Nicalon NLM202® SiC fiber woven fabric-mullite matrix composites pressure sintered at 1350°C: (a) polished section: a regular $3\text{Al}_2\text{O}_3\cdot 2\text{SiO}_2$ matrix cracking pattern is observed, mean intercrack distance ~ 1 mm; (b) detail of the fiber-matrix interface; the zirconia precipitates of the matrix appear in white (mean matrix composition: $6\text{Al}_2\text{O}_3\cdot 4\text{SiO}_2\cdot \text{ZrO}_2$). The zirconia-free interphase around the SiC fiber arises from the transformation of the interface precursor deposit TBB+3SiAl (mean composition: $\text{Al}_2\text{O}_3\cdot 2\text{SiO}_2$ with B_2O_3 traces); (c) fracture of a Nextel 440 fiber fabric-mullite matrix composite pressure sintered at 1200°C (interface precursor: TBP+SiAl).

Interface precursor-matrix precursor reaction

Figure 2 gives an illustration of the interphase formation between the fiber and the matrix. The matrix composition was chosen to be $6\text{Al}_2\text{O}_3\cdot 4\text{SiO}_2\cdot \text{ZrO}_2$. The interface precursor is the mixture of TBB and SiAl ester (oxide composition: $\text{Al}_2\text{O}_3\cdot 2\text{SiO}_2\cdot n\text{B}_2\text{O}_3$). We can observe the homogeneous, submicronic dispersion of zirconia precipitates in the mullite matrix and a zirconia free contour around the SiC fiber can be observed (zirconia appears white in the SEM photomicrograph due to the high number of electrons of Zr). The contour corresponds to a silica-rich mullite glass-ceramic with nanometric mullite crystals created by the pyrolysis of the interface precursor gel. However, some zirconia crystals are observed at the fiber periphery because of zirconia precipitation through reaction with the temporary liquid sintering aid.

Techniques

The expansion measurement was achieved using an Adamel Lhormargy DI24 apparatus (Instrument SA, Longjumeau, France) with silica glass rod and support. Dilatometric curves were drawn under vacuum at heating and cooling rates of 5°C/min from room-temperature up to 900°C. Sample dimensions were $25 \times 10 \times 10$ mm³.

Flexural strength was recorded by three point bending tests using a bar specimen (35 or 50 mm length) over a 30 mm span at a cross-head speed of 0.1 mm/min. Tests were performed at room temperature and at 900°C in air after 30 min stabilization (heating rate 300°C/h). Typically three samples were broken for each composition at both temperatures.

Fracture surfaces and sliced or polished sections of the samples were observed using an optical microscope or by scanning electron microscopy (Cambridge Scan 200 KV). TEM investigations were performed using 200 KV microscopes (Jeol 2000 FX and Topcon 002-B) both equipped with EDX analysis with optimal 5 nm spatial resolution. The standardless metallurgical thin film (SMTF) method was used to determine the local composition.

Local Young's modulus, microhardness and interfacial frictional stress (IFS: τ) were determined using a home-made Vickers microindenter instrument and models described in Ref. 15. The load cell measures loads up to 1 N with an accuracy of about 500 μN . The capacitive displacement gauge has an accuracy of some nanometers. The loading rate is load-controlled and varies from 7 to 30 mN/s. The position of the indenter relative to the polished surface of the sample and the applied

load were measured continuously during testing. This enables the hardness and Young's modulus to be determined without the need for direct imaging of the indentation. However, the size and shape of the indentation were always checked afterwards and the indentation axis position was checked using the method described in Ref. 15.

Micro-Raman spectra were recorded at the 514.5 nm exciting wavelength of an Ar⁺ laser using a XY Dilor multichannel microprobe (Lille, France) equipped with a liquid nitrogen cooled Wright CCD (1200-300) array detector.

Results and Discussion

Porosity and macroscopic mechanical properties

SiC-mullite composites

Preliminary work has shown that 2D fabric SiC fiber/mullite matrix composites prepared by the above method exhibit a RT dissipative fracture (Fig. 3) and a rather good linear limit of strength behavior when a 1TBB + 3SiAl (volume ratio) interface precursor was used.⁷ On the other hand, the deposit only the TBB precursor leads to a brittle composite.¹⁶ Optimisation of the enduction process lowers the open porosity to about 9% and

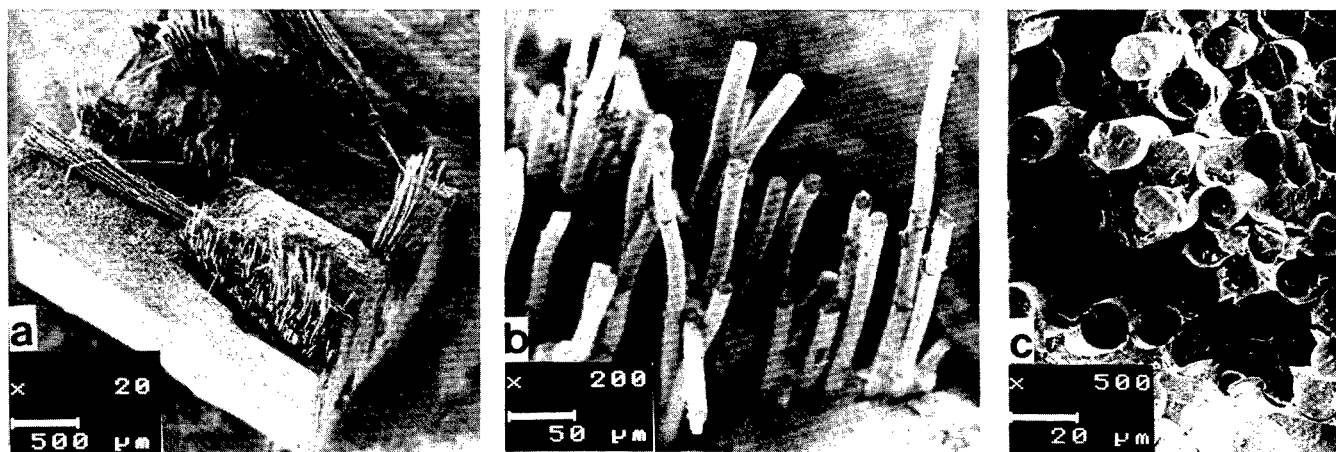


Fig. 3. Photomicrograph of a SiC fiber woven fabric-mullite matrix composite pressure sintered at 1350°C (TBB+3SiAl interface precursor). Fiber volume: 0.3; open porosity: 12%: (a) fracture at RT; (b) detail of the fiber pull-out at RT, and (c) after 900°C.

Table 1. Open porosity (*P*) and flexural strength (σ) of composites prepared using various interface and matrix precursors

Fabrics (fibers)	Matrix	Interface precursors ^c (volume ratio)	Sintering temperature and dwell-time	σ (MPa) ^d	<i>P</i> (%)
4 dir (NLM202) ^a	3Al ₂ O ₃ ·2SiO ₂	TBB	1350°C (45 min)	<100 (brittle) ^e	~15
	6Al ₂ O ₃ ·4SiO ₂	1TBB	1350°C	~120–130	9–14
	ZrO ₂	3SiAl	45 min	(100) ^f	
			1300°C	(dissipative) ^e	
			90 min	~150–180	9
				(120) ^f	
Satin (Nextel 440) ^b	3Al ₂ O ₃ ·2SiO ₂	1ZP	1300°C	150 μm	
	0.1TiO ₂	1TEOGGe	90 min	RT ~260 ± 30	3 ± 0.5
	3Al ₂ O ₃ ·2SiO ₂	+ 1TBB		900°C ~280 ± 20	
	0.1B ₂ O ₃	3SiAl		(190) ^f	
				(dissipative) ^e	
				500–2000 μm	
	3Al ₂ O ₃ ·2SiO ₂	1SiAl + 1TBP	1200°C	100 (brittle)	8%
	0.1TiO ₂			70	20%
	3Al ₂ O ₃ ·2SiO ₂	ZP	1200°C	50–100 μm	
	0.1B ₂ O ₃			(dissipative) ^e	

^aNicalon®, Nippon Carbon; the volume of fiber is about to 35–40%.

^b3M Co.

^cTBB: tributylborate; SiAl: SiAl 084 Dynasyl ester; ZP: zirconium i-propoxide. TBP: tributylphosphate; TEOGe: tetraethoxygermane.

^dIn air, at RT or at 900°C.

^eFracture behaviour, fiber pull-out.

^fLinear limit.

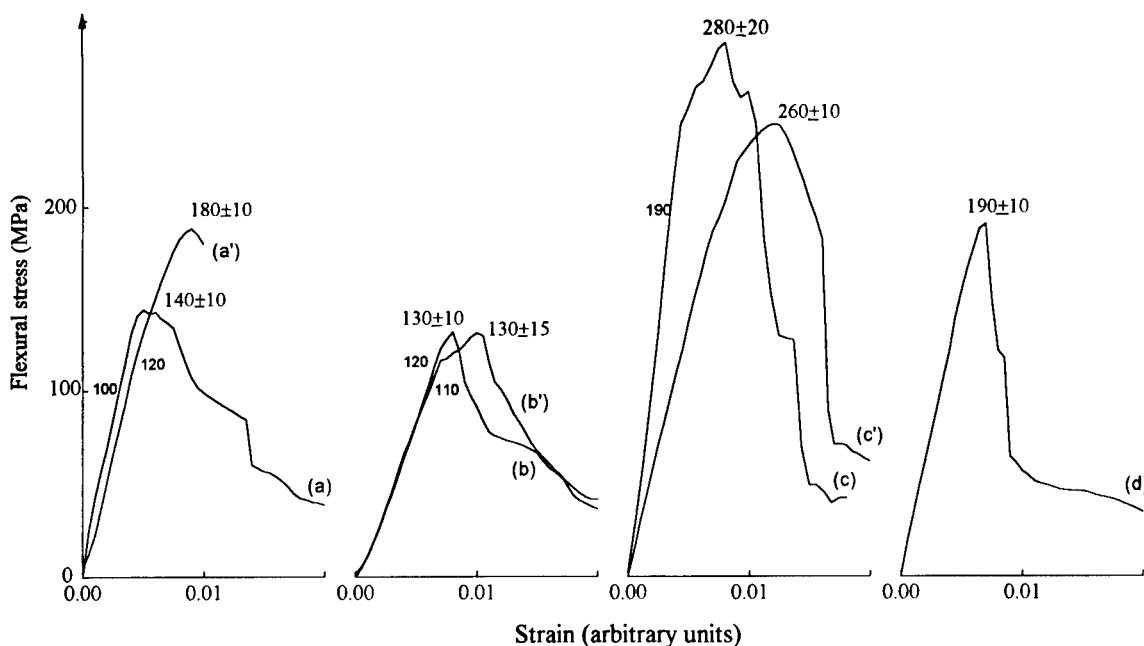


Fig. 4. Flexural stress-strain plots for various composites made with a $6\text{Al}_2\text{O}_3\text{4SiO}_2\text{ZrO}_2$ matrix. Curves are recorded at RT (a, b, c, d) or at 900°C (a', b', c') in air. Samples are made with the TBB+3SiAl interface precursor, with (c, c', d) or without (a, a', b, b') addition of zirconium propoxide and tetra-ethoxygermane. The samples were sintered for 90 min at 1300°C (a, a', c, c', d) or at 1350°C with a 5 min excursion to 1450°C (b, b'). Curve d was recorded at RT after 30 h annealing at 1200°C , in air. Arbitrary relative scales are used in x-axis: the comparison is made for similar bar specimens (same number of fabrics sheets, same thickness).

the corresponding ultimate strength reaches 150 MPa at RT and at 900°C (Table 1 and Fig. 4) for zirconia containing mullite matrices. The calculated strain values are close to 0.5%. Decreasing the sintering temperature from 1350 to 1300°C is possible without increase of the porosity if the dwelling time is increased to 90 min. At the same time, the linear strength limit is increased up to 120 MPa. With the addition of $\text{ZrO}_2\text{-GeO}_2$ interface precursor, the densification begins below 800°C (instead of 950°C) and open porosity of $\sim 3\%$ is obtained after hot-pressing at 1300°C . The ultimate strength reaches 250 MPa at RT and 300 MPa at 900°C , in air. Furthermore, the equivalent strain calculated for the fibers located in the medium plane is $\sim 0.9\%$ at the ultimate strength which corresponds to the typical value measured for SiC fibers heated at $1200\text{--}1300^\circ\text{C}$. The linear limit is close to 180 MPa and is not lowered after 30 h annealing in air at 1200°C (Fig. 4, size of annealed samples: $35 \times 5 \times 4$ mm). Good mechanical properties are thus observed for 2D SiC fiber and mainly tetragonal zirconia particulates-reinforced mullite matrix composites.

Mullite-mullite composites

Using mullite fiber woven fabrics, the achievement of low porosity composites without fiber-matrix reaction is much more difficult due to the high reactivity of the mullite fibers. When the interface precursor consisted of a mixture of SiAl ester and TBP as sintering aid, a rather good densification

of the composite is obtained (open porosity $\sim 8\%$). Neither matrix microcracking nor fiber pull-out can be deduced from the stress-strain plots (a straight line up to the failure); however fiber pull-out, typically in the range of $5\text{--}50 \mu\text{m}$, can be observed in the fracture micrograph (Fig. 2). In order to prevent reaction between the matrix and the reinforcing fibers, we deposited an inert layer between the mullite matrix and the mullite fibers. This interphase may be selected from refractory compositions which should remain stable during the hot-pressing and at the working temperature. Thus zirconia has been chosen as interphase.

A significant work of fracture is observed on the strain-stress plot measured at samples consisting of the Nextel® 440 satin coated with ZrO_2 interphase in a B_2O_3 doped mullite matrix. X-ray diffraction patterns indicate that the zirconia interphase has monoclinic symmetry. The mechanical performances remain poor ($\sigma \sim 70$ MPa, Table 1) because of the high open porosity ($\sim 20\%$) and the low fiber volume fraction ($\sim 30\%$). Further work is needed to know whether the remaining porosity promotes or inhibits the dissipative character of the fracture, and to improve the mechanical strength.

Matrix, fiber and interphase characterization methodologies

The measurement of local mechanical properties is an important step in the understanding of the macroscopic behaviour of composites. The indentation hardness test is probably the simplest

Table 2. Local Young's modulus (E) and Vickers microhardness (H_v) of various mullite samples and fibers

Samples	E (GPa)	H_v (GPa)	Remarks
$3\text{Al}_2\text{O}_3\cdot 2\text{SiO}_2$	180 ± 17	12.4 ± 2	Hot-pressed — 1600°C (porosity $<0.5\%$)
$3\text{Al}_2\text{O}_3\cdot 2\text{SiO}_2^a$ with zirconia precipitates (10%, molar)	240 ± 15	16 ± 2	Hot-pressed — 1600°C (porosity $<0.5\%$)
$3\text{Al}_2\text{O}_3\cdot 2\text{SiO}_2\cdot 0.1\text{B}_2\text{O}_3$ (matrix of a composite)	160 ± 20	12.5 ± 5	Hot-pressed — 1350°C (composite porosity $\sim 12\%$)
$6\text{Al}_2\text{O}_3\cdot 4\text{SiO}_2\cdot \text{ZrO}_2^b$ (matrix of a composite)	150 ± 20	17 ± 3	Hot-pressed — 1300°C (composite porosity $\sim 9\%$)
$6\text{Al}_2\text{O}_3\cdot 4\text{SiO}_2\cdot \text{ZrO}_2^b$ (matrix of a composite)	200 ± 20	18 ± 3	Hot-pressed — 1350°C (composite porosity $\sim 9\%$)
$\text{Al}_2\text{O}_3\cdot 2\text{SiO}_2$ (interphase of a composite)	90 ± 10	8 ± 2	Hot-pressed — 1350°C (composite porosity $\sim 9\%$)
SiC fiber in composite pressure sintered at $1000\text{--}1200^\circ\text{C}$	210 ± 20	25 ± 0.5	
1350°C	200 ± 30	20 ± 1	
1350°C^d		17.5 ± 1	

^aMicron dispersion; ^bSubmicron dispersion; ^cMeyer law: $h = \alpha F^\beta$ with $\alpha = 0.1 \pm 0.01$ and $\beta = 0.623 \pm 0.03$ (F in g, d in μm); ^da 180 min annealing at 900°C in air was performed after preparation.

method of measuring the mechanical properties of materials. The use of load-controlled depth-sensing hardness tester which operates in the (sub)micron range enables the study of each component of the composite. Following the work of Loubet *et al.*,¹⁷ we extract Young's modulus (E) and the Vickers microhardness (H_v) from the load-displacement

plot during the unloading displacement.¹⁵ Results are given in Table 2. Typical applied load–penetration depth plots are shown in Fig. 5 for the indentation of the silica-rich interphase and of the tetragonal zirconia reinforced mullite matrix. E and H_v values are calculated using Loubet's model:

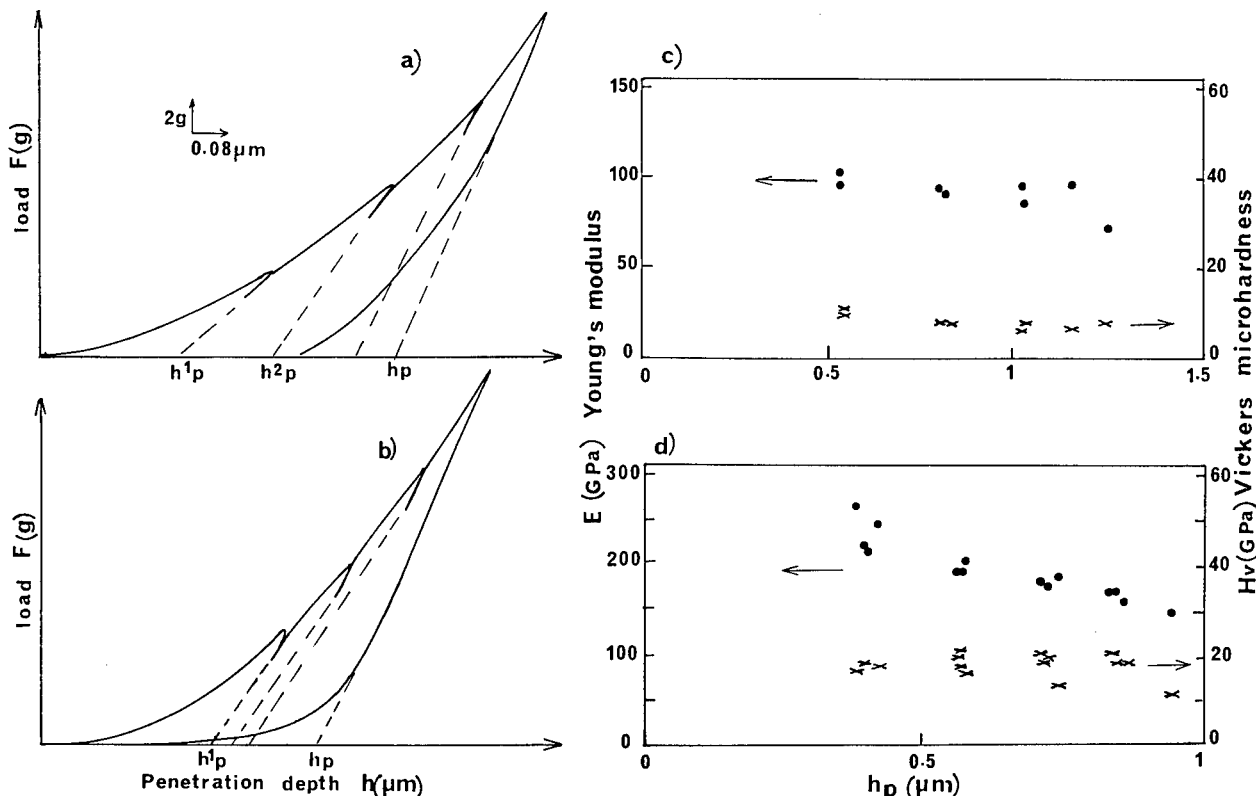


Fig. 5. $6\text{Al}_2\text{O}_3\cdot 4\text{SiO}_2\cdot \text{ZrO}_2$ mullite matrix; Indentation plots of applied load (F) against penetration depth (h) for (a) the fiber matrix interphase (TBB+3SiAl interface precursor, mean composition after sintering: $\text{Al}_2\text{O}_3\cdot 2\text{SiO}_2$) and (b) the matrix (mean composition $6\text{Al}_2\text{O}_3\cdot 4\text{SiO}_2\cdot \text{ZrO}_2$) region for a composite pressure sintered at 1350°C . Partial unloadings are made in order to determine the microhardness H_v and the Young's modulus E for different loads as described in Ref. 15. The H_v and E values are deduced from the plateau observed in the plots given in (c) and (d) for the interphase and the matrix, respectively.

$$E = \frac{\partial F}{\partial h} \left(\frac{\pi}{2} \right)^{1/2} \frac{1}{2 \sqrt{2h_p} \tan \theta} \text{ and } H_v = \frac{F \cos^2 \theta}{4h_p^2 \sin \theta}$$

2θ being the angle of the Vickers pyramidal indenter and h_p the plastic depth deduced from the intersection between the extrapolation of the straight line occurring when the load is lowered (unloading cycle) and the abscissa. At very small penetration depth the measurement error is large due to the diamond tip defect and the difficulty of determining the contact point ($F = 0$ origin). At high penetration depth cracks may occur deforming the unloading trace.¹⁵ Thus the observation of a plateau is needed to determine the true E and H_v values (Fig. 5 (c,d)).

Comparison is made with pure mullite and zirconia reinforced mullite monolithic ceramics hot-pressed at 1600°C for 1 h (Table 2). The local mechanical properties of mullite matrices sintered at 1350°C are very similar to those of dense hot-pressed monoliths. A large increase in the E and

H_v values is observed for zirconia containing samples. The Young's modulus of the silica-rich mullite glass surrounding the fibers, arising from the thermal treatment of the alumino(boro)silicate interface precursor is much lower: ~90 GPa (H_v ~8 GPa). This low value corresponds to that usually measured for glass-ceramics.¹⁸

Indentation of the fiber allows one to observe the degradation of the fiber properties as a function of the processing and the thermal ageing. No degradation is evident in composites prepared below 1300°C: E and H_v values remain unchanged. On the other hand, the indentation of fibers of composites sintered above 1300°C indicates a lowering of both Young's modulus and micro-hardness. Similar conclusions can be made after air annealing at 900°C (Table 2).

Examination of the indentation figures shows that fiber fractures are numerous and if the applied load exceeds the threshold load (F_s) (Fig. 6), the fiber slides within the matrix and a black circle

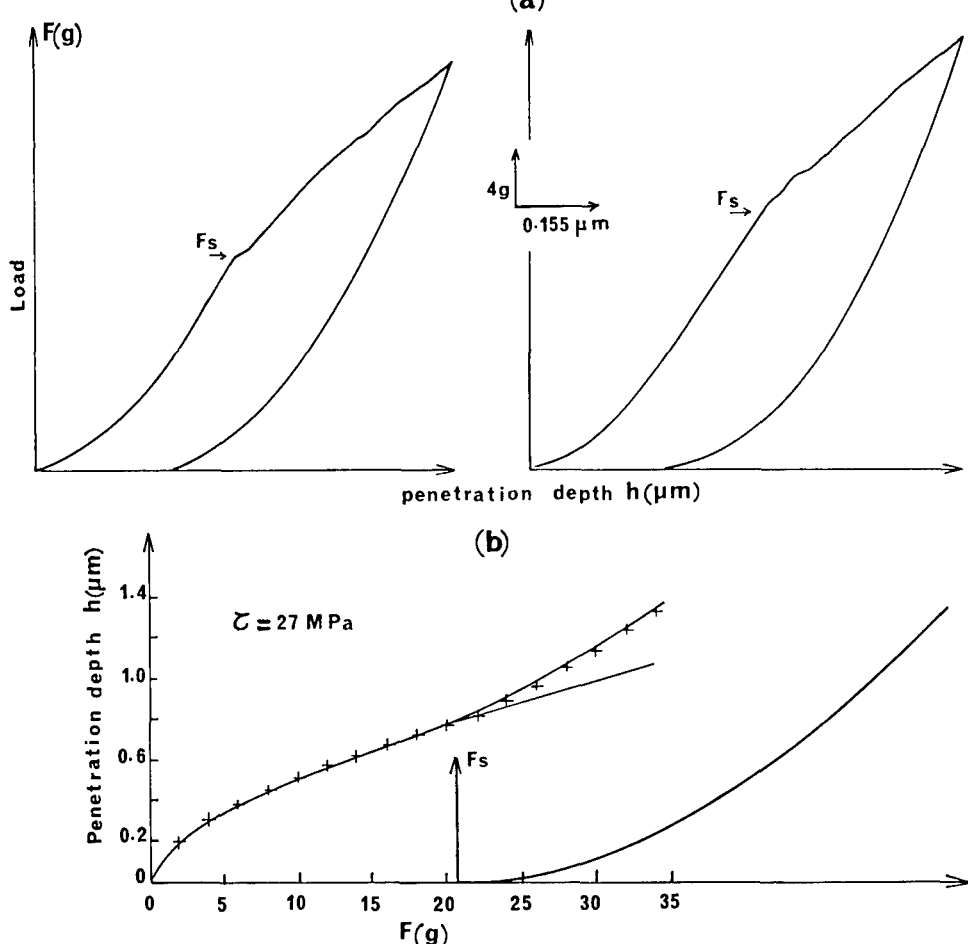


Fig. 6. (a) Typical indentation plots of applied load (F) against penetration depth (h) for various SiC fibers embedded in a silica rich-mullite glass-ceramic matrix. The steps (arrows) correspond to the debonding and the onset of the sliding regime. (b) Example of the calculation of the interfacial shear stress (τ). Crosses: experimental data from the indentation plots. Lines: calculations. The results are interpreted using a Meyer law ($h = \alpha F^\beta$) which describes the fiber hardness before the threshold load (F_s) plus the Marshall model in the sliding regime, after the threshold:

$$F > F_s : h = \alpha F^\beta + \frac{(F - F_s)^2}{4\pi^2 r^3 E \tau}$$

(E : fiber Young's modulus, r : fiber radius).



Fig. 7. SEM photomicrographs (secondary electron mode) showing SiC Nicalon® indented fibers (left); see the white contour due to the fiber debonding and the remaining step (right).

becomes visible at the fiber periphery (Fig. 7) due to the step formation: part of the fiber push-down is permanent.

Comparison of the thermal expansion coefficient measured parallel or perpendicularly to the woven fabrics gives further information about the composite. The parallel value corresponds to that imposed by the SiC fibers whereas the perpendicular value is the mean of the thermal expansion of the matrix and that of the SiC fibers. Thermal expansion coefficients are given in Table 3. A rather good agreement is obtained. No significant discrepancies are observed for zirconia-free and zirconia reinforced matrix. On the other hand, a slight shrinkage is observed above 900°C, perpendicularly, which could indicate some softening of the glassy mullite-like second phase.

Fiber/matrix interface

Figure 8 compares the line scan profiles across SiC fibers in two composites prepared using the TBB+3SiAl interface precursor with or without the addition of the ZP+TEOG interface precursors.

In both cases, we observe that some aluminium ions replace silicon ions at the fiber periphery (penetration depth $\sim 3 \mu\text{m}$ after 45 min sintering at 1350°C). Germanium is present in the fiber periphery.

Typical transmission electron microscopy thin film micrographs are shown in Fig. 9. Four interphases are found in the interfacial region. The SiC fiber (phase no. 1) is identified by its typical electron diffraction pattern which exhibits the 111, 220 and 311 rings of the cubic βSiC structure. EDX spectra show a 5% atomic aluminum concentration. This result confirms the 'macroscopic' electron microprobe analysis of Fig. 8. The fiber crust near the interface is enriched in oxygen and depleted in silicon and carbon. Moreover, we notice in Fig. 8 that the oxygen peak of the macroscopic line scan is more intense at the fiber periphery corresponding to the Si depleted region. This indicates a superficial oxidation of the fiber. At a very fine scale the transmission electron microscope image shows an external (phase no. 2), amorphous layer of several tens of nanometers

Table 3. Mean thermal expansion coefficients (α) of 4 dir SiC fiber^a-mullite matrix composites

Sintering ^b temperature	Open porosity (%)	$\alpha_{25-800^\circ\text{C}} (10^{-6}\text{C}^{-1})$		$\alpha_{25-1000^\circ\text{C}} (10^{-6}\text{C}^{-1})$	
		//	\perp	//	\perp
1300 ^c	12	3.7	3.2	3.7	2.6
1350 ^d	13.5	3.5	3.1	3.4	2.3
1300 ^e (30 h in air at 1200°C)	3	4	— ^f	3.8	— ^f

^aNicalon NLM202®, the fibers are woven along four directions in a plane.

^bDwell-time: 30 min.

^cMatrix $6\text{Al}_2\text{O}_3\cdot4\text{SiO}_2\cdot\text{ZrO}_2$, interface precursor: 1TBB+3SiAl (see Table 1 for definition).

^dMatrix $3\text{Al}_2\text{O}_3\cdot2\text{SiO}_2\cdot0.1\text{B}_2\text{O}_3$, interface precursor: 1TBB+3SiAl.

^eMatrix $6\text{Al}_2\text{O}_3\cdot4\text{SiO}_2\cdot\text{ZrO}_2$, 1TBB+3SiAl and ZP+TEOG interface precursors are simultaneously used.

^fNot measured.

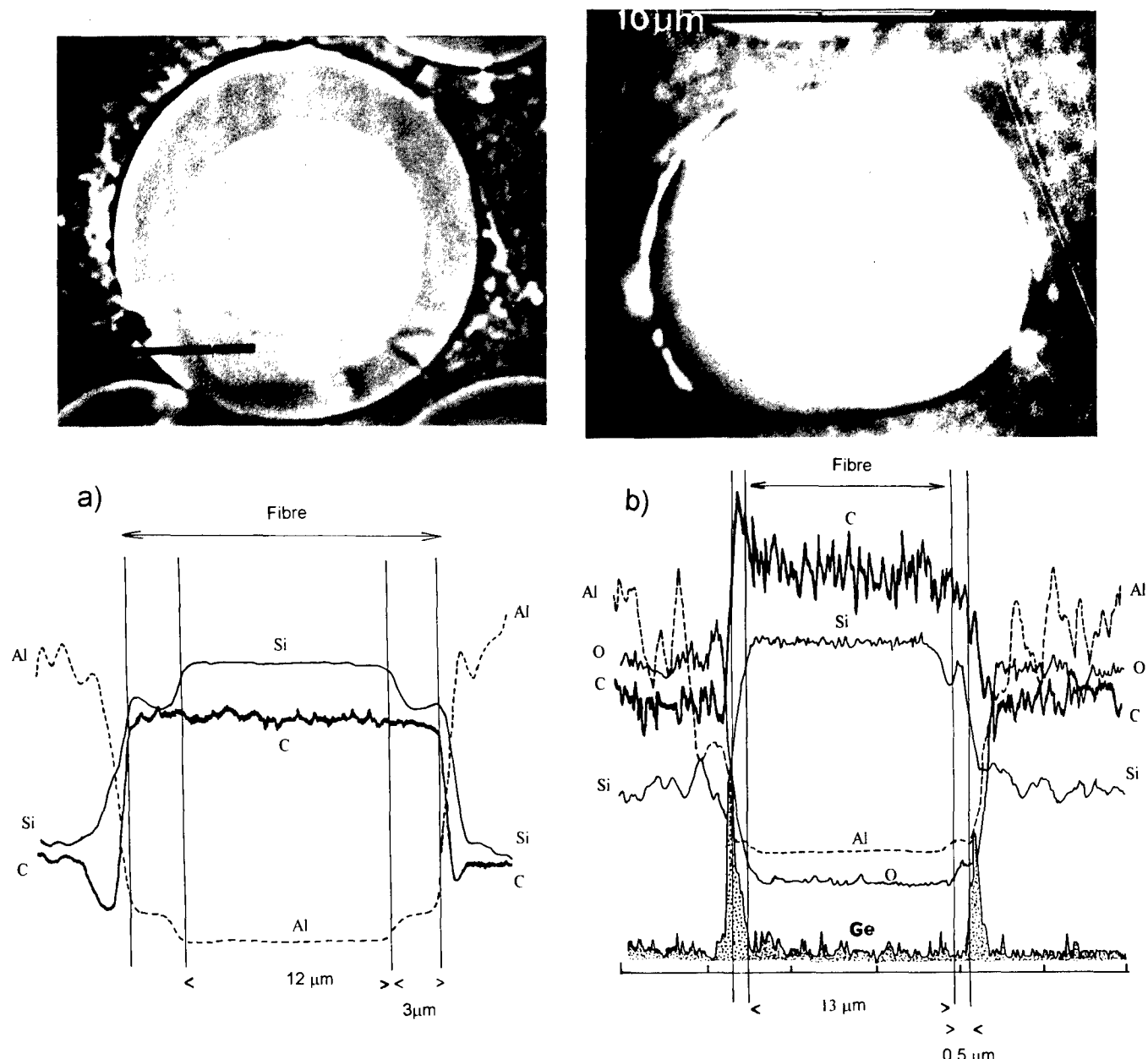


Fig. 8. SEM photomicrographs and X-ray line scan profiles recorded with a CAMEBAX electron microprobe across SiC Nicalon® fiber sections of composites prepared using the TBB+3SiAl interface precursor without (a) or with (b) addition of the ZP+TEOG interface precursor. Al, Si, C, O, Zr and Ge profiles are measured (sintering temperature: (a) 1350°C; (b) 1300°C).

thickness. This oxide phase contains about 10 at% Al and 90% Si, respectively. Only carbon traces are detected by EDX and electron diffraction and this zone did not display the 'white' layer and the corresponding rings of graphitic carbon as observed in many other composites.^{4,19-21} The interface precursor leads to small acicular $3\text{Al}_2\text{O}_3\cdot\text{SiO}_2$ mullite crystals (phase no. 3) dispersed in a glassy phase (phase no. 4). The composition of this last phase is 60 mol% SiO_2 , 40 mol% Al_2O_3 with a relatively intense carbon signal (the size of the analyzed area is about $10 \times 10 \text{ nm}^2$). The origin of the relatively high carbon content of this phase can be found in the organic traces arising from the pyrolysis of the interface precursor. Incompletely hydrolyzed branches often remain in the *in situ* gelated interface precursor. The interfaces appear to be free of a carbon

film. However, these observations do not exclude the presence of a few atomic carbon planes around the SiC fibers, as observed at the interface of SiC whiskers.²² The carbon film, if such a film is present, is thinner than that usually observed in composites made with alkali or earth-alkali-containing matrices.¹⁹⁻²¹ Furthermore, TEM examination of the fiber/matrix interface of a composite annealed for a few hours in air at 1470°C (Fig. 9(b)) shows that the main changes are: (i) the growth of the mullite crystals; (ii) the punctuation of the SiC fiber rings which indicates the onset of the crystallization.

Fiber/matrix sliding properties

The high strength and toughness of glass-ceramic matrix composites result directly from the low

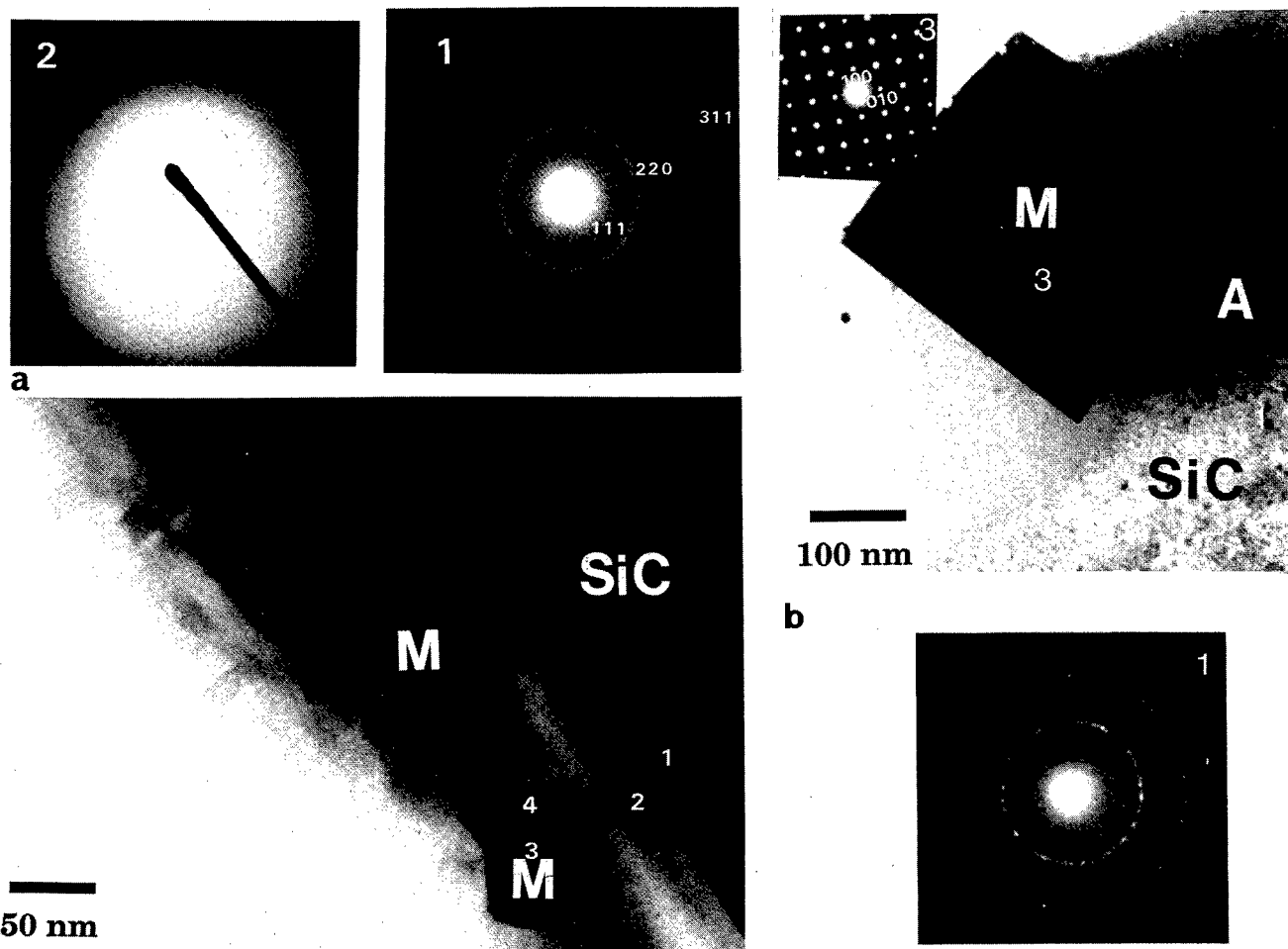


Fig. 9. TEM image of a SiC Nicalon® NLM202 fiber woven fabric-embedded in $(3\text{Al}_2\text{O}_3 \cdot 2\text{SiO}_2 \cdot 0.1\text{B}_2\text{O}_3)$ mullite matrix composite elaborated using the TBB+3SiAl interface precursor and pressure sintered at 1350°C. (a) Interfacial regions are: (1) fiber; (2) external region; (3) mullite crystal; (4) amorphous aluminosilicate phase. (b) After annealing for 3 h at 1470°C, in air.

fiber/matrix bonding originates in the processing. Usually, a reaction between SiC Nicalon fibers and an alkali- or earth-alkali-containing matrix leads to the formation of a thin carbon-rich interfacial layer (~ 100 nm) referred to as the carbon interphase.¹⁹⁻²¹ This interphase acts as a 'fuse', deflecting the matrix microcracks parallel to the fiber axis and thus avoiding the early failure of the fibers. This interphase is formed *in situ* during the hot-pressing as a result of the fiber/matrix chemical reaction or results from the deposit of a thin coating of C or BN when non-reactive matrices are used.²³

Another important parameter controlling the fiber/matrix bonding is the sign and the level of the residual mechanical stresses in the composite after processing arising from the thermal coefficient expansion mismatch. Too high a radial compressive residual stress increases the fiber/matrix bonding and is usually detrimental.

The sliding strength is usually measured on 1D composites using instrumented or non-instrumented micro-hardness tester following the method of Marshall.²⁴⁻²⁶ The fiber to be tested is selected

with regard to its axial position (circular section) and to have a uniform arrangement of distances from neighbouring fibers. Its diameter is measured after indentation. If the indent is not centered or if there is the least sign of fiber splitting, the measurement is rejected. Examples of applied load indentor/tip displacement are given in Fig. 6. Three regions are clearly distinguished on the load (F)-depth (h) plots:

- the first polynomial regime $h = \alpha F^\beta$ related to the fiber indentation and its elastoplastic deformation under the sharp indenter (see above, Loubet's model, $F < F_s$),
- a region characterized by a lower rate of load increase, a few steps often being observed at the limit between the elastoplastic response of the fiber and the debonding-plus-sliding regime ($F \sim F_s$),
- a third region can be observed when the pyramidal diamond tip comes into contact with the matrix ($F > F_s$).

The interfacial frictional stress (τ) related to sliding may be measured in 2D material if the fiber curvature is larger than the debonding length

induced by fiber sliding. The very large yarn curvature in 4-direction woven fabrics (curvature radius > a few tens of centimetres whereas debonding length ranges between 50 and 500 μm , typically e.g. see Fig. 3) makes possible experiments and calculations.

The calculation of the interfacial stress (or sliding strength) τ is made using Marshall's uniaxial model. The elastoplastic contribution of the fiber before the sliding threshold (F_s : threshold load) is assumed to follow a Meyer law:¹⁵

$$h = \alpha F^\beta \quad (\forall F \leq F_s)$$

h : penetration depth, F : applied load

In the sliding regime $\forall F > F_s$:

$$h = \alpha F^\beta + \frac{(F - F_s)^2}{4\pi^2 r^3 E \tau} \quad (1)$$

E : Young's modulus, r : radius of the fiber, respectively.

A more accurate model has been proposed:¹⁵

$$h = \alpha F^\beta + \frac{F^2 - F_s^2}{4\pi^2 r^3 E \tau} \quad (2)$$

This last model gives a τ -value 2–3 times larger than that calculated from model 1. In fact, it is very difficult to determine the true interfacial frictional stress and to compare the τ values calculated by different authors. Only comparative studies using the same model—and the same apparatus—are significant. The main results are summarized in Table 4 and typical curves are shown in Fig. 6. Comparison of the experimental data with the calculation (model no. 1) shows a rather good agreement. A similar agreement is obtained using model no. 2. A criterion for choosing between model no. 1 and model no. 2 is the height of the residual step after indentation.¹⁵ However, the measurement is difficult and the thermally induced stress should also be taken into consideration.²⁶ Our τ values may be considered as comparative data. The τ value is rather constant whatever the sintering temperature (1350–1450°C temperature range). On the other hand, the threshold load

is lowered when zirconia reinforced mullite is used as matrix. Comparison with experiments (using the same model and instrument) on SiC/LAS (or MLAS) matrix composites shows that our F_s values remain large ($\tau_{\text{LAS}} \sim 3\text{--}8 \text{ MPa}$). The fibers can be initially debonded in the LAS (MLAS) matrix ($F_2 \leq 2 \text{ g}$).¹⁵ A large increase in the τ value is observed after annealing in air. This is consistent with the decrease in the area of the strain–stress plot (Fig. 4) and with the TEM examination: the fiber/matrix boundary is well-defined in the 1350°C sintered sample whereas a corrugated front is observed in the sample annealed for 3 h at 1470°C (Fig. 9). Benoit *et al.*²⁷ have demonstrated that the interface sliding behaviour is controlled by the difference between the roughness induced misfit and the thermally induced gap. The lack of a visible C film in our SiC-mullite composites could explain why our τ values remain 4–5 times larger than those measured on composites exhibiting a well-defined carbon-rich interface (e.g. SiC/LAS matrix composite). This also explains why the thermally induced degradation is slower in SiC/mullite composites than for example in SiC/LAS composites.

Thermal degradation of the matrix and fiber/matrix interphase

TEM investigation and microindentation analysis have demonstrated that the fibre–matrix interface changes after thermal annealing. Transformations are also seen in the matrix. Figure 10 shows micro-Raman spectra recorded in different places for a germanium containing composite annealed for 30 h at 1200°C in air. This annealing being performed on a very small sliced rod, it represents a brutal thermal ageing. After annealing, we observe that zircon (ZrSiO_4) replaces the (tetragonal and monoclinic) zirconia precipitates in the matrix. The complete disappearance of tetragonal zirconia indicates that the smaller grains have been first transformed into zircon, even though the heating temperature is lower than the usual limit for the reaction mullite + zirconia \rightarrow zircon + alumina ($> 1300^\circ\text{C}$). The germanium phase exhibiting the strong 300 cm^{-1} Raman peak remains present (white

Table 4. Interfacial shear stress (τ) and threshold load (F_s) of SiC fiber/mullite matrix composites^a

Matrix	Sintering temperature	F_s (g)	τ_1^c (MPa)	τ_2^c (MPa)
$3\text{Al}_2\text{O}_3\cdot2\text{SiO}_2\cdot0.1\text{B}_2\text{O}_3$	1350°C	15–25	20 ± 5	~ 50
$6\text{Al}_2\text{O}_3\cdot4\text{SiO}_2\cdot\text{ZrO}_2$	1350°C +2 h at 900°C in air	10–18	22 ± 5	~ 50
	1450°C		≥ 80	≥ 200
		15–25	24 ± 7^b	~ 50

^aAt least 12 fibers are studied.

^bMany fibers are crushed under indentation

^c τ_1 : model of eqn (1); τ_2 model of eqn (2).

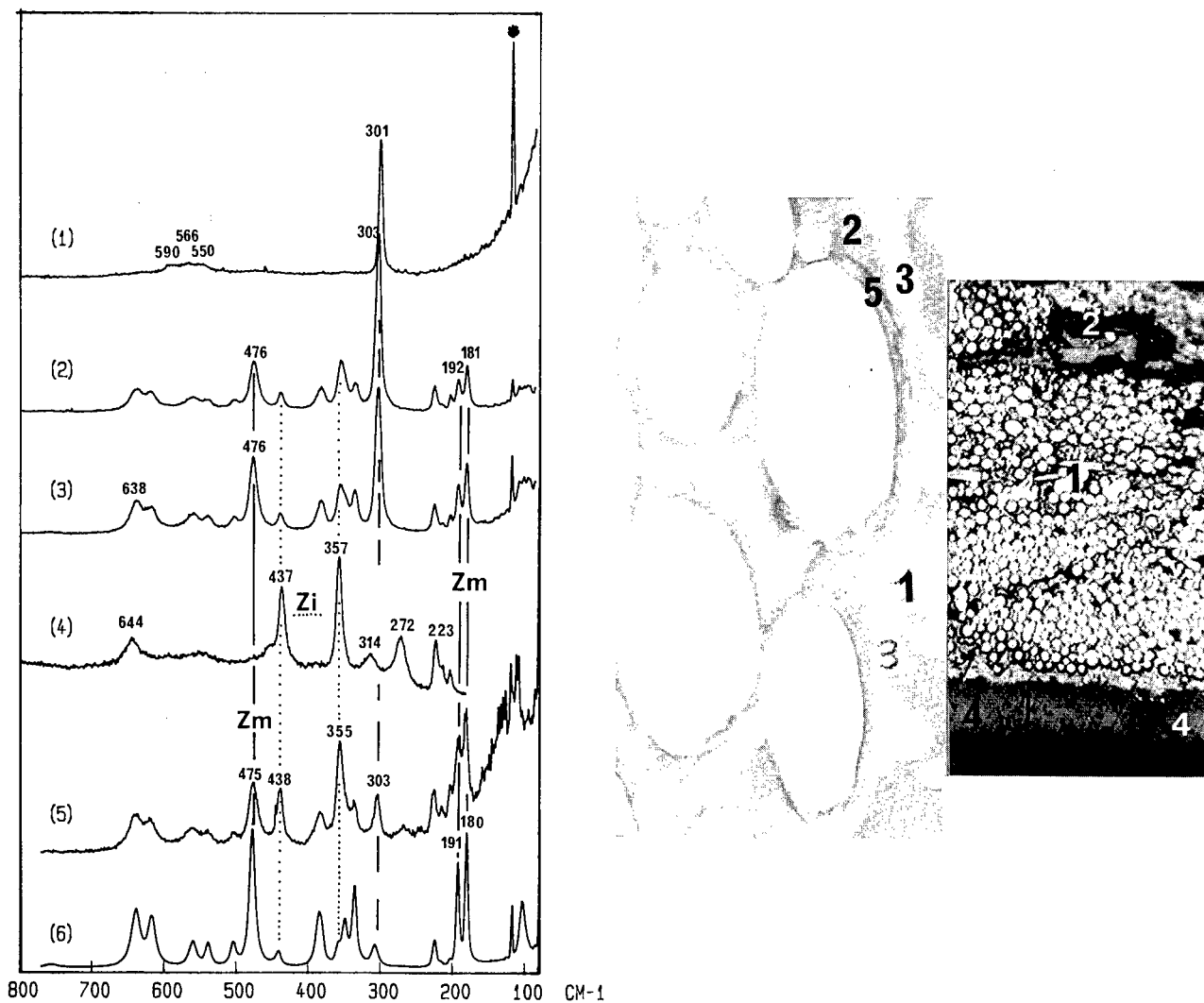


Fig. 10. Optical photomicrographs showing the reaction contour at the SiC fiber periphery in composite prepared using the ZP+TEOG interface precursor and annealed for 30 h at 1200°C in air. The corresponding micro-Raman spectra are given: (1) Ge rich 'white' precipitate; (2) black region (main phases: Ge+Zm+Zi); (3) grey region (Zm+Zi+Ge); (4) matrix surface (Zi); (5) region around the fiber. Zm: monoclinic zirconia, Zi: zircon; (6) comparison is made with Raman spectra recorded before annealing or after annealing below 800°C (star: laser line).

grains). The interphase at the fiber contour is made of monoclinic zirconia and of zircon. This zircon crust can be formed by reaction with silicon evolving from the fiber as observed in many composites.⁴

Conclusions

From the results which have been presented and discussed the following conclusions can be drawn:

(i) Almost fully dense woven fabric mullite matrix composites have been prepared by a prepreg sol-gel route using tailored interface precursors compatible with SiC Nicalon NLM202® and/or mullite Nextel 440® fibers. Low porosity SiC-mullite composites are obtained with the help of transient liquid sintering aids (first a B₂O₃ rich phase and then a Ge/GeO₂ containing phase). The porosity of oxide fiber/mullite

composites remains high and further work must be done to improve their densification.

- (ii) In the as-processed composite the matrix composition changes gradually from the intersheet region to the fiber environment due to the use of two kinds of precursors, the interface and the matrix precursors. This accommodates the thermal expansion coefficient mismatch. Multilevel reinforcement is achieved (fibers, particulates).
- (iii) Good (bending) mechanical properties are obtained for SiC/mullite composites (~300 MPa at RT and at 900°C). The high linear limit (180 MPa) is maintained after 30 h annealing in air. However, a gradual transformation of the zirconia precipitates into zircon is observed. The mechanical properties of mullite-mullite composites show the potential interest of such materials in air if the porosity can be lowered.

(iv) The SiC Nicalon NLM202® fiber/silica-rich mullite interphase appears to be free of a carbon film. This behaviour is consistent with the rather good preservation of sliding behaviour at the fiber/matrix interface after air annealing. On the other hand the interfacial shear stress is 3–4 times larger than that measured when the usual carbon interface is present (e.g. SiC/LAS composite). These carbon-film-free SiC-mullite composites as well as the mullite–mullite composites are promising materials for structural applications at medium temperature in an oxygenizing atmosphere.

Acknowledgements

Dr D. Michel is kindly acknowledged for his help for the TEM examination. Dr M. Parlier is acknowledged for fruitful discussions.

References

1. Colomban, Ph., *Ceramics Int.*, **15** (1989) 23–50.
2. Klein, L. C., *Sol–Gel Technology*, Noyes Publication, New Jersey, 1988.
3. Colomban, Ph. & Mazerolles, L., *J. Mater. Sci.*, **26** (1991) 3503–10.
4. Bruneton, E., Michel, D. & Colomban, Ph., *J. de Physique IV*, **C7** (1993) 1937–40.
5. Guney, V., Jones, F. R., James, P. F. & Bailey, J. E., *Int. Phys. Conf. Ser. III*, IOP Publishing Ltd, 1990, pp. 217–26; Chen, M., Jones, F. R., James, P. F. & Bailey, J. E., *ibid.* 227–37.
6. Qui, D. & Pantano, C. G., *3rd Int. Conf. Ultrastructure Processing of Ceramics, Glasses and Composites*, eds J. D. Mackenzie & D. R. Ulrich, 1987, pp. 635–44.
7. Colomban, Ph. & Mouchon, E., *High Temperature Ceramic Matrix Composites*, Proc. HT-CMC1, 20–24 Sept. 1993, Bordeaux, eds R. Naslain, J. Lamon & D. Doumeingts, Woodhead Publ. Ltd, Abington, Cambridge, 1993, pp. 159–66.
8. Colomban, Ph. & Vendage, V., *J. Non-Crystalline Solids*, **147/148** (1992) 245–50.
9. Colomban, Ph., Menet, M., Mouchon, E., Courtemanche, C. & Parlier, M., French patent 2672283 (1991), European patent 92400235.5, US patent 07/8303510.
10. Prewo, K. M., *Ceram. Bull.*, **68** (1989) 395–401; Lipowitz, J., *ibid.* **70** (1991) 1888–92.
11. Colomban, Ph., *Ceramics Today–Tomorrows Ceramics*, ed. P. Vencenzini, Elsevier, Amsterdam, 1991, pp. 599–605.
12. Colomban, Ph. & Mouchon, E., *Solid State Ionics*, **73** (1994) 209–20.
13. Colomban, Ph., *J. Mater. Sci.*, **24** (1989) 3011–20.
14. Low, I. M. & MacPherson, R., *J. Mater. Sci.*, **24** (1989) 926–35.
15. Lagrange, J. L., Passilly, B., Parlier, M. & Colomban, Ph., *Proc. JNC-8 (8èmes Journées Nationales sur les Composites)*, 16–18 Nov. 1992, Palaiseau, France, eds O. Allix, J. P. Favre & P. Ladevèze, AMAC, Paris, 1992, pp. 241–52.
16. Parlier, M., Grenier, T., Renevey, S., Passilly, B., Mouchon, E., Bruneton, E. & Colomban, Ph., *Proc. 4th Int. Symp. on Ceramic Materials and Components for Engines*, 10–12 Jun. 1992, eds R. Göteborg, Carlsson, T. Johansson & L. Kahlmann, Elsevier Appl. Sci. Ltd, UK, 1992, pp. 440–8.
17. Loubet, J. L., Georges, J. M., Marchesini, O. & Meille, G., *J. Tribology*, **106** (1984) 43–8; Loubet, J. L., Georges, J. M. & Meille, G., *Microindentation Techniques in Materials Science and Engineering*, eds J. P. Blau & B. R. Lawn, ASTM STP 889, Philadelphia, 1980, pp. 72–89.
18. Ashcroft, I. A., Lawrence, C. W., Weihs, T. P. & Derby, B., *J. Am. Ceram. Soc.*, **75** (1992) 1284–6.
19. Cooper, R. F. & Chyung, K., *J. Mater. Sci.*, **22** (1987) 3148–60.
20. Brennan, J. J., *Fiber-reinforced Ceramic Composites, Materials, Processing and Technology*, ed. K. S. Mazdiyasi, 1990, pp. 223–59; Colomban, Ph. & Mouchon, E., *High Temperature Ceramic Matrix Composites*, Proc. HT-CMC1, 20–24 Sept. 1993, Bordeaux, eds R. Naslain, J. Lamon & D. Doumeingts, Woodhead Publ. Ltd, Abington, Cambridge, 1993, pp. 269–83.
21. Bleay, S., Scott, V. D., Harris, B., Cooke, R. G. & Habis, F. A., *J. Mater. Sci.*, **27** (1992) 2811–22.
22. Lin, F., Moriels, T., Morrone, A. & Nutt, S., *Mat. Res. Symp. Proc.*, **120** (1988) 323.
23. Naslain, R., *JNC-8 (8èmes Journées Nationales sur les Composites)*, 16–18 Nov. 1992, Palaiseau, France, eds O. Allix, J. P. Favre & P. Ladevèze, AMAC, Paris, 1992, pp. 199–212.
24. Marshall, D. B., *J. Am. Ceram. Soc.*, **67** (1984) C259–60.
25. Marshall, D. B. & Evans, A. G., *J. Am. Ceram. Soc.*, **68** (1985) 225–31.
26. Sudre, O., Passilly, B. & Parlier, M., *Proc. 17th Ann. Conf. Composites and Adv. Ceramics*, Cocoa Beach, FL, 10–15 Jan. 1993, *Ceram. Eng. Sci. Proc.*, (1994), July–August, 1994, pp. 180–7.
27. Benoit, M., Brenet, P. & Rouby, D., *High Temperature Ceramic Matrix Composites*, Proc. HT-CMC1, 20–24 Sept. 1993, Bordeaux, eds R. Naslain, J. Lamon & D. Doumeingts, Woodhead Publ. Ltd, Abington, Cambridge, 1993, pp. 329–36.

Processing and Mechanical Properties of Laminated Composites of Mullite/Woven Fabrics of Si-Ti-C-O Fibers

Yoshihiro Hirata,^a Manabu Matsuda,^a Kumiko Takeshima,^a Ryoko Yamashita,^a Masaki Shibuya,^b Martin Schmücker^c & Hartmut Schneider^c

^aDepartment of Applied Chemistry and Chemical Engineering, Faculty of Engineering, Kagoshima University, 1-21-40 Korimoto, Kagoshima 890, Japan

^bTyranno Fiber Development Project, Ube Industries, Ltd, 1978-10 Kogushi, Ube 755, Japan

^cGerman Aerospace Research Establishment, (DLR), Institute for Materials Research, D-51140 Köln, Germany

(Accepted 22 July 1995)

Abstract

A sol-gel-processed mullite powder and Si-Ti-C-O fiber woven fabrics were formed into laminated composites by filtration or doctor blade method using aqueous mullite suspensions containing polyacrylic ammonium (PAA) and methyl cellulose (MC) at pH 8.5. The laminate green composites with 6 and 10 vol% fabrics were hot-pressed to near full density at 1500–1650°C for 1 h under a pressure of 39 MPa in a N_2 atmosphere. However, the composites with 20 and 30 vol% fabrics resulted in delaminated porous ones after hot-pressing due to the exfoliation of filament yarn in woven fabrics. A linear relation of stress-displacement in fracture behavior of monolithic mullite changed to a non-linear relation in the composites with 10–30 vol% of Si-Ti-C-O fabrics and hot-pressed at 1650°C. Addition of Si-Ti-C-O fabrics decreased the four point flexural strength of monolithic mullite (328 MPa) to 292 MPa at 6 vol%, 271 MPa at 10 vol% and 59–78 MPa at 20–30 vol% of fabrics whereas the fracture toughness by the single edge precracked beam (SEPB) method increased from 1.6 MPa $m^{0.5}$ for the monolithic mullite to 4.7 MPa $m^{0.5}$ for the composites with 10 vol% of Si-Ti-C-O fabrics. Enhancement of the mechanical properties can be interpreted by the partial decomposition of Si-Ti-C-O fibers during hot-pressing at 1500–1650°C, which caused the diffusion of C and Ti elements of fibers to the interfaces between the fibers and mullite matrix. The diffusion of Al from mullite matrix into fibers was also observed. The change of composition, microstructure and strength at the interfaces would increase debonding or pull-out effect of fibers.

1 Introduction

Mullite ($3Al_2O_3 \cdot 2SiO_2$) is a candidate oxide for high temperature structural applications because of a high melting point, a low thermal expansion coefficient, good thermal shock fracture resistance, a low true density and high creep resistance. For increase of mechanical reliability of mullite ceramics with a low fracture toughness (1–2 MPa $m^{0.5}$), some papers reported the increase of fracture toughness by addition of SiC whiskers, long carbon or Si-Ti-C-O fibers to mullite matrix.^{1–5} Especially, the long fiber-reinforced mullite matrix composites are attractive materials because this type of composites show usually high fracture toughness and non-linear fracture behaviour of stress-displacement curves, along with remarkably high fracture energy. A typical mullite composite reinforced by 35 vol% of uniaxial carbon fiber showed significantly high strength above 800 MPa and high fracture toughness reaching 29 MPa $m^{0.5}$ at 1200°C.³ The most important factor in the processing of fiber-reinforced composites would be the control of strength of interface between fiber and matrix. An adequate interface strength that is not too strong or too weak can lead to the excellent mechanical properties of composite materials.^{6–8} The objective of this research was to study the processing, mechanical properties, and microstructure of the laminated mullite/woven fabric composites with high fracture toughness and high strength. In this study, mullite green sheets formed by doctor blade of aqueous mullite suspensions and woven fabrics of Si-Ti-C-O long fibers were laminated to sinter by hot-pressing at 1500–1650°C. The Si-Ti-C-O long fibers show

high tensile strength (3.2 GPa), high oxidation resistance, and good wettability to oxide ceramics.⁹

2 Experimental Procedure

2.1 Starting materials and colloidal processing

A sol-gel-processed mullite powder (Fig. 1(a)) was mixed with aqueous solutions to form thick green sheets or to pour into the spaces separated with the woven fabrics of Si-Ti-C-O fibers. The mullite powder used was supplied from Chichibu Cement Co., Ltd, Japan. It has the following properties: particle size distribution: 0.1–1.5 µm, specific surface area: 3.2 m²/g (equivalent diameter of spherical particle: 0.59 µm), chemical composition: 71.80 mass% Al₂O₃, 28.05 mass% SiO₂, 0.10 mass% TiO₂, and 0.01 mass% Na₂O. The Si-Ti-C-O woven fabrics of 270 µm thick (Ube Industries, Ltd, Yamaguchi, Japan), were made of long fibers with an average diameter of 8.5 µm (Fig. 1(b)), and a chemical composition of 50.4 mass% Si, 29.7 mass% C, 17.9 mass% O, and 2.0 mass% Ti. The surface characteristics of the mullite and crushed Si-Ti-C-O fibers in dilute aqueous suspensions (0.02 mass%) were studied by measuring the electrophoretic mobility. The pH of each suspension was adjusted using 0.01N HCl and 0.01N NH₄OH solutions. Electrosterically stabilized mullite suspensions of 40 vol% solid at pH 8.5 were prepared by adding 0.75 mass% of polyacrylic ammonium (PAA, (HCOONH₄CH₂)_n, average molecular weight: 10000) and 2.0 mass% of methyl cellulose (MC) against the weight of mullite to give flexibility and strength for handling of thick films formed.

The suspensions were stirred for 24 h and ultrasonic vibration at 20 kHz was applied for an additional 5 min to disperse particle agglomerates. Air bubbles in the suspensions were eliminated in a bell jar connected to a vacuum pump. These suspensions were formed into thick films by doctor blade of a blade clearance of 500 µm at a transfer rate of 15 cm/min of polyethylene carrier tape (DP-100, Tsugawa Seiki Seisakusho, Tokyo, Japan). In the preparation of composite with 6 vol% fabrics, the mullite suspensions of 52 vol% solid containing 0.75 mass% of PAA at pH 8.5–8.8 were poured into the rectangular spaces separated at 2.7 mm intervals of four Si-Ti-C-O fabric sheets (thickness, 270 µm, 38 mm long and 25 mm wide) which were set on a gypsum mold.

2.2 Hot-pressing and measurement of mechanical properties

Before hot-pressing in a N₂ atmosphere, a set of 5–7 layers of a mullite sheet (thickness, 200–250 µm) and one layer of Si-Ti-C-O fabric sheet, (thickness, 270 µm, 38 mm long and 25 mm wide) were alternately laminated to 10–12 mm in thickness. The green laminated composites of 6–30 vol% Si-Ti-C-O fabrics were pressed with a carbon die under a pressure of 39 MPa at room temperature and heated to 1500 or 1650°C at the rate of 10°C/min, and sintered for 1 h in a N₂ atmosphere (FVH-5 type, Fuji Denpa Kogyo Co., Osaka, Japan). The densities of hot-pressed composites were measured in distilled water by the Archimedes method. A hot-pressed sample was cut into five test specimens 38 mm long, 3–4 mm wide and 4–7.5 mm thick, parallel to the hot-pressing direction.

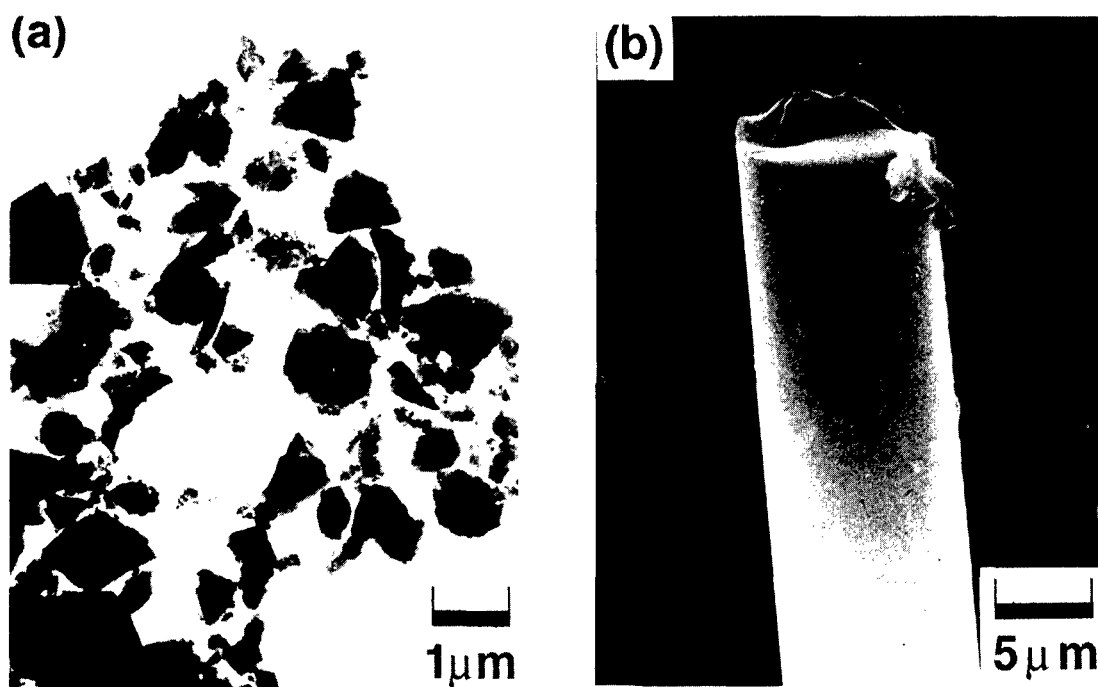


Fig. 1. Photographs of: (a) sol-gel-processed mullite powder and (b) Si-Ti-C-O long fiber.

The flexural strength of test specimens parallel to the hot-pressing direction was measured at room temperature by the four-point flexural method over spans of 30 mm (lower span) and 10 mm (upper span) at a crosshead speed of 0.5 mm/min. The test specimens were prepared by grinding with a No. 400 diamond wheel and finished with No. 2000 abrasive paper. The average strength was calculated from the data for 3–4 specimens. The fracture toughness was evaluated by single edge precracked beam (SEPB) method. The strengths of the flexural specimens, precracked by a Vickers indenter (model MVF-K, Akashi Seisakusho Co., Tokyo, Japan) of 98 N to induce microcracks, were measured by three-point loading over a span of 30 mm at a crosshead speed of 0.5 mm/min, and then calculated to fracture toughness.¹⁰ Data for 3–4 test specimens were used to calculate the average fracture toughness. Microstructures of the composites were observed by scanning electron microscopy with energy dispersive X-ray spectroscopy (EDX: S-5000 Type, Hitachi Co., Tokyo, Japan) and analytical transmission electron microscopy (TEM: EM430, Philips Co., Eindhoven, Netherlands).

3 Results and Discussion

3.1 Forming of laminated composites

As shown in Fig. 2, the isoelectric points for the suspensions of the mullite particles and crushed Si-Ti-C-O fibers were pH 4.9 and 3.5, respectively. The electrophoretic mobility of both of the negatively charged powders reached the maximum values of $-4 - 5 \mu\text{m s}^{-1} \text{V}^{-1} \text{cm}$ in the pH range of 8–10. The above result suggests that: (1) the mullite particles are to be dispersed due to the strong electric repulsion at high pH and (2) strong repulsive interaction is also formed between the negatively charged mullite particles and Si-Ti-C-O fibers at

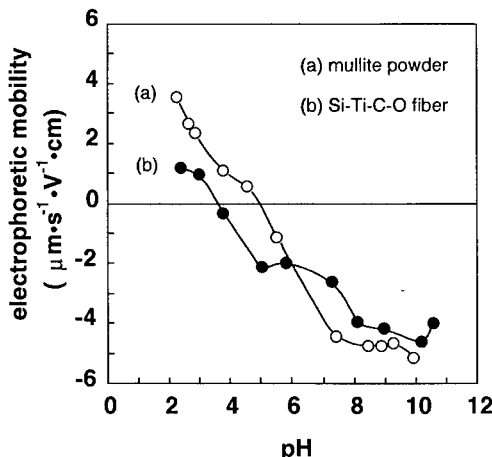


Fig. 2. Electrophoretic mobility of: (a) mullite particles and (b) Si-Ti-C-O fibers in aqueous suspensions.

high pH. Thus, the mullite suspensions in this experiment were adjusted at pH 8.5 to enhance the dispersion state of mullite powder. In the doctor blade method, 2.0 mass% of MC and 0.75 mass% of PAA against the weight of mullite were added to the suspensions to give an apparent viscosity of 45.1 Pa s at a shear rate of 3.83 s⁻¹. For the preparation of laminated composites with 6 vol% fabrics by filtration of the mullite suspension in the space separated with Si-Ti-C-O fabrics, 0.75 mass% of PAA was added to the concentrated mullite suspensions of 52 vol% solid at pH 8.5–8.8.⁵ This electrosterically stabilized mullite suspensions behaved as a Newtonian flow and the viscosity was 122 mPa s. The green compacts obtained from this suspension was 63% of the theoretical density (TD).¹¹

3.2 Hot-pressing and mechanical properties of laminated composites

The monolithic mullite and mullite/Si-Ti-C-O fiber fabric (6 and 10 vol%) composites were densified to near full densities (99.7–99.9% TD) at 1500 to 1650°C for 1 h by hot-pressing under a pressure of 39 MPa. However, the composites with 20 and 30 vol% fabrics resulted in delaminated porous bodies and the filament yarns in the woven fabrics exfoliated. The density of the composites with 30 vol% fabrics was 64% TD. Since the Si-Ti-C-O fabrics introduce a high porosity, the increase of fabrics content may cause the insufficient packing of mullite particles in the open spaces of fabrics. The above phenomenon indicates a limit of fiber loading in this type of laminated composites.

Figure 3 shows the stress–displacement curves

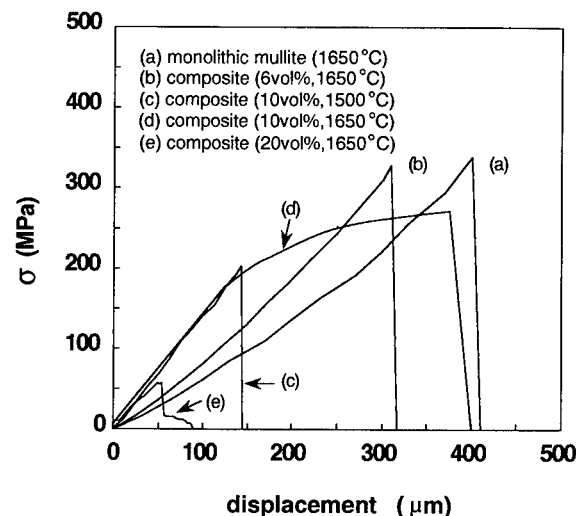


Fig. 3. Stress–displacement curves at room temperature for: (a) monolithic mullite hot-pressed at 1650°C; (b) mullite/Si-Ti-C-O fabrics composites with 6 vol% fabrics hot-pressed at 1650°C; (c) composites with 10 vol% fabrics hot-pressed at 1500°C; (d) composites with 10 vol% fabrics hot-pressed at 1650°C and (e) composites with 20 vol% fabrics hot-pressed at 1650°C.

for monolithic mullite and mullite/Si-Ti-C-O fabric composites. The fracture behavior of composites was affected by two factors, i.e. hot-pressing temperature and Si-Ti-C-O fabrics content. The stress-displacement curve of the composites with 10 vol% fabrics hot-pressed at 1500°C was similar to that of mullite hot-pressed at 1650°C. This result suggests that the inserted fabrics behaved like a part of mullite matrix and they fractured in the clear absence of pseudoplastic behavior. Increase in the hot-pressing temperature of the composites with 10 vol% fabrics to 1650°C caused a non-linear fracture behavior with a high fracture energy as seen in Fig. 3(d). This effect of hot-pressing temperature may be corresponding to decrease in strength of interface between the mullite matrix and Si-Ti-C-O fabrics. Increase in the Si-Ti-C-O fabric content from 6 to 10 vol% in the composites hot-pressed at 1650°C was effective to achieve the non-linear fracture behavior and to increase fracture energy as shown in Fig. 3. On the other hand, the delaminated porous composites with 20–30 vol% fabrics showed a non-linear fracture behavior with a low fracture strength. It is also noted that the composites with 10 vol% fabrics hot-pressed at 1650°C and precracked by a Vickers indenter of 98 N showed a clear non-linear fracture behavior as shown in Fig. 4, indicating a high damage tolerance. However, the precracked composite with 6 vol% fabrics fractured with a linear relation of stress-displacement.

Figure 5 summarizes the mechanical properties of mullite/Si-Ti-C-O fabric composites hot-pressed at 1650°C. Increase of the Si-Ti-C-O fabric content caused a slight decrease of flexural strength up to 10 vol% fabrics but gave a drastic decrease at 20 and 30 vol% fabrics. The fracture toughness that was calculated at the highest stress

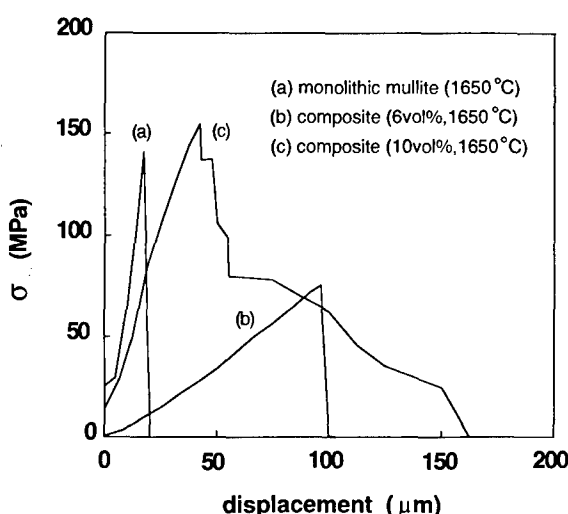


Fig. 4. Stress-displacement curves for: (a) monolithic mullite; (b) composites with 6 vol% fabrics and (c) composites with 10 vol% fabrics, precracked by a Vickers indenter of 98 N.

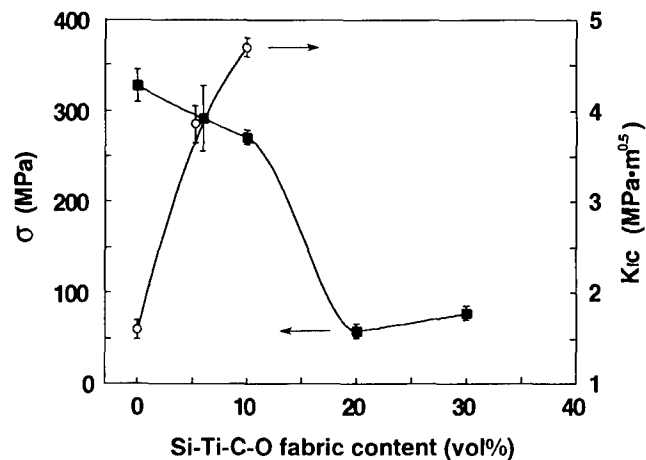


Fig. 5. Dependence of flexural strength and fracture toughness on Si-Ti-C-O fabric content for composites hot-pressed at 1650°C.

of samples with precracks in SEPB method, increased from $1.6 \text{ MPa m}^{0.5}$ for monolithic mullite to $4.7 \text{ MPa m}^{0.5}$ for the composite with 10 vol% fabrics. That is, it was possible to increase fracture toughness of the laminated composites significantly with a comparable strength to monolithic mullite.

Figures 6 and 7 show the SEM photographs

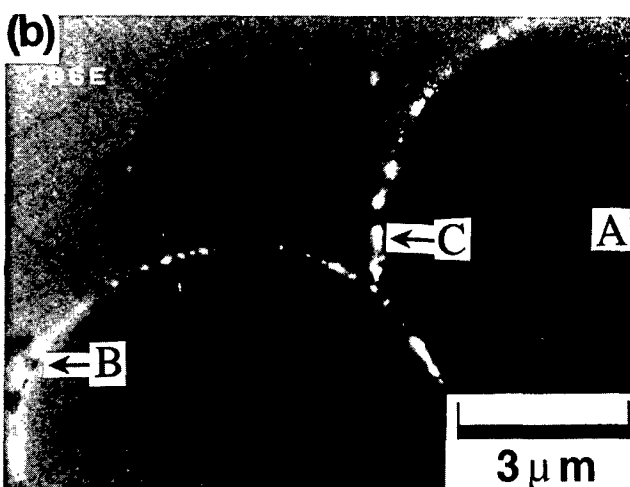
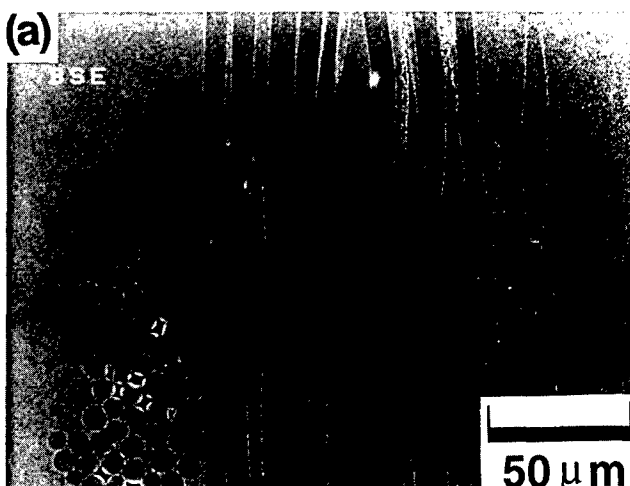


Fig. 6. SEM photographs of composites with 10 vol% fabrics hot-pressed at 1650°C.

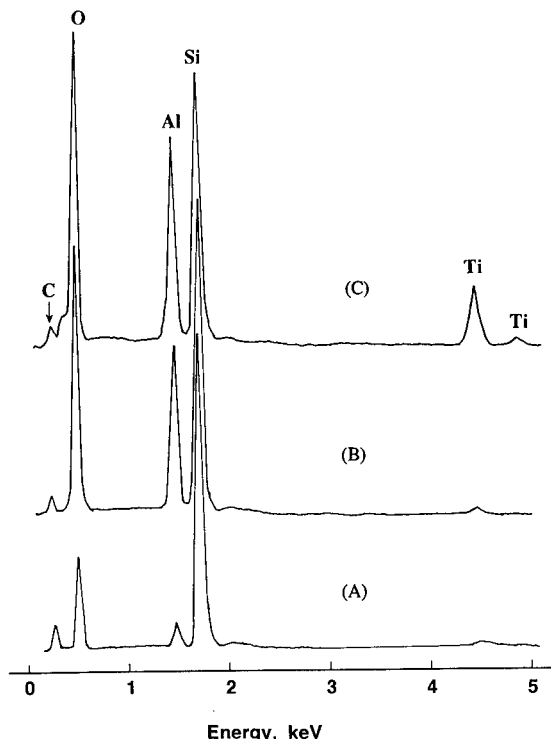


Fig. 7. EDX analysis of Si-Ti-C-O fiber (point A) and interface (points B and C).

and corresponding EDX spectra of the composites with 10 vol% fabrics hot-pressed at 1650°C. Pore-free microstructure was observed in the mullite matrix of the composites. A few pores remained in the spaces surrounded by the Si-Ti-C-O fibers (Fig. 6(a)). The interface between the mullite matrix and Si-Ti-C-O fibers contained a light colored precipitate (Fig. 6(b)). The EDX analysis for Si-Ti-C-O fibers and the interface indicates that: (1) the inside of Si-Ti-C-O fibers contained the elements of Si, C, O and Al; (2) the chemical composition of the interface without precipitate was more enriched in Al and O than that of the center of Si-Ti-C-O fiber and (3) the light color precipitate in the interface contained a relatively high concentration of Ti in addition to the elements of Si, Al, O and C. The above results suggest that Ti in fibers diffused into interfaces and Al in mullite diffused into fibers during hot-pressing. Similar EDX spectra were measured in the composites with 10 vol% fabrics hot-pressed at 1500°C but the interfaces were enriched in C than the inside of fibers. These results can be explained by the thermal decomposition of Si-Ti-C-O fibers in the mullite matrix above 1500°C.¹² In the observation of the interfaces of the mullite/Si-Ti-C-O fabric (6 vol%) composites hot-pressed at 1650°C by transmission electron microscopy (Fig. 8), the following phenomena were shown: (1) formation of thin graphite layer (30–50 nm) at interface and (2) formation of fine SiC particles (<50 nm) in the Si-Ti-C-O fiber. The basal planes of graphite

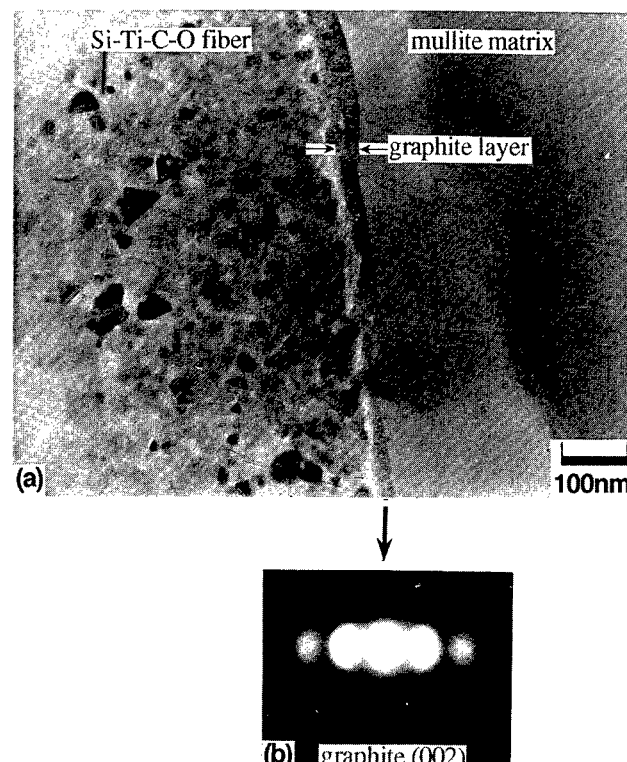


Fig. 8. TEM photograph (a) and selected area electron diffraction pattern (b) at the interface between Si-Ti-C-O fiber and mullite matrix of composites hot-pressed at 1650°C.

were parallel to the interface. The observation of graphite layer was also reported by Sato *et al.*⁴ in the interfaces of the composites of mullite/choiced Si-Ti-C-O fiber hot-pressed at 1650°C. In respect to the thermal stability of Si-Ti-C-O fiber, Yamamura *et al.*^{13,14} reported that: (1) the oxygen content of Si-Ti-C-O fibers hot-pressed in Ar atmosphere decreases above 1500°C and reaches below 1 mass% at 1800–2100°C and (2) the atomic ratio of C/(Si + Ti) decreases from 1.5 to 1.0. Decomposition of Si-Ti-C-O fiber to form SiC–TiC fiber, therefore, releases excess carbon at the interfaces of the composites above 1500°C. The graphite layer formed would reduce the interface strength and enhance the debonding or pull-out effect of Si-Ti-C-O fibers. The precipitate enriched with Ti and the compositional gradient of Al element at the interfaces may also contribute to the improvement of mechanical properties.

Figure 9 shows a transmission electron micrograph of the mullite grains in the composites hot-pressed at 1650°C. The mullite matrix consisted of granular-shaped grains of 0.8–1.1 μm in size. Since the granular shape of mullite grains is correlated to little existence of glassy phase in the grain boundaries,^{15,16} it may be expected to show high possibility of mechanical strength at high temperatures.



Fig. 9. TEM photograph showing granular-shaped mullite grains in the matrix of composites hot-pressed at 1650°C.

4 Conclusions

Laminated green compacts of mullite/Si-Ti-C-O fiber fabrics (6–30 vol%) were formed by the doctor blade method or filtration of aqueous mullite suspensions (40–52 vol% solid) containing 0.75 mass% of polyacrylic ammonium and 2.0 mass% of methyl cellulose against the weight of mullite at pH 8.5. These green compacts with 6–10 vol% fabrics were densified to nearly full density (>99% of theoretical density) by hot-pressing under a pressure of 39 MPa in a N₂ atmosphere at 1500–1650°C. Increase of the fabric content to 20 or 30 vol%, however, resulted in a delaminated porous composite. The fracture toughness of monolithic mullite hot-pressed at 1650°C (1.6 MPa m^{0.5}) was enhanced to 4.7 MPa m^{0.5} in the composites with 10 vol% Si-Ti-C-O fabrics which showed a non-linear fracture behavior at room temperature. The strength of monolithic mullite (328 MPa) at room temperature decreased slightly with addition of Si-Ti-C-O fabrics to 292 MPa at 6 vol% and to 271 MPa at 10 vol% of fabrics. The composites with 20–30 vol% fabrics showed a non-linear fracture behavior but their strengths were significantly lower (59–78 MPa) compared to the strength of monolithic mullite. The improvement of mechanical properties in the mullite/Si-Ti-C-O fabric composites was interpreted by the thermal decomposition of Si-Ti-C-O fibers

above 1500°C, which caused the diffusion of C and Ti from the fibers to the interfaces between Si-Ti-C-O fibers and mullite matrix of granular-shaped grains (~1 μm). The diffusion of Al from mullite matrix to fiber was also observed. These change of composition, microstructure, and strength of the interface would enhance the debonding or pull-out effect of Si-Ti-C-O fibers in the composites.

References

1. Kumazawa, T., Ohta, S., Tabata, H. & Kanzaki, S., Mechanical properties of mullite-SiC whisker composites. *J. Ceram. Soc. Japan*, **97**(9) (1989) 895–902.
2. Becker, P. F. & Tiegs, T. N., Toughening behavior involving multiple mechanisms: whisker reinforcement and zirconia toughening. *J. Am. Ceram. Soc.*, **70**(9) (1987) 651–4.
3. Somiya, S. & Hirata, Y., Mullite powder technology and application in Japan. *Am. Ceram. Soc. Bull.*, **70**(10) (1991) 1624–32.
4. Sato, M., Shibuya, M., Ohtsubo H., Hiratsuka, T., Harada, Y. & Yamamura, T., Properties of ceramic matrix composite using chopped Si-Ti-C-O fibers. In *Proceedings of 2nd International SAMPE Symposium*, 1991, pp. 844–51.
5. Hirata, Y. & Takeshima, K., Colloidal processing for preparation of laminated composites of mullite/woven fabrics of Si-Ti-C-O fibers. *Mater. Lett.*, **17**(6) (1993) 374–8.
6. Prouhet, S., Camus, G., Labrugere, C., Guette, A. & Martin, E., Mechanical characterization of Si-C(O) fiber/Si(CVI) matrix composites with a BN interphase. *J. Am. Ceram. Soc.*, **77**(3) (1994) 649–56.
7. Bender, B. A. & Jessen, T. L., Comparison of the interfaces development and ultimate strength between nicalon and Tyranno silicon carbide-fiber-reinforced zirconia titanate matrix composites. *Ceram. Eng. Sci. Proc.*, **14**(7–8) (1993) 931–8.
8. Jessen, T. L., Powers, J. & Bender, B. A., The effect of fiber arrangement on the mechanical properties of an unidirectional CFCC. *Ceram. Eng. Sci. Proc.*, **14**(7–8) (1993) 991–7.
9. Mah, T., Mendiratta, M. G., Katz, A. P. & Mazdiyasi, K. S., Recent development in fiber-reinforced high temperature ceramic composites. *Am. Ceram. Soc. Bull.*, **66**(2) (1987) 304–8.
10. Japanese Industrial Standard, JIS R 1607-1990. Testing methods for fracture toughness of high performance ceramics.
11. Hirata, Y. & Takeshima, K., Effect of particle classification on colloidal processing of mullite. *Mater. Lett.*, **16**(4) (1993) 169–74.
12. Yamamura, T., Ishikawa, T., Shibuya, M., Tamura, M., Nagasawa, T. & Okamura, K., A new type of ceramic matrix composite using Si-Ti-C-O fiber. *Ceram. Eng. Sci. Proc.*, **10**(7–8) (1989) 736–47.
13. Jero, P. D., Parthasarathy, T. A., Kerans, R. J., A comparison of single and multi-fiber pushout techniques. *Ceram. Eng. Sci. Proc.*, **14**(7–8) (1993) 147–55.
14. Wereszczak, A. A., Feber, M. K. & Lowden, R. A., Development of an interfacial test system for the determination of interfacial properties in fiber reinforced ceramic composites. *Ceram. Eng. Sci. Proc.*, **14**(7–8) (1993) 156–67.
15. Pask, J. A., Zhag, X. W., Tomsia, A. P. & Yoldas, B. E., Effect of sol-gel mixing on mullite microstructure and phase equilibria in the α -Al₂O₃-SiO₂ system. *J. Am. Ceram. Soc.*, **70**(10) (1987) 704–7.
16. Ismail, M. G. M. U., Nakai, Z. & Soma, S., Microstructure and mechanical properties of mullite prepared by the sol-gel method. *J. Am. Ceram. Soc.*, **70**(1) (1987) C-7–8.

SEND FOR A FREE SAMPLE COPY OF...

COMPOSITES PART B: ENGINEERING

An International Journal

Former title: *Composites Engineering*

Editor-in-Chief: David Hui, *Department of Mechanical Engineering, University of New Orleans, USA*

AIMS AND SCOPE

The aim of *Composites Part B: Engineering* is to provide a balance between mechanics and materials science aspects, basic and applied research, and high technology and high volume (low cost) composite development.

The Journal aims to provide a forum for the prompt publication of original research on all areas of composites, with emphasis being placed on evaluation and modelling of engineering details and concepts. Basic research papers are welcomed, but authors are encouraged to discuss the issues relative to application in the short or long-term in various areas, such as aerospace, automotive and other surface transportation, infrastructure, shipbuilding, off-shore piping, and recreational products.

Current topics of interest to readers include durability, functionally gradient materials, interfaces, interlaminar fracture, joints and adhesion, smart composites, textile composites, thermoplastics, wave propagation, and non-destructive testing.

Audience: Materials Scientists, Aeronautical, Structural & Mechanical Engineers, Stress Analysts.

ABSTRACTED/INDEXED IN:
Adhesive Abstracts, Current Contents/Engineering, Computing and Technology, INSPEC, MSCI, Rapra Abstracts, Research Alert, SciSearch, Science Citation Index.

1996: Volume 27B (6 issues)
Associated Personal price:
£67.00 (US\$107.00)
Subscription price:
£500.00 (US\$795.00)
ISSN 1359-8368 (00984)

Forthcoming contents services now available.....



For more details;
contentsdirect@elsevier.co.uk



ELSEVIER

An imprint of Elsevier Science

Please send me a FREE SAMPLE COPY of:
 Please enter my FREE ContentsDirect subscription to:
Composites Part B: Engineering (00984)

Name _____ Position _____

Organization _____ Department _____

Address _____

Post/Zip Code _____

E-Mail/Internet No. _____

Return to: Elsevier Science Ltd, The Boulevard, Langford lane, Kidlington, Oxford OX5 1GB, UK

Telephone: +44 (0) 1865 843479/843781 Fax: +44 (0) 1865 843952

or Elsevier Science Inc., 660 White Plains Road, Tarrytown, NY 10591-5153, USA

Telephone: +1-914-524-9200 Fax: +1-914-333-2444

E-mail: freesamples@elsevier.co.uk (quoting journal title and your full name and postal address).

For even faster service use e-mail, fax or telephone number

SEND FOR A FREE SAMPLE COPY OF...

CANADIAN METALLURGICAL QUARTERLY

Published by the Metallurgical Society of the Canadian Institute of Mining and Metallurgy

Editor-in-Chief:

H. Henein, *Department of Mining, Metallurgical and Petroleum Engineering, 606 Chemical-Mineral Engineering Building, University of Alberta, Edmonton, Alberta T6G 2G6, Canada*

AIMS AND SCOPE

Devoted to the science, practice and technology of metallurgy, this journal provides a forum for the discussion and presentation of both basic and applied research developments in the areas of metallurgy and materials. Research papers are published on topics such as mineral processing, extractive metallurgy, alloy development and metal working. Critical reviews of current research activities in extractive and physical metallurgy of Canadian interest are also encouraged.

Audience: Metallurgists, Mineralogists, Materials Scientists.

ABSTRACTED/INDEXED
IN: *Chemical Abstracts Service, Current Contents, Engng Ind Monthly Author Index, Materials Science Citation Index, Metal Abstr, World Alum Abstr.*

1996: Volume 35 (5 issues)
Subscription price:
£334.00 (US\$530.00)
ISSN 0008-4433 (00345)
PERGAMON: Oxford

Forthcoming contents services now available.....



For more details;
contentsdirect@elsevier.co.uk



PERGAMON

An imprint of Elsevier Science

Please send me a FREE SAMPLE COPY of:
 Please enter my FREE ContentsDirect subscription to:
Canadian Metallurgical Quarterly (00345)

Name _____ Position _____

Organization _____ Department _____

Address _____

Post/Zip Code _____

E-Mail/Internet No. _____

Return to: Elsevier Science Ltd, The Boulevard, Langford Lane, Kidlington, Oxford OX5 1GB, UK

Telephone: +44 (0) 1865 843479/843781 Fax: +44 (0) 1865 843952

or: Elsevier Science Inc., 660 White Plains Road, Tarrytown, NY 10591-5153, USA

Telephone: +1-914-524-9200 Fax: +1-914-333-2444

E-mail: freesamples@elsevier.co.uk (quoting journal title and your full name and postal address).

For even faster service use e-mail, fax or telephone number

JOURNAL OF THE EUROPEAN CERAMIC SOCIETY

NOTES FOR AUTHORS

The Journal will publish the results of original research relating to the structure, properties and processing of ceramic materials. Papers of either an experimental or theoretical character will be welcomed on a fully international basis. Papers may cover any of the branches of ceramic science and may relate to any of the so-called categories, structural, functional and traditional ceramics. The central objective will be to sustain a high standard with rigorous reviewing procedures.

Submission of papers

Submission of a manuscript implies that it is not being considered for publication elsewhere. Submission of a multi-authored manuscript implies the consent of all the participating authors. All papers should be written in English. Upon acceptance of an article by the journal the author(s) will be asked to transfer the copyright of the article to the publisher. This transfer will ensure the widest possible dissemination of information.

Contributors should submit their papers to Professor R. J. Brook, either at the University of Oxford, Department of Materials, Parks Road, Oxford OX1 3PH, UK, tel. (44) 1865 273781 or (44) 1865 273697; fax. (44) 1865 273783, or at the Max Planck Institute for Metals Research, Heisenbergstrasse 5, 7000 Stuttgart 80, Germany, tel. (49) 711-6861-202; fax. (49) 711-6861-131. Contributors in the Americas may send their papers to the North American Co-ordinator, Dr R. N. Katz, Department of Mechanical Engineering, Worcester Polytechnic Institute, 100 Institute Road, Worcester, Massachusetts 01609-2280, USA, and those in Asia to the Japanese Co-ordinator, Professor S. Sōmiya, Nishi Tokyo University, 3-7-19 Seijo, Setagaya, Tokyo 157, Japan.

All papers will be independently refereed.

Types of contributions

Original papers, short communications and review articles.

Manuscript preparation

Three copies should be provided, in **double-spaced typing** on pages of uniform size, with a wide margin at the left. Generally, the size of the manuscript should be a minimum consistent with clarity. Each paper should be provided with an Abstract of about 100-150 words, reporting concisely on the purpose and results of the paper.

Authors should consult an issue of the journal for style and layout if possible. The Editor reserves the right to adjust style to certain standards of uniformity.

The title of the paper should unambiguously reflect its contents. Where the title exceeds 70 characters a suggestion for an abbreviated running title should be given.

The name(s) and address(es) should follow the title. Where an author has moved permanently or temporarily to a new address, this should be indicated as a footnote on the first page. All joint communications must indicate the author to whom correspondence should be addressed if this is not the first-mentioned author.

The SI system should be used for all scientific and laboratory data; if, in certain instances, it is necessary to quote other units, these should be added in parentheses. Temperatures should be given in degrees Celsius. The unit 'billion' (10⁹ in America, 10¹² in Europe) is ambiguous and should not be used.

Abbreviations for units should follow the suggestions of the British Standards publication BS 1991. The full stop should not be included in abbreviations, e.g. m (not m.), ppm (not p.p.m.), '%' and '°' should be used in preference to 'per cent' and 'per'. Where abbreviations are likely to cause ambiguity or not be readily understood by an international readership, units should be put in full.

Tables (numbered consecutively with arabic numerals), references and legends to illustrations should be typed on separate sheets and placed at the end of the paper.

Footnotes should be avoided especially if they contain information which could equally well be included in the text.

The use of proprietary names should be avoided. Papers essentially of an advertising nature will not be accepted.

Disks

For papers produced using a word-processor or *T_EX*, please submit a disk with the **final revised version** of the manuscript. The file on disk should correspond exactly to the hard copy. The operating system and the word-processor used should be specified clearly.

Illustrations or chemical structures in electronic format may be supplied provided that the file format and the program used to produce them is clearly indicated and that a hard copy is also supplied.

More detailed guidelines and further information are available from the publisher.

References

References should be cited at the appropriate point in the text by a superscript numeral. A list of references, in numerical order, should appear at the end of the paper. All references in this list should be indicated at some point in the text and vice versa. Unpublished data or private communications should not appear in the list. Examples of layout of references are given below.

1. Lee, J. G. & Cutler, I. B., Sinterable sialon powder by reaction of clay with carbon and nitrogen. *Am. Ceram. Soc. Bull.*, **58** (1979) 869-71.
2. Paris, R. A. & Grollier-Baron, T., Procédé de préparation de sialons, produits obtenus et articles fabriqués de ces produits. European Patent 23869, 2 Nov. 1981.
3. Siddiqi, S. A., Higgins, I. & Hendry, A., Production of β -sialon by carbothermal reaction of clay. In *Proceedings of the International Conference Non-oxide Technical and Engineering Ceramics*, ed. S. Hampshire. Elsevier Applied Science, London, 1986, pp. 119-20.
4. Briggs, D. & Seah, M. P., *Practical Surface Analysis by Auger and X-ray Photoelectron Spectroscopy*. John Wiley and Sons, New York, 1984, pp. 15-17.
5. Marra, R. A., Homogeneous nucleation and growth of silicon powder from laser heated gas phase reactions. PhD thesis, Massachusetts Institute of Technology, Cambridge, MA, 1983.

Illustrations

The *original* and two copies, which may be of a reduced size, of each illustration should be provided. Line drawings may be submitted in any medium providing that the image is black and very sharp. They should preferably all require the same degree of reduction; large diagrams, more than four times final size, are discouraged due to handling difficulties. The type area of the journal is 177 mm wide \times 240 mm deep, in two columns per page, each 85 mm wide, and lettering should therefore be large enough to be legible after reduction of the illustration to fit (ideally 7pt lettering after reduction). Photographs should be submitted as contrasting black-and-white prints on glossy paper. Each illustration must be clearly numbered and the name(s) of the author(s) of the paper written on the reverse side.

Proofs

The author (or the selected author where several are involved) will receive a set of proofs for checking. No new material may be inserted in the text at the time of proof reading unless accepted by the Editor.

Page charges and offprints

There will be no page charges. Twenty-five offprints of each paper will be supplied free of charge. Additional copies can be ordered at current printing prices.

Published for the EUROPEAN CERAMIC SOCIETY

by

ELSEVIER SCIENCE LIMITED

The Boulevard, Langford Lane, Kidlington, Oxford, UK, OX5 1GB

JOURNAL OF THE EUROPEAN CERAMIC SOCIETY



0955-2219(1996)16:2;1-S

(Abstracted/Indexed in: *Applied Mechanics Reviews*; *ASM International/Materials Information*; *Ceramics Abstracts*; *Current Contents/Engineering, Computing and Technology*; *Current Contents/Physical, Chemical and Earth Sciences*; *Fluid Engineering Abstracts (BHRA)*; *FLUIDEX*; *INSPEC*; *Materials Science Citation Index*; *Science Citation Index*)

CONTENTS

Volume 16 Number 2 1996

Special Issue: Mullite '94

For Contents see p. iii

ECRS

ELSEVIER

02036